

ADAM MICKIEWICZ UNIVERSITY

FACULTY OF PHYSICS

**Determination of charge transfer dynamics
and efficiency in solar cells sensitized with
carbazole, indoline and triphenylamine dyes**

PhD Thesis

by

M.Sc. Eng. Adam Glinka



Supervised by:

Prof. dr hab. Marcin Ziólek

Dr Mateusz Gierszewski

Poznań 2021

Acknowledgements

First of all I would like to thank my PhD thesis supervisor Prof dr hab. Marcin Ziółek, for his always encouraging and supporting attitude which made my work in his group not only developing and challenging but also enjoyable and rewarding.

Dr Mateusz Gierszewski for all his help and commitment, especially on the beginning of my PhD studies.

Prof Marina Freitag for giving me the opportunity to work in her lab and learn so much during my internship in Uppsala.

All the co-authors of the papers constituting this work, whose work and knowledge made it actually possible.

Next, I would like to thank all the colleagues from Quantum Electronics Laboratory and the Faculty of Physics, thanks to whom being a PhD student at the Faculty was something more than just learning and working.

I would also like to thank my former supervisor dr inż. Adam Buczek Prof. PP who started introducing me into experimental physics almost ten years ago.

I must mention “The Congress of Physicists” and say thanks for a good reason to meet and study (or not) since we were in high school.

I would like to express my gratitude to my parents and the whole family for believing in my abilities since I remember, and being curious about my work, even though I had no idea how to explain it.

Last but not least I need to thank Marta for supporting me in every possible way and being the bright side of my life.

I kindly acknowledge the financial support from the Polish National Science Centre under project 2015/18/E/ST4/00196.

Table of Contents

Abstract	4
Streszczenie	6
List of Published Articles Constituting the Thesis	8
1. Introduction	9
1.1 The Energy Demand	9
1.2 Solar Energy	9
1.3 Photovoltaics	10
2. Dye Sensitized Solar Cells	12
2.1 Principles of Operation	13
2.1.1 Charge Separation	13
2.1.2 Power Conversion Efficiency	14
2.1.3 The Limitations of Photovoltaic Performance	15
2.2 DSSC Components and Architecture	17
2.2.1 Semiconductor Layer	18
2.2.2 Dyes	19
2.2.3 Electrolytes	21
2.2.4 Counter Electrodes	23
2.2.5 Semiconductor/Dye/Electrolyte Interface Modifications	23
2.3 Strategies of Enhancing DSSC Efficiency	24
3. The Aims of the Thesis	26
4. Methods	28
4.1 DSSC Manufacturing Procedure	28
4.1.1 Glass Cleaning Procedure	28
4.1.2 Photoanodes Fabrication	28
4.1.3 Counter Electrode Preparation	30
4.1.4 DSSC Assembly	31
4.2 Full DSSC and Components Characterization Techniques	32
4.2.1 Current-Voltage Characterization	32
4.2.2 Incident Photon to Current Efficiency Spectra	33
4.2.3 UV-VIS Absorption Spectroscopy	34
4.2.4 Electrochemical Impedance Spectroscopy	35
4.2.5 Transient Absorption Spectroscopy	37
5. Realization of the Aims of the Thesis	45
Paper I	45

Paper II.....	46
Paper III.....	47
Paper IV	48
Paper V.....	50
Paper VI	51
6. Conclusions.....	53
References.....	55
Full texts of published articles constituting the thesis	
Appendix	

Abstract

The main concern of this thesis is the dynamics of charge transfer processes occurring in Dye Sensitized Solar Cells (DSSC) comprising a top efficient carbazole, indoline and triphenylamine dyes. This dissertation is based on a series of papers reporting the effects of different modifications applied to improve DSSCs on ultrafast and fast charge transfer processes and relation between the dynamics of particular charge transfer phenomena and the overall DSSC performance.

One of the most important modifications studied in the context of charge transfer dynamics and solar cell efficiency was the substitution of the most commonly used carboxylic anchoring moiety by a stronger alkoxy-silyl group (in MK-2 carbazole dye, D149 and D205 indoline dyes). Next, different semiconductor/dye/electrolyte interface modifications were examined (molecular capping, atomic layer deposition of Al₂O₃ layers and dye moieties encapsulation by cucurbit[7]uril macrocyclic molecules). Furthermore, the influence of different electrolyte compositions was investigated, including the impact of varying the redox couple (I⁻/I₃⁻, Co^{2+/3+}(bpy)₃ (bpy = 2,2'-bipyridine), Co^{2+/3+}(phen)₃ (phen = 2,2'-phenanthroline), Cu⁺²⁺(tmby)₂ (tmby = 4,4',6,6'-tetramethyl-2,2'-bipyridine), the use of additional Lewis' base (4-*tert*-butylpyridine or 1-methylbenzimidazole) or a solvent (acetonitrile, water or their mixture). Moreover, the effects of different titania layer morphology - different porosity, thickness as well as contents of large scattering particles in mesoporous layer were studied. Another modification tested was the interface alteration by continuous irradiation of solar cells. Finally, the dynamics of charge transfer processes between the benchmark Y123 triphenylamine dye and titania photoanode was thoroughly studied.

In order to gain the information on the dynamics of charge transfer processes, their efficiency and relationship with the overall photovoltaic performance of studied devices, a broad range of experimental techniques was applied, including basic photovoltaic characterization methods (current-voltage characterization of illuminated cells, incident photon to current efficiency spectra measurements), electrochemical impedance spectroscopy, stationary absorption in the visible range and time-resolved optical spectroscopy methods: transient absorption in ns – ms time window in visible range

(nanosecond flash photolysis), and femtosecond transient absorption (in fs-ns time window) in visible, near and mid infrared spectral ranges.

The opening part of the dissertation (chapters 1 – 4) provides an introduction to the current state of knowledge on DSSC operation and a review of materials applied in DSSCs. Meanwhile, the main research problems along with strategies of their overcoming are outlined. Main experimental methods including fabrication and key characterization techniques used for purposes of this thesis are thoroughly described. The scientific papers making the basis of this thesis are described in chapter 5 and attached after chapter 6 presenting the conclusions. Finally, the appendix contains the detailed description of the contribution of the author of this dissertation to the papers, the declarations on the contribution of other co-authors (partially in Polish), a list of other scientific papers published by the author during his PhD studies, and a list of attended conferences.

Streszczenie

Niniejsza praca została poświęcona badaniom dynamiki procesów transferu ładunku zachodzących w ogniwach słonecznych sensybilizowanych barwnikiem (ang. Dye Sensitized Solar Cells – DSSC), zawierających wysoko wydajne barwniki karbazolowe, indolinowe i trifenylaminowe. W opublikowanych artykułach, wchodzących w skład cyklu stanowiącego przedmiot tej rozprawy, opisaliśmy, jak różnorodne modyfikacje, stosowane w celu poprawienia funkcjonowania ogniw, wpływają na ultraszybkie i szybkie procesy transferu ładunku oraz jak dynamika poszczególnych procesów związana jest z całościowym funkcjonowaniem ogniw.

Jedną z najbardziej istotnych modyfikacji, przebadanych w kontekście dynamiki transferu ładunku i wydajności ogniw, była zamiana najczęściej stosowanej karboksylowej grupy przyłączeniowej przez silniejszą grupę alkoksylilową w karbazolowym barwniku MK-2 oraz indolinowych barwnikach D149 i D205. Następnie, stosowane były różne modyfikacje na styku między powierzchnią półprzewodnika, warstwą barwnika i elektrolitem, takie jak molekularna pasywacja (ang. molecular capping), atomowa pasywacja poprzez depozycję warstwy Al_2O_3 czy enkapsulacja niektórych ugrupowań molekuł barwnika przez makrocykliczne cząsteczki cucurbit[7]urilu. W dalszej kolejności, zbadany został wpływ zmiany użytej pary redoks (I^-/I_3^- , $\text{Co}^{2+/3+}(\text{bpy})_3$ ($\text{bpy} = 2,2'$ -bipirydyna), $\text{Co}^{2+/3+}(\text{phen})_3$ ($\text{phen} = 2,2'$ -fenantrolina), $\text{Cu}^{+/2+}(\text{tmby})_2$. ($\text{tmby} = 4,4',6,6'$ -tetrametylo-2,2'-bipirydyna) w składzie elektrolitu oraz różnych stężeń zasad Lewis'a (4-*tert*-butylopirydyny lub 1-metylobenzoimidazolu). Wykorzystano również różne rozpuszczalniki (acetonitryl lub woda). Ponadto przeanalizowano wpływ zastosowania warstw tlenku tytanu o różnych morfologiach – różnej porowatości i grubości oraz zawierających duże (~ 400 nm) cząstki tlenku tytanu rozpraszające światło. Zbadano również zmiany wywołane przez ciągłe oświetlanie próbek. Wreszcie, zbadane zostały również ultraszybkie procesy transferu ładunku pomiędzy wzorcowym barwnikiem trifenylaminowym Y123 a nanocząstkami tlenku tytanu tworzącymi fotoanodę DSSC.

W celu uzyskania informacji o dynamice procesów transferu ładunku, ich wydajności oraz o powiązaniu tych cech z parametrami fotowoltaicznymi ogniw, wykorzystano szeroki zakres technik eksperymentalnych, obejmujący podstawową charakterystykę

prądowo napięciową oświetlanych ogniw, pomiary widm czynnościowych (ang. Incident Photon to Current Efficiency – IPCE), elektrochemiczną spektroskopię impedancyjną oraz różnorodne metody spektroskopii optycznej – absorpcję stacjonarną w zakresie widzialnym, oraz absorpcje przejściową w nanosekundowej rozdzielczości czasowej (w zakresie widzialnym) oraz w femtosekundowej rozdzielczości czasowej (w zakresie widzialnym oraz bliskiej i średniej podczerwieni).

Część wstępna (rozdziały 1 – 4) zawiera wprowadzenie opisujące stan wiedzy na temat funkcjonowania ogniw DSSC oraz przegląd materiałów stosowanych do ich wytwarzania. Zarysowano w niej również główne problemy oraz najważniejsze strategie ich rozwiązania. Praca zawiera również dokładne objaśnienie metodyki wytwarzania ogniw DSSC jak również opis najważniejszych technik wykorzystanych do ich badań. Publikacje naukowe, wchodzące w skład niniejszej pracy, podsumowane zostały w rozdziale piątym i zamieszczone za rozdziałem nr 6, gdzie podsumowano konkluzje pracy. Załącznik do pracy zawiera dokładny opis wkładu autora rozprawy (oraz pozostałych współautorów) w poszczególne prace naukowe, listę innych prac naukowych z udziałem autora rozprawy oraz listę konferencji, na których prezentował on wyniki badań.

List of Published Articles Constituting the Thesis

- 1 **Effects of Post-Assembly Molecular and Atomic Passivation of Sensitized Titania Surface: Dynamics of Electron Transfer Measured from Femtoseconds to Seconds.**
Gierszewski, M.; **Glinka, A.**; Gradzka, I.; Jancelewicz, M.; Ziółek, M.
ACS Appl. Mater. Interfaces **2017**, *9*, 17102–17114. IF=8.7, MNiSW points = 200
- 2 **Effects of Aqueous Electrolyte, Active Layer Thickness and Bias Irradiation on Charge Transfer Rates in Solar Cells Sensitized with Top Efficient Carbazole Dyes.**
Glinka, A.; Gierszewski, M.; Ziółek, M.
J. Phys. Chem. C **2018**, *122*, 8147–8158. IF=4.2, MNiSW points = 140
- 3 **Testing New Concepts in Solar Cells Sensitized with Indoline Dyes—Alkoxysilyl Anchoring Group, Molecular Capping, and Cobalt-Based Electrolyte.**
Gierszewski, M.; **Glinka, A.**; Grądzka, I.; Gierczyk, B.; Ziółek, M.
J. Phys. Chem. C **2018**, *122*, 25764–25775. IF=4.2, MNiSW points = 140
- 4 **Interface Modification and Exceptionally Fast Regeneration in Copper Mediated Solar Cells Sensitized with Indoline Dyes.**
Glinka, A.; Gierszewski, M.; Gierczyk, B.; Burdziński, G.; Michaels, H.; Freitag, M.; Ziółek, M.
J. Phys. Chem. C **2020**, *124*, 2895–2906. IF=4.2, MNiSW points = 140
- 5 **Impact of Improvements in Mesoporous Titania Layers on Ultrafast Electron Transfer Dynamics in Perovskite and Dye-Sensitized Solar Cells.**
Pydzińska-Białek, K.*; **Glinka, A.***; Drushliak, V.; Nowaczyk, G.; Florczak, P.; Ziółek, M.
Phys. Chem. Chem. Phys. **2020**, *22*, 21947–21960. IF=3.6, MNiSW points = 100
* authors contributed equally
- 6 **Complexity of Electron Injection Dynamics and Light Soaking Effects in Efficient Dyes for Modern DSSC**
Glinka, A.; Kubicki, J.; Ziółek, M.
Energies, **2021**, *14*, 407. IF=2.7, MNiSW points = 140

1. Introduction

1.1 The Energy Demand

Due to continuous rise of world human population, economic growth and technological development, the energy demand is inevitably increasing.¹ Satisfaction of these needs using fossil deposits, biomass or even nuclear fission does not ensure sustainability of global economy, since utilization of these resources proceeds much faster than their creation. Moreover, combustion of enormous amounts of fuels, affects the global climate in increasingly pronounced way.¹⁻⁴ In order to avoid severe consequences threatening humanity and its culture as well as the whole terrestrial environment, radical measures must be taken straight off. First of all a reduction in consumption of conventional energy sources and focus on renewable ones is necessary. In order to accelerate these changes, there is a need of development of efficient, cheap and environmentally friendly renewable energy sources.

1.2 Solar Energy

As a matter of fact, almost all of the energy sources available on earth originate from the power of the Sun which was converted to chemical energy by living organisms performing photosynthesis, or to thermal and consequently, partly to mechanical energy of biotope. Over 120 PJ of solar energy reaches the Earth every second. It is by orders of magnitude more than we could consume,¹ thus its direct utilization seems to be the most reasonable way to meet the energy demand.

Solar energy can be exploited in numerous ways, including the use of thermal collectors to heat up water (often applied in small household installations) or large scale solar furnaces converting sunlight to heat, used by conventional thermal power plants. However, a direct conversion to electricity by photovoltaic cells is probably the most applicable of them, thanks to the ease of output management as well as feasibility of up and down-scaling.

1.3 Photovoltaics

Photovoltaic cells take the advantage of internal photoelectric phenomenon occurring in semiconductors, in which an exciton (a pair of electron in conduction band and hole in a valence band of a semiconductor) is created after an act of photon absorption and subsequently split to an electron and a hole on the interface of electron and hole transporting materials (p-n junction). Starting from the first experiments performed by Becquerel in 1839, the knowledge on the photovoltaic effect has been expanded until the construction of the first solar cell in Bell Labs in 1954. Since then, the idea of photovoltaic solar energy conversion has gained many possible realizations including application of a variety of different materials and architectures in pursue of efficiency improvement, lowering their cost and gaining many other desirable features. The technologies and their certified record performances over years are gathered at the National Renewable Energy Laboratory (NREL) of USA (Figure 1).

Special attention has been attracted to the so-called emerging photovoltaic technologies, exhibiting the fastest pace of development. In general, they aim at utilizing low amounts of cheap and abundant materials, and low energy consuming fabrication processes to obtain as highly efficient devices as possible. Thanks to their low price, they have a chance to be applied not only in conventional applications (large solar panels connected to the electrical grid) but also in powering small devices, wearable electronics etc.

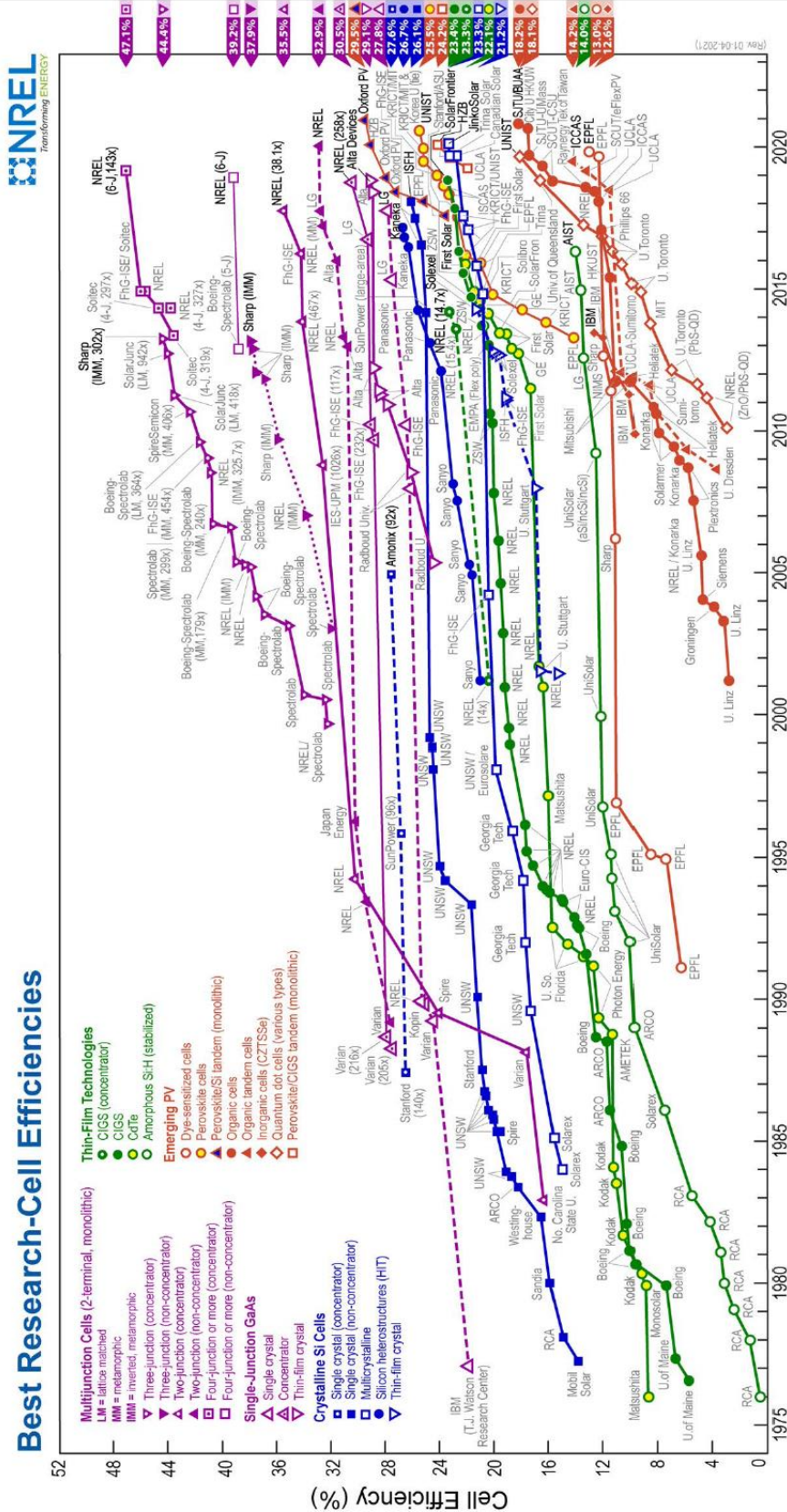


Figure 1. A chart of best solar cell efficiencies exhibited by most important photovoltaic technologies, published by NREL in February 2021.

2. Dye Sensitized Solar Cells

Dye Sensitized Solar Cells (DSSC) are photovoltaic devices (belonging to emerging technologies) in which typical p-n semiconductor junction is replaced by wide bandgap semiconductor/electrolyte interface, taking advantage of photocatalytic properties of metal oxide semiconductors⁵ (e.g. TiO₂, ZnO etc.). In order to broaden the photoresponse of metal oxides (absorbing in UV spectral region), dyes were introduced to sensitize the semiconductor's surface.^{6,7} Ultimately, bulk semiconductor anodes were replaced by mesoporous layers, tremendously boosting surface area available for the sensitizing dye, and consequently enhancing light harvesting, achieving for the first time attainable ~7 % efficiency and establishing new solar cell technology.⁸ Since 1991, when the breakthrough paper by O'Regan and Gratzel was published,⁸ DSSCs have attracted significant interest of scientific community, as potentially cheaper and more environmentally friendly alternative to ubiquitous silicon solar cells.⁹ As a result tremendous advances have been achieved in the field of new materials development as well as device operation understanding.⁹⁻¹² Nowadays the best laboratory efficiencies of DSSCs reach 13-14 %¹³⁻¹⁶ (certified 13.0 % - see Figure 1). DSSCs have also gained successor technologies, namely Quantum Dot Sensitized Solar Cells¹⁷ (QDSC) and Perovskite Solar Cells^{18,19} (PSC) established on the foundations of many years' DSSC community research efforts. Both QDSC and PSC outperform DSSC in terms of power conversion efficiency in full sunlight conditions, currently reaching impressive 18.1 % and 25.5 % respectively (Figure 1). Nevertheless, DSSCs are regaining scientific interest thanks to their superior performance among all photovoltaic technologies, exhibiting PCE in indoor ambient lighting conditions²⁰ reaching 32-34 %.^{21,22} This feature is especially important in the advent of Internet of Things (IoT) technology expansion which is currently taking place.²³ Photovoltaic cells or photo-capacitor devices²⁴ can make the devices networking in IoT, independent of additional power supply, wiring or disposal batteries (which is also an opportunity for a variety of different low power electric widgets). Thus, in 30 years after their introduction, DSSCs are still an attractive field of both fundamental and application research.

2.1 Principles of Operation

2.1.1 Charge Separation

The charge separation in DSSC begins with absorption of a photon (process 1 in Figure 2) by the dye molecule adsorbed on the mesoporous surface of a wide bandgap n-type semiconductor (most frequently TiO_2). Subsequently, an electron is injected from the dye's excited state to the semiconductors conduction band (CB) (process 2). Then the electron in CB is diffusively transported (process 4) to the anode consisting of a glass plate coated with a transparent and conducting layer of fluorine doped tin oxide (FTO). After giving the electron away, the dye molecule stays in its oxidized state until it is regenerated by the reduced form of the redox mediator (process 3), contained in the electrolyte solution. This reaction is followed by diffusion of the oxidized redox mediator molecule to the counter electrode. The counter electrode is the FTO glass plate coated with a catalyst (most frequently activated platinum or poly(3,4-ethylenedioxythiophene) – PEDOT). The catalyst participates in reduction of the oxidized form of the redox mediator (process 5) closing the electrical circuit.

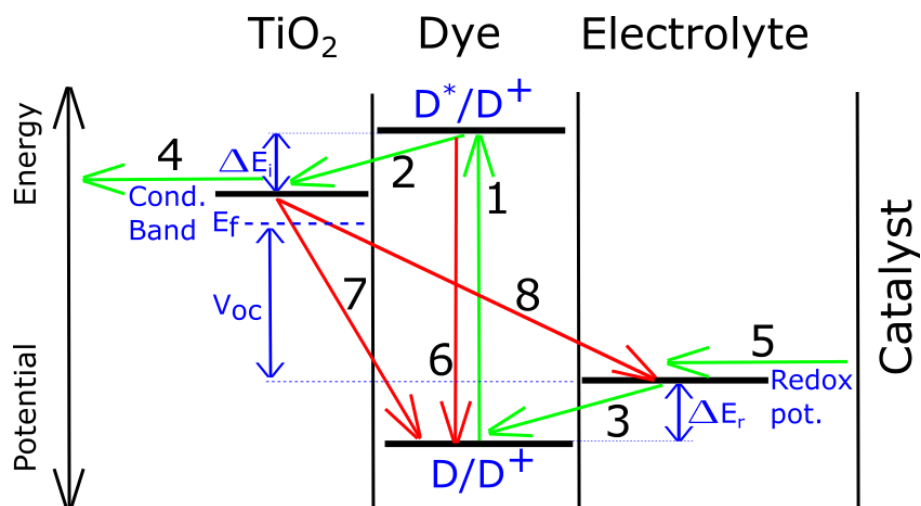


Figure 2. Energetic diagram of DSSC with indicated desired electron transfer processes (green arrows) and undesired electron transfer processes (red arrows). Description in the text.

The aforementioned processes are accompanied by undesired phenomena occurring in DSSC. These processes include internal conversion (process 6), and recombination: between semiconductor's CB and oxidized dye (process 7) as well as oxidized form of the redox mediator (process 8). All of them compete with the desired phenomena and consequently limit the quantum yields of partial charge separation affecting the overall power conversion efficiency.^{9,25,26}

2.1.2 Power Conversion Efficiency

The power conversion efficiency (PCE) of operating cell is obtained on the basis of current-voltage curve, usually measured under standardized AM 1.5G illumination conditions (Figure 3).

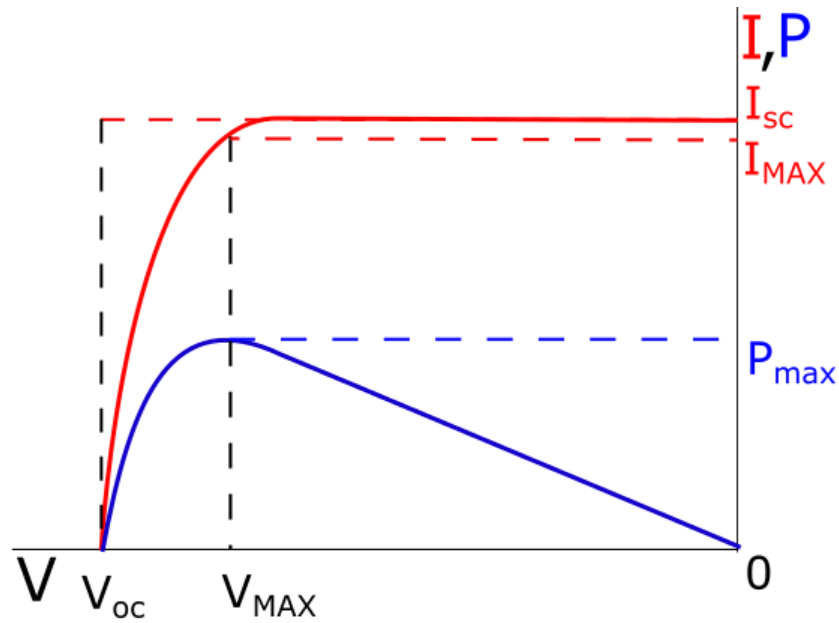


Figure 3. Typical I(V) and P(V) curves ($P = I V$), with the most important parameters indicated: P_{MAX} – maximal output power, I_{SC} – short circuit photocurrent, V_{OC} – open circuit voltage, I_{MAX} – photocurrent at maximal power point, V_{MAX} – voltage at maximal power point.

The PCE is calculated according to the following equation:

$$PCE = \frac{J_{sc} V_{oc} FF}{P_{in}} \quad , \quad (1)$$

where:

P_{in} – input power density,

FF – fill factor:

$$FF = \frac{P_{MAX}}{J_{SC} V_{OC}}, \quad (2)$$

J_{SC} – short circuit photocurrent density:

$$J_{SC} = \frac{I_{SC}}{A}, \quad (3)$$

where:

A – illuminated photoanode surface.

2.1.3 The Limitations of Photovoltaic Performance

Theoretical limit of power conversion efficiency for the solar cell using a single p-n junction, was calculated by Shockley and Queisser to be 33.7%²⁷ assuming AM 1.5 (solar spectrum corrected by the air mass coefficient, which defines the length of the optical path through the atmosphere) and on the basis of the principle of detailed balance which was derived from basic physical laws. DSSCs highest reported PCE are currently about 13-14%^{13,15,16} so there is much room for improvement of particular photovoltaic parameters determining the solar cells output power (equation 1 numerator).

J_{SC} of a complete device is determined by the photon flux of incident light and limited by the external quantum efficiency of a solar cell according to the equation:

$$J_{SC} = e \int_{\lambda_{min}}^{\lambda_{max}} \Phi_{ph}(\lambda) IPCE(\lambda) d\lambda, \quad (4)$$

where:

e – elementary charge

$\lambda_{min}, \lambda_{max}$ – the limits of incident light spectra

Φ_{ph} – incident photon flux,

IPCE – incident photon to current efficiency (also called external quantum efficiency):

$$IPCE(\lambda) = LHE(\lambda) \eta_{sep}, \quad (5)$$

where:

LHE – light harvesting efficiency (a ratio of absorbed and incident photon numbers)

η_{sep} – overall charge separation efficiency which is a product of particular charge separation processes efficiencies:

$$\eta_{sep} = \eta_{inj} \eta_{reg} \eta_{cc}, \quad (6)$$

where:

η_{inj} – electron injection efficiency,

η_{reg} – oxidized dye regeneration efficiency,

η_{cc} – charge collection efficiency.

In principle η_{sep} is a wavelength function, however the approach may be simplified assuming average charge separation efficiency. Then, η_{sep} is identical to the total absorbed photon to current efficiency (*total_APCE* - defined in the Chapter 4). Particular charge separation processes efficiencies depend on the relationship between rate constants of charge separation and respective competing charge recombination process.^{9,25} Thus characterization of dynamics of particular desired and undesired charge transfer processes is the way to find a bottleneck limiting a photocurrent density of given system.^{11,25}

V_{OC} of an operating cell is determined by the difference between the redox potential of electrolyte and quasi Fermi level potential in TiO_2 in open circuit conditions. Recombination processes 7 and 8 may also limit V_{OC} of a solar cell by lowering of the quasi-fermi level energy.^{9,25}

FF can be limited due to discrepancy between highest possible photocurrent value generated by the photoanode and counter electrode capability of reduction of the oxidized redox compound. Other reasons may be additional series and parallel resistances originating from poor contacts, not tight interfaces, mass transport limitations for the redox mediator and resistance of electron transport in TiO_2 mesoporous layer.^{9,25,26}

2.2 DSSC Components and Architecture

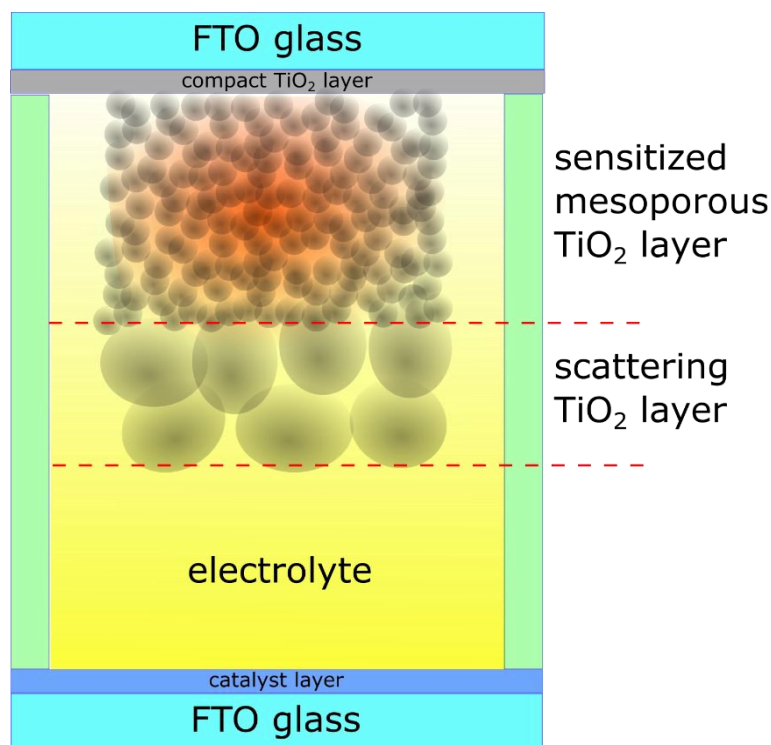


Figure 4. Typical DSSC architecture.

In the most established DSSC architecture (Figure 4), the device consists of a photoanode sandwiched with counter electrode with the electrolyte solution injected in between.⁹ The use of liquid electrolyte involves the risk of leakage or solvent evaporation, largely limiting the stability and possible applications of the devices.²⁸ However, this architecture provides still the highest reported Power Conversion Efficiencies (PCE) reaching 14%.^{13,15} It is also being used as excellent platform for fundamental studies of dye-semiconductor interactions and charge transfer processes, important not only for DSSCs but also for dye sensitized photo electrochemical cells (DSPECs) used as water splitting systems,^{29–31} electrochromic devices,³² photocatalytic CO₂ reduction,³³ photo-capacitors²⁴ etc.

Many different device architectures have been introduced in the attempt to eliminate liquid electrolyte, including quasi solid state electrolytes and solid state hole transporting

materials²⁸ both fully organic as well as based on copper (I/II) coordination complexes,^{34,35} formed by evaporation of the solvent from the electrolyte based on copper (I/II) redox couple.^{22,28,36,37} The latter, the so-called zombie cells have the greatest potential to outperform liquid DSSCs and already permit achieving nearly 12% PCEs.^{16,29}

2.2.1 Semiconductor Layer

The DSSC's photoanode is based on an n-type, wide bandgap semiconductor layer – predominantly titanium dioxide. Since Fujishima and Honda presented their work⁵ on the electrochemical photooxidation of water on the semiconductor electrode, titania has been extensively studied for different photocatalytic applications such as water splitting and hydrogen generation,^{29–31} photo-degradation of water pollutants³⁸ and many others.

Typical DSSC photoanode consists of three morphologically different titania layers sequentially deposited onto the FTO glass (Figure 4),^{25,26} namely: compact layer³⁹ – dense ~50 nm thick layer usually deposited by spray-pyrolysis⁴⁰ or TiCl₄ treatment, mesoporous layer – 2-20 μm thick composed of 20-30 nm titania nanoparticles typically in the polymorphic form of anatase, with addition of rutile and deposited by screen printing method, using paste containing titania nanoparticles, and subsequently sintered. Finally, the scattering layer ~3 μm thick, containing ~400 nm titania nanoparticles⁴¹ is deposited in the same way as the mesoporous layer. Detailed description of photoanodes preparation is provided in Chapter 4. “Methods”.

The size of titania nanoparticles, mesoporous layer's thickness and porosity are parameters that need optimization in order to obtain the highest possible efficiency of any dye-redox mediator system.⁴² Increasing the titania layer thickness rises light harvesting efficiency of the photoanode at the expense of increased series resistance and consequently, decreased charge collection efficiency (η_{cc}). Further, the size of pores is proportional to the size of nanoparticles and the content of cellulose in the screen-printable paste. The pore size may be also modified along with the tuning of porosity, which is defined as the ratio between the pores volume and overall photoanode volume and depends mainly on the ratio between the content of titania nanoparticles and that of cellulose in the screen-printable paste. Too small size of pores, may impede redox species

diffusion and cause mass transport limitations, especially in the thick mesoporous layer.^{43,44}

The application of scattering particles (forming distinct scattering layer or their presence within the mesoporous layer) provides backscattering of non-absorbed light, enhancing light harvesting of the photoanode.^{41,45} However, in fundamental studies relying on optical measurements in transmission mode, this modification is usually skipped in order to maintain proper transmittance of the specimens.¹¹

Besides TiO₂, several different semiconductors showing similar physical properties e.g. ZnO,⁴² SnO₂,⁴³ Nb₂O₅⁴⁸ and their numerous composites with TiO₂ have been studied by scientific community for the purpose of use in DSSC photoanodes.⁴⁹ Also different morphologies of nanoparticles ranging from simple nanobeads, through nanorods,⁴⁵ nanotubes,⁵⁰ and a variety of different nanostructured morphologies⁵¹ have been tested, aiming at obtaining high conductivity, active surface and low impedance for electrolyte species diffusion. The modifications with metal nanoparticles enhancing light harvesting taking the advantage of plasmonic interactions,⁵² photoanode patterning^{53,54} for better light trapping and a great deal of refinements not mentioned here, have been reported.

2.2.2 Dyes

Since the absorption onset of anatase is at about 400 nm, it is not possible to harvest significant part of the solar spectrum. To expand its spectral response, dyes with high extinction coefficient over broad absorption spectra are needed.^{7,55} In order to attach dye molecules to the semiconductor surface, compounds with moieties capable of bonding to metal oxides (predominantly carboxylic group but also other including phosphonic, pirydyl, picolinic and finally alkoxy-silyl⁵⁶⁻⁵⁸ unit which was studied in this work) were employed.⁵⁹ Different anchoring groups, provide various bonding strength as well as distinct electron transfer properties.⁶⁰ The other requirements for sensitizer dyes are that the energy of its lowest unoccupied molecular orbital (LUMO) must be higher than the CB edge of the semiconductor. Also the highest occupied molecular orbital (HOMO) energy level needs to be lower than the redox level of the redox mediator used in the system.^{9,61}

The first widely used sensitizers were the group of polypyridyl ruthenium coordination complexes.^{9,61,62} Due to their strong and tunable metal to ligand charge transfer (MLCT) transitions as well as high attainable dye-load, they reached about 12% PCE with remarkable stability.⁶³ It is also worth mentioning that despite of rare earth element content, Ru complexes are among the cheapest sensitizers, thanks to their relatively easy synthesis and purification paths.⁶¹ Thus, they are still the first choice in the commercial applications as well as in the DSSC fundamental studies focused on the semiconductor layer's or counter electrode's modifications. However, they are being replaced by fully organic dyes due to modest performance with redox mediators other than iodide/triiodide, which precludes reaching open circuit voltages higher than about 0.8 V and consequently, excludes ruthenium sensitizers from reaching efficiencies relevantly higher than the mentioned 12% due to its elevated loss in potential.⁶⁴ The other drawbacks are: relatively low extinction coefficients ($1-2 \times 10^4 \text{ M}^{-1} \text{ cm}^{-1}$) and the above-mentioned low abundance of ruthenium.⁶³ Thus, scientists attempt to replace ruthenium ions in polypyridyl coordination complexes by iridium,⁶⁵ iron^{66,67} or copper,⁶⁸ unfortunately, with no significant success yet.

The other worth mentioning metal coordination complexes used as sensitizers in DSSC are porphyrin derivatives, reaching impressive 13%,¹⁶ however, the complexity of their synthesis and low stability in working devices does not promise their broad application in DSSC systems.

Ultimately, fully organic dyes adapting the donor - π conjugated linker - acceptor (D- π -A) architecture have been extensively studied,⁵⁵ providing a variety of interesting compounds. As the donor group, the dyes comprise such moieties as carbazole,^{56,69} indoline,⁷⁰ perylene,⁷¹ coumarine⁵⁵ or triphenylamine⁷²⁻⁷⁷ - notably well performing in the state of the art DSSC systems. The linker group usually consists of thiophene ring, its oligomers or derivatives, providing strong π -orbitals conjugation.^{69,74} Finally, the acceptor moiety very often simultaneously acts as the anchoring unit. Most frequently, cyanoacrylic moiety (comprising carboxylic group) is applied.⁵⁹ The choice of the donor and acceptor as well as the length and structure of the π -linker determine the HOMO and LUMO energy levels as well as the extinction coefficient (for such a compound usually relatively high - $3-5 \times 10^4 \text{ M}^{-1} \text{ cm}^{-1}$).⁵⁵ Apart from the D- π -A core, well performing organic dyes usually contain bulky auxiliary moieties e.g. phenyl rings and alkyl chains,

preventing from the aggregation of dye molecules as well as from redox mediator's approach to the semiconductor's surface.^{78,79} Both mentioned phenomena may cause undesired recombination processes and diminish the device performance.⁹

2.2.3 Electrolytes

The electrolyte solution in DSSC acts as a hole transporting medium. The solution contains most importantly a redox couple which is a pair of reducing and oxidizing agents. In DSSC such a mediator has to be capable of reducing dye molecules oxidized after the electron injection process and being diffusively transported to the counter electrode, where it is reduced again by the catalyst.

2.2.3.1 Redox Mediators

Since the introduction of DSSCs, the most commonly used redox couple was I^-/I_3^- due to its exceptional redox properties and low recombination rates in DSSC. However, I^-/I_3^- redox reaction is two-step and involves two electrons. As a result, it consumes about 0.5 V overpotential (ΔE_r in Figure 2) to regenerate the dye efficiently, which causes a significant loss of open circuit voltage and in consequence, significant PCE limitation.⁶⁴

In order to overcome this problem and enhance the efficiency of DSSCs, a variety of one electron redox mediators have been introduced.⁸⁰ The replacement of I^-/I_3^- redox couple led to a decrease in ΔE_r from ~ 0.5 V to ~ 0.3 V for Co^{2+}/Co^{3+} ^{72,81–83} and even ~ 0.1 V for Cu^+/Cu^{2+} ^{34,35,84,85} maintaining the η_{reg} close to unity. It was possible thanks to a simpler, in comparison with the I^-/I_3^- one, electron redox reaction occurring in cobalt and copper mediated systems. Particularly, for Cu^+/Cu^{2+} the internal reorganization energy is significantly lower than in Co^{2+}/Co^{3+} , where high-spin (d^7) to low-spin (d^6) transition is a serious drawback consuming driving force for dye regeneration.^{34,86} According to the Marcus's theory, the reorganization energy is equal to the work which needs to be performed due to a change in the conformation of the compound and its surrounding, upon the change in the oxidation state.^{87,88} Thus, it is a potential barrier for electron transfer process. Lowering the reorganization energy of the redox mediator leads to reduction of the required ΔE_r to the mentioned 0.1 V permitting over 1.24 V V_{oc}

achievement in highly efficient DSSCs.⁷⁷ It is worth noting that the redox couples consisting of coordination compounds have the advantage of being tuned by ligand modifications. It gives e.g. the opportunity of introducing additional steric hindrance limiting changes in the complex geometry (in the case of Cu^+ to Cu^{2+} it is a transition from tetrahedral to square planar) forced by the change in the oxidation state, which means a lower contribution to reorganization energy. Thanks to the ligand modification by introducing additional electron donating or withdrawing moieties, it is also possible to obtain different redox potentials of the synthesized redox couples.³⁴

Nevertheless, the improvement of photovoltage output observed in cobalt and copper mediated DSSCs is not as high as could be anticipated on the basis of the difference in the redox potentials between I^-/I_3^- and its substitutes.⁸⁹ The common issue of all metal coordination complexes based redox mediators and a probable explanation of the above-mentioned issues are the undesired titania-redox couple electron recombination processes which are much more intensive than in the systems employing I^-/I_3^- . However, cobalt and copper mediated DSSCs have already reached impressive PCEs records about 12-14%^{13,15,22,73,84} already outperforming I^-/I_3^- based counterparts.

2.2.3.2 Potential Determining Additives

The other important components of electrolyte solutions are the so-called potential determining additives. Lewis bases – predominately 4-*tert*-butylpyridine (TBP)⁹⁰ or imidazole derivatives,^{91,92} provide upshift of the titania conduction band resulting in a higher voltage output.⁹³ They may also limit the undesired charge recombination processes, by passivation of titania surface states.^{90,94} Despite their addition at the early stage of DSSC technology development, they are still revealing new roles in the state of the art systems.^{91,95,96} In contrast, lithium salts, which provide Li^+ ions, induce a downshift of the CB edge, which may help in reaching higher photocurrent output.⁹³ Generally, the optimized electrolyte solutions should contain both Lewis base and lithium salt in appropriate concentrations.⁹

2.2.3.3 Solvents

Thanks to their excellent physical properties (i.e. high dielectric constants, low viscosity and high solubility of variety of compounds) organic solvents, like acetonitrile (ACN), 3-methoxypropionitrile or valeronitrile, are the most commonly used for DSSC's electrolyte solutions.⁹⁷ The choice between them is usually conditioned by the relationship between viscosity and volatility, determining performance and stability trade-off.

In the pursue of obtaining environmentally friendly devices, also water is investigated as an alternative for organic solvents,⁹⁸ however, despite appreciable researchers' effort, its performance and stability still need much improvement before aqueous DSSCs could be considered as applicable. Nevertheless, significant advances are frequently reported in this field,^{92,99–102} including the topics of efficiency and stability improvements, as well as describing progress in the understanding of aqueous DSSC operation.

2.2.4 Counter Electrodes

While the efforts of scientists attempting to improve DSSCs efficiency, have been mainly focused on the photoanode side of the cell and to a lesser degree on the electrolyte system's enhancements, activated platinum was used as a catalyst enabling reduction of the oxidized form of the redox mediator on the counter electrode, since the very beginning of works on DSSC.^{8,9,25} However, notable advances have also been made in this field aimed at replacing precious platinum by more available carbon materials.¹⁰³ In particular, electrodeposited porous PEDOT films,^{104,105} graphene or carbon nanotube composites and most recently metal-organic frameworks¹⁰⁶ have been successfully applied.

2.2.5 Semiconductor/Dye/Electrolyte Interface Modifications

Much effort has been devoted to deal with the undesired strong titania-redox couple electron recombination in the presence of transition metal complexes.

The most common and probably also the most effective approach is to employ the dye engaging bulky blocking moieties (alkyl chains, phenyl rings etc.) preventing oxidized

redox mediator molecules from approaching the semiconductor's surface and interception of electrons from CB.^{72,81,107} Alkyl chains may also prevent undesirable dye molecules aggregation on the semiconductor's surface.^{69,70} This approach is usually combined with the application of co-adsorbing electronically inert molecules added to sensitizing dye solution, e.g. chenodeoxycholic acid (CDCA).⁷⁰

Alternative methods aim at limiting the back electron transfer by filling the voids between dye molecules adsorbed at titania surface. It can be obtained by adsorption of different acids with long alkyl chains, providing additional steric hindrance for the approach of oxidized redox molecules to the semiconductor's surface.^{13,56,108} This is gained by sequential immersion of the sensitized photoanode in different acid solutions and is known as multi-capping. Unfortunately, in this process significant dye amount can be desorbed from the titania surface. For this reason alternative anchoring moieties, which provide stronger bond to titania than most frequently used carboxylic group, are applied.¹⁰⁸

Additional steric hindrance can be provided by treatment of the sensitized semiconductor with cucurbit[7]uril aqueous solution.¹⁰⁹ Cucurbit[n]uriles¹¹⁰ are macrocyclic n-glycourile oligomers. The sevenfold oligomer is large enough to encapsulate small chemical moieties, particularly alkyl chains and phenyl rings, building dye molecules.¹¹¹ Literature provides also reports of cyclodextrins application for the same purpose.¹¹²

Another applied approach is atomic passivation of titania surface between the dye molecules, by deposition of a high bandgap semiconductor (e.g. Al₂O₃, HfO₂ etc.) on the sensitized photoanode by atomic layer deposition (ALD) method.¹¹³⁻¹¹⁵ There are reports on pre- and post-assembly (before and after sensitization) ALD.

2.3 Strategies of Enhancing DSSC Efficiency

Further photocurrent density enhancements will be realized by broadening the solar spectra absorption by application of more broadly panchromatic dyes or co-sensitization,^{77,116,117} which means the use of at least two different dyes with complementary absorption spectra. Furthermore, higher photocurrent values may be achieved by enhancing the efficiency of partial charge separation processes.^{9,25} In

particular, it may be obtained by the reduction of reorganization energy of the used compounds (dyes and redox mediators) to accelerate electron injection to the semiconductor's conduction band and regeneration of a dye by a redox compound.^{34,88} Furthermore, the use of dyes providing stronger electron coupling with the semiconductor's CB may also be beneficial for electron injection rate constants.¹¹⁸ Moreover, the charge separation phenomena can be additionally hasten by increment of energy intervals (ΔE_i and ΔE_r) creating driving force for respective injection and regeneration processes.^{88,119} Unfortunately, almost every modification aimed at particular photovoltaic parameter or charge separation process improvement, comes at the expense of another one. Namely, the reduction of redox mediator's reorganization energy, causes intensified recombination between semiconductor's CB and the oxidized form of the redox compound. Further modifications aimed at electron injection acceleration may simultaneously boost undesirable back electron transfer (from CB to oxidized dye), while increase in ΔE_i and ΔE_r directly consume attainable photovoltage.

In contrast, a decrease in ΔE_i and ΔE_r is an obvious way to improve V_{OC} , but at the same time maintenance of high efficiency of electron injection (process 2 in Figure 2) and oxidized dye regeneration (process 3) is essential.¹²⁰ Such a scenario has been recently realized by introduction of the aforementioned novel redox couples based on transition metal coordination complexes.⁸⁹ At the same time, the reduction of reorganization energy caused escalation of the recombination between semiconductor's CB and the oxidized form of the redox mediator.¹¹⁷ Thus, stopping this undesired process is currently one of the most important topic in the DSSC research.

3. The Aims of the Thesis

The main aim of the thesis was to characterize charge transfer dynamics, charge separation yield and their impact on DSSC efficiency depending on the applied different modifications. State of the art compounds were used for DSSC fabrication, including the dyes from the carbazole (MK-2), indoline (D149 and D205) and triphenylamine (Y123) families. The following modifications were investigated:

- Substitution of the most commonly used carboxylic anchoring moiety by alkoxyethyl group resulting in:
 - ADEKA-1 dye (modification of MK-2 dye),
 - D149Si dye (modification of D149 dye),
 - D205Si dye (modification of D205 dye).
- Semiconductor/dye/electrolyte interface modifications:
 - Molecular capping and multi-capping (applied in the systems with all studied dyes),
 - Atomic Layer Deposition of Al_2O_3 (ADEKA-1 and MK-2 sensitized cells),
 - Encapsulation of some sensitizer moieties by cucurbit[7]uril macrocyclic molecules (D205, D205Si and Y123 sensitized cells).
- Different electrolyte compositions including changes in.
 - Redox couple (I^-/I_3^- , $\text{Co}^{2+/3+}(\text{bpy})_3$ (bpy = 2,2'-bipyridine), $\text{Co}^{2+/3+}(\text{phen})_3$ (phen = 2,2'-phenanthroline), $\text{Cu}^{+2+}(\text{tmby})_2$ (tmby = 4,4',6,6'-tetramethyl-2,2'-bipyridine),
 - Solvent (standard organic acetonitrile vs. water) in systems with $\text{Co}^{2+/3+}(\text{phen})_3$ and MK-2 and ADEKA-1 sensitized cells,
 - Lewis' base concentration (4-*tert*-butylpyridine (TBP) or 1-methylbenzimidazole (MBI) in water based systems).
- Different titania layer morphologies:
 - Content of large (~ 400nm) particles within mesoporous layer (ADEKA-1 and MK-2 sensitized cells),
 - Different layer thickness (ADEKA-1 and MK-2 sensitized cells),
 - Different porosity of mesoporous layer (MK-2 sensitized cells),

- Modification caused by continuous irradiation of solar cells (MK-2 or Y123 sensitized cells).

4. Methods

This section contains description of the experimental methods including manufacturing of DSSC samples as well as characterization of full devices and their components. The methodology was established on the foundation of many years of the DSSC community research and published literature.^{9,11,25,26} In particular, the chapter describes the procedures and equipment used in the Quantum Electronics Laboratory, Faculty of Physics, Adam Mickiewicz University, where the author performed the vast majority of his investigations described in papers 1 - 6 attached to this dissertation.

4.1 DSSC Manufacturing Procedure

4.1.1 Glass Cleaning Procedure

The glass cleaning procedure includes three-step sequential sonication in aqueous detergent solution, distilled water and ethanol, 15 min each. To get rid of any residual traces, the substrates are dried with compressed air between the steps. Subsequently, for superior purity another 15 min step of UV-ozone cleaning can be applied.

4.1.2 Photoanodes Fabrication

When the FTO glass (a glass coated with a thin layer of transparent and conducting fluorine doped tin oxide) is cleaned, a compact TiO₂ layer is deposited. The glass substrates are immersed in 40 mM TiCl₂ aqueous solution at 70 °C for 30 min. Next, the substrate is rinsed with distilled water to remove residual titania precipitate and sintered for 60 min at 450 °C. The substrate is gradually warmed up in the stove to 150 °C and 300 °C for 5 min each, then it is left to cool down slowly after sintering process to avoid cracks.

The abovementioned 40 mM TiCl₄ aqueous solution is unstable and should be made each time before use by addition of appropriate 2M TiCl₄ aqueous solution to water. The storable 2M TiCl₄ solution is obtained by very slow dropwise addition of an appropriate volume of concentrated TiCl₄ to deionized water. During the TiCl₄ addition, the solution

is vigorously stirred on a magnetic stirrer and cooled in an ice bath. It is also important to cool down water to close to 0 °C and TiCl₄ in a refrigerator (approximately to -20 °C). The obtained solution must be transparent and free of precipitate. For long lasting storage, 2M TiCl₄ solution should be kept in a refrigerator. After the compact TiO₂ layer is deposited on the FTO glass, the mesoporous titania layer is deposited by screen printing method. First of all, a clean substrate is carefully placed under the screen and immobilized by scotch tape. Subsequently, some amount of screen-printable paste containing semiconductor's nanoparticles, is put on the screen, across the field of mesh spots (Figure 5A). The first slide of the rubber squeegee is applied without pressure to spread the paste firmly along the field of mesh spots (Figure 5B). This stage can be repeated if necessary (Figure 5B). The second move has to be performed very firmly. The squeegee should be aligned at an angle of approximately 45 ° to the screen surface and drawn with moderate pressure applied. The squeegee gathers almost all the paste from the mesh spot field (Figure 5C), except a small amount which is transferred through the mesh spots onto the substrate. It is helpful to spread some paste on the whole working edge of the squeegee to reduce friction between the rubber and the screen and to provide a firm slide. Gathered paste can be reused many times unless it gets contaminated.

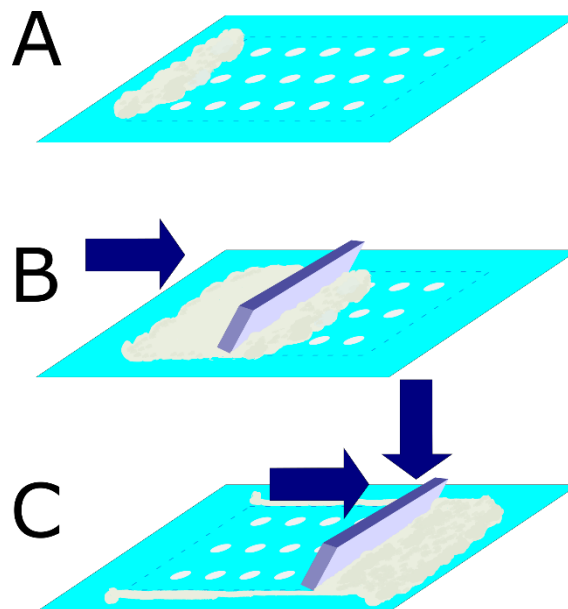


Figure 5. Screen-printing procedure steps. Description is provided in the text.

The substrate with screen-printed spots is left under coverage for 5-10 min to allow cohesion forces to even the mesh pattern. Subsequently, the layer is sintered for 60 min at 450 °C following the same warm up and cool-down precautions as described for TiCl₄ treatment. If another layer is needed (e.g. scattering or another mesoporous) the screen printed layer is dried in a stove or on a hotplate at 120 °C instead of sintering. Next, it is precisely realigned in the screen-printer to avoid mismatch between subsequent layers.

Once the titania layers are sintered, the TiCl₄ treatment is repeated according to the same procedure as described previously for the compact layer.

So prepared titania photoanodes may be stored for years, in a dry and clean container.

Next, in the process of sensitization, titania photoanodes are immersed in a dye solution. During this stage, dye molecules are adsorbed on the titania surface creating covalent bonds to the semiconductor's surface. Sensitizer's solution may also contain co-adsorbate which is an electronically inert compound, applied to limit dye aggregation as well as to fill the voids between dye molecules. Predominately chenodeoxycholic acid (CDCA) is used for this purpose. Sensitization process should last between 4 and 24 hours and is performed in the dark to avoid dye degradation photo-catalyzed by titania. Too short time, may not provide proper dye coverage of the surface, while on the other hand, too long time may cause formation of aggregates.

The titania photoanodes should be still warm (~70 °C) after sintering while they are immersed in the dye solution. If the titania photoanodes were previously stored, they should be heated before sensitization, to get rid of water and additional contaminants deposited in the porous structure during storage. Sensitized photoanodes are taken out of the sensitizer's solution and rinsed with a solvent capable of solubilizing a given dye. After that they must be assembled into a complete DSSC as soon as possible or put into acetonitrile and stored in the dark.

4.1.3 Counter Electrode Preparation

For the purpose of this work, two different catalysts have been used. Namely activated platinum for all I⁻/I₃⁻ and Co²⁺/Co³⁺ based electrolytes and PEDOT: poly(3,4-ethylenedioxythiophene) for all samples with Cu⁺/Cu²⁺ redox couple.

The substrates are first drilled with 1 mm wide ball shaped diamond drill bit, under water immersion. Two holes are needed per each plate – one for electrolyte injection and the second one for venting the cell during electrolyte injection. Then, they are cleaned according to the glass cleaning procedure described above.

The activated platinum is deposited on the plates by spreading of the colloidal platinum solution in ethanol (Platisol, provided by Solaronix) using a paintbrush. Next, the plates are sintered in a stove according to the same procedure as described for TiO₂.

The PEDOT is electrodeposited from 0.01 M 3,4-ethylenedioxythiophene (EDOT) and 0.1 M of sodium dodecyl sulfate (SDS) aqueous solution. The electrodeposition procedure is conducted as follows. Two FTO electrodes are immersed in the solution face to face in parallel in approximately 1 cm distance. The counter electrode should have at least the same area as the working electrode. Subsequently, the 0.16 mA cm⁻² constant current is supplied from a potentiostat in galvanostatic mode for 175 s. After deposition, the PEDOT layer is rinsed with distilled water and left to dry.

4.1.4 DSSC Assembly

In order to assemble a solar cell, first a circular Surlyn gasket needs to be placed on the active side of counter electrode (Figure 6B). Such a gaskets can be cut from Surlyn foil by a plotting device. The counter electrode with a gasket on it is then placed on a hotplate warmed up to 120 °C. When the gasket melts, a dye sensitized photoanode (previously taken out of a sensitizer's solution, rinsed and dried in ambient atmosphere) is sandwiched with the counter electrode, placing the active surface within the gasket (Figure 6C). Such a sandwich is pressed strongly with a rubber presser for 5-10 s and quickly removed from the hotplate. It is important to evaluate the surlyn gasket tightness visually and repeat pressing if needed. However, the time of the cells exposure to heating should be kept as short as possible, in order to avoid dye's degradation.

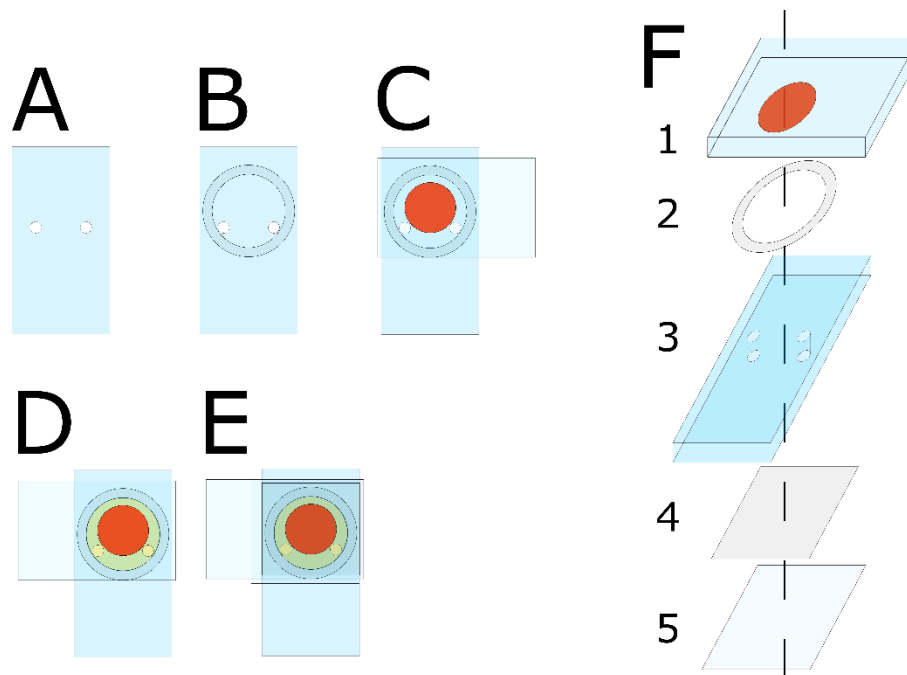


Figure 6. (A-E) Steps of DSSC assembly. (F) Exploded view of DSSC.

When the photoanode and the counter electrode are sandwiched, the assembly is cooled down to room temperature and then it is filled with 7 μl of electrolyte solution, through one of the predrilled holes (Figure 6D). Any excess of the electrolyte spilled on the glass surface, must be removed with tissue. Ultimately, the holes in the counter electrode have to be covered by square Surlyn sheet and a glass coverslip (Figure 6E). Next, the coverslip needs to be stuck to the glass substrate by melting the Surlyn sheet, situated in between, using soldering iron tip warmed up to 200 $^{\circ}\text{C}$.

4.2 Full DSSC and Components Characterization Techniques

4.2.1 Current-Voltage Characterization

Basic photovoltaic cell characterization includes primarily Current-Voltage (C-V) curve measurement under standard AM 1.5 G simulated solar light illumination. The conditions are ensured by a photoelectric spectrometer (Instytut Fotonowy, Figure 7) equipped with a solar simulator which comprises an AM 1.5 G spectral filter fitted to the light source (150 W Xenon lamp) spectra. The light intensity is adjusted to 100 mW/cm^2 using ABET 15151 calibration cell and controlled in the light stabilization mode of the spectrometer.

The surface of illuminated sample is confined by a mask and the photocurrent is measured by a potentiostat (model M101 Autolab), while voltage is scanned, starting at a negative value exceeding V_{OC} , corresponding to the open-circuit conditions and reaching at least 0 V (short-circuit conditions). The information and photovoltaic parameters obtained from C-V characterization are described in section 2.1.2 entitled Power Conversion Efficiency.



Figure 7. Photoelectric spectrometer with solar light simulation.

4.2.2 Incident Photon to Current Efficiency Spectra

Incident Photon to Current Efficiency (IPCE) can be defined as:

$$IPCE = \frac{J_{SC}(\lambda)}{e \Phi(\lambda)} \quad (7)$$

According to equation 7, the IPCE assessment is based on J_{SC} measurement for each wavelength interval, provided by the monochromator of the photoelectrical spectrometer (Figure 7). At the same time, incident photon flux - $\Phi(\lambda)$ is measured in the reference beam separated by a beamsplitter situated right ahead of sample. In order to get net photocurrent values for each monochromator step, assigned to a given wavelength, the

current measurement is performed alternately under illumination and in the dark (with open or closed illumination shutter).

4.2.3 UV-VIS Absorption Spectroscopy

UV-VIS Absorption spectroscopy is a fundamental technique providing primary information on interactions with light and electronic structure of a studied system. In particular, UV-VIS Absorption spectroscopy is applied to study dyes applied as sensitizers in DSSC in order to characterize their light harvesting abilities - broad absorption bands and high extinction coefficient (ϵ), which can be calculated on the basis of the measured absorbance:

$$Abs = \log \frac{I_0}{I} , \quad (8)$$

where:

I_0 – incident light intensity,

I – transmitted light intensity,

and the Lambert-Bear law:

$$Abs = \epsilon lc \quad , \quad (9)$$

where:

l – length of optical path in the sample,

c – molar concentration of studied solution.

Absorption measurements may also be applied for sensitized titania films in order to determine light harvesting efficiency also known as absorptance.

$$LHE(\lambda) = 1 - 10^{-Abs(\lambda)} \quad (10)$$

This knowledge of the LHE allows calculation of the total absorbed photon to current efficiency (*total_APCE*):

$$total\ APCE = \frac{J_{sc}}{N_{Phe}} , \quad (11)$$

where N_{Ph} is the number of absorbed photons (under AM 1.5 G illumination in visible 400 nm – 800 nm wavelength range):

$$N_{Ph} = \int_{400}^{800} LHE(\lambda)\Phi(\lambda)d\lambda \quad (12)$$

Due to notable scattering properties of titania photoanodes, the absorption spectra measurements are conducted in the JASCO V-770 spectrophotometer setup including LN-925 integrating sphere module in order to collect both transmitted and scattered light (in such mode the samples are placed before the integrating sphere).

4.2.4 Electrochemical Impedance Spectroscopy

Electrochemical Impedance Spectroscopy (EIS) is a technique applied to study various processes occurring in electrochemical systems including interfacial processes like adsorption, electrocatalytic reactions, redox reactions, but also diffusive mass transport in a solution and many others. Impedance is a frequency dependent, complex quantity, describing the relationship between the applied voltage and the flowing current in alternating current circuit. Impedance includes real resistance (Z' - related to in-phase current) and imaginary reactance (Z'' - related to $\pm \frac{\pi}{2}$ shifted current) parts. In the EIS the impedance of DSSC systems is measured in a broad range of frequencies (0.1 Hz – 100 kHz, thus the processes occurring on time scale from sub-ms to seconds can be detected) by application of sine voltage perturbation and measurement of in-phase and $\frac{\pi}{2}$ shifted current realized by frequency response analyzer. As a result the Nyquist plot (exemplary Nyquist plot is shown in Figure 8), depicting imaginary vs. real impedance values for each frequency is obtained. The Nyquist plot consist of semi-arcs representing impedance originating from different processes. The use of proper modeling for fitting experimental data permits obtaining parameters attributed to physicochemical properties of a studied system. Figure 8 presents an example of equivalent circuit, which can be used to model DSSC impedance and obtain the parameters.

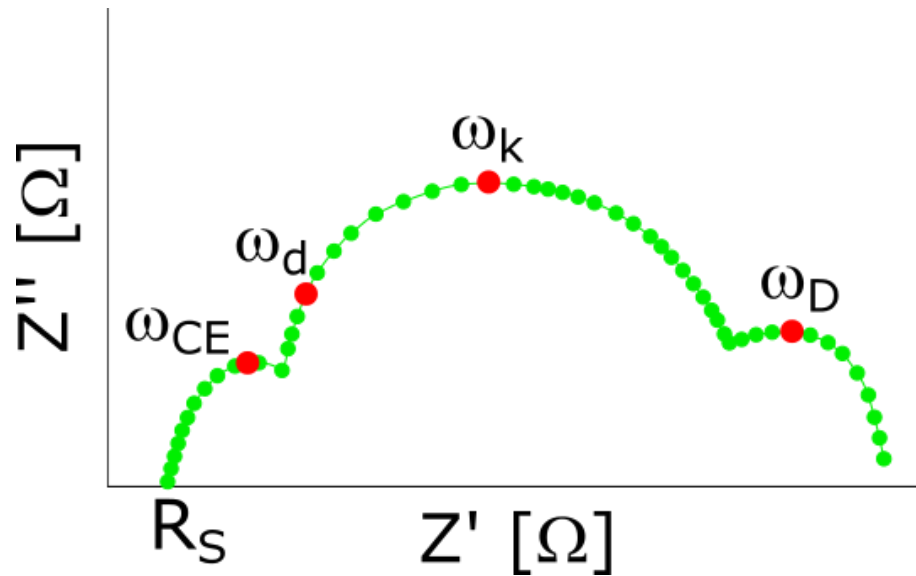


Figure 8. Typical Nyquist plot obtained for DSSC in V_{OC} conditions. R_S – series resistance, ω_{CE} , ω_d , ω_k , ω_D correspond to the charge transfer processes at the counter electrode, electron diffusion in mesoporous TiO_2 , back electron transfer from TiO_2 to oxidized redox agent in the electrolyte, and diffusion of redox species in the electrolyte, respectively.

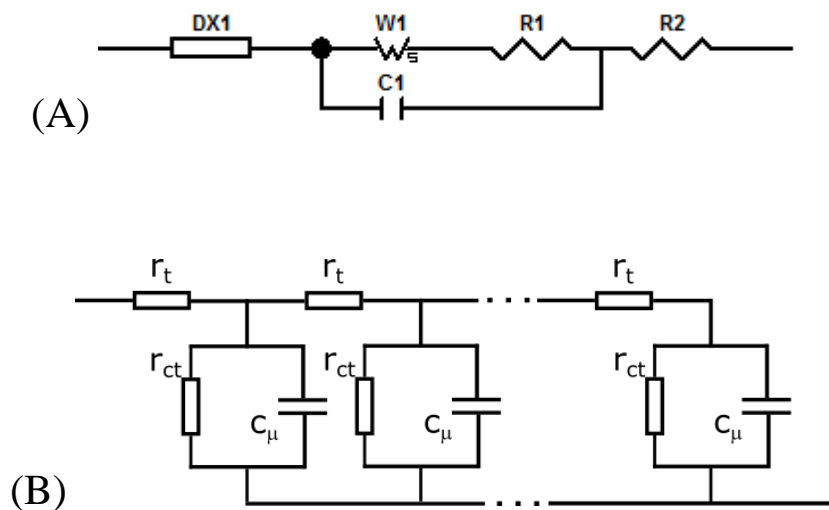


Figure 9. (A) A model applied to fit experimental data obtained in EIS of DSSC samples. DX1 is the transmission line element introduced to model mesoporous titania films DSSC, by Fabregat-Santiago et al.⁵ W1 is the Warburg diffusion element. (B) Transmission line elements - r_t , r_{ct} and C_μ are distributed components of overall electron transport resistance (through mesoporous TiO_2 net) R_T , charge transfer resistance (from TiO_2 to the oxidized redox mediator) R_{CT} and chemical capacitance of TiO_2 C_μ respectively.

Particularly, the information on chemical capacitance and charge transfer resistance obtained from scans performed at different bias voltage is very useful in assessment of the extent of TiO₂ – electrolyte recombination as well as conduction band edge position and distribution of trap states within the semiconductors bandgap.

4.2.5 Transient Absorption Spectroscopy

Transient Absorption Spectroscopy (TAS) is a method used in investigation of dynamic properties of various systems in photophysical, photochemical and photobiological studies. It is a powerful tool in particular in investigations of different charge transfer processes occurring in DSSCs in a wide range of temporal scales spanning from milliseconds to sub-picoseconds.

In general, TAS techniques is based on pump-probe approach which takes advantage of two different light beams. A probe is a pulse analyzing the sample and a pump is a more powerful pulse, introducing perturbation to the investigated system. The difference in absorbance measured with and without the pump pulse can be defined as:

$$\Delta A = Abs_{pump} - Abs_{No\ pump}, \quad (13)$$

which according to equation 8 can be expressed as:

$$\Delta A = \log \frac{I_0}{I_{pump}} - \log \frac{I_0}{I_{No\ pump}} = \log \frac{I_{No\ pump}}{I_{pump}}. \quad (14)$$

Thus, only measurements of transmitted probe light with and without the pump are needed and no reference beam is required.

Experimental realizations of this idea take different forms, depending on the desired time resolution and spectral ranges of the pump and probe.

The positive transient absorption (TA) signals in the visible (VIS) range may originate from the absorption of light associated with transitions from the excited state to another excited state (higher in energy) or the presence of new species (e.g. oxidized or deprotonated forms of a studied compound). The negative signals originate mainly from depopulation of the ground state of a studied compound (the so-called ground state bleach – GSB) or stimulated emission from excited state. To identify the abovementioned bands,

the data from stationary absorption, emission or photo-induced absorption may be needed. Another possible transient absorption feature in DSSC TAS measurements is the spectrum shaped like a derivative of the stationary absorption one (positive and negative adjacent bands) due to the shift of absorption band associated with the Stark effect.^{121,122}

In DSSC the decays of TA signals can be assigned to charge transfer processes. The dynamics of deactivation of dye's excited state (observed through a decay of stimulated emission and absorption associated with transitions to higher excited states in VIS range) is determined by the electron injection process (from the excited state of organic dye to CB of the semiconductor - process 2 in Figure 2). It is because the injection of electron is a process occurring much faster (fs – ps time scale) than the internal conversion (ps – ns time scale) (process 6 in Figure 2), the latter can be e.g. determined from the deactivation of the dye's excited state in solution. The injection of electrons to the semiconductor's CB can be also directly observed by the evaluation of kinetics in mid-IR spectral region, where electrons in CB have nonspecific broad absorption spectra. A wavelength free of contributions from oscillation band has to be chosen in this range. Moreover, the measurements in mid-IR should be performed on half-cells assembled on sapphire plates instead of ordinarily used FTO glass, because FTO glass is not transparent to mid-IR.

Another charge transfer process which can be observed in fs TAS experiments is CB-oxidized dye recombination (process 7). This recombination can be associated with the decay of GSB and the decay of oxidized dye's absorption. It must be noted that the excitation by laser pulse in fs TAS provides many times higher concentration of the oxidized form of dye, resulting in possible severe acceleration of this second order process in comparison with AM 1.5 G standard operation conditions. However, fs TAS is still a source of useful information on recombination assessment and comparison between variously modified systems.

In TAS measurements in ns- μ s timescale, the recovery of dye's ground state should be majorly assigned to desired process of regeneration of oxidized dye (process 3) by the reduced form of redox mediator present in the electrolyte. In order to compare its dynamics with competing process 7, the reference samples with electrolyte deprived of redox mediator are applied. For the latter samples, the kinetics due to process 7 are typically observed in μ s-ms timescales.

4.2.5.1 Nanosecond Laser Flash Photolysis

In the experimental setup (Figure 10) for TAS in ns-ms timescale (often called nanosecond flash photolysis), 8 ns pump pulses (full width at half of maximum – FWHM) are provided by 10 Hz Q-switched Nd-YAG (Continuum Surelite II, Coherent) laser with optical parametric oscillator (OPO) unit for wavelength tuning. A scheme of the setup is given in Figure 10. Probe light is generated by 150W Xe arc lamp with 1 Hz pulse mode, which is synchronized with the pump laser by external triggering signal. The shutter in the probe beam path is opened every 1 second, and is synchronized with triggering the signal acquisition by a Tektronix TDS 680 C oscilloscope (by another shutter, passing a fraction of light separated from pumping beam by a beam splitter in order to reach a photodiode). The shutter in the pump beam path (before the sample) is opened once per 2 probe pulses. A white light beam guided by an optical fiber from Xe arc lamp, is focused on a sample by a lens terminating the fiber. Subsequently it is spectrally confined by interference band-pass filter (10 nm at FWHM) to minimize irradiation of the sample by the probe light. A diameter of the beam is set by diaphragms situated on either sides of a sample. Subsequently the probe beam is filtered again in order to stop scattered photons originating from the pump. The beam is finally focused on the monochromator's (SpectraPro 300i) slit by the set of two lenses. The light signal is detected by R928 Hamamatsu photomultiplier coupled with oscilloscope. For a sufficient signal to noise ratio, multiple kinetics are measured and averaged.

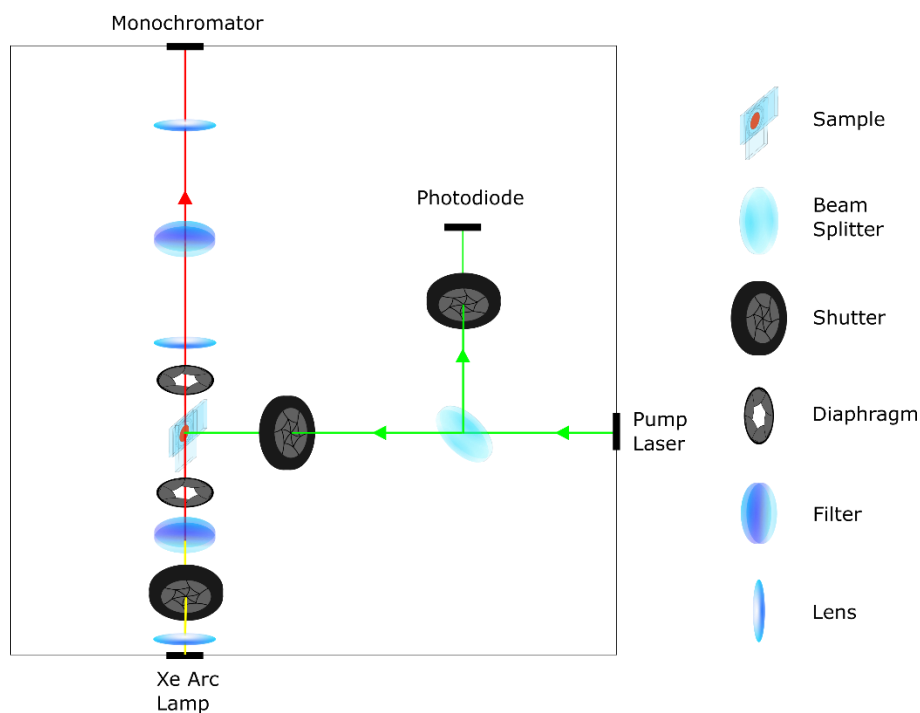


Figure 10. Simplified scheme of the ns TAS setup. Description in the text.

4.2.5.2 UV-VIS-NIR Femtosecond Transient Absorption Spectroscopy

The experimental setup (Figure 11) used for UV-VIS-NIR (where NIR is near infrared) TAS in 0.2 ps – 3 ns time window is a commercial Helios Femtosecond Transient Absorption Spectrometer, provided by Ultrafast Systems. The light source for the spectrometer, is a laser system provided by Spectra Physics, consisting of a Mai Tai Diode-Pumped, Mode-Locked Ti:Sapphire laser emitting <100 fs light pulses, which are subsequently amplified in Spitfire Ace Ti:Sapphire Regenerative Amplifier, which is pumped by a high power Empower Q-Switched Nd:YLF laser. The beam of light pulses ($\lambda = 800 \text{ nm}$ ~100 fs long (FWHM) with 1 kHz repetition frequency) is subsequently split into the pump and probe beams. The probe beam is then directed to the Helios spectrometer.

The pump beam of higher power is introduced to the TOPAS Prime (Spectra Physics, Light Conversion) unit which is an optical parametric amplifier (OPA), where primary photons are converted to pairs of signal and idler photons of different wavelengths, depending on the OPA tuning. The signal and idler wavelengths are then mixed in a NIRUVIS (Spectra Physics, Light Conversion) unit and a desired wavelength is separated

from the residual signal and idler photons on dichroic mirrors. Ultimately, the pump beam is guided to the Helios Spectrometer.

In the Helios Spectrometer section, prior to reaching the sample, the pump beam is properly prepared. First, the beam passes through a depolarizer. Subsequently, the pulse power is adjusted by neutral density filter to achieve a desired pulse energy. Then, every second pulse is stopped by the chopper. Finally, the pump beam passes through the lens, which focuses it on a sample.

The probe beam is first directed to the delay line, which is a system of mirrors where the optical path length can be adjusted by the position of the retroreflector placed on the motorized stage. In this way the time delay between pump and probe pulses is adjusted with fs resolution. In the next step, the power of the primary probe beam at 800 nm is adjusted by a neutral density filter, to provide proper conditions for white light continuum (WLC) generation (also called supercontinuum generation) by focusing the 800 nm pulses in the proper crystal. There quasi-monochromatic pulse is converted to the pulse of continuous wavelengths spanning in the range that depends on the crystal used: UV-VIS for CaF₂, VIS for sapphire and NIR for YAG crystal. After white light pulses are formed, the beam passes through 750 nm low pass interference filter in order to cut out residual 800 nm photons (primary pump beam wavelength). The beam is then focused on the sample at the site tightly overlapping that of the pump pulse. After transmission through the sample, the beam power can be again adjusted by a neutral density filter to prevent detector's saturation. Finally the system of two lenses focuses the beam on the entrance to the optical fiber leading the light to the broadband detector. For a better signal to noise ratio and for assessment of the examined sample stability, multiple scans are performed and subsequently averaged.

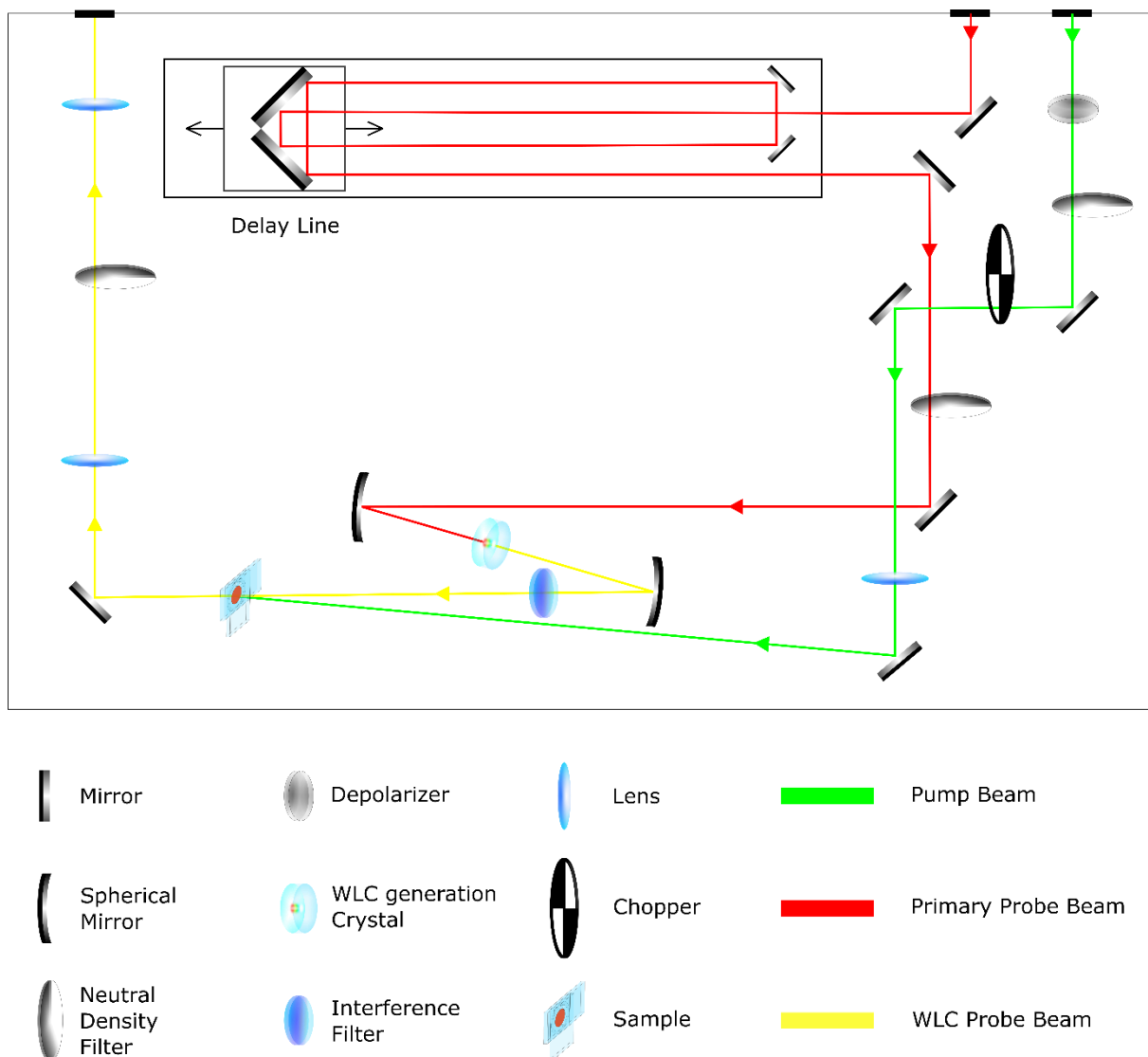


Figure 11. Simplified scheme of Helios transient absorption spectrometer, in VIS mode.

The courses of the beams are described in the text.

In the above described experiment, a matrix of data in the form $\Delta A(\lambda_i, t_j)$ is obtained. After proper conditioning, including reducing of the artifacts caused by scattered light reaching the detector and temporal dispersion of white light continuum components (the so-called chirp) the data can be further processed.

Since $\Delta A(\lambda, t)$ may be difficult for direct interpretation, a global analysis can be applied to distinguish n_k different time constants k of the observed transient absorption decays and wavelength dependent amplitudes $a(\lambda)$ associated with them (sometimes also called decay

associated difference spectra). Moreover, the measured TA signal is the convolution of the fitted multi-exponential function with the instrument response function ($IRF(\lambda, t)$):

$$\Delta A(\lambda, t) = IRF(\lambda, t) \otimes \sum_{i=1}^{n_k} a_n(\lambda) e^{-k_n t} \quad (15)$$

IRF is the pump-probe temporal cross-correlation function, and in the fitting procedure it is usually modelled as a Gaussian function of certain FWHM (~ 200 fs).

Global analysis does not require assuming any model before fitting.¹²³ However, such an operation on a large data matrix would require considerable computing resources, thus singular value decomposition (SVD) is applied first, to substantially simplify the problem.¹²⁴ All described operations can be performed by Surface Explorer software provided by the Ultrafast Systems.

SVD used before fit, provides a set of principal components which include basis spectra and associated with them time dependent amplitude vectors. These spectra are not the recorded ones, but are determined by the mathematical properties of SVD. The minimal number of necessary principle components can be determined by visual inspection of signal to noise ratio in successive amplitude vectors. Usually, a subset of first 2 - 3 principle components contains nearly the whole relevant information carried by the data matrix and is enough to describe $\Delta A(\lambda_i, t_j)$ within experimental resolution, which means a great reduction of the number of data to be fitted.⁹ Once the SVD is executed, the global analysis can be easily accomplished on the basis of a set of principal components: the fitting given by equation (15) is only performed on the limited number of principle kinetics vectors, instead of fitting the kinetics at all wavelengths. The number of global analysis components (n_k) can be presumed by estimation of the anticipated number of relaxation processes in the system, however, due to spectral and temporal overlapping of different species contributions, it is possible that some components may not represent particular processes, but a superposition of more than one of them. In order to give interpretation of global analysis components, a careful evaluation of their pre-exponential factor spectra is necessary.

4.2.5.3 MIR Femtosecond Transient Absorption Spectroscopy

The idea of fs TAS experiment in MIR (mid infrared) is the same as in VIS range, but the realization varies significantly. The first difference is that the MIR setup uses another TOPAS prime OPA coupled with NDFG (Spectra Physics, Coherent) unit to tune the probe beam to a desired wavelength in the MIR spectral range. A 2DQuick IR Transient spectrometer supplied by PHASETECH was used in the standard VIS-pump MIR-probe mode, which makes detailed description of this setup redundant. The important feature is a delay line in the VIS pump beam course, in which a beam needs to be carefully aligned. A probe beam is detected in a Horiba iHR 320 spectrograph by a Liquid Nitrogen cooled HgCdTe array detector (InfraRed associates Inc.). In order to enhance the signal to noise ratio, multiple scans can be performed. Furthermore for accurate measurement of kinetics of TA with nonspecific spectra (like originating from electrons in semiconductors CB) the kinetics may be averaged over some range of wavelengths.

5. Realization of the Aims of the Thesis

Paper I

In this paper the dynamics of electron injection from dye to titania and recombination from titania to oxidized dye or oxidized redox agent was studied on titania/dye/electrolyte interfaces modified by two different post-assembly passivation treatments (Atomic Layer Deposition of Al_2O_3 and hierarchical multi-capping by a sequence of different compounds possessing various acidic moieties and alkyl chain lengths). The treatments were applied to solar cells sensitized with top efficient carbazole dye ADEKA-1, possessing alkoxy-silyl anchoring unit and its popular carboxylic analogue MK-2 (Figure 12), and mediated by $\text{Co}^{2+/3}(\text{bpy})_3$ redox couple (Figure 13A).

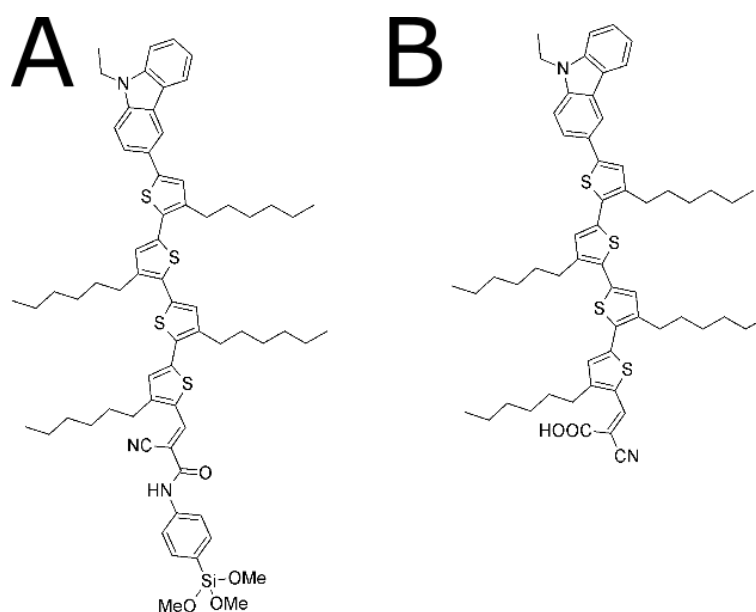


Figure 12. (A) ADEKA-1 dye and (B) MK-2 dye molecular structures.

Both methods of passivation, improved V_{OC} and FF of the cells, due to extension of lifetime of the electrons injected to titania CB. However, the value J_{SC} corrected for the number of absorbed photons ($total_APCE$) was reduced in both cases. Moreover, the value of $total_APCE$ was found to be proportional to the amplitude of residual TA signal (at 3 ns time delay), originating from the oxidized dye, thus representing the amount of successfully separated charge. This relationship indicates a dependence between J_{SC} and

ultrafast and fast charge separation efficiency. Although the recombination from titania CB to the oxidized dye was found to be slowed down upon passivation, it affected a greater fraction of injected electrons. The injection process was also found to be slowed down in modified systems. Additional conclusion coming from this study was that alkoxy-silyl anchoring group limits desorption of the dye in the multi-capping process, however, it does not suppress it entirely within applied set of acids and its concentrations. Alkoxy-silyl anchoring derivative was also more resistant to high temperature applied in ALD reactor in comparison with the carboxylic one. The efficiency of DSSCs with MK-2 was also found to be enhanced by the addition of CDCA co-adsorbing agent.

Paper II

The same carbazole sensitizers as in Paper I were applied in the systems comprising aqueous electrolyte based on $\text{Co}^{2+/3+}(\text{phen})_3$ redox couple (Figure 13B) and with different pH values (different 1-methylbenzimidazole (MBI) base concentration). Furthermore, different morphologies of photoanodes – transparent mesoporous titania layer containing ~ 30 nm beads and opaque layers with incorporated large ~ 400 nm particles were applied in photoanodes of different thicknesses. In the samples prepared on transparent titania, ultrafast and fast electron transfer processes were studied in the cells containing different electrolyte compositions and were compared with standard systems based on organic solvent (acetonitrile). Also a thoughtful comparison of photovoltaic performances of different systems was provided.

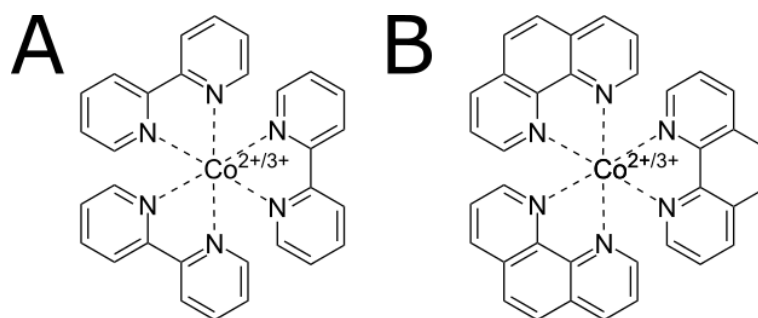


Figure 13. (A) $\text{Co}^{2+/3+}(\text{bpy})_3$ redox couple and (B) $\text{Co}^{2+/3+}(\text{phen})_3$ redox couple molecular structures.

In general the DSSCs with aqueous electrolyte performed much worse than those based on ACN. However, alkoxyethyl anchoring moiety was found to be advantageous in comparison with carboxylic one, providing ~ 60 % higher V_{OC} in aqueous electrolyte. On the other hand, J_{SC} of the cells with ADEKA-1 was always about 75 % of those with MK-2 dye. Also the stability of the devices was enhanced thanks to a stronger anchoring group. Finally, the concentration of MBI was found to be crucial for wettability of the cells with ADEKA-1 dye and OTMS as co-adsorbate. The situation was different for the cells with MK-2 and co-adsorbing CDCA, which is known to raise mesoporous titania wettability.

As in Paper I, the $total_APCE$ parameter was also closely related to ultrafast (up to 3 ns) charge separation dynamics. In the solar cells based on photoanodes with incorporated light scattering particles, the $total_APCE$ was found to be reduced in comparison with that in the transparent ones. Moreover, increasing the thickness of the photoanodes did not provide a clear enhancement in efficiency, which points out that in the solar cells sensitized with organic dyes (having high extinction coefficients), the small gains in LHE provided by modifications of photoanodes morphology, may be easily frustrated by increased recombination.

The rate constants of electron injection from the dye to titania and of back electron transfer to the oxidized dye, were found to be well correlated in different systems, and the conclusion was that the dynamics of both processes were controlled mainly by electronic coupling between the dye's molecular orbitals and titania CB. In aqueous electrolyte, both charge transfer processes were retarded due to possible adsorption of water molecules on the titania surface.

Another conclusion coming from this study was the possibility of application of bias irradiation to change the position of quasi-Fermi level in TAS experiment in order to study charge transfer processes in the conditions more similar to the operating conditions of solar cells.

Paper III

In this paper a new sensitizer D149Si, which is a alkoxyethyl anchoring derivative of popular indoline D149 dye, was introduced (Figure 14). The performances of both derivatives were compared in the presence of standard electrolyte comprising I^-/I_3^- redox

couple or more modern $\text{Co}^{2+/3+}(\text{bpy})_3$ mediator, providing higher attainable V_{OC} . Additionally, two different molecular-capping procedures were applied.

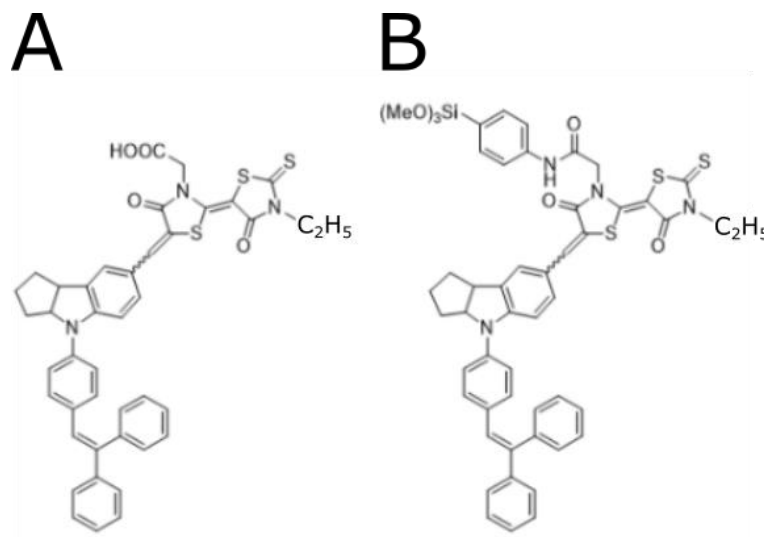


Figure 14. (A) D149 dye and (B) D149Si dye molecular structures.

The alkoxy silyl anchoring group was confirmed to be more resistant to desorption from titania surface, but photovoltaic performance of both derivatives was very similar. In the cells comprising I^-/I_3^- based electrolyte, the use of alkoxy silyl derivative permitted reaching higher efficiency due to slightly higher V_{OC} and J_{SC} . Furthermore, substitution of I^-/I_3^- based electrolyte by Co complex based one, also led to an increase in efficiency. Another advantage of using the Co based electrolyte was a significant enhancement of the stability of the devices. Ultimately the surface modification by molecular-capping brought enhancements in J_{SC} and total_APCE which was explained as a result of retardation of the decay of dyes' excited states due to limited self-quenching. Thus, capping of the molecules reduced the interactions between adjacent dye molecules and hence increased the quantum yield of electron injection.

Paper IV

This paper reports the effects of modification of another popular and highly efficient indoline sensitizer (D205) by substitution of carboxylic anchoring group by alkoxy silyl moiety (Figure 15A-B). The modified sensitizer was studied in combination with

$\text{Cu}^{+/2+}(\text{tmby})_2$ based electrolyte (Figure 15C) and original interface modifications. A newly developed multi-capping procedure was introduced (optimized to be used with D205 dye derivatives) and titania/dye/electrolyte interface was modified by cucurbit[7]uril molecules (Figure 15D). The latter are able to encapsulate some dye molecule's sections. The above-mentioned modifications were applied in attempt to block increased back electron transfer from titania to oxidized redox agent, occurring in systems comprising one-electron redox mediators based on transition metal complexes. In order to evaluate the effectiveness of this approach, a reference system comprising benchmark Y123 triphenylamine dye (Figure 16), with bulky moieties blocking the approach of oxidized redox species to titania surface, was applied.

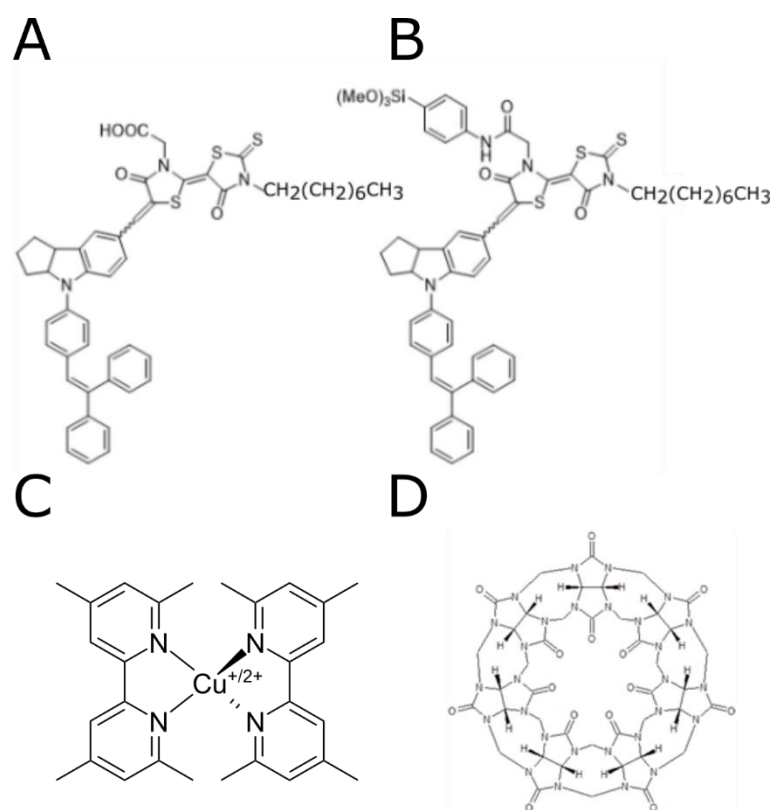


Figure 15. (A) D205 dye, (B) D205Si dye, (C) $\text{Cu}^{+/2+}(\text{tmby})_2$ redox couple and (D) cucurbit[7]uril molecular structures.

In the cells comprising photoanodes without modifications, the PCE values of the solar cells sensitized with indoline dyes were much lower than that of the cell with Y123, due

to the mentioned severe recombination in the absence of bulky blocking moieties. However, the interface modifications were found to enhance the photovoltaic performance of D205 dye derivatives (especially of the one with alkoxyethyl anchoring group) due to additional steric hindrance causing a rise in charge transfer resistance (confirmed in EIS) and increasing the electron lifetime in the titania's CB. Interestingly, the same modifications did not improve the performance of Y123 sensitized cells.

Another important outcome of the study was the observation of exceptionally fast reduction of oxidized indoline dyes by $[\text{Cu}(\text{tmby})_2]^+$ occurring with a time constant smaller than 100 ns, which has been up to date the fastest ever observed dye regeneration in DSSC with liquid non-tandem electrolyte.

Paper V

This paper concerns the performance of DSSCs and perovskite solar cells (PSCs), however only the part including the study of DSSCs is considered relevant for this thesis.

Titania photoanodes modification was introduced on the stage of screen-printable paste preparation, namely a solution of ethyl-cellulose in a mixture of α -terpineol and ethanol, was added in order to provide higher porosity of titania substrates. The layers prepared from the so-modified paste, were compared with the ones made with the use of unmodified commercially available paste in the standard liquid DSSC configuration (comprising MK-2 sensitizer and $\text{Co}^{2+/3+}(\text{bpy})_3$ or $\text{Co}^{2+/3+}(\text{phen})_3$ based electrolytes) as well as in the solid state (S-DSSC) architecture comprising Spiro-OMeTAD as hole transporting material and sputtered golden electrode. The S-DSSCs were also prepared on thin spin-coated titania layers such as used for PSCs.

As a result of the screen-printable paste dilution, not only the size of pores has grown but also the thickness of the layers has decreased. Despite that, high LHE was maintained (absorbance > 1.5 at maximum and only 10 ~ 12% lower number of absorbed photons - N_{Ph}) indicating higher dye-load on the "diluted" photoanodes. Consequently, PCE of the so-modified solar cells was higher, mainly thanks to the rise in V_{OC} . Also the *total_APCE* was enhanced pointing to a higher charge separation efficiency. The latter was explained in broadband VIS femtosecond TAS measurements confirming retardation of fast titania-oxidized dye recombination.

The effect of screen-printable paste “dilution” was also beneficial for S-DSSCs whose efficiency was enhanced due to the rise of V_{OC} and FF . This result was assigned to better pore-filling which was the best in the cells comprising spin-coated mesoporous titania layers, however, in this case LHE was very low due to low titania thickness, limiting attainable J_{SC} .

Paper VI

This paper was focused on electron transfer dynamics between Y123 triphenylamine dye (Figure 16) and titania mesoporous scaffold. The study was performed on DSSCs prepared on transparent titania films in combination with $Co^{2+/3+}(bpy)_3$ or $Cu^{+/2+}(tmbpy)_2$ based electrolytes, by broadband VIS femtosecond TAS measurements. Also half-cells were prepared on sapphire substrates (instead of FTO coated glass) in order to provide sufficient transparency in MIR to enable femtosecond TAS measurements in this spectral range, which was essential for proper characterization of electron injection process. Moreover, the effects of continuous steady-state irradiation (the so-called light soaking effects) on ultrafast and fast electron transfer processes were studied and a comparison with MK-2 dye sensitized cells was made.

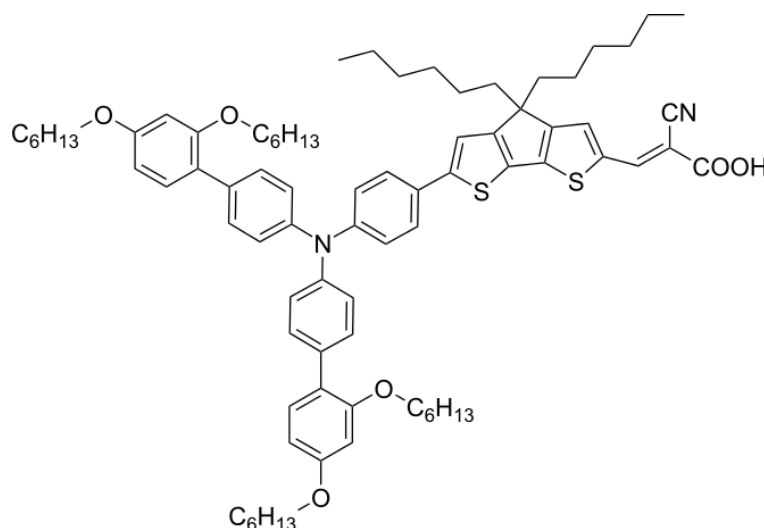


Figure 16. Y123 dye molecular structure.

The electron injection from the excited state of Y123 dye to titania CB was found to occur biphasically with the faster time constant of about 350 fs and the slower - within 80 – 95 ps. We ascribed the fastest component to the injection occurring from hot S_1 (Frank-

Condon) state and the slower one happening from the relaxed S_1 state. The contribution of the fastest process was significantly decreasing along with decreasing pump pulse energy densities, thus the slower one can be considered as dominating in the operating conditions.

Furthermore, in systems comprising both studied dyes (Y123 and MK-2), we observed the acceleration of injection process caused by light soaking effects associated with the down-shift of titania CB edge energy. In the cells with MK-2 sensitizer, a back electron transfer from titania CB to the oxidized dye was slowed down. Moreover, higher estimated charge separation efficiency (up to 3 ns) was observed in the systems comprising both dyes, which was directly correlated with the photocurrent increase upon illumination.

6. Conclusions

Dye Sensitized Solar Cells are pretty complex systems. In-depth understanding of their operation requires knowledge of solid state physics, molecular physics, electrochemistry, surface physics, nanomaterials science and a variety of other related fields. Continuous development of the components and processes applied in composition and production of DSSC needs endless efforts aimed at characterization of new materials and explanation of phenomena taking place in them and their interrelations. For this reason, we studied the effects of diverse modifications applied in order to potentially improve DSSCs, how they affect the ultrafast and fast charge transfer processes, and we investigated the relation between the dynamics of particular charge transfer phenomena and to the overall DSSC performance. The modifications were studied in complete operating DSSC devices, using a variety of experimental methods.

One of the main approaches to improve the DSSC performance studied in this thesis was to check the effects of different treatments of semiconductor's surface, previously sensitized by a dye with alkoxy-silyl anchoring moiety (which is stronger than the commonly used carboxylic group). Such a remedy for undesired charge recombination processes can be considered as an alternative to more commonly used application of bulky aromatic moieties and alkyl chains, functionalizing the sensitizers. Limiting titania-electrolyte recombination is especially important (and intensified in the research) in the systems containing novel one-electron redox mediators, based on organometallic transition metal complexes (in comparison to the standard I/I_3^- based electrolyte). Although this approach has been successfully applied by Prof. Hanaya group,^{13,56,108} establishing the long standing laboratory DSSC efficiency record, it turns out to be advantageous only in some particular conditions including high additional steric hindrance provided by applied modification and very high dye-load. These requirements are difficult to meet simultaneously, which was shown in our contributions. Nevertheless, we have significantly furthered the knowledge on the impact of this kind of modifications on charge transfer processes dynamics and their relationships with overall device performance in a considerable set of systems comprising highly efficient carbazole and indoline dyes as well as various, up-to-date redox mediators.

Furthermore, the effects of using water, instead of organic solvent in the electrolyte solution, together with varying of its basicity, on the charge transfer dynamics were described in the thesis. Moreover, the influence of the changes in titania films morphology (content of large light-scattering particles, modification of film's thickness and pore size) on the overall performance and charge transfer processes kinetics was investigated. In our studies we have also thoroughly described the phenomenon of electron injection occurring from the benchmark triphenylamine Y123 dye to TiO₂. Ultimately, some modifications caused by continuous illumination of the solar cells were examined. One of the most important results revealed in this dissertation was also observation of the direct correlation between the relative photocurrent of the cells and the efficiency of fast charge separation (measured at few nanoseconds after excitation). Such correlations were confirmed for various systems, suggesting that it is a universal feature of many DSSC systems.

Summarizing, the studies described in this thesis, have substantially broadened the knowledge on the charge transfer processes occurring on the semiconductor/dye/electrolyte interface in DSSCs. We believe that our efforts have already contributed to the development of the field and will help in further progress in future.

References

- (1) Dansgaard, W.; Johnsen, S. J.; Clausen, H. B.; Dahl-Jensen, D.; Gundestrup, N. S.; Hammer, C. U.; Hvidberg, C. S.; Steffensen, J. P.; Sveinbjörnsdóttir, A. E.; Jouzel, J.; et al. *Nature* **1993**, *364*, 218–220.
- (2) Cox, P. M.; Betts, R. A.; Jones, C. D.; Spall, S. A.; Totterdell, I. J. *Nature* **2000**, *408*, 184–187.
- (3) Parmesan, C.; Yohe, G. *Nature* **2003**, *421*, 37–42.
- (4) Engström, G.; Gars, J.; Jaakkola, N.; Lindahl, T.; Spiro, D.; van Benthem, A. A. *Environ. Resour. Econ.* **2020**, *76*, 789–810.
- (5) Fujishima, A.; Honda, K. *Nature* **1972**, *238*, 37–38.
- (6) Gerischer, H.; Michel-Beyerle, M. E.; Rebentrost, F.; Tributsch, H. *Electrochim. Acta* **1968**, *13*, 1509–1515.
- (7) Augustynski, J.; Vlachopoulos, N.; Liska, P.; Grätzel, M. *J. Am. Chem. Soc.* **1988**, *110*, 1216–1220.
- (8) O'Regan, B.; Gratzel, M. *Nature* **1991**, *353*, 737–740.
- (9) Hagfeldt, A.; Boschloo, G.; Sun, L.; Kloo, L.; Pettersson, H. *Chem. Rev.* **2010**, *110*, 6595–6663.
- (10) Freitag, M.; Boschloo, G. *Curr. Opin. Electrochem.* **2017**, *2*, 111–119.
- (11) Martín, C.; Ziólek, M.; Douhal, A. *J. Photochem. Photobiol. C Photochem. Rev.* **2016**, *26*, 1–30.
- (12) Vlachopoulos, N.; Hagfeldt, A.; Benesperi, I.; Freitag, M.; Hashmi, G.; Jia, G.; Wahyuono, R. A.; Plentz, J.; Dietzek, B. *Sustain. Energy Fuels* **2021**, *5*, 367–383.
- (13) Kakiage, K.; Aoyama, Y.; Yano, T.; Oya, K.; Fujisawa, J.; Hanaya, M. *Chem. Commun.* **2015**, *51*, 15894–15897.
- (14) Yella, A.; Lee, H.-W.; Tsao, H. N.; Chenyi, Y.; Chandiran, A. K.; Nazeeruddin, M. K.; Diao, E. W.-G.; Yeh, C.-Y.; Zakeeruddin, S. M.; Grätzel, M. *Science* (80-

-). **2011**, *334*, 629–634.
- (15) Ji, J. M.; Zhou, H.; Eom, Y. K.; Kim, C. H.; Kim, H. K. *Adv. Energy Mater.* **2020**, *10*, 1–12.
- (16) Mathew, S.; Yella, A.; Gao, P.; Humphry-Baker, R.; Curchod, B. F. E.; Ashari-Astani, N.; Tavernelli, I.; Rothlisberger, U.; Nazeeruddin, M. K.; Grätzel, M. *Nat. Chem.* **2014**, *6*, 242–247.
- (17) Chebrolu, V. T.; Kim, H.-J. *J. Mater. Chem. C* **2019**, *7*, 4911–4933.
- (18) Jena, A. K.; Kulkarni, A.; Miyasaka, T. *Chem. Rev.* **2018**, *119*, 3036–3103.
- (19) Roy, P.; Kumar Sinha, N.; Tiwari, S.; Khare, A. *Sol. Energy* **2020**, *198*, 665–688.
- (20) Freitag, M.; Teuscher, J.; Saygili, Y.; Zhang, X.; Giordano, F.; Liska, P.; Hua, J.; Zakeeruddin, S. M.; Moser, J.-E.; Grätzel, M.; et al. *Nat. Photonics* **2017**, *11*, 372–378.
- (21) Cao, Y.; Liu, Y.; Zakeeruddin, S. M.; Hagfeldt, A.; Grätzel, M. *Joule* **2018**, *2*, 1108–1117.
- (22) Michaels, H.; Rinderle, M.; Freitag, R.; Benesperi, I.; Edvinsson, T.; Socher, R.; Gagliardi, A.; Freitag, M. *Chem. Sci.* **2020**, *11*, 2895–2906.
- (23) Shafique, K.; Khawaja, B. A.; Sabir, F.; Qazi, S.; Mustaqim, M. *IEEE Access* **2020**, *8*, 23022–23040.
- (24) Ng, C. H.; Lim, H. N.; Hayase, S.; Harrison, I.; Pandikumar, A.; Huang, N. M. *J. Power Sources* **2015**, *296*, 169–185.
- (25) Tian, H.; Boschloo, G.; Hagfeldt, A. *Molecular Devices for Solar Energy Conversion and Storage*, 1st ed.; Tian, H., Boschloo, G., Hagfeldt, A., Eds.; Springer, 2018.
- (26) Sharma, S.; Ali, K. *Solar Cells From Materials to Device Technology*, 1st ed.; Sharma, S., Ali, K., Eds.; Springer International Publishing, 2020.
- (27) Shockley, W.; Queisser, H. J. *J. Appl. Phys.* **1961**, *32*, 510–519.
- (28) Benesperi, I.; Michaels, H.; Freitag, M. *J. Mater. Chem. C* **2018**, *6*, 11903–11942.

- (29) Xu, P.; McCool, N. S.; Mallouk, T. E. *Nano Today* **2017**, *14*, 42–58.
- (30) Swierk, J. R.; Mallouk, T. E. *Chem. Soc. Rev.* **2013**, *42*, 2357–2387.
- (31) Grätzel, M. *Nature* **2001**, *414*, 338–344.
- (32) Cinnsealach, R.; Boschloo, G.; Rao, S. N.; Fitzmaurice, D. *Sol. Energy Mater. Sol. Cells* **1999**, *57*, 107–125.
- (33) Ola, O.; Maroto-Valer, M. M. *J. Photochem. Photobiol. C Photochem. Rev.* **2015**, *24*, 16–42.
- (34) Saygili, Y.; Söderberg, M.; Pellet, N.; Giordano, F.; Cao, Y.; Munoz-García, A. B.; Zakeeruddin, S. M.; Vlachopoulos, N.; Pavone, M.; Boschloo, G.; et al. *J. Am. Chem. Soc.* **2016**, *138*, 15087–15096.
- (35) Freitag, M.; Giordano, F.; Yang, W.; Pazoki, M.; Hao, Y.; Zietz, B.; Gra, M.; Hagfeldt, A.; Boschloo, G. *J. Phys. Chem. C* **2016**, *120*, 9595–9603.
- (36) Freitag, M.; Daniel, Q.; Pazoki, M.; Sveinbjörnsson, K.; Zhang, J.; Sun, L.; Hagfeldt, A.; Boschloo, G. *Energy Environ. Sci.* **2015**, *8*, 2634–2637.
- (37) Cao, Y.; Saygili, Y.; Ummadisingu, A.; Teuscher, J.; Luo, J.; Pellet, N.; Giordano, F.; Zakeeruddin, S. M.; Moser, J.-E.; Freitag, M.; et al. *Nat. Commun.* **2017**, *8*, 15390.
- (38) Hsien, Y. H.; Chang, C. F.; Chen, Y. H.; Cheng, S. *Appl. Catal. B Environ.* **2001**, *31*, 241–249.
- (39) Burke, A.; Ito, S.; Snaith, H.; Bach, U.; Kwiatkowski, J.; Grätzel, M. *Nano Lett.* **2008**, *8*, 977–981.
- (40) Kavan, L.; Grätzel, M. *Electrochim. Acta* **1995**, *40*, 643–652.
- (41) Zhang, Z.; Ito, S.; O'Regan, B.; Kuang, D.; Zakeeruddin, S. M.; Liska, P.; Charvet, R.; Comte, P.; Nazeeruddin, M. K.; Péchy, P.; et al. *Zeitschrift für Phys. Chemie* **2007**, *221*, 319–327.
- (42) Ito, S.; Murakami, T. N.; Comte, P.; Liska, P.; Grätzel, C.; Nazeeruddin, M. K.; Grätzel, M. *Thin Solid Films* **2008**, *516*, 4613–4619.
- (43) García-Rodríguez, R.; Jiang, R.; Canto-Aguilar, E. J.; Oskam, G.; Boschloo, G.

- Phys. Chem. Chem. Phys.* **2017**, *19*, 32132–32142.
- (44) Jiang, R.; Boschloo, G. *Inorganics* **2018**, *6*.
- (45) Zhu, L.; Zhao, Y. L.; Lin, X. P.; Gu, X. Q.; Qiang, Y. H. *Superlattices Microstruct.* **2014**, *65*, 152–160.
- (46) Vittal, R.; Ho, K. C. *Renew. Sustain. Energy Rev.* **2017**, *70*, 920–935.
- (47) Li, Z.; Zhou, Y.; Sun, R.; Xiong, Y.; Xie, H.; Zou, Z. *Chinese Sci. Bull.* **2014**, *59*, 2122–2134.
- (48) Guo, P.; Aegerter, M. A. *Thin Solid Films* **1999**, *351*, 290–294.
- (49) Shakeel Ahmad, M.; Pandey, A. K.; Abd Rahim, N. *Renew. Sustain. Energy Rev.* **2017**, *77*, 89–108.
- (50) Mor, G. K.; Varghese, O. K.; Paulose, M.; Shankar, K.; Grimes, C. A. *Sol. Energy Mater. Sol. Cells* **2006**, *90*, 2011–2075.
- (51) Ko, S. H. *Smart Sci.* **2014**, *2*, 54–62.
- (52) Gangadharan, D. T.; Xu, Z.; Liu, Y.; Izquierdo, R.; Ma, D. *Nanophotonics* **2017**, *6*, 153–175.
- (53) Yun, M. J.; Sim, Y. H.; Cha, S. I.; Seo, S. H.; Lee, D. Y. *Sci. Rep.* **2017**, *7*, 1–10.
- (54) Bella, F.; Verna, A.; Gerbaldi, C. *Mater. Sci. Semicond. Process.* **2018**, *73*, 92–98.
- (55) Shalini, S.; Balasundaraprabhu, R.; Satish Kumar, T.; Prabavathy, N.; Senthilarasu, S.; Prasanna, S. *Int. J. Energy Res.* **2016**, *40*, 1303–1320.
- (56) Kakiage, K.; Aoyama, Y.; Yano, T.; Oya, K.; Kyomen, T.; Hanaya, M. *Chem. Commun.* **2015**, *51*, 6315–6317.
- (57) Fournier, M.; Hoogeveen, D. A.; Bonke, S. A.; Spiccia, L.; Simonov, A. N. *Sustain. Energy Fuels* **2018**, *2*, 1707–1718.
- (58) Castellucci, E.; Monini, M.; Bessi, M.; Iagatti, A.; Bussotti, L.; Sinicropi, A.; Calamante, M.; Zani, L.; Basosi, R.; Reginato, G.; et al. *Phys. Chem. Chem. Phys.* **2017**, *19*, 15310–15323.

- (59) Zhang, L.; Cole, J. M. *ACS Appl. Mater. Interfaces* **2015**, *7*, 3427–3455.
- (60) Wiberg, J.; Marinado, T.; Hagberg, D. P.; Sun, L.; Hagfeldt, A.; Albinsson, B. *Chart* **2009**, 3881–3886.
- (61) Aghazada, S.; Nazeeruddin, M. K. *Inorganics* **2018**, *6*.
- (62) Nazeeruddin, M. K.; Kay, A.; Rodicio, I.; Humphry-Baker, R.; Mueller, E.; Liska, P.; Vlachopoulos, N.; Graetzel, M. *J. Am. Chem. Soc.* **1993**, *115*, 6382–6390.
- (63) Sekar, N.; Gehlot, V. Y. *Resonance* **2010**, *15*, 819–831.
- (64) Hardin, B. E.; Snaith, H. J.; McGehee, M. D. *Nat. Photonics* **2012**, *6*, 162–169.
- (65) Ning, Z.; Zhang, Q.; Wu, W.; Tian, H. *J. Organomet. Chem.* **2009**, *694*, 2705–2711.
- (66) Harlang, T. C. B.; Liu, Y.; Gordivska, O.; Fredin, L. A.; Ponceca, C. S.; Huang, P.; Chábera, P.; Kjaer, K. S.; Mateos, H.; Uhlig, J.; et al. *Nat. Chem.* **2015**, *7*, 883–889.
- (67) Wang, J.; Li, C.; Wong, W. L.; Chow, C. F. *Russ. J. Electrochem.* **2018**, *54*, 1164–1175.
- (68) Dragonetti, C.; Magni, M.; Colombo, A.; Melchiorre, F.; Biagini, P.; Roberto, D. *ACS Appl. Mater. Interfaces* **2018**, *1*, 751–756.
- (69) Wang, Z. S.; Koumura, N.; Cui, Y.; Takahashi, M.; Sekiguchi, H.; Mori, A.; Kubo, T.; Furube, A.; Hara, K. *Chem. Mater.* **2008**, *20*, 3993–4003.
- (70) Ito, S.; Miura, H.; Uchida, S.; Takata, M.; Sumioka, K.; Liska, P.; Comte, P.; Péchy, P.; Grätzel, M. *Chem. Commun.* **2008**, *41*, 5194–5196.
- (71) Cappel, U. B.; Karlsson, M. H.; Pschirer, N. G.; Eickemeyer, F.; Scho, J.; Erk, P.; Boschloo, G.; Hagfeldt, A. *J. Phys. Chem. C* **2009**, 14595–14597.
- (72) Feldt, S. M.; Gibson, E. A.; Gabrielsson, E.; Sun, L.; Boschloo, G.; Hagfeldt, A. *J. Am. Chem. Soc.* **2010**, *132*, 16714–16724.
- (73) Ren, Y.; Flores-Díaz, N.; Zhang, D.; Cao, Y.; Decoppet, J. D.; Fish, G. C.; Moser, J. E.; Zakeeruddin, S. M.; Wang, P.; Hagfeldt, A.; et al. *Adv. Funct.*

Mater. **2020**, 2004804, 1–7.

- (74) Ellis, H.; Eriksson, S. K.; Feldt, S. M.; Gabrielsson, E.; Lohse, P. W.; Lindblad, R.; Sun, L.; Rensmo, H.; Boschloo, G.; Hagfeldt, A. *J. Phys. Chem. C* **2013**, *117*, 21029–21036.
- (75) Xu, W.; Peng, B.; Chen, J.; Liang, M.; Cai, F. *J. Phys. Chem. C* **2008**, *112*, 874–880.
- (76) Mahmood, A. *Sol. Energy* **2016**, *123*, 127–144.
- (77) Zhang, D.; Stojanovic, M.; Ren, Y.; Cao, Y.; Eickemeyer, F. T.; Socie, E.; Vlachopoulos, N.; Moser, J.-E.; Zakeeruddin, S. M.; Hagfeldt, A.; et al. *Nat. Commun.* **2021**, *12*, 2–11.
- (78) Jiang, X.; Marinado, T.; Gabrielsson, E.; Hagberg, D. P.; Sun, L.; Hagfeldt, A. *J. Phys. Chem. C* **2010**, *114*, 2799–2805.
- (79) Hao, Y.; Tian, H.; Cong, J.; Yang, W.; Bora, I.; Sun, L.; Boschloo, G.; Hagfeldt, A. *ChemPhysChem* **2014**, *15*, 3476–3483.
- (80) Iftikhar, H.; Sonai, G. G.; Hashmi, S. G.; Nogueira, A. F.; Lund, P. D.; Fl, A. *Materials (Basel)*. **2019**, *12*, 1998.
- (81) Feldt, S. M.; Lohse, P. W.; Kessler, F.; Nazeeruddin, M. K.; Grätzel, M.; Boschloo, G.; Hagfeldt, A. *Phys. Chem. Chem. Phys.* **2013**, *15*, 7087–7097.
- (82) Feldt, S. M. Uppsala University, 2013.
- (83) Yum, J.-H. H.; Baranoff, E.; Kessler, F.; Moehl, T.; Ahmad, S.; Bessho, T.; Marchioro, A.; Ghadiri, E.; Moser, J.-E. E.; Yi, C.; et al. *Nat. Commun.* **2012**, *3*, 631.
- (84) Zhang, W.; Wu, Y.; Bahng, H. W.; Cao, Y.; Yi, C.; Saygili, Y.; Luo, J.; Liu, Y.; Kavan, L.; Moser, J. E.; et al. *Energy Environ. Sci.* **2018**, *11*, 1779–1787.
- (85) Saygili, Y.; Stojanovic, M.; Flores-d, N.; Zakeeruddin, S. M.; Vlachopoulos, N.; Grätzel, M.; Hagfeldt, A. *Inorganics* **2019**, *7*, 30.
- (86) Mosconi, E.; Yum, J.-H. H.; Kessler, F.; Gomez Garcia, C. J.; Zuccaccia, C.; Cinti, A.; Nazeeruddin, M. K.; Graetzel, M.; De Angelis, F.; Garcia, C. J. G.; et

- al. *J. Am. Chem. Soc.* **2012**, *134*, 19438–19453.
- (87) Marcus, R. A. *J. Chem. Phys.* **1965**, *43*, 679–701.
- (88) Marcus, R. A. Sutin, N. *Biochim. Biophys. Acta* **1985**, *811*, 265–322.
- (89) Pradhan, S. C.; Hagfeldt, A.; Soman, S. *J. Mater. Chem. A* **2018**, *6*, 22204–22214.
- (90) Boschloo, G.; Ha, L.; Hagfeldt, A. *J. Phys. Chem. B* **2006**, *110*, 13144–13150.
- (91) Furer, S. O.; Milhuisen, R. A.; Kashif, M. K.; Raga, S. R.; Acharya, S. S.; Forsyth, C.; Liu, M.; Frazer, L.; Duffy, N. W.; Ohlin, C. A.; et al. *Adv. Energy Mater.* **2020**, *2002067*, 1–13.
- (92) Ellis, H.; Jiang, R.; Ye, S.; Hagfeldt, A.; Boschloo, G. *Phys. Chem. Chem. Phys.* **2016**, *18*, 8419–8427.
- (93) Yang, X.; Zhang, S.; Zhang, K.; Liu, J.; Qin, C.; Chen, H.; Islam, A.; Han, L. *Energy Environ. Sci.* **2013**, *6*, 3637–3645.
- (94) Nazeeruddin, M. K.; Kay, A.; Miiller, E.; Liska, P.; Vlachopoulos, N.; Gratzel, M.; Lausanne, C.-; April, R. *J. Am. Chem. Soc.* **1993**, *115*, 6382–6390.
- (95) Gao, J.; Yang, W.; El-zohry, A. M.; Prajapati, G. K.; Fang, Y.; Dai, J.; Hao, Y.; Leandri, V.; Svensson, P. H.; Boschloo, G.; et al. **2019**, 19495–19505.
- (96) Hoffeditz, W. L.; Katz, M. J.; Deria, P.; Cutsail, G. E.; Pellin, M. J.; Farha, O. K.; Hupp, J. T. *J. Phys. Chem. C* **2016**, *120*, 3731–3740.
- (97) Iftikhar, H.; Sonai, G. G.; Hashmi, S. G.; Fl, A. *Materials (Basel)*. **2019**, *12*, 1998.
- (98) Bella, F.; Gerbaldi, C.; Barolo, C.; Gratzel, M. *Chem. Soc. Rev.* **2015**, *44*, 3431–3473.
- (99) Bella, F.; Galliano, S.; Falco, M.; Viscardi, G.; Barolo, C.; Gratzel, M.; Gerbaldi, C. *Green Chem.* **2017**, *19*, 1043–1051.
- (100) Galliano, S.; Bella, F.; Bonomo, M.; Giordano, F.; Gratzel, M.; Viscardi, G.; Hagfeldt, A.; Gerbaldi, C.; Barolo, C. *Sol. RRL* **2021**.

- (101) Xiang, W.; Huang, F.; Cheng, Y.-B.; Bach, U.; Spiccia, L. *Energy Environ. Sci.* **2013**, *6*, 121–127.
- (102) Saito, H.; Uegusa, S.; Murakami, T. N.; Kawashima, N.; Miyasaka, T. *Electrochemistry* **2004**, *72*, 310–316.
- (103) Chen, M.; Shao, L.-L. *Chem. Eng. J.* **2016**, *304*, 629–645.
- (104) Ellis, H.; Vlachopoulos, N.; Häggman, L.; Perruchot, C.; Jouini, M.; Boschloo, G.; Hagfeldt, A. *Electrochim. Acta* **2013**, *107*, 45–51.
- (105) Wei, W.; Wang, H.; Hu, Y. H. *Int. J. Energy Res.* **2014**, *38*, 1099–1111.
- (106) Yang, A.-N.; Lin, J. T.; Li, C.-T. *ACS Appl. Mater. Interfaces* **2021**, *13*, 8435–8444.
- (107) Saygili, Y.; Stojanovic, M.; Michaels, H.; Tjepelt, J.; Teuscher, J.; Massaro, A.; Pavone, M.; Giordano, F.; Zakeeruddin, S. M.; Boschloo, G.; et al. *ACS Appl. Energy Mater* **2018**, *1*, 4950–4962.
- (108) Kakiage, K.; Aoyama, Y.; Yano, T.; Otsuka, T.; Kyomen, T.; Unno, M.; Hanaya, M. *Chem. Commun.* **2014**, *50*, 6379–6381.
- (109) Glinka, A.; Gierszewski, M.; Gierczyk, B.; Burdziński, G.; Michaels, H.; Freitag, M.; Ziółek, M. *J. Phys. Chem. C* **2020**, *124*, 2895–2906.
- (110) Freeman, W. A.; Mock, W. L.; Shih, N. Y. *J. Am. Chem. Soc.* **1981**, *103*, 7367–7368.
- (111) Koner, A. L.; Nau, W. M. *Supramol. Chem.* **2007**, *19*, 55–66.
- (112) Choi, H.; Kang, S. O.; Ko, J.; Gao, G.; Kang, H. S.; Kang, M. S.; Nazeeruddin, M. K.; Grätzel, M. *Angew. Chemie - Int. Ed.* **2009**, *48*, 5938–5941.
- (113) Kim, D. H.; Losego, M. D.; Hanson, K.; Alibabaei, L.; Lee, K.; Meyer, T. J.; Parsons, G. N. *Phys. Chem. Chem. Phys.* **2014**, *16*, 8615–8622.
- (114) Parsons, G. N.; George, S. M.; Knez, M. *MRS Bull.* **2011**, *36*, 865–871.
- (115) Gierszewski, M.; Glinka, A.; Gradzka, I.; Jancelewicz, M.; Ziółek, M. *ACS Appl. Mater. Interfaces* **2017**, *9*, 17102–17114.

- (116) Cole, J. M.; Pepe, G.; Al Bahri, O. K.; Cooper, C. B. *Chem. Rev.* **2019**, *119*, 7279–7327.
- (117) Boschloo, G. *Front. Chem.* **2019**, *7*, 1–9.
- (118) Katoh, R.; Furube, A. *J. Photochem. Photobiol. C* **2014**, *20*, 1–16.
- (119) Daeneke, T.; Mozer, A. J.; Uemura, Y.; Makuta, S.; Fekete, M.; Tachibana, Y.; Koumura, N.; Bach, U.; Spiccia, L. *J. Am. Chem. Soc.* **2012**, *134*, 16925–16928.
- (120) Yao, Z.; Guo, Y.; Wang, L.; Hao, Y.; Guo, Y.; Franchi, D.; Zhang, F.; Kloo, L.; Sun, L. *Sol. RRL* **2019**, *3*, 1–9.
- (121) Ardo, S.; Sun, Y.; Staniszewski, A.; Castellano, F. N.; Meyer, G. J.; Regan, O. *J. Am. Chem. Soc.* **2010**, *132*, 6696–6709.
- (122) Burdziński, G.; Karolczak, J.; Ziółek, M. *Phys. Chem. Chem. Phys.* **2013**, *15*, 3889–3896.
- (123) Van Stokkum, I. H. M.; Larsen, D. S.; Van Grondelle, R. *Biochim. Biophys. Acta - Bioenerg.* **2004**, *1657*, 82–104.
- (124) Henry, E. R.; Hofrichter, J. *Methods Enzymol.* **1992**, *210*, 129–192.

Paper I

Effects of Post-Assembly Molecular and Atomic Passivation of Sensitized Titania Surface: Dynamics of Electron Transfer Measured from Femtoseconds to Seconds.

Gierszewski, M.; **Glinka, A.**; Gradzka, I.; Jancelewicz, M.; Ziółek, M.

ACS Appl. Mater. Interfaces **2017**, 9, 17102–17114.

Effects of Post-Assembly Molecular and Atomic Passivation of Sensitized Titania Surface: Dynamics of Electron Transfer Measured from Femtoseconds to Seconds

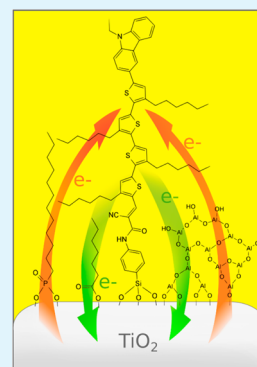
Mateusz Gierszewski,[†] Adam Glinka,[†] Iwona Grądzka,[†] Mariusz Jancelewicz,[‡] and Marcin Ziólek^{*,†,§}

[†]Quantum Electronics Laboratory, Faculty of Physics, and [‡]NanoBioMedical Centre, Adam Mickiewicz University in Poznań, Umultowska 85, 61-614 Poznań, Poland

S Supporting Information

ABSTRACT: The dynamics of electron transfer at the dye–titania and titania–electrolyte interfaces is investigated in two post-sensitization processes: (i) atomic layer deposition of blocking alumina coating and (ii) hierarchical molecular multicapping. To measure the electron transfer dynamics, time-resolved spectroscopic methods (femtosecond transient absorption on the time scale from femtoseconds to nanoseconds and electrochemical impedance spectroscopy on the time scale from milliseconds to seconds) are applied to the complete dye-sensitized solar cells with cobalt-based electrolyte and champion ADEKA-1 dye (with silyl-anchor unit) or its popular carboxyl-anchor analogue, MK-2 dye. Both molecular capping and alumina blocking layers slow down the electron injection process (the average rate constant decreases from 1.1 ps⁻¹ to 0.4 ps⁻¹) and partial sub-nanosecond back electron transfer from titania to the dye (from ca. 10 ns⁻¹ to 5 ns⁻¹). Very small alumina layers (of 0.1 nm thickness) have the highest impact on reducing the rate constants of these electron transfer processes, and for the thicknesses greater than 0.3 nm the rate constants hardly change. In contrast, the electron recombination between titania and electrolyte, occurring on the millisecond time scale, starts to be significantly suppressed for the blocking layers of 0.3 nm or more in thickness (up to ca. 20 times for 0.5 nm thickness with respect to that for untreated sample), improving open circuit voltage and fill factor of the cells. The amplitude of the relative photocurrent (short circuit current per number of absorbed photons) is found to depend almost exclusively on the ultrafast and fast processes taking place in the first nanoseconds after dye excitation. The positive impact of coadsorbents on the solar cells performance for both ADEKA-1 and MK-2 is also studied.

KEYWORDS: TiO₂ passivation, molecular multicapping, atomic layer deposition, ADEKA-1 dye, MK-2 dye, femtosecond transient absorption, electrochemical impedance spectroscopy



INTRODUCTION

The interfaces between mesoporous titania and dyes that sensitize the titania surface, and between titania and hole transporting medium (e.g., electrolyte), are key elements in the operation of dye-sensitized solar cells (DSSC)^{1,2} and dye-sensitized photoelectrochemical cells (DSPEC) for water splitting.^{3,4} After absorption of light, the electrons are injected from the excited dyes to the conduction band of titania nanostructure, and they should reach the photoanode with high quantum yield for efficient charge separation. However, unwanted electron recombination at the above interfaces (titania–dye and titania–electrolyte) is among the main limitations in further development of DSSC and DSPEC devices. For example, the problem of titania–electrolyte recombination has become a fundamental issue for the recently proposed cobalt-based electrolytes in DSSC, offering higher open circuit voltage of the cells than that obtained with the traditional iodide/triiodide redox pair. When the recombination process was properly suppressed, the use of such one-electron redox couples led to the best laboratory efficiencies of DSSC.^{5–9} However, without a special surface treatment and/or dye design, the titania–electrolyte recombination results in a

much worse performance of cobalt-based cells with respect to that of iodide-based ones.^{10–12}

Many attempts have been made to passivate titania surface with thin layers of insulating materials. One of the most frequently used approaches has been the deposition of thin layers of large-bandgap semiconductors (like Al₂O₃) via chemical methods or atomic layer deposition (ALD) techniques.^{13–15} The latter conformal technique gave very homogeneous layers with atomic precision even on topographically complex surfaces, for example, on porous networks. However, almost all these approaches have been applied to the titania nanostructures before dye sensitization. Therefore, the dyes were actually attached to such insulating layers, and, simultaneously with suppressing recombination, the electron injection was also slowed down, so its efficiency was lowered. Recently, novel and interesting approaches have been proposed based on surface passivation after the dye-sensitization process (often called the post-assembly methods): hierarchical

Received: March 7, 2017

Accepted: May 8, 2017

Published: May 8, 2017

Table 1. Averaged Photovoltaic Parameters of the Studied Solar Cells^a

no.	abbreviation	description	V_{OC} [V]	FF	J_{SC} [mA cm ⁻²]	Eff [%]	total APCE	S_{res}
1	A	ADEKA-1	0.81	0.56	5.9	2.7	0.44	0.33
2	A_CAPP	ADEKA-1 + multi capping	0.78	0.65	2.5	1.3	0.25	0.27
3	A_OTMS	ADEKA-1 + OTMS	0.83	0.46	7.0	2.5	0.57	0.40
3b	A_OTMS ^b	ADEKA-1 + OTMS ^b	0.79	0.51	5.8	2.4	0.57	0.43
4	A_OTMS_CAPP	ADEKA-1 + OTMS + multi capping	0.76	0.63	1.7	0.8	0.20	0.32
5	A_OTMS_200C	ADEKA-1 + OTMS + temp. 200 °C	0.84	0.48	6.5	2.6	0.54	0.47
6	A_OTMS_1ALD ^b	ADEKA-1 + OTMS + 0.1 nm Al ₂ O ₃	0.83	0.55	6.0	2.7	0.47	0.37
7	A_OTMS_3ALD ^b	ADEKA-1 + OTMS + 0.3 nm Al ₂ O ₃	0.82	0.71	1.8	1.1	0.22	0.22
8	A_OTMS_5ALD	ADEKA-1 + OTMS + 0.5 nm Al ₂ O ₃	0.87	0.73	2.0	1.3	0.17	0.14
9	A_OTMS_noTBP ^b	ADEKA-1 + OTMS – TBP (in electrolyte)	0.59	0.40	6.4	1.5	0.58	0.57
10	M	MK-2	0.83	0.45	8.1	3.0	0.63	0.42
11	M_CAPP	MK-2 + multi capping	0.51	0.50	0.7	0.2	0.51	0.54
12	M_CDCA	MK-2 + CDCA	0.81	0.53	7.8	3.4	0.84	0.58
13	M_CDCA_200C	MK-2 + CDCA + temp. 200 °C	0.82	0.46	8.4	3.2	0.92	0.61
14	M_CDCA_5ALD	MK-2 + CDCA + 0.5 nm Al ₂ O ₃	0.85	0.69	2.0	1.2	0.30	0.29
15	M_CDCA_noTBP	MK-2 + CDCA – TBP (in electrolyte)	0.58	0.55	4.7	1.4	0.57	0.76

^aOpen circuit voltage (V_{OC}), fill factor (FF), photocurrent density (J_{SC}), efficiency (Eff), corrected photocurrent efficiency (Total APCE), and the amplitude of the normalized residual signal of transient absorption kinetic at 750 nm (S_{res} , ratio of the amplitude after 3 ns to the initial one). ^bInitial number of absorbed photons smaller by about 15% in this series than in other ones are related to smaller titania thickness.

molecular multicapping^{7,9} and ALD of blocking coating (ref 16 and references therein). In principle, such methods keep the sensitizing dye anchored to the titania surface. The lack of wider and earlier use of such approaches is probably due to the fact that the post-assembly methods can affect the chemical bond between dyes and titania, up to destroying the sensitized photoanode. Molecular multicapping is based on the surface passivation with molecules having alkyl chains of various lengths (from the longest to the shortest) resulting in filling the voids between the sensitizing dye and reducing the aggregation of the dye on the titania surface. This method has been successfully used to the novel organic dye ADEKA-1, having a silyl-anchor unit that forms stronger bonds with TiO₂ than the traditional carboxyl groups.⁷ The efficiency of DSSC with ADEKA-1, cobalt-based electrolytes, and multicapping passivation reached almost 13%.⁸ The use of co-sensitization of ADEKA-1 with LEG4 dye resulted in currently the best laboratory efficiency of over 14%.⁹ Post-assembly ALD of TiO₂ layers has been proposed to stabilize ruthenium RuP dye in DSPEC,¹⁷ water oxidation catalyst in DSPEC,¹⁸ and donor-acceptor organic dye OrgD in DSSC with aqueous electrolyte.¹⁹ Atomic layer deposition of Al₂O₃ on TiO₂ was applied after sensitization with RuP,²⁰ standard ruthenium dye N719,²¹ and OrgD.²²

According to our knowledge, the impact of the two post-assembly passivation methods above on the dynamics of interfacial electron transfer has been poorly studied so far. Some aspects of electron recombination after molecular multicapping for ADEKA-1 with cobalt-phenanthroline electrolyte have been studied by us recently, but without investigation of electron injection.²³ For the TiO₂-RuP system in water, electron injection and back electron transfer rate constants were observed to decrease with increasing cycles of Al₂O₃ deposition.²⁰ Similar trends have been found for ALD films on N719 sensitized meso-TiO₂ electrodes.²¹ On the contrary, for OrgD dye, ultrathin layers of either TiO₂ or Al₂O₃ reduced negative dye aggregation effects and improved electron injection quantum yield.²²

Therefore, in this work we present thorough studies of DSSC modified with molecular multicapping and post-sensitization

atomic deposition of Al₂O₃ layers of different thicknesses (0.1–0.5 nm). As dyes, we used the champion ADEKA-1 and its commercially available and efficient carboxyl-anchor analogue, MK-2 dye.^{24–27} The same complete cells were characterized by the basic photovoltaic measurements (J - V curves, IPCE spectra, photovoltage and photocurrent decays, steady-state absorption of the photoanodes) and by time-resolved spectroscopic methods. Using femtosecond transient absorption and electrochemical impedance spectroscopy we were able to simultaneously determine the dynamics of all 3 interfacial electron transfer processes that take place on the time scales from femtoseconds to seconds: electron injection, back electron transfer from titania to the dye, and electron recombination between the titania nanoparticles and the cobalt tris(bipyridyl) based electrolyte. Besides the effect of post-assembly passivation, we also investigated the impact of coadsorbent, high temperature (200 °C) treatment, the lack of a Lewis base in the electrolyte, and the details of ultrafast injection and fast recombination mechanisms.

DSSCs with MK-2 and ADEKA-1 dyes have been studied by some of us before, by time-resolved laser spectroscopy methods. In our previous work for MK-2, we have revealed the presence of a fast partial recombination on the sub-nanosecond time scale for which the dynamics depended on the conduction band potential.²⁸ For ADEKA-1 we have observed that sub-nanosecond recombination can be suppressed by the optimized dye synthesis methods and upon addition of a coadsorbent.²³ The effects of alumina overlayers prepared on titania nanoparticles before dye sensitization have been also studied for ADEKA-1.²³

We believe that our present work will significantly improve the basic understanding of the impact of post-assembly surface passivation for the most efficient dyes and cobalt-based electrolytes. Many of our findings should also be valid for other classes of dyes, which might help further progress in optimization of DSSC and DSPEC devices.

EXPERIMENTAL SECTION

Preparation of the Solar Cells. Glass plates (final size 12 × 17 mm²) were cut from the FTO glass sheet (Sigma-Aldrich, 2.2 mm

thickness, 13 Ω /sq). They were cleaned using sequentially (i) the solution of commercially available dishwashing detergent in distilled water, (ii) distilled water, and (iii) ethanol in ultrasonic bath, with each cleaning procedure lasting for 15 min. Next, using the screen printing technique (DN-HM02 screen-printer, Dyenamo, with polyester screen of mesh count 250, Sefar) an approximately 2–3- μ m-thick single layer of mesoporous titania was deposited using the commercially available screen-printable transparent TiO₂ paste with 28–31 nm particles (DN-GPS-30TS, Dyenamo). After screen printing, the glass plates with mesoporous titania were gradually heated at 150 °C for 5 min, 300 °C for 5 min, and 450 °C for 60 min. After that, the hot plates were submerged in 50 mM aqueous solution of TiCl₄ for 30 min at 70 °C, rinsed in water, and again heated at 150 °C for 5 min, 300 °C for 5 min, and 450 °C for 30 min.

For photoanode sensitization, the glass plates with titania layers were immersed in dye solutions at 5 °C for about 16 h to enable efficient adsorption of the dyes (the sensitization temperature was low in accordance to the procedure used for ADEKA-1⁷). We used two different organic dyes, ADEKA-1 (100% monomeric form obtained by the synthesis route described in our previous article²³) and MK-2 (from Sigma-Aldrich) with or without coadsorbent molecules, isooctyltrimethoxysilane (OTMS, Sigma-Aldrich) for ADEKA-1 and chenodeoxycholic acid (CDCA, Sigma-Aldrich) for MK-2 in the following concentrations and solvents: (i) the 0.2 mM solution of a dye without coadsorbent in toluene and (ii) 0.2 mM dye + 0.1 mM of coadsorbent in 9:1 mixture of toluene and acetonitrile. Dye structures are shown in Scheme S1 (in the Supporting Information, SI).

Counter electrodes were prepared from the same FTO glass plates and by the same cleaning procedure as that used for photoanodes. Afterward, they were dried in air and one layer of activated platinum (Platisol T, Solaronix) was deposited by paintbrush. Finally, the plates were heated at 400 °C for 30 min in order to remove any organic contamination. Photoanodes and counter electrodes were bonded together by a polymer seal (25 μ m Surllyn, Meltronix, Solaronix SA) with conducting surfaces facing inward. Afterward, the devices were filled with electrolyte through 1 mm holes in the counter electrode and sealed with the cover glass on the top. We used the electrolyte with the following components and concentrations: 0.25 M Co²⁺ bis-(trifluoromethane)sulfonimide (TFSI), 0.035 M of Co³⁺TFSI, 0.1 M of LiTFSI, and 0.5 M *tert*-butylpyridine (TBP). The cobalt redox couple was a cobalt-bipyridine complex (Co-Bpy) in all cases. The cells with this electrolyte are abbreviated as presented in Table 1: **A** means the cell was sensitized with only ADEKA-1, **A_OTMS** – with ADEKA-1 and OTMS, **M** – with only MK-2, and **M_CDCA** – with MK-2 and CDCA. For control and comparison experiments, for both ADEKA-1 with OTMS and MK-2 with CDCA photoanodes, electrolyte without TBP was also used (cells labeled as **A_OTMS_noTBP** and **M_CDCA_noTBP**).

ALD and Multicapping Procedure. The atomic layer deposition (ALD) technique was used to deposit alumina shell on the photoanodes after dye deposition, for the cells fabricated with ADEKA-1 with OTMS and MK-2 with CDCA. For ADEKA-1 with OTMS the thickness of the alumina shell was 0.1 nm (**A_OTMS_1ALD**), 0.3 nm (**A_OTMS_3ALD**), and 0.5 nm (**A_OTMS_5ALD**). For MK-2 with CDCA it was 0.5 nm (**M_CDCA_5ALD**). The influence of temperature inside the ALD reactor on the properties of the cells was tested for both ADEKA-1 with OTMS (**A_OTMS_200C**) and MK-2 with CDCA (**M_CDCA_200C**) at 200 °C. ALD was performed using an R-200 reactor (Picosun) with deionized water and trimethylaluminum as oxygen and aluminum sources, respectively. An individual cycle of Al₂O₃ deposition, at the precursor pulse time of 2 s and purge time of 8 s, resulted in generation of a layer close to 0.1 nm thick.

The hierarchical molecular capping treatment was performed on photoanodes after the dye deposition for ADEKA-1 (**A_CAPP**), ADEKA-1 with OTMS (**A_OTMS_CAPP**), and MK-2 (**M_CAPP**). The electrodes were dipped in the appropriate solutions and then rinsed with toluene. The treatment was performed just after taking them out of the dye solution and immediately before sealing the cells. The solutions used for multicapping treatment contained a relevant

acid in 1 mM concentration and a mixture of 1:1 toluene:acetonitrile as a solvent. For **A_CAPP** and **A_OTMS_CAPP** the electrodes were submerged in the following substances with varying alkyl-chain lengths: *n*-octadecyl succinic acid (ODSA, 5 min), *n*-hexadecyl malonic acid (HMA, 5 min), tetradecylphosphonic acid (TDPA, 2 min), octylphosphonic acid (OPA, 1 min), isooctyltrimethoxysilane (OTMS, 10 min), heptanoic acid (HA, 5 min), and finally ethylphosphonic acid (EPA, 1 min). Due to the stronger desorption process of MK-2 from the titania surface, compared to ADEKA-1, the immersion time for **M_CAPP** was shorter—the photoanodes were dipped in ODSA for 2 min, HMA for 2 min, TDPA for 30 s, OPA for 30 s, CDCA for 2 min, HA for 2 min, and finally EPA for 30 s. The molecules for hierarchical multicapping were similar but not exactly the same as those proposed for the record efficiencies of ADEKA-1.^{7,9}

Cell Characterization. Stationary absorption spectra of the photoanodes (before cell assembly) were recorded on a UV–vis–NIR JASCO V-770 spectrophotometer equipped with a 150 mm integrating sphere (LN-925). The samples were placed in front of the integrating sphere to measure both transmitted and scattered light. A potentiostat (model M101 with a frequency response analyzer FRA32 M module, Autolab) coupled to a photoelectric spectrometer equipped with a solar simulator (Photon Institute, Poland) was used to make a current–voltage characterization (for calculation of photovoltaic parameters of the cells) and IPCE (incident photon to current efficiency) spectra of the solar cells obtained. The measurements were made 1 h and 1 day after cell preparation. The sunlight conditions were simulated by a Xe lamp with AM 1.5 G spectral filter and intensity adjusted to 100 mW/cm² using a calibrated cell (1S151, ABET). Electrochemical impedance spectroscopy (EIS) measurements were performed using the previously mentioned potentiostat. The ZView software was employed to make an analysis of the obtained curves (Nyquist plot representation) by fitting typical equivalent circuits for the DSSC system with a transmission line element.²⁹

The transient absorption measurements were performed for the same complete solar cells as those for current–voltage and impedance characterization. More details about the ultrafast broadband transient absorption system have been described already (Helios spectrometer from Ultrafast Systems and Spectra Physics laser system).³⁰ The pump pulses were set at 500 nm and the IRF (pump–probe cross correlation function) was about 250 fs (fwhm). Global analysis of the transient absorption data was performed using Surface Explorer software (Ultrafast Systems). The program fits a multiexponential function (convoluted with IRF) to the kinetic vectors of a selected number of singular values. As a result of the analysis the characteristic time constants as well as the wavelength-dependent amplitudes associated with them were obtained.

RESULTS AND DISCUSSION

Stationary Absorption. The sensitized photoanodes for all configurations were first investigated by stationary absorption measurements with integrating sphere (to include the effect of the light scattered by TiO₂ nanoparticles), and the baseline measured for unsensitized TiO₂ electrodes was subtracted in all cases. We would like to stress the importance of such data in our studies, because they allow us to calculate the relative photocurrent, which is the short circuit current per the number of absorbed photons, N_{ph} (see *total APCE* parameter in the next section), and which is used to compare the charge separation efficiency for the cells of different dye absorption. The value of N_{ph} was obtained from integration of stationary absorbance spectrum multiplied by the photon flux spectrum from AM 1.5G data. Typically, such data are gained from dye desorption experiments, but they often suffer from high uncertainty, not to mention the problem of desorption of ADEKA-1 dye with strong binding to titania surfaces. To check, we performed chemical desorption of MK-2 dye from the titania surface by ethylphosphonic acid (0.001 M, 1:1 acetonitrile:toluene, 16 h)

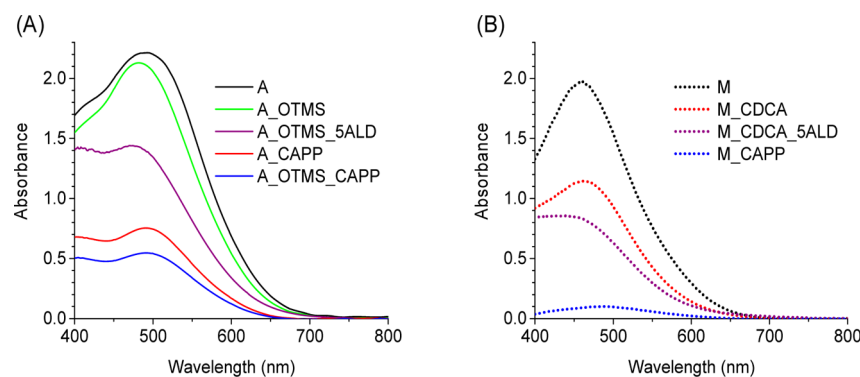


Figure 1. Stationary absorption of selected sensitized films with TiO_2 contribution subtracted: (A) ADEKA-1 and (B) MK-2 cells.

and the calculated results were the same as those obtained from photoanode absorption measurements. Therefore, we propose stationary absorption as a much better and more reliable method. The measured relative errors in the determination of the absorbance and N_{ph} were 5% and 2%, respectively (the relative error is defined as the standard deviation of the mean divided by the mean value and multiplied by 100%).

Figure 1 shows the representative spectra of photoanodes for selected configurations. Addition of coadsorbents during sensitization (silyl-anchor OTMS to ADEKA-1 and carboxyl-anchor CDCA to MK-2) results in lowering the absorbance of the sample, more pronounced for MK-2 dye (compare samples **M** and **M_CDCA** in Figure 1B) than for ADEKA-1 dye (samples **A** vs **A_OTMS** in Figure 1A). In the standard ALD method that we used a minimum temperature necessary for Al_2O_3 deposition was 200 °C. Therefore, we had to check if the dyes used in our studies were able to withstand such a high temperature for at least 2 min, required for ALD. In the experiment with a hot plate at normal pressure conditions, some changes in the absorption spectra were evident for both dyes, slightly more pronounced for MK-2 than ADEKA-1 (see Figure S1 in the Supporting Information, SI). By the way, a small decrease in absorbance was already observed after the exposure to 120 °C, a temperature that was used for sealing in preparation of solar cells. After Al_2O_3 deposition in the ALD chamber with low pressure some decrease in the absorbance was also observed (the spectra of **A_OTMS_5ALD** and **M_CDCA_5ALD** in Figure 1, corresponding to post-assembly deposition of 0.5 nm layer of Al_2O_3). However, the highest decrease in absorbance was observed for molecular multicapping: for ADEKA-1 dye only around 30% of the dye molecules were left (the spectra of **A_CAPP** and **A_OTMS_CAPP** in Figure 1A) and more than 90% of MK-2 molecules were desorbed (the spectrum of **M_CAPP** in Figure 1B).

Finally, additional tests were made of the dye desorption using relatively strong ethylphosphonic acid (Figure S1). As expected, from among reference photoanodes of both dyes with coadsorbents, MK-2 showed much lower stability than ADEKA-1, confirming the difference between the bond strength of carboxyl and silyl anchoring groups (and also explaining the low absorbance of MK-2 photoanodes after multicapping passivation). In line with several reports for dye stabilization after post-assembly ALD,^{19–21} our Al_2O_3 -coated samples also exhibit smaller desorption effect, but not for the smallest layer thickness of 0.1 nm (Figure S1).

Photovoltaic Parameters. In total, 60 solar cells in 15 different configurations were prepared for our studies. Their photovoltaics parameters, obtained from the current–voltage

curves measured under 1Sun illumination, are presented in Table 1: open circuit voltage (V_{OC}), short circuit current density (J_{SC}), fill factor (FF), and efficiency (Eff). These values were averaged from at least 3 different cells of particular configuration, for each cell measurements were performed twice, on the day of preparation and 1 day later (no consistent changes were observed after 1 day, so the samples were stable in terms of single days). The statistics of the obtained parameters are shown in Table S1 for each configuration. On average, the mean values of the photovoltaic parameters presented in Table 1 were based on 7 measurements, and the relative errors were 2% for V_{OC} , 4% for FF, 8% for J_{SC} , and 10% for the efficiency. Besides the typically observed variation in the performance of handmade prepared DSSCs, the errors in the photocurrent values might be slightly increased due to limited beam homogeneity of our sunlight source with respect to professional solar simulators (thus, additional deviations might be due to sample positioning in the current–voltage measurements). IPCE spectra for the best cells of each configuration are presented in Figure S2, while Table S2 shows the parameters for these cells.

The efficiencies of our cells are relatively low in comparison to the champion DSSCs sensitized with ADEKA-1 (about 12%) and MK-2 (about 10%) dyes. The main reason is the small thickness of the mesoporous titania layer (2–3 μm) and the lack of scattering particles in our cells, which is because of the necessity to have sufficiently transparent samples for transient absorption measurements. For example, the highly efficient cells with ADEKA-1 had 10–11 μm titania layer with semitransparent and scattering layers, which results in significantly better light harvesting efficiency and higher photocurrents.⁷ However, it does not influence the generality of our results, since the observed differences in electron transfer dynamics should also be valid for the thicker devices optimized for the record efficiencies.

As can be seen from Table 1, multicapping causes a decrease in V_{OC} of the cells while Al_2O_3 deposition causes its gradual increase (e.g., from 0.83 V for **A_OTMS** to 0.87 V for **A_OTMS_5ALD**, and from 0.81 V for **M_CDCA** to 0.85 V for **M_CDCA_5ALD**). The lowest V_{OC} was found for **M_CAPP** cell (0.51 V) and for the control cells without 4-*tert*-butylpyridine (TBP) in electrolyte (**A_OTMS_noTBP**: 0.59 V and **M_CDCA_noTBP**: 0.58 V). Changes in V_{OC} indicate differences in the titania conduction band potential, as will be verified in the next section. More positive potential (lower energy) for the electrolytes without TBP is a well-known phenomenon, while molecular capping with acidic molecules might increase protonation of the titania surface, which is

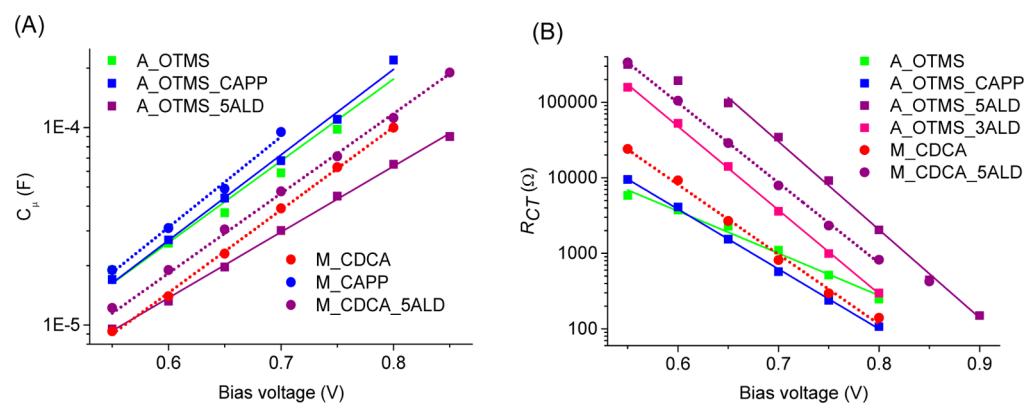


Figure 2. Plots of (A) chemical capacitance (C_{μ}) and (B) charge transfer resistance (R_{CT}) versus applied bias obtained from the equivalent circuit fits to impedance spectroscopy results for selected ADEKA-1 and MK-2 cells. The results for the rest of configurations are in SI (Figure S3).

especially enhanced for MK-2 with most of the dyes desorbed (Figure 1B for M_{CAPP}).

Both post-assembly passivation methods improve the FF parameter of the solar cells. For example, in the cells with the thickest alumina layer (A_{OTMS_5ALD} and M_{CDCA_5ALD}) FF was equal to about 0.7, while in the reference cells (A_{OTMS} and M_{CDCA}) it was about 0.5. This suggests a reduced titania–electrolyte recombination when the passivation is applied, which will also be further confirmed in the next section.

As mentioned above, the values of J_{SC} are generally relatively low, because our cells were optimized for transient absorption conditions. Moreover, as evidenced in the previous section, addition of a coadsorbent and application of molecular and atomic post-assembly passivation resulted in large variation in the dye coverage and absorption of the cells. Therefore, we focus our attention on another parameter, also shown in Table 1, which we call the total absorbed photon to current efficiency (APCE), and calculate as $total\ APCE = J_{SC}/(e N_{ph})$, where e is the value of elementary charge. In principle, the cells with better $total\ APCE$ exhibit better charge separation efficiency, and should have better J_{SC} in the thicker solar cells optimized for best efficiencies and maximum light absorption.

First of all, addition of a coadsorbent (OTMS or CDCA) improves the $total\ APCE$ by about 30% (A_{OTMS} vs A , and M_{CDCA} vs M ; see Table 1). For ADEKA-1 this finding has already been reported in our recent studies²³ and it can be expected since we used the same concentrations of ADEKA-1 and OTMS as in the reports for the champion efficiencies.^{7,9} However, for the best cells of MK-2 no coadsorbent has been used so far.^{24–27} Therefore, our observation with commonly used coadsorbent CDCA might result in obtaining even better efficiency for this dye. Next, for the cells with photoanodes treated by high temperature in ALD chamber (but without any deposition, A_{OTMS_200C} and M_{CDCA_200C}), $total\ APCE$, as well as other parameters of the cells, were roughly the same as for the reference cells (A_{OTMS} and M_{CDCA}). This means that, despite some changes in the absorption spectrum (Figures 1 and S1), both dyes are well suited for the ALD processing at 200 °C.

In spite of that, $total\ APCE$ for a single cycle of alumina deposition (A_{OTMS_1ALD}) was smaller than that for the reference cell (A_{OTMS_200C} or A_{OTMS}), and it gradually decreased with increasing alumina overlayer thickness (A_{OTMS_3ALD} and A_{OTMS_5ALD}). For the largest alumina layer thickness studied (0.5 nm), $total\ APCE$ was only

about 30% of that of the reference cells, for both ADEKA-1 and MK-2. Similarly, molecular multicapping resulted in lowering the $total\ APCE$ values; namely, for A_{OTMS_CAPP} it was placed between the values for A_{OTMS_3ALD} and A_{OTMS_5ALD} .

Finally, our control cells without TBP (A_{OTMS_noTBP} and M_{CDCA_noTBP}) were prepared to check whether an excessively high energetic position of titania conduction band edge does not limit the photocurrent of the cells. In fact, J_{SC} and $total\ APCE$ values did not increase and were even lower for these samples (Table 1), which indicates that titania conduction band was not too negative with respect to the redox potential of the excited states of ADEKA-1 and MK-2.

Electrochemical Impedance. Electrochemical impedance spectroscopy (EIS) studies brought the information about the time constants of electron recombination between titania and the redox pair in the electrolyte (time scale from milliseconds to seconds), and also explained the variation in V_{OC} and FF values for different cells. The impedance measurements were applied to all studied solar cell samples without illumination and for different applied bias voltages scanning from 200 mV to V_{OC} in 50 mV increments. The data were analyzed using a typical equivalent circuit for DSSC that includes a transmission line element.²⁹ The details of the EIS analysis are presented in SI, and below only the most important conclusions regarding post-assembly passivation are summarized. Two basic parameters extracted from the EIS data analysis, namely, chemical capacitance (C_{μ}) and charge transfer resistance (R_{CT}), are presented in Figure 2 in semilog representation as a function of applied bias voltage for selected samples. Figure S3 shows the same plots for other samples and in the extended bias range. The data were obtained as the average of at least two different measurements of the best cells in each configuration. The shift in C_{μ} values is a good estimation of the relative movement of titania conduction band. As can be seen in Figure 2A, for ADEKA-1 cells the molecular multicapping results in a very small down-shift of conduction band position (cell A_{OTMS} vs A_{OTMS_CAPP}), while ALD passivation causes the conduction band to be shifted toward higher energy (up to 100 mV for the thickest Al_2O_3 layer, cell A_{OTMS_5ALD} vs A_{OTMS}). For MK-2 cells the situation is different; the conduction band is shifted significantly down as a result of the multicapping passivation (about 100 mV, cell M_{CAPP} vs M_{CDCA}), while Al_2O_3 coating does not result in conduction band upshift, but in a small downshift. However, the conduction band potential in the reference samples is already

Table 2. Electron Lifetimes for Two Selected Applied Biases, Extracted from Electrochemical Impedance Measurements^a

sample/ configuration	lifetime at 0.55 V bias, s	lifetime at 0.65 V bias, s	S ₁ state decay from VIS part, ps	S ₁ state decay from NIR part, ps	recombination from VIS part, ps	recombination from NIR part, ps
A	0.16	0.080	0.5	1.3	100	70
A_CAPP	0.16	0.071	2.2	1.6	250	100
A_OTMS	0.11	0.084	0.5	1.3	110	80
A_OTMS_CAPP	0.16	0.068	2.0	1.6	220	100
A_OTMS_200C	0.14	0.087	0.5	1.1	150	70
A_OTMS_1ALD	0.16	0.095	1.5	1.5	180	110
A_OTMS_3ALD	1.50	0.30	2.9	1.9	210	140
A_OTMS_5ALD	3.01	1.93	3.0	1.9	260	180
A_OTMS_noTBP	0.014	-	0.2	0.3	65	12
M	0.084	0.066	0.2	0.5	17	18
M_CAPP	0.081	0.044	0.2	0.8	40	80
M_CDCA	0.22	0.062	0.8	1.1	70	35
M_CDCA_200C	0.28	0.067	0.4	0.5	100	13
M_CDCA_5ALD	4.10	0.38	2.9	1.5	190	110
M_CDCA_noTBP	0.015	-	0.2	0.2	12	4.6

^aAveraged time constants for S₁ state decay and recombination based on the global analysis of transient absorption data in VIS and NIR ranges.

more negative for MK-2 than ADEKA-1 cells by about 50 mV (cell M_CDCA vs A_OTMS). The slope of linear fits in the semilog plots of C_{μ} vs bias voltage can be used to compare the distribution of trap states below the conduction band (parameter α collected in Table S3).^{29,31} The values of α become slightly smaller for the cells with coadsorbents (both for ADEKA-1 and MK-2) and further decrease for alumina coating, which indicates a more stretched distribution of trap states.

Most of the variations in C_{μ} can probably be explained by a known dependence of conduction flat-band position in nanoparticles on pH, taking into account different acidic strength of the attached sensitizing molecules, coadsorbents, and molecules for multicapping. For example, the highest downshift in Figure 2A is observed for the M_CAPP cell, for which the titania surface coverage by multicapping components is the highest due to the detachment of most of MK-2 molecules (the absorption spectra in Figure 1B). As for alumina deposition, this semiconductor has much a higher conduction band edge than that of titania, so its thin layer can induce an effective conduction band upshift of the nanoparticle.

A strong effect of alumina post-assembly deposition is also visible in the R_{CT} plots in Figure 2B, with R_{CT} values roughly 1 order of magnitude higher for the cells with 0.3 nm Al₂O₃ layer than for those without any coating, and further 1 order higher for those with 0.5 nm coating. It confirms the expected protective role of alumina in suppressing electron recombination between nanoparticles and cobalt-based electrolyte. The slope of linear fits in the semilog plots of R_{CT} vs bias voltage enables determination of the cell ideality factor m (recombination reaction order), which is gathered in Table S3. Generally, steeper slopes (smaller m parameters) are observed again for the cells with alumina passivation. The values of m can be correlated with the fill factor of the cell (smaller m indicates better FF),^{29,31} although, in principle, the impedance measurements in the dark correspond to the shape of the dark current–voltage curve. Illumination accelerates recombination for the corresponding bias voltages, and parameter m increases as we verified in additional impedance measurements under 1Sun (Figure S4). However, the positive impact of alumina passivation was manifested in the results obtained both in the dark and under 1Sun conditions.

Electron lifetimes for different cells, calculated as the product $C_{\mu}R_{CT}$, are shown in Figure S5 as plots vs bias voltage. In Table 2, the electron lifetime values at two exemplary biases (0.55 and 0.65 V) are also collected. Roughly, for ADEKA-1 cells, the lifetimes were similar irrespective of the use of coadsorbent, applying molecular capping, or deposition of the thinnest 0.1 nm alumina layer. A significant improvement in the lifetimes (thus suppression of the recombination) was observed for greater thickness of the alumina layer. For example, electron lifetimes at 0.55 V were 1.5 s for A_OTMS_3ALD and 3.0 s for A_OTMS_5ALD, which is 10 and 20 times longer than for the other ADEKA-1 configurations (about 150 ms, Table 2). For MK-2 cells, the lifetimes at low and medium biases (<0.65 V) were higher for the cells with coadsorbent than those without CDCA, while for all applied voltages the lifetimes for 0.5 nm alumina layer were at least 10 times longer than those for the other configurations. These values are similar to those obtained as the effect of preassembly alumina coating, reported by us recently for ADEKA-1, for which the gradual increase in electron lifetime was observed, about 2 times per 0.2 nm thick layer.²³

Finally, we have also made additional chronoamperometric test measurements (Figure S6) which confirm the behavior of the electron lifetimes observed in the impedance studies. Photovoltage decays, photovoltage increases, and photocurrent decays are similar for A_OTMS and A_OTMS_1ALD samples, while they become gradually longer for A_OTMS_3ALD and A_OTMS_5ALD cells.

Transient Absorption. Femtosecond transient absorption was performed under excitation at 500 nm in 3 ns time window in two spectral ranges: 520–850 nm (VIS) and 800–1500 nm (NIR). The samples studied were the same as those used in photovoltaic and impedance studies, i.e., the complete solar cells.³² The pump pulse energy was set at 60 nJ, which corresponds to the energy density of about 30 $\mu\text{J}/\text{cm}^2$. This energy was optimized taking into account a sufficient signal-to-noise ratio and the fact that in the control measurements at lower energy (20 nJ) the transient absorption kinetics hardly changed, while at higher energy (150 nJ) the acceleration of the kinetics was observed. Measurements were performed for at least the two best cells of each configuration (often more than once), and the summarized time constants presented below

correspond to the values averaged over these experiments. The main aim of transient absorption studies was the determination of the rate constants of the two fastest interfacial electron transfer processes: electron injection and titania–dye electron recombination. As will be shown below, the measurements also explained the differences between J_{SC} of the studied cells (or, strictly speaking, *total APCE*).

Figure S7 shows representative transient absorption (ΔA) spectra for selected time delays between the pump and probe pulse of ADEKA-1 in toluene solution and in the exemplary solar cell (A_OTMS). The interpretation of the data in solution is similar to that for MK-2 in our previous work.²⁸ The negative signal below 550 nm is due to the ground state depopulation (bleach), while the negative band between 580 and 720 nm is assigned to the stimulated emission from the excited state (S_1) that suffers from spectral shift caused by solvation. Another characteristic absorption band of S_1 state is in NIR range with a maximum around 920 nm. The amplitudes of S_1 bands decay according to its lifetime (see global analysis below), and the final transient absorption spectrum at long delays (2 ns) is due to the triplet state.

The analysis of the solar cell spectra is much more complicated. The positive signal with a maximum around 750 nm is due to a combined contribution of the oxidized dye (dye radical cation formed after electron injection to titania nanoparticles) and the electrons in titania (those in the trap states and free electrons).^{23,28} The decay of this band on the time scale of tens and hundreds of picoseconds is due to unwanted partial recombination of injected electrons with the oxidized dye.^{23,28} The first, rough evaluation of the time scales of electron transfer processes in solar cells can be made by analysis of the kinetics at two characteristic wavelengths: 700 and 750 nm. These kinetics are presented in Figure 3A,B for ADEKA-1 cells (and Figure S8A–B for MK-2 cells). The kinetics at 700 nm contains the contribution of the stimulated emission from the S_1 state; therefore the rise times fitted at this wavelength reflect the decay of the excited state due to electron injection. The obtained time constants of the rise component are gathered in Table S4, and from both this table and Figures 3A and S8A it is evident that sub-picosecond electron injection of nonpassivated samples extends to single picoseconds for the solar cells with molecular or atomic surface passivation.

On the contrary, the kinetics at 750 nm (Figures 3B and S8B) is better suited to monitor the dynamics and contribution of electron recombination. Residual amplitudes obtained at 3 ns delay at this wavelength (S_{res}) are collected in the last column of Table 1 for all studied solar cell configurations. The values of S_{res} , normalized to the initial signal at 750 nm, are proportional to the relative population of successfully separated charges with respect to the population of initially excited dyes. Therefore, similarly to our previous studies of ADEKA-1,²³ we examined the correlation between *total APCE* and S_{res} . As can be observed in Figure 3C, for most of the samples a very good linear correlation takes place. The residual amplitude S_{res} is the highest for the cells with the best *total APCE* values (dyes with coadsorbents), while it is the lowest for the passivated cells, for which *total APCE* is also poor. The only exceptions are the samples with multicapping (A_OTMS_CAPP and M_CAPP in Figure 3C) and the samples without TBP (A_OTMS_noTBP and M_CDCA_noTBP, Table 1), for which *total APCE* seems to be lower than could be expected on the basis of S_{res} value and the linear correlations for the other samples (Figure 3C). This means that there are other processes on a

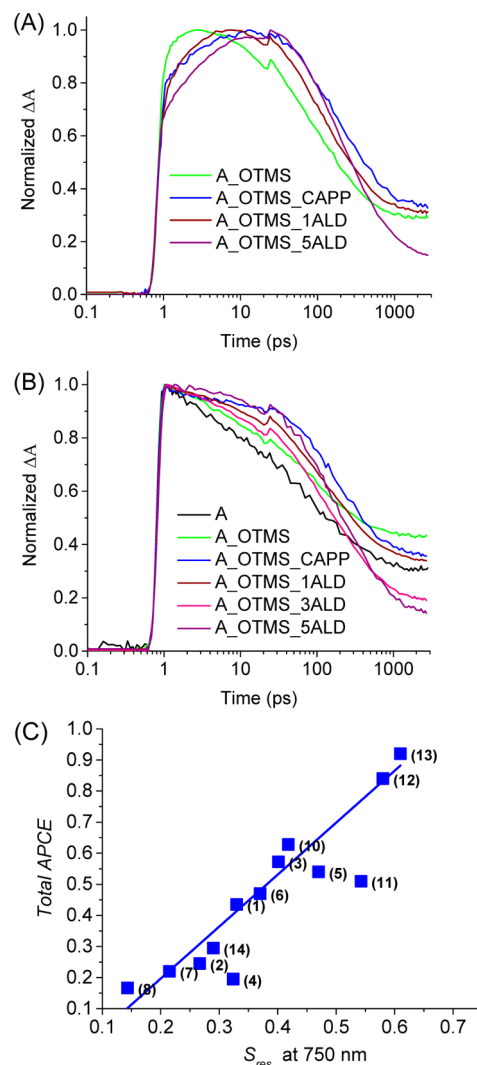


Figure 3. Transient absorption kinetics at (A) 700 nm and (B) 750 nm for ADEKA-1 cells (the corresponding kinetics for MK-2 cells are in Figure S8). Time zero was shifted to 1 ps in order to present the time axis in logarithmic scale. (C) Correlation of *total APCE* with the amplitude of residual signal at 750 nm in transient absorption experiment measured after 3 ns after sample excitation (S_{res}); numbers in brackets indicate different cells according to Table 1.

longer time scale, not observed in our 3 ns time window, which lower charge separation efficiency in these particular samples more than in the other cells. However, for the majority of the cells studied a good correlation between *total APCE* and S_{res} indicates that the differences in the photocurrent of the cells (J_{SC}) are totally determined by the processes occurring on the ultrafast and fast time scales, up to 3 ns, and by the dye absorption in the cells. We would like to stress this conclusion, as it is in line with several recent findings in our group for DSSC with organic dyes,^{23,28,33–35} and it highlights the importance of using time-resolved laser spectroscopy to characterize DSSC systems and find improvements.

Next, to get more accurate values of rate constants of electron injection and electron recombination, we took advantage of the broadband detection and used global analysis in VIS and NIR ranges. As concluded from the previous studies of ADEKA-1²³ and MK-2,²⁸ the interpretation of such analysis is complex, because both electron injection and recombination processes are non-single exponential and take place from many

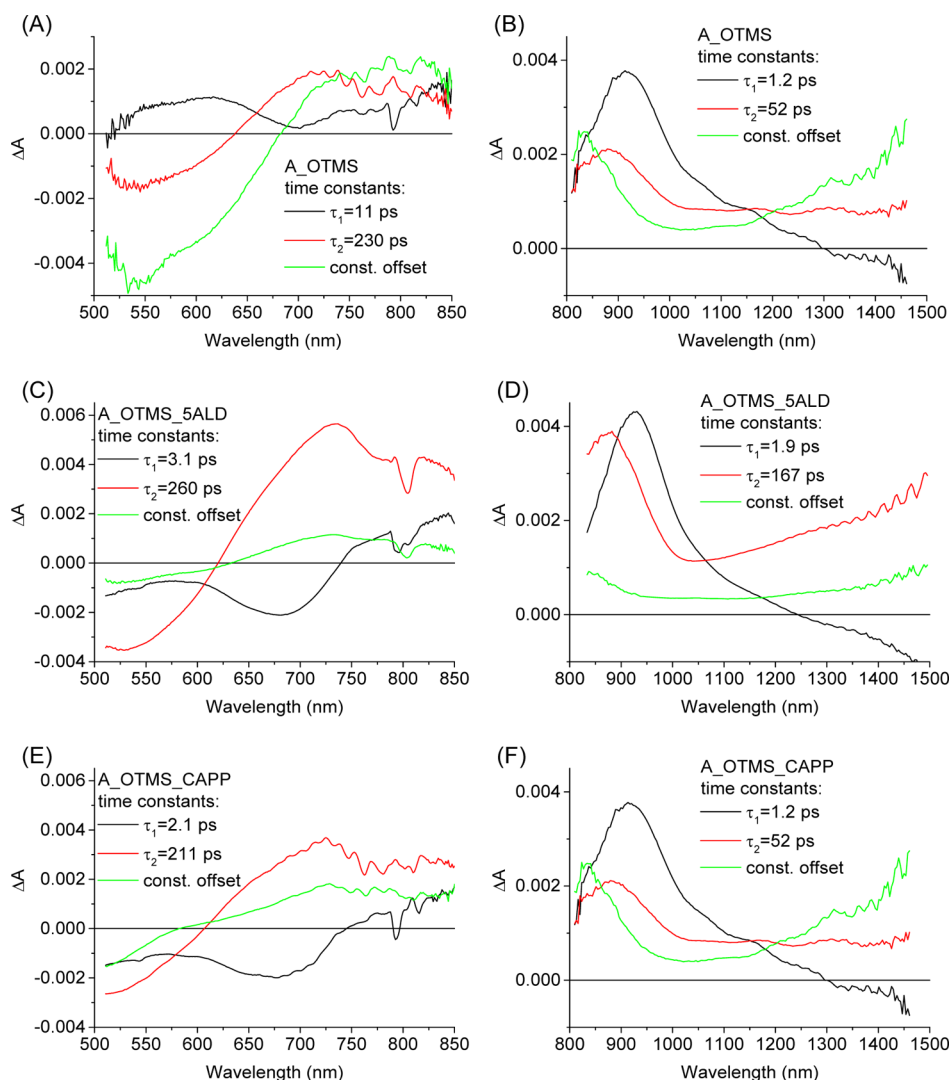


Figure 4. Wavelength dependent amplitudes of the indicated time constants obtained from global analysis (two exponential with constant offset) of transient absorption spectra of solar cells in selected configurations, sensitized with ADEKA-1 in the VIS (left: A, C, E) and NIR (right: B, D, F) spectral ranges. The results for other configurations are presented in SI (Figures S9–S12).

states (e.g., electron injection from hot and relaxed excited state of a dye, electron recombination from semiconductor trap states, free electrons, and from intermediate nonfully charge separated states). To get completely satisfactory global fit quality, four-exponential fit with constant offset was necessary in most cases. Such a detailed analysis is included in the SI. However, for the sake of clarity, and to get one average rate constant for injection and one for electron recombination, a simplified, two-exponential analysis is presented below. The characteristic bands are similar for ADEKA-1 and MK-2, so they will be discussed together.

As a result of two-exponential global analysis, the two characteristic time constants were obtained as well as the wavelength-dependent amplitudes associated with them (also called pre-exponential factor spectra). They are collected in Figures 4, 5, and S9–S12 for the representative experiments for all studied configurations. First, the interpretation of the results in solution (Figures S9A for ADEKA-1 and S11A for MK-2) is rather obvious: the faster component of a few picoseconds is due to relaxation in the S_1 state and solvation dynamics, and its amplitude spectrum reflects the shifts of the transient absorption and emission bands (negative amplitudes in pre-

exponential factor spectra correspond to the rise of ΔA signal, while the positive amplitudes to decay of ΔA). The constant offset component is due to the triplet state of the dye,²⁸ while the longer component of about 500 ps duration (average of the fitted time constants of 460 ps in VIS range and 580 ps in NIR range, Figure S9A,B) is due to the decay of the relaxed S_1 state (S_1 lifetime) and exhibits characteristic negative amplitudes in the range 580–720 nm due to stimulated emission, and a positive band with a maximum around 920 nm, as discussed above. These two characteristic features will be used to identify the presence of S_1 state decay (thus, the dynamics of electron injection) in solar cell samples.

As for the solar cells, the component assignment is easier in the NIR range (right parts in Figures 4, 5, and S9–S12). The amplitude of the constant offset component is determined by the oxidized dye band (maximum around 820 nm) and free or shallow trapped electrons in titania (the increasing positive amplitude from 1000 to 1500 nm). The ratio of the constant offset component amplitude to the sum of the amplitudes of the other components agrees with the S_{res} values from the kinetics at 750 nm (Table 1). The faster component is related to the decay of the S_1 state; it has a maximum at 920 nm; while

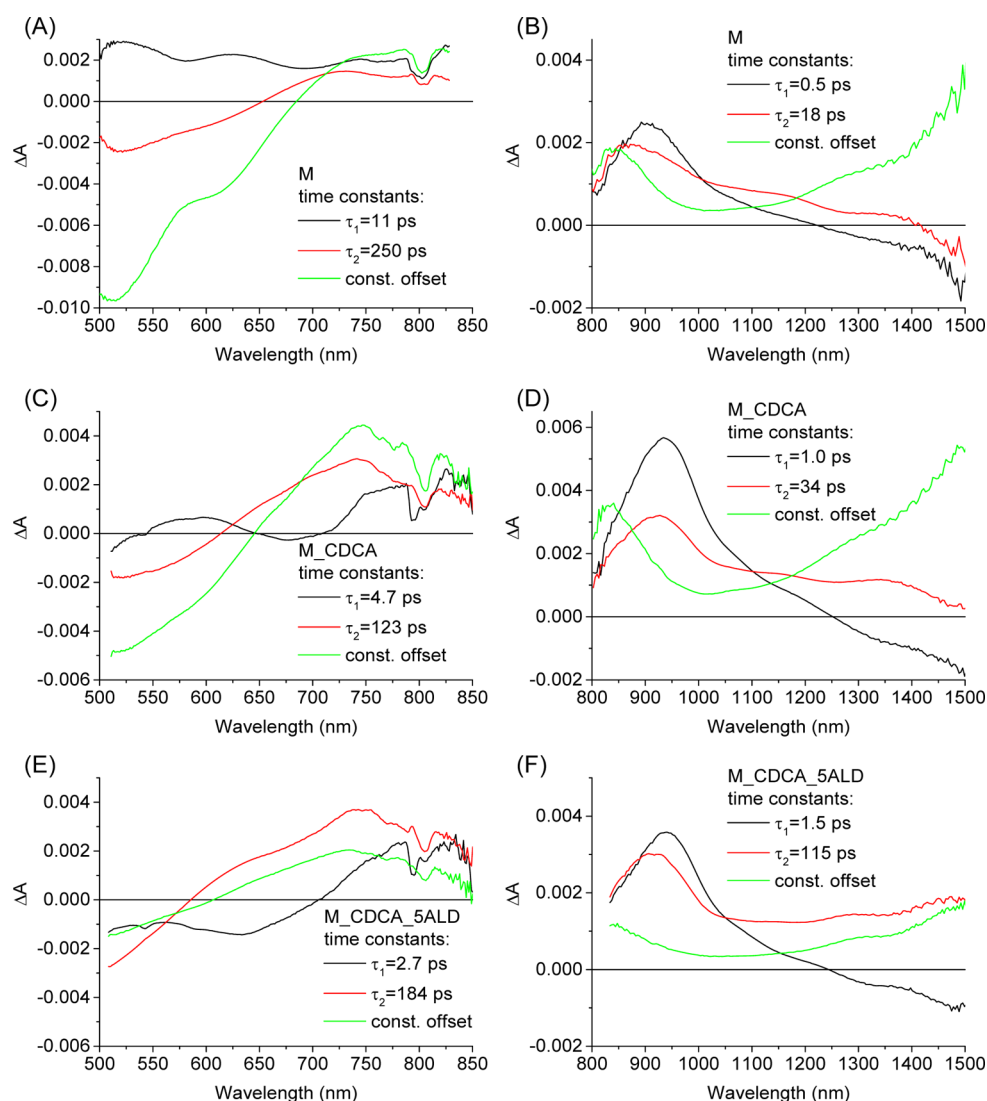


Figure 5. Wavelength dependent amplitudes of the indicated time constants obtained from global analysis (two exponential with constant offset) of transient absorption spectra of solar cells in the selected configurations, sensitized with MK-2 in the VIS (left: A, C, E) and NIR (right: B, D, F) spectral ranges. The results for other configurations are presented in SI (Figures S9–S12).

the negative amplitudes for the wavelengths longer than 1200 nm are probably a result of an increase in the free electron population in the electron injection process. The longer component has a maximum between that of the S_1 state (920 nm) and that of the oxidized dye (820 nm), so it probably corresponds to the decay of the intermediate dye–electron complex, in which electrons are not fully separated but localized in the titania trap states, close to the parent dye from which they were injected. The decay of such a complex leads partially to the fully separated charges (free electrons and oxidized dye) and partially to the unwanted recombination. Therefore, the two time constants from the NIR analysis can be directly related to the electron injection (faster component) and electron recombination (longer component), and their average values are collected in Table 2.

In the VIS region (left parts in Figures 4, 5, and S9–S12) the decay of the S_1 state (electron injection to titania nanoparticles) is manifested as a negative amplitude in the range 600–730 nm (stimulated emission, slightly red-shifted with respect to that in solution). For the samples for which the amplitude of the faster component is negative in this range (i.e., all cells with alumina

passivation and both ADEKA-1 cells with multicapping), the time constant of this component is directly taken as that of electron injection, while the time constant of slower component as that of electron recombination. The average values of both of them are collected in Table 2. For the rest of the samples, in the VIS range (with faster S_1 state decay) the situation is more difficult when both time constants are left to be optimally fitted. In such cases, the decay of S_1 state only partially contributes to the faster component (manifested in the corresponding amplitude spectra as indentation toward negative values in the range 600–730 nm), while the rest of this component represents the faster part of electron recombination which is a consequence of spectral overlap of the features characteristic for both injection and recombination. Therefore, the average time constants for electron injection and recombination summarized in Table 2 were calculated differently for these samples. The characteristic time of electron recombination was taken from one-exponential plus constant offset global fit (the contribution of subpicosecond electron injection is negligible in this case). In contrast, the proper values of the time constant for electron injection were

estimated from the shortest component in three-exponential plus constant offset global fit. The time constant of this component was fixed to the maximum value at which its amplitude is negative below 730 nm (see Figure S13 as an example of such fit). As can be seen comparing the values from Table 2 and Table S4, the injection time constants extracted in the protocol described earlier are in agreement with the rise times obtained from the single kinetics analysis at 700 nm (Figures 3A and S8A).

The trends in variation of the average injection and recombination time constants for different samples are the same in VIS and NIR ranges; however, the values for electron injection extracted from the NIR part are longer than those from the VIS part, while for recombination the situation is the opposite (Table 2). This observation can be rationalized by the complicated nature of both processes of injection (e.g., faster from hot than from relaxed S_1 state) and recombination (e.g., faster from the dye–electron complex than from free electrons), and that different constituents of these processes bring different contributions to the signals in VIS and NIR regions. Our aim is to get one mean rate constant for interfacial electron injection and one for recombination; therefore we decided to calculate them as the reciprocal of the averaged two time constants in VIS and NIR ranges from Table 2. Such rate constants are presented in Figure 6. Figure 6A depicts a good correlation between the average electron injection and electron recombination rate constants. In our previous work for MK-2 cells we observed that addition of TBP to the electrolyte slows

down both electron injection and recombination dynamics.²⁸ Our present results indicate that the relationship between the dynamics of these two processes is even more universal. For the corresponding cell configurations, the electron injection and recombination are faster in MK-2 than ADEKA-1 cells. It might be explained by the differences in the structures of both molecules and the previously reported results of molecular modeling.⁹ The LUMO orbital is localized in both molecules near the cyano group, so it is closer to the titania surface in MK-2 than in ADEKA-1, since in the latter the additional phenyl and amide groups are present between the cyano group and the anchoring part (Scheme S1). The effect of coadsorbent is more pronounced for the MK-2 cells since both recombination and injection are slowed down by about 3 times in M_CDCA with respect to the values for M cell. For ADEKA-1 cells the differences between A_OTMS and A samples are much smaller, but it should be recalled that OTMS lowered the ADEKA-1 coverage to a much smaller extent than CDCA affected the number of attached MK-2 molecules (Figure 1). For ADEKA-1 both hierarchical molecular multicapping and alumina passivation resulted in significantly slower injection and recombination rate constants with respect to those for the uncoated samples. Interestingly, the position of A_OTMS_CAPP and A_CAPP samples in Figure 6A is between A_OTMS_IALD and A_OTMS_3ALD, which means that the effect of the capping molecules corresponds to that of the Al_2O_3 coating between 0.1 and 0.3 nm. For MK-2 with multicapping, the time constant of electron injection still lies in the sub-picosecond regime, although recombination is slower for M_CAPP than for the M sample. It can probably be explained by a significant downshift of the titania conduction band for the M_CAPP sample (most of the dye molecules are desorbed by stronger acidic capping molecules, Figure 1), as in the samples without TBP, which exhibit the fastest injection and recombination rates with respect to those of the other cells of the same dyes (M_CDCA_noTBP, A_OTMS_noTBP in Figure 6A).

Finally, Figure 6B presents the dependence of time constants of both electron injection and electron recombination in ADEKA-1 cells on the thickness (x) of deposited alumina layer. The data can be fitted with the exponential function $k = k_0 + k_d \exp(-x/d)$ in which the characteristic quenching distance d is about 0.1 nm. The initial rate constants (without alumina layer, $k_0 + k_d$) are 1.1 ps⁻¹ for injection and 10.4 ns⁻¹ for recombination, while the residual rate constants (for sufficiently thick alumina layer, k_0) are 0.4 ps⁻¹ and 4.8 ns⁻¹, respectively. This important result means that after one or two ALD cycles (0.1 nm layer per cycle) the rate constants are significantly suppressed, and further coating hardly changes them. It explains why the time constants are similar for A_OTMS_3ALD and A_OTMS_5ALD cells (Table 2 and Figure 6).

With all the results in hand, two important questions should be asked. The first is why electron injection is slower for post-assembly passivation methods, for which the chemical bond between the dye and titania is preserved. In the typical understanding of the operation of DSSC, the electrons are injected through the anchoring part of the molecule and the overlap between dye LUMO orbital and electron acceptor states in titania is the determining parameter. In the studies reporting post-assembly ALD passivation for N719 and RuP dyes, mentioned in the Introduction,^{20,21} a possible increase in the conduction band energy (which lowers the density of acceptor states) upon alumina coating has been suggested as

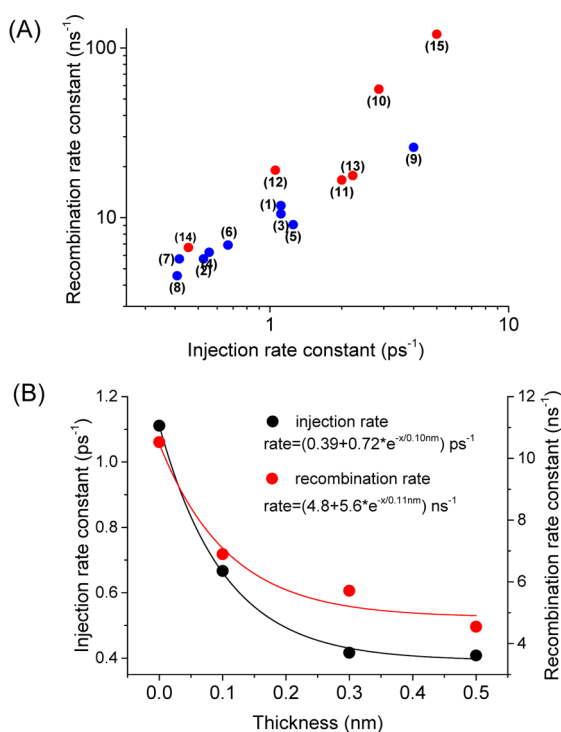


Figure 6. (A) Correlation of the averaged (from VIS and NIR ranges) electron recombination rate constant with the average electron injection rate constants calculated from the global fit of transient absorption spectra; numbers in brackets indicate different cells according to Table 1 (red points for MK-2 cells, blue points for ADEKA-1 cells). (B) Electron injection and recombination rate constants versus the thickness (x) of post-assembly alumina coating for ADEKA-1 cells. The inset shows the exponential fit to the data.

the reason for slower electron injection. However, in our case slower electron injection is observed for both ADEKA-1 samples with alumina (that exhibit conduction band upshift) as with multicapping (which shows even small energetic downshift of titania conduction band). Therefore, a different mechanism must operate, and perhaps the concept of the electron injection “through space”, recently proposed for DSSCs with zinc-porphyrin^{36,37} and zinc-phthalocyanines³⁸ dyes, could be adopted here. In this model, electron injection does not involve charge “flow” through the anchoring unit, but tunneling between electron donor part in the molecule and electron acceptor in titania. The rate depends thus on the distance and the potential barrier height for tunneling,³⁸ which, in our case, could be increased by the presence of capping molecules or alumina coating. Moreover, this model also explains the correlation between the injection and recombination rate constants, because the recombination process is based on the same tunneling process, but with much lower probability of the back electron transfer (e.g., see TOC).

The second question is why the passivated cells with slower electron injection exhibit worse *total APCE* and worse overall DSSC efficiency. The average injection time constant is only slowed down to single picoseconds, which, with the lifetime of S_1 state in solution of both dyes (about 500 ps) in mind, should still be enough to maintain the injection quantum yield close to 100%. The possible explanation is that the relaxation process in the S_1 state plays a key role, since the studies in solution indicate that its dynamics can be described also on the single picoseconds time scale. Electron transfer from the relaxed S_1 state of lower energy might lead to enhanced injection into deep trap states in titania and higher population of intermediate states from which recombination is more probable than from free or shallowly trapped electrons. Despite longer lifetime (longer recombination) of such intermediate states in passivated cells, the contribution of recombination increases with respect to that for nonpassivated samples. It could be noted that slowing down electron injection (and recombination) to a certain value is beneficial (better *total APCE* and cell performance for M_CDCA than M cell), but a further decrease in electron injection rate results in worse charge separation (M_CDCA_SALD vs M_CDCA).

CONCLUSIONS

Two post-sensitization passivation processes of titania surface (atomic layer deposition of blocking alumina coating and hierarchical molecular multicapping) were investigated and their influence on the dynamics of electron transfer at the dye–titania and titania–electrolyte interfaces were discussed. DSSCs with cobalt-based electrolyte, champion ADEKA-1 dye with silyl-anchor unit, and its popular and efficient carboxyl-anchor analogue, MK-2 dye, were examined from the point of view of electron injection, titania–dye and titania–electrolyte recombination, on the basis of femtosecond transient absorption and electrochemical impedance measurements. Both passivation processes improved the fill factor of the cells, additionally electron lifetime and open circuit voltage were significantly increased for alumina coating of the thickness greater than 0.3 nm. On the other hand, the relative photocurrent of the cells (short circuit current per number of absorbed photons) was reduced upon both treatments, and the decrease was greater with increasing alumina layer thickness. The amplitude of this relative photocurrent was found to depend almost exclusively

on the ultrafast and fast processes taking place in the first nanoseconds after dye excitation.

Both molecular capping and atomic blocking layers slowed down electron injection process (from sub-picoseconds to single picosecond average time constant), and this is a probable reason for the smaller relative photocurrent in the passivated cells. We interpret the results taking into account the dye relaxation, existence of intermediate dye–titania charge transfer complex, and charge transfer processes occurring “through space” rather than through the dye anchoring unit. The decreasing rate constant of electron injection correlates with the decreasing rate constant of partial back electron transfer occurring on the time scale of tens and hundreds of picoseconds. Significant extension of electron injection and recombination processes occurs for alumina layer thickness smaller than 0.3 nm. Therefore, unfortunately, the negative impact of the passivation (decrease in charge separation yield in the first nanoseconds) occurs for the coating layers thinner than that from which the positive impact of the passivation (longer electron lifetime) starts.

Besides, our studies revealed that short (single minutes) exposure of the electrodes sensitized with both dyes to 200 °C temperature hardly changes the interfacial dynamics and does not decrease the DSSC performance. We also observed that addition of coadsorbent (CDCA) to MK-2 dye has a positive impact on all interfacial charge transfer processes, and it significantly improves the relative photocurrent of the cell. This finding seems to have not been reported so far and should lead to the improved efficiency of DSSC with this dye.

ASSOCIATED CONTENT

Supporting Information

The Supporting Information is available free of charge on the ACS Publications website at DOI: 10.1021/acsami.7b03288.

Photovoltaic parameters, structures, stationary absorption–stability tests, IPCE spectra, and the details of electrochemical impedance and transient absorption studies (PDF)

AUTHOR INFORMATION

Corresponding Author

*E-mail: marziol@amu.edu.pl.

ORCID

Marcin Ziólek: 0000-0003-1882-6022

Notes

The authors declare no competing financial interest.

ACKNOWLEDGMENTS

This work was supported by NCN (National Science Centre, Poland) under project 2015/18/E/ST4/00196. Dr. hab. Błażej Gierczyk from the Faculty of Chemistry, Adam Mickiewicz University in Poznań, Poland, who synthesized ADEKA-1 dye is kindly acknowledged.

REFERENCES

- (1) O'Regan, B.; Grätzel, M. A Low-Cost, High-Efficiency Solar Cell Based on Dye-Sensitized Colloidal TiO_2 Films. *Nature* **1991**, *353*, 737–740.
- (2) Hagfeldt, A.; Boschloo, G.; Sun, L.; Kloo, L.; Pettersson, H. Dye-Sensitized Solar Cells. *Chem. Rev.* **2010**, *110*, 6595–6663.

- (3) Yu, Z.; Li, F.; Sun, L. Recent Advances in Dye-Sensitized Photoelectrochemical Cells for Solar Hydrogen Production Based on Molecular Components. *Energy Environ. Sci.* **2015**, *8*, 760–775.
- (4) Swierk, J. R.; Mallouk, T. E. Design and Development of Photoanodes for Water-Splitting Dye-Sensitized Photoelectrochemical Cells. *Chem. Soc. Rev.* **2013**, *42*, 2357–2387.
- (5) Yella, A.; Lee, H.-W.; Tsao, H. N.; Yi, C.; Chandiran, A. K.; Nazeeruddin, M. K.; Diah, E. W.-G.; Yeh, C.-Y.; Zakeeruddin, S. M.; Grätzel, M. Porphyrin-Sensitized Solar Cells with Cobalt (II/III)-Based Redox Electrolyte Exceed 12% Efficiency. *Science* **2011**, *334*, 629–634.
- (6) Mathew, S.; Yella, A.; Gao, P.; Humphry-Baker, R.; Curchod, B. F. E.; Ashari-Astani, N.; Tavernelli, I.; Rothlisberger, U.; Nazeeruddin, M. K.; Grätzel, M. Dye-Sensitized Solar Cells with 13% Efficiency Achieved through the Molecular Engineering of Porphyrin Sensitizers. *Nat. Chem.* **2014**, *6*, 242–247.
- (7) Kakiage, K.; Aoyama, Y.; Yano, T.; Otsuka, T.; Kyomen, T.; Unno, M.; Hanaya, M. An Achievement of over 12% Efficiency in an Organic Dye-Sensitized Solar Cell. *Chem. Commun.* **2014**, *50*, 6379–6381.
- (8) Kakiage, K.; Aoyama, Y.; Yano, T.; Oya, K.; Kyomen, T.; Hanaya, M. Fabrication of a High-Performance Dye-Sensitized Solar Cell with 12.8% Conversion Efficiency Using Organic Silyl-Anchor Dyes. *Chem. Commun.* **2015**, *51*, 6315–6317.
- (9) Kakiage, K.; Aoyama, Y.; Yano, T.; Oya, K.; Fujisawa, J.-i.; Hanaya, M. Highly-Efficient Dye-Sensitized Solar Cells with Collaborative Sensitization by Silyl-Anchor and Carboxy-Anchor Dyes. *Chem. Commun.* **2015**, *51*, 15894–15897.
- (10) Mosconi, E.; Yum, J.-H.; Kessler, F.; Gómez García, C. J.; Zuccaccia, C.; Cinti, A.; Nazeeruddin, M. K.; Grätzel, M.; De Angelis, F. Cobalt Electrolyte/Dye Interactions in Dye-Sensitized Solar Cells: A Combined Computational and Experimental Study. *J. Am. Chem. Soc.* **2012**, *134*, 19438–19453.
- (11) Marchena, M. J.; de Miguel, G.; Cohen, B.; Organero, J. A.; Pandey, S.; Hayase, S.; Douhal, A. Real-Time Photodynamics of Squaraine-Based Dye-Sensitized Solar Cells with Iodide and Cobalt Electrolytes. *J. Phys. Chem. C* **2013**, *117*, 11906–11919.
- (12) Pazoki, M.; Lohse, P. W.; Taghavinia, N.; Hagfeldt, A.; Boschloo, G. The Effect of Dye Coverage on the Performance of Dye-Sensitized Solar Cells with a Cobalt-Based Electrolyte. *Phys. Chem. Chem. Phys.* **2014**, *16*, 8503–8508.
- (13) Hamann, T. W.; Farha, O. K.; Hupp, J. T. Outer-Sphere Redox Couples as Shuttles in Dye-Sensitized Solar Cells. Performance Enhancement Based on Photoelectrode Modification Via Atomic Layer Deposition. *J. Phys. Chem. C* **2008**, *112*, 19756–19764.
- (14) Moser, J. E. Dynamics of Interfacial and Surface Electron Transfer Processes. In *Dye-Sensitized Solar Cells*, 2010 ed.; Kalyanasundaram, K., Ed.; EPFL Press: Lausanne, 2010; pp 403–456.
- (15) Antila, L. J.; Heikkilä, M. J.; Mäkinen, V.; Humalampi, N.; Laitinen, M.; Linko, V.; Jalkanen, P.; Toppari, J.; Aumanen, V.; Kemell, M.; Myllyperkiö, P.; Honkala, K.; Häkkinen, H.; Leskelä, M.; Korppi-Tommola, J. E. I. ALD Grown Aluminum Oxide Submonolayers in Dye-Sensitized Solar Cells: The Effect on Interfacial Electron Transfer and Performance. *J. Phys. Chem. C* **2011**, *115*, 16720–16729.
- (16) Kim, D. H.; Losego, M. D.; Peng, Q.; Parsons, G. N. Thin Films: Atomic Layer Deposition for Sensitized Solar Cells: Recent Progress and Prospects. *Adv. Mater. Interfaces* **2016**, *3*, 1 DOI: 10.1002/admi.201670102.
- (17) Hanson, K.; Losego, M. D.; Kalanyan, B.; Parsons, G. N.; Meyer, T. J. Stabilizing Small Molecules on Metal Oxide Surfaces Using Atomic Layer Deposition. *Nano Lett.* **2013**, *13*, 4802–4809.
- (18) Vannucci, A. K.; Alibabaei, L.; Losego, M. D.; Concepcion, J. J.; Kalanyan, B.; Parsons, G. N.; Meyer, T. J. Crossing the Divide between Homogeneous and Heterogeneous Catalysis in Water Oxidation. *Proc. Natl. Acad. Sci. U. S. A.* **2013**, *110*, 20918–20922.
- (19) Son, H.-J.; Prasittichai, C.; Mondloch, J. E.; Luo, L.; Wu, J.; Kim, D. W.; Farha, O. K.; Hupp, J. T. Dye Stabilization and Enhanced Photoelectrode Wettability in Water-Based Dye-Sensitized Solar Cells through Post-Assembly Atomic Layer Deposition of TiO₂. *J. Am. Chem. Soc.* **2013**, *135*, 11529–11532.
- (20) Hanson, K.; Losego, M. D.; Kalanyan, B.; Ashford, D. L.; Parsons, G. N.; Meyer, T. J. Stabilization of [Ru(Bpy)₂(4,4'-(PO₃H₂)Bpy)]²⁺ on Mesoporous TiO₂ with Atomic Layer Deposition of Al₂O₃. *Chem. Mater.* **2013**, *25*, 3–5.
- (21) Kim, D. H.; Losego, M. D.; Hanson, K.; Alibabaei, L.; Lee, K.; Meyer, T. J.; Parsons, G. N. Stabilizing Chromophore Binding on TiO₂ for Long-Term Stability of Dye-Sensitized Solar Cells Using Multicomponent Atomic Layer Deposition. *Phys. Chem. Chem. Phys.* **2014**, *16*, 8615–8622.
- (22) Son, H.-J.; Kim, C. H.; Kim, D. W.; Jeong, N. C.; Prasittichai, C.; Luo, L.; Wu, J.; Farha, O. K.; Wasielewski, M. R.; Hupp, J. T. Post-Assembly Atomic Layer Deposition of Ultrathin Metal-Oxide Coatings Enhances the Performance of an Organic Dye-Sensitized Solar Cell by Suppressing Dye Aggregation. *ACS Appl. Mater. Interfaces* **2015**, *7*, 5150–5159.
- (23) Sobuś, J.; Gierczyk, B.; Burdziński, G.; Jancelewicz, M.; Polanski, E.; Hagfeldt, A.; Ziólek, M. Factors Affecting the Performance of Champion Silyl-Anchor Carbazole Dye Revealed in the Femtosecond to Second Studies of Complete ADEKA-1 Sensitized Solar Cells. *Chem. - Eur. J.* **2016**, *22*, 15807–15818.
- (24) Koumura, N.; Wang, Z.-S.; Mori, S.; Miyashita, M.; Suzuki, E.; Hara, K. Alkyl-Functionalized Organic Dyes for Efficient Molecular Photovoltaics. *J. Am. Chem. Soc.* **2006**, *128*, 14256–14257.
- (25) Hara, K.; Wang, Z.-S.; Cui, Y.; Furube, A.; Koumura, N. Long-Term Stability of Organic-Dye-Sensitized Solar Cells Based on an Alkyl-Functionalized Carbazole Dye. *Energy Environ. Sci.* **2009**, *2*, 1109–1114.
- (26) Kashif, M. K.; Axelson, J.; Duffy, N. W.; Forsyth, C. M.; Chang, C. J.; Long, J. R.; Spiccia, L.; Bach, U. A New Direction in Dye-Sensitized Solar Cells Redox Mediator Development: In Situ Fine-Tuning of the Cobalt(II)/(III) Redox Potential through Lewis Base Interactions. *J. Am. Chem. Soc.* **2012**, *134*, 16646–16653.
- (27) Murakami, T. N.; Koumura, N.; Uchiyama, T.; Uemura, Y.; Obuchi, K.; Masaki, N.; Kimura, M.; Mori, S. Recombination Inhibitive Structure of Organic Dyes for Cobalt Complex Redox Electrolytes in Dye-Sensitized Solar Cells. *J. Mater. Chem. A* **2013**, *1*, 792–798.
- (28) Sobuś, J.; Kubicki, J.; Burdziński, G.; Ziólek, M. Carbazole Dye-Sensitized Solar Cells Studied from Femtoseconds to Seconds—Effect of Additives in Cobalt- and Iodide-Based Electrolytes. *ChemSusChem* **2015**, *8*, 3118–3128.
- (29) Fabregat-Santiago, F.; Garcia-Belmonte, G.; Mora-Seró, I.; Bisquert, J. Characterization of Nanostructured Hybrid and Organic Solar Cells by Impedance Spectroscopy. *Phys. Chem. Chem. Phys.* **2011**, *13*, 9083–9118.
- (30) Idígoras, J.; Burdziński, G.; Karolczak, J.; Kubicki, J.; Oskam, G.; Anta, J. A.; Ziólek, M. The Impact of the Electrical Nature of the Metal-Oxide on the Performance in Dye-Sensitized Solar Cells: New Look at Old Paradigms. *J. Phys. Chem. C* **2015**, *119*, 3931–3944.
- (31) Anta, J. A.; Guillén, E.; Tena-Zaera, R. ZnO-Based Dye-Sensitized Solar Cells. *J. Phys. Chem. C* **2012**, *116*, 11413–11425.
- (32) Martín, C.; Ziólek, M.; Douhal, A. Ultrafast and Fast Charge Separation Processes in Real Dye-Sensitized Solar Cells. *J. Photochem. Photobiol. C* **2016**, *26*, 1–30.
- (33) Pydzińska, K.; Ziólek, M. Solar Cells Sensitized with near-Infrared Absorbing Dye: Problems with Sunlight Conversion Efficiency Revealed in Ultrafast Laser Spectroscopy Studies. *Dyes Pigm.* **2015**, *122*, 272–279.
- (34) Idígoras, J.; Sobuś, J.; Jancelewicz, M.; Azaceta, E.; Tena-Zaera, R.; Anta, J. A.; Ziólek, M. Effect of Different Photoanode Nanostructures on the Initial Charge Separation and Electron Injection Process in Dye Sensitized Solar Cells: A Photophysical Study with Indoline Dyes. *Mater. Chem. Phys.* **2016**, *170*, 218–228.
- (35) Wendel, M.; Kumorkiewicz, A.; Wybraniec, S.; Ziólek, M.; Burdziński, G. Impact of S₁→S₀ Internal Conversion in Betalain-Based Dye Sensitized Solar Cells. *Dyes Pigm.* **2017**, *141*, 306–315.

(36) Imahori, H.; Kang, S.; Hayashi, H.; Haruta, M.; Kurata, H.; Isoda, S.; Canton, S. E.; Infahsaeng, Y.; Kathiravan, A.; Pascher, T.; Chábera, P.; Yartsev, A. P.; Sundström, V. Photoinduced Charge Carrier Dynamics of Zn-Porphyrin-TiO₂ Electrodes: The Key Role of Charge Recombination for Solar Cell Performance. *J. Phys. Chem. A* **2011**, *115*, 3679–3690.

(37) Ye, S.; Kathiravan, A.; Hayashi, H.; Tong, Y.; Infahsaeng, Y.; Chabera, P.; Pascher, T.; Yartsev, A. P.; Isoda, S.; Imahori, H.; Sundström, V. Role of Adsorption Structures of Zn-Porphyrin on TiO₂ in Dye-Sensitized Solar Cells Studied by Sum Frequency Generation Vibrational Spectroscopy and Ultrafast Spectroscopy. *J. Phys. Chem. C* **2013**, *117*, 6066–6080.

(38) Matsuzaki, H.; Murakami, T. N.; Masaki, N.; Furube, A.; Kimura, M.; Mori, S. Dye Aggregation Effect on Interfacial Electron-Transfer Dynamics in Zinc Phthalocyanine-Sensitized Solar Cells. *J. Phys. Chem. C* **2014**, *118*, 17205–17212.

Supporting information

for

Effects of post-assembly molecular and atomic passivation of sensitized titania surface: dynamics of electron transfer measured from femtoseconds to seconds.

Mateusz Gierszewski ¹, Adam Glinka ¹, Iwona Grądzka ¹,
Mariusz Jancelewicz ² and Marcin Ziólek^{1*}

¹ *Quantum Electronics Laboratory, Faculty of Physics, Adam Mickiewicz University in
Poznań, Umultowska 85, 61-614 Poznań, Poland.*

² *NanoBioMedical Centre, Adam Mickiewicz University in Poznań, Umultowska 85, 61-614
Poznań, Poland.*

* corresponding author, email: marziol@amu.edu.pl

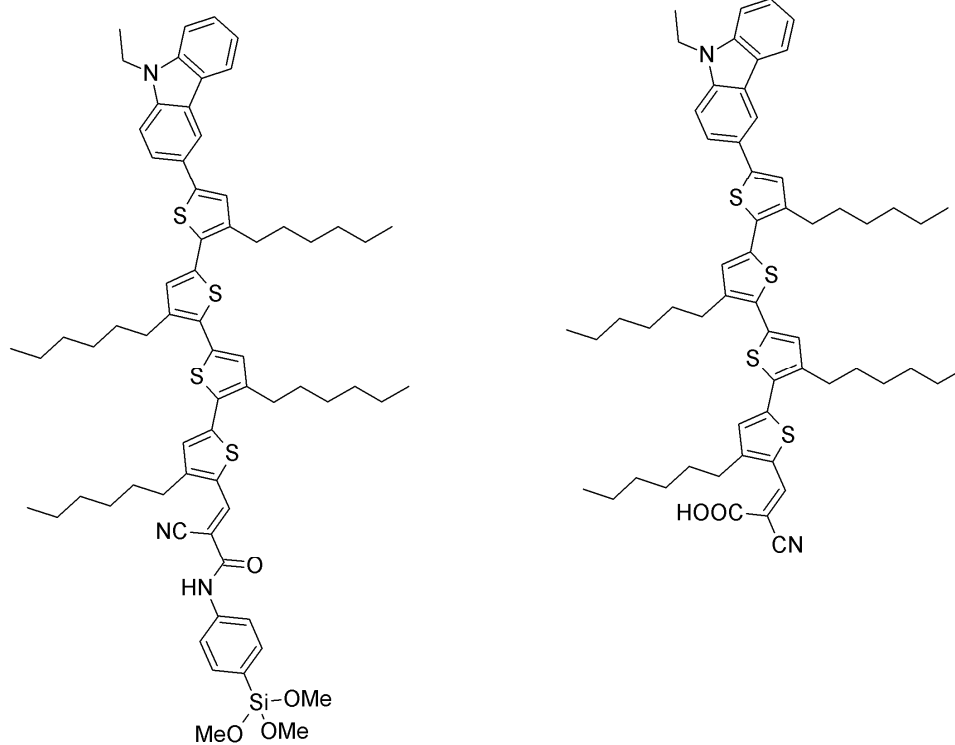
Photovoltaic parameters

Table S1. Number of measured samples (N) and relative errors of the calculated averaged photovoltaic parameters (given in Table 1) for the studied solar cells. The relative error of parameter p is defined as the standard deviation of the mean (Δp) divided by the mean value (from Table 1) and multiplied by 100 %.

Cell	N	$\frac{\Delta V_{oc}}{\overline{V_{oc}}}$ [%]	$\frac{\Delta FF}{\overline{FF}}$ [%]	$\frac{\Delta J_{sc}}{\overline{J_{sc}}}$ [%]	$\frac{\Delta Eff}{\overline{Eff}}$ [%]
A	7	0.8	2.6	4.6	6.3
A_CAPP	7	1.2	2.6	8.4	10.5
A_OTMS	7	1.2	11.2	10.5	4.8
A_OTMS_CAPP	5	2.0	4.5	13.6	17.4
A_OTMS_200C	5	0.9	3.0	6.8	7.7
A_OTMS_1ALD	6	0.4	3.1	2.6	3.2
A_OTMS_3ALD	6	2.7	1.6	6.3	4.4
A_OTMS_5ALD	6	0.6	0.8	10.3	10.3
A_OTMS_noTBP	4	4.2	1.4	5.0	10.8
M	15	0.9	4.1	4.6	6.8
M_CAPP	9	11.7	9.4	18.3	36.1
M_CDCA	6	0.7	3.0	4.2	6.1
M_CDCA_200C	6	0.7	7.0	2.2	8.5
M_CDCA_5ALD	6	0.5	1.4	9.9	7.7
M_CDCA_noTBP	3	2.6	10.0	9.6	2.4

Table S2. Photovoltaic parameters of the best solar cells sensitized with ADEKA-1 and MK-2 of each configuration: open circuit voltage (V_{OC}), fill factor (FF), photocurrent density (J_{SC}), efficiency (Eff) number of absorbed photons at 1Sun illumination (N_{ph}), absorption in the maximum (A_{max}) and corrected photocurrent efficiency ($Total APCE$).

Cell	V_{OC} [V]	FF	J_{SC} [mAcm ⁻²]	Eff [%]	N_{ph} [10 ²⁰ s ⁻¹ m ⁻²]	A_{max}	$Total APCE$
A	0.82	0.58	6.5	3.1	8.9	2.83	0.46
A_CAPP	0.80	0.67	3.6	1.9	6.6	1.14	0.34
A_OTMS	0.85	0.36	9.1	2.8	8.4	2.25	0.68
A_OTMS_CAPP	0.80	0.69	2.4	1.3	6.1	0.54	0.24
A_OTMS_200C	0.83	0.51	7.3	3.0	7.9	1.50	0.58
A_OTMS_1ALD	0.83	0.61	5.9	3.0	7.9	1.38	0.47
A_OTMS_3ALD	0.81	0.64	2.6	1.3	6.5	0.93	0.25
A_OTMS_5ALD	0.85	0.71	2.4	1.5	7.5	1.30	0.20
A_OTMS_noTBP	0.65	0.41	7.2	1.9	7.1	1.26	0.64
M	0.85	0.47	9.7	3.9	7.2	1.50	0.84
M_CAPP	0.75	0.65	1.5	0.7	1.8	0.15	0.51
M_CDCA	0.81	0.54	8.4	3.6	5.9	0.93	0.89
M_CDCA_200C	0.83	0.48	9.0	3.6	5.9	0.89	0.95
M_CDCA_5ALD	0.84	0.67	2.7	1.5	5.2	0.63	0.32
M_CDCA_noTBP	0.59	0.49	5.3	1.5	5.8	0.82	0.57



Scheme S1. The structures of ADEKA-1 (left) and MK-2 (right).

Stationary absorption – stability tests

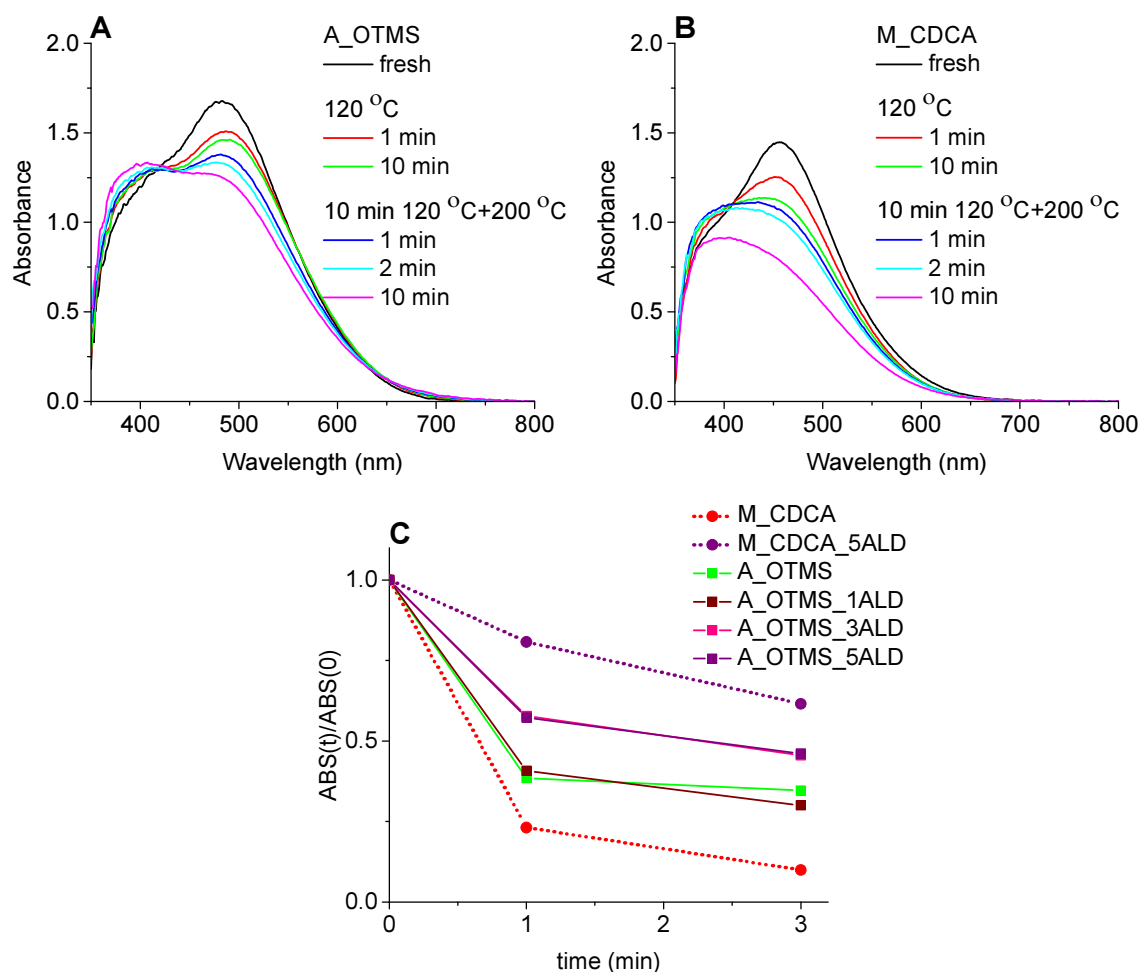


Figure S1. (A, B) Temperature effects in stationary absorption spectra in selected time intervals for ADEKA-1+OTMS (A, **A_OTMS**) and MK-2+CDCA (B, **M_CDCA**) photoanodes. (C) Test of desorption of ADEKA-1 and MK-2 dyes from titania surface by ethylphosphonic acid (EPA). The relative decrease in the absorbance of the sensitized photoanodes ($ABS(t)/ABS(0)$, where $ABS(t)$ is absorbance after time t and $ABS(0)$ is the initial absorbance) as a function of the immersion time in ethylphosphonic acid (0.01 M) solution in 1:1 acetonitrile:toluene mixture.

Comment:

The characteristic absorption band with the maximum at 483 nm and the absorption shoulder at about 396 nm can be observed in the absorption spectra of fresh photoanodes sensitized with ADEKA-1 and OTMS (Figure S1A). During the heating with a hotplate at normal pressure conditions at 120 °C, the values of absorbance around the absorption maximum (483 nm) decreased, while those close to the absorption shoulder (~ 396 nm) increased. The most rapid change was observed within the first 1 minute of heating. Next, higher temperature was applied (200 °C) which resulted in further lowering of absorbance at 483 nm and creation of new absorption band in the short-wavelength part of absorption spectrum with maximum at about 396 nm. A clear isosbestic point around 420 nm can be noted. Much more pronounced changes in the absorption spectra during the heating were observed for photoanodes sensitized with MK-2 and CDCA (Figure S1B). In the absorption spectrum of fresh photoanodes the maximum at 458 nm and small absorption shoulder at 388 nm were observed. After heating for 1 min. at 120 °C we noted ~ 14% decrease in the absorbance when compared to the fresh sample, and after 10 min heating ~ 23% decrease in amplitude of the longest-wavelength absorption band. At the same time the value of absorbance at about 388 nm increased, similarly as for ADEKA-1. Heating at 200 °C caused further absorbance decrease (checked after 1 min., 2 min. and 10 min.) with the most pronounced changes after 10 min. (in the spectral range between 350 nm and 800 nm only one absorption band was found with maximum at 396 nm).

IPCE spectra

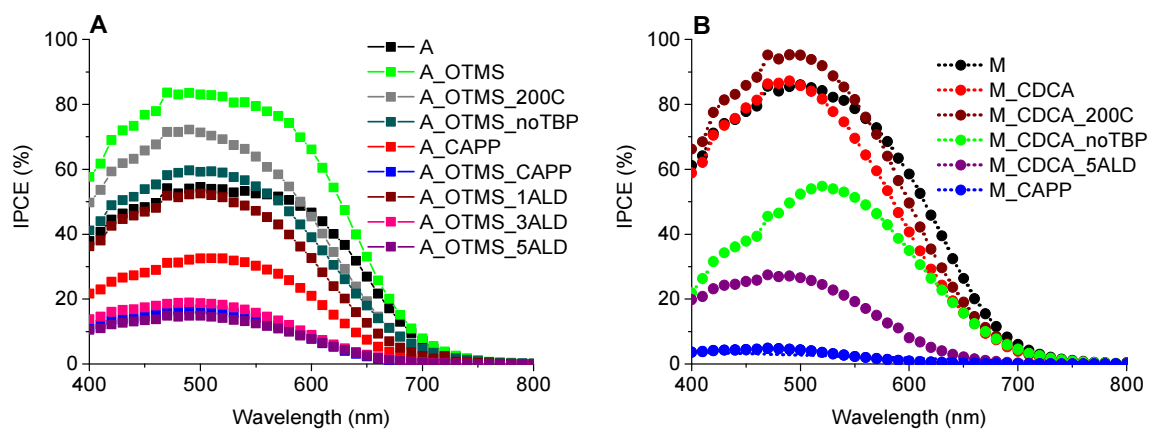


Figure S2. IPCE spectra of selected cells sensitized with ADEKA-1 (A) and MK-2 (B) dyes in the different, indicated configurations.

Comment:

Figure S2 shows the incident-photon to current efficiency (IPCE) spectra for the best cells sensitized with ADEKA-1 (A) and MK-2 (B) dyes. Generally, the order in maximum IPCE values is in agreement with J_{SC} presented in Table S1, and for the samples of $A_{max} > 1$, the IPCE maxima are similar to *total APCE* values, confirming the compatibility of both experiments. Among ADEKA-1 cells the highest IPCE values were obtained for ADEKA-1 with OTMS (**A_OTMS**, close to 84%) and ADEKA-1 with OTMS after 200 °C treatment (**A_OTMS_200C**, close to 72%). The cells prepared with ADEKA-1 (A) produced maximum IPCE value ~ 55%. For the cells sensitized with ADEKA-1 and OTMS after ALD post-treatment, the IPCE values changed in the sequence: **A_OTMS_1ALD** > **A_OTMS_3ALD** > **A_OTMS_5ALD**. Further, comparison between multi-capping treatment for ADEKA-1 with OTMS and ADEKA-1 shows decrease in IPCE values for **A_OTMS_CAPP** (~ 17%) when compared to **A_CAPP** (~ 32%). Interestingly, the changes Lewis base additives (TBP) in electrolyte caused significantly decrease in the IPCE values for the cells without *tert*-butylpyridinie (**A_OTMS_noTBP**) when compared to the cells with TBP (**A_OTMS**). The location of the IPCE maxima slightly depended on the cell configurations (in line with stationary absorption shifts): for **A_OTMS** it was found at about 490 nm, the shifts to longer wavelengths were observed for **A** (~ 500 nm, due to aggregation effects) and **A_CAPP** (~ 510 nm, due to more acidic environment), while the shift to shorter wavelengths was noted for **A_OTMS_5ALD** (~470 nm, due to the temperature effects).

For cells sensitized with MK-2 dye (Figure S2B) the highest IPCE value, close to 95%, was obtained for **M_CDCA_200C** (MK-2 and CDCA after 200 °C inside the ALD reactor). Slightly lower IPCE values were noted for **M** and **M_CDCA** (close to 85%). The changes in electrolyte compositions decreased IPCE values from ~ 85% (**M_CDCA**) to ~ 55% (**M_CDCA_noTBP**). Significantly, the lowest IPCE values were noted for the cells sensitized with MK-2 and CDCA after ALD treatment (**M_CDCA_5ALD**, ~ 27%) and MK-2 after multi-capping process (**M_CAPP**, ~ 5%). The location of IPCE maxima for cells sensitized with MK-2 dye depended on the cells configurations, similar as for the cells sensitized with ADEKA-1 dye. For **M_CDCA** and **M_CDCA_200C** the maximum was found at about 490 nm, while for **M** at about 500 nm (aggregation effects). The shift to longer wavelengths was noted also for **M_CDCA_noTBP** (520 nm, more acidic environment) and the shift to shorter wavelengths – for **M_CDCA_5ALD** (470 nm, due to temperature effects). Additionally, the cells sensitized with ADEKA-1 dye delivered IPCE spectra broader than the cells with MK-2 (under the same conditions and for the same cell modifications), in accordance with slightly broader stationary spectra of the former dye than the latter one.

Electrochemical impedance spectroscopy (EIS)

A:

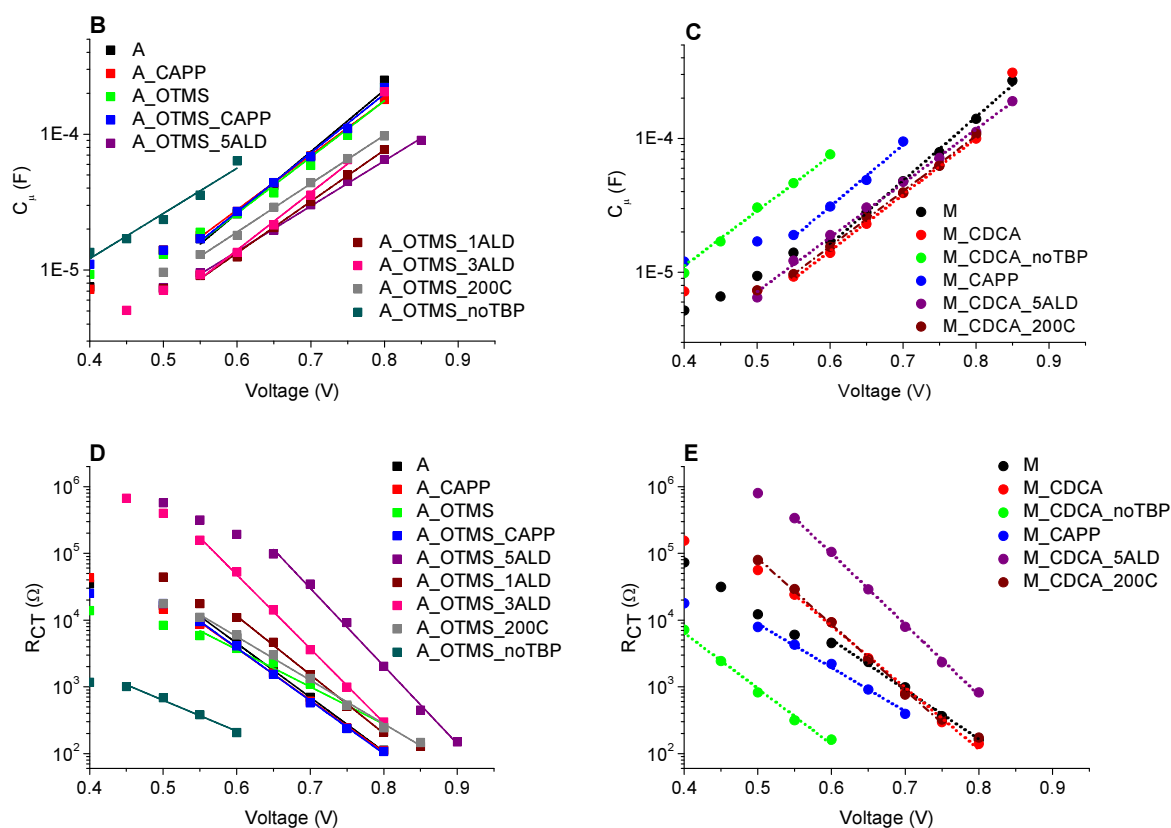
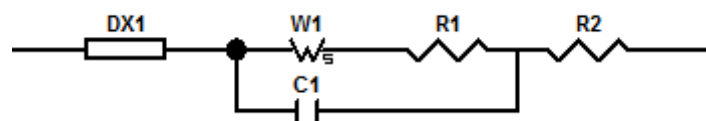


Figure S3. (A) Equivalent circuits for DSSCs based on ADEKA-1 and MK-2 dyes, DX1 is transmission line element ¹. Chemical capacitance (B-C) and charge transfer resistance (D-E) of different cells sensitized with ADEKA-1 and MK-2 dye in different cell configurations. Line shows the fits with the parameters given in Table S3.

Comment:

The following main elements were extracted from fitting equivalent circuit (Figure S3A) to Nyquist plots: (i) charge transfer resistance (R_{CT}) related to electron recombination at the TiO_2 / electrolyte interface, (ii) the capacitance at this contact (C_{μ}) and (iii) electron transport resistance (R_T). These elements were included in the transmission line of finite length for diffusion-recombination described as DX-11 (Bisquert#2).¹ Besides, the equivalent circuit contains also: the Warburg element (W1) due to the diffusion of a redox pair in the electrolyte, the resistance and the capacitance at the counter electrode/electrolyte interface

(R1 and C1, respectively), and series resistance (R2) due to sheet resistance of FTO substrate and electrolyte resistance.

The plot of extracted C_{μ} values vs bias voltage are shown in Figure S3B-C for the cells sensitized with ADEKA-1 and MK-2 in different configurations. The shift in C_{μ} values is a good estimation of the relative movement of titania conduction band. For the cells with ADEKA-1 and OTMS cells the lack of TBP caused down-shift of conduction band position of about 100 mV (**A_OTMS_noTBP**) when compared to the cells with TBP in electrolyte (**A_OTMS**). Similarly, for MK-2 with CDCA the down-shift of conduction band position of about 150 mV was found (**M_CDCA_noTBP** compared to **M_CDCA**). The effect of exposure to the temperature inside the ALD reactor (200 °C) resulted in some up-shift of conduction band position (**A_OTMS_200C**) with respect to that of **A_OTMS** cells while only negligible changes in the conduction band position were noted for **M_CDCA_200C** when compared to **M_CDCA**. Comparison between the samples after ALD treatment (**A_OTMS_1ALD**, **A_OTMS_3ALD** and **A_OTMS_5ALD**) shows that the highest up-shift of conduction band was observed for **A_OTMS_5ALD** (the thickest layer of alumina).

The variation in charge transfer resistance (R_{CT}) vs bias voltage for cells sensitized with ADEKA-1 and MK-2 dye in different configurations is presented in Figure S3D-E. Firstly, for both ADEKA-1 with OTMS and MK-2 with CDCA devices a marked reduction (roughly two orders of magnitude) in R_{CT} values was observed for the samples without TBP in electrolyte with respect to those with TBP. The down-shift of the conduction band position resulted in the increased recombination between electrons in titania nanoparticles and Co-Bpy electrolyte (at the same applied bias). It should be noted that the values of R_{CT} in the cells without TBP are still lower even taking into account the shift of the titania conduction band between **A_OTMS_noTBP** and **A_OTMS** cells (i.e. after the correction for Fermi level position). Secondly, examination of the cells after ALD treatment (**A_OTMS_1ALD**, **A_OTMS_3ALD** and **A_OTMS_5ALD**) reveals that thicker layer of alumina resulted in increased R_{CT} values compared to the cells without such post-treatment (**A_OTMS**). This confirms that more layers of alumina protect better against unwanted electron recombination between titania nanoparticles and Co-Bpy electrolyte. Similar trend was observed for MK-2 with CDCA cells. Thirdly, multi-capping treatment, both for the cells sensitized with ADEKA-1 and MK-2 dyes resulted in slight decrease in R_{CT} values compared to those of the same cells but without the multi-capping treatment. It is in some contrast to our previous report for ADEKA-1, where an increase in R_{CT} values upon single-capping, and further increase upon multi-capping was observed, in line with corresponding increase in V_{OC} values.² We account this difference to the distinct titania nanoparticles used in the current study, which give V_{OC} higher than previously already for the cells without capping treatment.² Control experiments were made for **A** and **A_OTMS** cells using the photoanodes from our previous studies, both for ADEKA-1,² and MK-2,³ and they showed that the current electrodes gives better V_{OC} and about an order of magnitude higher R_{CT} values for the same applied bias.

Table S3. Calculated ideality factor (m) and trap distribution parameter (α) for the cells sensitized with ADEKA-1 and MK-2 dye in different configurations. The parameters α and m were obtained from the fit (Figure S3) of the following functions: $C_{\mu}=C_0 \exp(\alpha Ve/kT)$ and $R_{ct}=R_0 \exp(-Ve/m kT)$.⁴

Sample / configuration	m	α
A	2.1	0.27
A_CAPP	2.1	0.24
A_OTMS	3.0	0.24
A_OTMS_CAPP	2.2	0.25
A_OTMS_200C	2.6	0.21
A_OTMS_1ALD	1.9	0.22
A_OTMS_3ALD	1.5	0.25
A_OTMS_5ALD	1.5	0.19
A_OTMS_noTBP	3.7	0.19
M	2.3	0.28
M_CAPP	2.6	0.27
M_CDCA	1.8	0.25
M_CDCA_200C	1.7	0.24
M_CDCA_5ALD	1.6	0.24
M_CDCA_noTBP	2.0	0.24

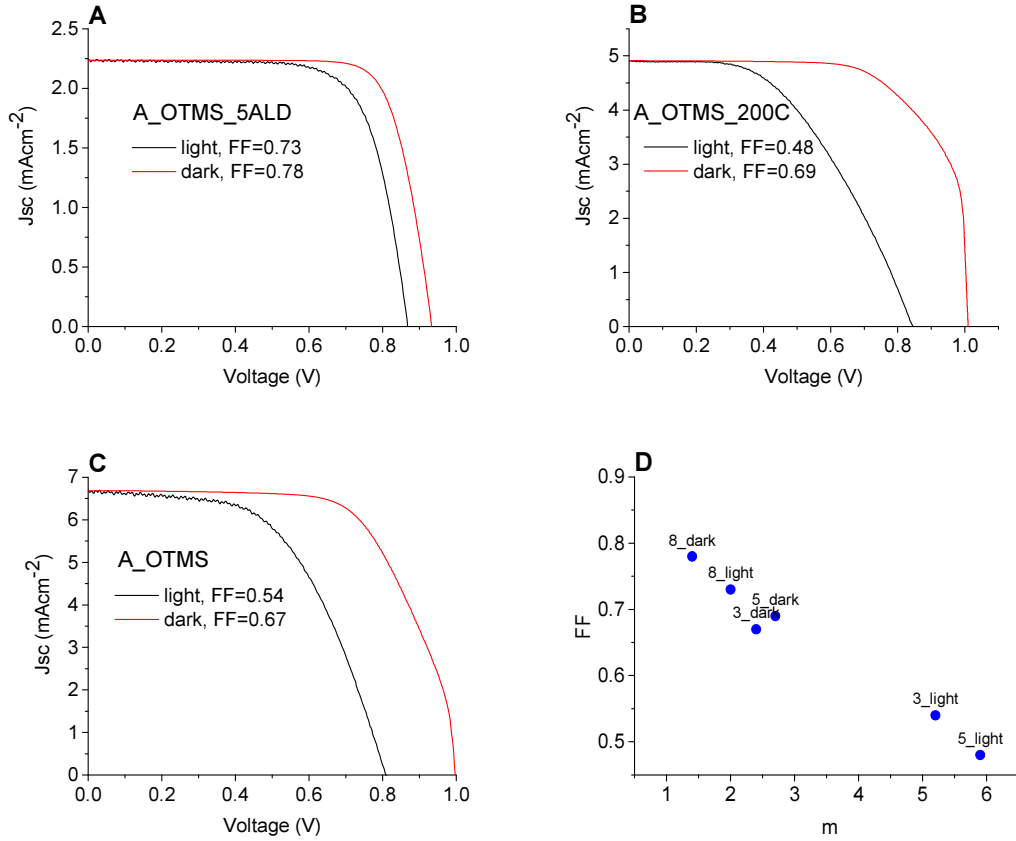


Figure S4. (A-C) C-V curves measured at 1Sun illumination (black) and simulated ideal C-V curves (red) for the indicated samples; the simulated ideal C-V curves were obtained adding J_{SC} value to the current from dark C-V curves of the corresponding cells. (D) Plot of FF (calculated from the C-V curves in figures A-C) as a function of ideality factor m (from EIS measurements at 1Sun and in the dark, numbers indicate the cell configuration in line with Table 1; 8: A_OTMS_5ALD, 5: A_OTMS_200C, 3: A_OTMS).

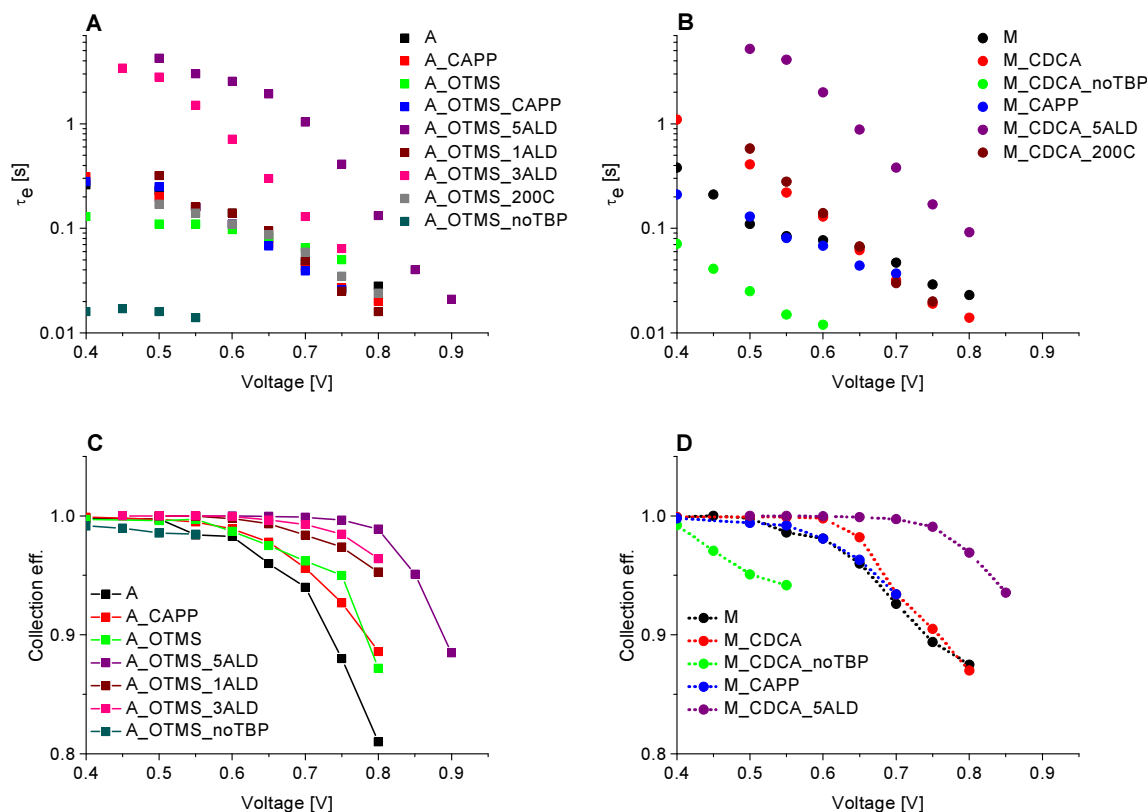


Figure S5. Electron lifetime (A-B) and charge collection efficiency (C-D) of different cells sensitized with ADEKA-1 and MK-2 dye in different configurations.

Comment:

Charge collection efficiency values, calculated as the ratio of R_{CT} and R_T according to the following equation: $R_{CT}/(R_{CT} + R_T)$, are presented in Figure S5C-D for the cells sensitized with ADEKA-1 and MK-2 dyes in different, selected configurations. Both for ADEKA-1 and MK-2 cells, the ratio $R_{CT}/(R_{CT} + R_T)$ is improved at high voltage after the post-treatment of titania surface (including multi-capping, ALD and addition of co-adsorbent molecules such as OTMS or CDCA). For example, at applied bias 0.7 V, the charge collection efficiency values are: A: 94%, A_CAPP: 95.6%, A_OTMS: 96.2%, A_OTMS_1ALD: 98.4%, A_OTMS_3ALD: 99.3% and A_OTMS_5ALD: 99.9%. It can be also noted that the drop in collection efficiency values occurs at the biases for which the photocurrent in C-V curves starts to decrease (e.g. Figure S4), thus it reflects the differences in FF values.

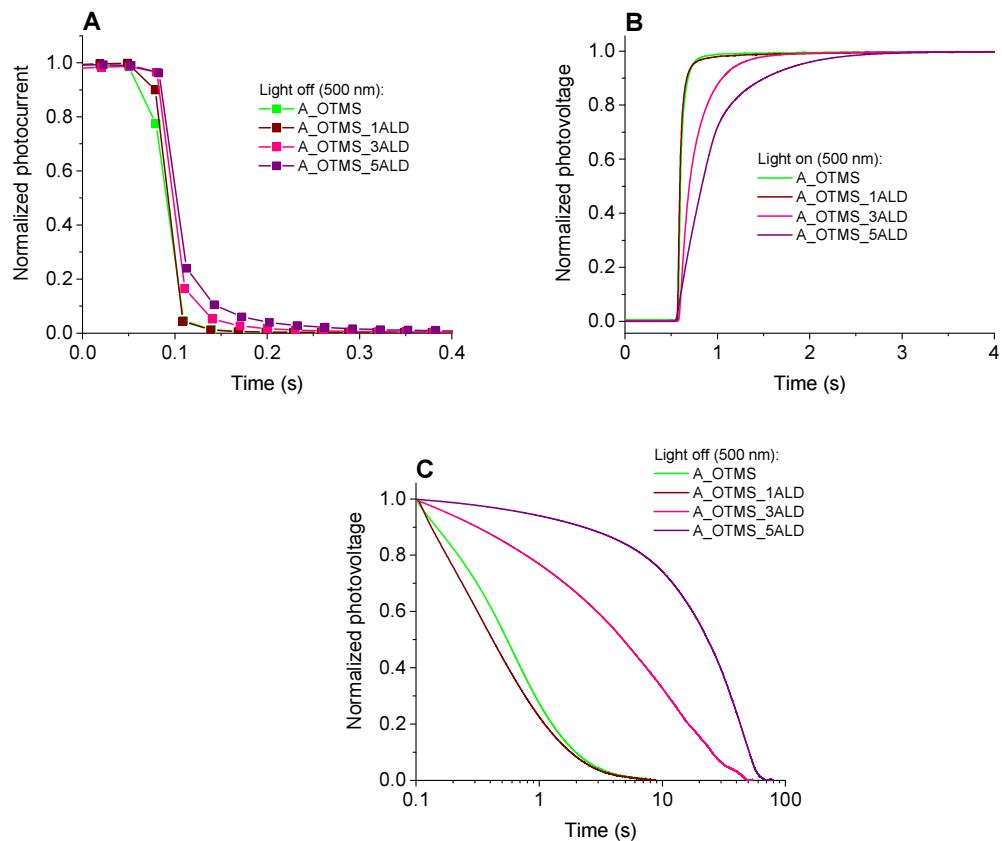


Figure S6. Chronoamperometric studies for **A_OTMS**, **A_OTMS_1ALD**, **A_OTMS_3ALD** and **A_OTMS_5ALD**: (A) normalized photocurrent decay after turning the continuous light off ($\lambda = 500$ nm, 0.7 mW/cm²); (B) normalized photovoltage rise after turning the light on; (C) normalized photovoltage decay after turning the light off .

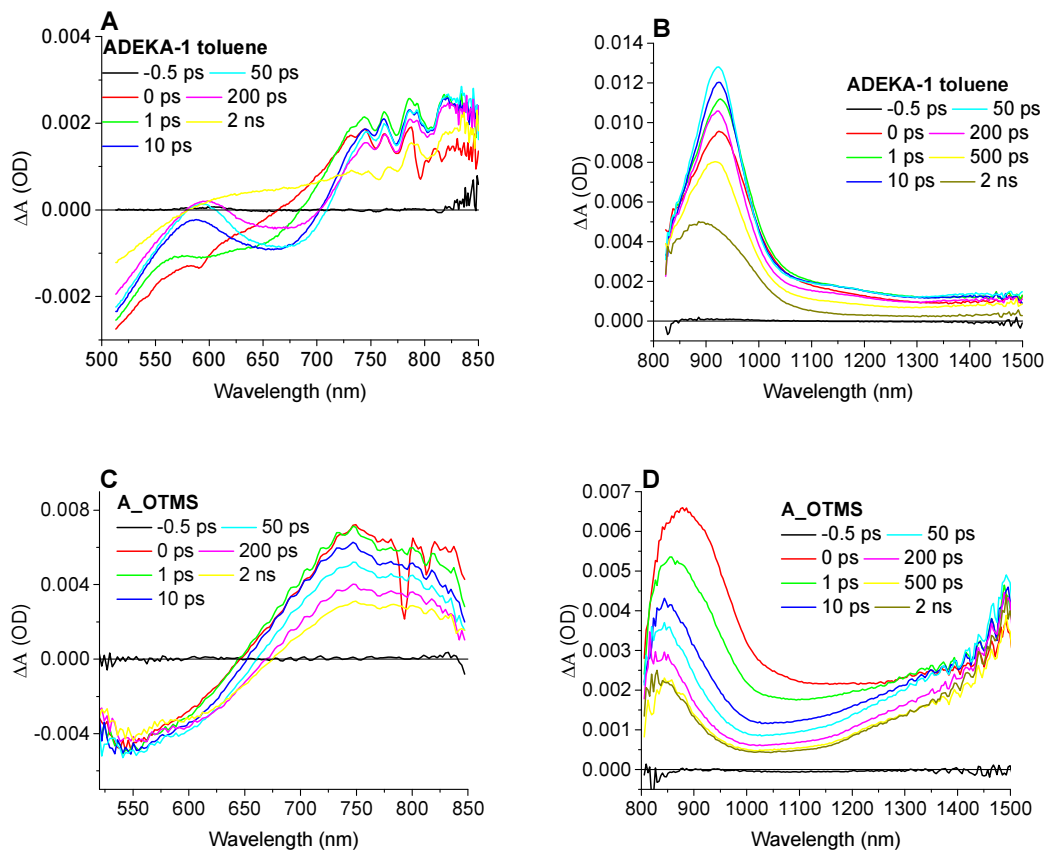


Figure S7. Representative transient absorption spectra for selected time delays between pump and probe pulse of ADEKA-1 in toluene solution (A-B) and cell sensitized with ADEKA-1+OTMS (C-D).

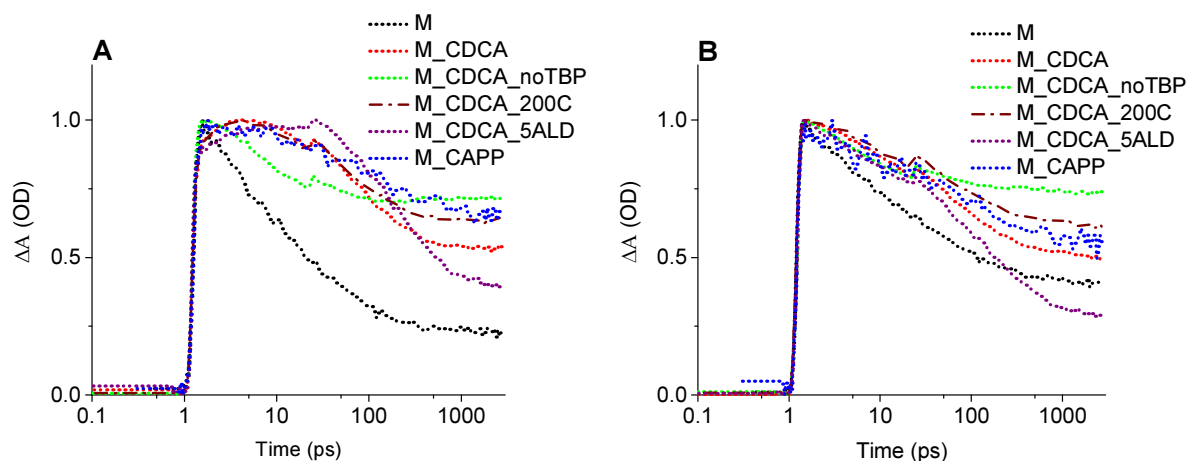


Figure S8. Transient absorption kinetics at 700 nm (A) and 750 nm (B) for MK-2 cells in selected configurations. Time zero was shifted to 1 ps in order to present the time axis in logarithmic scale.

Table S4. Time constants for the rise of kinetic signals measured at 700 nm and their normalized contribution. The data for each configuration were obtained from the average of transient absorption measurements for 2-5 independent solar cell samples.

Sample / configuration	Time constant, ps	Contribution, %
A	0.4	28
A_CAPP	2.5	30
A_OTMS	0.4	23
A_OTMS_CAPP	6.0	43
A_OTMS_200C	0.3	39
A_OTMS_1ALD	1.1	31
A_OTMS_3ALD	2.6	18
A_OTMS_5ALD	2.9	33
A_OTMS_noTBP	0.1	50
M	0.3	18
M_CAPP	0.2	22
M_CDCA	0.4	17
M_CDCA_200C	0.4	24
M_CDCA_5ALD	2.4	16
M_CDCA_noTBP	0.1	63

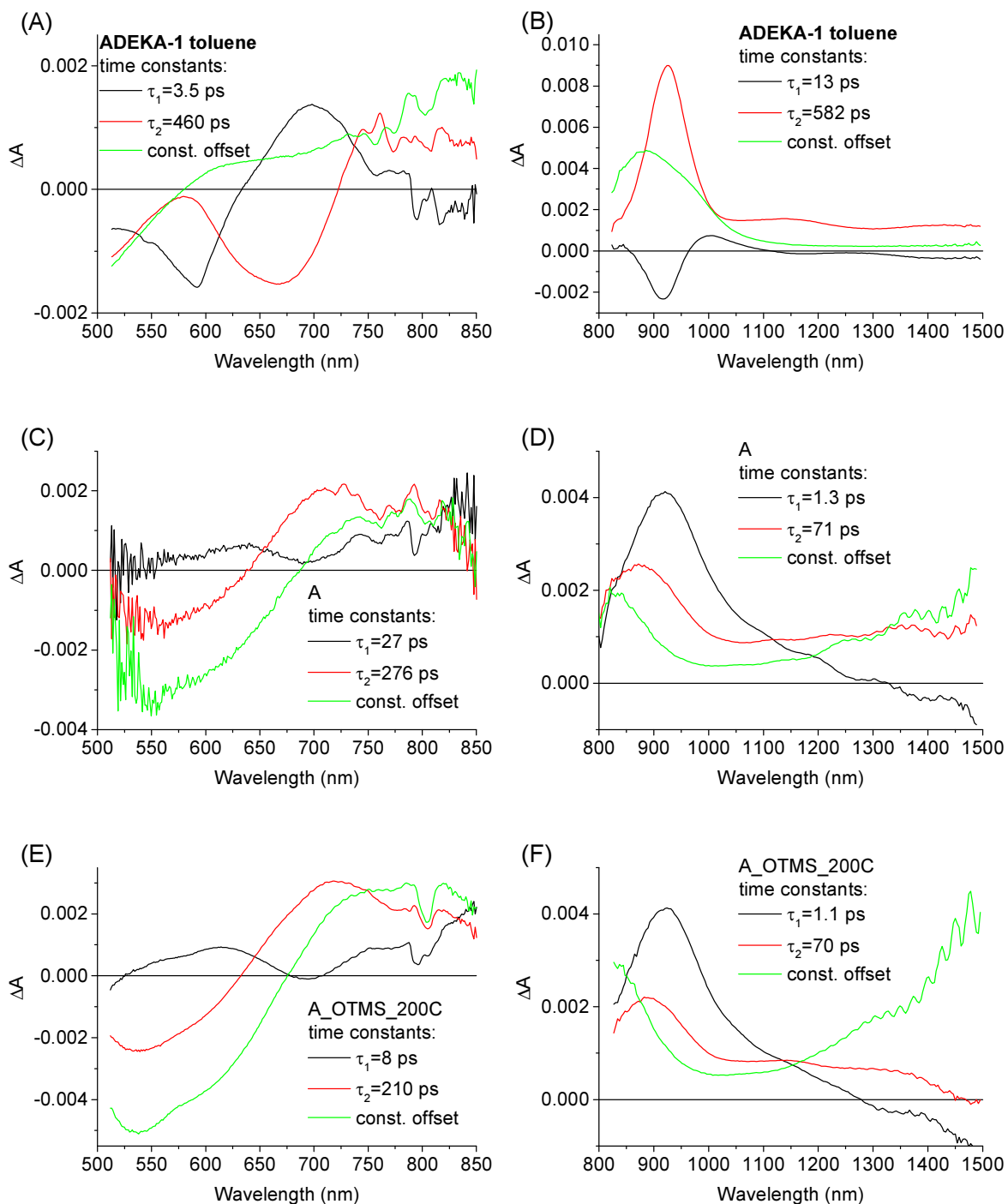


Figure. S9. Wavelength dependent amplitudes of the indicated time constants obtained from global analysis (two exponential with constant offset) of transient absorption spectra of ADEKA-1 in toluene solution (A-B) and of the solar cells with ADEKA-1: A (C-D) and A_OTMS_200C (E-F). The left parts show VIS while the right part shows NIR spectral ranges.

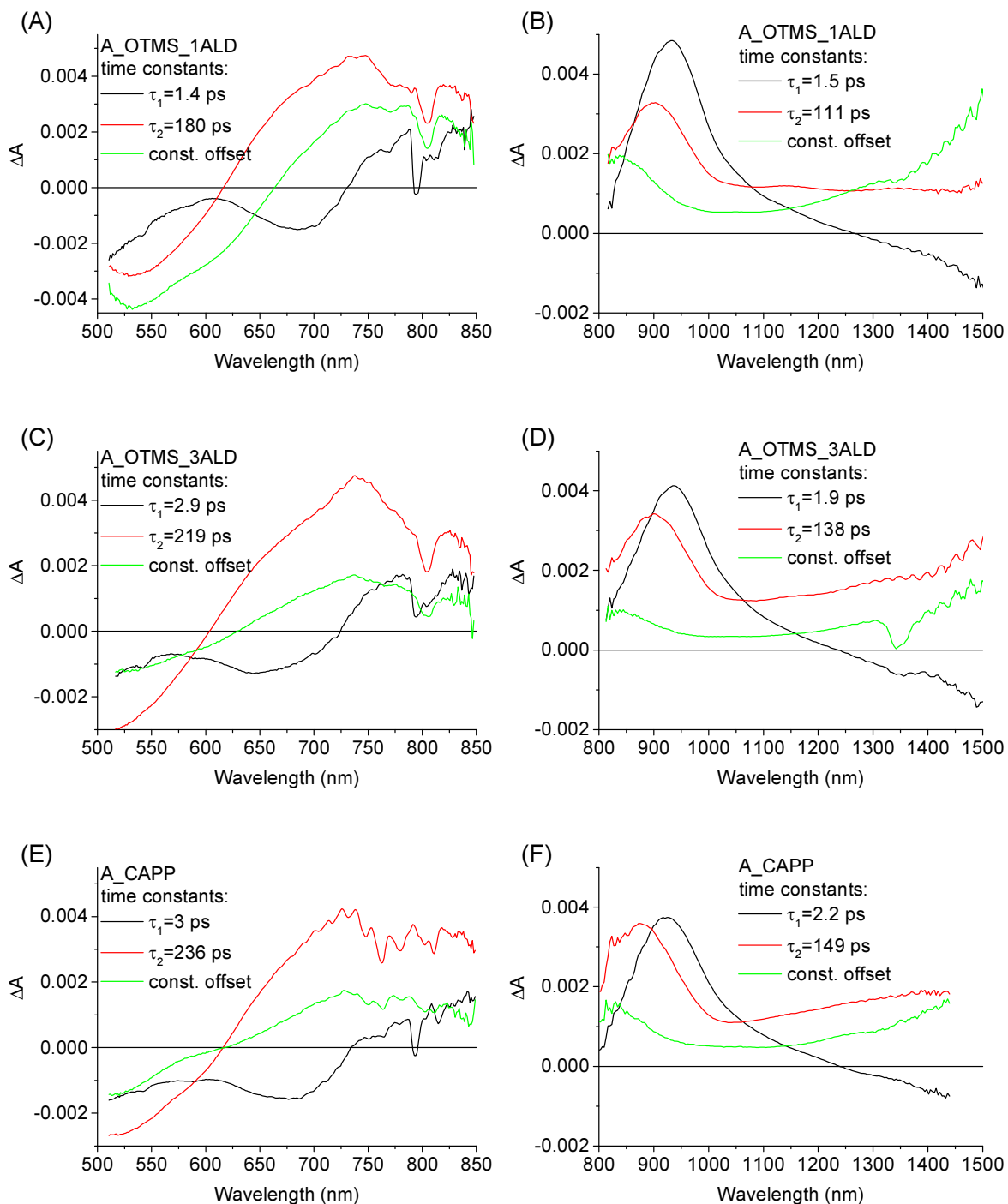


Figure S10. Wavelength dependent amplitudes of the indicated time constants obtained from global analysis (two exponential with constant offset) of transient absorption spectra of the sensitized with ADEKA-1: A_OTMS_1ALD (A-B), A_OTMS_3ALD (C-D) and A_CAPP (E-F). The left parts show VIS while the right part shows NIR spectral ranges.

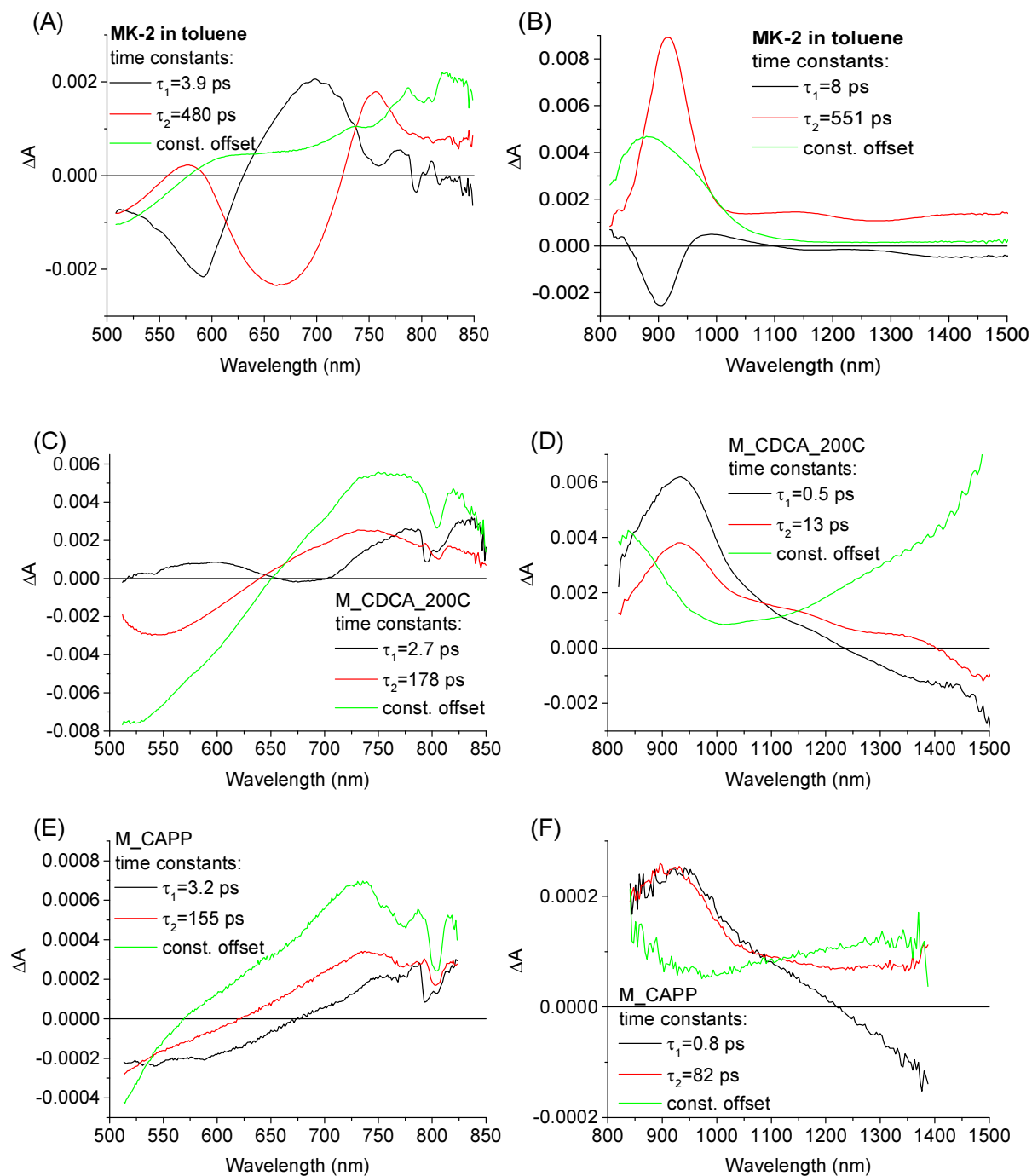


Figure S11. Wavelength dependent amplitudes of the indicated time constants obtained from global analysis (two exponential with constant offset) of transient absorption spectra of MK-2 in toluene solution (A-B) and of the solar cells sensitized with MK-2: **M_CDCA_200C** (C-D) and **M_CAPP** (E-F). The left parts show VIS while the right part shows NIR spectral ranges.

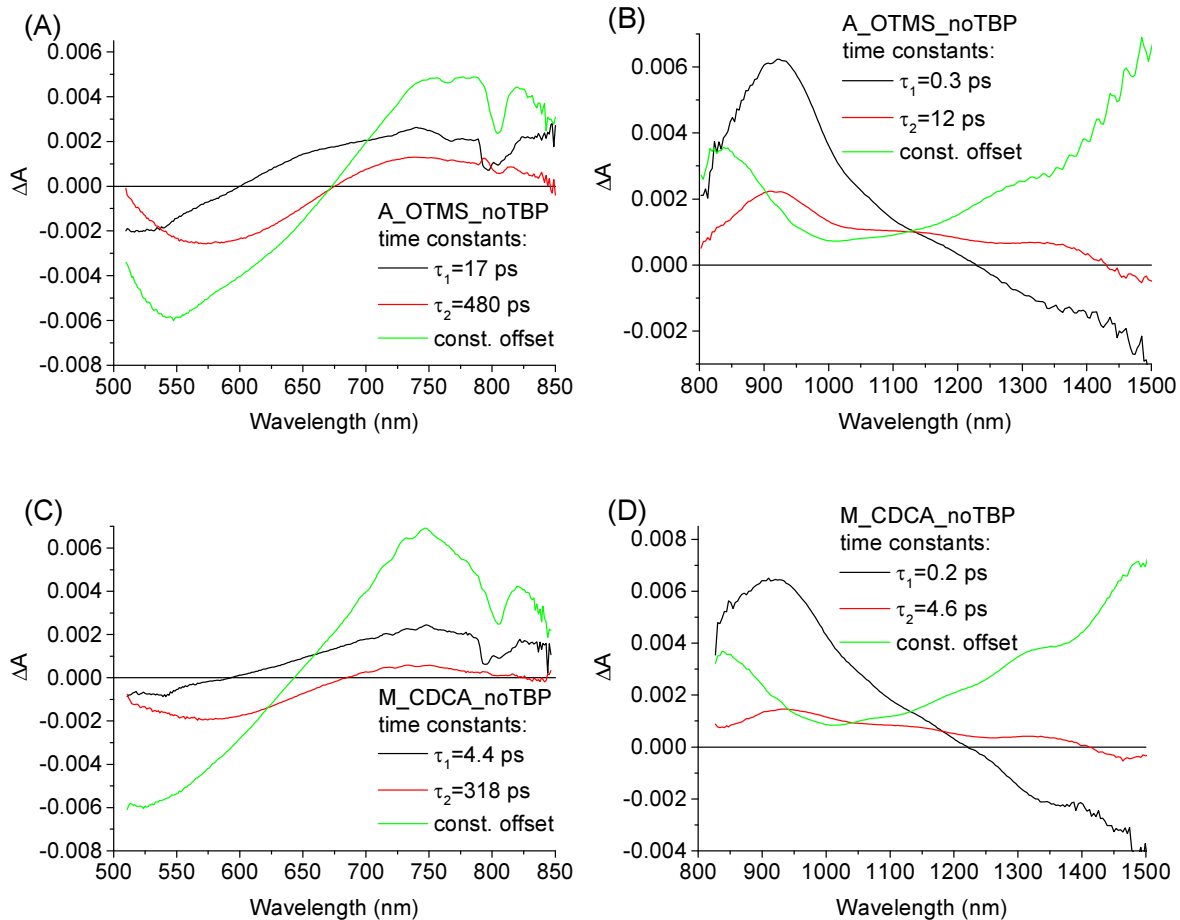


Figure S12. Wavelength dependent amplitudes of the indicated time constants obtained from global analysis (two exponential with constant offset) of transient absorption spectra of solar cells without TBP in electrolyte: **A_OTMS_noTBP** (A-B) and **M_CDCA_noTBP** (C-D). The left parts show VIS while the right part shows NIR spectral ranges.

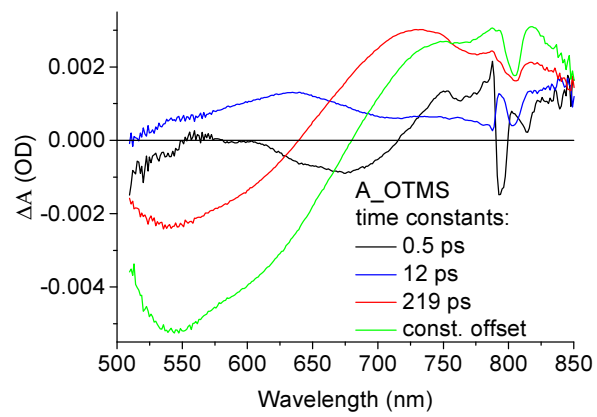


Figure S13. Example of 3-exponential global fit of A_OTMS cell, used to estimate the time constant of electron injection (the fastest component).

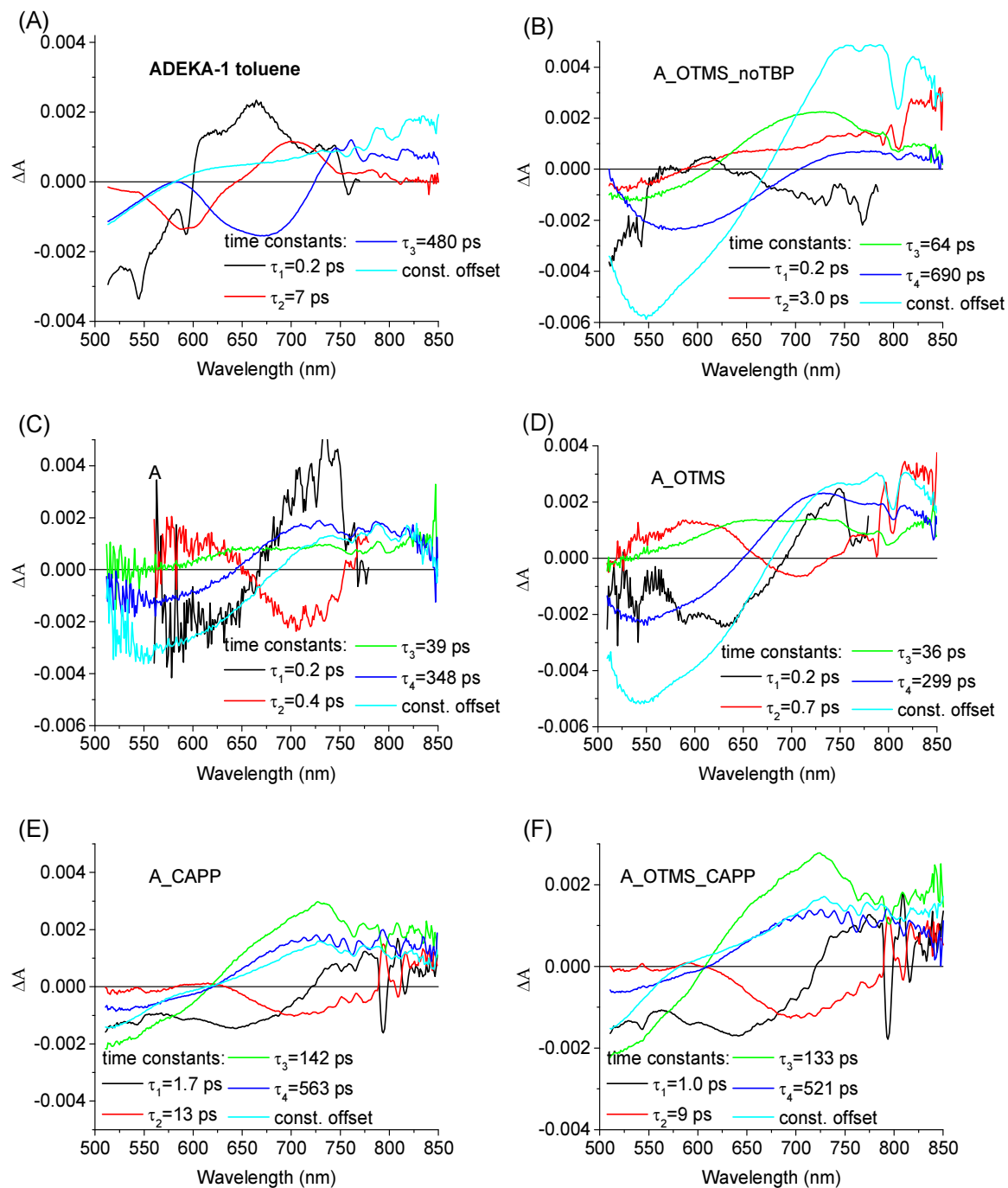


Figure S14. Four-exponential global fit of transient absorption in VIS range for the ADEKA-1 samples: ADEKA-1 in toluene solution (A), A_OTMS_noTBP (B), A (C), A_OTMS (D), A_CAPP (E) and A_OTMS_CAPP (F).

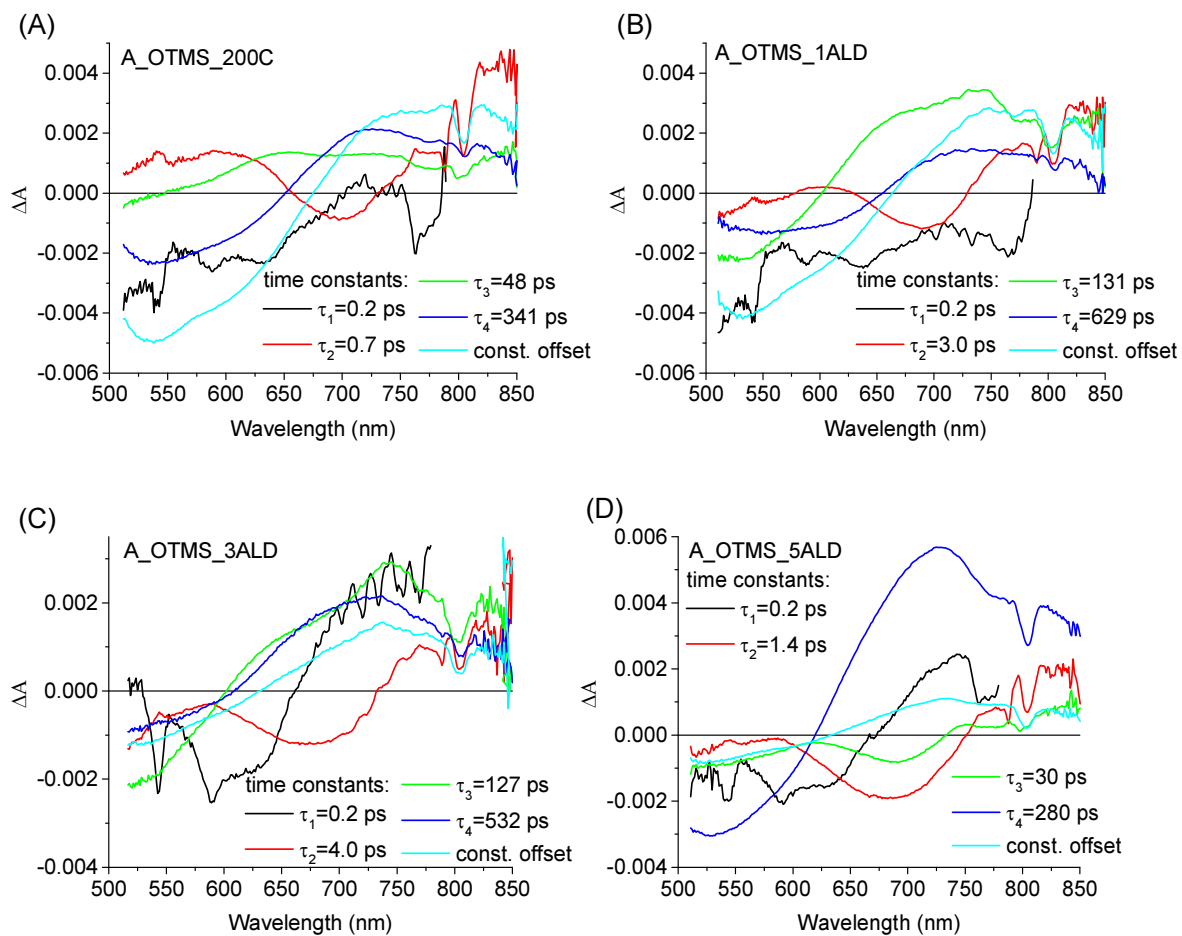


Figure S15. Four-exponential global fit of transient absorption in VIS range for the ADEKA-1 samples: **A_OTMS_200C** (A), **A_OTMS_1ALD** (B), **A_OTMS_3ALD** (C) and **A_OTMS_4ALD** (D).

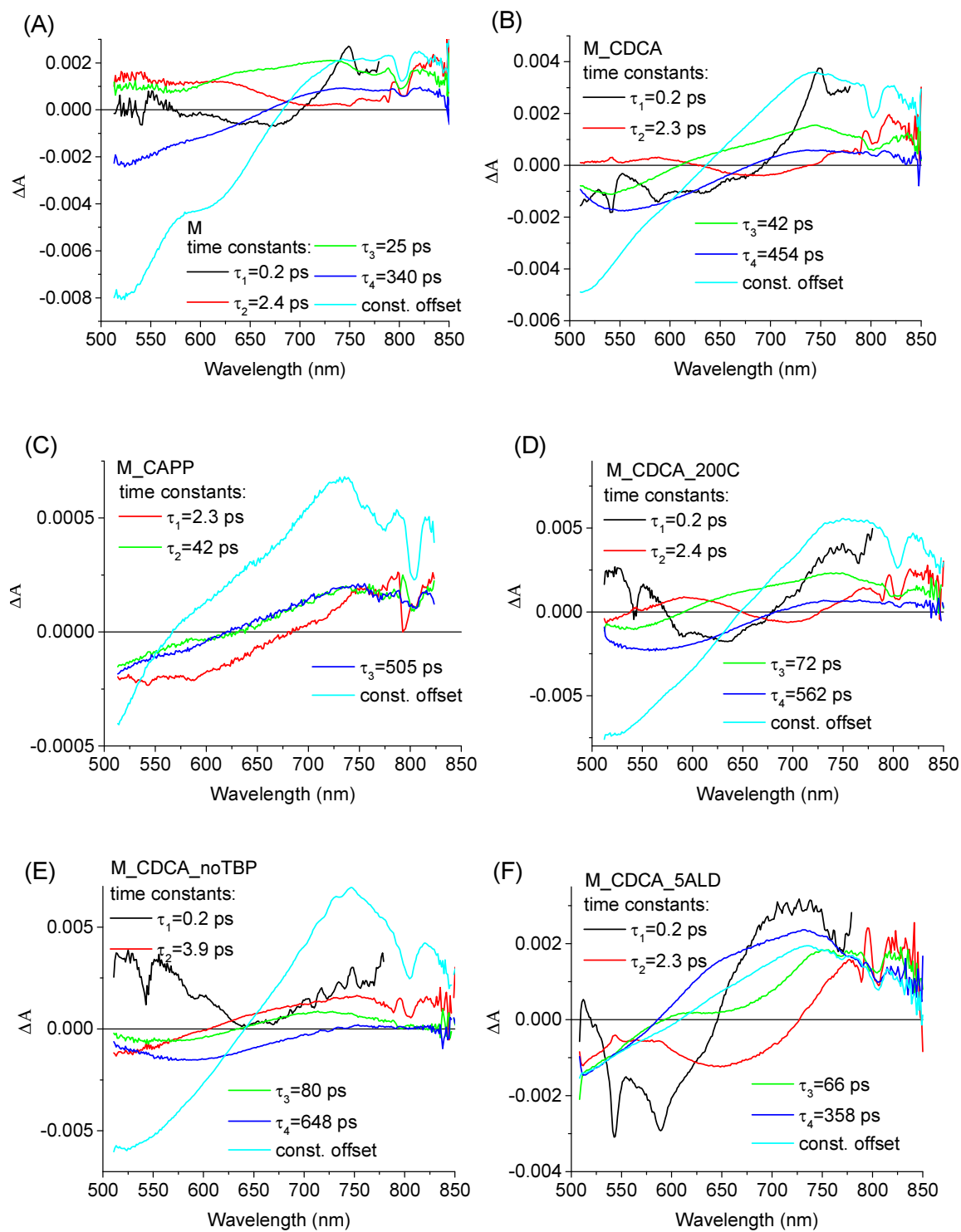


Figure S16. Four-exponential global fit of transient absorption in VIS range for the ADEKA-1 samples: **M** (A), **M_CDCA** (B), **M_CAPP** (C), **M_CDCA_200C** (D), **M_CDCA_noTBP** (E) and **M_CDCA_5ALD** (F).

Comments:

In the main text global transient absorption analysis with 2-exponential fits was used to calculate the average electron injection and recombination time constants. To have the best quality of the global fits more exponential components are necessary. For ADEKA-1 in toluene solution, a model with 3-exponential function and constant offset was used (Figure S14A). Compared to the simplified 2-exponential model discussed in the main part, it reveals the presence of two separate short time constants (0.2 ps and 7 ps in Figure S14A) instead of one (3.5 ps in Figure S9A), both due to the relaxation in S_1 state and the solvation dynamics. The amplitude of the faster component (0.2 ps) is negative below 600 nm and positive above this wavelength, while the crossing point ($\Delta A=0$) of the longer component (7 ps) is shifted to longer wavelength (650 nm). Negative amplitudes reflect the decay of stimulated emission in shorter-wavelength part while the positive amplitude show the increase in stimulated emission at longer wavelengths. Thus, this behaviour reflects the red-shift of the stimulated emission band during the energy stabilization in S_1 state, which is better described by two time constants.

For the solar cell samples, 4-exponential fit with constant offset had to be applied. Figures S14-S15 present the results obtained for ADEKA-1 cells, while those for MK-2 cells are shown in Figure S16. All the time constants were set free during the fit except for the fastest one, which was fixed at 0.2 ps if it tended to go below IRF of the setup (0.2 ps). The interpretation of the results is similar to our previous studies for MK-2 and ADEKA-1 cells, although slightly simplified approach was used before: for MK-2 samples we applied 3-exponential fit,³ while for ADEKA-1 cells the second and third components were fixed at averaged values.² Therefore, the present studies use the most general analysis. Usually (Figures S14-S16), the two fastest components are due to the electron injection process. The amplitude of the fastest one (typically 0.2 ps) is negative for wavelengths below 680 nm which is shorter than those of the second component (below 750 nm). Thus these components are accounted for the stimulated emission from the hot (the first component) and relaxed (the second component) S_1 state of the dyes, respectively.

On the contrary, the third (typically several tens of ps) and the fourth (several hundreds of ps) components represent electron recombination process. Their amplitude spectra are different, and the spectrum of fourth, longest component is more similar to the spectrum of the constant offset. Thus, and in line with our previous interpretations,²⁻³ we assign the faster recombination component to the process involving deep trap states and dye-titania charge transfer complexes, while the longer component – to the recombination between free or shallowly trapped electron in titania with the oxidized dye. However, for some cells with fast electron injection, the second component contains some contribution of recombination (positive amplitudes below 650 nm apart from negative stimulated emission indentation for samples: **A**, **A_OTMS**, **A_OTMS_200C**, **M**, **M_CDCA**, **M_CDCA_200C**) or the second component can be exclusively accounted for the recombination (samples: **A_OTMS_noTBP**, **M_CAPP** and **M_CDCA_noTBP**).

Examination of 4-exponential analysis presented in Figures S14-S16 confirms slower electron injection and slower recombination of the cells with alumina post-assembly passivation (**A_OTMS_1ALD**, **A_OTMS_3ALD**, **A_OTMS_5ALD**, **M_CDCA_5ALD**)

and molecular capping passivation (**A_CAPP** and **A_OTMS_CAPP**) with respect to the non-passivated samples. However, the differences in the dynamics of injection and recombination processes are not only reflected in the fitted time constants, but also in the relative contribution of the different components assigned to injection and recombination. Therefore, the simplified global analysis presented in the main part is more suitable to extract the average rates.

References:

1. Fabregat-Santiago, F.; Bisquert, J.; Garcia-Belmonte, G.; Boschloo, G.; Hagfeldt, A., Influence of Electrolyte in Transport and Recombination in Dye-Sensitized Solar Cells Studied by Impedance Spectroscopy. *Sol. Energy Mater Sol. Cells* **2005**, *87*, 117-131.
2. Sobuś, J.; Gierczyk, B.; Burdziński, G.; Jancelewicz, M.; Polanski, E.; Hagfeldt, A.; Ziólek, M., Factors Affecting the Performance of Champion Silyl-Anchor Carbazole Dye Revealed in the Femtosecond to Second Studies of Complete ADEKA-1 Sensitized Solar Cells. *Chem. Eur. J.* **2016**, *22*, 15807-15818.
3. Sobuś, J.; Kubicki, J.; Burdziński, G.; Ziólek, M., Carbazole Dye-Sensitized Solar Cells Studied from Femtoseconds to Seconds - Effect of Additives in Cobalt- and Iodide-Based Electrolytes. *ChemSusChem* **2015**, *8*, 3118-3128.
4. Anta, J. A.; Guillén, E.; Tena-Zaera, R., Zno-Based Dye-Sensitized Solar Cells. *J. Phys. Chem. C* **2012**, *116*, 11413-11425.

Paper II

Effects of Aqueous Electrolyte, Active Layer Thickness and Bias Irradiation on Charge Transfer Rates in Solar Cells Sensitized with Top Efficient Carbazole Dyes.

Glinka, A.; Gierszewski, M.; Ziótek, M.

J. Phys. Chem. C **2018**, *122*, 8147–8158.

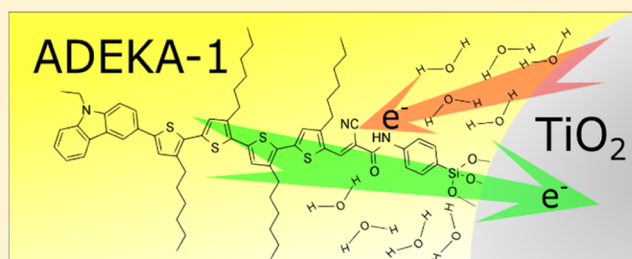
Effects of Aqueous Electrolyte, Active Layer Thickness and Bias Irradiation on Charge Transfer Rates in Solar Cells Sensitized with Top Efficient Carbazole Dyes

Adam Glinka, Mateusz Gierszewski, and Marcin Ziółek*

Quantum Electronics Laboratory, Faculty of Physics, Adam Mickiewicz University in Poznań, Umultowska 85, 61-614 Poznań, Poland

Supporting Information

ABSTRACT: The photovoltaic performance and electron-transfer dynamics from femtoseconds to milliseconds are explored for very efficient carbazole sensitizers applied in solar cells, including the champion dye ADEKA-1. The photocurrent in the novel, environmentally friendly aqueous electrolyte is about 40% of that in the standard acetonitrile one, both based on cobalt complexes as a redox pair. The drop in the photocurrent is found to be correlated with increased electron recombination between sensitized titania particles and dyes, taking place with a time constant of several hundreds of picoseconds. Electron injection and recombination between titania and dye are slowed down under the presence of water (about 10 times) and with additional 1 sun bias irradiation (about 2 times). These effects are interpreted as due to reduced electronic coupling between the electron donors (dyes) and acceptor framework (titania). Moreover, a decrease in the relative photocurrent, photovoltage, and fill factor of the cells with increasing thickness of titania layers are observed. The obtained results should be relevant for the optimization of solar cells with a large class of organic sensitizers, especially when looking for nontoxic configurations and determining true charge transfer rates under operating solar cell conditions.



INTRODUCTION

Dye-sensitized solar cells (DSSCs) have attracted major concern in recent years as a cheaper alternative for commercially available semiconductor solar energy conversion devices. After a breakthrough in 1991¹ when DSSCs based on mesoporous TiO₂ photoanodes sensitized with a ruthenium complex dye, combined with an electrolyte consisting of iodide/triiodide (I⁻/I₃⁻) redox couple solution in an organic solvent, reached 7.9% power conversion efficiency (PCE), the technology has been intensively developed, which has led to the current of over 14% of the efficiency record.² The champion solar cells were constructed using titania photoanodes, cosensitized with ADEKA-1—a carbazole dye, having an alkoxy-silyl-anchoring group in combination with cobalt-based electrolytes, which despite of some stability issues,³ provide higher open-circuit voltages (V_{OC}) than I⁻/I₃⁻^{4–6} thanks to a simpler dye-regeneration mechanism.⁷

Because acetonitrile (ACN) and other organic solvents, thanks to their excellent physical properties (i.e., high dielectric constants, low viscosity, and high solubilization ability of various additives), were introduced as high-efficiency electrolyte main ingredients, water has been forsaken as an electrolyte component. Moreover, it was believed to be evidently lethal for DSSC efficiency and long-term stability.^{8,9} However organic solvents have some serious drawbacks, especially high volatility, flammability, and toxicity for humans and the environment. Aqueous electrolytes were called back in 2010 by O'Regan et al.,¹⁰ and the interest in them is constantly growing.⁸ In

addition, recently, they reached over 5% PCE, basing on a cobalt bipyridine-pyrazole redox couple¹¹ in a 100% aqueous solution without any surfactant addition. Another approach that should be mentioned is the application of quasi-solid electrolytes based on water and jellifying agents, which provide remarkable stability of devices without toxicity problems.^{3,12–14} Nevertheless, construction of high-performing and durable aqueous DSSCs is still a challenge.

To the best of our knowledge, the effects of changing the composition of aqueous electrolytes on the performance and electron-transfer dynamics in solar cells, sensitized with the champion alkoxy-silyl-anchoring dye, have not been studied so far. Moreover, studies of dye-sensitized wide band gap semiconductor structures, able to operate in aqueous environments, can be useful for developing dye-sensitized photo-electrochemical cells for water splitting applications.^{15,16} The understanding of charge-transfer dynamics of dye-sensitized mesoporous systems in water environment is generally much more limited compared to the information gathered on organic solvents.

In this study, photovoltaic performance and electron-transfer dynamics were compared in solar cells based on the champion ADEKA-1 alkoxy-silyl-anchoring dye and its benchmark carboxylic-anchoring analogue MK-2^{17,18} (Scheme S1 in the

Received: February 27, 2018

Revised: March 29, 2018

Published: March 30, 2018

Supporting Information, whose performance was also described in combination with aqueous electrolytes^{19,20}) combined with 100% aqueous electrolytes based on tris(1,10-phenanthroline)-cobalt(II/III) complexes at different pH values, which were obtained by varying the concentration of 1-methylbenzimidazole (MBI) base. The performance and operation of devices with a water-based electrolyte was compared with those of the cells containing electrolytes based on standard organic solvents, including ACN, and tris(1,10-phenanthroline)cobalt(II/III) (Co-Phen), tris(2,2'-bipyridine)cobalt(II/III) (Co-Bpy), or iodide/triiodide as redox couples. It should be pointed out that ADEKA-1 cells with stronger anchoring unit of the sensitizer reach their top efficiencies only under complex titania surface passivation (including molecular multicapping).²¹ Without such treatments, the efficiencies of the reference cells with MK-2 dye can be even higher than those achieved using ADEKA-1 because of the less pronounced back electron transfer from titania to the oxidized dye.^{22,23} In this work, for easier interpretation of the studied effects, we used a simplified procedure to suppress recombination, that is, we added appropriate coadsorbents: isoctyltrimethoxysilane (OTMS) with an alkoxysilyl-anchoring unit for ADEKA-1²¹ and chenodeoxycholic acid (CDCA) with a carboxyl-anchoring unit for MK-2.²³

Another important issue for optimizing DSSC assembly is the choice of proper thickness and morphology of the photoanode. Increasing the thickness of the titania layer and addition of larger light-scattering particles (diameter > 100 nm) to the lattice enlarges the amount of the adsorbed dye, which increases the light-harvesting efficiency.^{24,25} However, above a certain thickness, the series resistance of the mesoporous titania lattice, diffusion limitations in pores, and interfacial charge recombination balance the gain in the amount of separated charge carriers.^{26,27} Consequently, the optimal photoanode thickness and morphology can vary depending on the used sensitizer, electrolyte solvent, and redox shuttle as well as other special photoanode treatment methods.

Therefore, we studied the effects of different thicknesses of the titania layer containing light-scattering particles on the performance of solar cells sensitized with champion ADEKA-1 and MK-2 dyes assembled with Co-Bpy electrolyte based on ACN. Furthermore, we checked the differences in the photovoltaic performance and charge-transfer properties of ADEKA-1- and MK-2-sensitized cells assembled with aqueous Co-Phen electrolyte depending on the photoanode morphology (i.e., transparent and containing scattering particles in titania layers).

Within this work, solar cells were characterized not only by basic photovoltaic measurements, such as $J-V$ curves under AM1.5G illumination, incident photon-to-current efficiency (IPCE) spectra, and stationary absorption, but also by time-resolved spectroscopic measurements: electrochemical impedance spectroscopy (EIS) and transient absorption (TA) spectroscopy, which provide information about charge-transfer dynamics from millisecond to second for EIS and from subpicosecond to nanosecond timescale for TA. We also investigated the effects of additional irradiation of the solar cells during TA measurements. Such an improvement allowed us to observe ultrafast charge-transfer dynamics in conditions closer to real operation circumstances and compare it with the results obtained with TA measurements without additional illumination, which is a very well-established technique to obtain

information about ultrafast and fast processes in photovoltaic systems.^{28,29}

EXPERIMENTAL SECTION

Preparation of the Solar Cells. To utilize the DSSCs, we followed the same procedure as in our previous work.²³ The procedure for the preparation of scattering photoanodes of different thicknesses (from 3 to 9 μm) is described elsewhere.³⁰

The prepared photoanodes were dipped into dye solutions for sensitization. We used two solutions of different carbazole dyes, MK-2 (from Sigma-Aldrich) with CDCA (Sigma-Aldrich) as a coadsorbent and 100% monomeric ADEKA-1 dye obtained in previously described synthesis²² with OTMS (Sigma-Aldrich) as a coadsorbent. Both solutions were prepared in the following concentrations: 0.2 mM dye + 0.1 mM coadsorbent in 9:1 toluene and ACN mixture. Sensitization was performed for 16 h at 5 °C according to the procedure used for ADEKA-1.^{21,23}

The composition of water-based electrolytes was as follows: 0.13 M Co(phen)₃Cl₂, 0.035 M Co(phen)₃Cl₃, and different concentrations of MBI: 0, 0.072, and 0.8 M for pH \approx 6, pH \approx 9, and pH \approx 10, respectively. The redox couple was cobalt-phenanthroline (Co-Phen) complex. All components were dissolved in distilled water. The reference ACN-based electrolytes were drawn up according to the following compositions: 0.13 M Co(phen)₃(TFSI)₂, 0.035 M Co(phen)₃(TFSI)₃, 0.1 M of LiTFSI, and 0.5 M *tert*-butylpyridine (TBP). The cobalt redox couple was Co-Phen or cobalt-bipyridine (Co-Bpy) complex. Additionally, for one configuration, we tested the electrolyte with the following components and concentrations: 0.13 M Co(phen)₃Cl₂, 0.035 M Co(phen)₃Cl₃, 0.1 M of LiTFSI, and 0.5 M TBP in a 1:5 mixture of ACN:water. For the cells constructed with photoanodes with different thicknesses, we used the Co-based electrolyte with the following components and concentrations: 0.25 M Co(bpy)₃(TFSI)₂, 0.035 M Co(bpy)₃(TFSI)₃, 0.1 M LiTFSI, and 0.5 M TBP in ACN. The iodide/triiodide composition was: 0.08 M I₂, 0.6 M 1,2-dimethyl-3-propylimidazolium iodide, 0.1 M LiI, 0.1 M guanidine thiocyanate (GuSCN), and 0.5 M of TBP.

To distinguish different DSSC configurations studied in this work, we introduced the following abbreviations: **A** and **M** for different dyes (ADEKA-1 and MK-2, respectively); **Phen** and **Bpy** for different redox couples (cobalt-phenanthroline and cobalt-bipyridine, respectively); **ACN**, **H₂O**, and **H₂O + ACN** for different electrolyte solvents (ACN, water, or their mixture, respectively); **pH6**, **pH9**, and **pH10** (to distinguish aqueous electrolytes with different MBI concentrations); **T** and **S** for different titania photoanode types (transparent and scattering, respectively); and, if needed, **x2** or **x3** (to distinguish between double and triple screen-printed titania layers from single layers).

Cell Characterization. A UV-vis-NIR spectrophotometer (V-770, Jasco), equipped with an integrating sphere (150 mm LN-925, Jasco), was used to measure the stationary absorption spectra of different photoanodes. To detect the scattered as well as transmitted light, the specimens were mounted before the integrating sphere.

To perform the current-voltage measurements under simulated sunlight AM 1.5 G conditions and to obtain the IPCE spectra, a potentiostat (model M101 with a frequency response analyzer FRA32M module, Autolab) coupled with a photoelectric spectrometer equipped with a solar simulator (Photon Institute, Poland) was used. Simulated sunlight was

Table 1. Photovoltaic Performance of Studied Systems: Open-Circuit Voltage (V_{OC}), Short-Circuit Photocurrent Density (J_{SC}), Fill Factor (FF), PCE(Eff), Number of Absorbed Photons (N_{PH}), Absorbance at 500 nm (A_{500}), and Corrected Photocurrent ($total_APCE$)

cell	V_{OC} [V]	FF	J_{SC} [mA/cm ²]	Eff [%]	N_{PH} [10 ²⁰ s ⁻¹ m ⁻²]	A_{500}	$total_APCE$
(A) ACN Solution							
M_Bpy_ACN_T ^a	0.81	0.53	7.8	3.4	5.9	0.93	0.84
M_Phen_ACN_T	0.87	0.56	6.5	3.1	6.4	1.09	0.63
M_Bpy_ACN_S	0.82	0.53	6.5	2.8	5.1	1.51	0.79
M_Bpy_ACN_Sx2	0.80	0.40	8.4	2.7	8.3	1.77	0.63
M_Bpy_ACN_S	0.74	0.37	8.0	2.2	9.3	1.97	0.54
A_Bpy_ACN_T ^a	0.83	0.46	7.0	2.5	8.4	2.25	0.57
A_Phen_ACN_T	0.87	0.55	6.1	2.9	7.7	1.68	0.49
A_Bpy_ACN_S	0.84	0.48	5.7	2.3	6.5	1.65	0.55
A_Bpy_ACN_Sx2	0.79	0.44	7.9	2.7	9.3	1.95	0.54
A_Bpy_ACN_Sx3	0.75	0.44	8.0	2.6	10.4	2.11	0.48
(B) Water Electrolyte							
M_Phen_H ₂ O_pH10_T	0.42	0.21	2.6	0.2	6.4	1.09	0.26
M_Phen_H ₂ O_pH10_S	0.43	0.24	3.0	0.3	6.3	1.21	0.30
M_Phen_H ₂ O_pH9_S	0.32	0.37	2.4	0.3	6.3	1.21	0.23
M_Phen_H ₂ O_pH6_S	0.34	0.42	2.0	0.3	5.1	0.73	0.25
M_Phen_H ₂ O + ACN_S	0.28	0.29	1.6	0.1	7.2	1.29	0.14
A_Phen_H ₂ O_pH10_T	0.68	0.26	2.2	0.4	7.7	1.68	0.20
A_Phen_H ₂ O_pH10_S	0.70	0.31	2.5	0.5	7.7	1.42	0.20
A_Phen_H ₂ O_pH9_S	0.54	0.50	0.9	0.2	7.7	1.42	0.07
A_Phen_H ₂ O_pH6_S	0.56	0.60	0.2	0.1	6.5	1.09	0.02
A_Phen_H ₂ O + ACN_S	0.37	0.34	1.5	0.2	8.6	1.70	0.11

^aCells from our previous work.²³

provided by an Xe lamp with an AM 1.5 G spectral filter. The irradiance was adjusted to 100 mW cm⁻² using a calibrated cell (15151, ABET).

The same previously mentioned potentiostat equipped with a frequency response analyzer was used to perform EIS measurements. To accomplish the analysis of the obtained data by fitting standard equivalent circuits for DSSCs, the ZView software was used.

TA measurements were performed using a commercial Helios spectrometer from Ultrafast Systems connected with a Spectra Physics laser system described before.³¹ The duration of instrument response function (IRF), that is, pump-pulse cross-correlation function of our setup, was about 200 fs at full width at half-maximum. TA spectra were measured in 3 ns time window in the range of 510–850 nm. The excitation wavelength was tuned to 500 nm, and the pulse energy was set to 60 nJ (default value) or 180 nJ (if stated), which correspond to the energy density of 30 and 90 μJ cm⁻¹, respectively. We also used additional white light-emitting diode (LED) (MWWHF2, Thorlabs) illumination of the cell to simulate normal operation conditions of the solar cells. Unless otherwise stated, the intensity of illumination was adjusted to obtain the same J_{SC} value as measured on the solar simulator described before. To perform global analysis of TA data, we used the Surface Explorer software from Ultrafast Systems, which allows fitting the multiexponential function convoluted with IRF to experimental data, so that we can obtain wavelength-dependent amplitudes corresponding to time constants associated with particular processes.

RESULTS AND DISCUSSION

Stationary Absorption and Photovoltaic Performance. Stationary absorption spectra of the sensitized films were measured to determine the number of absorbed photons

(N_{PH}) and relative photocurrent of the cells ($total_APCE$ parameter, see below). Figure S1 (in Supporting Information) compares the exemplary absorption spectra for transparent and scattering photoanodes of mesoporous films of different thicknesses (from 1 to 3 titania layers, corresponding to the thickness from about 3 to 9 μm). The absorbance close to the maximum absorption of both dyes (400–500 nm) is already higher than 1 for the thinnest transparent films (almost all light absorbed in this spectral range). Therefore, modifications with scattering particles and additional layers do not improve the number of absorbed photons below 500 nm but systematically increase the light-harvesting efficiency on the long-wavelength absorption onset (above 500 nm). This is also confirmed in the normalized IPCE spectra shown in Figure S2. A beneficial, slight red shift in the photoaction spectra of ADEKA-1 versus MK-2 can be noticed.

Table 1 presents averaged values of open-circuit voltage (V_{OC}), short-circuit photocurrent density (J_{SC}), FF, and PCE (Eff) obtained from the $J(V)$ curves measured under AM 1.5G illumination conditions. For each cell, a $J(V)$ curve was measured twice (1 h and one day after assembling) and there were at least three cells drawn up for each system. The other parameters, including the number of absorbed photons (N_{PH}), A_{500} , and $total_APCE$, were gained from stationary absorption measurements. The value of N_{PH} was obtained by numerical integration of the absorption spectrum ($1 - 10^{-A(\lambda)}$, where $A(\lambda)$ is the absorbance) in range from 400 to 800 nm and multiplication by the function of photon flux for AM 1.5 G spectrum for 100 mW cm⁻¹ irradiance. The $total_APCE$ parameter can be described as the photocurrent density corrected for the number of absorbed photons and is calculated as $J_{SC} e^{-1} N_{PH}^{-1}$. The value of A_{500} is the absorbance of the photoanode at the wavelength $\lambda = 500$ nm, which is close to the maximum of the absorption band of ADEKA-1 and MK-2 dyes

and was chosen as the pumping wavelength in TA measurements (discussed later). It should be noted that real J_{SC} and Eff values were slightly higher (by a factor of 1.19). Because of our previous overestimation of active surface of photoanodes, we still assume it to be higher (0.283 cm^2 instead of the real 0.237 cm^2) to keep the results in this work comparable with our previous study on these dyes.²³

Table 1A shows the changes in photovoltaic parameters for the cells with standard ACN-based electrolytes in response to different thicknesses of photoanodes and the content of the light-scattering titania particles. The addition of scattering particles slightly enhances V_{OC} (by about 10 mV) but the *total APCE* parameter is reduced (e.g., compare samples **A_Bpy_ACN_T** vs **A_Bpy_ACN_S** and **M_Bpy_ACN_T** vs **M_Bpy_ACN_S**). We have previously observed a similar effect for the cells with N719.³⁰ It can be explained by the higher density of injected electrons per nanoparticle for scattering samples, which enhances the recombination. Along with increasing the thickness of photoanodes, the V_{OC} values decrease for both MK-2 (from 0.82 V for **M_Bpy_ACN_S** to 0.74 V for **M_Bpy_ACN_Sx3**) and ADEKA-1 (from 0.84 V for **A_Bpy_ACN_S** to 0.75 V for **A_Bpy_ACN_Sx3**). It is due to the enlargement of the surface area of the film, which enhances the recombination between electrons from titania and the redox shuttle,³² and due to a shift of the conduction band (CB), which will be explored in the impedance section below. The same recombination phenomenon is responsible for decreasing the FF of the cells with thicker photoanodes. Higher recombination also affects the *total APCE* parameter, and hence, the photocurrent does not increase proportionally to the number of absorbed photons. Consequently, efficiencies of the solar cells drop with increasing layer thickness for the MK-2 dye (from 2.8 to 2.2%) and reach a maximal value of 2.7% for an intermediate ($\sim 6 \mu\text{m}$) thickness of the photoanode sensitized with the ADEKA-1 dye. This is in contrast to our earlier results on the cells with ruthenium dye N719, whose efficiency increased with increasing thickness up to $9 \mu\text{m}$. A possible interpretation is the higher absorption coefficients of MK-2 and ADEKA-1 dyes ($35800 \text{ M}^{-1} \text{ cm}^{-1}$ ¹⁷ and $43200 \text{ M}^{-1} \text{ cm}^{-1}$ ²¹ respectively) with respect to that of N719 ($14100 \text{ M}^{-1} \text{ cm}^{-1}$ ²⁷). For the organic sensitizers studied in this work, the relatively high absorption is already realized for thinner titania layer, and further increase in thickness worsens the recombination more than it improves the absorption.

The effect of different ligands coordinating $\text{Co}^{2+/3+}$ cations is very distinctly expressed in V_{OC} values for both dyes, that is, V_{OC} increases from 0.81 to 0.87 V for MK-2 and from 0.83 to 0.87 V for ADEKA-1, when 2,2'-bipyridine is replaced by 1,10-phenanthroline (Table 1A), which corresponds to the difference between the redox potential of electrolytes: 0.56 V versus normal hydrogen electrode (NHE) for Co-Bpy and 0.62 V versus NHE for Co-Phen. On the other hand, J_{SC} of the cells is lowered. It can be explained by the slower regeneration of the oxidized dye by the redox couple as a result of lower driving force for the reduction reaction.²² This effect is more significant for MK-2 because its highest occupied molecular orbital (HOMO) level (0.96 V vs NHE)¹⁸ is less positive when compared to that of ADEKA-1 HOMO level (0.99 V vs NHE).² This beneficial alignment of the energetic levels of ADEKA-1 and Co-Phen redox shuttle results in enhanced efficiency with respect to the cells with Co-Bpy redox couple (2.9% for **A_Phen_ACN_T** vs 2.5% for **A_Bpy_ACN_T**). On the contrary, the performance of the cells with MK-2 and Co-

Phen electrolyte is lower (3.1% for **M_Phen_ACN_T** vs 3.4% for **M_Bpy_ACN_T**). Another contribution to the smaller relative photocurrent for the cells with Co-Phen might come from fast titania–dye recombination processes that will be revealed in the **Transient Absorption** section.

Replacement of ACN by water as a solvent in the electrolyte leads to lower efficiencies of the solar cells (Table 1B). It is connected both with photocurrent and photovoltage limitation. The V_{OC} is initially reduced due to the 0.3 V negative shift of the reduction potential of Co-Phen redox couple because it is dissolved in water.¹¹ A further drop in V_{OC} is associated with lowering the edge of CB in titania by reducing the pH of the electrolyte³³ according to the well-established Nernstian dependence. It will be further investigated by the electrochemical impedance measurements, whose results are presented in the next section. Table 1B demonstrates that, on average, the relative photocurrent (*total APCE*) of the solar cells with water electrolyte reaches only about 40% of those with ACN electrolytes and the same redox couple (Co-Phen). This huge decrease points to a severe limitation in the charge-separation efficiency, and its reasons are provided by TA experiments discussed later.

Even smaller photocurrents are observed for ADEKA-1 cells with water electrolyte of $\text{pH} \approx 9$ or lower (samples **A_Phen_H2O_pH9_S** and **A_Phen_H2O_pH6_S** in Table 1B). A severe drop in J_{SC} and *total APCE* for ADEKA-1-sensitized cells (about 65% for $\text{pH} \approx 9$ and over 90% for $\text{pH} \approx 6$) along with lowering the pH of the electrolyte is associated with insufficient wetting, when the concentration of MBI is reduced. There was no such issue for MK-2-sensitized cells, where CDCA possessing hydroxyl groups was used as a coadsorbent. Its improvement of hydrophilic properties of mesoporous photoanodes and its positive influence on overall PCE have been reported before.^{10,20,34} On the contrary, OTMS used as a coadsorbent for ADEKA-1 does not improve the hydrophilic properties of the photoanode; thus, a high concentration of MBI (0.8 M) is necessary for proper contact of sensitized titania and the electrolyte. Interestingly, for the cell filled with a mixture of water and ACN (**A_Phen_H2O + ACN_S**), the photocurrent is increased, despite V_{OC} even smaller than that for $\text{pH} \approx 6$, which confirms the problem with wetting in only-water ADEKA-1 cells at low MBI concentrations.

Another problem observed for the solar cells with water electrolyte is the stability, which is presented in Figure S3. Both ADEKA-1 and MK-2 cells filled with cobalt- and ACN-based electrolytes exhibit remarkably constant V_{OC} and J_{SC} parameters (relatively decrease less than 5% after 20 days). On the contrary, in the cells with water electrolyte, a significant drop in photovoltaic parameters is already observed after 5 days (about 40% decrease in V_{OC} and 20% decrease in J_{SC}). Moreover, the decomposition of the system in water electrolyte can be also seen, several days old cells become more pale, which is shown in Figure S3C. Remarkably, this effect is more severe for MK-2 cells, which could be explained by weaker attachment to titania due to different anchoring groups in MK-2 and ADEKA-1.

Finally, the *total APCE* is similarly smaller in all ADEKA-1 cells, about three-fourth of that in the corresponding MK-2 cells (Table 1A,B, neglecting the ADEKA-1 cells with water electrolyte at $\text{pH} \approx 9$ and $\text{pH} \approx 6$ because of the problem of wetting). It is in line with our previous reports,^{22,23} which means that a special photoanode treatment with (e.g., multicapping) is necessary to lift the photocurrent in

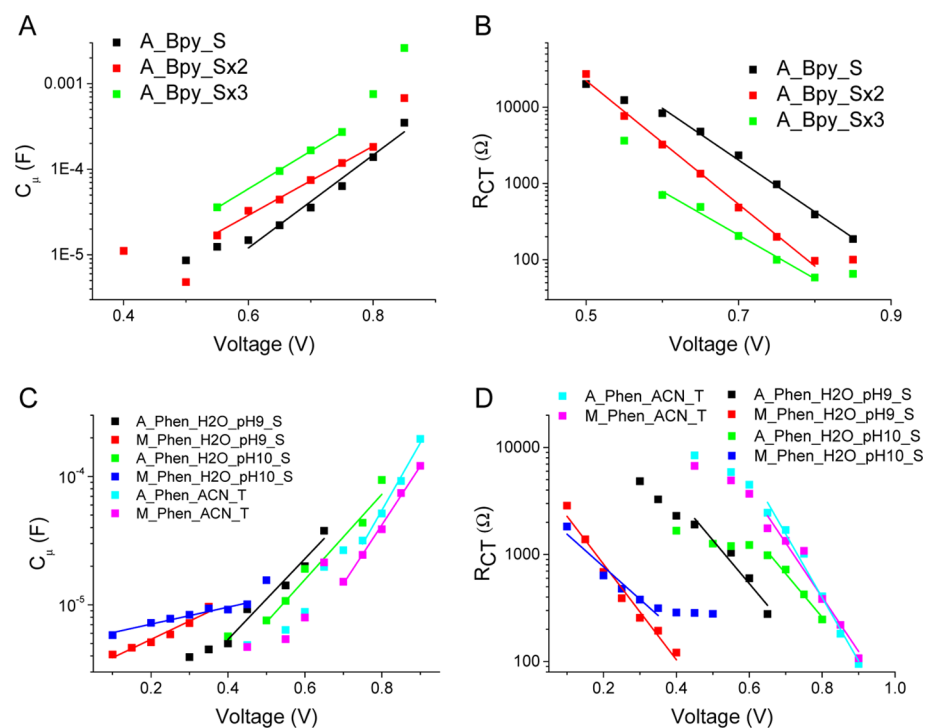


Figure 1. (A,B) C_{μ} and R_{CT} as a function of bias voltage obtained from EIS for cells with different thicknesses of titania layers sensitized with ADEKA-1 dye (analogous collection for MK-2 is in the Supporting Information Figure S4) and (C,D) C_{μ} and R_{CT} obtained from EIS for ADEKA-1- and MK-2-sensitized cells, assembled with various electrolytes.

ADEKA-1 cells to the champion efficiencies.² We have also made preliminary tests for the solar cells made with ZnO instead of TiO₂ nanoparticles (Table S1) and observed that the same relation between the relative photocurrent (always smaller for ADEKA-1) is maintained in the photoanodes made of different metal oxides. Besides, we observed that *total APCE* was about twice smaller for ZnO photoanodes than TiO₂ ones, both sensitized with the same dye solutions. Interestingly, MK-2 cells showed a slightly higher relative photocurrent in the iodide electrolyte than in the Co-Bpy electrolyte, whereas for ADEKA-1 cells, the situation was reversed (Table S1, for both TO₂ and ZnO photoanodes).

Electrochemical Impedance Spectroscopy. The impacts of changing the photoanode thickness and substituting standard ACN-based electrolytes with aqueous ones in the context of recombination and transport dynamics in our DSSCs were studied by means of EIS. Series of Nyquist impedance plots were obtained for different bias potentials. The fit to the obtained curves was made with the typical DSSC model with a transmission line.³⁵

Along with increasing the thickness of the titania nanoparticle layer, we can observe a rise in chemical capacitance (C_{μ}) values for each applied potential for the cells sensitized with ADEKA-1 dye (Figure 1A) or MK-2 dye (Figure S4A). This shift corresponds to the displacement of CB edge with respect to the redox potential of a given electrolyte, which adversely affects V_{OC} (Table 1A). We have already observed this influence of titania thickness in our previous study with N719.³⁰ Another effect of increasing the photoanode thickness is a decrease in the interfacial charge-transfer resistance (Figure 1B for ADEKA-1 and S4B for MK-2), which points to a higher recombination of electrons injected to the CB with cations in the electrolyte when the surface area of photoanode/electrolyte interface is enlarged. It results in lowering the FF parameter

(Table 1A). The trap-state distribution parameter (α) does not show a clear linear dependence on the thickness; however, it is remarkable that it rises along with the photoanode thickness. Similarly, the ideality factor (m) is getting worse with increasing thickness. Values of α and m parameters for cells in various configurations are summarized in Table S2.

Substituting an organic solvent by water in the electrolyte solution causes a shift in C_{μ} toward lower values when ACN is replaced by water and further displacement when pH is lowered from pH \approx 10 to the pH \approx 9 (Figure 1C). This effect results in severe lowering of the V_{OC} value (Table 1A), which unfavorably affects the PCE. Interestingly, we can see that this effect is less pronounced for the cells sensitized with ADEKA-1 dye than with MK-2 (A_Phen_H₂O_pH9_S and A_Phen_H₂O_pH10_S vs M_Phen_H₂O_pH9_S and M_Phen_H₂O_pH10_S). It suggests larger uptake of H⁺ ions from the aqueous solution by titania for the photoanodes with hydrophilic CDCA as a coadsorbent. It should be noted that titania uptake of H⁺ cations from the aqueous solution occurs even for high pH values (up to pH = 12).³³ ADEKA-1 aqueous cells are also characterized by higher values of α parameter than those of MK-2 ($\alpha = 0.18$ and $\alpha = 0.19$ for A_Phen_H₂O_pH9_S and A_Phen_H₂O_pH10_S, respectively, vs $\alpha = 0.08$ and $\alpha = 0.04$ for M_Phen_H₂O_pH9_S and M_Phen_H₂O_pH10_S, respectively), which indicates a narrower distribution of trap states below the CB edge. Similar to the systems described in the previous paragraph, lowering of the R_{CT} is reflected in decreasing FF values (Table 1B).

In Figure 1D, we compare the charge-transfer resistance (R_{CT}) between the same systems as in Figure 1C. Substitution of the organic electrolyte solvent with water generally increases the probability of recombination between electrons injected to the titania CB and the oxidized redox mediator. It is mainly because of the drop in the charge-transfer resistance (compare

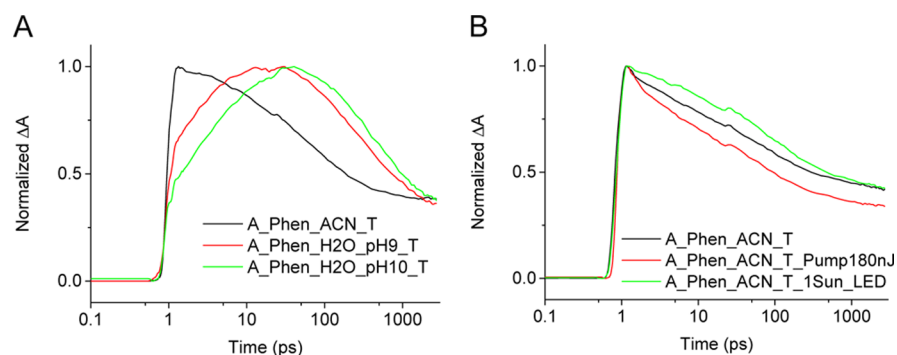


Figure 2. TA kinetics of ADEKA-1-sensitized cells (A) 700 and (B) 750 nm. Analogous results for MK-2-sensitized cells are presented in the Supporting Information Figure S7.

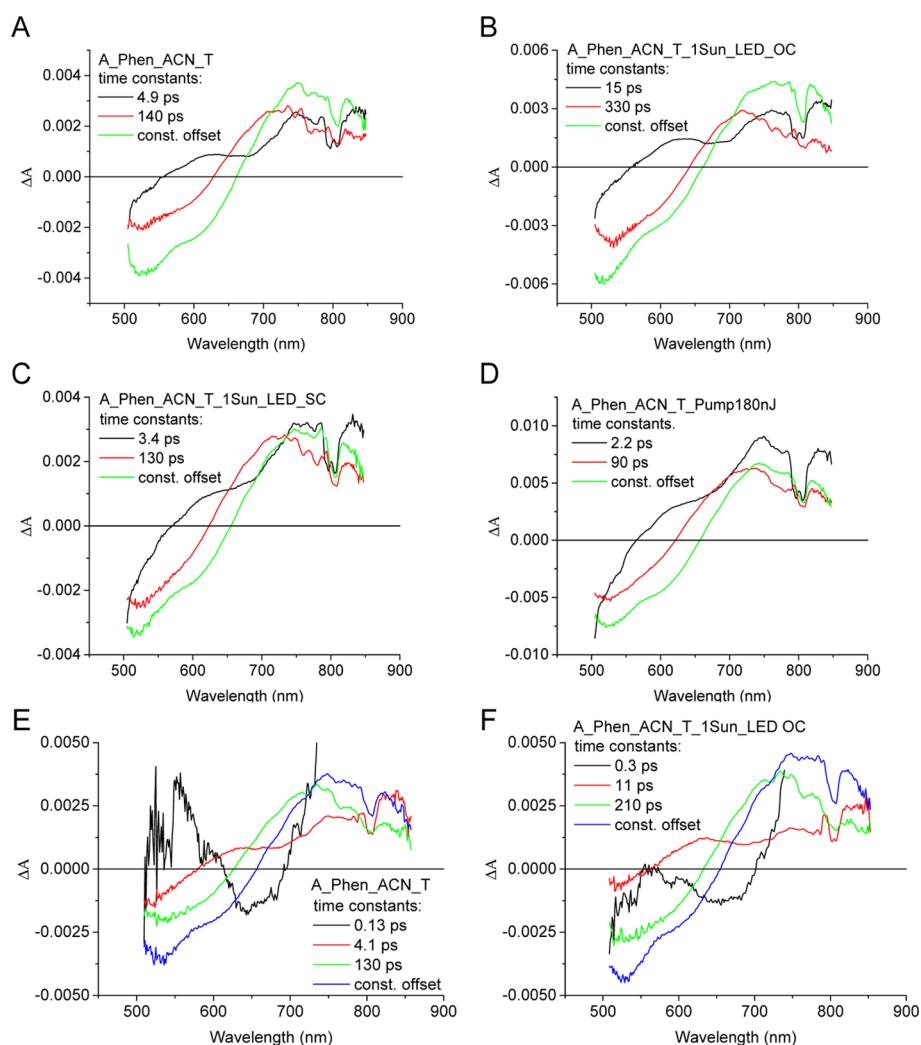


Figure 3. Wavelength-dependent amplitudes of characteristic time constants obtained from global analysis of TA spectra of ADEKA-1-sensitized cells assembled with ACN-based Co-Phen electrolyte by two-exponential fitting with a constant offset (A–D) and three-exponential fitting with a constant offset (E,F). Data are summarized to exhibit effects of: LED illumination (A vs B), open-/short-circuit (OC/SC) configuration of illuminated cell (B vs C), and different pump pulse energies (60 nJ—no indication or 180 nJ—abbreviation “pump 180 nJ”) (A vs D). Analogous collection for MK-2 sensitized cells is in the Supporting Information [Figures S8(A–D) and S9(A,C)].

A_Phen_ACN_T vs **A_Phen_H₂O_pH10_S** and **M_Phen_ACN_T** vs **M_Phen_H₂O_pH10_S** in Figure 1D). Again, this undesired effect is enlarged by lowering pH from ≈ 10 to ≈ 9 (compare **A_Phen_H₂O_pH10_S** vs **A_Phen_H₂O_pH9_S** and **M_Phen_H₂O_pH10_S** vs **M_Phen_H₂O_pH9_S** in Figure 1D). The result of lowering the R_{CT}

values is much more pronounced for MK-2 cells (compare **A_Phen_H₂O_pH10_S** vs **M_Phen_H₂O_pH10_S** and **A_Phen_H₂O_pH9_S** vs **M_Phen_H₂O_pH9_S** in Figure 1D), which again supports our explanation of more tight contact between the aqueous electrolyte and MK-2 + CDCA-functionalized titania surface with respect to that of ADEKA-1

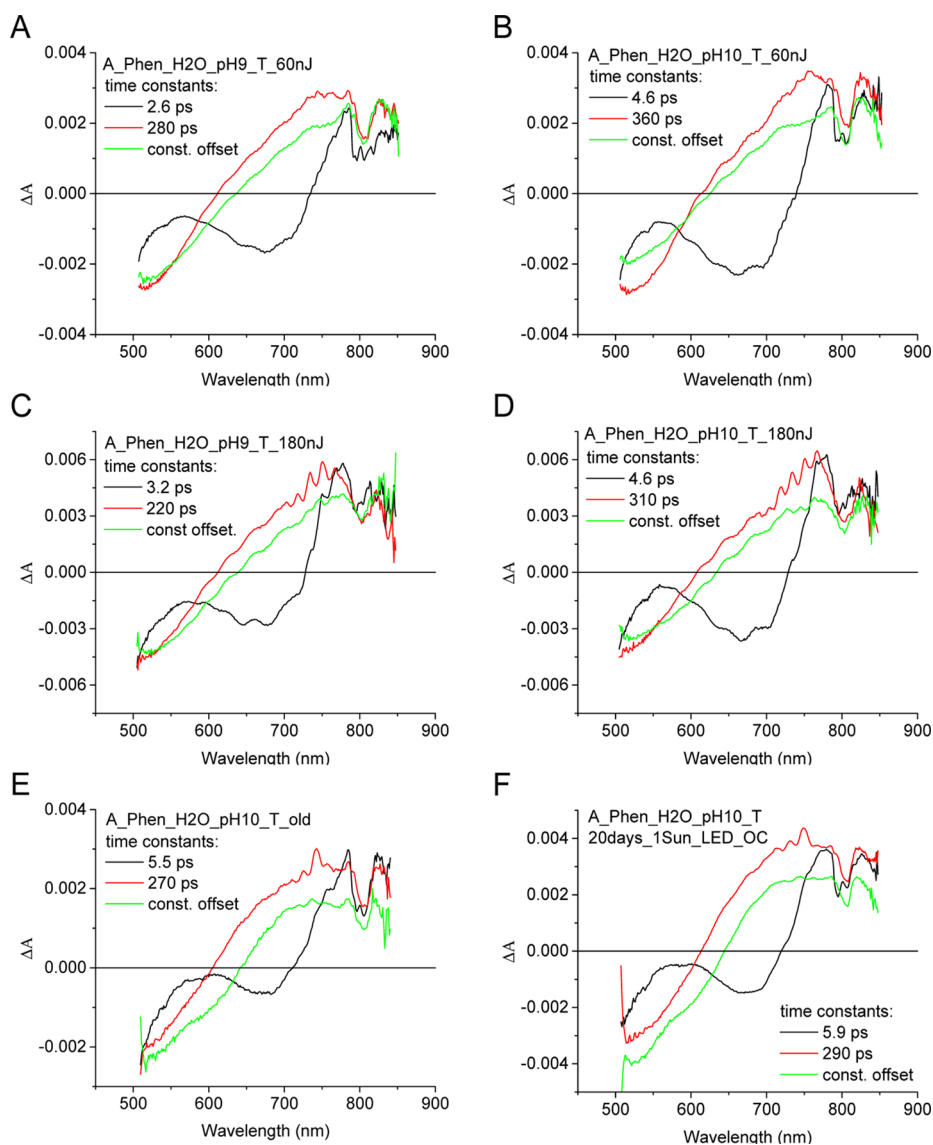


Figure 4. Wavelength-dependent amplitudes of characteristic time constants obtained from global analysis of TA spectra of ADEKA-1-sensitized cells by two-exponential fitting with a constant offset set to compare the effects: of the assembly with H₂O-based Co-Phen electrolyte of different pH values (A vs B and C vs D), different pump energies (A vs C and B vs D), and aging (B vs E) and of LED illumination (E vs F). Supplementary results for MK-2-sensitized cells are in the [Supporting Information](#) (Figure S10).

+ OTMS. Decrease in R_{CT} with respect to the transport resistance of titania scaffold results in a decreasing lifetime of electrons in the semiconductor CB, especially for the MK-2-sensitized cells with aqueous electrolyte—by about 1 order of magnitude (Figure S5A). As a result, we observe a shift in the onset of the decrease in charge-collection efficiency toward lower potentials, when the organic solvent is substituted by water and a further shift when the pH value is reduced (Figure S5B).

Another issue is the impact of 1 sun irradiation on R_{CT} , which can be directly associated with rise of the Fermi level due to electron injection. Irradiation increases the probability of recombination with an oxidized redox mediator as a result of enlarging the energy difference between the Fermi level and redox potential of the electrolyte; therefore, R_{CT} parameters are lower for the same applied bias potential, and the slopes of R_{CT} versus bias are smaller (Figure S6).

Transient Absorption. Within this work, we have compared TA measurements: kinetics of TA for selected

representative wavelengths (700 and 750 nm, Figure 2 for ADEKA-1 samples) and wavelength-dependent amplitudes of time constants obtained from global analysis (Figures 3 and 4 for ADEKA-1). Transparent cells were analyzed in 500–850 nm spectral range for pump-probe delays up to 3 ns. In this way, we evaluate the effects of assembling the solar cells with different Co-Phen electrolytes as well as results of higher pump pulse energy and additional illumination on the kinetics of electron injection from the excited dye to the titania CB (observed at $\lambda = 700$ nm) and recombination between electrons from titania CB and dye radical cation for ADEKA-1-sensitized solar cells (for $\lambda = 750$ nm). The kinetics and global analysis of TA spectral data of MK-2-sensitized cells are included in the [Supporting Information](#) (Figures S7–S10).

The interpretation of TA data is similar for all of the studied systems and analogous to our analysis in the previous works on ADEKA-1 and MK-2 dyes.^{22,23} The obtained wavelength-dependent amplitudes are characterized by different time constants so that we can compare the rates of the studied

processes (electron injection from the excited dye to the CB of TiO₂ and electron recombination between the CB of TiO₂ and oxidized dye) in various systems. Furthermore, we can estimate a contribution of different deactivation processes on the basis of comparative analysis of wavelength-dependent amplitudes of characteristic time constants. Another process occurring in DSSCs in the fast scale is the radical cation reduction by the redox shuttle (dye regeneration); however, the contribution of this process to the TA signal is negligible in 3 ns timescale.²²

In all samples, negative signals in the range from 510 nm to about 650 nm corresponding to stationary absorption spectra of both ADEKA-1 and MK-2 can be assigned to the ground state bleaching of the dye. In the longer wavelength range, we can find a positive band with maximum at around 750 nm, which comes from the combined absorption spectra of radical cation and electrons in titania trap states as well as free electrons in CB of TiO₂. Decay of these signals corresponds to recombination between injected electrons in titania and the oxidized dye. To observe the recombination process with minimized contribution of injection, we can examine the decay in TA kinetics for the wavelength 750 nm (Figures 2B and S7B). The ratio (parameter S_{RES}) between the residual signal (value for 3 ns delay between the probe and pump pulses) and the maximal signal of the kinetics is proportional to the number of successfully separated charge carriers.

Negative amplitudes (the rise of TA signal) in the range from 600 to 720 nm come from the reduction of stimulated emission accompanying the transition between S_1 and S_0 states. Injection of the electron from the S_1 state to the CB of the titania is the alternative way of deactivating the excited state of the dye; therefore, by observing the stimulated emission decay, we can monitor the dynamics of electron injection. Similar to the recombination process, we can monitor injection dynamics by analyzing the rise of the signal for 700 nm (Figures 2A and S7A).

It is not trivial to obtain average rate constants of injection and recombination because both injection and recombination processes cannot be characterized by monoexponential decays and, moreover, S_1 and S_0 absorption bands, the stimulated emission band (whose decay indicates the process of injection), and the absorption band of the radical cation of the dye (whose decay is caused by recombination) overlap spectrally. Similarly, as in our previous work,²³ for the cells with relatively slow electron injection (slow enough comparing to IRF of the setup), the characteristic times can be directly obtained from the biexponential global fit (slower component is assigned to recombination and faster to injection of electron). In this work, it operates for the cells based on aqueous electrolytes and it can be verified by the negative amplitude of the faster component in the range of 600–720 nm because of the stimulated emission decay (Figures 4 and S10). For the cells based on ACN electrolyte, the injection process occurs much faster (subpicosecond injection is comparable with IRF); therefore, in the biexponential global fit, both components mainly contain the contribution of recombination, with only a small indentation in the spectra of the faster component in the range of 600–720 nm because of electron injection (Figures 3A–D and S8). Thus, when the data are fitted with monoexponential dependence + a constant offset, the contribution from subpicosecond injection is negligible; therefore, we can take its rate constant as the average for recombination (not shown). To obtain the injection rate constant, we need to fit the data with a triexponential dependence and try different fits, with the

fastest component fixed on the value, which is increased until the signal between 600 and 720 nm is still negative and hence unaffected by the contribution of recombination (Figures 3E,F and S9). The same approach was applied in our previous work.²³ Constant offset components in all cases are due to the signal of radical cation and electrons; therefore, they represent the successfully separated charges (similar to S_{RES} parameters for single kinetics at 750 nm).

The obtained time constants for injection and recombination are gathered in Table 2. It should be noted that the averaged

Table 2. Average Injection and Recombination Times Obtained from TA in Vis for Different Solar Cell Samples^a

sample	injection time constant [ps]	recombination time constant [ps]
M_Bpy_ACN_T ^b	0.6	85
M_Phen_ACN_T	0.08	26
M_Phen_ACN_T LED	0.27	71
M_Phen_H ₂ O_pH10_T	3.8	240
M_Phen_H ₂ O_pH9_T	4.6	260
M_Phen_H ₂ O_pH10_T old	6.6	151
M_Phen_H ₂ O_pH10_T old LED	7.1	204
A_Bpy_ACN_T ^b	0.5	110
A_Phen_ACN_T	0.16	41
A_Phen_ACN_T LED	0.3	91
A_Phen_H ₂ O_pH10_T	4.6	360
A_Phen_H ₂ O_pH9_T	2.6	280
A_Phen_H ₂ O_pH10_T old	5.5	270
A_Phen_H ₂ O_pH10_T old LED	5.9	290

^aThe abbreviations “Old” and “LED” stand for 20 days old samples and additional illumination simulating 1 sun conditions, respectively
^bCells from our previous work.²³

time constants from several experiments are presented there, whereas the plots in Figures 3, 4, and S8–S10 show the results for particular samples. Very serious differences in ultrafast charge-transfer processes kinetics are observed when the ACN-based electrolyte is substituted with an aqueous electrolyte. Both processes are slowed down, for example, injection from 0.16 to 4.6 ps for A_Phen_ACN_T and A_Phen_H₂O_pH10_T, respectively, and recombination from 41 to 360 ps. This effect is less pronounced for the A_Phen_H₂O_pH9_T cell, for which we obtained the injection and recombination time constants of 2.6 and 280 ps, respectively. The downturn in injection is also well-pronounced in the set of kinetics for $\lambda = 700$ nm (Figure 2A). We can assign this effect to charge-transfer blocking properties of water molecules interacting with titania within the voids between the dye molecules attached to the titania surface.^{36,37} Water adsorption is assisted by the presence of MBI as it enhances wettability of the photoanode so that the effect of downturn of injection is more pronounced for higher MBI concentrations. On the other hand, for MK-2-dyed photoanodes, whose hydrophilic properties are determined by the coadsorbed CDCA molecules, the injection rate seems to be hardly affected by the reduction of MBI concentration (time constant of injection rises from 3.8 to 4.6 ps and recombination slows down from 240 to 260 ps). The differences in electron injection dynamics are in line with the changes in photovoltaic performance—slower injection in the samples with aqueous electrolyte correlates with worse *total APCE* parameter (Table 1). Similarly, as in our earlier study for insulating layer,²³ we explain it by higher contribution

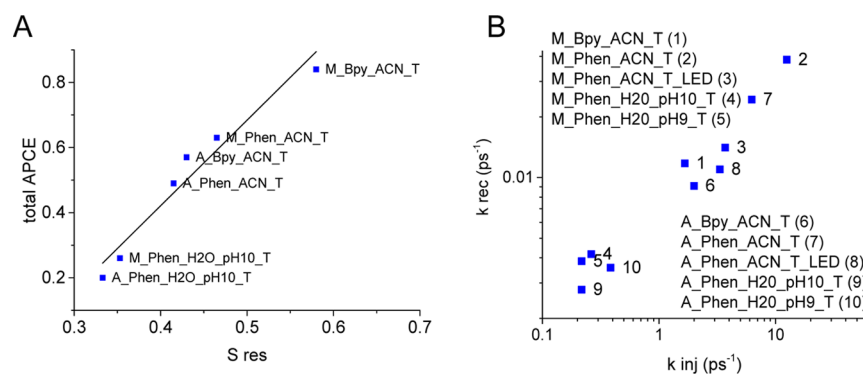


Figure 5. (A) Correlation of $total_APCE$ and S_{RES} . (B) Correlation of injection and recombination rates for different solar cell samples.

of injection to the trap states from which the recombination occurs with higher probability (although the dynamics of recombination is slower, its amplitude is higher).

Other differences in the obtained time constants were related to different experimental conditions applied for the same cells. We noticed that additional LED illumination (equivalent of 1 sun conditions) in the open-circuit configuration increases the time of injection and recombination about twice for the **A_Phen_ACN_T** cell (from 0.16 to 0.30 ps and from 41 to 91 ps, respectively, Figure 3E,F) and about three times for **M_Phen_ACN_T** (from 0.08 to 0.27 ps and from 26 to 71 ps, respectively, Figure S9). For better visualization of this phenomenon, we present the kinetics of TA for $\lambda = 750$ nm (Figures 2B and S7B). Interestingly, no such effect is observed when illumination is applied in the short-circuit configuration (e.g. Figures 3A–C and S8A–C) and the increase in time constants in the open-circuit conditions occurs already when about three times less intense illumination is used (Figures 3E vs 3F and S9D,A vs S9B,C). It indicates that longer time constants are associated with the position of Fermi level in TiO₂. The change in electron-transfer dynamics in this case could be explained by the reduction of electron coupling between the dye molecular orbital [lowest unoccupied molecular orbital (LUMO)] and titania CB because of the created electric field, which repels electrons from the dye LUMO away from the titania surface. A similar mechanism has been proposed for the action of potential-determining additives that create additional dipole moments at the dye/TiO₂ interface and thus influence the electronic coupling by redistribution of electron wave function in LUMO.³⁸ A similar but less pronounced trend is observed for aqueous cells (Table 2, Figure 4E,F) where electron coupling is already seriously limited by water molecules. Another explanation is that the electron-transfer dynamics is affected by a higher population (under 1 sun illumination) of long-living trap states lying toward more positive potentials. Injected electrons do not get trapped so likely and are less prone to recombine with the dye radical cation; thus, the initial charge separation is more efficient.

In contrast, increasing the energy of pump pulses accelerates the recombination (kinetics in Figures 2B and S7B, global analysis in Figures 3A vs 3D, S8A vs S8D, 4A,B vs 4C,D), which could be expected as it is a second-order reaction, and the concentrations of both electrons in titania CB and dye radical cations are increased. Similar effects have also been observed by us previously for these dyes,^{22,23} and we have concluded that it occurs for pump pulse energies above 60 nJ. Therefore, important differences should be highlighted between

increasing pump energy and adding continuous illumination in TA experiments. In the first case (pulse excitation), the same number of electrons and radical cations per titania nanoparticle is created, which leads to an increased recombination rate. In the latter situation (stationary excitation), in the open-circuit conditions, only the population of electrons increases (as radical cations have about 3 orders of magnitude shorter lifetime), and these electrons probably occupy long-living trap states (e.g., at particle grain boundaries). Therefore, they do not contribute to the second-order recombination reaction but change the electric field on the dye/TiO₂ interface, which decreases electron injection and recombination rates.

The parameter S_{RES} obtained from the kinetics of TA for $\lambda = 750$ nm is found to correlate linearly with the photocurrent corrected for the number of absorbed photons ($total_APCE$ parameter). The data are presented in Figure 5A. The correlation is in line with our previous studies^{22,23} and supports the thesis on general dependence of relative photocurrent density on the ultrafast processes of charge separation. Interestingly, the correlation of the TA signal at 3 ns with the relative photocurrent of the cells also operates for the ACN-based samples with Co-Bpy and Co-Phen redox couples. It means that fast recombination plays a more important role in the photocurrent variation than the different driving forces for dye regeneration between these two redox couples, as assumed so far.

Finally, another important dependence, which results from our ultrafast electron-transfer studies, is the correlation between injection and recombination rate constants presented in Figure 5B. It confirms that dye–titania electronic coupling is the main factor that drives the dynamics of these two charge-transfer processes in fresh cells, although they occur on different timescales. However, the times of injection and recombination are found to change unfavorably with aqueous cells aging. For **A_Phen_H2O_pH10_T_old** (20 days after preparation), the time of injection of electron is about 20% longer and the recombination time accelerates by 25% in respect to that for the **A_Phen_H2O_pH10_T** sample (measurement performed on the day of cell assembly). This effect is even more pronounced for **M_Phen_H2O_pH10_T** (over 70% slower injection and about 40% faster recombination), as MK-2 is less stable because of the weaker double C–O–Ti bond when compared to the triple Si–O–Ti bond anchoring ADEKA-1, and can be easily desorbed. This observation is in line with the results of cell aging tests (Figure S3).

Table 3. Summary of the Comparison between ACN-Based and Water-Based Electrolytes in Solar Cells Sensitized with ADEKA-1 Dye and OTMS as a Coadsorbent (Co-phen Redox Couple Used in Both Electrolytes)

solar cell property	ACN-based electrolyte	water-based electrolyte
<i>total_APCE</i>	moderate (~50%)	low (~20%)
<i>total_APCE</i> (ADEKA-1)/ <i>total_APCE</i> (MK-2)	~70–80%	~70–80%
V_{OC}	high (~870 mV)	moderate (~700 mV)
electron injection rate constant	fast (~6 ps ⁻¹)	slow (~0.3 ps ⁻¹), decreases upon cell aging
electron recombination rate constant	fast (~20 ns ⁻¹)	slow (~3 ns ⁻¹), increases upon cell aging
stability of the solar cell	good	bad
wettability of the photoanode	good	poor at pH < 9 ([MBI] < 0.1 M)

CONCLUSIONS

The performances of ADEKA-1, a champion dye for DSSCs with a carbazole moiety and an alkoxy-silyl-anchor unit, and its popular analogue with a carboxylic anchor, MK-2, are compared in different solar cell configurations, including those with water-based electrolytes. Particular attention is paid to the determination of charge-transfer dynamics measured from femtoseconds to milliseconds in the real conditions for solar cells. The samples are fully assembled devices (filled with cobalt-based electrolyte in water or ACN solution) with characterized photovoltaic performance. The charge-transfer dynamics is studied with or without 1 sun bias irradiation.

Without special a photoanode treatment (mesoporous titania layers are sensitized only with the photoactive dyes containing coadsorbents: OTMS for ADEKA-1 and CDCA for MK-2), the photocurrent corrected for the number of absorbed photons is always lower for ADEKA-1 (on average it is about 75% of that of MK-2), whereas the initial open-circuit voltage (V_{OC}) is higher for ADEKA-1 (about 1% higher for ACN electrolyte and 60% higher for water electrolyte). The *total_APCE* parameter for both dyes correlates very well with the amplitude of the residual TA signal measured at 3 ns after excitation, which indicates that the initial electron recombination process, occurring on the time scale from sub-ns to single nanoseconds is the main reason for the limited photocurrent of the devices. The validity of this explanation includes the effect of water (*total_APCE* in aqueous electrolyte is about 40% of that in analogous ACN electrolyte) and cobalt redox species of different potentials (corrected photocurrent for the Co-phenanthroline complex is about 85% of that for the Co-bipyridine complex).

The corrected photocurrent decreases when a scattering titania layer is used instead of a transparent one and upon further increasing the thickness of the scattering layers (from about 3 to 9 μm). Simultaneously, V_{OC} drops because of the shift of the titania CB, and the FF decreases because of the more pronounced electron recombination between titania and the electrolyte (on ms time scale). It means that for the studied organic dyes with high extinction coefficients, the thickness of the photoanode should not be too high to obtain the best efficiency.

The rate of electron injection is correlated with the rate of electron recombination between titania and ADEKA-1 or MK-2 dyes. It means that higher electronic coupling between the dye and titania accelerates both processes. In aqueous electrolytes, the average rate constants of electron injection (0.15–0.40 ps⁻¹) and recombination (3–4 ns⁻¹) are significantly smaller than those in the corresponding ACN electrolyte (injection 1–12 ps⁻¹, recombination 10–40 ns⁻¹). This indicates that water

molecules form an insulating layer on the titania surface leading to the decrease in the dye–titania electronic coupling.

The 1 sun bias irradiation causes a decrease in electron-transfer rates between the dye and titania (both injection and recombination are about twice slower when compared to those in the nonirradiated samples) in the open-circuit conditions. No such effect is observed when the cells are kept at short circuit. We explain this observation by the electric field present on the titania particle surface and induced by the long-living trapped electrons, whose population is created under stationary irradiation conditions. Most probably, such an electric field weakens the electronic coupling between the dyes and titania.

The samples with ACN electrolyte show good stability (relative decrease in V_{OC} and J_{SC} is less than 5% after 20 days). In contrast, the cells with aqueous electrolyte exhibit significant decrease in photovoltaic efficiency, mainly caused by the drop in V_{OC} (e.g., about 40% drop after 5 days) and in J_{SC} (~20% drop after 5 days). Upon the cell aging, the electron injection rate decreases but the electron recombination rate increases, which might explain the observed degradation in the photovoltaic performance in the presence of water. Moreover, the degradation of photoanodes in water environment is also observed, more pronounced for MK-2 than ADEKA-1. Finally, for ADEKA-1 with OTMS coadsorbent, the problems with wetting of electrodes in aqueous electrolyte are observed, leading to a drastic decrease in the photocurrent of the cell with the electrolyte at a low pH \approx (6–9) (in contrast to MK-2-sensitized photoanodes with coadsorbed CDCA, which are characterized by higher wettability). MBI addition improves wetting at the concentrations of 0.8 M, corresponding to pH \approx 10 of the electrolyte solution. Comparison between aqueous and ACN-based electrolytes is summarized in Table 3.

ASSOCIATED CONTENT

Supporting Information

The Supporting Information is available free of charge on the ACS Publications website at DOI: 10.1021/acs.jpcc.8b01986.

Structures of ADEKA-1 and MK-2; stationary absorption spectra; IPCE spectra; stability tests and cell photography; EIS data; TA data for MK-2; photovoltaic parameters of preliminary studied systems; ideality factors; and trap distribution parameters (PDF)

AUTHOR INFORMATION

Corresponding Author

*E-mail: marziol@amu.edu.pl.

ORCID

Marcin Ziółek: 0000-0003-1882-6022

Notes

The authors declare no competing financial interest.

ACKNOWLEDGMENTS

This work was supported by the NCN (National Science Centre, Poland) under project 2015/18/E/ST4/00196. Dr. hab. Błażej Gierczyk from the Faculty of Chemistry, who synthesized the ADEKA-1 dye, and Iwona Grądzka from the Faculty of Physics, Adam Mickiewicz University in Poznań, Poland, who helped with solar cell sample preparation are kindly acknowledged.

REFERENCES

- (1) O'Regan, B.; Grätzel, M. A Low-Cost, High-Efficiency Solar-Cell Based on Dye-Sensitized Colloidal TiO₂ Films. *Nature* **1991**, *353*, 737–740.
- (2) Kakiage, K.; Aoyama, Y.; Yano, T.; Oya, K.; Fujisawa, J.-i.; Hanaya, M. Highly-Efficient Dye-Sensitized Solar Cells with Collaborative Sensitization by Silyl-Anchor and Carboxy-Anchor Dyes. *Chem. Commun.* **2015**, *51*, 15894–15897.
- (3) Bella, F.; Galliano, S.; Gerbaldi, C.; Viscardi, G. Cobalt-Based Electrolytes for Dye-Sensitized Solar Cells: Recent Advances towards Stable Devices. *Energies* **2016**, *9*, 384.
- (4) Feldt, S. M.; Gibson, E. A.; Gabrielson, E.; Sun, L.; Boschloo, G.; Hagfeldt, A. Design of Organic Dyes and Cobalt Polypyridine Redox Mediators for High Efficiency Dye-Sensitized Solar Cells. *J. Am. Chem. Soc.* **2010**, *132*, 16714–16724.
- (5) Yella, A.; Lee, H.-W.; Tsao, H. N.; Yi, C.; Chandiran, A. K.; Nazeeruddin, M. K.; Diau, E. W.-G.; Yeh, C.-Y.; Zakeeruddin, S. M.; Grätzel, M. Porphyrin-Sensitized Solar Cells with Cobalt (II/III)-based Redox Electrolyte Exceed 12 Percent Efficiency. *Science* **2011**, *334*, 629–634.
- (6) Yum, J.-H.; Baranoff, E.; Kessler, F.; Moehl, T.; Ahmad, S.; Bessho, T.; Marchioro, A.; Ghadiri, E.; Moser, J.-E.; Yi, C.; et al. A Cobalt Complex Redox Shuttle for Dye-Sensitized Solar Cells with High Open-Circuit Potentials. *Nat. Commun.* **2012**, *3*, 631.
- (7) Sapp, S. A.; Elliott, C. M.; Contado, C.; Caramori, S.; Bignozzi, C. A. Substituted Polypyridine Complexes of cobalt(II/III) as Efficient Electron-Transfer Mediators in Dye-Sensitized Solar Cells. *J. Am. Chem. Soc.* **2002**, *124*, 11215–11222.
- (8) Bella, F.; Gerbaldi, C.; Barolo, C.; Grätzel, M. Aqueous Dye-Sensitized Solar Cells. *Chem. Soc. Rev.* **2015**, *44*, 3431–3473.
- (9) De Angelis, F.; Fantacci, S.; Gebauer, R. Simulating Dye-Sensitized TiO₂ heterointerfaces in Explicit Solvent: Absorption Spectra, Energy Levels, and Dye Desorption. *J. Phys. Chem. Lett.* **2011**, *2*, 813–817.
- (10) Law, C.; Pathirana, S. C.; Li, X.; Anderson, A. Y.; Barnes, P. R. F.; Listorti, A.; Ghaddar, T. H.; O'Regan, B. C. Water-Based Electrolytes for Dye-Sensitized Solar Cells. *Adv. Mater.* **2010**, *22*, 4505–4509.
- (11) Ellis, H.; Jiang, R.; Ye, S.; Hagfeldt, A.; Boschloo, G. Development of High Efficiency 100% Aqueous Cobalt Electrolyte Dye-Sensitized Solar Cells. *Phys. Chem. Chem. Phys.* **2016**, *18*, 8419–8427.
- (12) Bella, F.; Galliano, S.; Falco, M.; Viscardi, G.; Barolo, C.; Grätzel, M.; Gerbaldi, C. Approaching Truly Sustainable Solar Cells by the Use of Water and Cellulose Derivatives. *Green Chem.* **2017**, *19*, 1043–1051.
- (13) Nath, N. C. D.; Lee, H. J.; Lee, J.-J. Effect of Water on the Performance of Dye-Sensitized Solar Cells with Quasi-Solid-State Electrolytes. *J. Nanosci. Nanotechnol.* **2016**, *16*, 10575–10582.
- (14) Park, S. J.; Yoo, K.; Kim, J.-Y.; Kim, J. Y.; Lee, D.-K.; Kim, B.; Kim, H.; Kim, J. H.; Cho, J.; Ko, M. J. Water-Based Thixotropic Polymer Gel Electrolyte for Dye-Sensitized Solar Cells. *ACS Nano* **2013**, *7*, 4050–4056.
- (15) Yu, Z.; Li, F.; Sun, L. Recent Advances in Dye-Sensitized Photoelectrochemical Cells for Solar Hydrogen Production Based on Molecular Components. *Energy Environ. Sci.* **2015**, *8*, 760–775.
- (16) Swierk, J. R.; Mallouk, T. E. Design and Development of Photoanodes for Water-Splitting Dye-Sensitized Photoelectrochemical Cells. *Chem. Soc. Rev.* **2013**, *42*, 2357–2387.
- (17) Koumura, N.; Wang, Z.-S.; Mori, S.; Miyashita, M.; Suzuki, E.; Hara, K. Alkyl-Functionalized Organic Dyes for Efficient Molecular Photovoltaics. *J. Am. Chem. Soc.* **2006**, *128*, 14256–14257.
- (18) Wang, Z.-S.; Koumura, N.; Cui, Y.; Takahashi, M.; Sekiguchi, H.; Mori, A.; Kubo, T.; Furube, A.; Hara, K. Hexylthiophene-Functionalized Carbazole Dyes for Efficient Molecular Photovoltaics: Tuning of Solar-Cell Performance by Structural Modification. *Chem. Mater.* **2008**, *20*, 3993–4003.
- (19) Xiang, W.; Huang, F.; Cheng, Y.-B.; Bach, U.; Spiccia, L. Aqueous Dye-Sensitized Solar Cell Electrolytes Based on the cobalt(II)/(III) Tris(bipyridine) Redox Couple. *Energy Environ. Sci.* **2013**, *6*, 121–127.
- (20) Galliano, S.; Bella, F.; Gerbaldi, C.; Falco, M.; Viscardi, G.; Grätzel, M.; Barolo, C. Photoanode/Electrolyte Interface Stability in Aqueous Dye-Sensitized Solar Cells. *Energy Technol.* **2017**, *5*, 300–311.
- (21) Kakiage, K.; Aoyama, Y.; Yano, T.; Otsuka, T.; Kyomen, T.; Unno, M.; Hanaya, M. An Achievement of over 12 Percent Efficiency in an Organic Dye-Sensitized Solar Cell. *Chem. Commun.* **2014**, *50*, 6379–6381.
- (22) Sobuś, J.; Gierczyk, B.; Burdziński, G.; Jancelewicz, M.; Polanski, E.; Hagfeldt, A.; Ziólek, M. Factors Affecting the Performance of Champion Silyl-Anchor Carbazole Dye Revealed in the Femtosecond to Second Studies of Complete ADEKA-1 Sensitized Solar Cells. *Chem.—Eur. J.* **2016**, *22*, 15807–15818.
- (23) Gierszewski, M.; Glinka, A.; Grądzka, I.; Jancelewicz, M.; Ziólek, M. Effects of Post-Assembly Molecular and Atomic Passivation of Sensitized Titania Surface: Dynamics of Electron Transfer Measured from Femtoseconds to Seconds. *ACS Appl. Mater. Interfaces* **2017**, *9*, 17102–17114.
- (24) Sengupta, D.; Das, P.; Mondal, B.; Mukherjee, K. Effects of Doping, Morphology and Film-Thickness of Photo-Anode Materials for Dye Sensitized Solar Cell Application - A Review. *Renewable Sustainable Energy Rev.* **2016**, *60*, 356–376.
- (25) Lee, J.-K.; Jeong, B.-H.; Jang, S.-I.; Yeo, Y.-S.; Park, S.-H.; Kim, J.-U.; Kim, Y.-G.; Jang, Y.-W.; Kim, M.-R. Multi-Layered TiO₂ Nanostructured Films for Dye-Sensitized Solar Cells. *J. Mater. Sci.: Mater. Electron.* **2009**, *20*, 446–450.
- (26) Tsao, H. N.; Comte, P.; Yi, C.; Grätzel, M. Avoiding Diffusion Limitations in cobalt(III/II)-Tris(2,2'- Bipyridine)-Based Dye-Sensitized Solar Cells by Tuning the Mesoporous TiO₂ Film Properties. *ChemPhysChem* **2012**, *13*, 2976–2981.
- (27) Wang, Z.-S.; Kawachi, H.; Kashima, T.; Arakawa, H. Significant Influence of TiO₂ Photoelectrode Morphology on the Energy Conversion Efficiency of N719 Dye-Sensitized Solar Cell. *Coord. Chem. Rev.* **2004**, *248*, 1381–1389.
- (28) Martín, C.; Ziólek, M.; Douhal, A. Ultrafast and Fast Charge Separation Processes in Real Dye-Sensitized Solar Cells. *J. Photochem. Photobiol., C* **2016**, *26*, 1–30.
- (29) Ponseca, C. S.; Chábera, P.; Uhlig, J.; Persson, P.; Sundström, V. Ultrafast Electron Dynamics in Solar Energy Conversion. *Chem. Rev.* **2017**, *117*, 10940–11024.
- (30) Gierszewski, M.; Grądzka, I.; Glinka, A.; Ziólek, M. Insights into the Limitations of Solar Cells Sensitized with Ruthenium Dyes Revealed in Time-Resolved Spectroscopy Studies. *Phys. Chem. Chem. Phys.* **2017**, *19*, 20463–20473.
- (31) Idígoras, J.; Burdziński, G.; Karolczak, J.; Kubicki, J.; Oskam, G.; Anta, J. A.; Ziólek, M. The Impact of the Electrical Nature of the Metal Oxide on the Performance in Dye-Sensitized Solar Cells: New Look at Old Paradigms. *J. Phys. Chem. C* **2015**, *119*, 3931–3944.
- (32) Ito, S.; Liska, P.; Comte, P.; Charvet, R.; Péchy, P.; Bach, U.; Schmidt-Mende, L.; Zakeeruddin, S. M.; Kay, A.; Nazeeruddin, M. K.; et al. Control of Dark Current in Photoelectrochemical (TiO₂/I⁻/I³⁻) and Dye-Sensitized Solar Cells. *Chem. Commun.* **2005**, 4351–4353.
- (33) Lyon, L. A.; Hupp, J. T. Energetics of the Nanocrystalline Titanium Dioxide/Aqueous Solution Interface: Approximate Conduction Band Edge Variations between H₀ = -10 and H₋ = +26. *J. Phys. Chem. B* **1999**, *103*, 4623–4628.

(34) Galliano, S.; Bella, F.; Piana, G.; Giacona, G.; Viscardi, G.; Gerbaldi, C.; Grätzel, M.; Barolo, C. Finely Tuning Electrolytes and Photoanodes in Aqueous Solar Cells by Experimental Design. *Sol. Energy* **2018**, *163*, 251–255.

(35) Bisquert, J. Theory of the Impedance of Electron Diffusion and Recombination in a Thin Layer. *J. Phys. Chem. B* **2002**, *106*, 325–333.

(36) Tilocca, A.; Selloni, A. Vertical and Lateral Order in Adsorbed Water Layers on Anatase TiO₂(101). *Langmuir* **2004**, *20*, 8379–8384.

(37) Herman, G. S.; Dohnálek, Z.; Ruzycki, N.; Diebold, U. Experimental Investigation of the Interaction of Water and Methanol with Anatase–TiO₂ (101). *J. Phys. Chem. B* **2003**, *107*, 2788–2795.

(38) Yang, X.; Zhang, S.; Zhang, K.; Liu, J.; Qin, C.; Chen, H.; Islam, A.; Han, L. Coordinated Shifts of Interfacial Energy Levels: Insight into Electron Injection in Highly Efficient Dye-Sensitized Solar Cells. *Energy Environ. Sci.* **2013**, *6*, 3637–3645.

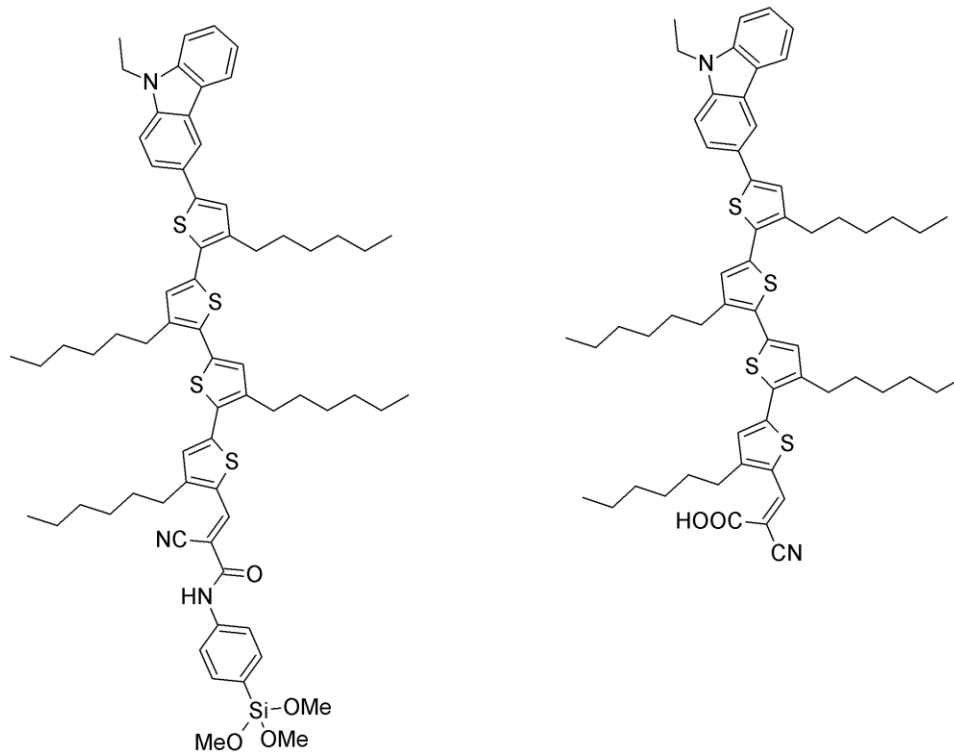
Supporting information

for

Effects of Aqueous Electrolyte, Active Layer Thickness and Bias Irradiation on Charge Transfer Rates In Solar Cells Sensitized with Top Efficient Carbazole Dyes

Adam Glinka ¹, Mateusz Gierszewski ¹, and Marcin Ziółek^{1*}

¹ *Quantum Electronics Laboratory, Faculty of Physics, Adam Mickiewicz University in Poznań, Umultowska 85, 61-614 Poznań, Poland.*



Scheme S1. The structures of ADEKA-1 (left) and MK-2 (right).

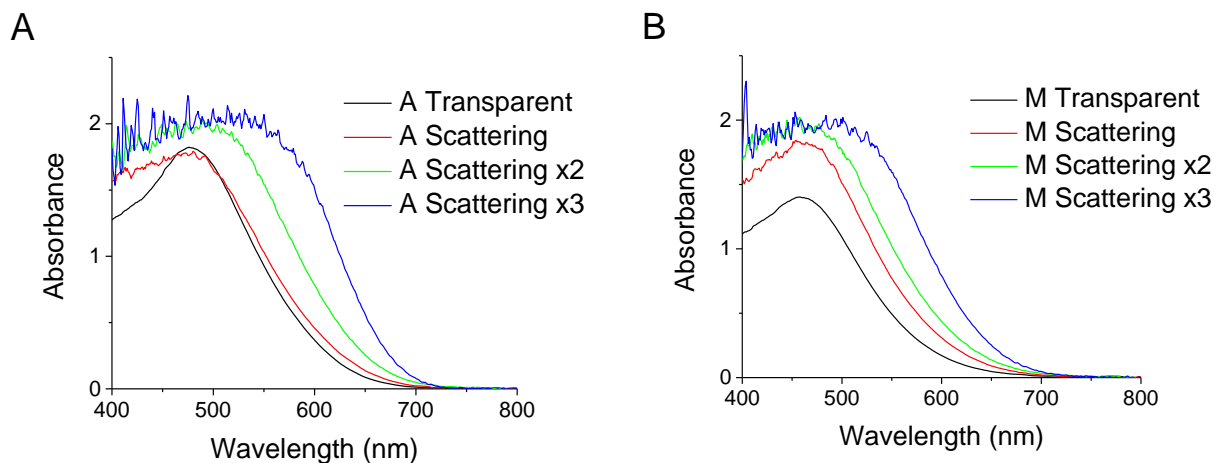


Figure S1. Stationary absorption of the films sensitized with (A) ADEKA-1 and (B) MK-2 dye.

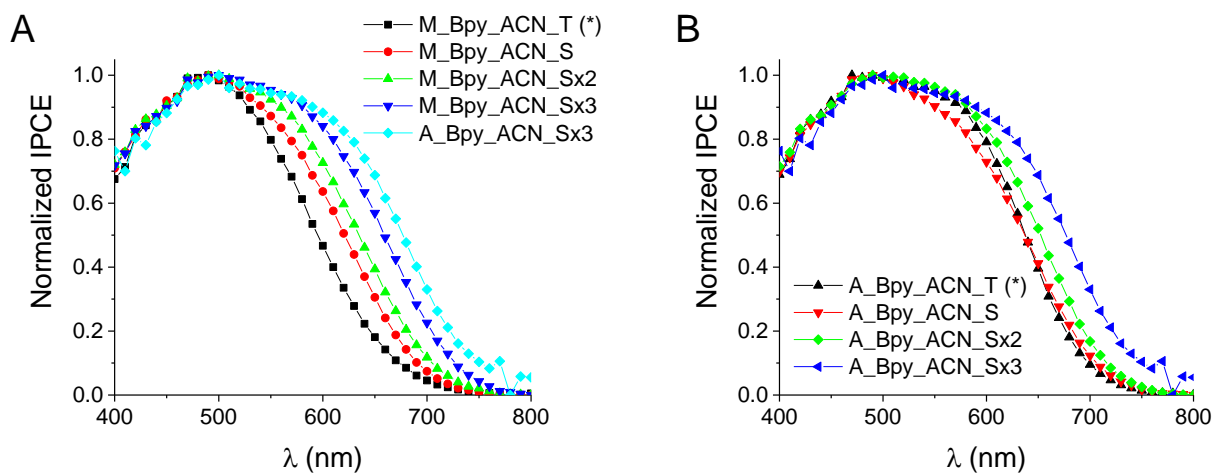


Figure S2. Normalized IPCE spectra of cells with ACN Co(Bpy) electrolyte.

(*) the cells from our previous work¹

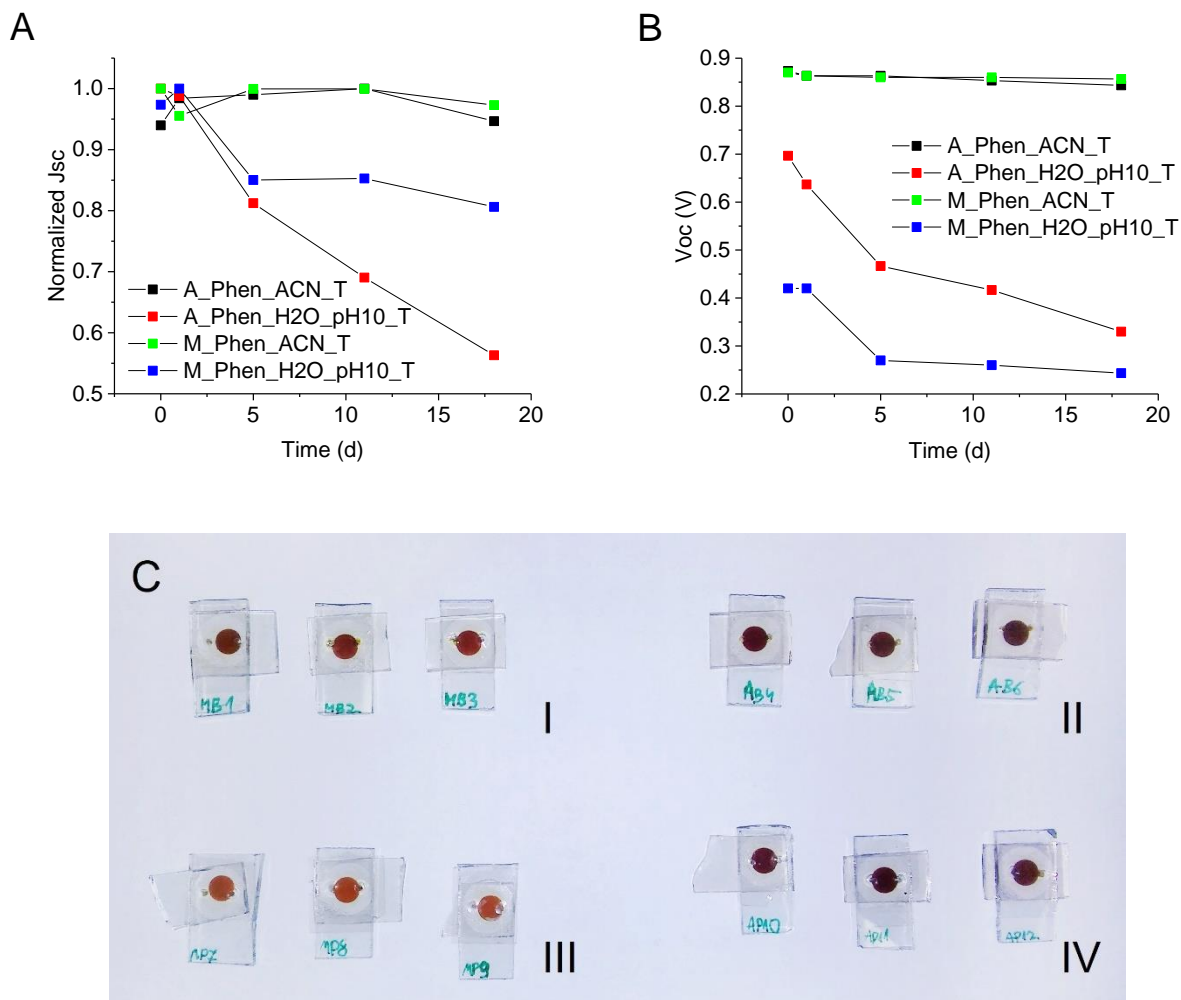


Figure S3. Effect of aging: A - decrease in normalized J_{sc} , B - decrease in V_{oc} , C - picture of several day-old cell samples, fading of MK-2 sensitized photoanodes in aqueous DSSCs (more pale cells with respect to those in ACN), ADEKA-1 sensitized cells hardly affected. I - M_Bpy_ACN_S, II - A_Bpy_ACN_S, III - M_Phen_H2O_pH10_S, IV - A_Phen_H2O_pH10_S.

Table S1. Photovoltaic performance of cells made up with old solutions for sensitization and ACN-based electrolyte: open circuit voltage (V_{OC}), short circuit photocurrent density (J_{SC}), fill factor (FF), power conversion efficiency (Eff), number of absorbed photons (N_{PH}), absorbance at 500 nm (A_{500}) and corrected photocurrent ($total_APCE$).

(A) TiO_2 , I stands for iodide/triiodide redox couple.

Cell	Voc [V]	FF	Jsc [mA/m ²]	Eff [%]	N_{PH} [10 ²⁰ s ⁻¹ m ⁻²]	A_{500}	$total_APCE$
M_I_ACN_S old	0.74	0.60	8.5	3.7	7.5	1.51	0.70
M_Phen_ACN_S old	0.83	0.52	7.0	3.0	7.2	1.29	0.61
M_Bpy_ACN_S old	0.83	0.43	7.6	2.8	7.5	1.51	0.66
A_I_ACN_S old	0.68	0.59	5.9	2.4	8.2	1.65	0.45
A_Phen_ACN_S old	0.81	0.62	4.6	1.0	8.6	1.7	0.33
A_Bpy_ACN_S old	0.78	0.41	6.7	2.2	8.2	1.65	0.51

(B) ZnO (doctor blade deposition method giving the thickness of about 1 μm^2 , N stands for reference N719 dye.

Cell	Voc [V]	FF	Jsc [mA/m ²]	Eff [%]	N_{PH} [10 ²⁰ s ⁻¹ m ⁻²]	A_{480}	$total_APCE$ (*)
M_Bpy_ACN_ZnO	0.71	0.47	3.7	1.23	4.9	0.74	0.35
M_I_ACN_ZnO	0.64	0.57	1.8	0.66	4.0	0.53	0.34
A_Bpy_ACN_ZnO	0.69	0.61	2.2	0.93	4.1	0.44	0.31
A_I_ACN_ZnO	0.64	0.59	1.0	0.38	4.8	0.55	0.15
N_Bpy_ACN_ZnO	0.50	0.50	1.4	0.35	2.1	0.11	0.42
N_I_ACN_ZnO	0.69	0.62	3.6	1.54	1.9	0.10	1.00

(*) averaged from J-V and IPCE data

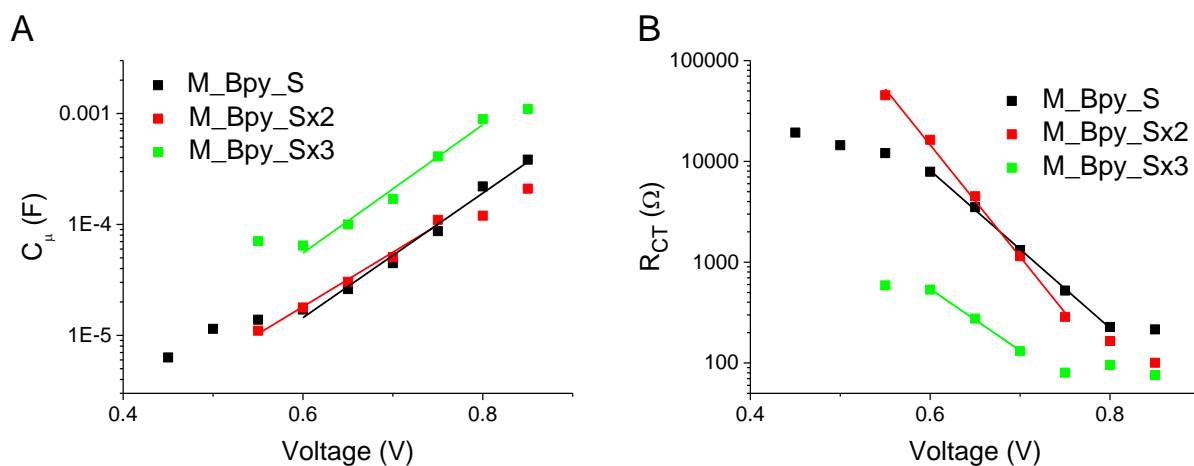


Figure S4. EIS for MK-2 sensitized cells with different photoanode thicknesses (supplement for Figure 1).

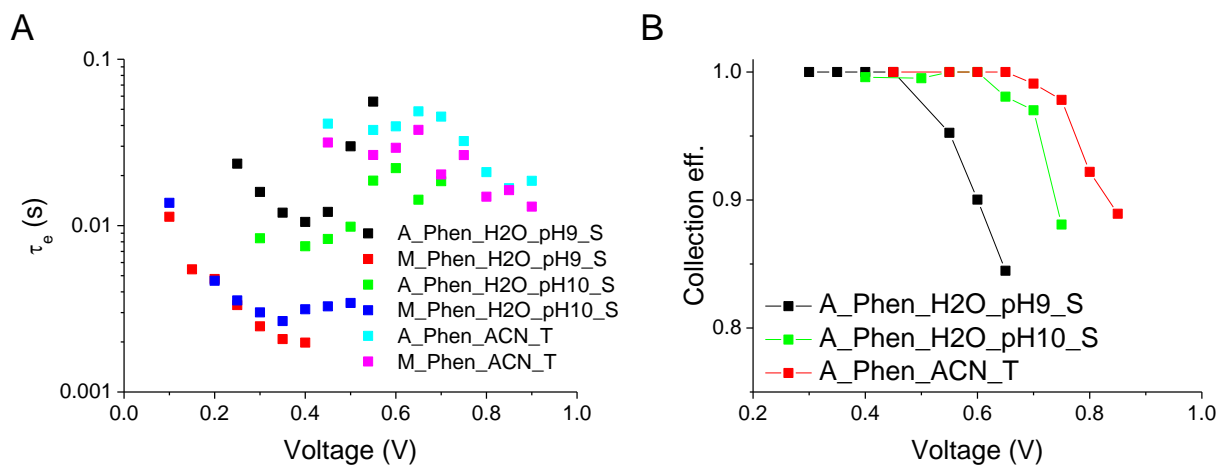


Figure S5. Supplement for Figure 1 : (A) - The lifetime of electron in titania CB, (B) – Charge collection efficiency of cells sensitized with ADEKA-1 dye.

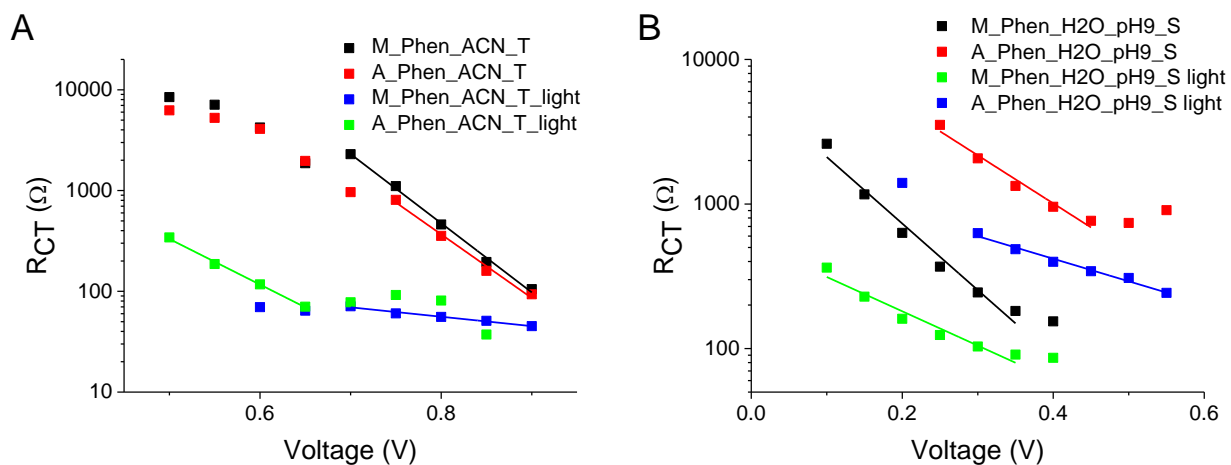


Figure S6. Effect of 1 sun light on charge recombination resistance in EIS, (A)– acetonitrile electrolyte, (B) – aqueous electrolyte. The values of the calculated ideality factor (m) parameter for the samples measured under illumination were as follows: $m=18.20$ for **M_Phen_ACN_T_light**, $m=3.76$ for **A_Phen_ACN_T_light**, $m=7.16$ for **M_Phen_H2O_pH9_S_light** and $m=10.90$ for **A_Phen_H2O_pH9_S_light**. For the rest of the samples, m values are given in Table S2.

Table S2. Calculated ideality factor (m) and trap distribution parameter (α): $C_{\mu}=C_0 \exp(\alpha V_e/kT)$ and $R_{CT}=R_0 \exp(-V_e/m kT)$. The values were averaged from the measurements on the first two days.

Sample / configuration	m	α
M_ Bpy _ACN_T (*)	1.8	0.25
M_ Phen _ACN_T	2.9	0.25
M_ Bpy _ACN_S	2.1	0.32
M_ Bpy _ACN_Sx2	1.7	0.29
M_ Bpy _ACN_Sx3	2.3	0.32
A_ Bpy _ACN_T (*)	3.0	0.24
A_ Phen _ACN_T	2.8	0.31
A_ Bpy _ACN_S	2.7	0.32
A_ Bpy _ACN_Sx2	2.3	0.26
A_ Bpy _ACN_Sx3	2.9	0.30
M_ Phen _H2O_pH10_S	6.7	0.04
M_ Phen _H2O_pH9_S	3.8	0.08
A_ Phen _H2O_pH10_S	4.1	0.19
A_ Phen _H2O_pH9_S	4.2	0.18
A_ Phen _H2O_pH10_T	4.0	0.32

(*) the cells from our previous work¹.

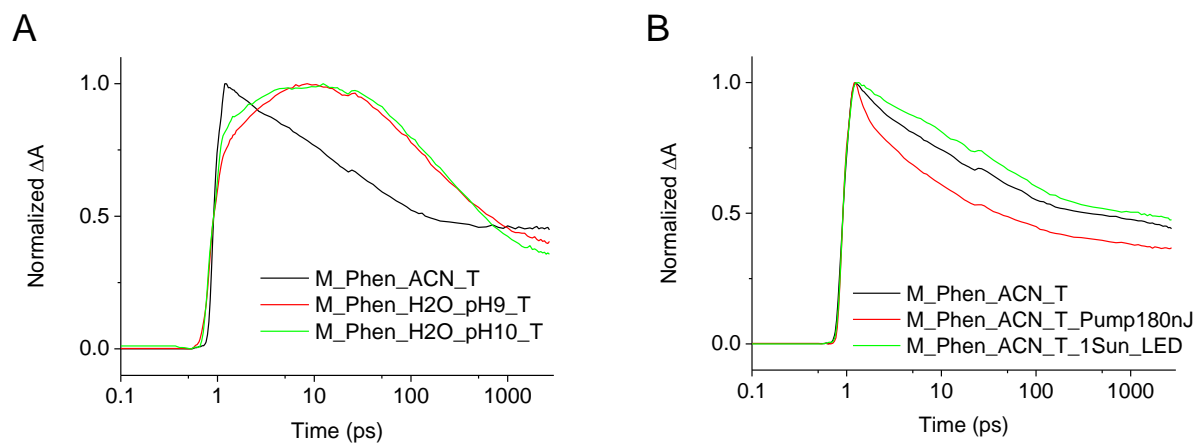


Figure S7. TA kinetics of MK-2 sensitized cells (A) 700 nm, and (B) 750 nm. Supplement for Figure 2.

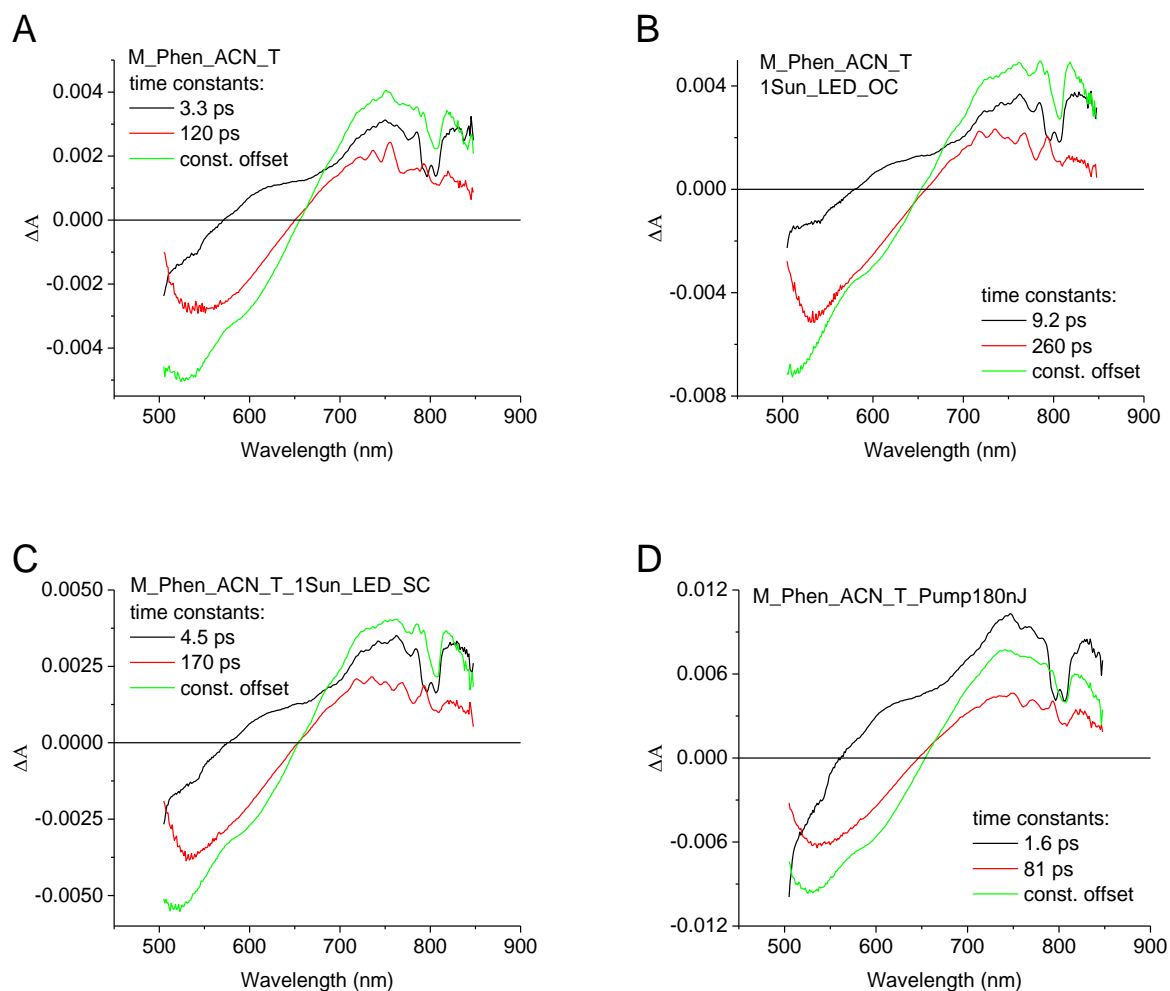


Figure S8. Wavelength dependent amplitudes of characteristic time constants obtained from global analysis of TA spectra of MK-2 sensitized cells assembled with ACN-based Co-Phen electrolyte by two-exponential fitting with constant offset. Data are summarized in order to exhibit effects of to exhibit effects of: LED illumination (A vs. B), open/short circuit (OC/SC) configuration of illuminated cell (B vs. C), different pump pulse energy (60 nJ/180nJ) (A vs. D). Supplement for Figure 3 (A-D).

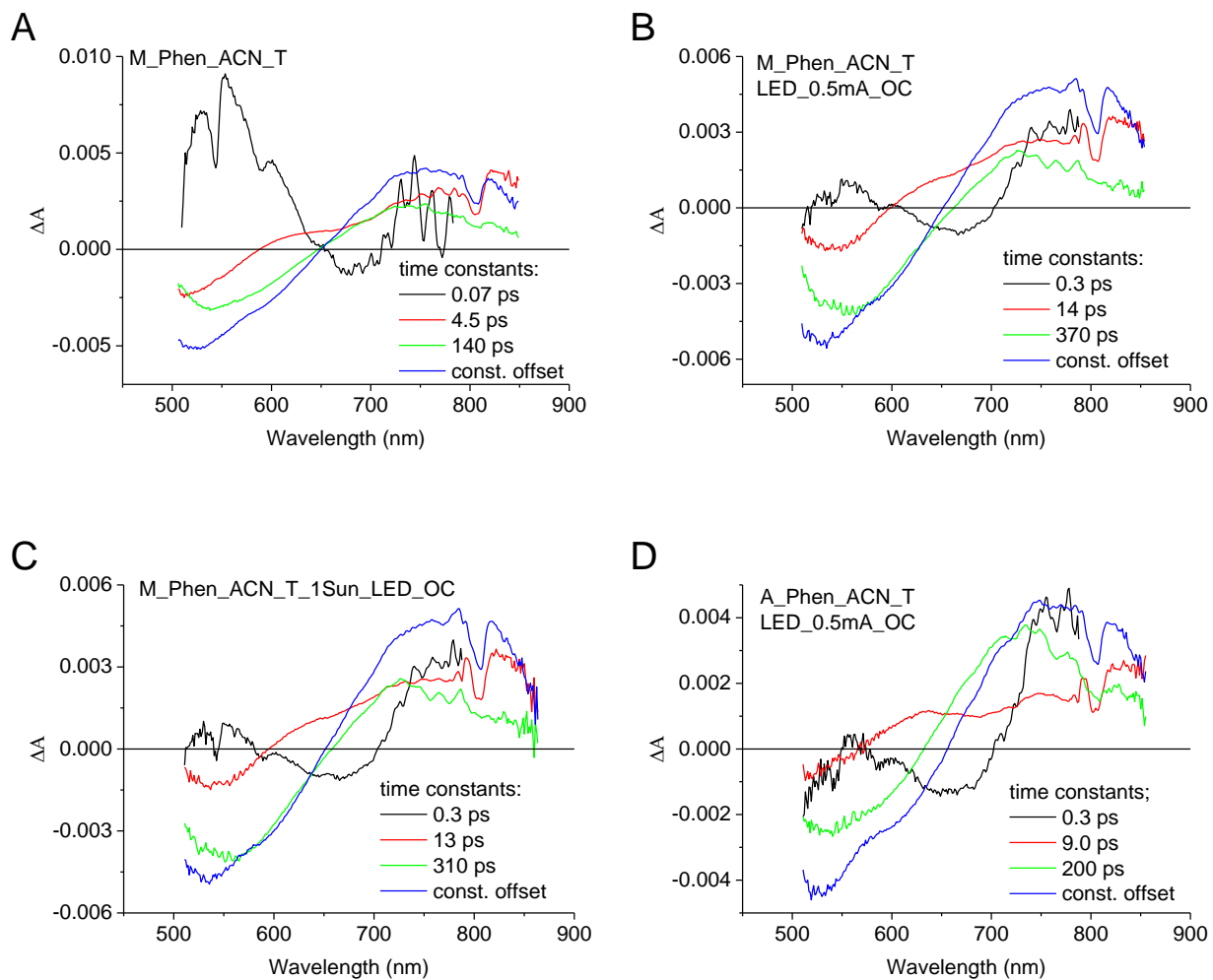


Figure S9. (A-C) - The effect of LED illumination on MK-2 sensitized cells assembled with ACN-based electrolyte (D) – ADEKA-1 sensitized cell illuminated with intermediate LED light intensity (0.5 mA vs. ~ 1.5 mA for 1 sun conditions). Measurements performed 20 days after cells assembly. Supplement for Figure 3 (E-F).

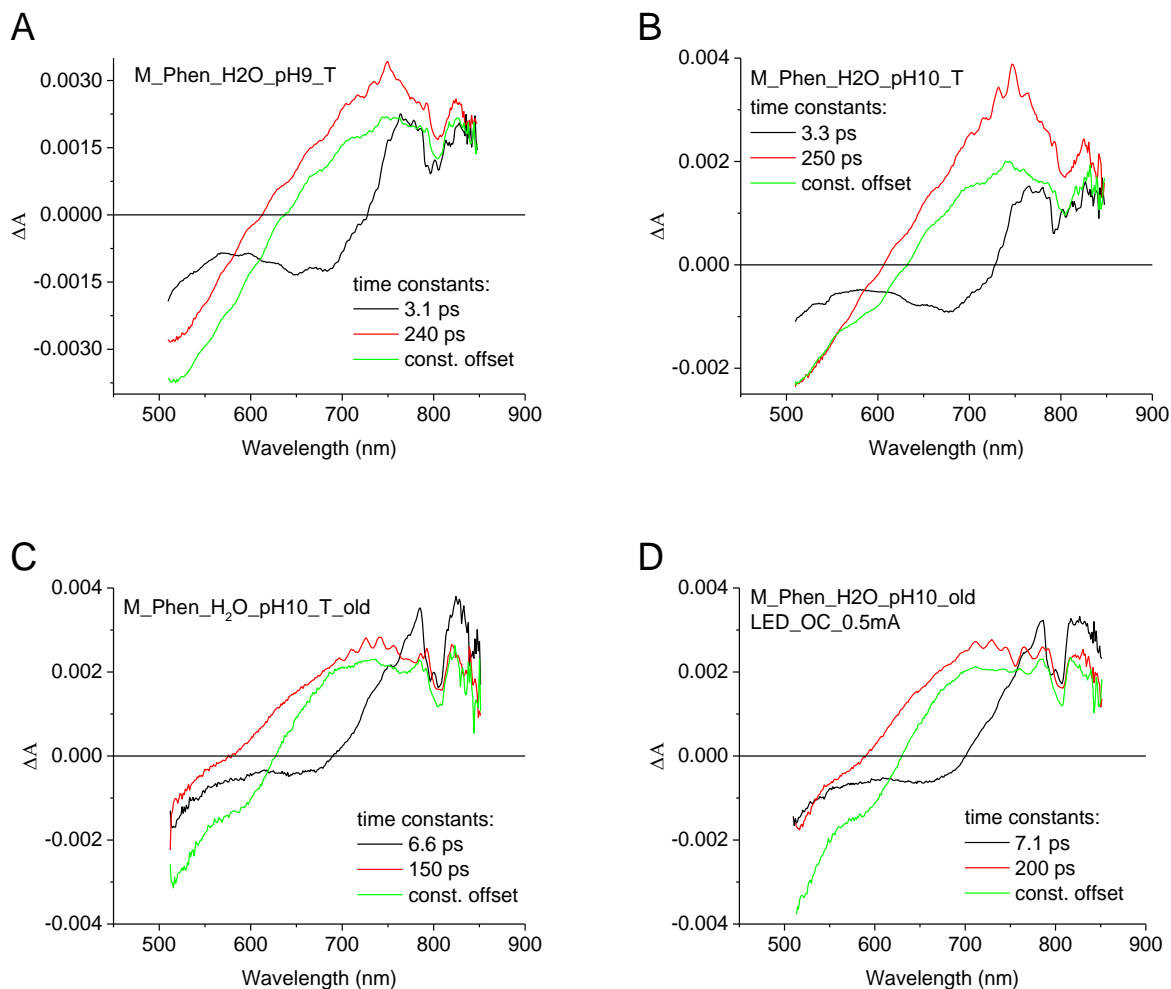


Figure S10. The effects of: assembly of MK-2-sensitized cells with H₂O-based Co-Phen electrolyte of different pH values (A vs. B), 20 days of ageing (B vs. C), of LED illumination (C vs. D). Supplement for Figure 4.

References

- 1 M. Gierszewski, A. Glinka, I. Grądzka, M. Jancelewicz and M. Ziółek, Effects of Post-Assembly Molecular and Atomic Passivation of Sensitized Titania Surface: Dynamics of Electron Transfer Measured from Femtoseconds to Seconds, *ACS Appl. Mater. Interfaces*, 2017, **9**, 17102–17114.
- 2 J. Sobuś, J. Karolczak, D. Komar, J. A. Anta and M. Ziółek, Transient states and the role of excited state self-quenching of indoline dyes in complete dye-sensitized solar cells, *Dye. Pigment.*, 2015, **113**, 692–701.

Paper III

**Testing New Concepts in Solar Cells Sensitized with Indoline Dyes—
Alkoxysilyl Anchoring Group, Molecular Capping, and Cobalt-
Based Electrolyte.**

Gierszewski, M.; **Glinka, A.**; Grądzka, I.; Gierczyk, B.; Ziółek, M.

J. Phys. Chem. C **2018**, *122*, 25764–25775.

Testing New Concepts in Solar Cells Sensitized with Indoline Dyes—Alkoxysilyl Anchoring Group, Molecular Capping, and Cobalt-Based Electrolyte

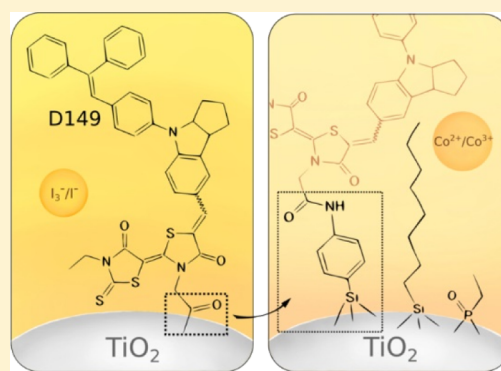
Mateusz Gierszewski,^{*,†} Adam Glinka,[†] Iwona Grądzka,[†] Błażej Gierczyk,[‡] and Marcin Ziółek^{*,†}

[†]Quantum Electronics Laboratory, Faculty of Physics, Adam Mickiewicz University in Poznań, Umultowska 85, 61-614 Poznań, Poland

[‡]Faculty of Chemistry, Adam Mickiewicz University in Poznań, Umultowska 89b, 61-614 Poznań, Poland

S Supporting Information

ABSTRACT: Basic photovoltaic parameters of the cells sensitized with a popular indoline D149 dye, containing the carboxyl anchoring group, were compared with those of the cells sensitized with the dye modified by the addition of the alkoxysilyl anchoring moiety. Desorption measurements of both compounds showed that the time constant of this process was longer for the modified dye. Two types of electrolytes were used, and the long-time stability and open-circuit voltage were significantly improved when the iodide electrolyte was replaced by the cobalt–bipyridine one. The dynamics of electron injection and titania–electrolyte recombination processes that occur in different time scales, from femtoseconds to seconds, were monitored by femtosecond transient absorption and electrochemical impedance spectroscopy. Additionally, the effect of molecular passivation by post-sensitization capping was checked. The cells after molecular capping showed better relative photocurrent and longer lifetime of the excited state, which was explained as resulting from the suppressed self-quenching of the dyes.



INTRODUCTION

The design of novel chemical dyes used for construction of dye-sensitized solar cell (DSSC) systems to improve the solar cell efficiency has been one of the most important challenges in recent years.^{1–6} Modification of the dye structure is accompanied by changes in the ligand structure, especially in ruthenium dyes, or a change in the anchoring groups that take part in the chemical bonds between the titania surface and dye molecules, including carboxyl, phosphonate, alkoxysilyl, or hydroxyl groups.^{7–12} Additionally, the design of metal-free dyes instead of the most popular ruthenium ones that would be attractive for DSSC application, is one of the most important steps in improving DSSC performance.^{13–15} On the other hand, the carboxyl group is the most popular anchoring moiety in organic dyes used for DSSC construction because of the relatively high solar cell efficiency.⁷ However, the long-time stability of solar cells working with the dyes with the carboxyl group is not satisfactory, especially in the presence of water-based or alkaline-containing electrolytes, because of the risk of hydrolysis of the dye from the titania surface.¹⁶ Recently, a series of organic dyes modified with the alkoxysilyl anchoring group, instead of the carboxyl one, has been proposed. It has been found that the replacement of the carbonyl group by the alkoxysilyl anchoring group improves the long-term stability of DSSC systems.^{13,17,18} The tridentate bonds created by Si–O–Ti, instead of the bidentate ones created by C–O–Ti linkage

to the titania surface, are relatively stronger.¹⁹ Alkoxysilyl anchoring also enables better post-sensitization passivation of the electrodes,^{13,20,21} which has recently led to champion DSSC efficiencies.^{13,17,18} Replacement of the carbonyl group by the triethoxysilane group in (dimethylamino)azobenzene derivatives has resulted in better performance of solar cells, including higher values of open-circuit voltage, and has restrained the electron recombination at the titania–electrolyte interface.¹⁹ It is especially important for the recently proposed Co-based electrolytes that are promising to improve the solar cell performance.^{15,22} In Co-based electrolytes, the blocking of the direct contact between the redox pair and the titania surface is necessary, which is realized, for example, by special photoanode treatments, including passivation by atomic layer deposition^{20,21,23,24} or the molecular-capping procedure.^{13,17,21}

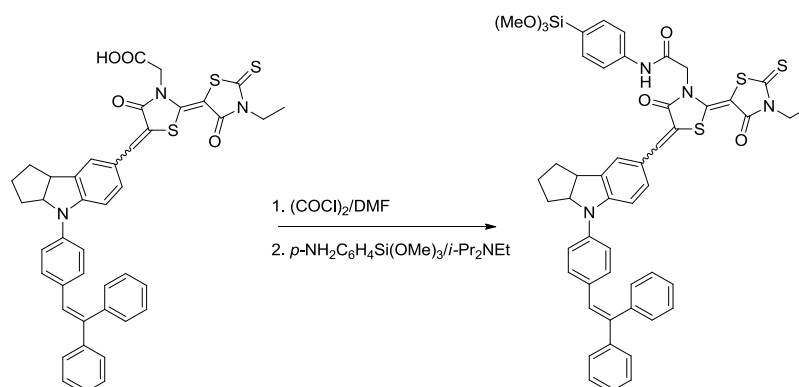
One of the first applications of D149 and other indoline dyes was proposed in 2004.²⁵ High-efficiency solar cells employing the D149 dye, with an iodide-based electrolyte and acetonitrile or ionic liquid as a solvent, were investigated as a function of the thickness of nanocrystalline titania film. The optimized thickness for the acetonitrile-based electrolyte was found to be 6.3 μm , which provided a solar cell efficiency of 6.67%.²⁶

Received: July 4, 2018

Revised: October 12, 2018

Published: October 21, 2018

Scheme 1. Synthesis Route Used for Conversion from D149 with a Carboxyl Group (Denoted as D149C in This Work) To Modified D149 with an Alkoxyethyl Anchoing Group (Denoted as D149Si)



Modification of the D149 structure by the *n*-octyl chain at the rhodanine ring and application of coadsorbent molecules such as chenodeoxycholic acid in different concentrations improved the solar cell efficiency.²⁷ Recently, for the cells made with indoline dyes, with a planar geometry and a high molar absorption coefficient adsorbed on the thin film of titanium dioxide, high power conversion efficiency values (up to 9.1%) were obtained depending on the alkyl chain length.²⁸ The cells with indoline dyes and Co(II/III)tris(1,10-phenanthroline)-based electrolyte (Co-phen) were studied with D-A- π -A indoline dyes (D—donor, A—acceptor part).²⁹ In that work, the basic photovoltaic parameters for the cobalt-based cells were lower than for the iodide-based ones. On the other hand, basic studies of D149 have also been widely reported. The dynamics of excited-state deactivation and electron injection efficiency of the D149 dye in organic solvents and attached to different semiconductors have been recently studied by different techniques.^{30–44} Moreover, systematic charge dynamics study of modifications of the D149 dye by anchoring alkyl chains of varying lengths have also been reported.^{45,46} Recently, time-resolved photoluminescence in combination with the electrical bias was used to study the charge-transfer (CT) process on solid-state solar cells sensitized with two indoline dyes (D131 and D149).⁴⁷

To the best of our knowledge, literature does not provide reports on systematic investigation of the dynamics of electron injection and electron recombination (and its correlation with photovoltaic properties) occurring on different time scales in dyes with the trimethoxysilyl anchoring group. We decided to perform the synthesis route described below using the popular indoline dye coded as D149, with its structure modified by the replacement of the anchoring group by the alkoxyethyl (trimethoxysilyl) one. We report for the first time such modification for the indoline class of chemical dyes. Application of two different types of electrolyte, based on iodide and tris(2,2'-bipyridine)cobalt(II/III) redox couple (Co-Bpy), provided information on the long-term stability of DSSC systems, both with carboxyl and alkoxyethyl groups. Our studies give the opportunity to better understand the dynamics of electron injection from the dye excited states to the conduction band of titania and further undesirable processes, including electron recombination at the titania–dye and titania–electrolyte interfaces. Additionally, we applied passivation of the titania surface by the molecular-capping post-treatment (after dye sensitization), which has been recently proposed for other metal-free organic dyes, to increase

the solar cell efficiency in the cobalt-based electrolyte because of charge recombination blocking.^{15,48} A comparison between the popular and well-known dye in the literature belonging to the indoline class of chemical compounds (D149) and its alkoxyethyl derivative may be important from the point of view of future modified dye performance in DSSC systems.

EXPERIMENTAL SECTION

Synthesis Route of D149Si. A solution of 50 mg of D149 dye (0.067 mmol) in dry deoxygenated chloroform (2 mL) was cooled to 5 °C. Then, 9.5 mg (0.075 mmol) of oxalyl chloride and 100 μ L of dimethylformamide were added. The mixture obtained was heated to room temperature and stirred for 2 h. Then, 14.3 mg of 4-(trimethoxysilyl)aniline (0.067 mmol) and 17.5 mg of diisopropylethylamine (0.135 mmol) were added. The purple-violet solution was stirred for the next 2 h, and the product was precipitated with anhydrous methanol. The obtained solid was separated by centrifugation, washed with methanol, and dried in vacuum. The product in the form of a dark violet powder was obtained in the amount of 45 mg (yield: 70%) (Scheme 1).

¹H NMR (CDCl₃, 298 K): δ 10.82 (br s, 1H, NH), 7.73 (s, 1H; SC=CHAr), 7.60 (m, 4H, ArH–Si), 7.32 (m, 13H, ArH), 7.04 (m, 4H, ArH & =CH), 6.95 (d, 1H, 1.4 Hz, ArH), 6.93 (d, 1H, 8.4 Hz, ArH), 4.90 (s, 2H, CH₂CON), 4.85 (m, 1H, N–CH), 4.06 (q, 2H, 7.2 Hz, CH₂CH₃), 3.83 (m, 1H, ArCH), 3.59 (s, 9H, SiOCH₃); 1.4–2.2 (m, 6H, CH₂), 1.17 (t, 3H, 7.2 Hz, CH₃).

Preparation of the Solar Cells. The photoanodes were prepared in a way similar to that described in our recently published articles.^{21,49} Generally, glass plates were cut out from the fluorine-doped tin oxide glass sheet (Sigma-Aldrich, 2.2 mm thickness, 13 Ω /sq) to a final size of 12 \times 17 mm². Next, they were cleaned using a commercially available dishwashing detergent, distilled water, and ethanol in an ultrasonic bath. Subsequently, one layer of mesoporous titania with 2–3 μ m thickness was deposited on the photoanode surface using the commercially available screen-printable transparent TiO₂ paste with 28–31 nm particles (DN-GPS-30TS, Dyenamo) and the screen printing technique (DN-HM02 screen-printer, Dyenamo, with a polyester screen of mesh count 250, Sefar). Finally, the hot plates were submerged in 50 mM aqueous solution of TiCl₄ for 30 min at 70 °C, rinsed with water, and again heated at 150 °C for 5 min, 300 °C for 5 min, and 450 °C for 30 min.

The glass plates with the mesoporous titania layer were immersed in the dye solutions for about 16 h to enable efficient

Table 1. Averaged Photovoltaic Parameters of the Studied Solar Cells: Open-Circuit Voltage (V_{OC}), Fill Factor (FF), Photocurrent Density (J_{SC}), Efficiency (Eff), Corrected Photocurrent Efficiency ($total_APCE$), Number of Absorbed Photons at 1 Sun Illumination (N_{ph}), and Absorption at 550 nm for Photoanodes without the Electrolyte (A_{550})^a

abbreviation	description	V_{OC} [V]	FF	J_{SC} [mA cm ⁻²]	Eff [%]	$total_APCE$	N_{ph} [1020 s ⁻¹ m ⁻²]	A_{550}
D149C_I	dye with carboxyl group, iodide electrolyte	0.72	0.68	3.8	1.9	0.30	7.9	1.5
D149C_I_MC1	dye with carboxyl group, iodide electrolyte, molecular-capping	0.68	0.66	4.0	1.8	0.38	6.6	0.92
D149Si_I	dye with silyl-anchor unit, iodide electrolyte	0.75	0.65	4.4	2.1	0.34	8.0	1.7
D149Si_I_MC1	dye with silyl-anchor unit, iodide electrolyte, molecular-capping	0.72	0.65	4.6	2.1	0.37	7.6	1.5
D149C_Co	dye with carboxyl group, Co-Bpy electrolyte	0.79	0.47	5.9	2.2	0.45	8.2	1.7
D149C_Co_MC2	dye with carboxyl group, Co-Bpy electrolyte, molecular-capping	0.78	0.46	5.4	2.0	0.45	7.6	1.3
D149Si_Co	dye with silyl-anchor unit, Co-Bpy electrolyte	0.79	0.57	5.0	2.2	0.36	8.6	2.1
D149Si_Co_MC2	dye with silyl-anchor unit, Co-Bpy electrolyte, molecular-capping	0.78	0.49	5.3	2.0	0.42	7.9	1.5

^aThe parameters were averaged after 1 h and 1 day measurements (for iodide cells) and after 1 h, 1 day, and 6 days (for more stable Co-based cells).

adsorption of the dyes. Two indoline compounds were used to sensitize the photoanodes: the first, D149 (Aldrich) commercial dye with a carboxyl group, and the second, modified D149 obtained by the synthesis route described above with a silyl anchoring group. The solutions of both dyes used for sensitization were dissolved in the 1:1 mixture of acetonitrile and *tert*-butanol. The dye structures are shown in Scheme 1.

Similarly, the counter electrodes were prepared according to the procedure described in our recently published articles.^{21,49} One layer of activated platinum (Platisol T, Solaronix) was deposited on the cleaned surface of the electrodes. The photoanodes and counter electrodes were joined through a polymer seal (25 μ m Surlyn, Meltronix, Solaronix SA) with the conducting surfaces facing inward. Afterward, the devices were filled with the electrolyte through 1 mm holes in the counter electrode and sealed with the cover glass on the top.

Two types of electrolytes were used for cell preparation. The first of them was the cobalt-based electrolyte made of the following components: 0.25 M Co(bpy)₃(TFSI)₂, 0.035 M Co(bpy)₃(TFSI)₃, 0.1 M LiTFSI, and 0.5 M *tert*-butylpyridine (TBP) dissolved in acetonitrile. The redox couple was cobalt-bipyridine complex (Co-Bpy). The second one was the iodide electrolyte made of the following components: 0.08 M I₂, 0.6 M 1,2-dimethyl-3-propylimidazolium iodide, 0.1 M LiI, 0.1 M guanidine thiocyanate, and 0.5 M TBP dissolved in acetonitrile.

Molecular-Capping Procedure and Dye Desorption

Tests. After the dye adsorption on the titania surface, molecular passivation by the hierarchical molecular capping was performed for the selected photoanodes. The cells after molecular-capping treatment were coded as MC1 and MC2. The procedure of molecular-capping treatment was similar to that used recently by us for carbazole dyes.²¹ The treatment was performed just after taking the photoanodes out of the dye solution and immediately before sealing the cells. The electrodes were dipped in the appropriate solutions and then rinsed with acetonitrile. In the first molecular-capping procedure (MC1), ethylphosphonic acid solution (EPA, 10⁻³ M, 1 or 3 min) in a 1:1 mixture of acetonitrile/toluene was used. It was applied for the cells with the iodide electrolyte. For the cells with Co-Bpy electrolyte, the second molecular-capping procedure was applied (MC2), in which we used the

following solutions with their concentration and immersion time: *n*-octadecyl succinic acid (ODSA, 10⁻³ M, 1 min), isoocetyltrimethoxysilane (OTMS, 10⁻² M, 1 min), and octylphosphonic acid (OPA, 10⁻³ M, 1 min). The solutions were dissolved in a 1:1 mixture of acetonitrile/*tert*-butanol. The cells' symbols are included in Table 1. The symbols D149C and D149Si mean the D149 dye with a carboxyl or trimethoxysilyl group, respectively, "I" describes the iodide/triiodide redox couple electrolyte, and "Co" stands for the Co-Bpy electrolyte. "MC1" or "MC2" stand for the molecular-capping post-treatment procedure.

We used the 1:9 mixture of water/acetonitrile at room temperature or the 1:1 mixture of dimethyl sulfoxide (DMSO)/water at 85 °C to perform the desorption reaction from the titania surface of both dyes under the same conditions. Additional experiment was carried out using pure distilled water, however, both dyes were stable in the experimental conditions for a few days. Desorption process was monitored by steady-state absorption spectroscopy.

Cell Characterization. A UV-vis-NIR JASCO V-770 spectrophotometer equipped with a 150 mm integrating sphere (LN-925) was used to measure the stationary absorption spectra in the ultraviolet-visible (UV-vis) range. The samples were mounted in front of the integrating sphere to detect both transmitted and scattered light. Absorption spectra were recorded in the spectral range from 400 to 800 nm with a UV-vis bandwidth of 1 nm. The baselines for the unsensitized TiO₂ electrodes were measured and subtracted from the absorption spectra of the photoanodes sensitized by the dyes. Current-voltage measurements and IPCE (incident photon-to-current efficiency) spectra for the studied solar cells were recorded using a potentiostat (model M101 with a frequency response analyzer FRA32M module, Autolab) coupled to a photoelectric spectrometer equipped with a solar simulator (Photon Institute, Poland). Current-voltage measurements were usually made 1 h and 1 day after cell preparation; however, for the cells with the Co-Bpy electrolyte, the measurements were also repeated on the 6th day, 17th day, and 1 month after preparation. The Xe lamp with an AM 1.5 G spectral filter and irradiance adjusted to 100 mW/cm² using a calibrated cell (15151, ABET) mimicked the sunlight conditions. Electrochemical impedance spectroscopy (EIS) measurements were performed using the abovementioned

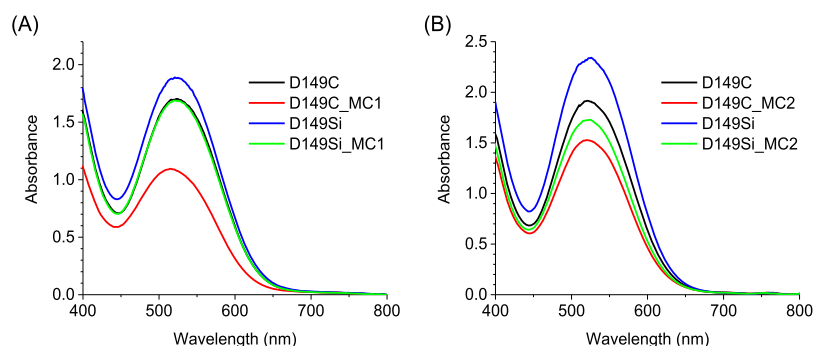


Figure 1. Stationary absorption of selected sensitized films by the D149 dye with the carboxyl or silyl anchor group with TiO₂ contribution subtracted; photoanodes used for the cells with iodide (A) and Co-Bpy (B) electrolyte. Absorption spectra were measured without the electrolyte.

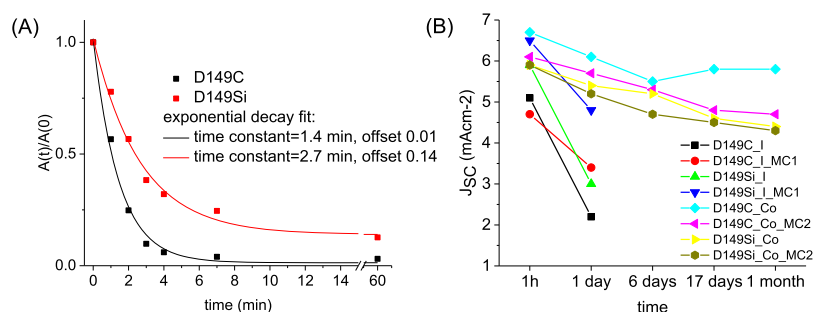


Figure 2. (A) Dependence of relative absorbance $A(t)/A(0)$ vs time t for D149C and D149Si electrodes immersed in the water environment, based on the data presented in Figure S1. (B) Plot of photocurrent density (J_{SC}) vs time after cell preparation for all configurations.

potentiostat. The typical equivalent circuit for the DSSC system with a transmission line element was used in all cases, and ZView software was employed to analyze the obtained curves typically in a Nyquist plot representation.^{50,51} The same complete solar cells as those for current–voltage and impedance measurements were used for the transient absorption studies. Transient absorption system has been described recently with more details (HELIOS spectrometer, Ultrafast Systems, and Spectra-Physics laser system).⁵² The laser pulses were set up at 550 nm and the instrument response function (IRF) (pump–probe cross correlation function) duration was about 200 fs (full width at half-maximum). The pump pulse energy was set to 50, 200, or 800 nJ, which corresponds to the energy density of 25, 100, or 400 $\mu\text{J cm}^{-2}$, respectively. The transient absorption measurements were analyzed using Surface Explorer software (Ultrafast Systems), including the global analysis. The program allowed fitting a multiexponential function (convoluted with IRF) to the kinetic vectors of a selected number of singular values. Finally, the characteristic time constants and the wavelength-dependent amplitudes associated with them were obtained.

RESULTS AND DISCUSSION

Stationary Absorption. Figure 1 shows the absorption spectra of photoanodes sensitized by the D149 dye with the carboxyl (D149C) and alkoxy-silyl (D149Si) anchoring groups. Table 1 summarizes the values of absorbance at 550 nm, as this wavelength was used for the excitation of complete cells in femtosecond transient absorption spectroscopy measurements. Table S1 shows the absorption maxima and the values of absorbance at a maximum wavelength for photoanodes at each configuration (without the electrolyte). Slightly higher absorbance for D149Si than for D149C is obtained, suggesting greater amount of adsorbed dye molecules, which might be

explained by the different anchoring unit (stronger and more flexible for D149Si). The absorption maximum is shifted to the red by 2–5 nm for D149Si with respect to that for D149C.

A significant decrease in the absorbance after molecular capping is observed because of the partial desorption during post-sensitization immersion in capping solutions. After molecular-capping passivation, a shift of the absorption maximum to shorter wavelengths is observed for both molecular-capping procedures (MC1 with EPA solution and MC2 with the solution of ODSA, OTMS, and OPA, which are less acidic than EPA). For example, absorption maximum for D149Si changes from 525 to 518 nm after 3 min molecular capping in EPA (Table S1). The effect of molecular capping is more pronounced for D149 with carboxyl than with the alkoxy-silyl anchoring group, when the same immersion solutions and experimental conditions are applied, for example, the absorbance values changed by 35% for D149C and by 12% for D149Si after molecular capping with EPA (MC1). As expected, the application of molecular-capping post-treatment with less acidic molecules (MC2) shows less pronounced absorption changes than in the molecular capping with EPA. The shifts of the position of the maximum absorption wavelength to shorter wavelengths and desorption of the dye molecules from the titania surface (manifested as decreased absorbance) are similar to those observed by us for ADEKA-1 and MK-2 dyes after molecular-capping passivation.²¹ It might be rationalized by the increased protonation of the titania surface (especially important when EPA solution was used) or the reduced aggregation of the dye molecules (absorption blue shift was also observed for D149 with increasing coadsorbent concentration).^{35,38,53}

The absorption spectra are also necessary for the interpretation of photovoltaic results because they were used for calculations of the number of absorbed photons (N_{ph}) and

the relative photocurrent (discussed below). The values of N_{ph} were obtained from the integration of the stationary absorbance spectrum multiplied by the photon flux spectrum from AM 1.5G and are also presented in Tables 1 and S1.

Desorption Tests. To test the chemical stability of D149 dyes attached to the titania surface, desorption tests were performed (Figures S1 and 2A). The photoanodes sensitized with D149C or D149Si dye were immersed in a mixture of 9:1 acetonitrile/water, and the absorption spectra were measured after 1 min, 2 min, 3 min, 4 min, 7 min, and 1 h. The results of absorption measurements were fitted to the monoexponential function with the characteristic decay times of 1.4 and 2.7 min for D149C and D149Si, respectively (Figure 2A). The results of the fit confirmed the difference in the bond strength between the carboxyl and alkoxyisyl groups anchoring to the titania surface and the observed lower stability of D149C than D149Si upon molecular-capping passivation. Additionally, desorption tests were performed for the photoanodes sensitized with both D149 derivatives using a mixture of DMSO/water 1:1 at 85 °C (data not shown). When using the photoanode sensitized with D149C, after 5 min of immersion, over 98% of the dye molecules underwent desorption from the titanium oxide surface, whereas in the same time, for D149Si, only 60% of the dye was desorbed. Finally, the photoanodes sensitized with D149Si and D149C were immersed in pure, distilled water for 5 days, and no changes in the absorption spectra were observed after this immersion time (data not shown). This interesting effect might be explained by the lack of wetting of the photoanodes sensitized by the dyes that are not water soluble. Thus, although water has a destructive effect, the presence of another solvent, such as acetonitrile or DMSO, is necessary to allow water to penetrate to the dye–titania interface. Therefore, we think that water is responsible for the hydrolysis of chemical bonds between the anchoring moiety and the titania surface, and the presence of an organic solvent, such as acetonitrile, is necessary to dissolve the detached dye.

Photovoltaic Parameters. Table 1 summarizes the averaged values of basic photovoltaic parameters measured for the studied solar cells, including the open-circuit voltage (V_{OC}), fill factor (FF), photocurrent density (J_{SC}), and efficiency (Eff). Measurements of the current–voltage curves of the cells with the iodide electrolyte were performed for each cell twice: 1 h and 1 day after preparation, and the final values were the averages from three different cells of each configuration. For the cells with the cobalt electrolyte, because of their better stability (discussed below), current–voltage curve for each cell was measured 3 times: 1 h, 1 day, and 6 days after preparation. Table S1 summarizes the photovoltaic parameters of the best solar cells (taking into account J_{SC}) of each configuration. Table S2 includes the values of the relative error of the averaged photovoltaic parameters given in Table 1. Both Tables 1 and S1 include the parameter representing the relative photocurrent and called the $total_APCE$ ($APCE = \text{absorbed photons per current efficiency}$), which is defined as $total_APCE = J_{\text{SC}}/eN_{\text{ph}}$, where e is the elementary charge. As the number of molecules of adsorbed dyes on the titania surface is different, this parameter allows us to compare the efficiency of charge separation between the cells. Moreover, for the best cells with the cobalt-based electrolyte, the IPCE spectra were also measured. The maxima of IPCE spectra (in the spectral region of photoanode absorbance >1) was 30–40%, which was in line with the values of $total_APCE$

parameters. The normalized IPCE spectra are presented in Figure S2, and they show a slight blue shift for the samples after molecular capping, in agreement with the absorption spectra.

Generally, the values of solar cell efficiency of our cells are relatively low compared to those of the champion DSSCs sensitized with the D149C dye (about 9% at a titania thickness of 12.6 μm).²⁶ The main reasons are the small thickness of the mesoporous titania layer (about 2–3 μm) and the lack of scattering nanoparticles layer in our cells, which should be transparent enough for transient absorption measurements. Moreover, for more clear comparison of the two dyes, we prepared our cells without addition of coadsorbent molecules, which typically improves the efficiency of indoline DSSCs.

First, the consequence of replacement of the anchoring carboxyl with the alkoxyisyl group will be discussed. The cells obtained with the use of D149 containing alkoxyisyl anchoring groups are characterized by higher solar cell efficiency than those with the carboxyl anchor in the iodide electrolyte, whereas it is the same in the cobalt-based electrolyte (Table 1). On the other hand, the relative photocurrent ($total_APCE$ parameter) is usually slightly lower for D149Si than for D149C cells. It can be explained by the slightly higher absorbance of D149Si photoanodes and thus possibly more negative effect of aggregation on the charge separation efficiency.³⁸

Another experimental factor that influences the photovoltaic parameters is the type of electrolyte used for the preparation of solar cells: iodide (I) or cobalt-based (Co). Generally, better values of V_{OC} were found for the cobalt-based cells than for the ones with the iodide electrolyte (e.g., D149Si_I: 0.75 V and D149Si_Co: 0.79 V). Similarly, the application of the cobalt-based electrolyte instead of the iodide one improves J_{SC} (e.g., D149Si_I: 4.4 mA cm^{-2} and D149Si_Co: 5.0 mA cm^{-2}), solar efficiency (e.g., D149C_I: 1.9% and D149C_Co: 2.2%), and $total_APCE$ (e.g., D149C_I: 0.30 and D149C_Co: 0.45). In contrast, the FF parameter is significantly worse in cells with the cobalt-based electrolyte than in those with the iodide one (e.g., D149C_I: 0.68 and D149C_Co: 0.47).

The third factor that influenced the fabricated cells performance is molecular-capping post-treatment. Molecular-capping post-treatment decreases the values of V_{OC} and FF parameter (e.g., D149C_I: 0.72 V and 0.68 with respect to D149C_I_MC1: 0.68 V and 0.66, respectively). The values of solar cell efficiency are slightly lower after molecular-capping post-treatment, irrespective of the type of electrolyte. It is mainly due to lower absorption caused by the partial desorption of the dyes after molecular capping. However, the higher values of $total_APCE$ for D149Si are obtained after molecular-capping (e.g., D149Si_I: 0.34 vs D149Si_I_MC1: 0.37 or D149Si_Co: 0.36 vs D149Si_Co_MC2: 0.42). The improvement of the relative photocurrent suggests that the efficiency of charge separation is increased after capping.

Solar Cell Stability. Additionally, the long-time stability test of the prepared solar cells was performed. Application of molecular capping and Co-based electrolyte instead of iodide improved the stability. Figure 2B shows the plot of photocurrent density (J_{SC}) vs time after cell preparation, for all studied configurations. One day after cell preparation, the photocurrent density of D149C_I decreased by $\sim 57\%$, but at the same time for D149C_Co, the change in J_{SC} was clearly smaller (about 9%). Recalling, molecular capping significantly affects the long-term stability. Generally, for most of the cells, 1 day after their preparation, the photocurrent density decrease

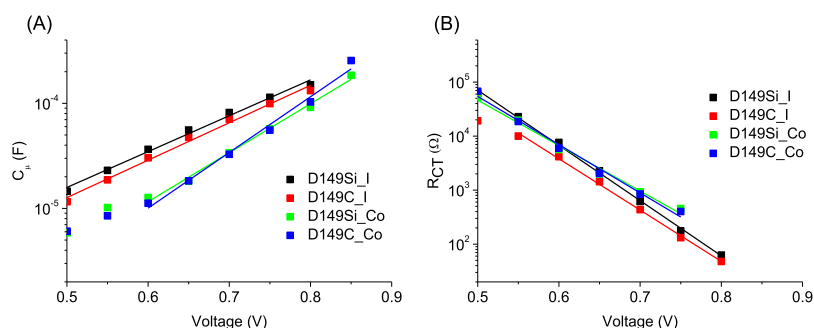


Figure 3. Plots of (A) chemical capacitance (C_{μ}) and (B) CT resistance (R_{CT}) vs applied bias obtained from the equivalent circuit fits to impedance spectroscopy results for selected cells. The results for the other configurations are in the Supporting Information (Figure S3).

was smaller when the molecular-capping post-treatment was applied (D149C_I: $\sim 57\%$ vs D149C_I_MC1: $\sim 28\%$ and D149C_Co: $\sim 9\%$ vs D149C_Co_MC2: $\sim 7\%$). Interestingly, the decrease in the solar cell performance is independent of the anchoring unit (similar for D149C and D149Si), despite slower desorption observed for the D149Si dye (e.g. Figure 2A). This means that cell degradation is rather not related to dye desorption, but other factors (e.g., change in the relative energetic position between the dye excited state and the TiO₂ valence band upon time) are responsible for this effect.

Electrochemical Impedance. EIS measurements were performed for the cells in all configurations in 2–3 h and 1 day after preparation. The results extracted from the Nyquist plots, such as the chemical capacitance at the TiO₂/electrolyte contact (C_{μ}) and the charge-transfer resistance at this interface (R_{CT}), were averaged from these two measurements. The impedance measurements were performed in the dark in 50 mV increments, starting from 400 mV and finishing slightly above the V_{OC} characteristic of each cell. The obtained results were analyzed using the ZView software for an equivalent circuit, with a transmission line typical of DSSC systems shown in Figure S3A. The examples of the Nyquist plots for different cells sensitized with D149 in selected configurations are included in Figure S4. The C_{μ} and R_{CT} data are presented in semilog plots as a function of the applied bias voltage and included in Figure 3 (cells without molecular-capping passivation) and Figure S3 (cells with molecular-capping post-treatment). Moreover, in Figures S5 and S6, the effect of molecular capping, for the same type of electrolyte, is illustrated.

The processes studied in EIS occurred in the time scale from milliseconds to seconds and may be helpful in the explanation of the variation in V_{OC} and FF values obtained from photovoltaic measurements of the cells. The shift in C_{μ} values is correlated with a relative shift of the titania conduction band with respect to the potential of the redox couple. Certain parameters or conditions of the process of solar cell preparation caused a down shift of the titania conduction band. First, the application of the Co–Bpy electrolyte instead of iodide (D149Si_I and D149C_I vs D149Si_Co and D149C_Co) causes an increase in the relative potential by about 100 mV, both for the samples with and without molecular capping (Figures 3A and S3B). On the other hand, only a slight down shift of the titania conduction band was observed for D149Si with respect to that observed for the D149C in the same type of electrolyte (Figures 3A and S3B). Irrespective of the type of electrolyte (iodide or Co–Bpy) and dye (D149C or D149Si), the molecular capping slightly shifts

down the position of the titania conduction band (Figures S5 and S6).

Moreover, the samples give the satisfactory linear fits of the semilog plots of C_{μ} vs the applied bias voltage. The slope of the above plots was used as a parameter, denoted as α , suitable for comparing distributions of the trap states below the conduction band.^{50,51} The values of this parameter are collected in Table S4, and they are significantly lower in the iodide cells (0.18–0.21) than those for the Co–Bpy cells (0.28–0.31). Our previous results with the same titania paste and photoanode preparation gave α of about 0.20 for the cells sensitized with the N719 dye in the iodide electrolyte⁴⁹ and α of about 0.24 for those sensitized with carbazole dyes in the Co–Bpy electrolyte.²¹ Thus, the presented results indicate that narrower distribution of the trap states in the Co–Bpy electrolyte than in the iodide one might be a more universal feature. It should also be pointed out that the changes in the type of anchoring group or the molecular-capping application have only a slight influence on the values of parameter α .

The second important parameter that can be extracted from EIS measurements is the charge-transfer resistance (R_{CT}). The results of R_{CT} vs the applied bias voltage of selected configurations are presented in Figures 3, S3C, S5B, and S6B. Analysis of the results presented in Figures 3B and S3C shows that the values of R_{CT} for the iodide electrolyte are slightly lower than those obtained for the Co–Bpy-based cells. Additionally, slightly lower values of R_{CT} were found for D149C than for D149Si in the same type of electrolyte. Further, the application of molecular-capping post-treatment led to significantly lower values of R_{CT} , irrespective of the electrolyte used (Figures S5B and S6B). For most samples, satisfactory linear fits of R_{CT} versus the applied bias voltage enable the extraction of the cells ideality parameter m (Figure S5). The values of parameter m are similar for all cells and vary between 1.8 and 2.2. Therefore, EIS measurements in the dark do not explain lower FF values for the Co–Bpy cells than those obtained for the iodide ones (Table 1), so a decrease in charge transport efficiency at high applied voltages in Co–Bpy cells must occur because of irradiation.

To further analyze the difference between the iodide and Co–Bpy electrolytes, we extracted three other parameters from the Nyquist plots. The results of the averaged values of the Warburg resistance, the counter electrode/electrolyte interface resistance, and the transport resistance for the different cells fabricated are shown and commented in detail in Figure S7. Similarly to our recent results obtained for the N719 dye,⁴⁹ all of the above resistances are higher for Co-based cells than for those with the iodide redox couple. It confirms the universal

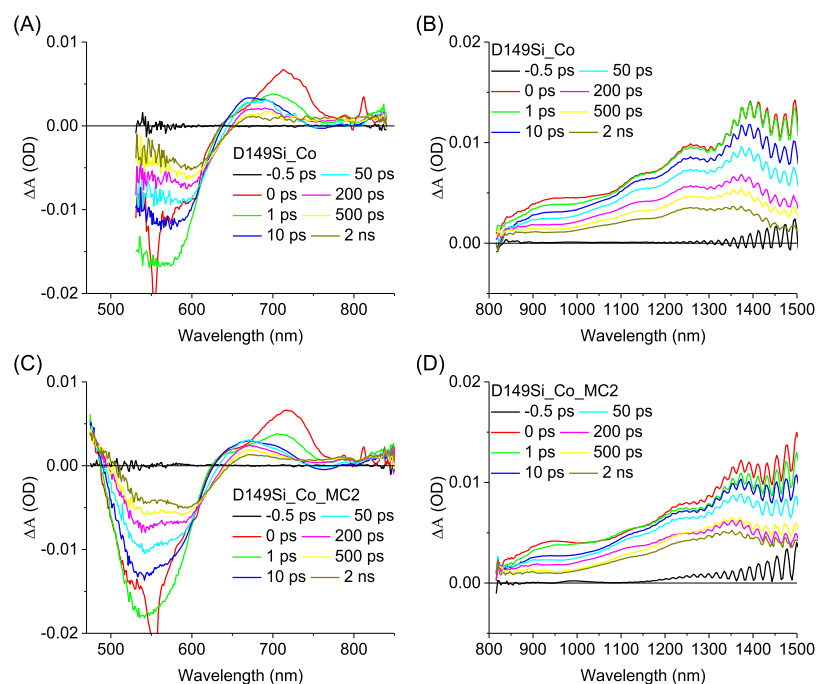


Figure 4. Exemplary transient absorption spectra for selected delay times between pump and probe pulses for D149Si_Co and D149Si_Co_MC2 in vis (A,C) and NIR (B,D) ranges. The results for other samples are presented in the Supporting Information (Figure S8).

feature and suggests that for both ruthenium and metal-free dyes, when the Co–Bpy electrolyte is used, the electron transport through titania nanoparticles, redox pair diffusion, and regeneration at the counter electrodes are slowed down, which can explain the lower FF values under 1 Sun conditions.

Transient Absorption: Spectra and Kinetics. Femto-second transient absorption measurements were performed for the cells with the cobalt-based electrolyte (showing higher stability) under excitation at 550 nm in a 3 ns time window in two spectral ranges in separate experiments: 480–840 nm (vis) and 800–1500 nm [near-infrared (NIR)]. The representative transient absorption spectra for selected delay times between pump and probe pulses both in vis and NIR ranges and the selected cell configuration are presented for D149Si_Co and D149Si_Co_MC2 in Figure 4 and for D149C_Co and D149C_Co_MC2 in Figure S8 (including exemplary two-dimensional representation of the transient data).

The residual spectrum (at long time delays) shows positive transient absorption at 670 nm (in the vis range) and at 1300–1400 nm (in the NIR range). These bands have been identified as characteristic of the free radical cation of D149.³² Additionally, some contribution in the NIR range might also be due to the band with a maximum at 1100 nm assigned to the bound radical cation–electron complex (intermediate state, living at least longer than the temporal window 3 ns of the experiment), on the basis of the transient absorption results of indoline dyes on the reference Al₂O₃ films^{38,54} and on ZnO films⁴⁶ (also called the ionic CT state). The negative signals contributing to the residual transient absorption spectra are related to the depopulation of the ground state of the dye (localized below 600 nm) and the negative part of the transient Stark shift (the signal originating from the electric field of injected electrons in titania and observed in the range 600–650 nm in previous studies of the D149 dye).^{32,36} The concentration of radical cations is proportional to the number of injected and successfully separated electrons in titania.

Therefore, the amplitude of the residual signal (at 3 ns) can be considered as a measure of efficiency of charge separation. This efficiency can be lowered as a result of self-quenching of the excited states (before electron injection) and back electron transfer in the bound complex of the radical cation and electron in titania (after electron injection).^{38,54} Figures S9 and S10 show the exemplary kinetics in the NIR range for different pump pulse intensities (50, 200, and 800 nJ). They confirm the faster decay of the signal and the smaller amplitude of residual transient absorption with increasing population of the excited state of the dye, which can be explained by the self-quenching effect.³⁸ Table 2 shows the residual signals at 1300 nm (band of free radical cation) for different cells measured upon 200 nJ excitation (from Figures S9 and S10).

Table 2. Averaged Time Constants (τ_1 and τ_2) Based on the of Global Analysis (Two-Exponential with a Constant Offset) of Transient Absorption Data in the NIR Range under 200 nJ Pump Pulse Intensity and the Amplitude of the Normalized Residual Signal of Transient Absorption Kinetics at 1300 nm (S_{res} , Ratio of the Amplitude after 3 ns to the Initial One) for the Selected Cells with the Co-Based Electrolyte

cell	τ_1 (NIR), ps	τ_2 (NIR), ps	S_{res} (1300 nm)
D149C_Co	7.2	190	0.37
D149C_Co_MC2	9.7	240	0.40
D149Si_Co	7.7	220	0.36
D149Si_Co_MC2	7.3	240	0.43

Transient Absorption: Global Analysis. To find detail information on the dynamics of excited state deactivation and electron injection, global analysis of the transient absorption spectra was applied. A three-exponential function plus a constant offset were applied to fit the experimental data and provide sufficient fit quality and low residuals (Figures 5 and

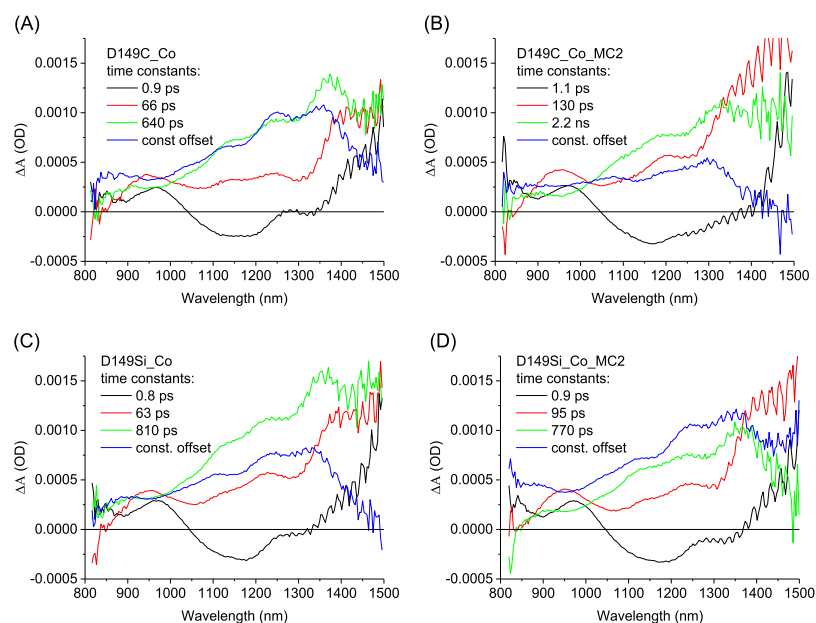


Figure 5. Wavelength-dependent amplitudes of the indicated time constants obtained from the global analysis (three-exponential with a constant offset) of transient absorption spectra for DSSCs with the D149 dye with carboxyl and silyl anchor groups and Co–Bpy electrolyte in the NIR spectral range for low energy (50 nJ).

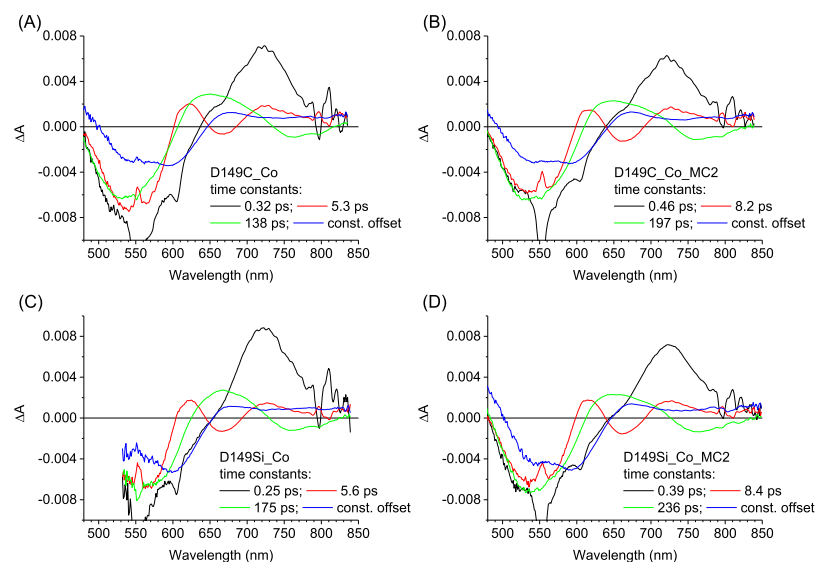


Figure 6. Wavelength-dependent amplitudes of the indicated time constants obtained from global analysis (three-exponential with constant offset) of transient absorption spectra for DSSCs with D149 dye with the carboxyl and silyl anchor groups and Co–Bpy electrolyte in the vis spectral range for high energy (200 nJ).

6). The positive amplitudes in the spectra of a given time constant represent the decay, whereas the negative amplitudes represent a rise of the transient absorption signal. Additionally, in the NIR range, the effect of different pump pulse intensities was studied (Figures S11 and S12). The interpretation of the spectra evolution follows from the previous assignments reported in our works about D149^{36–38} and a similar D358 dye.⁵⁴ The initial, short-living excited (Franck-Condon, FC) state was reported to have the transient absorption maximum around 720 nm, while the subsequent CT state shows a transient absorption maximum around 600 nm, the same for D149 in solution and on TiO₂ nanoparticles.^{38,54} Moreover, FC and CT states also give strong transient absorption signals in the NIR range (at least up to 1500 nm).³⁸ Therefore, the

direct detection of injected electrons in titania is not possible in the studied spectral range (probably further mid-IR range is required),⁴⁶ and we cannot separate the injection contribution from FC, hot CT, and relaxed CT states (the measured dynamics of the decay of all excited states can contain the contribution of both electron injection and internal deactivation), as is depicted in Scheme S1. However, the ratio of the residual signal (assigned to the radical cation) to the initial signal (due to FC state, so proportional to the population of excited dyes) can still be used to monitor the final charge separation efficiency (irrespective of from which state the electron injection occurs).

The fastest component in our global fit, having the amplitude spectrum with the maximum of positive part around

720 nm, is associated with the decay of the initially excited (FC) state.⁵⁴ It is characteristic that after the multicapping procedure, the time constant values increase for the D149 dye with both carboxylic and silyl anchoring moieties (e.g., D149C_Co: 0.32 ps vs D149C_Co_MC2: 0.46 ps and D149Si_Co: 0.25 ps vs D149Si_Co_MC2: 0.39 ps in Figure 6). A similar increase in the fastest component in the molecularly capped cells can also be observed in the NIR range (Figure 5). For the smallest pump pulse energy (50 nJ), a negative amplitude (rise of the signal due to the change from FC to CT state) can be observed in the range 1050–1250 nm, in line with the kinetics in Figures S9 and S10. When the global fit is narrowed to this range (data not shown), even clearer differences in the fastest components can be observed between the samples, with shorter time constants of 0.7 and 0.6 ps for D149C_Co and D149Si_Co, respectively, and significantly longer ones, 1.0 and 1.1 ps for D149C_Co_MC2 and D149Si_Co_MC2, respectively. The observed rise can be explained by higher absorption coefficients for the CT state and/or radical cation than that of FC state in the 1050–1250 nm range. For higher pump intensities, the rise is not observed (Figures S9 and S10) and only an indentation in the amplitude spectra is present (Figures S11 and S12), probably because of fast decay components of the CT state (due to self-quenching at high intensities) or cation radical disappearance (due to enhanced recombination at high intensities).

Further, the second and third components, with maxima of the amplitude spectra localized at 600–650 nm in vis and above 1400 nm in NIR, are associated with the decay of the CT state of D149 dye with simultaneous partial generation of population of the radical cation (Figures 5 and 6). The second component in the vis range has a negative amplitude around 680 nm and the third one (the longest) at around 770 nm. It can be attributed to the transient absorption rise due to the higher extinction coefficient of the radical cation than that of the CT state for these wavelengths.³⁸ Moreover, the negative amplitude might also originate from the decay of the stimulated emission (present for the CT state but absent for the radical cation), and its red shift with time indicates the contribution of a more relaxed CT state (emission shifted to longer wavelengths). It agrees with the fluorescence maximum of the D149 dye in acetonitrile solution at 664 nm,⁵⁵ taking into account that the stimulated emission is red-shifted with respect to the fluorescence spectra (scaling factor λ^4).⁵⁶ Moreover, we observed the negative signal of stimulated emission of D149 in solution extending up to 850 nm and the CT state relaxation taking place on the time scale of 2–40 ps because of the solvation process.^{38,54} Thus, the negative amplitude at around 680 nm in the second component is due to the stimulated emission and cation generation from the hot CT state dye, whereas the negative amplitude obtained in the third component around 770 nm is mainly related to the stimulated emission and cation generation from the relaxed CT states. It should be noted that we have observed previously the fluorescence decay time constants for D149/TiO₂ cells extending up to hundreds of picoseconds.³⁸ As for the NIR region, the spectra of the second and third components are similar to each other (Figure 5), probably because of less difference between the spectra of hot and relaxed CT states in this range. Table 2 summarizes the values of the time constants of the CT state decay averaged from several measurements in the NIR range at the pump pulse intensity of 200 nJ.

Similarly, as for the fastest component (of the FC state), global analysis of the transient absorption in vis and NIR shows that significant differences can be observed between the CT state dynamics of the samples with and without multicapping post-treatment. For the molecularly capped cells with either of the dyes, the fitted time constants of the CT state decay are on average 1.5 ± 0.2 times longer than those for samples without molecular capping (Figure 5 and Table 2 in NIR and Figure 6 in vis). It means that application of the molecular-capping post-treatment slows down the decay of both FC and CT states. Within the experimental error, no differences in the excited state dynamics can be observed between the dyes with the alkoxy-silyl and carboxyl anchoring moieties. An increase in the excited states lifetimes might be either a consequence of slower electron injection (generally decreasing the solar cell performance) or a slower self-quenching process (improved charge separation in the cells). In the case of molecular capping, we believe that the second mechanism operates, as the relative amplitude of the residual signal in the NIR range (Figures S9 and S10) increases with respect to that for the uncapped cells (Table 2). It also agrees well with the higher values of the *total_APCE* parameter for the cells after capping (Table 1); therefore, better charge separation correlates with the higher residual signal measured a few nanoseconds after excitation. It should be noted that a similar dynamical effect (lifetime increase) has been reported by us previously for D149 with increasing number of coadsorbed molecules (chenodeoxycholic acid).³⁸ It is not surprising because both the coadsorbed molecules and the molecules adsorbed after dye sensitization (in post-treatment capping) should increase the distance between adjacent indoline dye molecules on the titania surface, which suppresses self-quenching.

Finally, we would like to mention our preliminary results obtained for ZnO photoanodes sensitized with silyl-anchor modification of the D149 dye, which are presented in the Supporting Information (Table S5 and Figures S13 and S14).

CONCLUSIONS

The photovoltaic properties and dynamics of CT processes from picoseconds to seconds have been investigated for DSSCs with two different indoline dyes: commercially available D149 and its synthetic modification with the alkoxy-silyl anchoring group. We have observed that the dyes with the new, stronger anchoring group are more resistant to desorb from the titania surface. However, the photovoltaic parameters and CT dynamics were similar for both dyes. More changes were observed upon substitution of the standard iodide electrolyte with the recently widely explored new type of electrolyte with the cobalt-based redox couple (Co-Bpy in our work). The cells fabricated with the cobalt electrolyte showed significantly superior stability and slightly improved photovoltaic performance (higher V_{OC} , J_{SC} , and efficiency, although lower FF) than those with the iodide electrolyte.

Electrochemical impedance studies in the dark showed about 100 mV higher relative potential (of TiO₂ conduction band with respect to the redox couple), narrower distribution of trap states in titania, and slower titania–electrolyte recombination (at the same applied bias voltage) in the cobalt-based cells.

The application of novel molecular-capping post-treatment procedure resulted in the most pronounced changes of DSSCs in all aspects. The absorption spectra of the sensitized

Table 3. Summary of the Effects Studied for the Cells with the Indoline Sensitizer

	anchoring unit (carboxyl vs alkoxy-silyl)	type of electrolyte (cobalt- vs iodide-based)	molecular capping
stationary absorption	slightly higher absorbance and red shift for D149Si with respect to D149C		significant decrease of sensitizer's absorbance after capping
desorption tests	D149Si dye desorbs slower		
photovoltaic parameters	slightly better V_{OC} , J_{SC} , and efficiency for D149Si, but only with the iodide electrolyte	better V_{OC} , J_{SC} , and efficiency, worse FF for the Co-based electrolyte	worse V_{OC} , FF, and efficiency, usually better J_{SC} after capping
relative photocurrent	$total_APCE$ slightly worse for D149Si than D149C	better for Co-based electrolyte	better after capping
stability of the cells	no difference observed	better with Co-based electrolyte	capping slightly improves stability
electrochemical impedance	slight down shift of the titania conduction band and higher CT resistance for D149Si with respect to that observed for the D149C	higher relative potential and narrower distribution of trap states in the Co-based electrolyte	capping slightly shifts down the position of the titania conduction band and lowers the values of CT resistance at the same potential
fs–ns transient absorption	similar CT dynamics for both dyes		slower decay of the dye excited states and higher residual absorption signal after capping

photoanodes became modified upon molecular capping (lower absorbance and blue shift of the maximum), V_{OC} , FF, J_{SC} , and efficiency of the cells slightly decreased, but the relative photocurrent ($total_APCE$ parameter) was significantly higher than that of unmodified cells. Finally, slower decay of the sensitizer excited states was observed after molecular capping (FC state disappearing on the sub-picosecond time scale, hot CT state with single picosecond lifetime, and relaxed CT state with decay on the hundred picosecond time scale), and the effect was explained by suppressed self-quenching of the dyes. It was accompanied by an increase in the residual transient absorption signal after 3 ns that correlated with the improvement in the relative photocurrent.

Our observation of the effects caused by the three studied solar cell modifications (alkoxy-silyl anchoring group, molecular capping, and cobalt-based electrolyte) are summarized in Table 3. We believe that the presented studies of application of new DSSC concepts to the indoline-based solar cell will be of great importance for further optimization of the devices with this large class of efficient sensitizers.

■ ASSOCIATED CONTENT

■ Supporting Information

The Supporting Information is available free of charge on the ACS Publications website at DOI: 10.1021/acs.jpcc.8b06389.

Stationary absorption spectra; IPCE spectra; stability tests; EIS data; transient absorption data for D149Si and D149C; photovoltaic parameters of the best solar cells sensitized by D149C and D149Si; relative errors of the calculated averaged photovoltaic parameters; ideality factors and trap distribution parameters; and results for ZnO photoanodes (PDF)

■ AUTHOR INFORMATION

Corresponding Authors

*E-mail: mgiersz@amu.edu.pl (M.G.).

*E-mail: marziol@amu.edu.pl (M.Z.).

ORCID

Mateusz Gierszewski: 0000-0003-3021-4117

Marcin Ziólek: 0000-0003-1882-6022

Notes

The authors declare no competing financial interest.

■ ACKNOWLEDGMENTS

This work was supported by NCN (National Science Centre, Poland) under the project 2015/18/E/ST4/00196. Katarzyna Pydzińska-Białek is kindly acknowledged for the help in the preparation and characterization of the preliminary tested ZnO cells.

■ REFERENCES

- O'Regan, B.; Grätzel, M. A Low-Cost, High-Efficiency Solar Cell Based on Dye-Sensitized Colloidal TiO₂ Films. *Nature* **1991**, *353*, 737–740.
- Hagfeldt, A.; Boschloo, G.; Sun, L.; Kloo, L.; Pettersson, H. Dye-Sensitized Solar Cells. *Chem. Rev.* **2010**, *110*, 6595–6663.
- Han, L.; Islam, A.; Chen, H.; Malapaka, C.; Chiranjeevi, B.; Zhang, S.; Yang, X.; Yanagida, M. High-Efficiency Dye-Sensitized Solar Cell with a Novel Co-Adsorbent. *Energy Environ. Sci.* **2012**, *5*, 6057.
- Campbell, W. M.; Burrell, A. K.; Officer, D. L.; Jolley, K. W. Porphyrins as Light Harvesters in the Dye-Sensitized TiO₂ Solar Cell. *Coord. Chem. Rev.* **2004**, *248*, 1363–1379.
- Kumar, C. V.; Raptis, D.; Koukaras, E. N.; Sygellou, L.; Lianos, P. Study of an Indoline-Phenothiazine Based Organic Dye for Dye-Sensitized Solar Cells. Theoretical Calculations and Experimental Data. *Org. Electron.* **2015**, *25*, 66–73.
- Howie, W. H.; Claeysens, F.; Miura, H.; Peter, L. M. Characterization of Solid-State Dye-Sensitized Solar Cells Utilizing High Absorption Coefficient Metal-Free Organic Dyes. *J. Am. Chem. Soc.* **2008**, *130*, 1367–1375.
- Brennan, B. J.; Portolés, M. J. L.; Liddell, P. A.; Moore, T. A.; Moore, A. L.; Gust, D. Comparison of Silatrane, Phosphonic Acid, and Carboxylic Acid Functional Groups for Attachment of Porphyrin Sensitizers to TiO₂ in Photoelectrochemical Cells. *Phys. Chem. Chem. Phys.* **2013**, *15*, 16605.
- Nazeeruddin, M. K.; Humphry-Baker, R.; Officer, D. L.; Campbell, W. M.; Burrell, A. K.; Grätzel, M. Application of Metalloporphyrins in Nanocrystalline Dye-Sensitized Solar Cells for Conversion of Sunlight into Electricity. *Langmuir* **2004**, *20*, 6514–6517.
- Zhang, L.; Cole, J. M.; Dai, C. Variation in Optoelectronic Properties of Azo Dye-Sensitized TiO₂ Semiconductor Interfaces with Different Adsorption Anchors: Carboxylate, Sulfonate, Hydroxyl and Pyridyl Groups. *ACS Appl. Mater. Interfaces* **2014**, *6*, 7535–7546.
- Szpakowski, K.; Latham, K.; Rix, C.; Rani, R. A.; Kalantar-zadeh, K. Silane: A New Linker for Chromophores in Dye-Sensitized Solar Cells. *Polyhedron* **2013**, *52*, 719–732.
- Brennan, B. J.; Keirstead, A. E.; Liddell, P. A.; Vail, S. A.; Moore, T. A.; Moore, A. L.; Gust, D. 1-(3'-Amino)Propylsilatrane Derivatives As Covalent Surface Linkers To Nanoparticulate Metal

Oxide Films for Use in Photoelectrochemical Cells. *Nanotechnology* **2009**, *20*, 505203.

(12) Galoppini, E. Linkers for Anchoring Sensitizers to Semiconductor Nanoparticles. *Coord. Chem. Rev.* **2004**, *248*, 1283–1297.

(13) Kakiage, K.; Aoyama, Y.; Yano, T.; Otsuka, T.; Kyomen, T.; Unno, M.; Hanaya, M. An Achievement of over 12 Percent Efficiency in an Organic Dye-Sensitized Solar Cell. *Chem. Commun.* **2014**, *50*, 6379–6381.

(14) Yang, J.; Ganesan, P.; Teuscher, J.; Moehl, T.; Kim, Y. J.; Yi, C.; Comte, P.; Pei, K.; Holcombe, T. W.; Nazeeruddin, M. K.; et al. Influence of the Donor Size in D- π -A Organic Dyes for Dye-Sensitized Solar Cells. *J. Am. Chem. Soc.* **2014**, *136*, 5722–5730.

(15) Yella, A.; Lee, H.-W.; Tsao, H. N.; Yi, C.; Chandiran, A. K.; Nazeeruddin, M. K.; Diau, E. W.-G.; Yeh, C.-Y.; Zakeeruddin, S. M.; Grätzel, M. Porphyrin-Sensitized Solar Cells with Cobalt (II/III)-Based Redox Electrolyte Exceed 12 Percent Efficiency. *Science* **2011**, *334*, 629–634.

(16) O'Regan, B.; Xiaoe, L.; Ghaddar, T. Dye Adsorption, Desorption, and Distribution in Mesoporous TiO₂ Films, and Its Effects on Recombination Losses in Dye Sensitized Solar Cells. *Energy Environ. Sci.* **2012**, *5*, 7203.

(17) Kakiage, K.; Aoyama, Y.; Yano, T.; Oya, K.; Kyomen, T.; Hanaya, M. Fabrication of a High-Performance Dye-Sensitized Solar Cell with 12.8% Conversion Efficiency Using Organic Silyl-Anchor Dyes. *Chem. Commun.* **2015**, *51*, 6315–6317.

(18) Kakiage, K.; Aoyama, Y.; Yano, T.; Oya, K.; Fujisawa, J.-i.; Hanaya, M. Highly-Efficient Dye-Sensitized Solar Cells with Collaborative Sensitization by Silyl-Anchor and Carboxy-Anchor Dyes. *Chem. Commun.* **2015**, *51*, 15894–15897.

(19) Matta, S. K.; Kakiage, K.; Makuta, S.; Veamatahau, A.; Aoyama, Y.; Yano, T.; Hanaya, M.; Tachibana, Y. Dye-Anchoring Functional Groups on the Performance of Dye-Sensitized Solar Cells: Comparison between Alkoxy-silyl and Carboxyl Groups. *J. Phys. Chem. C* **2014**, *118*, 28425–28434.

(20) Sobuś, J.; Gierczyk, B.; Burdziński, G.; Jancelewicz, M.; Polanski, E.; Hagfeldt, A.; Ziółek, M. Factors Affecting the Performance of Champion Silyl-Anchor Carbazole Dye Revealed in the Femtosecond to Second Studies of Complete ADEKA-1 Sensitized Solar Cells. *Chem.—Eur. J.* **2016**, *22*, 15807–15818.

(21) Gierszewski, M.; Glinka, A.; Grządka, I.; Jancelewicz, M.; Ziółek, M. Effects of Post-Assembly Molecular and Atomic Passivation of Sensitized Titania Surface: Dynamics of Electron Transfer Measured from Femtoseconds to Seconds. *ACS Appl. Mater. Interfaces* **2017**, *9*, 17102–17114.

(22) Seo, K. D.; Choi, I. T.; Kim, H. K. D- π -A Organic Dyes with Various Bulky Amine-Typed Donor Moieties for Dye-Sensitized Solar Cells Employing the Cobalt Electrolyte. *Org. Electron.* **2015**, *25*, 1–5.

(23) Hamann, T. W.; Farha, O. K.; Hupp, J. T. Outer-Sphere Redox Couples as Shuttles in Dye-Sensitized Solar Cells. Performance Enhancement Based on Photoelectrode Modification via Atomic Layer Deposition. *J. Phys. Chem. C* **2008**, *112*, 19756–19764.

(24) Antila, L. J.; Heikkilä, M. J.; Mäkinen, V.; Humalämäki, N.; Laitinen, M.; Linko, V.; Jalkanen, P.; Toppari, J.; Aumanen, V.; Kemell, M.; et al. ALD Grown Aluminum Oxide Submonolayers in Dye-Sensitized Solar Cells: The Effect on Interfacial Electron Transfer and Performance. *J. Phys. Chem. C* **2011**, *115*, 16720–16729.

(25) Horiuchi, T.; Miura, H.; Sumioka, K.; Uchida, S. High Efficiency of Dye-Sensitized Solar Cells Based on Metal-Free Indoline Dyes. *J. Am. Chem. Soc.* **2004**, *126*, 12218–12219.

(26) Ito, S.; Zakeeruddin, S. M.; Humphry-Baker, R.; Liska, P.; Charvet, R.; Comte, P.; Nazeeruddin, M. K.; Péchy, P.; Takata, M.; Miura, H.; et al. High-Efficiency Organic-Dye-Sensitized Solar Cells Controlled by Nanocrystalline-TiO₂ Electrode Thickness. *Adv. Mater.* **2006**, *18*, 1202–1205.

(27) Ito, S.; Miura, H.; Uchida, S.; Takata, M.; Sumioka, K.; Liska, P.; Comte, P.; Péchy, P.; Grätzel, M. High-Conversion-Efficiency Organic Dye-Sensitized Solar Cells with a Novel Indoline Dye. *Chem. Commun.* **2008**, *41*, 5194.

(28) Jin, M. Y.; Kim, B.-M.; Jung, H. S.; Park, J.-H.; Roh, D.-H.; Nam, D. G.; Kwon, T.-H.; Ryu, D. H. Indoline-Based Molecular Engineering for Optimizing the Performance of Photoactive Thin Films. *Adv. Funct. Mater.* **2016**, *26*, 6876–6887.

(29) Wang, L.; Liang, M.; Zhang, Y.; Cheng, F.; Wang, X.; Sun, Z.; Xue, S. Influence of Donor and Bridge Structure in D-A- π -A Indoline Dyes on the Photovoltaic Properties of Dye-Sensitized Solar Cells Employing Iodine/Cobalt Electrolyte. *Dyes Pigm.* **2014**, *101*, 270–279.

(30) Flender, O.; Lohse, P. W.; Du, J.; Oekermann, T.; Scholz, M.; Oum, K.; Lenzer, T. Ultrafast Dynamics of the Indoline Dye D149 on Mesoporous ZnO and Al₂O₃ Thin Films. *Z. Phys. Chem.* **2015**, *229*, 1907–1928.

(31) Fakis, M.; Stathatos, E.; Tsigaridas, G.; Giannetas, V.; Persephonis, P. Femtosecond Decay and Electron Transfer Dynamics of the Organic Sensitizer D149 and Photovoltaic Performance in Quasi-Solid-State Dye-Sensitized Solar Cells. *J. Phys. Chem. C* **2011**, *115*, 13429–13437.

(32) Oum, K.; Lohse, P. W.; Flender, O.; Klein, J. R.; Scholz, M.; Lenzer, T.; Du, J.; Oekermann, T. Ultrafast Dynamics of the Indoline Dye D149 on Electrodeposited ZnO and Sintered ZrO₂ and TiO₂ Thin Films. *Phys. Chem. Chem. Phys.* **2012**, *14*, 15429–15437.

(33) Katoh, R.; Furube, A. Electron Injection Efficiency in Dye-Sensitized Solar Cells. *J. Photochem. Photobiol., C* **2014**, *20*, 1–16.

(34) Juozapavicius, M.; Kaucikas, M.; van Thor, J. J.; O'Regan, B. C. Observation of Multiexponential Pico- to Subnanosecond Electron Injection in Optimized Dye-Sensitized Solar Cells with Visible-Pump Mid-Infrared-Probe Transient Absorption Spectroscopy. *J. Phys. Chem. C* **2013**, *117*, 116–123.

(35) El-Zohry, A.; Orthaber, A.; Zietz, B. Isomerization and Aggregation of the Solar Cell Dye D149. *J. Phys. Chem. C* **2012**, *116*, 26144–26153.

(36) Burdziński, G.; Karolczak, J.; Ziółek, M. Dynamics of Local Stark Effect Observed for a Complete D149 Dye-Sensitized Solar Cell. *Phys. Chem. Chem. Phys.* **2013**, *15*, 3889–3896.

(37) Sobuś, J.; Burdziński, G.; Karolczak, J.; Idigoras, J.; Anta, J. A.; Ziółek, M. Comparison of TiO₂ and ZnO Solar Cells Sensitized with an Indoline Dye: Time-Resolved Laser Spectroscopy Studies of Partial Charge Separation Processes. *Langmuir* **2014**, *30*, 2505–2512.

(38) Sobuś, J.; Karolczak, J.; Komar, D.; Anta, J. A.; Ziółek, M. Transient States and the Role of Excited State Self-Quenching Of Indoline Dyes in Complete Dye-Sensitized Solar Cells. *Dyes Pigm.* **2015**, *113*, 692–701.

(39) Fakis, M.; Hrobárik, P.; Stathatos, E.; Giannetas, V.; Persephonis, P. A Time Resolved Fluorescence and Quantum Chemical Study of the Solar Cell Sensitizer D149. *Dyes Pigm.* **2013**, *96*, 304–312.

(40) Snaith, H. J.; Petrozza, A.; Ito, S.; Miura, H.; Grätzel, M. Charge Generation and Photovoltaic Operation of Solid-State Dye-Sensitized Solar Cells Incorporating a High Extinction Coefficient Indolene-Based Sensitizer. *Adv. Funct. Mater.* **2009**, *19*, 1810–1818.

(41) Cheng, H.-M.; Hsieh, W.-F. Electron Transfer Properties of Organic Dye-Sensitized Solar Cells Based on Indoline Sensitizers with ZnO Nanoparticles. *Nanotechnology* **2010**, *21*, 485202.

(42) Rohwer, E.; Richter, C.; Heming, N.; Strauch, K.; Litwinski, C.; Nyokong, T.; Schlettwein, D.; Schwoerer, H. Ultrafast Photodynamics of the Indoline Dye D149 Adsorbed to Porous ZnO in Dye-Sensitized Solar Cells. *ChemPhysChem* **2013**, *14*, 132–139.

(43) Cappel, U. B.; Feldt, S. M.; Schöneboom, J.; Hagfeldt, A.; Boschloo, G. The Influence of Local Electric Fields on Photoinduced Absorption in Dye-Sensitized Solar Cells. *J. Am. Chem. Soc.* **2010**, *132*, 9096–9101.

(44) Smortsova, Y.; Oher, H.; Miannay, F.-A.; Vanel, R.; Dubois, J.; Kalugin, O.; Idrissi, A. Solvatochromic Effects on a Class of Indoline Derivatives Organic Photosensitizers: About the Influence of Hydrogen-Bond Acceptor and Donor Abilities Parameters. *J. Mol. Liq.* **2017**, *245*, 76–84.

(45) Rohwer, E.; Minda, I.; Tauscher, G.; Richter, C.; Miura, H.; Schlettwein, D.; Schwoerer, H. Ultrafast Charge-Transfer Reactions of

Indoline Dyes with Anchoring Alkyl Chains of Varying Length in Mesoporous ZnO Solar Cells. *ChemPhysChem* **2015**, *16*, 943–948.

(46) Minda, I.; Ahmed, E.; Sleziona, V.; Richter, C.; Beu, M.; Falgenhauer, J.; Miura, H.; Schlettwein, D.; Schworer, H. Identification of Different Pathways of Electron Injection in Dye-Sensitized Solar Cells of Electrodeposited ZnO Using an Indoline Sensitizer. *Phys. Chem. Chem. Phys.* **2016**, *18*, 8938–8944.

(47) Meyenburg, I.; Hofeditz, N.; Ruess, R.; Rudolph, M.; Schlettwein, D.; Heimbrodt, W.; Meyenburg, I.; Hofeditz, N.; Ruess, R.; Rudolph, M.; et al. Optical Determination of Charge Transfer Times from Indoline Dyes to ZnO in Solid State Dye-Sensitized Solar Cells. *AIP Adv.* **2018**, *8*, 55218.

(48) Mathew, S.; Yella, A.; Gao, P.; Humphry-Baker, R.; Curchod, B. F. E.; Ashari-Astani, N.; Tavernelli, I.; Rothlisberger, U.; Nazeeruddin, M. K.; Grätzel, M. Dye-Sensitized Solar Cells with 13% Efficiency Achieved Through the Molecular Engineering of Porphyrin Sensitizers. *Nat. Chem.* **2014**, *6*, 242–247.

(49) Gierszewski, M.; Grądzka, I.; Glinka, A.; Ziólek, M. Insights into the Limitations of Solar Cells Sensitized with Ruthenium Dyes Revealed in Time-Resolved Spectroscopy Studies. *Phys. Chem. Chem. Phys.* **2017**, *19*, 20463–20473.

(50) Fabregat-Santiago, F.; Garcia-Belmonte, G.; Mora-Seró, I.; Bisquert, J. Characterization of Nanostructured Hybrid and Organic Solar Cells by Impedance Spectroscopy. *Phys. Chem. Chem. Phys.* **2011**, *13*, 9083–9118.

(51) Guillén, E.; Azaceta, E.; Peter, L. M.; Zukal, A.; Tena-Zaera, R.; Anta, J. A. ZnO Solar Cells with an Indoline Sensitizer: A Comparison Between Nanoparticulate Films and Electrodeposited Nanowire Arrays. *Energy Environ. Sci.* **2011**, *4*, 3400–3407.

(52) Idígoras, J.; Burdziński, G.; Karolczak, J.; Kubicki, J.; Oskam, G.; Anta, J. A.; Ziólek, M. The Impact of the Electrical Nature of the Metal-Oxide on the Performance in Dye-Sensitized Solar Cells: New Look at Old Paradigms. *J. Phys. Chem. C* **2015**, *119*, 3931–3944.

(53) Sakuragi, Y.; Wang, X.-F.; Miura, H.; Matsui, M.; Yoshida, T. Aggregation of Indoline Dyes as Sensitizers for ZnO Solar Cells. *J. Photochem. Photobiol., A* **2010**, *216*, 1–7.

(54) Idígoras, J.; Sobuś, J.; Jancelewicz, M.; Azaceta, E.; Tena-Zaera, R.; Anta, J. A.; Ziólek, M. Effect of Different Photoanode Nanostructures on the Initial Charge Separation and Electron Injection Process in Dye Sensitized Solar cells: A Photophysical Study with Indoline Dyes. *Mater. Chem. Phys.* **2016**, *170*, 218–228.

(55) Lohse, P. W.; Kuhnt, J.; Druzhinin, S. I.; Scholz, M.; Ekimova, M.; Oekermann, T.; Lenzer, T.; Oum, K. Ultrafast Photoinduced Relaxation Dynamics of the Indoline Dye D149 Inorganic Solvents. *Phys. Chem. Chem. Phys.* **2011**, *13*, 19632–19640.

(56) Deshpande, A. V.; Beidoun, A.; Penzkofer, A.; Wagenblast, G. Absorption and Emission Spectroscopic Investigation of Cyanovinyl-diethylaniline Dye Vapors. *Chem. Phys.* **1990**, *142*, 123–131.

Supporting information

for

Testing New Concepts in Solar Cells Sensitized with Indoline Dyes – Alkoxysilyl Anchoring Group, Molecular Capping and Cobalt-based Electrolyte

Mateusz Gierszewski ^{1*}, Adam Glinka ¹, Iwona Grądzka ¹, Błażej Gierczyk ² and Marcin Ziółek ^{1*}

¹ *Quantum Electronics Laboratory, Faculty of Physics, Adam Mickiewicz University in Poznań, Umultowska 85, 61-614 Poznań, Poland.*

² *Faculty of Chemistry, Adam Mickiewicz University in Poznań, Umultowska 89b, 61-614, Poznań, Poland.*

* corresponding authors, emails: mgiersz@amu.edu.pl (MG) and marziol@amu.edu.pl (MZ)

Table S1. Photovoltaic parameters of the best solar cells sensitized by D149 dye with carboxyl and silyl-anchor unit of each configuration: open circuit voltage (V_{OC}), fill factor (FF), photocurrent density (J_{SC}), efficiency (Eff) number of absorbed photons at 1Sun illumination (N_{ph}), absorbance at λ_{max} (A_{max}) and corrected photocurrent efficiency ($total_APCE$).

Cell	V_{OC} [V]	FF	J_{SC} [mAcm ⁻²]	Eff [%]	N_{ph} [10 ²⁰ s ⁻¹ m ⁻²]	A_{max} (λ_{max} [nm]) [#]	$total_APCE$
D149C_I	0.74	0.67	5.1	2.5	7.9	1.7 (523)	0.40
D149C_I_MC1	0.69	0.63	4.7	2.0	6.6	1.1 (515)	0.44
D149Si_I	0.76	0.63	5.9	2.8	8.0	1.9 (525)	0.47
D149Si_I_MC1(a)*	0.74	0.62	6.5	3.0	8.1	1.7 (521)	0.50
D149Si_I_MC1(b)*	0.73	0.65	4.7	2.2	7.4	1.5 (518)	0.40
D149C_Co	0.78	0.39	6.7	2.0	8.2	1.9 (521)	0.51
D149C_Co_MC2	0.79	0.45	6.1	2.2	7.7	1.5 (521)	0.50
D149Si_Co	0.79	0.53	5.9	2.4	8.6	2.3 (526)	0.43
D149Si_Co_MC2	0.79	0.5	5.9	2.3	7.9	1.7 (525)	0.46

*D149Si_I_MC1(a): D149 dye, silyl-anchor unit, iodide electrolyte, multi-capping post-treatment (1min EPA);

D149Si_I_MC1(b): D149 dye, silyl-anchor unit, iodide electrolyte, multi-capping post-treatment (3min EPA)

[#] relative error of λ_{max} includes between 0.1 – 0.3 %

Table S2. Number of measured samples (N) and relative errors of the calculated averaged photovoltaic parameters (given in Table 1) for the studied solar cells. The relative error of parameter p is defined as the standard deviation of the mean (Δp) divided by the mean value (from Table 1) and multiplied by 100 %.

Cell	N	$\frac{\Delta V_{oc}}{V_{oc}}$ [%]	$\frac{\Delta FF}{FF}$ [%]	$\frac{\Delta J_{sc}}{J_{sc}}$ [%]	$\frac{\Delta Eff}{Eff}$ [%]
D149C_I	4	1.4	2.9	18.2	17.7
D149C_I_MC1	2	1.5	3.8	16.4	13.9
D149Si_I	4	0.6	2.2	18.7	17.2
D149Si_I_MC1	6	0.9	1.1	9.7	10.2
D149C_Co	9	0.2	5.3	2.7	4.7
D149C_Co_MC2	6	0.6	4.9	4.6	5.2
D149Si_Co	9	0.3	2.1	4.9	2.8
D149Si_Co_MC2	9	0.3	3.1	2.3	3.1

Table S3. Photovoltaic parameters of the solar cells sensitized by D149 dye with carboxyl and silyl-anchor unit of each configuration after 1h; 1, 6, 17 days and 1 month after preparation with Co-Bpy electrolyte.

Cell	Time after preparation	V_{OC} [V]	FF	J_{SC} [mAcm ⁻²]	Eff [%]	N_{ph} [10^{20} s ⁻¹ m ⁻²]	$A_{500\text{ nm}}$	$total_APCE$
D149C_Co	1h	0.78	0.39	6.7	2.0	8.2	1.7	0.51
	1 day	0.78	0.48	6.1	2.3	8.2	1.7	0.47
	6 days	0.78	0.52	5.5	2.2	8.2	1.7	0.42
	17 days	0.78	0.54	5.8	2.4	8.2	1.7	0.44
	1 month	0.79	0.55	5.8	2.5	8.2	1.7	0.44
D149C_Co_MC2	1h	0.79	0.45	6.1	2.2	7.7	1.4	0.5
	1 day	0.77	0.49	5.7	2.1	7.7	1.4	0.46
	6 days	0.77	0.55	5.3	2.2	7.7	1.4	0.43
	17 days	0.77	0.60	4.8	2.2	7.7	1.4	0.4
	1 month	0.77	0.60	4.7	2.2	7.7	1.4	0.39
D149Si_Co	1h	0.79	0.53	5.9	2.4	8.6	2.1	0.43
	1 day	0.79	0.55	5.4	2.3	8.6	2.1	0.39
	6 days	0.79	0.56	5.2	2.3	8.6	2.1	0.38
	17 days	0.79	0.62	4.6	2.3	8.6	2.1	0.33
	1 month	0.8	0.64	4.4	2.3	8.6	2.1	0.32
D149Si_Co_MC2	1h	0.79	0.50	5.9	2.3	7.9	1.6	0.46
	1 day	0.79	0.54	5.2	2.2	7.9	1.6	0.41
	6 days	0.78	0.57	4.7	2.1	7.9	1.6	0.37
	17 days	0.78	0.60	4.5	2.1	7.9	1.6	0.36
	1 month	0.79	0.6	4.3	2.0	7.9	1.6	0.34

Open circuit voltage (V_{OC}), fill factor (FF), photocurrent density (J_{SC}), efficiency (Eff) number of absorbed photons at 1Sun illumination (N_{ph}), absorbance at 500 nm ($A_{500\text{ nm}}$) and corrected photocurrent efficiency ($Total\ APCE$).

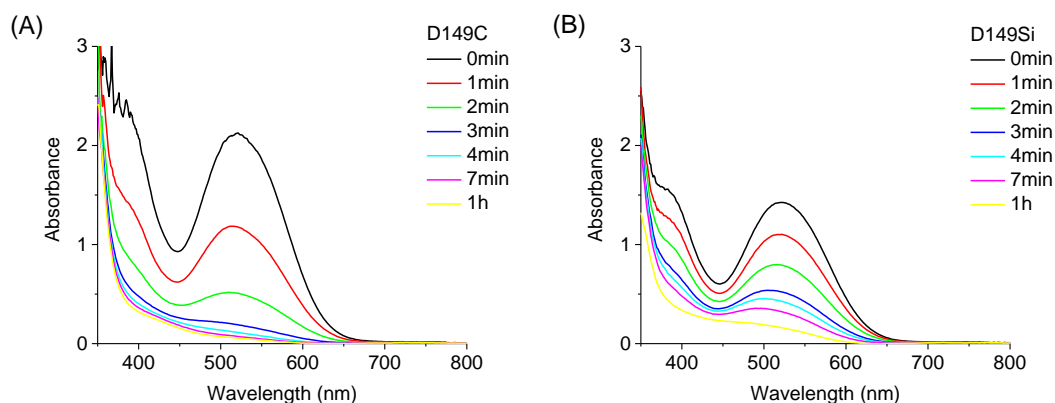


Figure S1. Absorption spectra of D149 dye with carboxyl (A) and silyl-anchor (B) groups upon immersion in mixture of 9:1 acetonitrile:water in time.

Comments to Figure S1:

It should be pointed that upon immersion of sensitized photoanodes, the absorption maximum shifts to the shorter-wavelengths, for D149C. Before immersion the maximum is noted at 521 nm, after 1min at 516 nm and after 2 min at 509 nm. Similar changes, however not so clearly, were observed for D149Si, whereas before immersion the absorption maximum is found at 521 nm and after 2 min at 517 nm. It might be rationalized by the presence of water in the mixture used to the desorption process or due to decreasing dye aggregation.

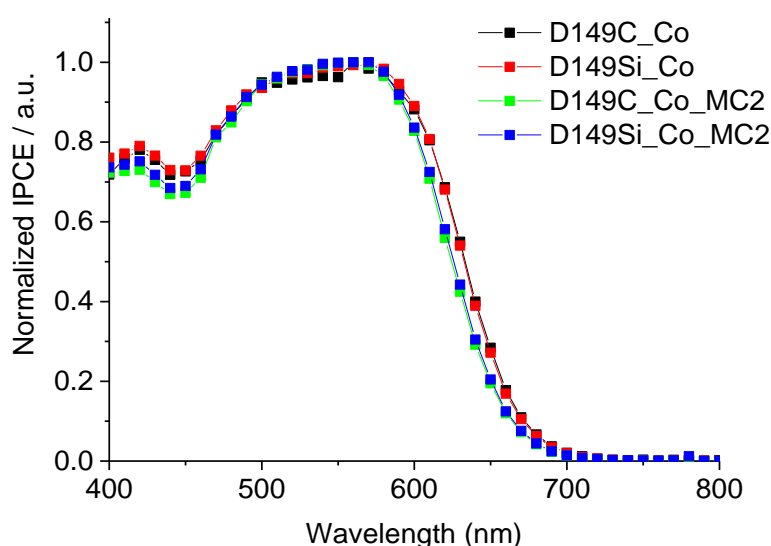


Figure S2. IPCE spectra of selected cells sensitized with D149 in the different, indicated configurations, all with Co-Bpy electrolyte.

Electrochemical impedance spectroscopy (EIS)

A:

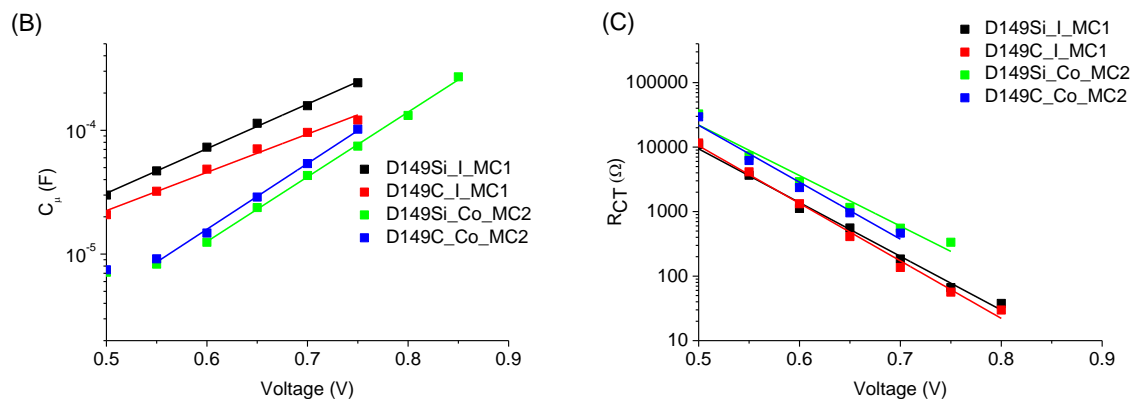
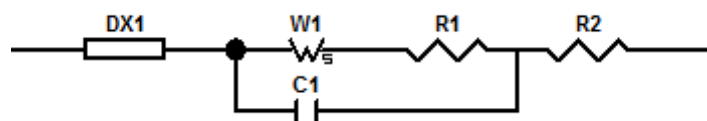


Figure S3. (A) Equivalent circuits for EIS of DSSCs, DX1 is transmission line element. Chemical capacitance (B) and charge transfer resistance (C) of different cells sensitized with D149 in different cell configurations after multi-capping post-treatment using iodide or Co-Bpy electrolyte.

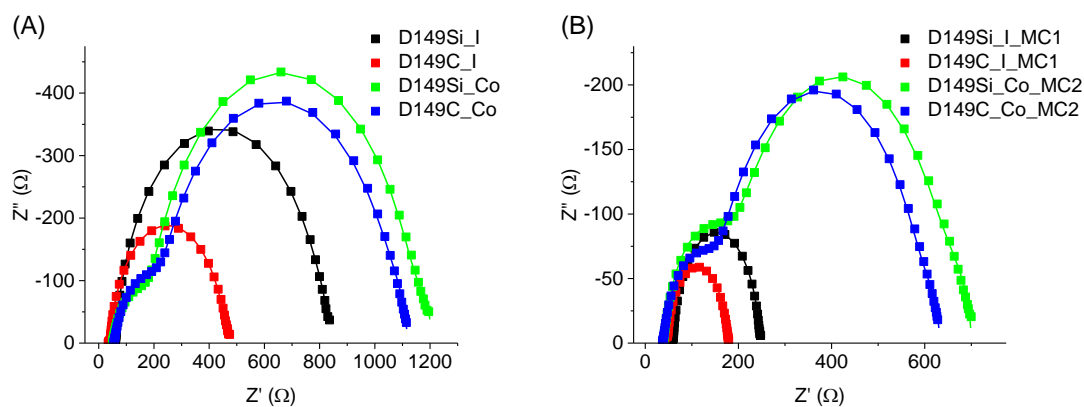


Figure S4. Nyquist plots for different cells sensitized by D149 in different configurations without (A) and after (B) multi-capping post-treatment at bias voltage of 0.7 V.

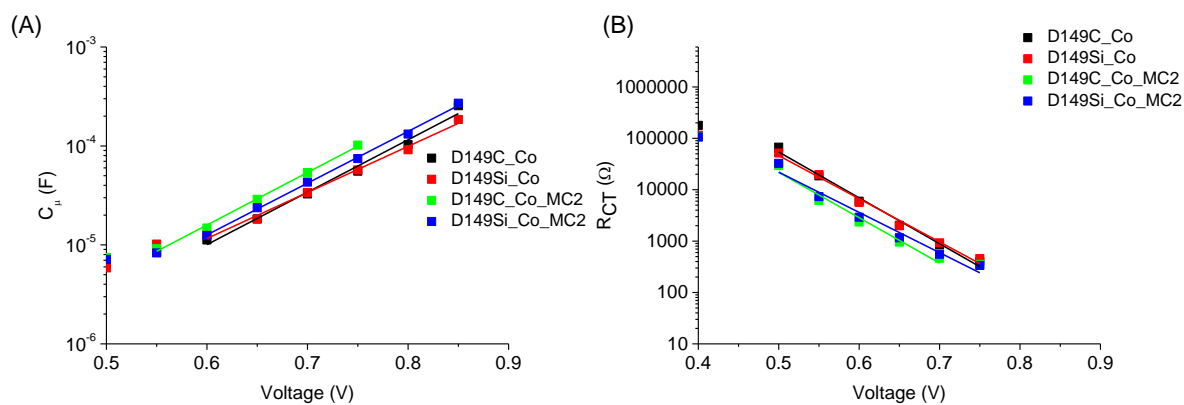


Figure S5. Chemical capacitance (A) and charge transfer resistance (B) of different cells sensitized by D149 in different cell configurations after or without multi-capping post-treatment using Co-Bpy electrolyte.

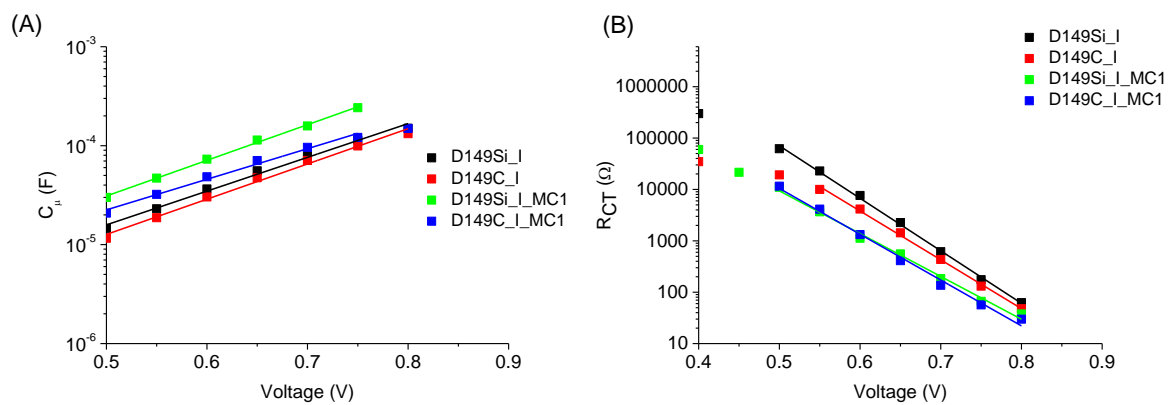


Figure S6. Chemical capacitance (A) and charge transfer resistance (B) of different cells sensitized by D149 in different cell configurations after or without multi-capping post-treatment using iodide electrolyte.

Table S4. Calculated ideality factor (m) and trap distribution parameter (α) for obtained cells sensitized by D149 in different configurations. The parameters α and m were obtained from the fit (Figures 3 and S3) of the following functions: $C_{\mu}=C_0 \exp(\alpha Ve/kT)$ and $R_{CT}=R_0 \exp(-Ve/m kT)$, relative errors of m includes between 5-20 % and of α - between 5-10 %.

Sample / configuration	m	α
D149C_I	1.8	0.21
D149C_I_MC1	1.9	0.18
D149Si_I	1.7	0.20
D149Si_I_MC1	2.0	0.21
D149C_Co	1.9	0.31
D149C_Co_MC2	1.9	0.31
D149Si_Co	2.0	0.28
D149Si_Co_MC2	2.2	0.31

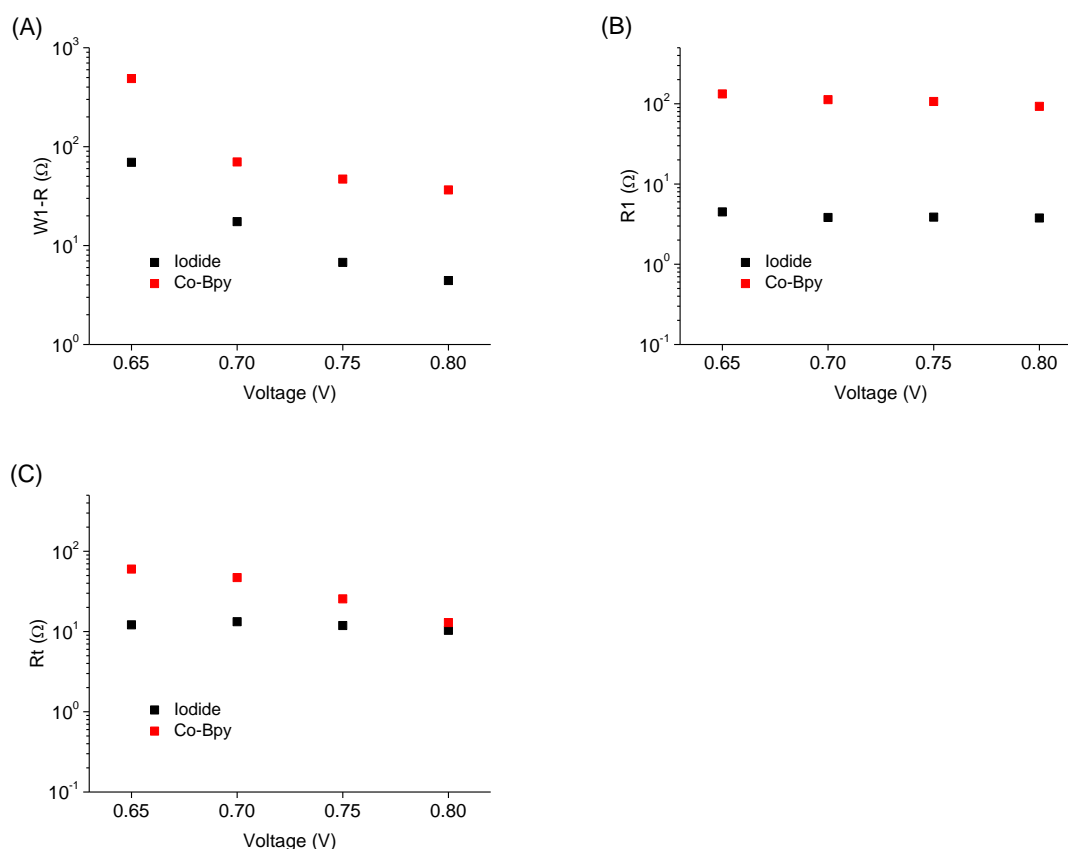


Figure S7. Averaged values of Warburg resistance ($W1_R$, Figure A), the counter electrode/electrolyte interface resistance ($R1$, Figure B) and transport resistance (Rt , Figure C) for different cells fabricated by D149 dye in different configurations with iodide and Co-Bpy electrolyte.

Comments to Figure S7:

Firstly, the values of Warburg resistance systematically increased both for iodide and Co-Bpy electrolyte. In the range of the applied bias voltage from 0.80 V to 0.65 V the values for iodide electrolyte changes from 4.4 Ω to 69.4 Ω and in the same range for Co-Bpy electrolyte the values of W_{I-R} appears from 36.5 Ω to 488 Ω . Similar trends for the change of Warburg resistance were observed for the solar cells fabricated by N719 dye with the same type of electrolyte¹. It suggests that the resistance responsible for the time of charge transport in electrolyte is independent of the type of dye used (ruthenium or metal-free). Further, the resistance responsible for the time scale of redox pair regeneration (R_I) for iodide electrolyte is practically the same from 0.80 V to 0.65 V ($\sim 4\Omega$) and systematically increase between 0.6 V and 0.5 V (from 4.5 Ω to 44 Ω). Significantly higher values of R_I are found in the Co-Bpy cells. Between 0.80 V and 0.50 V the values are similar ($\sim 92 \Omega$) with perturbation between

0.65 V and 0.55 V. Corresponding to the data obtained for N719 cells¹ it can be concluded that trends observed for R_l values are similar, so the values of R_l depend more on the type of electrolyte than used dye. Finally, the values of transport resistance for D149 in different configurations (Figure S7C) are weakly dependent on the electrolyte used. In the case of cobalt cells the values are higher with respect to the iodide one. Between 0.8V and 0.65V it was found that for iodide cells the values are practically the same (change from 10.3 Ω to 12.2 Ω) however increasing from 12.2 Ω to 40.7 Ω when bias voltage changes from 0.65V to 0.5V. In the case of cobalt cells, the values of R_t increases from 12.9 Ω to 60.1 Ω between applied bias voltage from 0.80V to 0.65V, but at lower values of bias voltage (from 0.65V to 0.5V) the values of R_t significantly decrease. It should be pointed that the differences between the R_t values for D149 dye for iodide and cobalt cells are not so high as observed for N719+CDCA¹ when the difference were about ten times higher for cobalt cells than iodide. It suggests, that electron transport through titania nanoparticles when the D149 dye is used instead of N719 is comparable, independently of the electrolyte used. The differences between cobalt and iodide cells fabricated by D149 dye are also clear show after comparison between Nyquist plots for different cells (Figure S4). For the iodide cells dominant semicircle is located in the intermediate frequency region, which corresponds to charge transfer resistance (R_{CT}), and only small semicircle in the high frequency part of the Nyquist plot is present, which can be associated to the counter electrode/electrolyte interface. On the other hand, in cobalt cells two clearly different semicircles were found, the first in the high frequency region (associated with R_l resistance) and the second, in the intermediate frequency region (associated with R_{CT}). In the low frequency part of Nyquist plots, both for iodide and cobalt cells no clearly semicircle is present and it is important difference between these cells and the cells sensitized by N719 dye.¹

Transient absorption spectroscopy

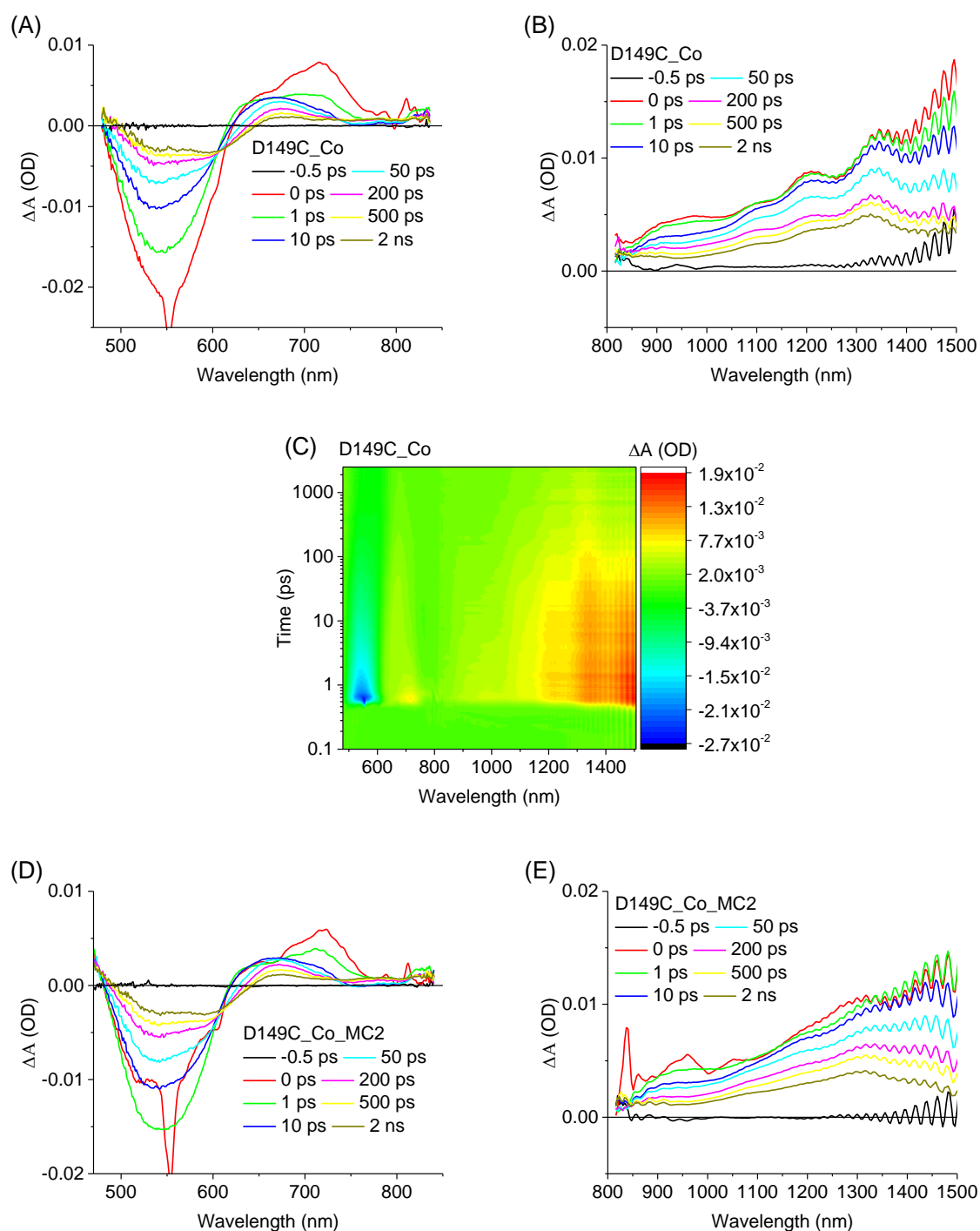


Figure S8. Exemplary transient absorption spectra for selected delay times between pump and probe pulses for D149C_Co and D149C_Co_MC2 in both VIS (A, D) and NIR (B, E) ranges; (C) 2D representation of the change of absorption (ΔA) plotted as a compilation of two individual example measurements in VIS and NIR range for D149C_Co sample.

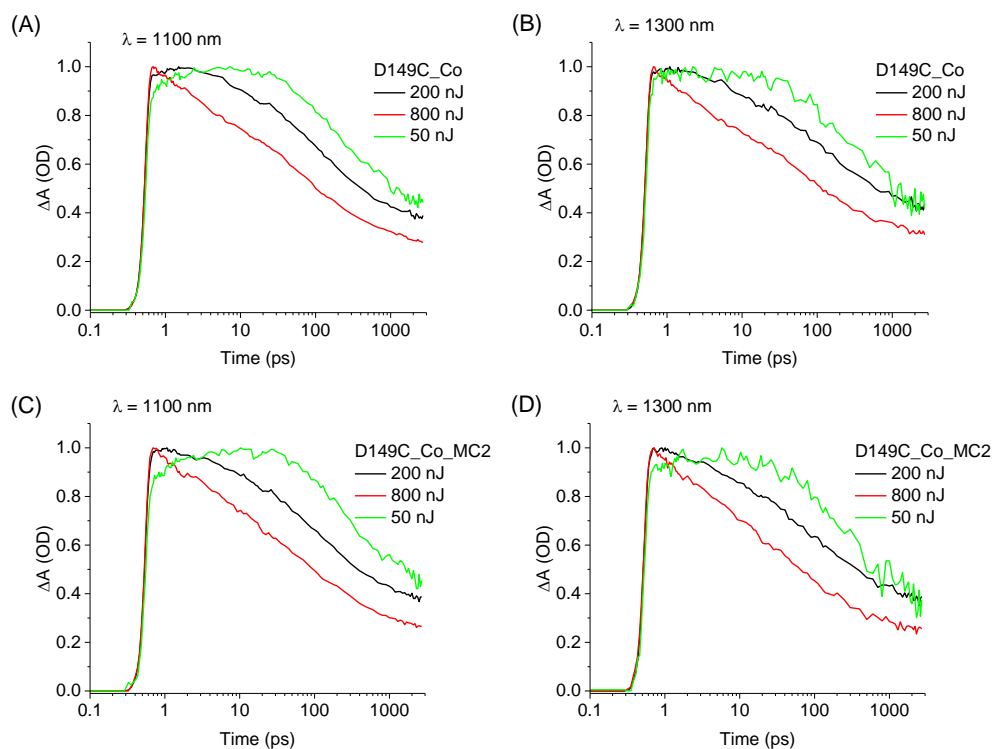


Figure S9. Kinetics at 1100 nm (A, C) and 1300 nm (B, D) for D149 dye with carboxyl group and Co-Bpy electrolyte under different pump pulse intensity (50, 200 and 800 nJ). The data for the cells after multi-capping post-treatment were included in C and D.

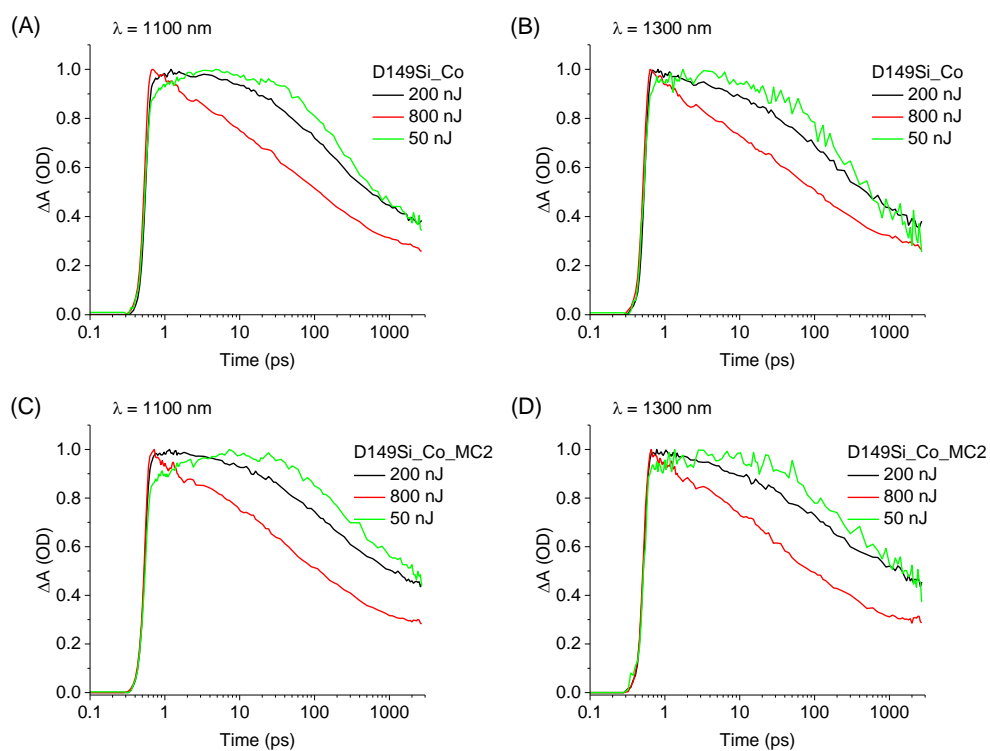


Figure S10. Kinetics at 1100 nm (A, C) and 1300 nm (B, D) for D149 dye with silyl-anchor unit and Co-Bpy electrolyte under different pump pulse intensity (50, 200 and 800 nJ). The data for the cells after multi-capping post-treatment were included in C and D.

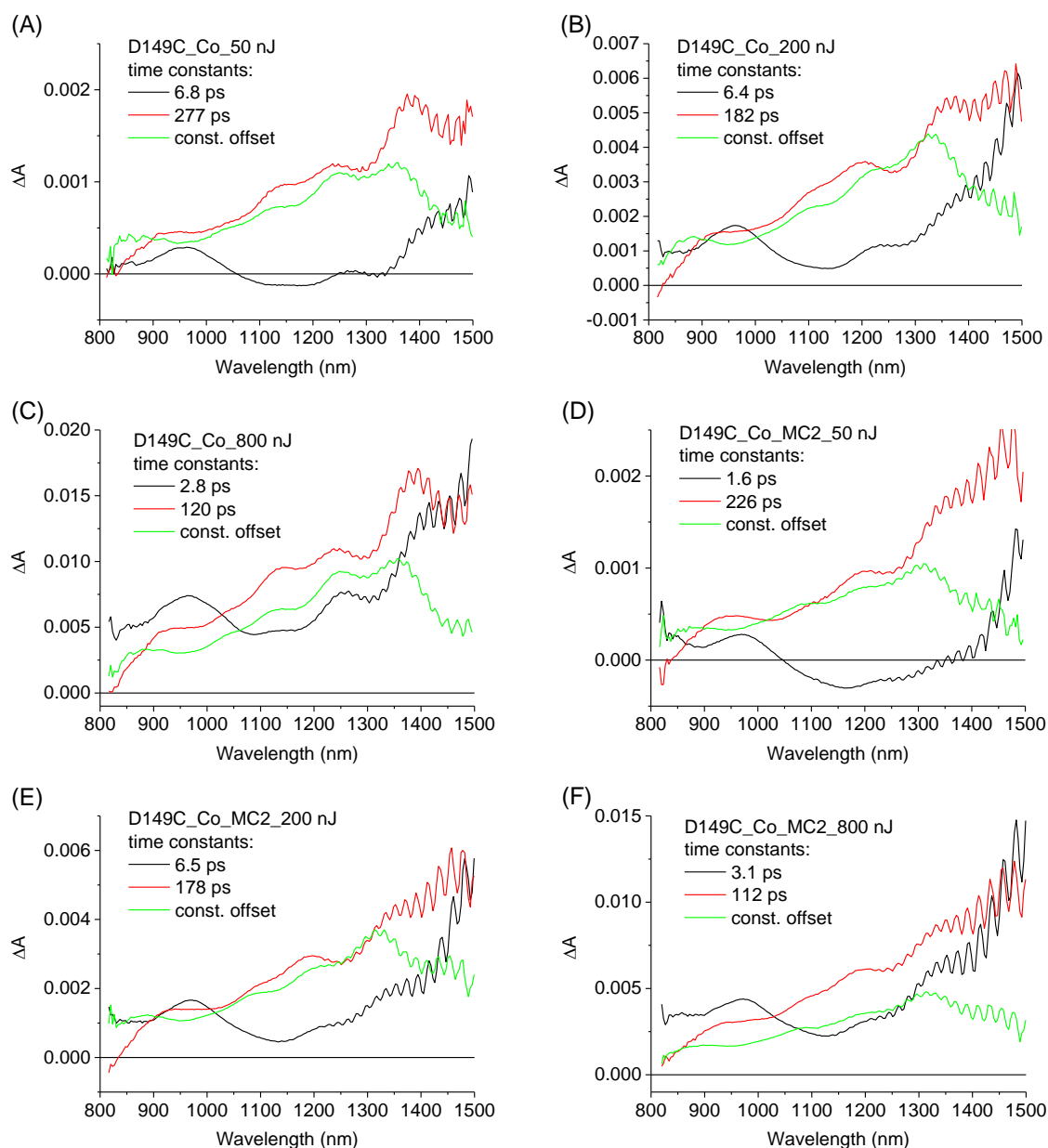


Figure S11. Wavelength dependent amplitudes of the indicated time constants obtained from global analysis: the effect of different pump pulse intensity (50, 200 and 800 nJ) in NIR range for DSSCs with D149 dye with carboxyl group and Co-Bpy electrolyte. For pulse energies ≥ 200 nJ the fastest component was not well resolved in NIR, therefore two-exponential fit plus a constant offset were used in this range. Samples in Figure D, E, F were after post-treatment multi-capping. The decay time constants decrease with higher pump pulse intensity, in agreement with the exemplary kinetics shown in Figure S9.

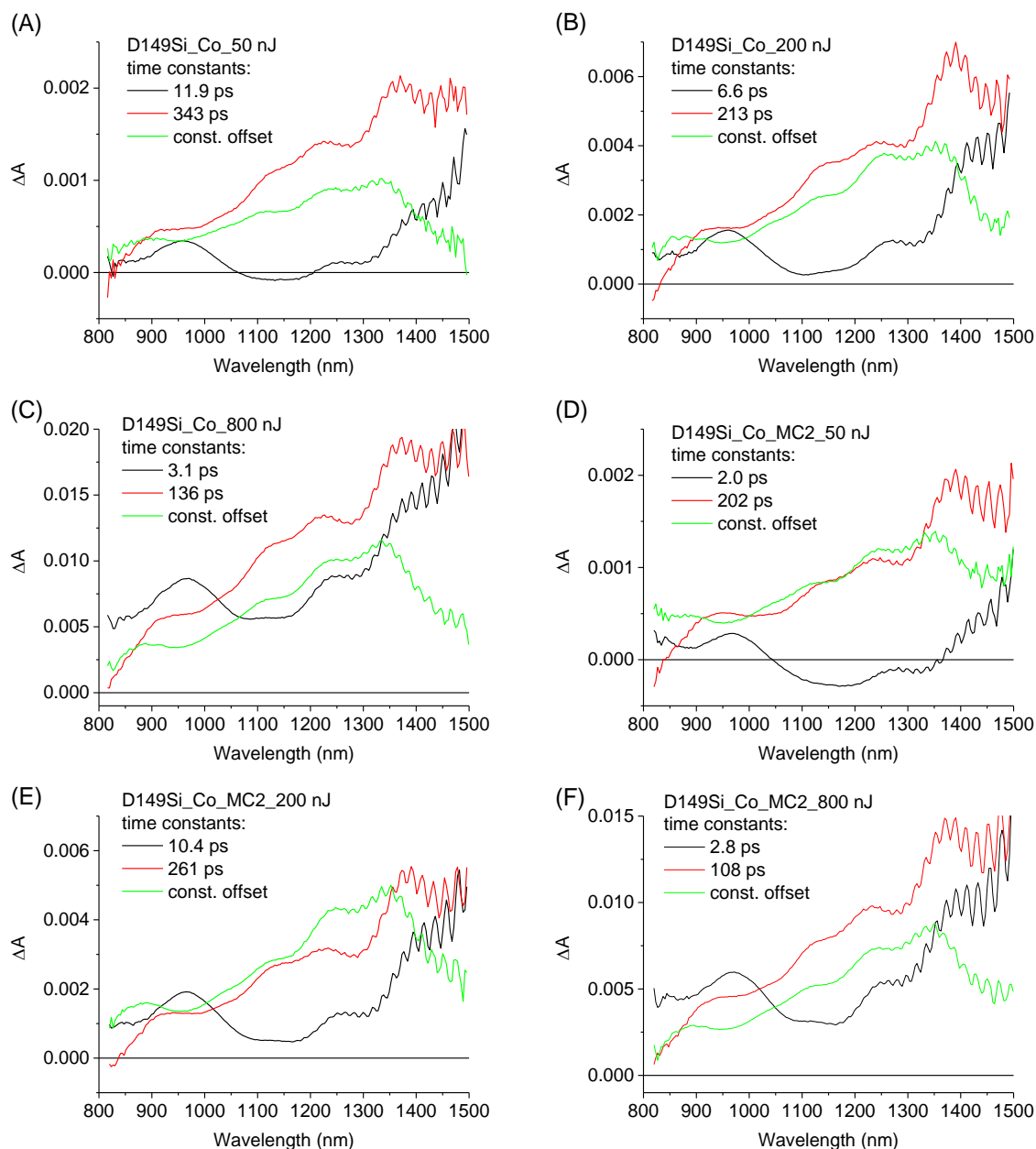


Figure S12. Wavelength dependent amplitudes of the indicated time constants obtained from global analysis: the effect of different pump pulse intensity (50, 200 and 800 nJ) in NIR range for DSSCs with D149 dye with alkoxysilyl-anchor group and Co-Bpy electrolyte. For pulse energies ≥ 200 nJ the fastest component was not well resolved in NIR, therefore two-exponential fit plus a constant offset were used in this range. Samples in Figure D, E, F were after post-treatment multi-capping. The decay time constants decrease with higher pump pulse intensity, in agreement with the exemplary kinetics shown in Figure S10.

Results for ZnO photoanodes

Our previous works for DSSC with indoline dyes have shown worse performance of the cells with different ZnO nanostructures with respect to those with TiO₂.²⁻⁴ One of the reasons was quick degradation in ZnO cells, probably due to dye desorption and formation of aggregates. We intended to test the possibility that stronger alkoxyethyl anchoring groups in the new dye might suppress this effect. However, we have not found any improvement in the solar cell performance (Table S5) or stability (Figures S13) of the dyes with alkoxyethyl anchor with respect to those previously studied (with carboxylic anchor). *Total_APCE* was even smaller (Table S5), lifetimes in femtosecond transient absorption experiments were shorter (Figure S14), and residual transient absorption signal smaller (Table S5) for alkoxyethyl dyes, which can be explained by slightly higher adsorption and thus, more pronounced self-quenching in these samples.

Table S5. Photovoltaic parameters for the cells prepared with photoanodes based on ZnO nanoparticles (the same as in⁴) and filled with iodide electrolyte. The values are averaged from 3 cells, each of them measured 3 times from 1 to 4 hours after preparation. The last column shows the normalized residual (after 3 ns) transient absorption signal measured at 730 nm.

Cell	V_{OC} [V]	FF	J_{SC} [mA/m ²]	Eff [%]	$Total_APCE$	S_{res} (730 nm), 50 nJ
D149C_ZnO	0.61	0.36	0.80	0.17	0.11	0.0051
D149Si_ZnO	0.57	0.33	0.56	0.10	0.08	0.0036

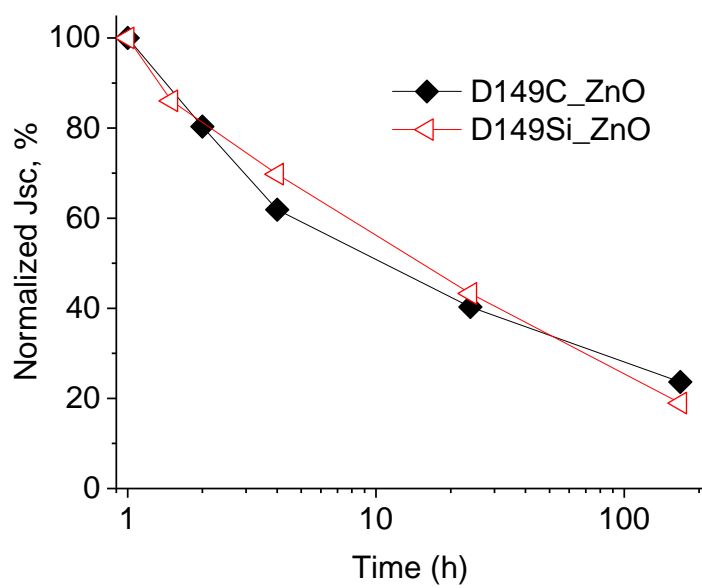


Figure S13. Decrease of the photocurrent with time for the cells with ZnO photoanodes and the two indoline dyes compared.

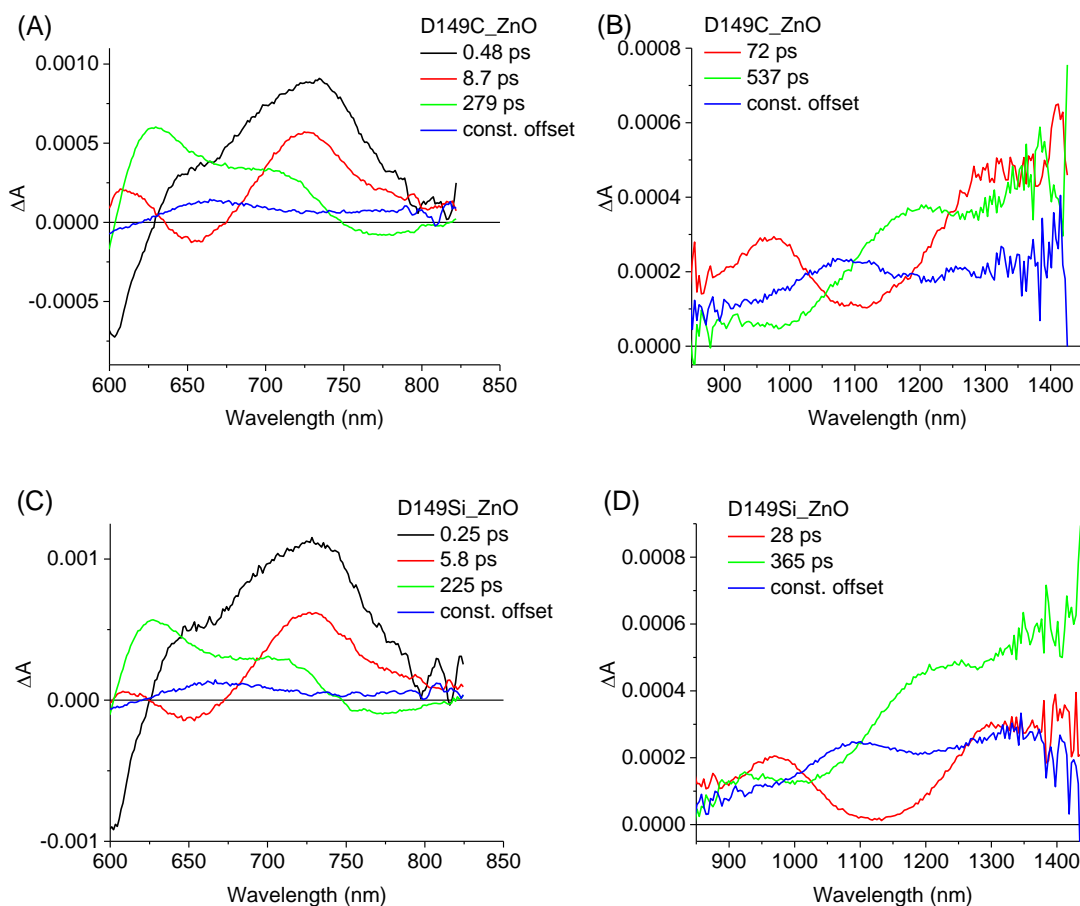
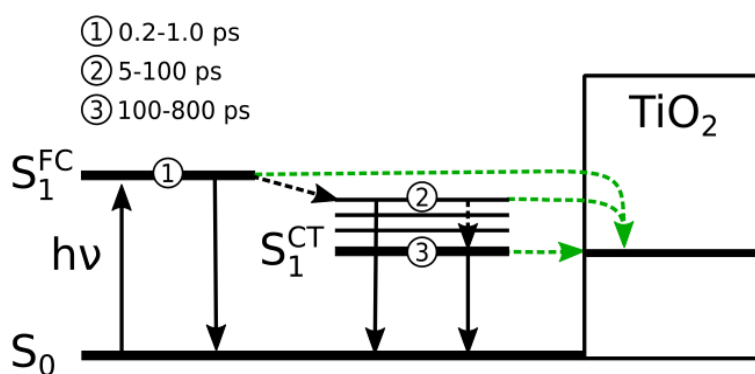


Figure S14. Wavelength dependent amplitudes of the indicated time constants obtained from global analysis of transient absorption spectra for ZnO cells sensitized with carboxyl-anchor (A, B) and alkoxysilyl-anchor (C, D) D149 dyes in the VIS (A, C) and NIR (B, D) spectral ranges. Pump pulse energy was 50 nJ, excitation at 555 nm.



Scheme S1. Schematic diagram of energy levels and charge transfer process upon photoexcitation of D149 dye in contact with electrolyte.

References:

- (1) Gierszewski, M.; Grądzka, I.; Glinka, A.; Ziółek, M. Insights into the Limitations of Solar Cells Sensitized with Ruthenium Dyes Revealed in Time-Resolved Spectroscopy Studies. *Phys. Chem. Chem. Phys.* **2017**, *19*, 20463–20473.
- (2) Sobuś, J.; Burdziński, G.; Karolczak, J.; Idígoras, J.; Anta, J. A.; Ziółek, M. Comparison of TiO₂ and ZnO Solar Cells Sensitized with an Indoline Dye: Time-Resolved Laser Spectroscopy Studies of Partial Charge Separation Processes. *Langmuir* **2014**, *30*, 2505–2512.
- (3) Sobuś, J.; Karolczak, J.; Komar, D.; Anta, J. A.; Ziółek, M. Transient States and the Role of Excited State Self-Quenching Of Indoline Dyes in Complete Dye-Sensitized Solar Cells. *Dye. Pigment.* **2015**, *113*, 692–701.
- (4) Idígoras, J.; Sobuś, J.; Jancelewicz, M.; Azaceta, E.; Tena-Zaera, R.; Anta, J. A.; Ziółek, M. Effect of Different Photoanode Nanostructures on the Initial Charge Separation and Electron Injection Process in Dye Sensitized Solar cells: A Photophysical Study with Indoline Dyes. *Mater. Chem. Phys.* **2016**, *170*, 218–228.

Paper IV

Interface Modification and Exceptionally Fast Regeneration in Copper Mediated Solar Cells Sensitized with Indoline Dyes.

Glinka, A.; Gierszewski, M.; Gierczyk, B.; Burdziński, G.; Michaels, H.; Freitag, M.; Ziółek, M.

J. Phys. Chem. C **2020**, *124*, 2895–2906.

Interface Modification and Exceptionally Fast Regeneration in Copper Mediated Solar Cells Sensitized with Indoline Dyes

Adam Glinka,* Mateusz Gierszewski, Błażej Gierczyk, Gotard Burdziński, Hannes Michaels, Marina Freitag, and Marcin Ziólek*

Cite This: *J. Phys. Chem. C* 2020, 124, 2895–2906

Read Online

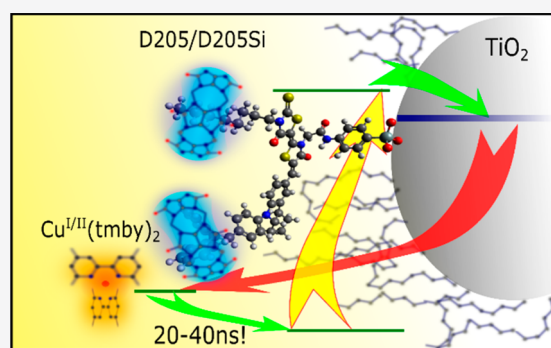
ACCESS |

Metrics & More

Article Recommendations

Supporting Information

ABSTRACT: The photovoltaic performance of solar cells sensitized with indoline D205 dye and its new derivative comprising an alkoxyethyl anchoring unit (D205Si) in the $[\text{Cu}(\text{tmby})_2](\text{TFSI})_{2/1}$ (tmby = 4,4',6,6'-tetramethyl-2,2'-bipyridine, TFSI = bis(trifluoromethane)sulfonimide) redox couple mediated systems was studied in the presence of various titania/dye/electrolyte interface modifications. Cucurbit[7]uril (CB7) was employed to encapsulate dye molecules, creating an electronically insulating layer, suppressing electron interception by redox mediator, and leading to the increase in the electron lifetime in the titania conduction band. For example, the electron lifetime increased from 2.2 to 6.5 ns upon CB7 encapsulation of D205 cells at 0.9 V voltage. Further, molecular multicapping was optimized to minimize dye desorption and prevent electron recombination. As a result, photovoltaic performance was found to be enhanced by the interface modifications in most cases, especially when applied to the alkoxyethyl anchoring derivative. The charge transfer processes (dye regeneration, titania-dye and titania-redox mediator recombination) in the above-mentioned system and in the reference $[\text{Co}(\text{bpy})_3](\text{TFSI})_{3/2}$ (bpy = 2,2'-bipyridine) redox couple mediated systems were investigated by means of small light perturbation electron lifetime measurements, electrochemical impedance spectroscopy, and nanosecond and femtosecond transient absorption spectroscopies. Indoline dyes were also found to be outstandingly fast regenerated by the Cu-based mediator (time constant shorter than 100 ns), which may open new opportunities for sensitizer improvements.



INTRODUCTION

Facing the effects of climate change and environmental pollution,^{1,2} abandonment of fossil fuel based energetics and turning to renewable energy sources is a necessity.³ Direct conversion of solar energy to electricity is one of the most promising ways of dealing with the current climate crisis; however, many technological challenges need to be overcome. Solving issues of energy storage and distribution, and efficient conversion have attracted tremendous interest from the scientific community. Dye sensitized solar cells⁴ (DSSCs) represent one of the third generation photovoltaic technologies, stimulating considerable research efforts⁵ aimed to provide higher stability (solid-state^{6–8}) and alternative applications (low light conditions and indoor applications).^{9,10} Increased performance in DSSCs can be reached by decreasing the overpotential losses and reducing recombination at the semiconductor/dye/electrolyte interface.⁸ Advances have been made in the field of alternative redox mediators based on coordination complexes (e.g., cobalt and copper)^{11,12} that use decreased voltage losses as compared to those based on iodide/triiodide (I^-/I_3^-), leading to open circuit voltages (V_{OC}) above 1.1 V in highly efficient copper complex mediated solar cells.^{6,13,14} High redox activity owed to one electron

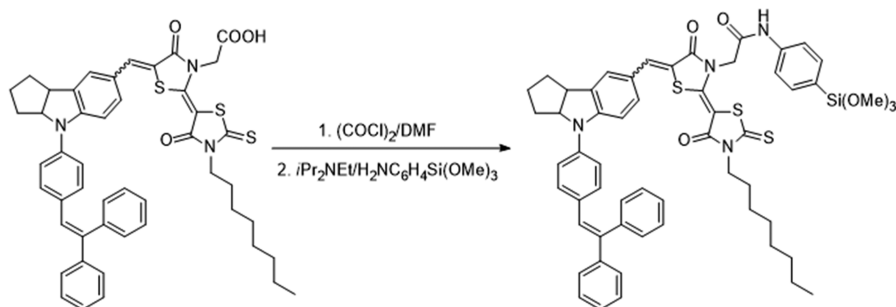
redox reactions and low reorganization energies in copper coordination complexes with modified ligand systems^{14,15} facilitates efficient dye regeneration, which is one of the photocurrent determining processes. However, enhanced redox activity allows easier recombination of electrons from the fluorine doped tin oxide (FTO) or from the titania conduction band (CB) and surface trap states.^{16,17} The widest used remedy for CB electron interception is the employment of dyes with bulky blocking moieties, alkyl chains and electron rich donor substituents,^{11,18} combined with the use of coadsorbing, electronically inert molecules (usually chenodeoxycholic acid, CDCA),¹⁹ insulating the TiO_2 surface from the contact with oxidized redox species. In particular, triphenylamine-based dyes have attracted interest thanks to the ease of synthesis, high extinction coefficients and broad absorption spectra, good photostability and temperature stability, and other features making them highly efficient

Received: December 20, 2019

Revised: January 9, 2020

Published: January 10, 2020

Scheme 1. Synthesis of D205Si Dye



photosensitizers.^{8,11,20–25} So far, the highest reported uncertified power conversion efficiencies (PCEs) of over 14% have been achieved for silyl-anchoring carbazole dye ADEKA-1 with the application of hierarchical molecular passivation, with the use of acids comprising alkyl chains of different lengths,^{26–28} which prevented electron recombination. In recent years, many different passivation techniques have been studied,²⁹ including molecular^{26,30–32} and atomic covering layers.^{32–34} However, to the best of our knowledge, there are very few systematic studies on molecular titania surface passivation and its effects on different charge transfer processes. Therefore, we have undertaken a study of the impact of several interface modifications, like the use of a dye anchoring unit, molecular capping, and encapsulation as well as alternate use of copper and cobalt complexes on the partial charge transfer steps occurring on time scales from femto-seconds to seconds.

We introduced a new silyl-anchoring D205Si sensitizer (Scheme 1), a derivative of the D205 dye, achieving a PCE of over 9% with I^-/I_3^- ,¹⁹ and we studied its photovoltaic properties in combination with $[Cu(tmby)_2]^{2+/+}$ ¹⁴ as a redox shuttle. As a reference system for these two indoline dyes, we used Y123 triphenylamine dye²⁴ (Scheme S1A in the Supporting Information, SI), well established in copper mediated systems. To find out more about the electronic structure of D205 and D205Si in their ground and excited states, density functional theory (DFT) and time-dependent DFT (TD-DFT) calculations were performed.

We further studied the effect of blocking the recombination processes on the semiconductor/dye/electrolyte interface by cucurbit[7]uril (CB7) molecules (Scheme S1B).³⁵ The CB7 compound belongs to the cucurbit[*n*]uril family of macrocyclic *n*-glycouril oligomers forming molecular cages in a similar manner as cyclodextrins.³⁶ The *n* = 7 homologue was chosen owing to its size (appropriate to encapsulate small organic moieties, e.g., aliphatic chains, but also bulkier, like phenyl rings³⁷) and fair solubility in water. Thanks to the ability of noncovalent binding to a variety of small molecules/guests through interactions with carbonyl-lined portal rims, CB7 can act as a molecular host for versatile applications, such as drug delivery, supramolecular polymers, catalysis, spectroscopy, or molecular machines.^{37–39} In this Article, we compared the CB7 effects with the results obtained when sequential molecular capping was applied and we found a higher increase in electron lifetime when the CB7 treatment was employed.

The recombination blocking properties were studied by means of electron lifetime measurements, electrochemical impedance spectroscopy (EIS), and nanosecond laser flash photolysis. The latter technique was also used to investigate dye regeneration kinetics. The results obtained for $[Cu-$

$(tmby)_2]^{2+/+}$ were compared with those collected for the systems employing $[Co(bpy)_3]^{2+/3+}$ as a redox mediator.

EXPERIMENTAL SECTION

Synthesis Route of D205Si. A solution of 50 mg of D205 dye (0.061 mM) in dry, deoxygenated chloroform (2 mL) was cooled to 5 °C. Then 8.9 mg (0.07 mM) of oxalyl chloride and 100 μ L of DMF were added. The mixture obtained was warmed to room temperature and stirred for over 2 h. After that, 13 mg of 4-(trimethoxysilyl)aniline (0.061 mM) and 17 mg (0.132 mM) of diisopropylethylamine were added. The purple-violet solution was stirred for over 2 h, and the product was precipitated with anhydrous methanol. The obtained solid was separated by centrifugation, washed with methanol, and dried in vacuum. The final product was a dark violet powder in the amount of 49 mg (yield: 78%) (Scheme 1).

The ¹H NMR spectrum is included in Figure S1A in the SI. ¹H NMR (CDCl₃, 298 K): δ 10.80 (bs, 1H; NH); 7.73 (s, 1H; SC=CHAr); 7.60 (bm, 4H; ArH-Si); 7.32 (m, 13H; ArH); 7.05 (m, 4H; ArH, =CH); 6.94 (d, 1H, 1.4 Hz; ArH); 6.93 (d, 1H, 8.4 Hz; ArH); 4.93 (s, 1H; CH₂CON); 4.85 (m, 2H; N-CH); 4.08 (m, 2H; NCH₂CH₂); 3.82 (m, 1H; ArCH); 3.61 (s, 9H; SiOCH₃); 1.2–2.2 (m, 18H; CH₂); 0.87 (t, 3H, 7.4 Hz; CH₃).

The ¹³C NMR spectrum is included in Figure S1B. ¹³C NMR in (CDCl₃, 298 K): δ 189.4 (C=S); 168.2 (CH₂CONH); 167.0 (C=O); 166.9 (C=O); 149.6 (NC=C); 146.7 (NAr^{C1}); 143.4; 141.6; 140.5; 139.7; 138.8 (SiAr^{C1}); 137.0 (SiAr^{C4}); 136.4; 135.6; 130.6; 130.3; 129.6 (SiAr^{C3}); 128.9; 128.2; 127.6; 127.5; 127.3; 124.2; 119.9 (SiAr^{C2}); 119.6 (NAr^{C2}); 113.23; 108.2; 93.7 (SC=C); 69.3 (cycloCH₂CHN); 50.8 (SiOCH₃); 46.3 (NCH₂CONH); 45.0 (cycloCH₂CHAr); 44.8 (CH₂N); 35.3 (cycloCH₂CHAr); 33.3 (cycloCH₂CHN); 31.7 (CH₂CH₂CH₂); 29.2 (CH₂CH₂CH₂); 30.0 (CH₂CH₂CH₂); 24.3 (cycloCH₂CH₂CH₂); 22.6 (CH₂CH₃); 14.1 (CH₂CH₃). Elemental analysis (%) calculated for C₅₇H₆₀N₄O₆S₃Si: C, 67.03; H, 5.92; N, 5.49; S, 9.42; found: C, 67.23; H, 5.66; N, 5.26; S, 9.33. Electrospray ionization mass spectrometry (ESI-MS) (*m/z*) calculated for C₅₇H₆₁N₄O₆S₃Si [*M* + H]⁺: 1021.3; found: 1021.3.

Computational Methods. Geometries of the studied molecules in the electronic ground state were optimized for both dyes in the gas phase using two different functionals, b3lyp and pbe1pbe, that had been used previously for theoretical calculations of D149 and D205 dyes^{40–44} together with a 6-31G(d) basis set in Gaussian 09.⁴⁵ The optimized geometries of D205 and D205Si have no imaginary frequencies, thereby representing an energy minimum. Assuming the optimized geometries of D205 and D205Si,

the shape and energy of molecular orbitals (MO), including HOMO and LUMO, were determined and the TD-DFT calculations were performed, both at the same levels of theory as DFT. Calculations of singlet–singlet excitations using the ground-state optimized geometries of D205 and D205Si allow description of the character of the $S_0 \rightarrow S_1$ electronic transitions. The calculated molecular orbitals (MO) were visualized using the Avogadro software.

Device Fabrication. Unless otherwise stated, all chemicals were purchased from Sigma-Aldrich. The dye Y123 and the copper coordination complexes were purchased from Dyname AB. TEC 15 FTO coated glass (Pilkington) was sequentially sonicated in aqueous RBS solution, pure deionized water, and ethanol, each step for 30 min. Afterward, a compact titania layer was deposited by spray pyrolysis of 0.2 M titanium tetraisopropoxide and 2 M acetylacetone solution in isopropanol, on the FTO heated up to 450 °C. Subsequently 4–5 μm (unless otherwise stated) mesoporous and 4–5 μm scattering layers were deposited by screen-printing. Samples for optical spectroscopy measurements were all prepared without the scattering layer. GreatCellSolar DSL 30 NRD-T paste containing 30 nm titania particles diluted with a saturated cellulose solution in α -terpineol at the ratio 4:1 was deposited. Subsequently, the layer was dried at 120 °C and GreatCellSolar WER2-0 paste containing 400 nm titania particles was screen-printed. Sintering was performed at 500 °C for 30 min and preceded by gradual stove warm up steps. After cooling down, the titania layers were immersed in 40 mM titanium tetrachloride aqueous solution at 70 °C for 30 min and sintered again in the same conditions as indicated previously.

Solutions of 0.1 mM of the dyes in an acetonitrile (ACN)/*tert*-butanol (*t*-BuOH) 1:1 mixture (for D205, D205Si and Y123 with 0.2 mM CDCA) were prepared. Sensitization was performed by immersing still warm (after sintering, 70–80 °C) photoanodes in the dye solution for 16 h at room temperature. Molecular multicapping (MC) was performed according to the following procedure (unless otherwise stated): sensitized photoanodes were sequentially immersed for 5 s in 1 mM solutions of lignoceric, stearic, heptanoic, and octylphosphonic acids in the ACN/toluene mixture. After each immersion, the photoanodes were rinsed with ACN. CB7 treatment was performed by overnight immersion of previously sensitized photoanodes in 0.5 mM CB7 solution in deionized water. Finally, the photoanodes were rinsed with water and ethanol (EtOH). The electrolyte solutions in ACN were prepared in the following concentrations: Cu-based, 0.2 M $[\text{Cu}(\text{tmbpy})_2]\text{TFSI}$, 0.04 M $[\text{Cu}(\text{tmbpy})_2](\text{TFSI})_2$, 0.1 M LiTFSI, 0.6 M *tert*-butylpyridine (TBP); and Co-based, 0.25 M $[\text{Co}(\text{bpy})_3](\text{TFSI})_2$, 0.035 M $[\text{Co}(\text{bpy})_3](\text{TFSI})_3$, 0.1 M LiTFSI, 0.5 M TBP.

For Cu-based mediated cells, the counter electrodes were fabricated by electropolymerization of 3,4-ethylenedioxythiophene (EDOT) from aqueous 0.01 mM solution containing 0.1 M sodium dodecyl sulfate (SDS). Co-based electrolyte cells were assembled using platinized counter electrodes which were fabricated by spreading activated platinum colloid (Platisol, Solaronix) on FTO glass using a paintbrush, followed by the same sintering procedure as described for titania. The assembly of cells was performed using 25 μm thick Surlyn frames, molten and pressed using a heat press from Heptachroma. The electrolyte was introduced by vacuum-injection through a predrilled hole in the counter electrodes and closed with cover

glass stuck by another piece of Surlyn. After cell assembly, electrical contacts were prepared using ultrasonic soldering station.

Dye and Device Characterization. Photoanodes were characterized by UV–vis absorption spectroscopy measurements performed using a JASCO V-770 spectrophotometer equipped with an LN-925 integrating sphere module working in the transmission mode. FT-IR ATR spectra of sensitized and CB7 treated titania films were acquired on a Thermo Electron. Corp. Nicolet 6700 FT-IR instrument. For photovoltaic characterization of the cells, a 0.16 cm^2 mask was used for accurate determination of the active solar cells surface. The $I(V)$ curves were obtained using a Keithley Source Meter 2400. Standard AM1.5G light conditions were provided by a Newport 91160 solar simulator. The monochromatic light for the incident photon to current conversion efficiency (IPCE) spectra was provided by an ASB-XE-175 xenon (10 mW cm^{-2}) light source focused on the entry slit of a CM110 Spectral Products monochromator. The photocurrent was measured using a LabJack U6 digital acquisition board. Both setups were calibrated using certified silicon reference cells from Fraunhofer ISE.

Electrochemical impedance spectroscopy (EIS) and cyclic voltammetry measurements were performed using an Autolab M101 potentiostat with an FRA32 M frequency analyzer module. Electrochemical cell consisted of a sensitized titania layer on FTO (working electrode), a platinum electrode (counter electrode) and Ag/AgNO₃ 0.01 M in ACN (reference electrode). As a supporting electrolyte, 0.1 M LiClO₄ in ACN was used. To calibrate the Ag/AgNO₃ electrode, 0.5 mM ferrocene solution in ACN was used. In order to obtain charge transfer resistance (R_{CT}) as a function of potential, the Nyquist impedance plots (measured for different bias voltages) were fitted using the transmission line model⁴⁶ in the ZView software. EIS measurements were performed for complete devices (two-electrode configuration).

Photoinduced absorption spectroscopy was performed using the setup described elsewhere.⁴⁷ Square modulated (9.33 Hz) LED (Luxeon Star 1W 460 nm –8 mW/cm^2 sample illumination intensity) pump and white probe lights (20 W tungsten–halogen 10 mW/cm^2 sample illumination intensity) were used. Transmitted probe light was focused on a monochromator (Acton Research Corporation SP-150) and detected via the UV-enhanced photodiode. The signal was extracted by a lock-in amplifier (Stanford Research Systems SR830) after previous amplification by a current amplifier (Stanford Research Systems SR 570).

Electron lifetimes were obtained using a Dyname Toolbox setup. Measurements were performed in open circuit conditions. A square wave modulated white light illumination was applied and the photovoltage response was acquired and analyzed by a dedicated software using the first order kinetics model.

Transient absorption kinetics in the nanosecond to millisecond time scale were recorded on a nanosecond flash photolysis setup based on a Q-switched Nd:YAG laser as the pump and a 150 W Xe arc lamp as the probe. The pump pulses were set to 532 nm wavelength with 0.2, 0.6, or 1.8 mJ energy. The probe spectrum was confined using a 10 nm at full width at half-maximum (fwhm) band-pass interference filter to limit the influence of high intensity probe light on the measured kinetics. The signal was detected by using a photomultiplier

(R928 Hamamatsu) coupled to a digital oscilloscope (Tektronix TDS 680 C).

The femtosecond transient absorption setup (HELIOS spectrometer, Ultrafast Systems and Spectra Physics femtosecond laser system) has been described in detail elsewhere.⁴⁸ The pump pulses were set to 505 nm wavelength with 50 or 200 nJ energy, which corresponds to 25 or 100 $\mu\text{J cm}^{-2}$ energy density, respectively. The instrument response function (IRF) duration was 0.3 ps at fwhm. The transient absorption data were analyzed in the Surface Explorer software (Ultrafast Systems) performing singular value decomposition and global analysis to obtain time constants of signal decays and wavelength dependent amplitudes related to them.

RESULTS AND DISCUSSION

Dye Characterization. Stationary absorption and emission spectra of D205 and D205Si dyes in ACN solution are shown in Figure S2. In order to characterize the energy levels of the studied dyes, the visible absorption spectra were taken (Figure S3) and cyclic voltammetry (Figure S4) was measured. The measurements were made on sensitized titania as it was more representative of DSSC system. The oxidized-dye/dye redox potentials of D205 and D205Si were found as -1.03 V vs SHE and -1.04 V vs SHE, respectively; thus, sufficient driving force for dye regeneration by both studied redox mediators was provided. The ΔE values and subsequently the LUMO levels were obtained on the basis of the absorption onset. The obtained values are juxtaposed in Figure 1. On average, the

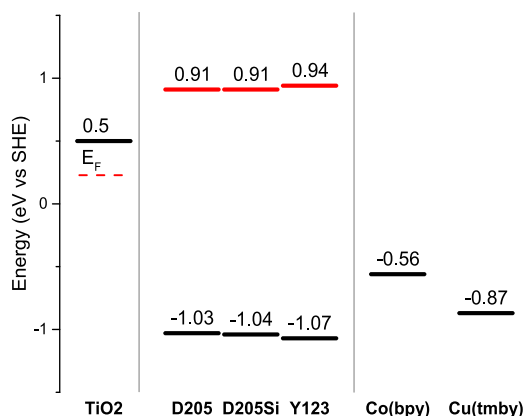


Figure 1. Diagram of energy level of HOMO measured by cyclic voltammetry (Figure S3) and LUMO calculated by addition of ΔE obtained from visible absorption measurements of dyes on TiO_2 (Figure S2). Y123 HOMO and LUMO as well as $[\text{Co}(\text{bpy})_3]^{2+/3+}$ and $[\text{Cu}(\text{tmby})_2]^{+/2+}$ redox potentials were taken from the literature.^{11,14,23}

absorbance at the maximum for the samples with D205Si is about 7% higher than that of D205 dye. It agrees with our previous observation for the silyl-modified D149 dye.³¹ The extinction coefficient (determined in ACN) is slightly lower for D205Si ($\sim 29\,000\ \text{M}^{-1}\ \text{cm}^{-1}$) than for D205 ($\sim 33\,000\ \text{M}^{-1}\ \text{cm}^{-1}$). Therefore, the higher absorbance of D205Si photoanodes can be explained by the stronger anchoring unit of D205Si dye, enhancing the dye loading.

To find out more about the character of the electronic transitions responsible for the absorption bands of D205 and D205Si, TD-DFT calculations were performed at the b3lyp/6-31G(d) and pbe1pbe/6-31G(d) levels. The computed

absorption maxima, oscillator strengths and coefficient values are included in Figure S5. The HOMO–LUMO energy gaps (ΔE) in D205 and D205Si are comparable, regardless of the applied functional. Namely, the energy gaps of 2.76 vs 2.73 eV were obtained for b3lyp/6-31G(d) and 3.04 vs 2.99 eV were calculated when using pbe1pbe/6-31G(d). We found that the calculations at the b3lyp/6-31G(d) level of theory resulted in a better correlation with the experimental absorption spectra maxima (520 and 518 nm for D205 and D205Si in *n*-hexane, respectively) than the data obtained at the level pbe1pbe/6-31G(d). It should be pointed out that differences in the values of oscillator strength and the coefficient of HOMO \rightarrow LUMO transition describing the electronic transition are negligible for both compounds at the same level of theory. It implies that the dye structure modification does not influence the character of electronic transitions, which is also confirmed by the calculated distributions of frontier HOMO and LUMO orbitals (Figure S6).

Interface Modifications. In the molecular multicapping (MC) procedure, the acid molecules are supposed to be adsorbed in the voids between dye molecules on the titania surface; however, an undesirable dye desorption process is difficult to avoid (Table S1 and Figure S7). To optimize the MC procedure, we started from that reported by us previously,³² adapted from the first reports of the MC procedure^{26–28} which employed a set of different type acids of various alkyl chain length and pK_a values (ensuring various steric and binding properties). Subsequently, we successively excluded the most desorbing compounds and shortened the exposure periods to maintain 90% of the dye load. To evaluate the MC influence on charge separation, regardless of the lower light harvesting efficiency of photoanodes, we fabricated batches of solar cells on a 2–3 μm mesoporous titania layer without a scattering layer to precisely measure the absorption spectra. Then we calculated the number of absorbed photons (N_{ph}) and the ratio of total absorbed photon to current efficiency, describing the relative photocurrent (total APCE), according to the following equations:^{32,49}

$$N_{\text{ph}} = \int_{400}^{800} (1 - 10^{-\text{Abs}(\lambda)}) \phi(\lambda) d\lambda \quad (1)$$

where $\phi(\lambda) = \text{AM 1.5 G photon flux}$.

$$\text{total APCE} = \frac{J_{\text{SC}}}{N_{\text{ph}} e} \quad (2)$$

where e is the elementary charge.

At this stage, an electrolyte containing $[\text{Co}(\text{bpy})_3]^{2+/3+}$ was used. As Figure 2 shows, only when the dye desorption is very slight (less than 10% of relative change in photoanodes maximal absorbance), the total APCE is enhanced (by 11% for D205 and 13% for D205Si), which is the result of both enhanced charge recombination resistance as well as accelerated dye regeneration kinetics, described in the following parts of this paper. Otherwise, a dramatic drop in the total APCE is observed, which indicates that too low dye/capping agent ratio facilitates unwanted recombination processes. Thus, we used the least harsh capping procedure (described in the Experimental Section) in our further experiments. A more detailed comparison of the impact of different acids on titania sensitized with D205 or D205Si is presented in Table S1 in the SI. It should be noted that, as expected, the alkoxy-silyl anchoring derivative of D205 dye was,

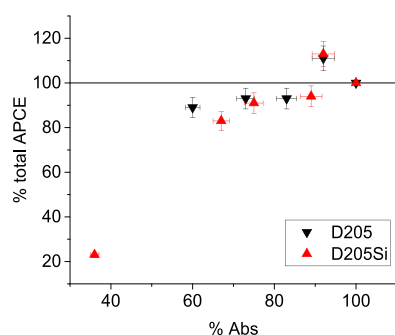


Figure 2. Percentage change in the total APCE as a function of the ratio of the absorption maxima of treated and untreated photoanodes (the points at % Abs = 100 correspond to the untreated ones). The errors were estimated by calculation of the standard deviation of mean values.

on average, 20% more stable against desorption from the titania surface. Additionally, we checked that the addition of CDCA to D205 and isooctyl trimethoxysilane (OTMS) to D205Si did not give a pronounced and unequivocal improvement of the device operation (Table S2). The number of absorbed dye molecules (N_{ph}) was not changed, and coadsorbates slightly decreased the total APCE and increased the fill factor (FF) of the cells. Therefore, no coadsorbates were employed in the further studies.

The effects of dye encapsulation by CB7 can be observed in the vis and IR spectroscopy measurements shown in Figure 3. The vis absorption reveals a 12 nm hypsochromic shift of the maximum (from 532 to 520 nm) which, however, does not affect the shape of the incident photon to current efficiency (IPCE) spectra (Figure S8). It is probable that the effect of polar electrolyte that can shift both spectra masks the differences observed for the isolated photoanodes. Furthermore, no desorption of the dye from titania surface occurred upon CB7 treatment, which is a significant advantage over the MC procedure. In the IR range, the spectra of D205 with CB7 show mostly the peaks assigned to CB7 with increased amplitude, which indicates that CB7 is certainly present on the surface and its amount is greater than that on the unsensitized film. Moreover, the intensities of the peaks attributed to D205 dye are diminished, which suggests that some moieties of the dye molecules are covered with CB7. Yet it is not possible to identify the encapsulation modes because of possible formation of a variety of feasible complexes. Furthermore, the changes in the binding mode and constant may occur dynamically when

dye molecules are oxidized after electron injection in the operating device when the distribution of charge of the dye molecule changes. The possibility of formation of different complexes discourages any attempts of quantifying the association constants in solution, since the basic requirements for application of continuous variation method are not satisfied.^{50,51}

Photovoltaic Performance. The photovoltaic parameters of the cells in Cu-based electrolyte are shown in Table 1. The power conversion efficiency (PCE) of the solar cells sensitized with indoline dyes is about 50% lower than that of Y123-sensitized cells (Table 1) due to a much lower J_{SC} but also because of V_{OC} reduction as a result of a much shorter electron lifetime in the conduction band of titania (Figure 4A). The differences in the electron lifetime are correlated to the electrochemical impedance results (Figures 5 and S9, and Table S3). The R_{CT} values measured during EIS in the dark show the electron recombination at the TiO_2 /electrolyte interface (the higher the resistance, the slower the recombination). The observed electron lifetimes of the cells with indoline dyes that are shorter than those of the cells with Y123 should be attributed to substantially different molecular structures of the dyes, i.e., the lack of bulky blocking moieties in the former two. Such moieties would prevent oxidized copper complexes from approaching the titania surface. Moreover, PCE of untreated cells sensitized with D205Si makes about 90% of its carboxylic-anchoring analogue, which is in line with our previous studies of indoline and carbazole silyl-anchoring dyes.^{31,32,49,52} This effect is probably due to the slightly less efficient initial charge separation for D205Si than D205 samples, which will be discussed in the section on femtosecond transient absorption.

When molecular multicapping (MC) was employed, the PCE rose slightly for D205 and greater for D205Si (about 10% relative rise) due to the J_{SC} enhancement, which can be explained by the rise in charge transfer resistance (R_{CT}) (Figure 5A,B) and, consequently, in the electron lifetime (Figure 4B). The photocurrent is also increased in Y123 sensitized cells; however, V_{OC} is decreased in this case, which resulted in slightly lower PCE. CB7 treatment enhanced V_{OC} of indoline dye cells (by 30 mV for D205 and 60 mV for D205Si) thanks to a greater rise of electron lifetime than that for MC cells (Figure 4B). For example, the electron lifetime increased from 2.2 to 6.5 ms upon CB7 encapsulation of D205 cells at 0.9 V voltage. Enhanced V_{OC} was also attributed to the rise of R_{CT} (Figure 5A, B). This led to a 13% relative rise of PCE of D205Si sensitized cells.

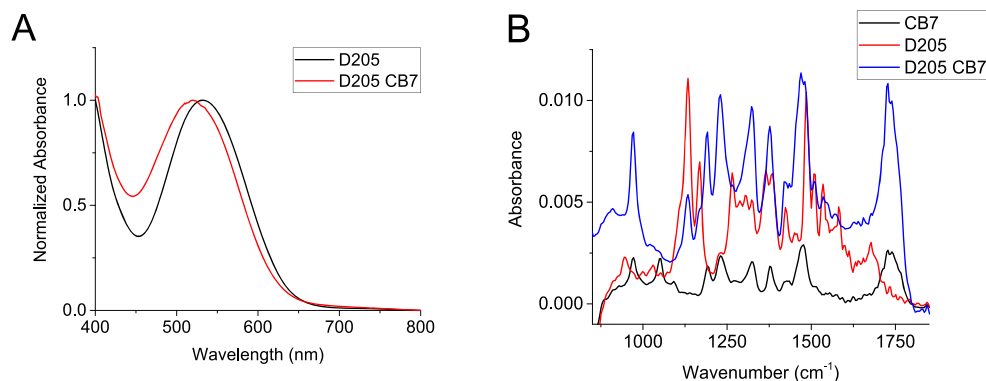


Figure 3. Visible absorption spectra (A) and FT-IR ATR spectra (B) of sensitized titania films (with titania contribution subtracted).

Table 1. Photovoltaic Parameters of the Studied Solar Cells^a

		pristine				MC				CB7			
		PCE [%]	V_{OC} [V]	J_{SC} [mA cm ⁻²]	FF	PCE [%]	V_{OC} [V]	J_{SC} [mA cm ⁻²]	FF	PCE [%]	V_{OC} [V]	J_{SC} [mA cm ⁻²]	FF
D205	best cell	4.70	0.90	6.52	0.80	5.00	0.90	6.70	0.82	4.60	0.92	6.12	0.82
	avg	4.43	0.89	6.25	0.79	4.57	0.89	6.33	0.81	4.38	0.92	5.86	0.82
	error	0.09	0.01	0.11	0.01	0.30	0.01	0.37	0.01	0.06	0.01	0.07	0.01
D205Si	best cell	4.19	0.92	6.07	0.75	4.61	0.89	6.54	0.79	4.75	0.95	6.40	0.78
	avg	3.92	0.89	5.76	0.77	4.37	0.88	6.22	0.80	4.41	0.95	5.98	0.78
	error	0.13	0.01	0.13	0.01	0.06	0.01	0.09	0.01	0.13	0.01	0.19	0.01
Y123	best cell	8.55	1.08	10.57	0.75	8.46	1.06	11.22	0.71	7.98	1.05	10.60	0.72
	avg	8.01	1.07	10.50	0.71	7.86	1.03	10.82	0.71	7.21	1.01	9.96	0.72
	error	0.18	0.01	0.12	0.01	0.24	0.01	0.19	0.01	0.28	0.02	0.34	0.01

^aPCE, power conversion efficiency; V_{OC} , open circuit voltage; J_{SC} , short circuit photocurrent density; FF, fill factor. Parameters were averaged from at least five devices. Errors were calculated as the standard deviation of a mean value.

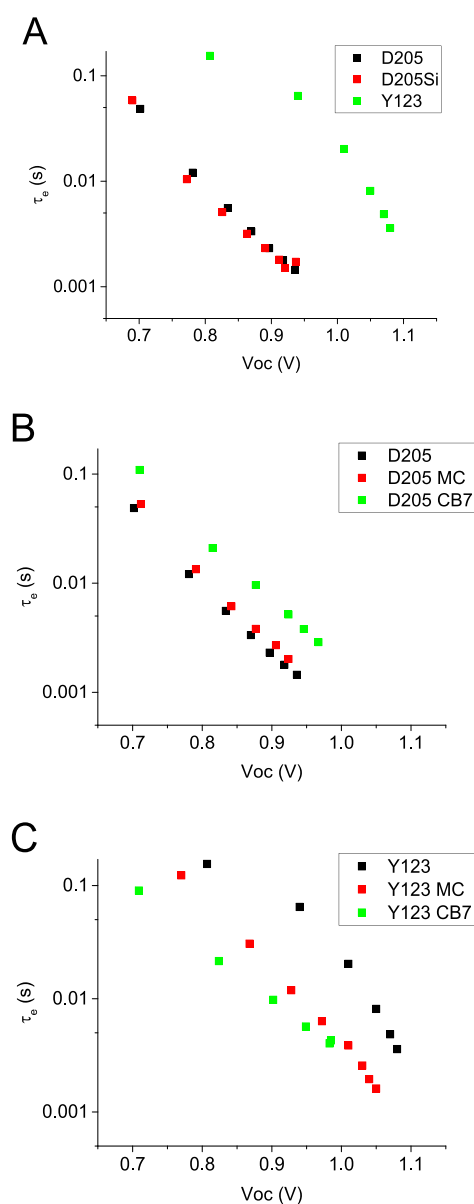


Figure 4. Small light perturbation electron lifetime measurements.

Unfortunately, both interface treatments diminished the electron lifetimes in Y123 sensitized cells, which resulted in

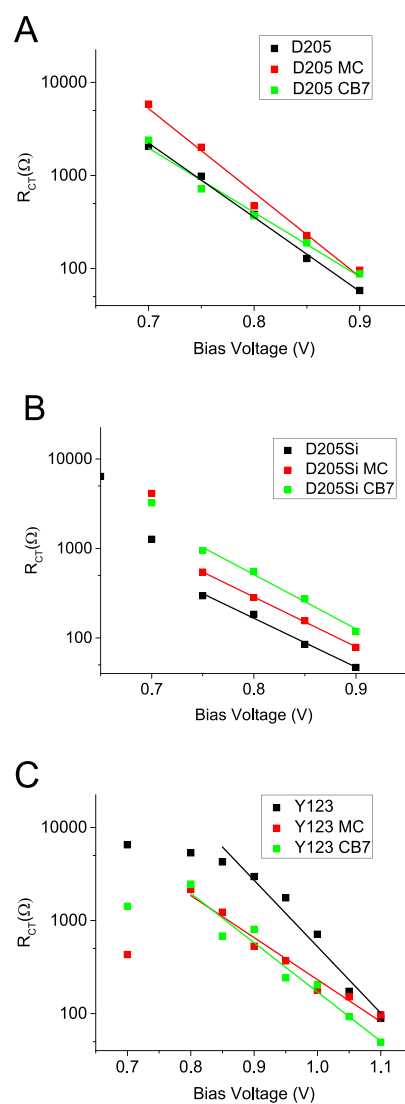


Figure 5. Charge transfer resistance extracted from EIS Nyquist plots.

lower V_{OC} of MC and CB7 treated systems with this dye. The recombination blocking properties of system employing Y123 were probably weakened, as can be deduced from the electron lifetime (Figure 4C) and R_{CT} (Figure 5C) measurements.

Photoinduced and Transient Absorption Spectroscopy. To determine the absorption spectra of the oxidized dye,

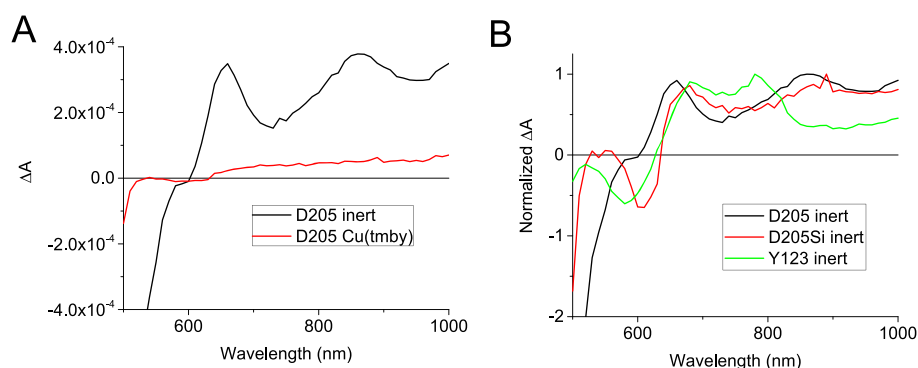


Figure 6. Photoinduced absorption spectra of D205 with inert electrolyte and in the presence of $[\text{Cu}(\text{tmby})_2]^{+2+}$ redox couple (A) and normalized photoinduced absorption spectra of dyes in the presence of inert electrolyte (B).

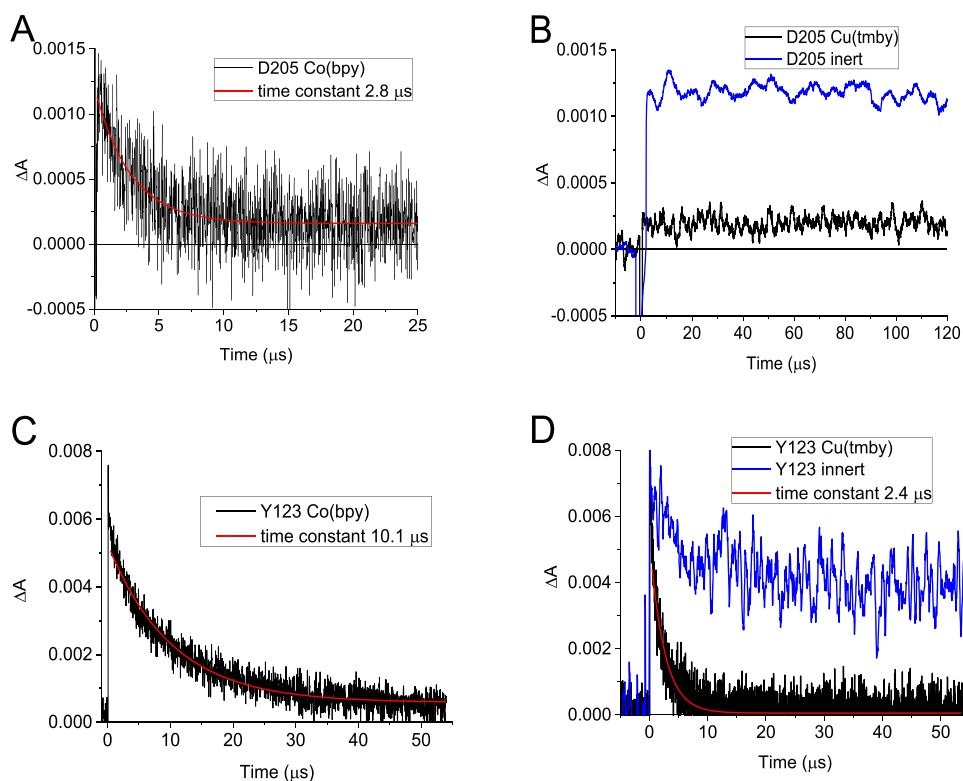


Figure 7. Transient absorption kinetics probed at $\lambda = 700$ nm. Pump pulse energy was 0.2 mJ, and $\lambda_{\text{pump}} = 532$ nm. Red lines show the best fit using a single exponential function with the indicated time constant.

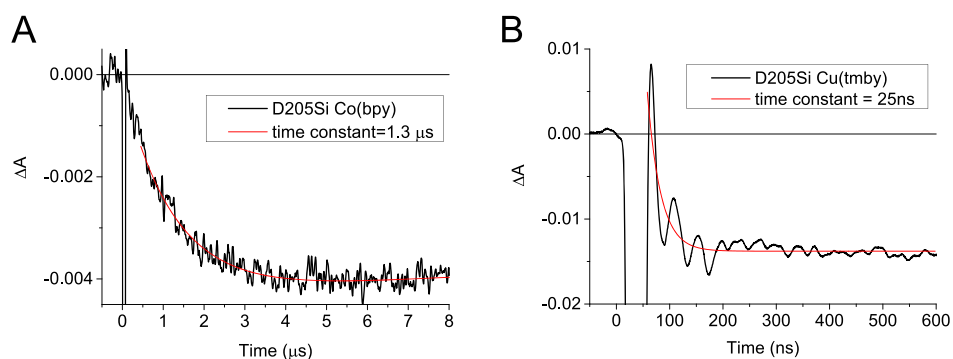


Figure 8. Transient absorption kinetics probed at $\lambda = 650$ nm. Red lines show the best fit using a single exponential function with the indicated time constant. Pump pulse energy was 0.6 and 1.8 mJ for $[\text{Co}(\text{bpy})_3]^{2+/3+}$ and $[\text{Cu}(\text{tmby})_2]^{+2+}$, respectively, and $\lambda_{\text{pump}} = 532$ nm.

we employed the photoinduced absorption (PIA) spectroscopy of photoanodes in the presence of an inert electrolyte (Figure 6). Indoline dyes show double band PIA spectra with onset between 600 and 640 nm. Below this range, we observed negative signals due to ground state bleach (which corresponded to the spectral range of stationary absorption band of these dyes) and a transient Stark shift of the dye absorption band induced by the electric field of electrons injected in titania.^{53–55} In the presence of redox couple, the PIA spectrum of oxidized D205 is reduced to low, positive but nonspecific absorption response of electrons injected to titania trap states. This change indicates efficient indoline dye regeneration by $[\text{Cu}(\text{tmby})_2]^{2+/+}$.

The dynamics of the oxidized state decay is the sum of the kinetics of electron recombination (taking place also in the samples with inert electrolyte) and the dye regeneration in full solar cells with an electrolyte containing a redox couple. In order to determine this dynamics, we used nanosecond flash photolysis and measured the kinetics of transient absorption at 700 nm (Figure 7) and 650 nm (Figure 8) wavelengths which are in the range of cation absorption of indoline and Y123 dyes (Figure 6). Measurements were performed on solar cells prepared without a scattering titania layer. Table 2 presents the

Table 2. Regeneration Times Statistics from Single Exponential Fits^a

cell configuration	time constant
D205 $[\text{Co}(\text{bpy})_3]^{2+/3+}$	$2.7 \pm 0.2 \mu\text{s}$
D205Si $[\text{Co}(\text{bpy})_3]^{2+/3+}$	$2.2 \pm 0.1 \mu\text{s}$
Y123 $[\text{Co}(\text{bpy})_3]^{2+/3+}$	$8.4 \pm 0.2 \mu\text{s}$
D205 MC $[\text{Co}(\text{bpy})_3]^{2+/3+}$	$2.3 \pm 0.2 \mu\text{s}$
D205Si MC $[\text{Co}(\text{bpy})_3]^{2+/3+}$	$2.2 \pm 0.3 \mu\text{s}$
Y123 MC $[\text{Co}(\text{bpy})_3]^{2+/3+}$	$6.9 \pm 0.3 \mu\text{s}$
D205/D205Si $[\text{Cu}(\text{tmby})_2]^{+/2+}$	$0.03 \pm 0.01 \mu\text{s}$
Y123 $[\text{Cu}(\text{tmby})_2]^{+/2+}$	$2.3 \pm 0.1 \mu\text{s}$
Y123 CB7 $[\text{Cu}(\text{tmby})_2]^{+/2+}$	$1.8 \pm 0.2 \mu\text{s}$

^aErrors were calculated as standard deviation from four measurements.

averaged time constants obtained by single exponential fit to the transient absorption decays at 700 nm for the full cells. For all cells with the $[\text{Co}(\text{bpy})_3]^{2+/3+}$ redox couple, the decays occur in the time scale of single microseconds. In this time scale, the signal coming from the inert samples is almost flat (e.g., Figure 7B, D). Moreover, the time constants do not change significantly for different pump pulse intensities (increasing pump pulse energy accelerates the electron recombination rates). Therefore, we can conclude that the regeneration efficiency is close to 100% for all studied systems and that the time constants in Table 2 represent the dye regeneration times.

The electron recombination between titania and the dye, measured in inert samples, takes place over many time scales. The average time constants from stretched exponential fit⁵⁶ (Figure S10 and Table S4) is in the sub-millisecond to single millisecond range. For example, for D205 at low pump pulse energy (0.15 mJ), the average time is 0.89 ms, and it decreases to about 0.39 ms for about four times higher excitation intensity (pump pulse energy 0.65 mJ). No changes in the recombination times are observed upon adding CB7 to indoline dye samples. In the same conditions, the averaged recombination time constants are slightly lower for Y123 (0.57

ms at 0.15 mJ and 0.24 ms at 0.65 mJ) and the decay is more stretched (smaller stretching parameter, see Table S3) than that for D205. Interestingly, for Y123, the recombination slows down on the time scale longer than 0.1 ms upon adding CB7, which results in higher average time constants (1.11 ms at 0.15 mJ and 0.27 ms at 0.65 mJ).

Nanosecond laser flash photolysis performed for the cells with $[\text{Co}(\text{bpy})_3]^{2+/3+}$ redox couple revealed that the dye regeneration was significantly faster in the cells sensitized with indoline dyes (2.7 and 2.2 μs for D205 and D205Si, respectively) as compared to that sensitized with Y123 (8.4 μs). It can be noted that the driving force is smaller for D205 and D205Si than for Y123 (Figure 1), so other factors (e.g., different reorganization energy) are responsible for faster regeneration in indoline dyes. A small difference (but greater than the measurement error, see Table 2) between the time constants of D205 and D205Si should be highlighted, which indicates that dye regeneration is slightly faster for alkoxyethyl derivative of D205. Furthermore, the MC procedure was found to accelerate slightly the dye regeneration in D205 and in Y123 sensitized cells (e.g., from 2.7 to 2.3 μs and from 8.4 to 6.9 μs , respectively), which should be attributed to the less polar dye environment contributing to lower outer-sphere reorganization energy and consequently faster dye regeneration.⁵⁷ The possible difference in the alignment of D205 and D205Si could probably explain the small difference in their regeneration times. Although the HOMO level of D205Si is slightly lower with respect to that of D205 (about 0.01 eV, Figure 1), it is rather too small to modify the regeneration time.

In the cells mediated by $[\text{Cu}(\text{tmby})_2]^{+/2+}$, for the Y123 reference cells, the 700 nm transient absorption decay time was determined to be 2.3 μs , which is consistent with literature results.¹⁴ CB7 interface modification was found to accelerate the regeneration slightly (to 1.8 μs). Strikingly, the regeneration kinetics could not be measured in the microsecond time scale for the cells sensitized with indoline dyes (both with and without CB7), which means that their regeneration time is significantly shorter. The signal at 700 nm for the samples with indoline dyes and $[\text{Cu}(\text{tmby})_2]^{+/2+}$ mediator is very low compared to that of oxidized species measured in the samples with indoline dyes and inert electrolyte (Figure 7B). It means that this small signal is only due to the electrons in titania and the dye regeneration took place faster, below 200 ns (which is determined by the time resolution of the flash photolysis setup and initial strong artifact signal due to pump scattering and/or stationary fluorescence of the dye, compare with Figure S2). It should be noted that a significantly faster regeneration time is observed also for Y123 dye when the redox couple is changed from $[\text{Co}(\text{bpy})_3]^{2+/3+}$ to $[\text{Cu}(\text{tmby})_2]^{+/2+}$, from 8.4 to 2.3 μs (Table 2). More detailed analysis of the transient absorption signal at a shorter wavelength (650 nm, for this wavelength the final signal is negative due to the transient Stark shift) indicates that the time constant for indoline dye regeneration by $[\text{Cu}(\text{tmby})_2]^{+/2+}$ is probably 20–40 ns (Figure 8). Such a time constant can be deduced from the single exponential kinetics fitted below 200 ns to the signal obscured by the oscillating artifact (Figure 8B). In electrolyte containing $[\text{Co}(\text{bpy})_3]^{2+/3+}$, the signal decay at 650 nm shows a similar character but is much longer (Figure 8A). The confirmation of the very short regeneration time constant for $[\text{Cu}(\text{tmby})_2]^{+/2+}$ will be

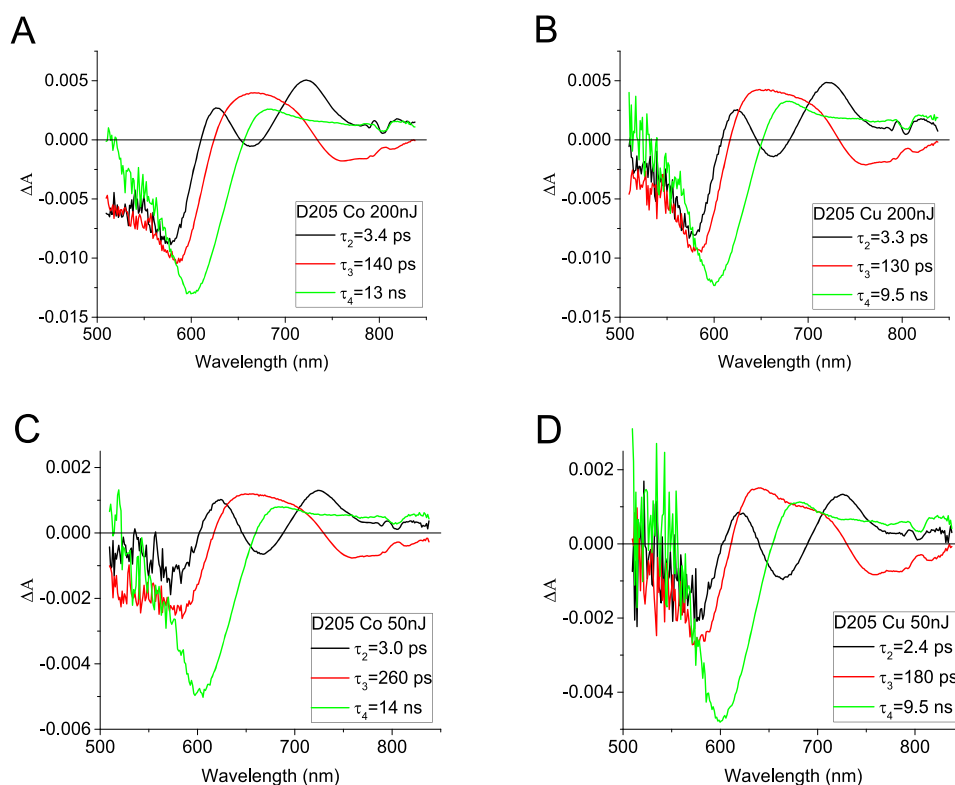


Figure 9. Results of the global fit to the femtosecond transient absorption data for the fresh D205 cells with Cu and Co mediated electrolytes at different pump pulse intensity ($\lambda_{\text{pump}} = 505 \text{ nm}$). Wavelength dependent amplitudes of transient absorption signal decays and time constants associated with them. The fastest component ($\tau_1 = 0.2 \text{ ps}$) is not shown for clarity.

provided by the femtosecond transient absorption data presented below.

To gain a deeper insight into the fast processes in D205 sensitized cells mediated by copper complexes, we performed transient absorption measurements in the time range 0.3–3000 ps. Broadband transient absorption data in 500–830 nm were subjected to global analysis, thereupon the time constants and wavelength dependent amplitudes associated with them were obtained. The transient absorption data were decomposed into four time constants with the fastest one (below temporal resolution of the setup) fixed to 0.2 ps (Figures 9 and S11). The interpretation of the time constants and the associated spectra follows from our previous assignments for solar cells with D149 and D358 indoline dyes.^{31,58,59} The smallest time constant (0.2 ps) is due to the decay of the initial short-living excited (Franck–Condon) state, while the second (3–6 ps) and the third (100–200 ps) time constants are assigned to the decay of the subsequent charge transfer (CT) state of the indoline dye. The spectra of Franck–Condon and CT states are similar to those measured for the free dyes in ACN solution (Figure S11E,F) with absorption maxima at 720 and 600 nm, respectively. Moreover, the decay of the CT state is accompanied by the negative amplitudes above 700 nm which are due to the disappearance of the stimulated emission from CT state (Figures S11E,F and S2) and the rise of the absorption of the oxidized dye (Figure 6). The decay of both states is due to the desired electron injection to titania and undesired self-quenching of the dyes. Therefore, upon increasing pump pulse intensity (more excited dyes on titania), the time constants decrease can be observed (e.g., compare Figures 9A vs C, 9B vs D, S11A vs C, and S11B vs D). Comparison of time constants obtained from global analysis of

TA data of $[\text{Co}(\text{bpy})_3]^{2+/3+}$ and $[\text{Cu}(\text{tmbpy})_2]^{+/2+}$ mediated cells does not show any significant difference in the fastest processes. It is not surprising as they are associated with dye–titania nanoparticle and dye–dye interactions rather than with the dye–redox complex charge transfers.

However, the slowest, fourth component (attributed mainly to the decay of the oxidized dye) is shorter for $[\text{Cu}(\text{tmbpy})_2]^{+/2+}$ than for $[\text{Co}(\text{bpy})_3]^{2+/3+}$ (9.5 vs 13–14 ns for the fresh cells, respectively, see Figure 9), which can be attributed to the partial contribution of fast dye regeneration in the transient absorption decay. Furthermore, no increase in the slowest component of the transient absorption decay for $[\text{Cu}(\text{tmbpy})_2]^{+/2+}$ when the pump energy is decreased (e.g., Figure 9B and D) may support its regenerative nature (unlike for $[\text{Co}(\text{bpy})_3]^{2+/3+}$ cell for which the fourth time constant increases for less intense pump pulse, e.g., Figure 9A and C). The charge recombination is a second order process, while the regeneration can be considered as the first order reaction in this time scale; thus, its kinetics is less prone to pump pulse energy changes. Figure S12 shows the examples of the fits to the decay traces of the kinetics vectors from global analysis, emphasizing the ability to distinguish between the 9.5 and 13–14 ns components in our setup. Interestingly, taking the longest time constant of 13 ns for $[\text{Co}(\text{bpy})_3]^{2+/3+}$ cells (only recombination contribution) and 9.5 ns for $[\text{Cu}(\text{tmbpy})_2]^{+/2+}$ cells (both recombination and regeneration), we can calculate the regeneration time constant of about 35 ns, which is in quite a good agreement with the estimation from nanosecond flash photolysis decay at 650 nm (Figure 8B). It should be noted that it is, as far as we know, the fastest ever observed interfacial dye regeneration process in DSSC with liquid single redox mediator electrolyte, not counting one report for a tandem

redox system, in which the first step of the regeneration (by the intermediate small electron donor) takes place in less than 1 ns.⁶⁰

Upon aging of the cells and with their photocurrent decreasing, the second and third time constants decrease (Figure S11A–D), which indicates more pronounced self-quenching. Moreover, the cells with D205Si dye also exhibit about 10% smaller time constants than the analogues with D205 (of the same electrolyte and age, e.g., compare Figures S11A with S13A). This suggests that the process of self-quenching is slightly more severe for alkoxysilyl derivative of D205 and this could be the reason for slightly worse photovoltaic performance of the untreated D205Si cells (with respect to the D205 ones). Interestingly, comparing different cells (fresh and old, with D205 and with D205Si), we find a good correlation between the total APCE parameter (indicating the charge separation efficiency) and the ratio of residual to the initial signal at 700 nm (proportional to the relative number of the oxidized dye with respect to the initially excited ones). Such a correlation is shown in Figure S13B. In particular, the total APCE and the residual signal at 700 nm of D205Si cells make about 80% of that of D205. Therefore, the slightly less efficient initial charge separation for D205Si than D205 samples can explain the lower photocurrent in the former samples, as indicated in the Photovoltaic Performance subsection.

CONCLUSIONS

In this study, we have shown the differences in charge transfer kinetics processes and overall solar cell efficiencies following from assuming specific approaches to titania–electrolyte recombination blocking. The solar cells were prepared using two different dyes: commercially available indoline dye, coded as D205, and its originally synthesized derivative with alkoxysilyl as an anchoring group (D205Si). Theoretical calculations indicated that the $S_0 \rightarrow S_1$ electronic transition showed the same intramolecular charge transfer character in both dyes. Molecular passivation of the titania surface by different acid molecules as well as macromolecular dye encapsulation can be applied to block charge recombination on the titania/dye/electrolyte interface. Moreover, it was confirmed that although the initial efficiency of solar cells sensitized with D205Si was lower, it was more prone to be enhanced by postassembly treatments. The attachment of D205Si to the titania surface was also found to be more stable than that of D205. Furthermore, both indoline dyes turned out to be regenerated outstandingly fast by the $[\text{Cu}(\text{tmby})_2]^{+2+}$ redox couple (in a few tens of ns). Thanks to the above-mentioned feature, the broad absorption spectrum and high robustness on the titania surface, our new D205Si dye can be considered as a promising cosensitizer in DSSC. The evidence of very fast regeneration (to the best of our knowledge, the fastest ever observed in liquid nontandem electrolyte DSSCs) should also be considered in further studies on new sensitizers dedicated to work with Cu-based redox systems.

ASSOCIATED CONTENT

Supporting Information

The Supporting Information is available free of charge at <https://pubs.acs.org/doi/10.1021/acs.jpcc.9b11778>.

NMR spectra; calculated HOMO and LUMO orbitals; absorption and emission spectra; cyclic voltammetry;

desorption tests; effects of coadsorbates; normalized IPCE spectra; EIS Nyquist plots and fitted parameters; recombination flash photolysis kinetics in inert samples; transient absorption of aged DSSCs and dyes in solution; correlation of total APCE and S_{res} parameters (PDF)

AUTHOR INFORMATION

Corresponding Authors

Adam Glinka – Quantum Electronics Laboratory, Faculty of Physics, Adam Mickiewicz University in Poznań, Poznań 61-614, Poland; orcid.org/0000-0002-1177-8534; Email: adagli@amu.edu.pl

Marcin Ziólek – Quantum Electronics Laboratory, Faculty of Physics, Adam Mickiewicz University in Poznań, Poznań 61-614, Poland; orcid.org/0000-0003-1882-6022; Email: marziol@amu.edu.pl

Authors

Mateusz Gierszewski – Quantum Electronics Laboratory, Faculty of Physics, Adam Mickiewicz University in Poznań, Poznań 61-614, Poland; orcid.org/0000-0003-3021-4117

Błażej Gierczyk – Faculty of Chemistry, Adam Mickiewicz University in Poznań, Poznań 61-614, Poland

Gotard Burdziński – Quantum Electronics Laboratory, Faculty of Physics, Adam Mickiewicz University in Poznań, Poznań 61-614, Poland; orcid.org/0000-0002-2947-1602

Hannes Michaels – Department of Chemistry, Ångström Laboratory, Uppsala University, Uppsala SE-75120, Sweden

Marina Freitag – Department of Chemistry, Ångström Laboratory, Uppsala University, Uppsala SE-75120, Sweden; Chemistry, School of Natural and Environmental Science, Bedson Building, Newcastle University, Newcastle upon Tyne NE1 8QB, United Kingdom; orcid.org/0000-0002-4954-6851

Complete contact information is available at: <https://pubs.acs.org/doi/10.1021/acs.jpcc.9b11778>

Notes

The authors declare no competing financial interest.

ACKNOWLEDGMENTS

This study was supported by the NCN (National Science Centre, Poland), under project 2015/18/E/ST4/00196. All theoretical calculations were performed at the PL-Grid project. Prof. Gerrit Boschloo from the Department of Chemistry, Ångström Laboratory, Uppsala University is kindly acknowledged for providing the opportunity of A.G.'s internship at the Ångström Laboratory.

REFERENCES

- (1) Dansgaard, W.; Johnsen, S. J.; Clausen, H. B.; Dahl-Jensen, D.; Gundestrup, N. S.; Hammer, C. U.; Hvidberg, C. S.; Steffensen, J. P.; Sveinbjörnsdóttir, A. E.; Jouzel, J.; et al. Evidence for General Instability of Past Climate from a 250-Kyr Ice-Core Record. *Nature* **1993**, *364*, 218–220.
- (2) Parmesan, C.; Yohe, G. A Globally Coherent Fingerprint of Climate Change Impacts across Natural Systems. *Nature* **2003**, *421*, 37–42.
- (3) Cox, P. M.; Betts, R. A.; Jones, C. D.; Spall, S. A.; Totterdell, I. J. Acceleration of Global Warming Due to Carbon-Cycle Feedbacks in a Coupled Climate Model. *Nature* **2000**, *408*, 184–187.

- (4) O'Regan, B.; Grätzel, M. A Low-Cost, High-Efficiency Solar-Cell Based on Dye-Sensitized Colloidal TiO₂ Films. *Nature* **1991**, *353*, 737–740.
- (5) Freitag, M.; Boschloo, G. The Revival of Dye-Sensitized Solar Cells. *Curr. Opin. Electrochem.* **2017**, *2*, 111–119.
- (6) Cao, Y.; Saygili, Y.; Ummadisingu, A.; Teuscher, J.; Luo, J.; Pellet, N.; Giordano, F.; Zakeeruddin, S. M.; Moser, J.-E.; Freitag, M.; et al. 11% Efficiency Solid-State Dye-Sensitized Solar Cells with Copper(II/I) Hole Transport Materials. *Nat. Commun.* **2017**, *8*, 15390.
- (7) Benesperi, I.; Michaels, H.; Freitag, M. The Researcher's Guide to Solid-State Dye-Sensitized Solar Cells. *J. Mater. Chem. C* **2018**, *6*, 11903–11942.
- (8) Zhang, W.; Wu, Y.; Bahng, H. W.; Cao, Y.; Yi, C.; Saygili, Y.; Luo, J.; Liu, Y.; Kavan, L.; Moser, J. E.; et al. Comprehensive Control of Voltage Loss Enables 11.7% Efficient Solid-State Dye-Sensitized Solar Cells. *Energy Environ. Sci.* **2018**, *11*, 1779–1787.
- (9) Freitag, M.; Teuscher, J.; Saygili, Y.; Zhang, X.; Giordano, F.; Liska, P.; Hua, J.; Zakeeruddin, S. M.; Moser, J.-E.; Grätzel, M.; et al. Dye-Sensitized Solar Cells for Efficient Power Generation under Ambient Lighting. *Nat. Photonics* **2017**, *11*, 372–378.
- (10) Cao, Y.; Liu, Y.; Zakeeruddin, S. M.; Hagfeldt, A.; Grätzel, M. Direct Contact of Selective Charge Extraction Layers Enables High-Efficiency Molecular Photovoltaics. *Joule* **2018**, *2*, 1108–1117.
- (11) Feldt, S. M.; Gibson, E. A.; Gabrielson, E.; Sun, L.; Boschloo, G.; Hagfeldt, A. Design of Organic Dyes and Cobalt Polypyridine Redox Mediators for High-Efficiency Dye-Sensitized Solar Cells. *J. Am. Chem. Soc.* **2010**, *132*, 16714–16724.
- (12) Bai, Y.; Yu, Q.; Cai, N.; Wang, Y.; Zhang, M.; Wang, P. High-Efficiency Organic Dye-Sensitized Mesoscopic Solar Cells with a Copper Redox Shuttle. *Chem. Commun.* **2011**, *47*, 4376.
- (13) Freitag, M.; Daniel, Q.; Pazoki, M.; Sveinbjörnsson, K.; Zhang, J.; Sun, L.; Hagfeldt, A.; Boschloo, G. High-Efficiency Dye-Sensitized Solar Cells with Molecular Copper Phenanthroline as Solid Hole Conductor. *Energy Environ. Sci.* **2015**, *8*, 2634–2637.
- (14) Saygili, Y.; Söderberg, M.; Pellet, N.; Giordano, F.; Cao, Y.; Muñoz-García, A. B.; Zakeeruddin, S. M.; Vlachopoulos, N.; Pavone, M.; Boschloo, G.; et al. Copper Bipyridyl Redox Mediators for Dye-Sensitized Solar Cells with High Photovoltage. *J. Am. Chem. Soc.* **2016**, *138*, 15087–15096.
- (15) Michaels, H.; Benesperi, I.; Edvinsson, T.; Muñoz-García, A. B.; Pavone, M.; Boschloo, G.; Freitag, M. Copper Complexes with Tetradentate Ligands for Enhanced Charge Transport in Dye-Sensitized Solar Cells. *Inorganics* **2018**, *6*, 53.
- (16) Feldt, S. M.; Cappel, U. B.; Johansson, E. M. J.; Boschloo, G.; Hagfeldt, A. Characterization of Surface Passivation by Poly-(Methylsiloxane) for Dye-Sensitized Solar Cells Employing the Ferrocene Redox Couple. *J. Phys. Chem. C* **2010**, *114*, 10551–10558.
- (17) Feldt, S. M.; Wang, G.; Boschloo, G.; Hagfeldt, A. Effects of Driving Forces for Recombination and Regeneration on the Photovoltaic Performance of Dye-Sensitized Solar Cells Using Cobalt Polypyridine Redox Couples. *J. Phys. Chem. C* **2011**, *115*, 21500–21507.
- (18) Saygili, Y.; Stojanovic, M.; Michaels, H.; Tjepelt, J.; Teuscher, J.; Massaro, A.; Pavone, M.; Giordano, F.; Zakeeruddin, S. M.; Boschloo, G.; et al. Effect of Coordination Sphere Geometry of Copper Redox Mediators on Regeneration and Recombination Behavior in Dye-Sensitized Solar Cell Applications. *ACS Appl. Energy Mater.* **2018**, *1*, 4950–4962.
- (19) Ito, S.; Miura, H.; Uchida, S.; Takata, M.; Sumioka, K.; Liska, P.; Comte, P.; Péchy, P.; Grätzel, M. High-Conversion-Efficiency Organic Dye-Sensitized Solar Cells with a Novel Indoline Dye. *Chem. Commun.* **2008**, *41*, 5194–5196.
- (20) Feldt, S. M.; Gibson, E. A.; Gabrielson, E.; Sun, L.; Boschloo, G.; Hagfeldt, A. Design of Organic Dyes and Cobalt Polypyridine Redox Mediators for High Efficiency Dye-Sensitized Solar Cells. *J. Am. Chem. Soc.* **2010**, *132*, 16714.
- (21) Feldt, S. M.; Lohse, P. W.; Kessler, F.; Nazeeruddin, M. K.; Grätzel, M.; Boschloo, G.; Hagfeldt, A. Regeneration and Recombination Kinetics in Cobalt Polypyridine Based Dye-Sensitized Solar Cells, Explained Using Marcus Theory. *Phys. Chem. Chem. Phys.* **2013**, *15*, 7087–7097.
- (22) Ellis, H.; Eriksson, S. K.; Feldt, S. M.; Gabrielson, E.; Lohse, P. W.; Lindblad, R.; Sun, L.; Rensmo, H.; Boschloo, G.; Hagfeldt, A. Linker Unit Modification of Triphenylamine-Based Organic Dyes for Efficient Cobalt Mediated Dye-Sensitized Solar Cells. *J. Phys. Chem. C* **2013**, *117*, 21029–21036.
- (23) Hao, Y.; Tian, H.; Cong, J.; Yang, W.; Bora, I.; Sun, L.; Boschloo, G.; Hagfeldt, A. Triphenylamine Groups Improve Blocking Behavior of Phenoxazine Dyes in Cobalt-Electrolyte-Based Dye-Sensitized Solar Cells. *ChemPhysChem* **2014**, *15*, 3476–3483.
- (24) Tsao, H. N.; Yi, C.; Moehl, T.; Yum, J. H.; Zakeeruddin, S. M.; Nazeeruddin, M. K.; Grätzel, M. Cyclopentadithiophene Bridged Donor-Acceptor Dyes Achieve High Power Conversion Efficiencies in Dye-Sensitized Solar Cells Based on the Tris-Cobalt Bipyridine Redox Couple. *ChemSusChem* **2011**, *4*, 591–594.
- (25) Jiang, N.; Sumitomo, T.; Lee, T.; Pellaroque, A.; Bellon, O.; Milliken, D.; Desilvestro, H. High Temperature Stability of Dye Solar Cells. *Sol. Energy Mater. Sol. Cells* **2013**, *119*, 36–50.
- (26) Kakiage, K.; Aoyama, Y.; Yano, T.; Otsuka, T.; Kyomen, T.; Unno, M.; Hanaya, M. An Achievement of over 12% Efficiency in an Organic Dye-Sensitized Solar Cell. *Chem. Commun.* **2014**, *50*, 6379–6381.
- (27) Kakiage, K.; Aoyama, Y.; Yano, T.; Oya, K.; Kyomen, T.; Hanaya, M. Fabrication of a High-Performance Dye-Sensitized Solar Cell with 12.8% Conversion Efficiency Using Organic Silyl-Anchor Dyes. *Chem. Commun.* **2015**, *51*, 6315–6317.
- (28) Kakiage, K.; Aoyama, Y.; Yano, T.; Oya, K.; Fujisawa, J.; Hanaya, M. Highly-Efficient Dye-Sensitized Solar Cells with Collaborative Sensitization by Silyl-Anchor and Carboxy-Anchor Dyes. *Chem. Commun.* **2015**, *51*, 15894–15897.
- (29) Shaikh, J. S.; Shaikh, N. S.; Mali, S. S.; Patil, J. V.; Pawar, K. K.; Kanjanaboos, P.; Hong, C. K.; Kim, J. H.; Patil, P. S. Nano-architectures in Dye-Sensitized Solar Cells: Metal Oxides, Oxide Perovskites and Carbon-Based Materials. *Nanoscale* **2018**, *10*, 4987–5034.
- (30) Aung, S. H.; Hao, Y.; Oo, T. Z.; Boschloo, G. 2-(4-Butoxyphenyl)-N-Hydroxyacetamide: An Efficient Pre-adsorber for Dye-Sensitized Solar Cells. *ACS Omega* **2017**, *2*, 1820–1825.
- (31) Gierszewski, M.; Glinka, A.; Grządka, I.; Gierczyk, B.; Ziólek, M. Testing New Concepts in Solar Cells Sensitized with Indoline Dyes—Alkoxy-silyl Anchoring Group, Molecular Capping, and Cobalt-Based Electrolyte. *J. Phys. Chem. C* **2018**, *122*, 25764–25775.
- (32) Gierszewski, M.; Glinka, A.; Grządka, I.; Jancelewicz, M.; Ziólek, M. Effects of Post-Assembly Molecular and Atomic Passivation of Sensitized Titania Surface: Dynamics of Electron Transfer Measured from Femtoseconds to Seconds. *ACS Appl. Mater. Interfaces* **2017**, *9*, 17102–17114.
- (33) Cheema, H.; Delcamp, J. H. Harnessing Photovoltage: Effects of Film Thickness, TiO₂ Nanoparticle Size, MgO and Surface Capping with DSCs. *ACS Appl. Mater. Interfaces* **2017**, *9*, 3050–3059.
- (34) Kim, D. H.; Losego, M. D.; Hanson, K.; Alibabaei, L.; Lee, K.; Meyer, T. J.; Parsons, G. N. Stabilizing Chromophore Binding on TiO₂ for Long-Term Stability of Dye-Sensitized Solar Cells Using Multicomponent Atomic Layer Deposition. *Phys. Chem. Chem. Phys.* **2014**, *16*, 8615–8622.
- (35) Freeman, W. A.; Mock, W. L.; Shih, N. Y. Cucurbituril. *J. Am. Chem. Soc.* **1981**, *103*, 7367–7368.
- (36) Choi, H.; Kang, S. O.; Ko, J.; Gao, G.; Kang, H. S.; Kang, M. S.; Nazeeruddin, M. K.; Grätzel, M. An Efficient Dye-Sensitized Solar Cell with an Organic Sensitizer Encapsulated in a Cyclodextrin Cavity. *Angew. Chem., Int. Ed.* **2009**, *48*, 5938–5941.
- (37) Barrow, S. J.; Kasera, S.; Rowland, M. J.; Del Barrio, J.; Scherman, O. A. Cucurbituril-Based Molecular Recognition. *Chem. Rev.* **2015**, *115*, 12320–12406.
- (38) Koner, A. L.; Nau, W. M. Cucurbituril Encapsulation of Fluorescent Dyes. *Supramol. Chem.* **2007**, *19*, 55–66.

- (39) Ni, X. L.; Xiao, X.; Cong, H.; Liang, L. L.; Cheng, K.; Cheng, X. J.; Ji, N. N.; Zhu, Q. J.; Xue, S. F.; Tao, Z. Cucurbit[n]Uril-Based Coordination Chemistry: From Simple Coordination Complexes to Novel Poly-Dimensional Coordination Polymers. *Chem. Soc. Rev.* **2013**, *42*, 9480–9508.
- (40) Ham, H. W.; Kim, Y. S. Theoretical Study of Indoline Dyes for Dye-Sensitized Solar Cells. *Thin Solid Films* **2010**, *518*, 6558–6563.
- (41) Lambert, C.; Mao, Y.; Zheng, Y.; Tao, X.; Hu, P.; Huang, M. Characterization of High-Performance Organic Dyes for Dye-Sensitized Solar Cell: A DFT/TDDFT Study. *Can. J. Chem.* **2016**, *94*, 1109–1118.
- (42) Howie, W. H.; Claeysens, F.; Miura, H.; Peter, L. M. Characterization of Solid-State Dye-Sensitized Solar Cells Utilizing High Absorption Coefficient Metal-Free Organic Dyes. *J. Am. Chem. Soc.* **2008**, *130*, 1367–1375.
- (43) Pastore, M.; De Angelis, F. Aggregation of Organic Dyes on TiO₂ in Dye-Sensitized Solar Cells Models: An Ab Initio Investigation. *ACS Nano* **2010**, *4*, 556–562.
- (44) Le Bahers, T.; Pauporte, T.; Scalmani, G.; Adamo, C.; Ciofini, I. A TD-DFT Investigation of Ground and Excited State Properties in Indoline Dyes Used for Dye-Sensitized Solar Cells. *Phys. Chem. Chem. Phys.* **2009**, *11*, 11276–11284.
- (45) Frisch, M. J.; Trucks, G. W.; Schlegel, H. B.; Scuseria, G. E.; Robb, M. A.; Cheeseman, J. R.; Scalmani, G.; Barone, V.; Mennucci, B.; Petersson, G. A.; et al. *Gaussian 09*, Revision E.01; Gaussian, Inc.: Wallingford, CT, 2013.
- (46) Fabregat-Santiago, F.; Garcia-Belmonte, G.; Mora-Seró, I.; Bisquert, J. Characterization of Nanostructured Hybrid and Organic Solar Cells by Impedance Spectroscopy. *Phys. Chem. Chem. Phys.* **2011**, *13*, 9083–9118.
- (47) Boschloo, G.; Hagfeldt, A. Photoinduced Absorption Spectroscopy as a Tool in the Study of Dye-Sensitized Solar Cells. *Inorg. Chim. Acta* **2008**, *361*, 729–734.
- (48) Idígoras, J.; Burdziński, G.; Karolczak, J.; Kubicki, J.; Oskam, G.; Anta, J. A.; Ziólek, M. The Impact of the Electrical Nature of the Metal Oxide on the Performance in Dye-Sensitized Solar Cells: New Look at Old Paradigms. *J. Phys. Chem. C* **2015**, *119*, 3931–3944.
- (49) Sobuś, J.; Gierczyk, B.; Burdziński, G.; Jancelewicz, M.; Polanski, E.; Hagfeldt, A.; Ziólek, M. Factors Affecting the Performance of Champion Silyl-Anchored Carbazole Dye Revealed in the Femtosecond to Second Studies of Complete ADEKA-1 Sensitized Solar Cells. *Chem. - Eur. J.* **2016**, *22*, 15807–15818.
- (50) Brynn Hibbert, D.; Thordarson, P. The Death of the Job Plot, Transparency, Open Science and Online Tools, Uncertainty Estimation Methods and Other Developments in Supramolecular Chemistry Data Analysis. *Chem. Commun.* **2016**, *52*, 12792–12805.
- (51) Ulatowski, F.; Dabrowa, K.; Balakier, T.; Jurczak, J. Recognizing the Limited Applicability of Job Plots in Studying Host – Guest Interactions in Supramolecular Chemistry. *J. Org. Chem.* **2016**, *81*, 1746–1756.
- (52) Glinka, A.; Gierszewski, M.; Ziólek, M. Effects of Aqueous Electrolyte, Active Layer Thickness and Bias Irradiation on Charge Transfer Rates in Solar Cells Sensitized with Top Efficient Carbazole Dyes. *J. Phys. Chem. C* **2018**, *122*, 8147–8158.
- (53) Cappel, U. B.; Feldt, S. M.; Schöneboom, J.; Hagfeldt, A.; Boschloo, G. The Influence of Local Electric Fields on Photoinduced Absorption in Dye-Sensitized Solar Cells. *J. Am. Chem. Soc.* **2010**, *132*, 9096–9101.
- (54) Ardo, S.; Sun, Y.; Staniszewski, A.; Castellano, F. N.; Meyer, G. J. Stark Effects after Excited-State Interfacial Electron Transfer at Sensitized TiO₂ Nanocrystallites. *J. Am. Chem. Soc.* **2010**, *132*, 6696–6709.
- (55) Burdziński, G.; Karolczak, J.; Ziólek, M. Dynamics of Local Stark Effect Observed for a Complete D149 Dye-Sensitized Solar Cell. *Phys. Chem. Chem. Phys.* **2013**, *15*, 3889–3896.
- (56) Nelson, J.; Haque, S. A.; Klug, D. R.; Durrant, J. R. Trap-Limited Recombination in Dye-Sensitized Nanocrystalline Metal Oxide Electrodes. *Phys. Rev. B: Condens. Matter Mater. Phys.* **2001**, *63*, 1–9.
- (57) Vaissier, V.; Barnes, P.; Kirkpatrick, J.; Nelson, J. Influence of Polar Medium on the Reorganization Energy of Charge Transfer between Dyes in a Dye Sensitized Film. *Phys. Chem. Chem. Phys.* **2013**, *15*, 4804–4814.
- (58) Sobuś, J.; Karolczak, J.; Komar, D.; Anta, J. A.; Ziólek, M. Transient States and the Role of Excited State Self-Quenching of Indoline Dyes in Complete Dye-Sensitized Solar Cells. *Dyes Pigm.* **2015**, *113*, 692–701.
- (59) Idígoras, J.; Sobuś, J.; Jancelewicz, M.; Azaceta, E.; Tena-Zaera, R.; Anta, J. A.; Ziólek, M. Effect of Different Photoanode Nanostructures on the Initial Charge Separation and Electron Injection Process in Dye Sensitized Solar Cells: A Photophysical Study with Indoline Dyes. *Mater. Chem. Phys.* **2016**, *170*, 218–228.
- (60) Hao, Y.; Yang, W.; Zhang, L.; Jiang, R.; Mijangos, E.; Saygili, Y.; Hammarstrom, L.; Hagfeldt, A.; Boschloo, G. A Small Electron Donor in Cobalt Complex Electrolyte Significantly Improves Efficiency in Dye-Sensitized Solar Cells. *Nat. Commun.* **2016**, *7*, 1–8.

Supporting Information

for

Interface Modification and Exceptionally Fast Regeneration in Copper Mediated Solar Cells Sensitized with Indoline Dyes

Adam Glinka*¹, Mateusz Gierszewski¹,
Błażej Gierczyk², Gotard Burdziński¹, Hannes Michaels³,
Marina Freitag^{3,4} and Marcin Ziółek*¹

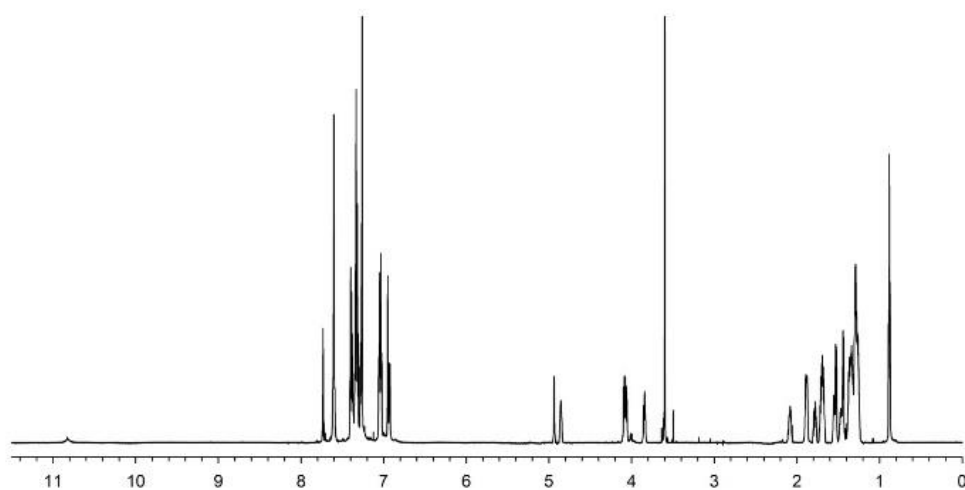
¹ *Quantum Electronics Laboratory, Faculty of Physics, Adam Mickiewicz University in Poznań, Uniwersytetu Poznańskiego 2, 61-614 Poznań, Poland.*

² *Faculty of Chemistry, Adam Mickiewicz University in Poznań, Uniwersytetu Poznańskiego 8, 61-614, Poznań, Poland.*

³ *Department of Chemistry, Ångström Laboratory, Uppsala University, P.O. Box 523, SE-75120 Uppsala, Sweden*

⁴ *Chemistry, School of Natural and Environmental Science, Bedson Building, Newcastle University, NE1 8QB Newcastle upon Tyne, UK*

A



B

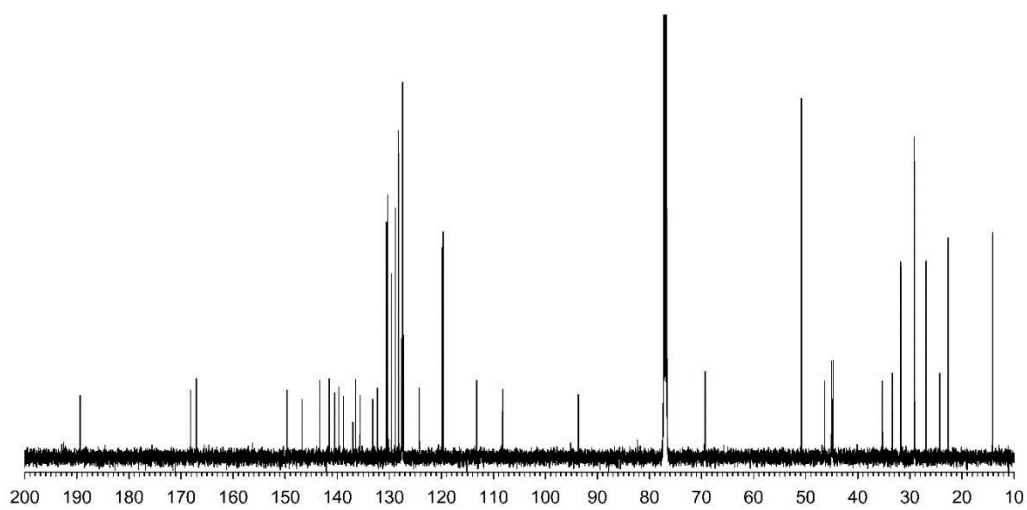
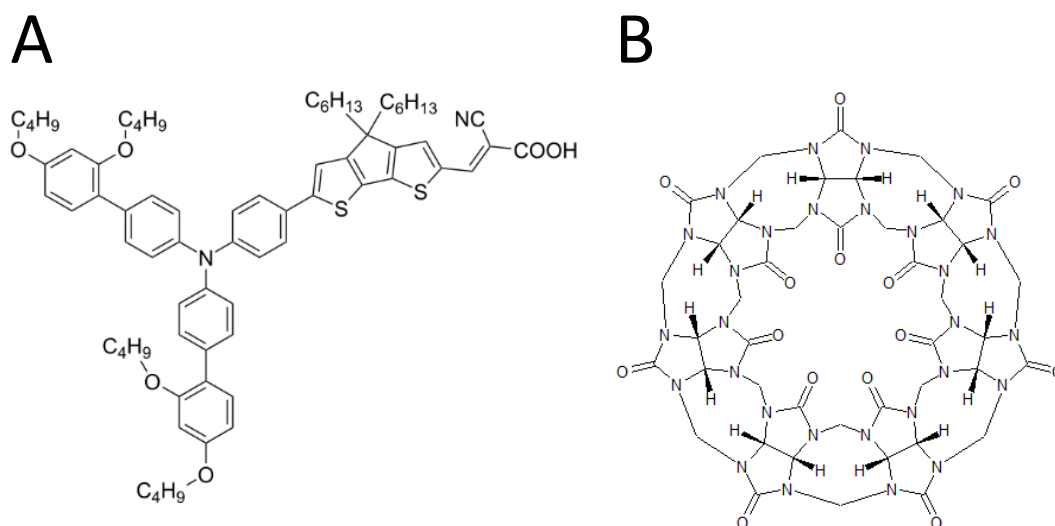


Figure S1. ^1H NMR spectrum of D205Si dye in CDCl_3 (A), ^{13}C NMR spectrum of D205Si dye in CDCl_3 (B).



Scheme S1. Y123 dye (A) and Cucurbit[7]uril (B) structures.

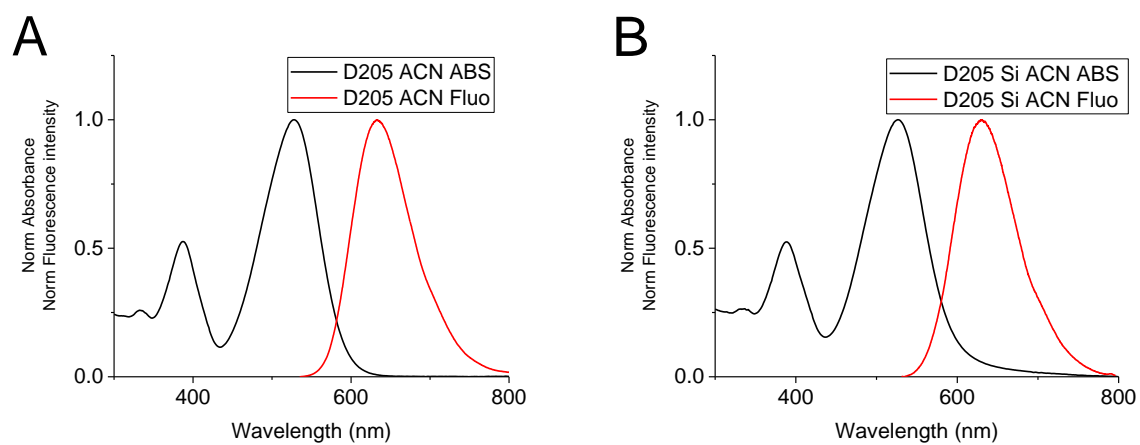


Figure S2. Visible absorption and fluorescence spectra of D205 and D205Si 10^{-5} M solutions in ACN. Fluorescence spectra were measured on Hitachi F-7000 Fluorescence spectrometer. The spectral slits were set to 2.5 nm and the excitation wavelength was set to 525 nm.

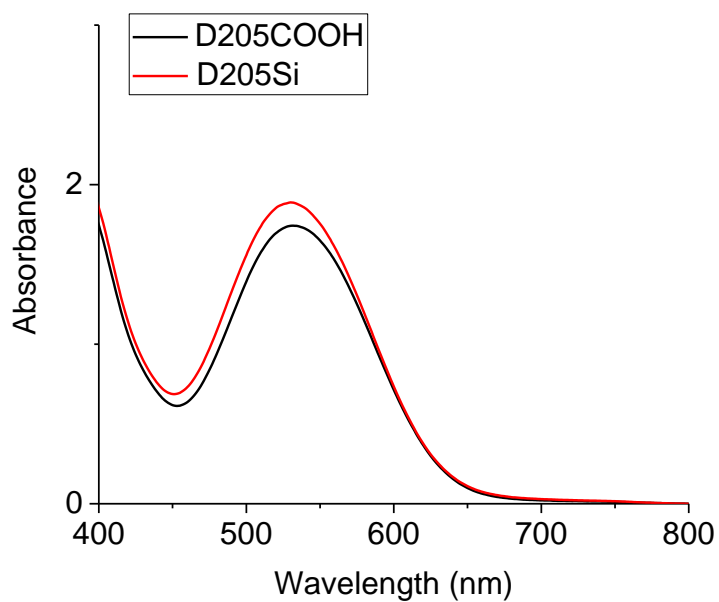


Figure S3. Visible absorption spectra of mesoporous titania films sensitized with D205 and D205Si dyes.

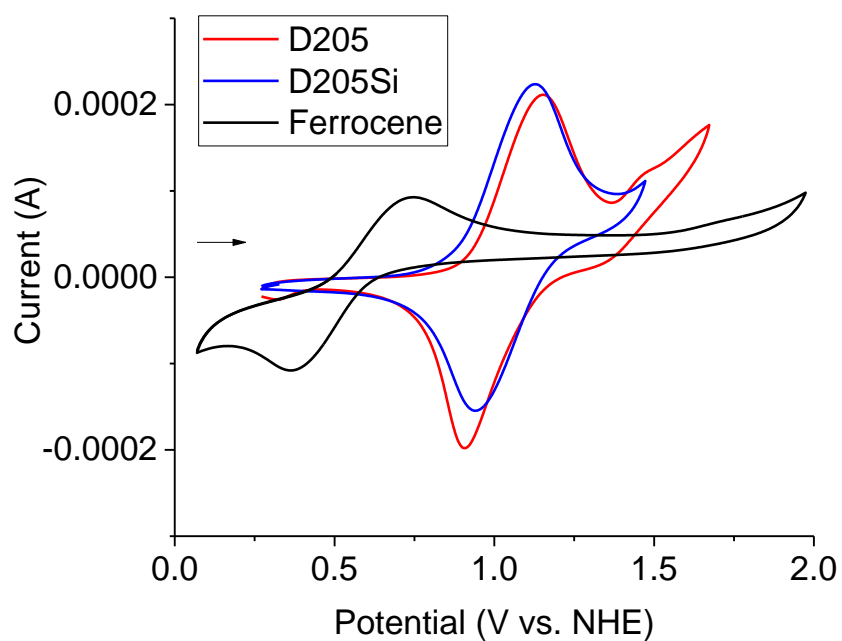


Figure S4. Cyclic voltammetry of dyes adsorbed on titania surface and ferrocene in solution.

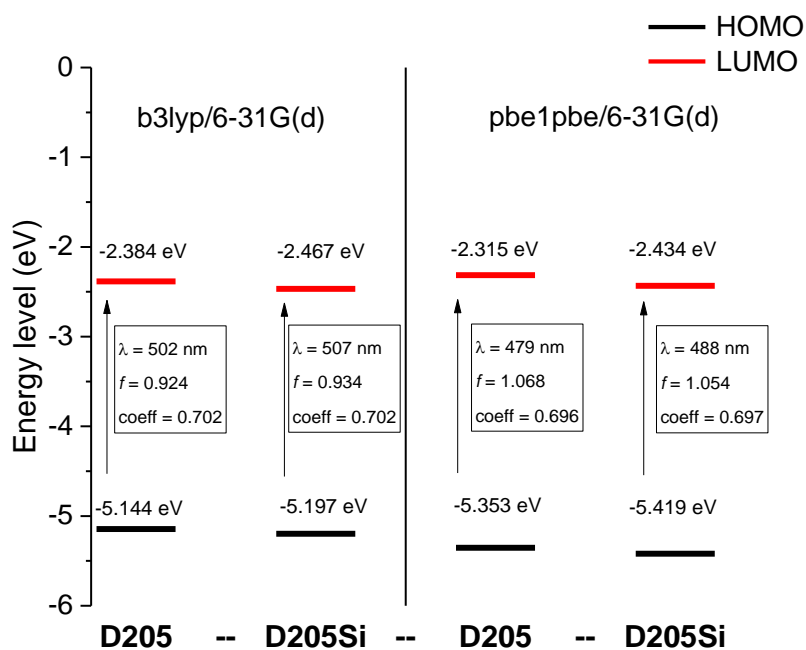


Figure S5. Diagram of energy level of HOMO and LUMO calculated at the b3lyp/6-31G(d) and pbe1pbe/6-31G(d) levels of theory for D205 and D205Si. The calculated values of wavelength of $S_0 \rightarrow S_1$ electronic transitions (λ), oscillator strength for this transition (f) and coefficient of HOMO \rightarrow LUMO transition were included. Energy gap (ΔE) between HOMO and LUMO of D205 and D205Si are comparable regardless of applied functional.

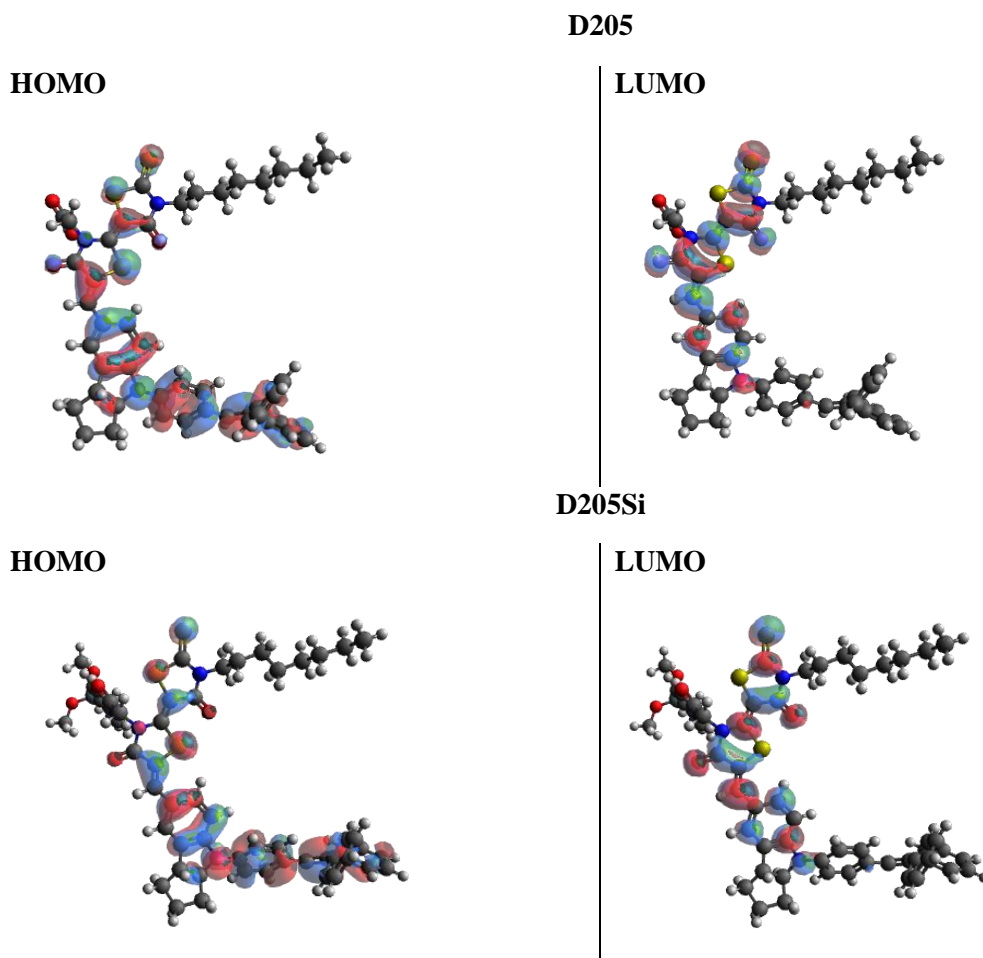


Figure S6. The distribution of HOMO and LUMO of D205 and D205Si at b3lyp/6-31G(d) theory level responsible for the $S_0 \rightarrow S_1$ electronic transition determined as isodensity surface plots.

To find the lowest-energy conformers of D205 molecule, by the first step, the possible structures were studied for D149 indoline dyes due to simpler structure. D149 and D205 dyes have the same chromophore system, however instead of an *n*-octyl group onto the rhodamine ring (D205) has an ethyl group (D149). After finding the lowest-energy conformer of D149 molecule, the alkyl substituent by the rhodamine ring was changed from ethyl- to octyl- one giving finally D205 molecule. In this form, finally the geometry in the gas phase as isolated molecules were optimized at b3lyp/6-31G(d) and pbe1pbe/6-31G(d) levels of theory. The D205Si molecule was obtained by the change of the carboxyl group, in D205 molecule, to the phenyl-amide moiety with trimethoxysilyl as an anchoring group.

Table S1.

Dyes' desorption tests in different acids at 1 mM concentration in ACN:TOL 1:1. Percentage of the initial maximal absorbance (~ 531nm) left after the indicated acid treatments. The last column presents the ratio of the percentage values of D205Si and D205 dyes, thus indicating by how much the alkoxysilyl dye is more stable.

Acid, time	D205 Si, %	D205 C, %	D205Si/D205
Stearic, 30 min	94	83	1.13
Stearic, 240 min	87	70	1.24
Lignoceric, 30 min	96	89	1.08
Lignoceric, 240 min	92	81	1.13
Tert butyl phosphonic, 30 min	78	65	1.20
Octadecylsulfonic, 30 min	79	65	1.22
Octadecylsulfonic, 60 min	73	51	1.43
Ocytylphosphonic, 30 min	83	62	1.34
Hexadecanoic, 30 min	86	81	1.06
Heptanoic, 30 min	95	87	1.09
Error	1	1	0.02

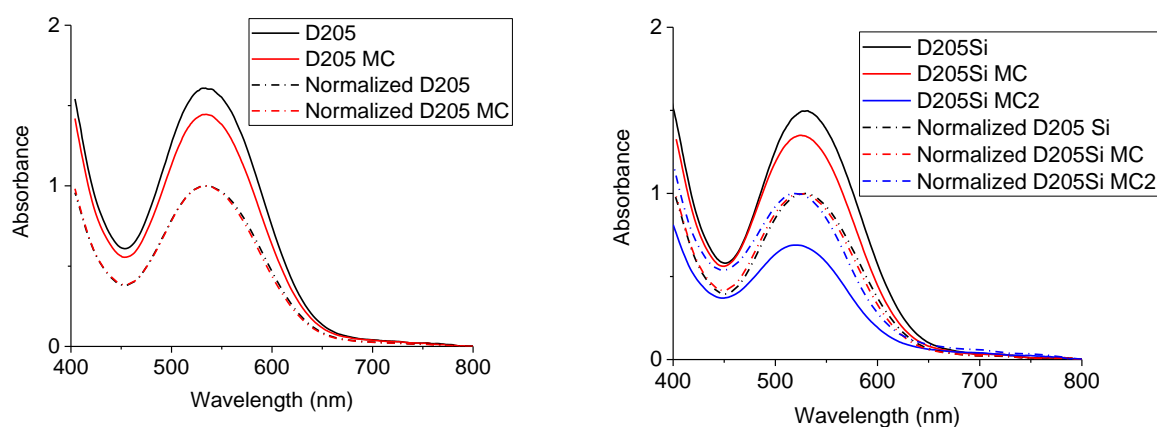


Figure S7. Absorption spectra of sensitized mesoporous titania films subjected to MC procedure. MC2 stands for extended multi-capping procedure. Extended multi-capping procedure was as follows: Lignoceric Acid – 2 min, stearic acid – 2min, tetradecyl phosphonic acid – 1 min, octyl phosphonic acid – 0.5 min, heptanoic acid – 1 min, *tert*-butyl phosphonic acid – 1 min, etylophosphonic acid 0.5 min. All acids solutions were prepared in 1mM concentration in ACN:Tol 1:1 mixture.

Table S2. Photovoltaic performance of solar cells sensitized with D205 and D205Si with and without addition of co-adsorbate (cheno-deoxycholic acid (CDCA) and isooctyl trimetoxysilane (OTMS)). The cells were prepared with thin (2-3 μm) transparent titania layer from DN-GPS-30TS paste (Dynamo) so the parameters cannot be directly compared with those in Table 1). The errors were estimated by calculation of the standard deviation of mean values.

Cell	Voc [V]	FF	Jsc [mA cm^{-2}]	EFF [%]	NPh [$10^{20}\text{s}^{-1} \text{m}^{-2}$]	ABS @ 530 nm	Total APCE
C_Co	0.86	0.54	6.9	3.2	7.9	1.8	0.54
C_CDCA_Co	0.86	0.57	6.4	3.1	7.8	1.8	0.52
Si_Co	0.83	0.49	6.1	2.4	8.2	2.0	0.46
Si_OTMS_Co	0.84	0.57	5.4	2.6	8.4	2.1	0.40
Error	0.01	0.03	0.3	0.2	0.1	0.1	0.02

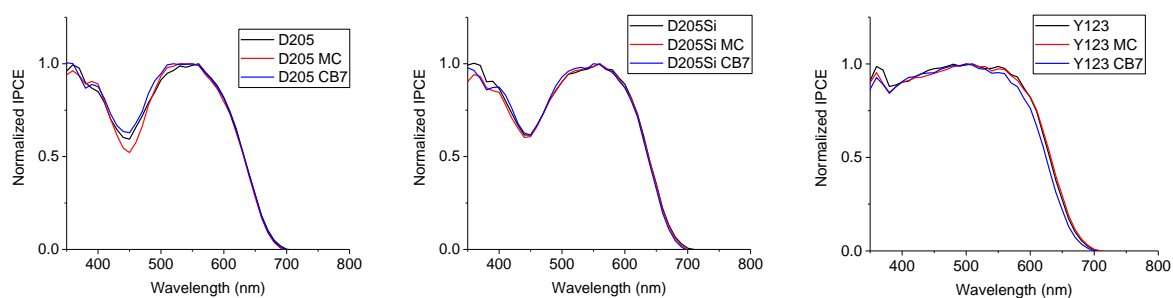


Figure S8. Normalized IPCE spectra.

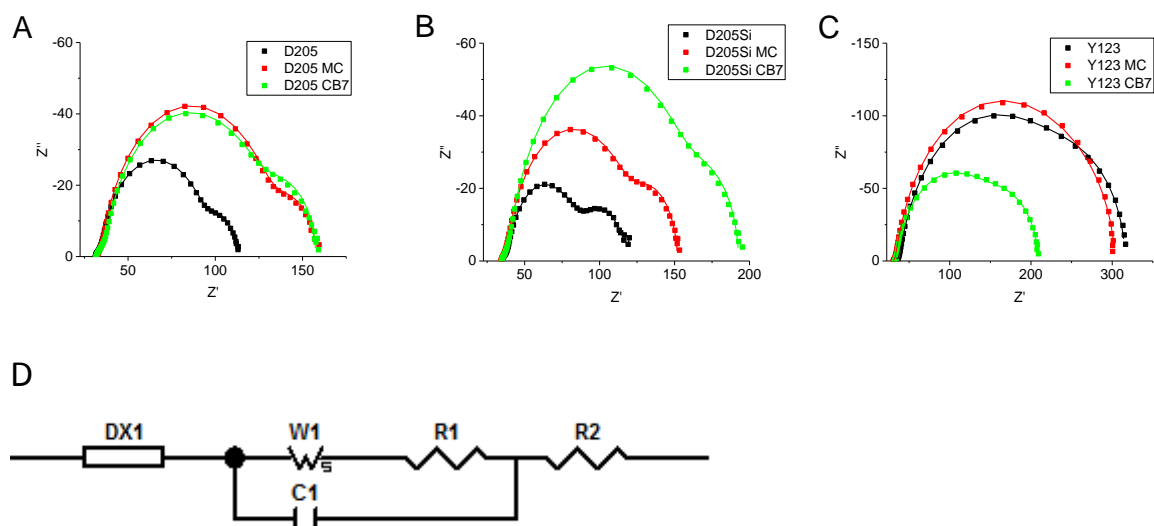


Figure S9. Example of Electrochemical Impedance Spectroscopy Nyquist plots and the fitted curves of DSSC's at V_{OC} (A-C). The data was fitted using the equivalent circuit (D). DX1 is transmission line element, W1 is the Warburg element.

Table S3. Table of basic EIS parameters obtained from Nyquist plots taken at V_{OC} . C_{μ} – chemical capacitance, R_{CT} – charge transfer resistance (both C_{μ} and R_{CT} were obtained from transmission line element - DX1), W1-R Warburg diffusion resistance, W1-T – Warburg diffusion time constant. Error values for each parameter were obtained from the fitting software (the highest values were taken).

	C_{μ} [F]	$R_{ct}[\Omega]$	W1-R $[\Omega]$	W1-T(s)
D205	0.00013	58.0	20.5	0.28
D205Si	0.00015	47.0	32.6	0.33
Y123	0.00024	173.0	107.2	0.48
D205 MC	0.00015	96.0	27.3	0.52
D205Si MC	0.00013	78.0	36.3	0.29
Y123 MC	0.00021	152.0	115.0	0.19
D205 CB7	0.00012	88.0	34.2	0.24
D205Si CB7	0.00012	118.0	36.6	0.33
Y123 CB7	0.00021	97.0	78.6	0.28
Error	0.00001	3.0	2.5	0.02

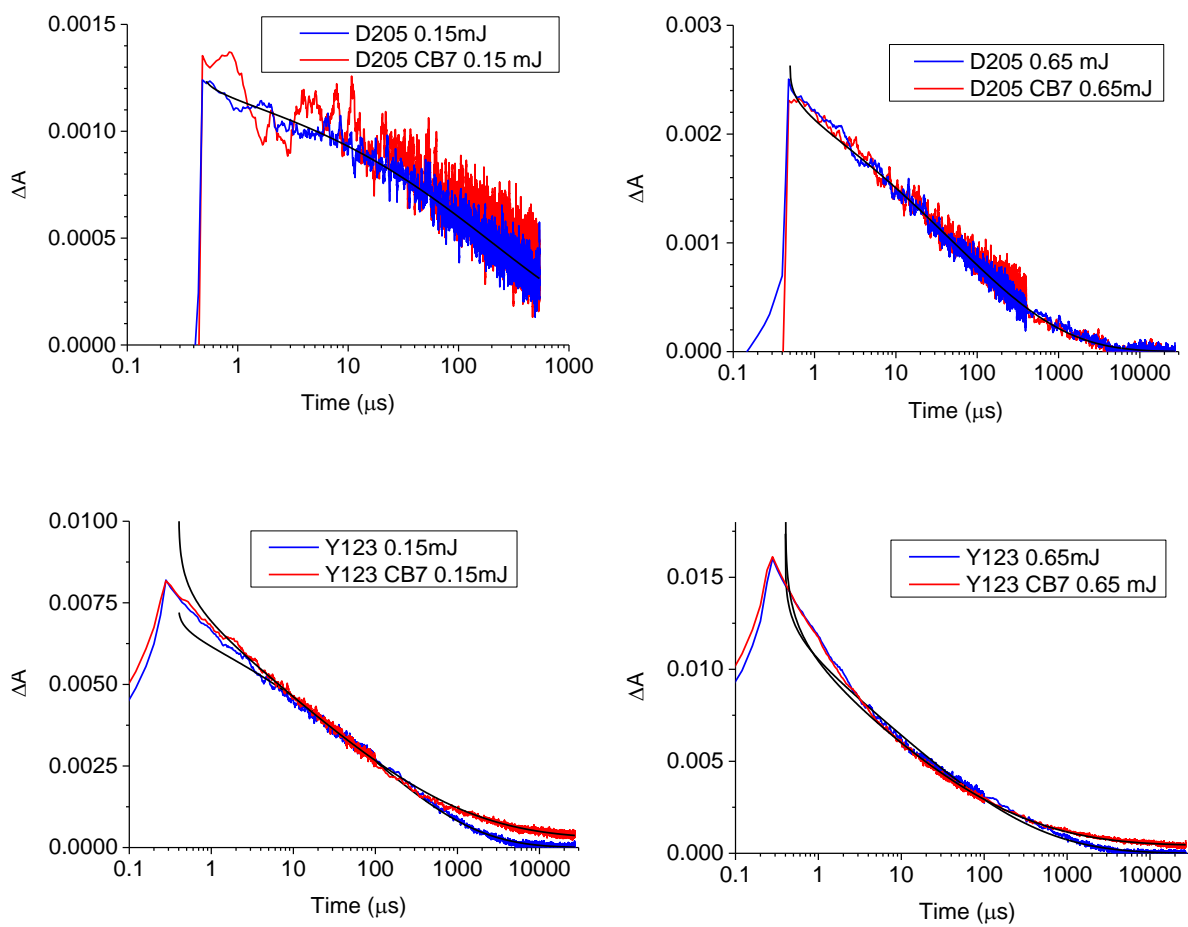


Figure S10. Kinetics probed at 700 nm measured by nanosecond flash photolysis for inert samples at different pump pulse energies ($\lambda_{\text{pump}} = 532 \text{ nm}$). Black lines show the stretched exponential fit with the parameters given in Table S4.

Table S4. Parameters of the stretched exponential fit to the nanosecond flash photolysis kinetics measured at 700 nm. The stretched exponential function is defined as $A(t) = A_0 e^{-(t/\tau)^\beta}$ where β is the stretching parameter and τ is the lifetime. The average time constants of stretched exponential function is defined as $\tau_{AVG} = \frac{\tau}{\beta} \Gamma\left(\frac{1}{\beta}\right)$. By the different measurements of the same sample we estimate the relative error of the averaged lifetime as 10%.

	τ (μ s)	β	τ_{AVG} (μ s)
D205/D205+CB7 0.15mJ	212	0.37	890
D205/D205+CB7 0.65mJ	54	0.32	390
Y123 0.15 mJ	88	0.33	570
Y123 CB7 0.15 mJ	9.3	0.20	1110
Y123 0.65 mJ	9.8	0.25	240
Y123 CB7 0.65 mJ	1.45	0.19	270

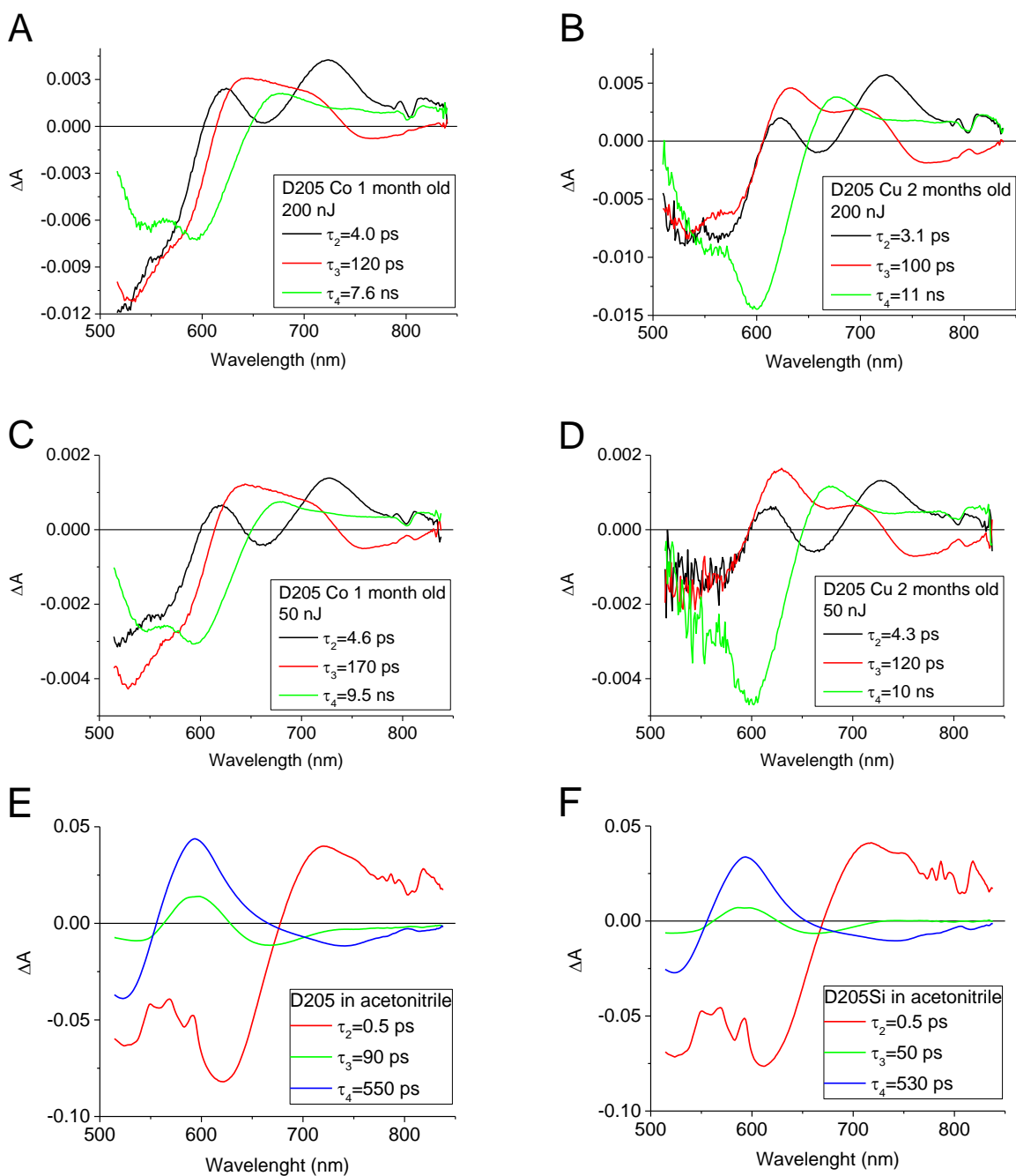


Figure S11. Results of the global fit to the femtosecond transient absorption data for the old D205 and D205Si cells with Cu and Co mediated electrolytes at different pump pulse ($\lambda_{\text{pump}} = 505$ nm) intensity (A-D) and for D205 and D205Si in acetonitrile solution ($C \sim 10^{-5}\text{M}$). Wavelength dependent amplitudes of transient absorption signal decays and the time constants associated with them. The fastest component ($\tau_1=0.2$ ps) is not shown for clarity. For the results in solution, the second component ($\tau_2=0.5$ ps) represents the decay of the Franck-Condon state, while the third (50-90 ps) and the fourth (530-550 ps) time constants are assigned to the decay of the subsequent charge transfer (CT) state at different stages of solvation. The negative signal above 620 nm is due to the stimulated emission of CT state (compare with the stationary emission spectra in Figure S2).

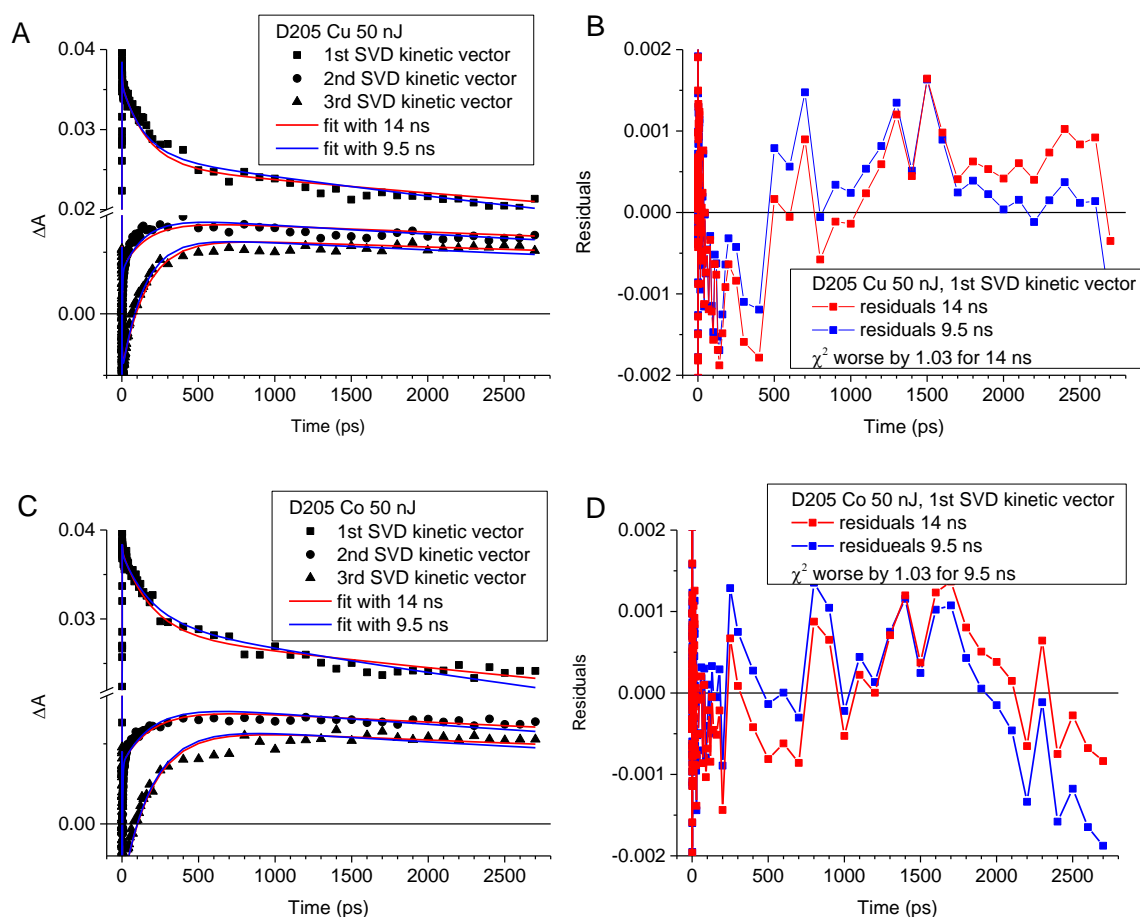


Figure S12. Examples of the global fits to the first three kinetic vectors obtained from singular value decomposition (SVD) analysis (left side) together with residuals (right side) for the transient absorption data presented in Figures 9C and 9D. In the global fits, the optimized values for the longest, τ_4 component, were 9.5 ns for D205 Cu sample (A, B) and 14 ns for D205 Co sample (C, D). For the comparison, the fit with τ_4 component fixed at longer value (14 ns) was added for D205 Cu sample, and the fit with τ_4 component fixed at shorter value (9.5 ns) was added for D205 Co sample. In both cases, the residuals are higher, and χ^2 value of the fit quality was worse by 3%.

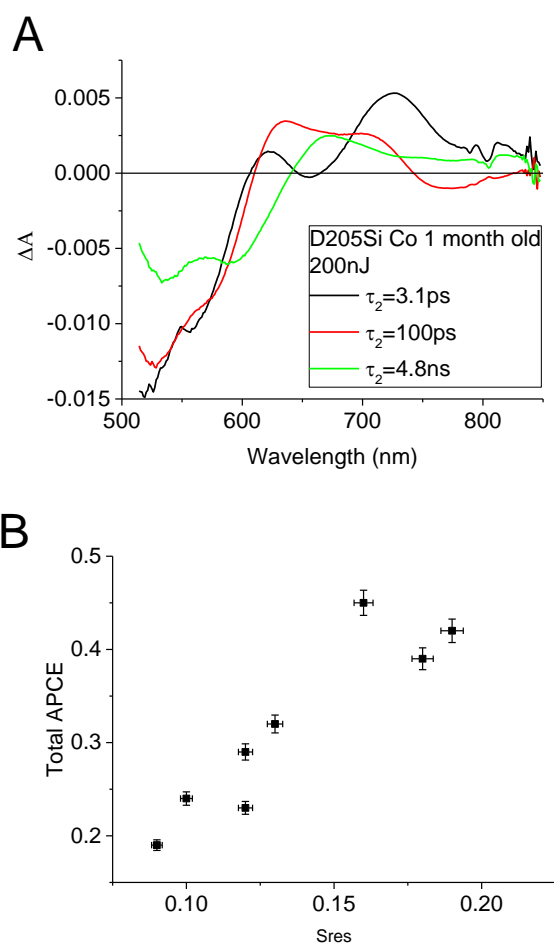


Figure S13. (A) Results of the global fit to the femtosecond transient absorption data for the old D205Si cell with Co mediated electrolyte. The pump pulse wavelength was $\lambda=505\text{nm}$. The fastest component ($\tau_1=0.2 \text{ ps}$) is not shown for clarity. (B) Correlation between total APCE parameter and residual signal (S_{res}) at 700 nm (ratio between maximum of signal and value for time delay 3ns). The errors were estimated by calculation of the standard deviation of mean values.

Paper V

Impact of Improvements in Mesoporous Titania Layers on Ultrafast Electron Transfer Dynamics in Perovskite and Dye-Sensitized Solar Cells.

Pydzińska-Białek, K.*; **Glinka, A.***; Drushliak, V.; Nowaczyk, G.;
Florczak, P.; Ziótek, M.







Phys. Chem. Chem. Phys. **2020**, 22, 21947–21960.

* authors contributed equally



Cite this: *Phys. Chem. Chem. Phys.*,
2020, 22, 21947

Impact of improvements in mesoporous titania layers on ultrafast electron transfer dynamics in perovskite and dye-sensitized solar cells†

Katarzyna Pydzińska-Białek, ^{‡a} Adam Glinka, ^{‡a} Viktoriia Drushliak, ^a
 Grzegorz Nowaczyk, ^b Patryk Florczak ^b and Marcin Ziótek ^{*a}

Improvement in the performance of perovskite solar cells (PSC) and dye-sensitized solar cells (DSSC) upon modifications of mesoporous titania layers has been studied. For PSC with triple cation perovskite (FA_{0.76} MA_{0.19} Cs_{0.05} Pb (I_{0.81} Br_{0.19})₃) about 40% higher photocurrent (up to ~24 mA cm⁻²) was found for more homogenous, made of larger particles (30 nm) and thinner (150–200 nm) titania layer. For DSSC (both with liquid cobalt-based electrolyte as well as with solid state hole transporter – spiro-OMeTAD), a greater dye loading, rise in photovoltage, and the enhancement in relative photocurrent were observed for the cells prepared from the diluted titania paste (2:1 w/w ratio) with respect to those prepared from undiluted one. The impact of these improvements in titania layers on charge transfer dynamics in the complete solar cells as well as in pristine TiO₂ layers was investigated by femtosecond transient absorption. Shorter photocarriers lifetime in perovskite material observed in better PSC, indicated that faster electron transfer at the titania interface was responsible for the higher photocurrent. Moreover, the photoinduced changes close to TiO₂ interface were revealed in better PSC, which may indicate that in the efficient devices halide segregation takes place in perovskite material. In liquid DSSC, the fast component of unwanted recombination was slower in the samples with the diluted titania paste than in those made with undiluted ones. In solid state DSSC, hole injection from MK2 dye to spiro-OMeTAD takes place on the very fast ps time scale (comparable to that of electron injection) and the evidence of better penetration of spiro-OMeTAD into thinner and more porous titania layers was provided.

Received 15th July 2020,
Accepted 25th August 2020

DOI: 10.1039/d0cp03780j

rsc.li/pccp

1. Introduction

Perovskite solar cells (PSCs) and dye-sensitized solar cells (DSSCs) belong to the very promising and potentially cheap emerging photovoltaic technologies. PSCs have been developed really rapidly in the latest few years, reaching the highest sunlight power conversion efficiency of 25%,¹ very close to the theoretical limit for single bandgap active material. The best efficiency of DSSC is about 14% achieved when using

cobalt-based electrolyte,^{2,3} but this environmentally friendly technology has been recently re-discovered as the best suited for indoor applications.⁴ It is because the efficiency of DSSC under low light intensity is greater than any of other common photovoltaic devices.⁵ Despite a large number of papers devoted to PSC (> 15 000 papers so far) and DSSC (> 24 000 publications up to now), the fundamental studies of charge transfer processes using time-resolved laser spectroscopies have been relatively rare, especially for the complete solar cell as samples.⁶

A very important element present in the most efficient PSCs and DSSCs is the mesoporous titania layer that accepts electrons from active materials and transfers them to the transparent conductive glass electrode.^{7,8} In DSSC, titania nanoparticles form a layer of a few microns in thickness (typically up to 10 μm). Sensitizing dyes are attached to such a scaffold and, after photo-excitation, inject electrons to TiO₂ conduction band in the very fast process (typically on fs and ps time scale), which is the primary charge separation step in DSSC operation. The regeneration of the dye (transfer of the electron to the oxidized form of the dye

^a Faculty of Physics, Adam Mickiewicz University, Uniwersytetu Poznańskiego 2, 61-614 Poznań, Poland. E-mail: marziol@amu.edu.pl

^b NanoBioMedical Centre, Adam Mickiewicz University, Wszechnicy Piastowskiej 3, 61-614 Poznań, Poland

† Electronic supplementary information (ESI) available: Fig. S1–S11: Additional SEM cross sections, stationary absorption, IPCE spectra, C–V curves, transient absorption spectra, temperature dependence, results of global analysis. Tables S1–S4: Parameters of the different TiO₂ layers, PV parameters of the samples, amplitude changes during consecutive scans in transient absorption experiment. See DOI: 10.1039/d0cp03780j

‡ Both authors contributed equally.

obtained after electron injection) in the cells with liquid electrolyte takes place on the time scale much longer than that of electron injection, typically from several hundreds of nanoseconds to single microseconds.^{6,8} However, if the electrolyte is substituted by solid state hole transporting material (*e.g.* the most popular spiro-OMeTAD) to enhance the stability of the cell, then the regeneration can occur much faster, even on the time scale comparable to that of electron injection (due to the hole hopping and higher density of charge conductive centers in the polymeric structure instead of redox pair diffusion in the electrolyte).^{9–11} Solid state DSSC still suffers from low efficiencies with respect to the cell with liquid electrolyte, mainly due to the problem of sufficient contact between all dyes and hole transporting materials.^{8,12,13} It should be noted that one of the most promising recent findings is the solidification of copper-based electrolytes (instead of the use of spiro-OMeTAD),⁵ which lead to record efficiency close to 12% for solid state DSSC.¹⁴

In PSC, the architecture is more similar to that of thin film solar cells where the active perovskite materials is placed between the charge selective layers of electron- and hole-transporting materials.¹⁵ However, in the most efficient devices, the titania mesoporous layer is still present (providing a base on which the perovskite crystalizes),¹⁶ although its thickness is much smaller (a few hundreds of nm) than that in DSSC. The optimization of the thickness and porosity of titania layers in PSC and DSSC is necessary for achieving high total power conversion efficiency. However, often it is unclear whether upon such optimization the fastest charge dynamics is changed and the efficiency of the primary charge separation step (the electron transfer at the interface between active material and titania) is improved.

Therefore, in the present work, we have constructed PSC and DSSC devices using the most efficient compounds and with different mesoporous titania layers to study the fully operating solar cell samples using the femtosecond transient absorption spectroscopy. For PSC, triple cation perovskite (containing methylammonium, formamidinium and cesium) was the active material¹⁷ and spiro-OMeTAD was the hole transporting layer, while titania layers of different thickness and porosity were tested. For DSSC, the efficient commercial carbazole dye MK2¹⁸ and cobalt-based liquid electrolytes^{19–21} were used to check the effect of dilution of popular commercial titania paste. Furthermore, also a solid state DSSC with spiro-OMeTAD and three types of titania layers were investigated. Our studies were aimed to establish whether the use of better titania layers (improving the sunlight conversion efficiency) correlates or not with the ultrafast dynamics of electrons and holes. Such information should be important for better understanding and further optimization of PSC and DSSC.

2. Experimental

Substrates for transparent electrodes for the cells were cut out from FTO glass sheet (Sigma-Aldrich, 2.2 mm thickness, 13 Ω sq⁻¹).

At first the glass plates were cleaned by sonication in a solution of commercially available dishwashing detergent (TRILLUX) mixed with distilled water, pure distilled water and ethanol, with each cleaning procedure lasting for 15 min. After drying by air flow, a UV ozone cleaner was used.

For PSC, spin-coating deposition was used in all steps of preparation. Electron transporting material (ETM) consisting of compact and mesoporous TiO₂ layers was deposited at first. A solution of titanium isopropoxide and ethanol was prepared in proportion of 1 : 9, respectively. Compact layer of TiO₂ was obtained by spin coating at 2000 rpm for 1 minute and then dried at 100 °C on a hot plate for 5 minutes. Next, the samples were gradually heated in the oven and kept at 450 °C for 30 min to form a compact TiO₂ layer. Two different mesoporous layers were used. The first one was prepared from TiO₂ paste for screen-printing of 18–20 nm-sized particle (DN-GPS-18TS, Dyenamo), dissolved in ethanol at the ratio of 1 : 6 (w:w). The second mesoporous layer was prepared from another TiO₂ paste of larger average particle size of 30 nm (GreatCell Solar, 30NR-D), similarly dissolved in ethanol at the ratio of 1 : 6 (w/w). The mixtures were preliminarily stirred continuously for 1 day. Mesoporous layers were spin coated at 2000 rpm for 10 s and then dried at 120 °C on the hot plate. Again, the substrates with titania layers were gradually heated in the oven and kept at 450 °C for 30 minutes. The abbreviations of the titania layers studied in this work refer to the deposition method, particles size and the possible use of dilution (see Table S1 in the ESI†). Thus, the two above paste are abbreviated as **SC18dil** and **SC30dil**.

Then, triple cation perovskite layer (FA_{0.76} MA_{0.19} Cs_{0.05} Pb (I_{0.81} Br_{0.19})₃, where MA is methylammonium and FA is formamidinium) was deposited by spin coating from 1.5 M precursor solution in DMF:DMSO (4:1 by volume, 10 s, 2000 rpm, then 20 s, 4000 rpm). Chlorobenzene (as anti-solvent) was applied 10 s before the end of the spinning. Subsequently, the substrates were annealed at 100 °C for 40 minutes. The hole transporting material (HTM) layer was obtained by spin-coating (4000 rpm, 30 s) from a solution consisting of 72.3 mg mL⁻¹ 2,2',7,7'-tetrakis[*N,N*-di(4-methoxyphenyl)amino]-9,9'-spirobifluoren (spiro-OMeTAD, Sigma-Aldrich), 28.8 μ L mL⁻¹ 4-*tert*-butylpyridine (TBP, Aldrich), and 17.5 μ L mL⁻¹ lithium bis(trifluoromethanesulfonyl) imide (LiTFSI, 520 mg mL⁻¹ in acetonitrile, Sigma-Aldrich), all dissolved in chlorobenzene (Sigma-Aldrich). The precursor solutions were prepared in oxygen free glovebox at a humidity RH = 6–7%, while the deposition of perovskite, annealing and deposition of HTM took place in another glovebox with oxygen presence at a humidity RH = 6–7%. Finally, gold electrodes were deposited on the top of HTM by sputtering technique for 60 s or 120 s, giving 25–50 or 50–100 nm layer thicknesses, respectively. The electrode sizes were of 0.05 or 0.20 cm² (0.125 cm² with the mask).

For DSSC studies, liquid cells (L-DSSC) with cobalt-based electrolyte and solid-state cells (S-DSSC) were constructed. At first, the blocking TiO₂ layer was formed on FTO electrodes by submerging them in 40 mM aqueous solution of TiCl₄

for 30 min at 70 °C, followed by rinsing with water, and heating at 150 °C for 5 min, 300 °C for 5 min, then at 450 °C for 30 min. At the next step, the two types of mesoporous titania layer were formed using the screen printing technique and nanoparticle paste of TiO₂ (DN-GPS-30TS, Dyenamo with 28–31 nm particles). The first one was made from the undiluted paste (abbreviated as **SP30**), The second, diluted-paste based mesoporous (**SP30dil**) layer, was prepared by mixing the above commercial paste with solution (6 g cellulose, 4 mL ethanol, 15 mL alpha-terpineol) at the ratio 2 : 1. After screen-printing of either diluted or undiluted pastes, the glass plates with mesoporous titania were gradually heated at 150 °C for 5 min, 300 °C for 5 min, and 450 °C for 60 min. After that, the glass plates were submerged in 40 mM aqueous solution of TiCl₄ (and treated in the same way as the blocking layer). For photoanode sensitization, the hot plates with TiO₂ layers were immersed in MK2 dye solutions in toluene for about 16 h to enable efficient adsorption of the dye. For MK2 sensitization we used either the solution of 0.2 mM dye and 0.1 mM of chenodeoxycholic acid (CDCA) as co-adsorbent or the solution of 0.2 mM dye without co-adsorbent.

Counter electrodes for L-DSSC were prepared from the same FTO glass plates and using the same cleaning procedure as that of photoanodes. Afterwards, they were dried in air and one layer of activated platinum (Platisol T, Solaronix) was deposited by paintbrush. Finally, the plates were heated at 450 °C for 30 min in order to remove any organic contamination. The photoanodes and counter electrode were bonded together by a polymer seal (25 μm Surlyn, Meltronix, Solaronix SA) with the conducting surfaces facing inwards. At the next step, the devices were filled with electrolyte through the 1 mm holes in the counter electrode and sealed with the cover glass on the top. We used the cobalt-bipyridine (bpy) or cobalt-phenanthroline (phen) complexes in acetonitrile solutions as the electrolytes for L-DSSC. The electrodes with MK2 and CDCA were used with the electrolyte consisting of 0.25 M [Co(bpy)₃](B(CN)₄)₂, 0.035 M [Co(bpy)₃](B(CN)₄)₃, 0.1 M LiClO₄ and 0.5 M TBP, and this configuration is abbreviated as **CBpy**. The electrodes without CDCA were used with the electrolyte consisting of 0.13 M [Co(phen)₃](TFSI)₂, 0.035 M [Co(phen)₃](TFSI)₃, 0.1 M of LiTFSI, and 0.5 M TBP, and this configuration is abbreviated as **Phen**. For S-DSSC, we used MK2 without CDCA for sensitization, and **SC30dil**, **SP30dil** or **SP30** titania layers. Spiro-OMeTAD as HTM and gold electrodes were deposited as described above for PSC.

A UV-VIS-NIR JASCO V-770 spectrophotometer equipped with a 150 mm integrating sphere (LN-925) was used to measure the stationary absorption spectra in the UV-VIS range. The samples were mounted in front of the integrating sphere in order to detect both transmitted and scattered light. The cross section images were recorded by Jeol 7001 TTLS field-emission scanning electron microscope (SEM) working at the acceleration voltage varying from 5 to 15 kV. Current-voltage measurements and IPCE (incident photon to current efficiency) spectra for the studied solar cells were recorded using a potentiostat (model M101, Autolab) coupled to a photoelectric spectrometer, equipped with a solar simulator (Instytut Fotonowy, Poland). A Xe lamp with AM 1.5G spectral filter and irradiance adjusted

to 100 mW cm⁻² using a calibrated cell (15151, ABET) mimicked the sunlight conditions. The same complete solar cells as those for current-voltage measurements were used for the transient absorption studies. Transient absorption system has been described recently in more details (Helios spectrometer, Ultrafast Systems, and Spectra Physics laser system).²² The laser pulses were set to 310, 355 or 500 nm and the IRF (pump-probe cross correlation function) duration was from 150 to 300 fs (FWHM). The transient absorption measurements were analyzed using the Surface Explorer software (Ultrafast Systems), including the global analysis. The program allowed fitting a multi-exponential function (convoluted with IRF) to the kinetic vectors of a selected number of singular values. Finally, the characteristic time constants and the wavelength-dependent amplitudes associated with them were obtained (they are also called the decay associated spectra or pre-exponential factor spectra). The fit quality was examined by the comparison of the multi-exponential fitted functions to the kinetic vectors.

3. Results and discussion

3.1. Morphology and stationary absorption

In order to determine the thickness of individual layers in solar cells SEM cross section images were carefully analyzed. The examples are shown in Fig. 1 and Fig. S1 (ESI[†]). Fig. 1A shows the cross section of **SP30dil** titania layer, while that of **SP30** layer is presented in Fig. S1A (ESI[†]). The estimated thickness of **SP30dil** layer is 1.3–1.5 μm, while that of **SP30** is 2.5–3 μm. Therefore, the use of diluted paste results in about twice smaller thickness of the mesoporous TiO₂ film. Moreover, the **SP30dil** structure has a higher porosity than that of **SP30** one, as indicated by the previous studies with different ethyl cellulose content in the titania paste.²³ The cross section of PVS solar cell made with a **SC30dil** thin titania layer is shown in Fig. 1B. The total thickness of the cell is about 850 nm, and the following layers deposited on the FTO glass substrate can be recognized: 150–200 nm of **SC30dil** (including very thin compact TiO₂ layer which is hard to be distinguished), 450–500 nm of pure triple cation PVS, 100–150 nm of spiro-OMeTAD and 50–100 nm of Au electrode. The average thickness of the solar cells made with a **SC18dil** layer is 1000 nm (Fig. S1B, ESI[†]), which indicates that the thickness of **SC18dil** layer is about twice higher than that of **SC30dil** one. Moreover, the homogeneity of the **SC18dil** is also worse with much higher variance in its thickness at different spots.

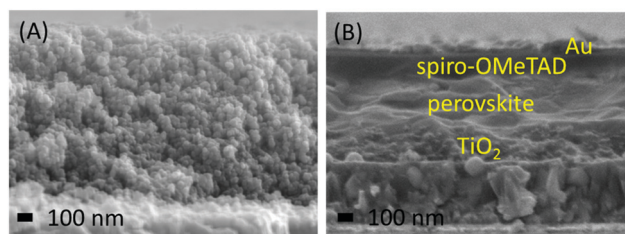


Fig. 1 SEM cross sections of **SP30dil** titania layer (A) and PSC made using **SC30dil** layer (B).

It also agrees with the eye observation of the electrodes (before perovskite deposition): those made with **SC18dil** are much more opaque, suggesting the presence of more scattering grains in **SC18dil** than in **SC30dil** layer. The differences in the thicknesses of the studied mesoporous layers are summarized in Table S1 (ESI[†]).

The differences in the thickness of **SP30dil** vs. **SP30** and **SC30dil** vs. **SC18dil** layers were also confirmed by stationary absorption measurements of the electrodes (Fig. S2, ESI[†]). The absorbance values below 400 nm (where TiO₂ absorbs) are higher for **SP30** than **SP30dil** and higher for **SC18dil** than **SC30dil**. However, the exact thickness ratio of different titania layers is hard to estimate in this way, because the absorbance is also affected by the scattering contribution, which results in the baseline signal increasing for shorter wavelength (and observed already at wavelength longer than 400 nm). Moreover, the absorption baseline is also affected by the oscillations appearing due to the light interference at the layers of sub μm sizes²⁴ present on the electrodes.

The stationary absorption measurements were also used to determine the absorption spectrum of active layers (dyes or perovskite) after the subtraction of titania layers contribution. The examples are shown in Fig. 2. These data are important to estimate the numbers of absorbed photons from 1 Sun irradiation (N_{ph}), which are necessary to calculate and compare the relative photocurrent of different cells (in the next section).

3.2. Photovoltaic parameters

Table 1 shows the photovoltaic parameters of the best cells prepared using different titania layers. The absorbance of the active material at selected wavelength and the number of absorbed photons (N_{ph}) from 1 Sun irradiation are given along with the standard photovoltaic parameters: open circuit voltage (V_{OC}), short circuit current density (J_{SC}), fill factor (FF) and sunlight power conversion efficiency (PCE). Moreover, Table 1 presents also the calculated parameter total APCE (APCE – absorbed photon to current efficiency), describing the relative

photocurrent of the cells per the number of absorbed photons. It is defined as the total APCE = $J_{\text{SC}}/e N_{\text{ph}}$, where e is elementary charge. This parameter allows us to compare the efficiency of charge separation between the cells with different amounts of adsorbed dyes, as we did in many of our previous studies.^{25–28} The average values of the photovoltaic parameters with errors based on the measurement of several cells of the same type are collected in Table S2 (ESI[†]).

At first, the DSSC samples with the liquid electrolyte (L-DSSC) will be described. The cells sensitized with popular carbazole dye called MK2 were studied in two configurations: without co-adsorbent in Co-phenanthroline electrolyte (**Phen**), and with CDCA in Co-bipyridine electrolyte (**CBpy**), using both **SP30dil** and **SP30** layers (Table 1A). The absorbance of MK2 (and thus the total amount of MK2 dyes on titania layer) is, as expected, smaller in the samples with the co-adsorption of CDCA. However, for both the cells with and without CDCA, the amount of dyes in **SP30dil** layers is as high as about 75% of that in the corresponding **SP30** layers. Having in mind that the thickness of **SP30** is about twice that of **SP30dil**, it means that the dye loading per layer thickness is significantly higher for the cells prepared with the diluted paste. It can be probably explained by higher porosity of the **SP30dil** titania layer. Furthermore, Table 1A shows that the photocurrent (J_{SC}) of the fresh cells is only slightly smaller for **SP30dil** cells, while IPCE spectra (Fig. S3, ESI[†]) indicate that it originates mainly from higher absorption on the rising, long-wavelength part of MK2 absorption band. Small difference in J_{SC} results in the higher relative photocurrent (total APCE) for **SP30dil** cells than **SP30** ones. Finally, L-DSSC from diluted titania paste exhibits higher V_{OC} (by about 0.04 V) indicating slightly smaller recombination losses in **SP30dil** cells. Our observations of the above improvements upon dilution of titania paste are consistent with previous reports.^{23,29} The layers with higher porosity permit a more effective transport of large redox shuttles like cobalt complexes. However, the studies of the impact of titania modifications on ultrafast charge transfer process, which we present in the next sections, has not been addressed so far.

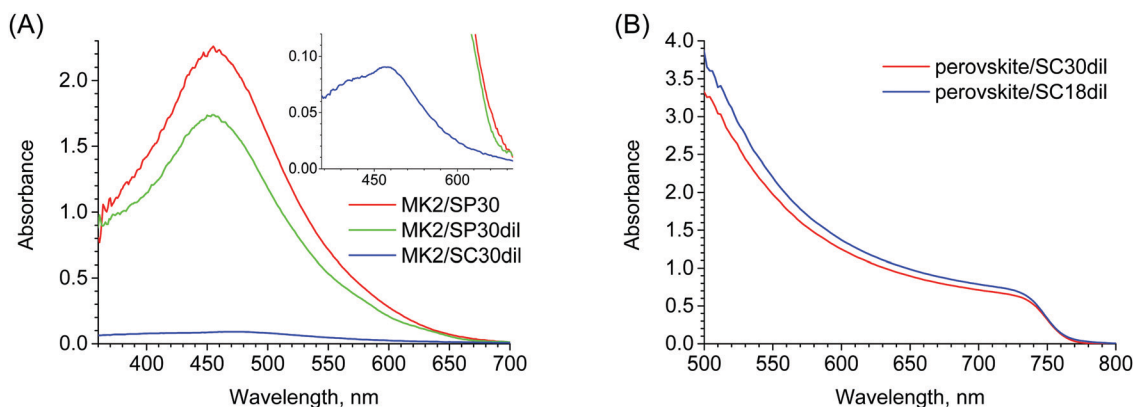


Fig. 2 Stationary absorption of the **SP30**, **SP30dil** and **SC30dil** electrodes sensitized with MK2 dye (without CDCA) (A) and triple cation perovskite on **SC30dil** and **SC18dil** layers (B). The contribution of titania has been subtracted in both figures. The inset in (A) presents the spectra with enlarged absorbance scale.

Table 1 Photovoltaic parameters of the best cells: V_{OC} – open circuit voltage, J_{SC} – short circuit photocurrent density, FF – fill factor, PCE – power conversion efficiency, N_{ph} – number of absorbed photons from 1 Sun, A – absorbance at 500 nm, total APCE – relative photocurrent

Sample	V_{OC} [V]	J_{SC} [mA cm ⁻²]	FF	PCE [%]	N_{ph} [10 ²⁰ s ⁻¹ m ⁻²]	A (500 nm)	Total APCE
(A) fresh L-DSSC:							
Phen/SP30	0.84	8.03	0.63	4.30	7.24	1.58	0.69
Phen/SP30dil	0.88	7.44	0.68	4.44	6.60	1.18	0.70
CBpy/SP30	0.79	7.04	0.70	3.93	6.44	1.12	0.68
CBpy/SP30dil	0.83	6.79	0.70	3.98	5.66	0.87	0.75
Sample	V_{OC} [V]	J_{SC} [mA cm ⁻²]	FF	PCE [%]	N_{ph} [10 ²⁰ s ⁻¹ m ⁻²]	A (500 nm)	Total APCE
(B) 20 days old L-DSSC:							
Phen/SP30	0.86	6.97	0.71	4.26	7.24	1.58	0.60
Phen/SP30dil	0.86	7.56	0.70	4.53	6.60	1.18	0.71
CBpy/SP30	0.79	7.82	0.70	4.34	6.44	1.12	0.76
CBpy/SP30dil	0.84	7.29	0.73	4.46	5.66	0.87	0.81
Sample	V_{OC} [V]	J_{SC} [mA cm ⁻²]	FF	PCE [%]	Total APCE		
(C) fresh PSC and S-DSSC:							
PSC/SC18dil	0.99	17.2	0.62	10.6	0.80		
PSC/SC30dil	1.07	24.4	0.68	17.8	1.17		
S-DSSC/SC30dil	0.71	0.98	0.57	0.40	0.52		
S-DSSC/SP30dil	0.58	3.20	0.42	0.79	0.49		
S-DSSC/SP30	0.46	3.74	0.34	0.58	0.38		

It should be noted that the same trends in the differences between **SP30dil** and **SP30** cells (higher V_{OC} and total APCE, better dye loading) were confirmed in our preliminary studies of L-DSSC with other dyes (indoline dye D205^{30,31} and the 2 : 1 mixture of MK2:D205 in Co-phenanthroline electrolyte). After 20 days, the parameters of L-DSSC were quite stable and most of them even improved, increasing the total efficiency of the cell (Table 1B). The best efficiency of about 4.5% was reached for the cells made with diluted paste. It is not very high comparing this value to that of the best L-DSSC (efficiencies 12–14%),^{2,3} however, it should be noted that our result was achieved on the very thin (1.3–1.5 μm) and transparent titania layer only.

PSC with triple cation perovskite, spiro-OMeTAD as hole transporting layer, and **SC18dil** or **SC30dil** titania layers as electron transporting material, were studied. Their photovoltaic parameters are collected in Table 1C. As can be seen, all parameters (V_{OC} , J_{SC} , FF and PCE) are better for the cells prepared on **SC30dil** than **SC18dil**, which confirms that more the homogenous thinner, and made of larger particles mesoporous titania layer is advantageous for the performance of this kind of cells. Better photovoltaic parameters obtained for larger nanoparticles and thinner TiO_2 layers are consistent with the previous reports.⁷ For example, the efficiency of PCS made of MAPbI_3 was 14.34% for 400 nm layer thickness of 25 nm particles, while it improved to 18.72% for 150 nm layer thickness with 41 nm particles.⁷ The improvement observed for larger particles was assigned to higher porosity and mean pore diameter of the resultant layer. However, according to our knowledge, the charge transfer dynamics (presented in the next sections) has not been compared so far.

The photovoltage (V_{OC} close to 1.1 V) and photocurrent (J_{SC} above 24 mA cm⁻²) of our best PSC with **SC30dil** layer are close to the top efficiencies reported for PSC. The very high value of the relative photocurrent (close to 100%) indicates

almost no charge recombination at low voltages. The constructed perovskite solar cells exhibit relatively small hysteresis with the hysteresis index of 0.03–0.05 (Fig. S4, ESI†). Our best PSC efficiency is about 18%, and the parameter which mainly limits our efficiency and which is significantly lower with respect to the best PSC devices, is the fill factor. The obtained values of FF below 0.7 in PSC are probably due to the sputtering method of gold electrode depositions used for our cells, instead of typically employed thermal evaporation technique. It is confirmed and explained in ESI† (Table S3 and the short discussion below, ESI†). However, it should be emphasized that low FF values of our PSC (and also our solid state DSSC described below) do not change the main conclusions following from our studies since we are mainly focused on the photocurrents and all samples compared are affected by gold sputtering in the similar way.

The solid state DSSC (S-DSSC) were prepared using **SC30dil** (the same as for PSC), **SP30dil** or **SP30** (the same as for L-DSSC) titania layers sensitized with MK2 dyes (without co-adsorbent). The electrodes were then covered with spiro-OMeTAD and gold electrodes. The photovoltaic parameters are collected in Table 1C. Although J_{SC} increases for thicker titania layers due to more adsorbed dyes, the other parameters (V_{OC} , FF and total APCE) significantly decrease when going from samples with **SC30dil** (thickness 150–200 nm) to **SP30dil** (1.3–1.5 μm) and further to **SP30** (2.5–3 μm). The common problem with S-DSSC is the penetration of spiro-OMeTAD to deeper titania layers sensitized with the dye,⁸ which is confirmed in our results. The best efficiency of about 0.8% is obtained for the cell with **SP30dil** layer. Fill factor values improve in both PSC and S-DSSC samples for more porous and thinner titania layer due to better pore filling by the precursor solution and spiro-OMeTAD, respectively.

The composition and deposition method of spiro-OMeTAD were optimized for PSC and it is probably one of the reasons

why the parameters and efficiencies of our S-DSSC are rather poor, comparing to other reports of S-DSSC with MK2 dye ($\sim 3\%$).^{32,33} Despite preferable match of HOMO levels of the dye (0.92 eV vs. NHE)³⁴ and the HTM (0.75 eV vs. NHE),³⁵ TiO₂ layer is not fully covered by the dyes as it is covered by the perovskite layer in PSC, allowing unwanted direct charge recombination at HTM/ETM interface. However, the total APCE values in our S-DSSC (from 0.52 to 0.38, compared to 0.60–0.80 for L-DSSC) indicate that still about half of the photoinduced charges are successfully separated at low voltages, therefore the findings from transient absorption studies presented in the next sections are still informative for the operation of S-DSSC.

3.3. Transient absorption of titania layers

We will begin with presentation of the transient absorption results obtained for isolated electrodes with titania layers excited at 310 or 355 nm. Such excitation leads to the direct absorption of light by TiO₂ and creation of electron-hole pairs. Fig. S5 (ESI[†]) shows the exemplary transient spectra for **SC30dil** in UV-VIS and NIR ranges at selected time delays between pump and probe pulses. The results of global three-exponential analysis of the same sample are presented in Fig. 3A and B. Initially, the negative bleach signal in the spectral range of TiO₂ stationary

absorption can be observed below 380 nm. At longer wavelength in the VIS range the positive signal from holes and trapped electrons can be observed, while the positive signals in NIR range are dominated by free and shallowly trapped electrons.³⁶ After 1 ns the majority of signals decay due to charge recombination, but below 400 nm a positive, a long-lasting band appears, which we assign to the thermal artifact – broadening of the titania absorption band upon local sample heating. Indeed, our stationary absorption measurements showed that TiO₂ electrodes increase their absorption in the range from 340 to 400 nm upon heating, with approximately 0.0008 change in absorption per 1 Celsius degree at 340 nm (Fig. S6, ESI[†]). This artifact, being responsible for the existence of transient absorption signal, even when no excited state population is present, has been reported recently for some metal oxide semiconductors: BiVO₄,³⁷ hematite, LaFeO₃ or LaMnO₃.³⁸ However, according to our knowledge, this effect has not been reported for TiO₂ as yet.

The multi-exponential global analysis reveals that the majority of free electrons decays occur with the time constant of about 1 ps (amplitudes of τ_1 component in Fig. 3B, increasing for longer wavelength in the infrared range)^{36,39} and that the signals of trapped electrons and holes do not decay in the single exponential way (components τ_1 and τ_2 in Fig. 3A). Fig. 3C and D

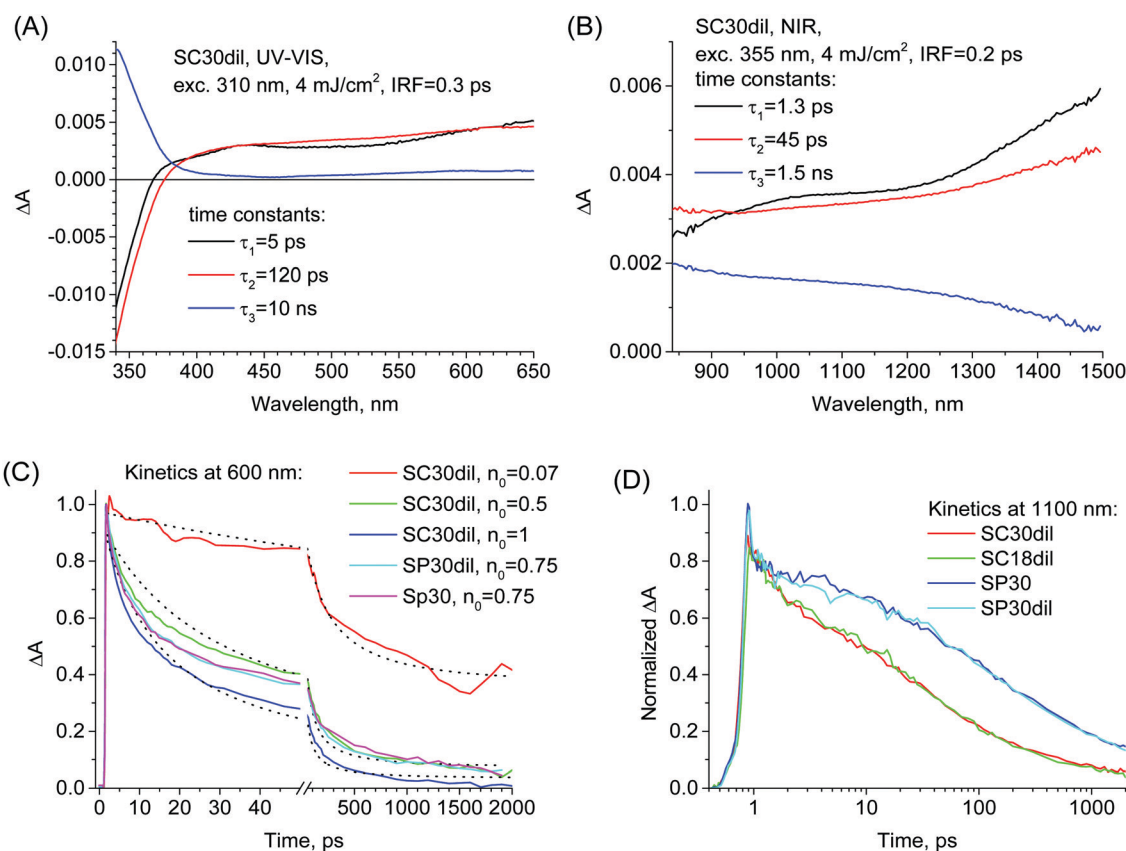


Fig. 3 Examples of the global analysis of transient absorption data using a three-exponential function with a constant offset for **SC30dil** electrode: in UV-VIS (A) and NIR ranges (B). The normalized kinetics at 600 nm for the indicated samples at fluences from 0.5 to 4 mJ cm⁻², together with mixed first and second order functions fitted (dotted lines) for **SC30dil** samples (C). The scaling factors for the initial photoexcited charge concentration (n_0) are also given. The normalized kinetics at 1100 nm for different titania samples measured at the same fluence (D). The amplitudes of **SC30dil** and **SC18dil** were multiplied by 1.85 in (D) to have the same value as those of **SP30** and **SP30dil** samples.

present the kinetics at 600 nm (dominated by holes) and 1100 nm (dominated by electrons). As can be seen, the dynamics of hole decay is similar for **SC30dil**, **SP30dil** and **SP30** layers (Fig. 3C). Interestingly, the decay of electrons is significantly slower for **SP30dil** and **SP30** layers than for **SC30dil** and **SC18dil** ones (Fig. 3D), indicating the difference in the distribution of trapped states below the titania conduction band. The decay of holes at 600 nm was analyzed at different excitation fluence (Fig. 3C). The higher the initial amplitude (and thus the population of the charges), the faster the decay. It can be justified by the contribution of second order process (hole-electron radiative recombination). Indeed, the mixed first and second order fit (see SI for the function definition) reveals trap-assisted first order rate constants $k_1 = 1 \text{ ns}^{-1}$ and second order rate constant $k_2 = 3.4 \text{ ns}^{-1} (m\Delta A)^{-1}$ (absorbance signal is used instead of charge concentration, because of difficult estimation of the latter). The fit is not perfect (Fig. 3C), which is probably due to the effect of the diffusion of charges in the sample of a certain thickness (therefore, the initial density of charges changes in time). The contribution of the second order process in the measured range of excitation fluence at 310 nm ($0.5\text{--}4 \text{ mJ cm}^{-2}$) varies from 81% to 98%.

3.4. Transient absorption of L-DSSC

Next, the transient absorption results for solar cell samples with different titania layers are presented and compared. L-DSSC, PSC and S-DSSC were excited at 500 nm, at which the light is absorbed by the active materials (MK2 dye or triple cation perovskite) and not by TiO_2 . The measurements for L-DSSC refer to a 20 days old cell, whose parameters were slightly improved with respect to the as-obtained one (Table 1B). The pump pulse was directed from the titania side and excitation fluence for L-DSSC was $100 \mu\text{J cm}^{-2}$. Fig. S7 (ESI[†]) shows the exemplary spectra of **CBpy/SP30dil** sample at selected time delays between the pump and probe pulses, while representative pseudo-color 2D spectra of transient absorption data are presented in Fig. 4A and B.

The transient absorption spectra and their evolution are analogous to those reported by us earlier for L-DSSC with MK2 dye.^{25,26,40,41} Similarly, global analysis assuming a two-exponential function and constant offset was employed to extract the characteristic time constants. The representative results are presented in Fig. 4C–F. The constant offset component with a bleach band below 650 nm (corresponding to stationary absorption of MK2 dye – compare with Fig. 2A) and a positive band with a maximum at 750 nm is assigned to the oxidized dye. Thus, its amplitude with respect to the initial one is proportional to the number of successfully separated charge carriers. The relative amplitude of the positive band is higher for the cells with CDCA (**CBpy**, Fig. 4C and D) than for those without co-adsorbent (**Phen**, Fig. 4E and F). It agrees with the higher total APCE values for the former than for the latter samples (Table 1B), and is in line with our previous findings.²⁵

The pre-exponential factor spectra of the second, longer component (τ_2 in the range from 130 to 180 ps, slightly faster for **Phen** than **CBpy** cells) have the shape similar to that of the constant offset spectra. Therefore, the second component is

assigned to the recombination of injected electron from titania to MK2 dye, decreasing the population of the oxidized dye. Finally, the fastest extracted component (τ_1 of several ps) is the only one for which the small but systematic differences between **SP30dil** and **SP30** samples can be observed. This component should be ascribed to the fast part of electron recombination (that occurs over many time scales), but it is also influenced by the electron injection; therefore, its pre-exponential factor spectra are different than those of τ_2 and constant offset components. In particular, the electron injection is accompanied with the decay of the S_1 state of the dye, and e.g. the indentation in the spectra in 600–750 nm range is due to the stimulated emission (Fig. 4C–F).²⁶ It is more visible in **CBpy** than **Phen** samples because, as we analyzed in more details earlier, the electron injection is slower for MK2 with CDCA than without CDCA.²⁵ Nevertheless, the electron injection times are below 1 ps in both cases, so the differences in values of τ_1 are mainly due to electron recombination. Thus, the fast component of recombination is slightly slower in the samples with the diluted titania phase (τ_1 of about 6 ps with respect to 4 ps for undiluted samples, Fig. 4C–F), which is beneficial for charge separation. It might be explained by a closer distance between the dyes on titania nanoparticle surface in **SP30** than **SP30dil** layer, which enhance fast recombination.^{25,41} Although dye loading is higher in **SP30dil** cells than **SP30** ones, it is the loading per the layer thickness that we consider, and due to higher porosity of **SP30dil** than **SP30** layer, the average distance between adjacent dyes might be even larger in **SP30dil** than **SP30**. It should be also noted that the charge transfer processes observed on the time scales up to few nanoseconds are only related to the interaction between dye molecules and single TiO_2 nanoparticle. Different titania thickness in DSSC samples can affect the kinetics on much longer time scales (e.g. electron transport through the titania nanoparticles net or titania-redox couple recombination).

3.5. Transient absorption of PSC

We will discuss now the transient absorption results obtained for as-obtained PSC. Fig. S8 (ESI[†]) presents the exemplary spectra at different time delays between the pump and probe pulses while representative pseudo-color 2D spectra of transient absorption data are shown in Fig. 5A and B. They are similar to many previous reports on standard MAPbI_3 perovskites,^{42–50} including our studies,^{28,51,52} as well as to our recent studies of the same triple cation perovskite compositions prepared under drybox or ambient air conditions.⁵³ The initial changes at times below 1 ps are due to the charge carrier relaxation.^{43,45,46,54} After that, the signals are dominated by the strong and sharp negative bleach close to the absorption edge, appearing due to the band filling mechanism and being proportional to the population of the excited carriers.^{42,46,47} The decay of this signal is due to the charge recombination, charge diffusion and charge transfer to contact layers (electron injection into TiO_2 and hole injection into spiro-OMeTAD).^{44,49,52,55}

To compare the charge dynamics in PSC with **SC30dil** and **SC18dil** layers, the global multi-exponential analysis was employed,

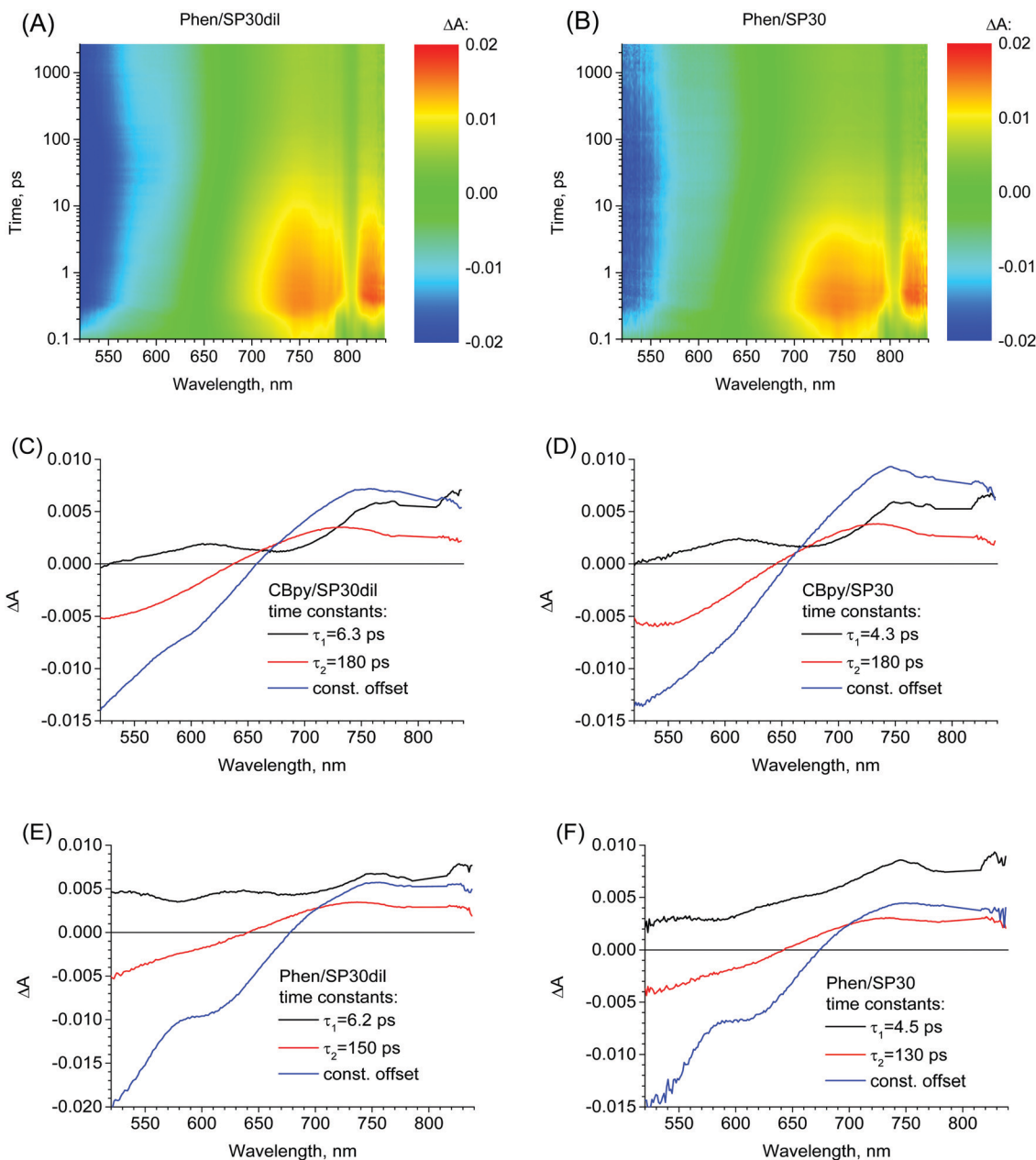


Fig. 4 Pseudo-color 2D spectra of original transient absorption data for L-DSSC with **SP30dil** and **SP30** titania layers (A and B). Examples of the global analysis of transient absorption data using a two-exponential function with a constant offset for L-DSSC samples (C–F). The graphs present pre-exponential factor spectra associated to the indicated time constants. The pump fluence was $100 \mu\text{J cm}^{-2}$ and IRF was 0.3 ps.

similarly as in our previous studies.^{28,51,52} As we have discussed,⁵² the exponential functions (being the solution of the first order kinetic equations) do not strictly follow the kinetics of charge population, which include *e.g.* second order radiative recombination and charge diffusion.^{47,48,56} However, the fitted time constants of exponential components and the associated pre-exponential factor spectra can be used to identify the occurring processes and compare their characteristic, average times. Fig. 5C–F shows the results of 3-exponential global analysis of the data obtained with the excitation fluence $30 \mu\text{J cm}^{-2}$ from both ETM (TiO_2) and HTM (spiro-OMeTAD) sides.

Due to the high absorbance of the samples at the excitation wavelength ($A > 3$ at 500 nm, see Fig. 2B), the initial excitation of perovskite is localized close to the contact layers, therefore the excitations from different sides of PSC probe more selectively the charge transfer to one, particular layer (ETM or HTM). The first, sub picosecond component has a shape characteristic of the band-edge shift, which is due to charge cooling and/or exciton dissociation.^{43,45,46} Its value of $\tau_1 = 0.3$ ps is the same for the samples with **SC30dil** and **SC18dil** titania layers. In contrast, the next two time components (having the amplitude spectra dominated by the bleach signal and showing the charge population decay) are

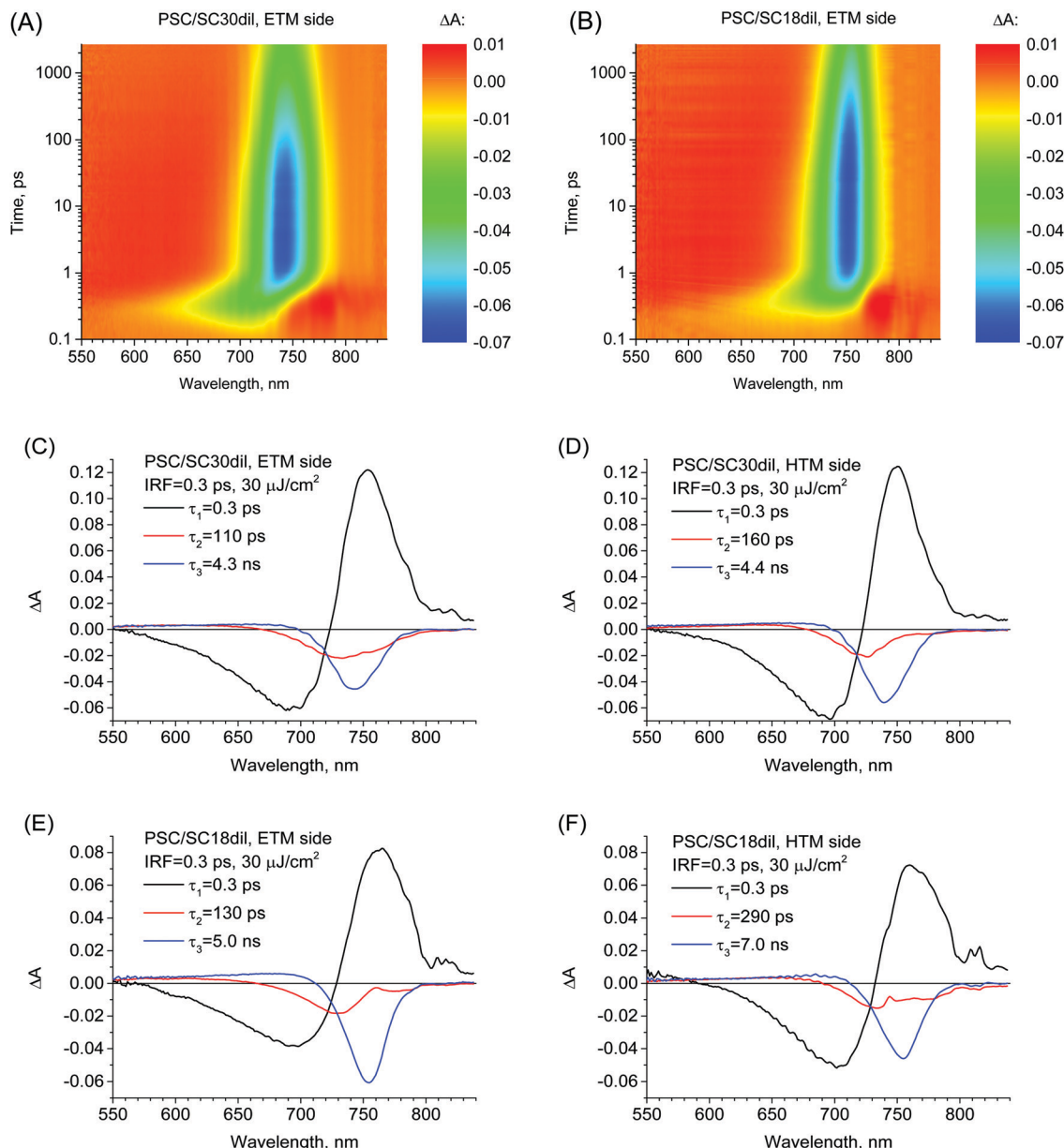


Fig. 5 Pseudo-color 2D spectra of original transient absorption data (A and B). Examples of the global analysis of transient absorption data using three-exponential function for PSC samples. The graphs present pre-exponential factor spectra associated to the indicated time constants. The pump fluence was $30 \mu\text{J cm}^{-2}$ and IRF was 0.3 ps.

always shorter for **SC30dil** than **SC18dil** layers, which indicates that the electron transfer to titania is faster for **SC30dil** cells with a higher photocurrent. The spectrum of the second component (τ_2 , from 100 to 300 ps in Fig. 5C–F) is usually blue-shifted with respect to that of the third one (τ_3 , in the nanosecond range) because the charges filling the bands of higher energy depopulate faster.⁵² It should be noted that the fitted time constant are only partly related to the charge injection times, because they are strongly affected by the second order charge recombination within the perovskite, as evidenced *e.g.* by the higher values of τ_2 and τ_3 at lower excitation fluence ($10 \mu\text{J cm}^{-2}$, see Fig. S9, ESI†).

To simplify the comparison between **SC30dil** and **SC18dil** layers, we have also performed 2-exponential global analysis,⁵¹

in which the second component reflects the average charge population decay (despite poor fit quality, at least for the excitation fluence $30 \mu\text{J cm}^{-2}$). The obtained mean values are the following: τ_{AVG} (**SC30dil**, ETM side) = 1.9 ns, τ_{AVG} (**SC30dil**, HTM side) = 2.5 ns, τ_{AVG} (**SC18dil**, ETM side) = 3.3 ns and τ_{AVG} (**SC18dil**, HTM side) = 3.3 ns, all with the error ± 0.1 ns based on standard deviation from 4–7 measurements.

As can be seen, the charge decay is faster for **SC30dil** than **SC18dil** samples, which is also visualized by the comparison of kinetics at bleach maximum presented in Fig. 6A or the pseudo-color 2D spectra in Fig. 5A and B. Moreover, the difference is higher for the excitation at ETM side where the contribution of electron injection to titania is higher than that at HTM side.

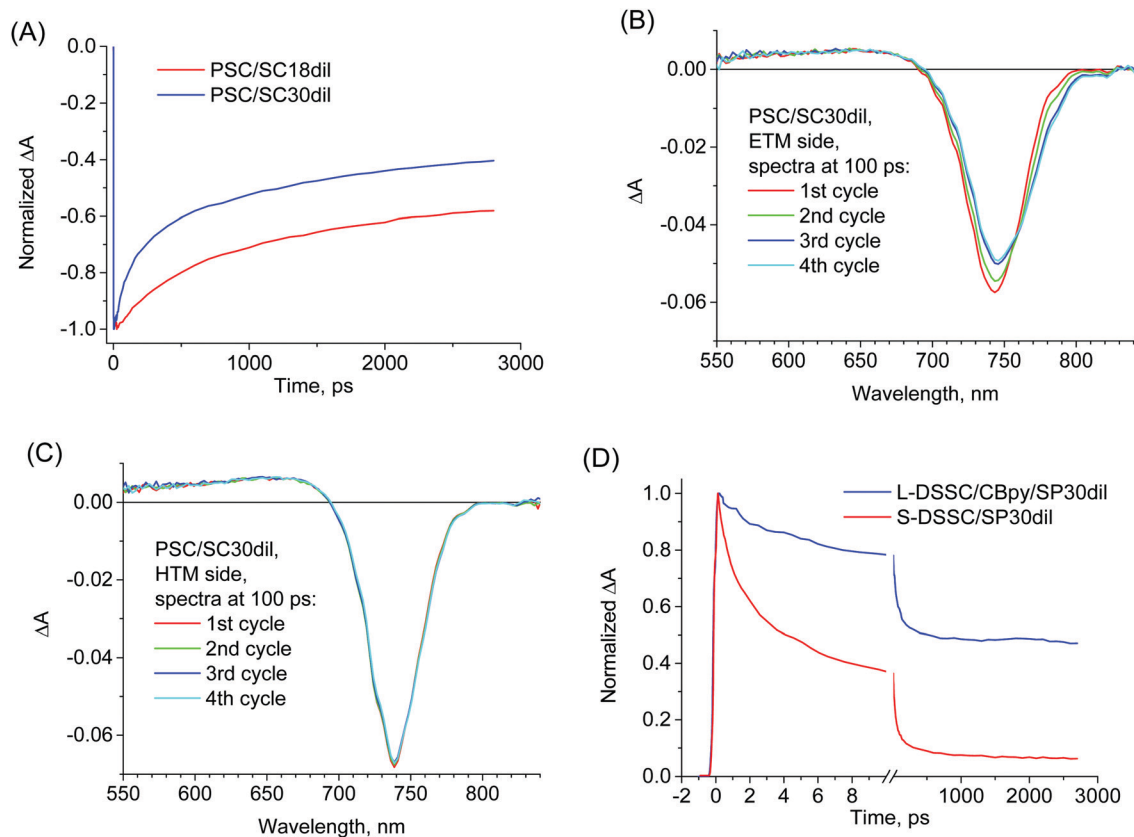


Fig. 6 Normalized kinetics for PSC measured from ETM side at the maximum of the bleach signal for **SC18dil** and **SC30dil** layers (A). Transient absorption spectra for PSC with **SC30dil** layer measured at 100 ps for different consecutive cycles at ETM (B) and HTM (C) sides. The pump fluence was $30 \mu\text{J cm}^{-2}$ in A–C. Normalized kinetics for L-DSSC and S-DSSC measured at 750 nm (D).

Therefore, it confirms that the faster electron injection from the perovskite to TiO_2 is responsible for the observed faster bleach recovery dynamics in the **SC30dil** samples, because all other parameters that might influence the population decay (excitation fluence, perovskite layer thickness, HTM material) are the same in both samples. However, it should be noted that the magnitude of lifetime shortening do not directly represent the values of intrinsic electron injection times, which might be much shorter than nanoseconds due to the occurrence of charge diffusion process. For example, it was shown that the half-decay of the bleach signal of the perovskite layer studied (of 80 nm in thickness) can decrease from 4 ns to 2 ns when the intrinsic electron transfer time is shortened from 50 ps to 10 ps.⁴⁷

Finally, we would also like to address another important issue related to the interface between triple-cation perovskite and the titania layer. In our recent contribution we have reported the differences in morphology (PbI_2 content) and spectra between the perovskite close to ETM and that near HTM interface.⁵³ In particular, the transient bleach band showed additional red-shifted spectral features of perovskite close to ETM side. One of the proposed explanations was the ion segregation leading to different ratios of bromide/iodide close to the TiO_2 that could modify the bandgap.⁵⁷ This effect can be enhanced by irradiation.⁵⁸ In the study presented here we

provide more evidence for this mechanism by comparing the changes in transient absorption spectra during the following cycles in the femtosecond experiment (each cycle lasted about 3 minutes). As can be seen in Fig. 6, upon increasing irradiation time, some clear changes (with isosbestic point) of bleach spectrum at 100 ps are observed at ETM side (Fig. 6B), while no such changes are visible at HTM side (Fig. 6C). This result was obtained for the PSC/**SC30dil** sample showing high photocurrent. On the contrary, for worse performing PSC/**SC18dil** cell the changes on ETM side were much smaller (Fig. S10A, ESI[†]). We have also passivated **SC30dil** layer by sensitization with MK2 dye (before perovskite deposition). For such test PSC the photocurrent was very small (total APCE = 0.61) and the changes on ETM side were also hardly observed (Fig. S10B, ESI[†]). Therefore, the photoinduced bleach changes near TiO_2 (due to probable ion segregation in mixed halide perovskite) occur efficiently only for the cells with high photocurrent. It is consistent with the recent supposition that ion segregation is enhanced by hole accumulation at the interface where electrons were efficiently injected.⁵⁸

3.6. Transient absorption of S-DSSC

In the last section we will present the transient absorption data measured for the as-obtained S-DSSC. Similarly as in the previous sections, the representative spectra at selected time

delays are shown in ESI† (Fig. S11), while representative pseudo-color 2D spectra of transient absorption data are shown in Fig. 7A. Fig. 7B–D presents the results of the global fit using the same model as for L-DSSC (two-exponential function with constant offset). The results for solid state cells should be compared with those of liquid solar cell made with the same dye (Fig. 4C–F).

The most important differences are the smaller contribution of the constant offset component and the shorter times τ_1 and τ_2 for S-DSSC (Fig. 7B–D) with respect to those of L-DSSC (Fig. 4C–F). The time constants obtained from the global fit are about three times shorter for S-DSSC than those for L-DSSC. The difference can be also clearly visualized by comparing the kinetics at the maximum of the oxidized dye band (750 nm), which are presented in Fig. 6D. Therefore, the additional quenching of the oxidized dye is observed for S-DSSC, which should be explained by fast regeneration of the dye by spiro-OMeTAD. In our systems, such a hole transfer occurs on the time scale of single and tens of ps. In the cells with liquid electrolyte the dye regeneration by redox couple (*e.g.* cobalt complex or iodide/iodine pair) occurs on the time scale of μs , but the hole injection from solid HTM can occur much faster, even competing with electron injection. Such a fast dye

regeneration has been reported for several systems,⁶ however, according to our knowledge, we show it for the first time for the popular carbazole dyes and spiro-OMeTAD.

In principle, the observed quenching of the oxidized MK2 dye in S-DSSC could be also explained by greatly enhanced electron recombination.³³ However, the decrease in the total APCE of S-DSSC is not more than half with respect to that of L-DSSC (Table 1), so we could expect not more than twice decrease in the residual signal in transient absorption.²⁵ The drop in the residual amplitude for S-DSSC is much larger than that, therefore, the quenching must be dominated by the fast hole transfer. Moreover, we can observe a clear correlation of the relative amplitude of constant offset component and lifetimes with the thickness of the mesoporous layer (Fig. 7B–D). The residual signal is the smallest and the time constants τ_1 and τ_2 are the shortest for **SC30dil** sample (thickness 150–200 nm). For **SP30dil** sample (1.3–1.5 μm) the values are intermediate, while for the thickest **SP30** layer (2.5–3 μm) the residual signal is the strongest and the time constants are the longest. As mentioned before, the problem in S-DSSC is the penetration of spiro-OMeTAD to deep parts of the mesoporous layer for the thickness above 1 μm . The limited penetration of HTM into titania can thus explain the trends we observe for

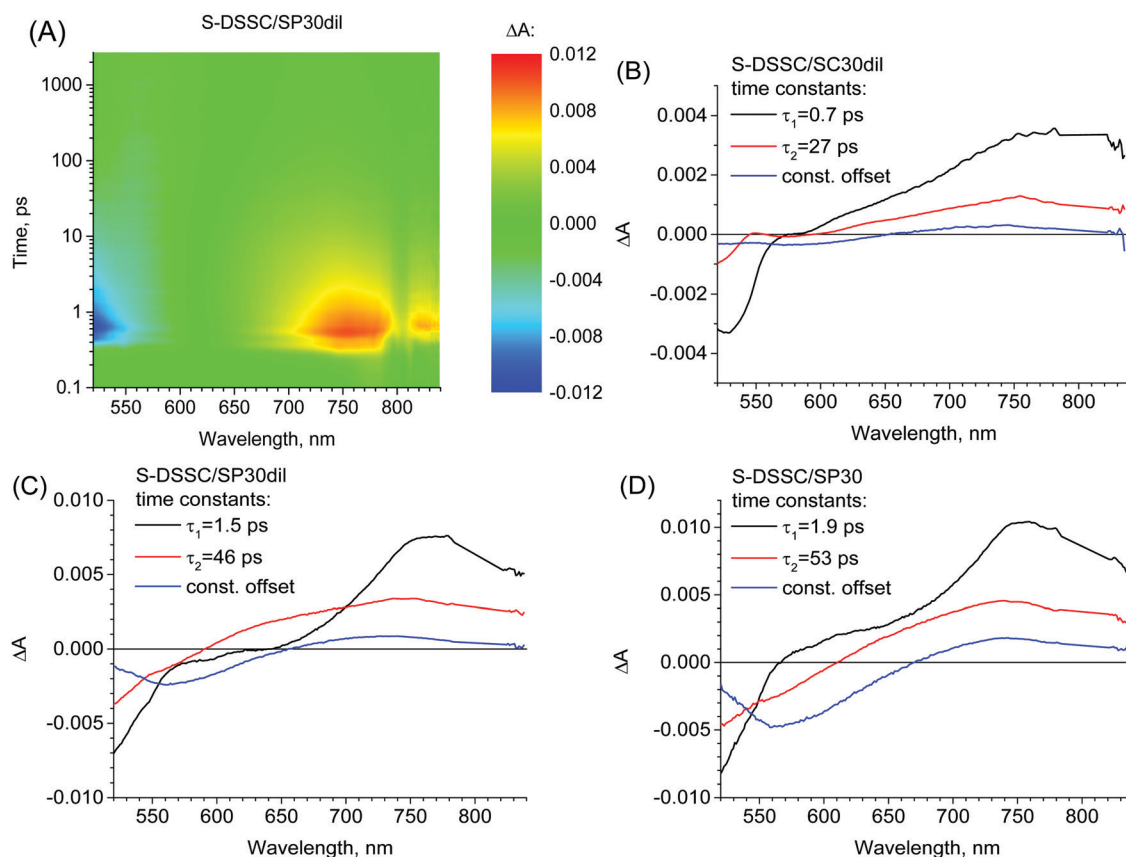


Fig. 7 Pseudo-color 2D spectra of original transient absorption data for S-DSSC with **SP30dil** titania layer (A). Examples of the global analysis of transient absorption data using two-exponential function with constant offset for S-DSSC samples with the indicated titania layers: **SC30dil** (B), **SP30dil** (C) and **SP30** (D). The graphs present pre-exponential factor spectra associated to the indicated time constants. The pump fluence was $100 \mu\text{J cm}^{-2}$, IRF was 0.3 ps and the excitation was from HTM side.

SC30dil, **SP30dil** and **SP30**: spiro-OMeTAD is probably not in contact with all dyes for **SP30dil** and especially for **SP30**, so their regeneration is slowed down. The observed differences in the quenching yield of oxidized MK2 by HTM correlates with the relative photocurrent (total APCE) of the cells: the highest for **SC30dil** and the lowest for **SP30** layers (Table 1C). It is in agreement with the previous reports about higher photocurrent in S-DSSC for better spiro-OMeTAD penetration and higher hole transfer yield.^{59–61}

Finally, another confirmation of poor pore filling in **SP30** samples comes from the analysis of the decomposition of the samples during transient absorption measurements (Table S4, ESI†). When the cell with **SP30** layer is excited from ETM side (which is hard to be reached by spiro-OMeTAD) a significant decrease (more than 12%) in the transient absorption signal for the consecutive cycles of the experiment is found. For the same **SP30** sample excited from HTM side, and for **SC30dil** and **SC30dil** samples excited at both sides, the changes in the signals are much smaller and probably random. The fast photodegradation under femtosecond pulse excitation occurs when the dyes are not in contact with regenerating medium (*e.g.* in the isolated sensitized electrodes) because the lifetime of the reactive oxidized state is very long.⁶

To summarize the transient absorption parts, the results prove that efficient charge transfer from perovskite to TiO₂ is responsible for improved performance in PSCs utilizing larger particle size. For DSSC utilizing liquid electrolyte a weaker electron recombination in TiO₂ films prepared with diluted TiO₂ is observed. For solid HTM based DSSC higher regeneration rates are observed for spin coated TiO₂ films whereas slower regeneration rates in screen printed films is found.

4. Conclusions

Improvement in the performance of perovskite solar cells (PSC) and dye-sensitized solar cells (DSSC) upon modifications of mesoporous titania layers has been studied. Its impact on the charge transfer dynamics in the complete solar cells as well as in pristine TiO₂ layers have been investigated by femtosecond transient absorption.

For PSC with triple cation perovskite (FA_{0.76} MA_{0.19} Cs_{0.05} Pb (I_{0.81} Br_{0.19})₃) the best efficiency of ~18% and photocurrent of ~24 mA cm⁻² were obtained for homogenous TiO₂ mesoporous layer made of 30 nm nanoparticles and with the thickness 150–200 nm. For about twice thicker, less homogenous and made of smaller particles (diameter 18 nm) titania layer, the best efficiency of only ~11% and photocurrent of ~17 mA cm⁻² were found. Shorter photocarriers lifetime in perovskite material was observed for the more efficient cells with respect to those with a worse TiO₂ layer (*e.g.* the average lifetime 1.9 ns vs. 3.3 ns when excited from TiO₂ side by 30 μJ cm⁻² pulse at 500 nm). It indicates that faster electron transfer from perovskite to the optimized TiO₂ is responsible for the higher photocurrent in these triple-cation PSC. Moreover, for better TiO₂ layer the photoinduced changes (appearance of red-shifted feature) in transient bleach signal were

revealed, which may indicate the occurrence of halide segregation in perovskite close to TiO₂ interface.

For DSSC, the effect of dilution of the commercial titania paste has been explored for popular MK2 dye and liquid cobalt-based electrolyte or solid state hole transporter (spiro-OMeTAD). The rise in the photovoltage (up to ~0.9 V), higher dye loading per layer thickness and the improvement in relative photocurrent were observed for the liquid cells prepared from the diluted paste (2:1 w/w ratio) with respect to those obtained for the cells prepared from undiluted one. The best efficiency of ~4.5% was obtained for DSSC having the titania mesoporous layer of thickness as small as 1.3–1.5 μm and in the absence of scattering layer. The dynamics of electron injection and recombination was similar in the cells with both diluted and undiluted titania pastes. However, the fast component of unwanted recombination was slightly slower (by about 30%) in the samples with the diluted titania phase than in those made with undiluted ones.

For solid state DSSC, the use of diluted paste results in higher voltage and better relative photocurrent, similar to those of liquid DSSC. The transient absorption studies reveal that the hole injection from MK2 dye to spiro-OMeTAD takes place on the very fast ps time scale (comparable to that of electron injection) and the evidence of the deeper penetration of spiro-OMeTAD into the mesoporous titania is presented.

Moreover, all titania layers (for PSC and DSSC) have been also studied separately in other transient absorption experiments by direct excitation in UV range and observation of electron and hole dynamics. The transient signals of different species have been identified in distinct spectral regions and compared between the samples of different layers: free and trapped electrons from 800 to 1500 nm, trapped holes around 600 nm and thermal artifacts below 400 nm. The decay of free electrons was observed to occur mainly with the time constants <1 ps, and the recombination of holes and electrons took place in the combined first and second order processes. The decay of trapped electrons was slower in the thicker titania layers used for DSSC than in the thinner layers in PSC.

Conflicts of interest

There are no conflicts to declare.

Acknowledgements

This work was supported by NCN (National Science Centre, Poland) under the project no. 2015/18/E/ST4/00196 and 0019/DIA/2017/46 (“Diamentowy Grant”) financed by the Polish Ministry of Science and Higher Education.

References

- 1 NREL, Best Res. Effic. Chart | Photovolt. Res. | NREL, 2019.
- 2 A. Yella, H.-W. Lee, H. N. Tsao, Ch. Yi, A. K. Chandiran, Md. K. Nazeeruddin, E. W.-G. Diau, Ch.-Y. Yeh, S. M. Zakeeruddin and M. Grätzel, *Science*, 2011, **334**, 629–634.

- 3 K. Kakiage, Y. Aoyama, T. Yano, K. Oya, J. I. Fujisawa and M. Hanaya, *Chem. Commun.*, 2015, **51**, 15894–15897.
- 4 H. Michaels, M. Rinderle, R. Freitag, I. Benesperi, T. Edvinsson, R. Socher, A. Gagliardi and M. Freitag, *Chem. Sci.*, 2020, **11**, 2895–2906.
- 5 M. Freitag, Q. Daniel, M. Pazoki, K. Sveinbjörnsson, J. Zhang, L. Sun, A. Hagfeldt and G. Boschloo, *Energy Environ. Sci.*, 2015, **8**, 2634–2637.
- 6 C. Martín, M. Ziólek and A. Douhal, *J. Photochem. Photobiol., C*, 2016, **26**, 1–30.
- 7 D. G. Lee, M. Ch. Kim, B. J. Kim, D. H. Kim, S. M. Lee, M. Choi, S. Lee and H. S. Jung, *Appl. Surf. Sci.*, 2019, **477**, 131–136.
- 8 A. Hagfeldt, G. Boschloo, L. Sun, L. Kloo and H. Pettersson, *Chem. Rev.*, 2010, **110**, 6595–6663.
- 9 U. Bach, D. Lupo, P. Comte, J. E. Moser, F. Weissörtel, J. Salbeck, H. Spreitzer and M. Grätzel, *Nature*, 1998, **395**, 583–585.
- 10 H. J. Snaith, A. Petrozza, S. Ito, H. Miura and M. Grätzel, *Adv. Funct. Mater.*, 2009, **19**, 1810–1818.
- 11 U. B. Cappel, A. L. Smeigh, S. Plogmaker, E. M. J. Johansson, H. Rensmo, L. Hammarström, A. Hagfeldt and G. Boschloo, *J. Phys. Chem. C*, 2011, **115**, 4345–4358.
- 12 I. K. Ding, N. Tétreault, J. Brillet, B. E. Hardin, E. H. Smith, S. J. Rosenthal, F. Sauvage, M. Grätzel and M. D. McGehee, *Adv. Funct. Mater.*, 2009, **19**, 2431–2436.
- 13 C. T. Weisspfennig, D. J. Hollman, C. Menelaou, S. D. Stranks, H. J. Joyce, M. B. Johnston, H. J. Snaith and L. M. Herz, *Adv. Funct. Mater.*, 2014, **24**, 668–677.
- 14 W. Zhang, Y. Wu, H. W. Bahng, Y. Cao, C. Yi, Y. Saygili, J. Luo, Y. Liu, L. Kavan, J. E. Moser, A. Hagfeldt, H. Tian, S. M. Zakeeruddin, W. H. Zhu and M. Grätzel, *Energy Environ. Sci.*, 2018, **11**, 1779–1787.
- 15 H. J. Snaith, *J. Phys. Chem. Lett.*, 2013, **4**, 3623–3630.
- 16 W. S. Yang, B. W. Park, E. H. Jung, N. J. Jeon, Y. C. Kim, D. U. Lee, S. S. Shin, J. Seo, E. K. Kim, J. H. Noh and S. I. Seok, *Science*, 2017, **356**, 1376–1379.
- 17 M. Saliba, T. Matsui, J.-Y. Seo, K. Domanski, J.-P. Correa-Baena, M. K. Nazeeruddin, S. M. Zakeeruddin, W. Tress, A. Abate, A. Hagfeldt and M. Grätzel, *Energy Environ. Sci.*, 2016, **9**, 1989–1997.
- 18 N. Koumura, Z. S. Wang, S. Mori, M. Miyashita, E. Suzuki and K. Hara, *J. Am. Chem. Soc.*, 2006, **128**, 14256–14257.
- 19 T. W. Hamann, *Dalton Trans.*, 2012, **41**, 3111–3115.
- 20 S. M. Feldt, E. A. Gibson, E. Gabrielsson, L. Sun, G. Boschloo and A. Hagfeldt, *J. Am. Chem. Soc.*, 2010, **132**, 16714–16724.
- 21 A. Pradhan, M. Sai Kiran, G. Kapil, S. Hayase and S. S. Pandey, *Sol. Energy Mater. Sol. Cells*, 2019, **195**, 122–133.
- 22 J. Idígoras, G. Burdziński, J. Karolczak, J. Kubicki, G. Oskam, J. A. Anta and M. Ziólek, *J. Phys. Chem. C*, 2015, **119**, 3931–3944.
- 23 H. S. Kim, S. B. Ko, I. H. Jang and N. G. Park, *Chem. Commun.*, 2011, **47**, 12637–12639.
- 24 P. D. T. Huibers and D. O. Shah, *Langmuir*, 1997, **13**, 5995–5998.
- 25 M. Gierszewski, A. Glinka, I. Gradzka, M. Jancelewicz and M. Ziólek, *ACS Appl. Mater. Interfaces*, 2017, **9**, 17102–17114.
- 26 A. Glinka, M. Gierszewski and M. Ziólek, *J. Phys. Chem. C*, 2018, **122**, 8147–8158.
- 27 M. Gierszewski, A. Glinka, I. Gradzka, B. Gierczyk and M. Ziólek, *J. Phys. Chem. C*, 2018, **122**, 25764–25775.
- 28 K. Pydzińska, P. Florczak, G. Nowaczyk and M. Ziólek, *Synth. Met.*, 2017, **232**, 181–187.
- 29 Y. Chen, F. Huang, W. Xiang, D. Chen, L. Cao, L. Spiccia, R. A. Caruso and Y. B. Cheng, *Nanoscale*, 2014, **6**, 13787–13794.
- 30 S. Ito, H. Miura, S. Uchida, M. Takata, K. Sumioka, P. Liska, P. Comte, P. Péchy and M. Grätzel, *Chem. Commun.*, 2008, 5194–5196.
- 31 A. Glinka, M. Gierszewski, B. Gierczyk, G. Burdziński, H. Michaels, M. Freitag and M. Ziólek, *J. Phys. Chem. C*, 2020, **124**, 2895–2906.
- 32 U. B. Cappel, T. Daeneke and U. Bach, *Nano Lett.*, 2012, **12**, 4925–4931.
- 33 A. Abate, M. Planells, D. J. Hollman, S. D. Stranks, A. Petrozza, A. R. S. Kandada, Y. Vaynzof, S. K. Pathak, N. Robertson and H. J. Snaith, *Adv. Energy Mater.*, 2014, **4**, 1400166.
- 34 I. R. Perera, A. Gupta, W. Xiang, T. Daeneke, U. Bach, R. A. Evans, C. A. Ohlin and L. Spiccia, *Phys. Chem. Chem. Phys.*, 2014, **16**, 12021–12028.
- 35 B. Xu, H. Tian, L. Lin, D. Qian, H. Chen, J. Zhang, N. Vlachopoulos, G. Boschloo, Y. Luo, F. Zhang, A. Hagfeldt and L. Sun, *Adv. Energy Mater.*, 2015, **5**, 1401185.
- 36 R. Katoh, M. Murai and A. Furube, *Chem. Phys. Lett.*, 2010, **500**, 309–312.
- 37 J. K. Cooper, S. E. Reyes-Lillo, L. H. Hess, C. M. Jiang, J. B. Neaton and I. D. Sharp, *J. Phys. Chem. C*, 2018, **122**, 20642–20652.
- 38 K. E. Knowles, M. D. Koch and J. L. Shelton, *J. Mater. Chem. C*, 2018, **6**, 11853–11867.
- 39 T. Berger, J. A. Anta and V. Morales-Flórez, *J. Phys. Chem. C*, 2012, **116**, 11444–11455.
- 40 J. Sobuś, J. Kubicki, G. Burdziński and M. Ziólek, *ChemSusChem*, 2015, **8**, 3118–3128.
- 41 J. Sobuś, B. Gierczyk, G. Burdziński, M. Jancelewicz, E. Polanski, A. Hagfeldt and M. Ziólek, *Chem. – Eur. J.*, 2016, **22**, 15807–15818.
- 42 J. S. Manser and P. V. Kamat, *Nat. Photonics*, 2014, **8**, 737–743.
- 43 F. Deschler, M. Price, S. Pathak, L. E. Klintberg, D. D. Jarausch, R. Higler, S. Hüttner, T. Leijtens, S. D. Stranks, H. J. Snaith, M. Atatüre, R. T. Phillips and R. H. Friend, *J. Phys. Chem. Lett.*, 2014, **5**, 1421–1426.
- 44 L. Wang, C. McCleese, A. Kovalsky, Y. Zhao and C. Burda, *J. Am. Chem. Soc.*, 2014, **110**, 12205–12208.
- 45 M. T. Trinh, X. Wu, D. Niesner and X.-Y. Zhu, *J. Mater. Chem. A*, 2015, **3**, 9285–9290.
- 46 T. C. Sum, N. Mathews, G. Xing, S. S. Lim, W. K. Chong, D. Giovanni and H. A. Dewi, *Acc. Chem. Res.*, 2016, **49**, 294–302.
- 47 J. Leng, J. Liu, J. Zhang and S. Jin, *J. Phys. Chem. Lett.*, 2016, **7**, 5056–5061.
- 48 T. W. Crothers, R. L. Milot, J. B. Patel, E. S. Parrott, J. Schlipf, P. Müller-Buschbaum, M. B. Johnston and L. M. Herz, *Nano Lett.*, 2017, **17**, 5782–5789.

- 49 E. Serpetzoglou, I. Konidakis, G. Kakavelakis, T. Maksudov, E. Kymakis and E. Stratakis, *ACS Appl. Mater. Interfaces*, 2017, **9**, 43910–43919.
- 50 P. Piatkowski, B. Cohen, F. Javier Ramos, M. Di Nunzio, M. K. Nazeeruddin, M. Grätzel, S. Ahmad and A. Douhal, *Phys. Chem. Chem. Phys.*, 2015, **17**, 14674–14684.
- 51 K. Pydzińska, J. Karolczak, I. Kosta, R. Tena-Zaera, A. Todinova, J. Idígoras, J. A. Anta and M. Ziólek, *ChemSusChem*, 2016, **9**, 1647–1659.
- 52 K. Pydzińska-Białek, J. Szeremeta, K. Wojciechowski and M. Ziólek, *J. Phys. Chem. C*, 2019, **123**, 110–119.
- 53 K. Pydzińska-Białek, V. Drushliak, E. Coy, K. Załęski, J. Flach, J. Idígoras, L. Contreras-Bernal, A. Hagfeldt, J. A. Anta and M. Ziólek, *ACS Appl. Mater. Interfaces*, 2020, **12**, 30399–30410.
- 54 T. R. Hopper, A. Gorodetsky, J. M. Frost, C. Müller, R. Lovrincic and A. A. Bakulin, *ACS Energy Lett.*, 2018, **3**, 2199–2205.
- 55 Q. Lin, Z. Wang, H. J. Snaith, M. B. Johnston and L. M. Herz, *Adv. Sci.*, 2018, **5**, 1–8.
- 56 L. M. Herz, *Annu. Rev. Phys. Chem.*, 2016, **67**, 65–89.
- 57 M. C. Brennan, A. Ruth, P. V. Kamat and M. Kuno, *Trends Chem.*, 2020, **2**, 282–301.
- 58 J. T. Dubose and P. V. Kamat, *J. Am. Chem. Soc.*, 2020, **142**, 5362–5370.
- 59 J. E. Kroeze, N. Hirata, L. Schmidt-Mende, C. Orizu, S. D. Ogier, K. Carr, M. Grätzel and J. R. Durrant, *Adv. Funct. Mater.*, 2006, **16**, 1832–1838.
- 60 J. Melas-Kyriazi, I. K. Ding, A. Marchioro, A. Punzi, B. E. Hardin, G. F. Burkhard, N. Tétreault, M. Grätzel, J. E. Moser and M. D. McGehee, *Adv. Energy Mater.*, 2011, **1**, 407–414.
- 61 Y. S. Kwon, J. Lim, I. Song, I. Y. Song, W. S. Shin, S. J. Moon and T. Park, *J. Mater. Chem.*, 2012, **22**, 8641–8648.

Supplementary Information

for

Impact of improvements in mesoporous titania layers on ultrafast electron transfer dynamics in perovskite and dye-sensitized solar cells

Katarzyna Pydzińska-Białek,^a Adam Glinka,^a Viktoriia Drushliak,^a
Grzegorz Nowaczyk,^b Patryk Florczak^b and Marcin Ziółek^{a*}

^a *Faculty of Physics, Adam Mickiewicz University,
Uniwersytetu Poznańskiego 2, 61-614 Poznań, Poland*

^b *NanoBioMedical Centre, Adam Mickiewicz University,
Wszehnicy Piastowskiej 3, 61-614 Poznań, Poland*

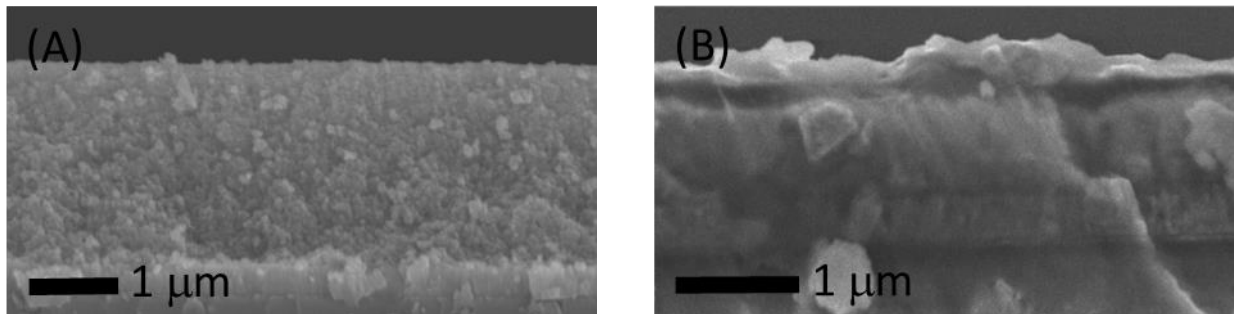


Figure S1. SEM cross sections of **SP30** titania layer (A) and PSC made using **SC18dil** layer (B).

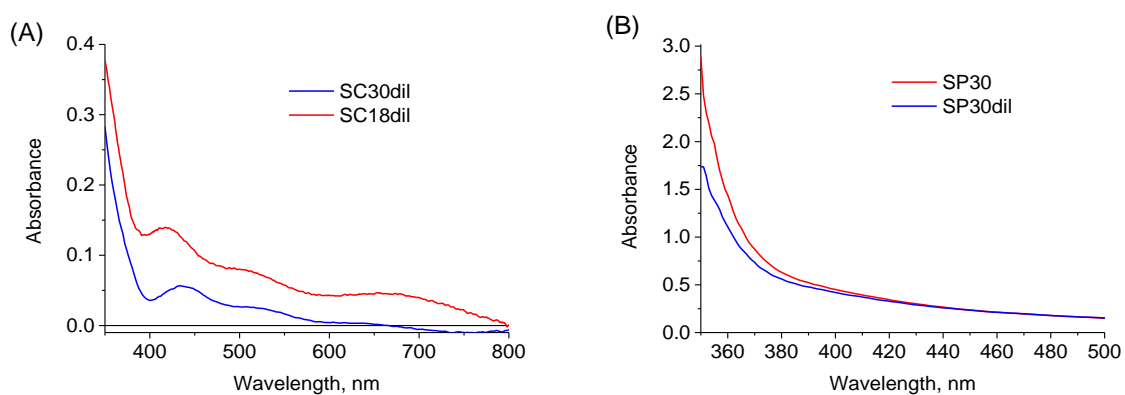


Figure S2. Stationary absorption of the electrodes with titania layers: **SC30dil** and **SC18dil** (A), **SP30dil** and **SP30** (B).

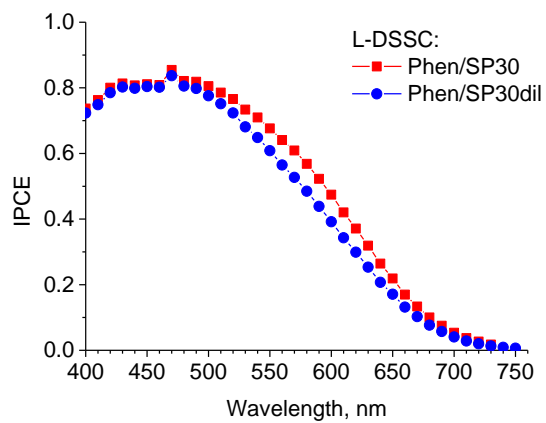


Figure S3. IPCE spectra of L-DSSC with **SP30dil** and **SP30** layers.

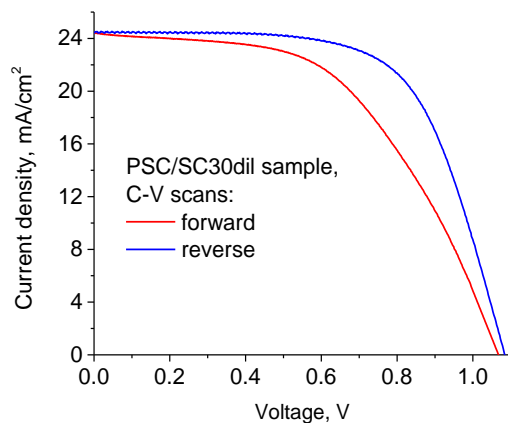


Figure S4. Example of current-voltage curves of PSC made using **SC30dil** layer measured at forward and backward directions (scanning rate 50mV/s). Hysteresis index HI obtained from the graph ($HI =$

$$\frac{J_{rev}\left(\frac{V_{oc}}{2}\right) - J_{for}\left(\frac{V_{oc}}{2}\right)}{J_{rev}\left(\frac{V_{oc}}{2}\right)}$$

) is equal to 0.05.

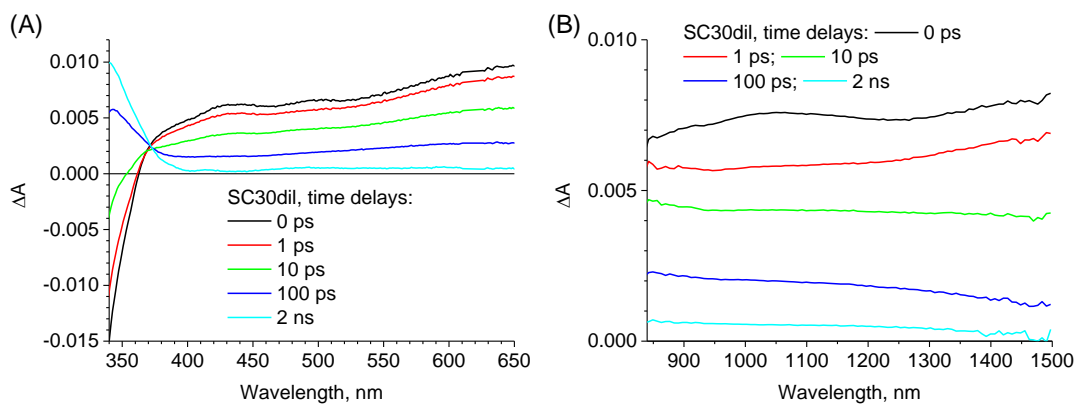


Figure S5. Transient absorption spectra at selected time delays between pump and probe pulses for electrode with SC30dil layer: in UV- VIS range excited at 310 nm with 4 mJ/cm² (A) and in NIR range excited at 355 nm with 4 mJ/cm² (B).

Mixed first and second order function:

The change of the population of the excited carriers (n) over time (t) in the semiconductor can be described by:

$$-\frac{dn}{dt} = k_1 n + k_2 n^2$$

The first order decay with the rate constant k_1 is related to the trap-assisted recombination (Shockley-Read-Hall recombination). The second order process described by the rate constant k_2 is due to free carrier recombination (band-to-band radiative recombination). Solution of the above equation can be given by the following analytical function, which is the mixed first and second order decay function:

$$n(t) = \frac{n_0 k_1}{k_1 \exp(k_1 t) + n_0 k_2 (\exp(k_1 t) - 1)},$$

where n_0 is initial number of excited carriers.

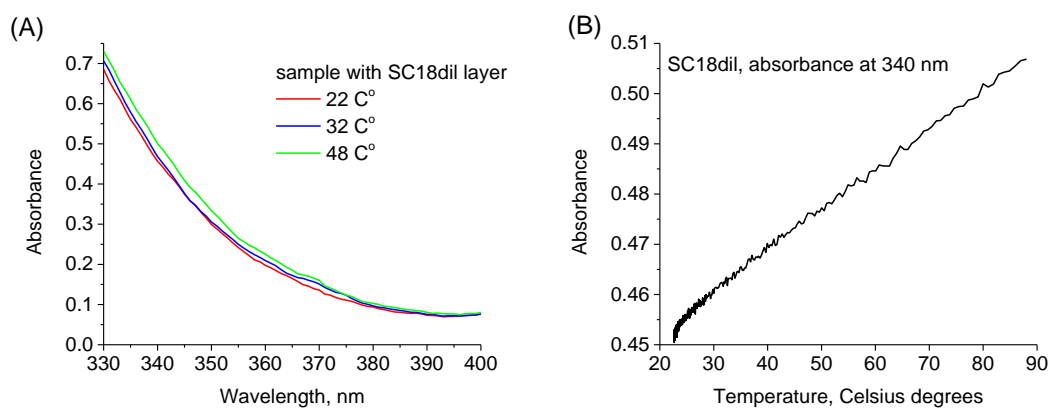


Figure S6. Temperature dependence of the stationary absorption of the electrodes with titania.

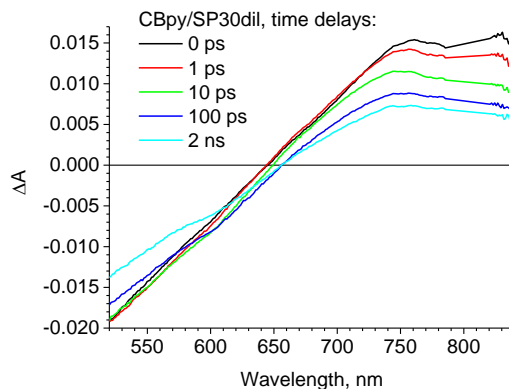


Figure S7. Transient absorption spectra at selected time delays between pump and probe pulses for **CBpy/SP30dil** liquid DSSC sample. The excitation wavelength was 500 nm with 100 $\mu\text{J}/\text{cm}^2$ fluence.

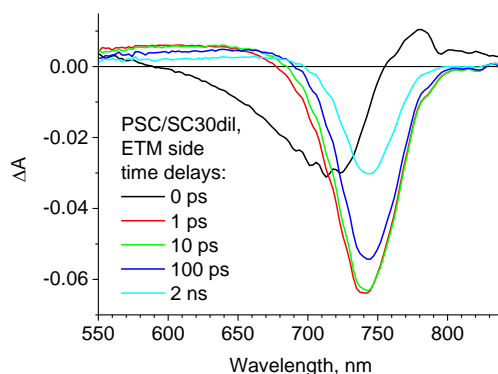


Figure S8. Transient absorption spectra at selected time delays between pump and probe pulses for **PSC/SC30dil** sample pumped from ETM side. The excitation wavelength was 500 nm with 30 $\mu\text{J}/\text{cm}^2$ fluence.

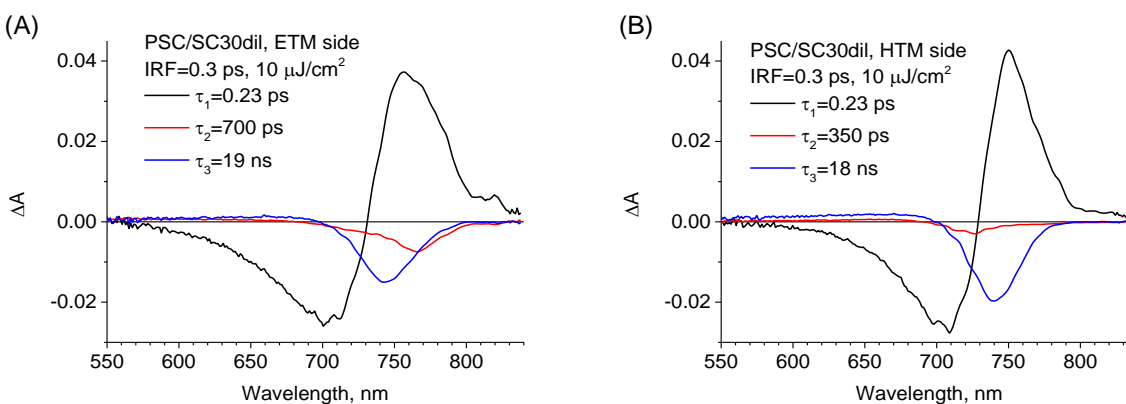


Figure S9. The results of global analysis of transient absorption data using three-exponential function for PSC samples. The graphs present pre-exponential factor spectra associated to the indicated time constants. The pump fluence was 10 $\mu\text{J}/\text{cm}^2$ and IRF was 0.3 ps.

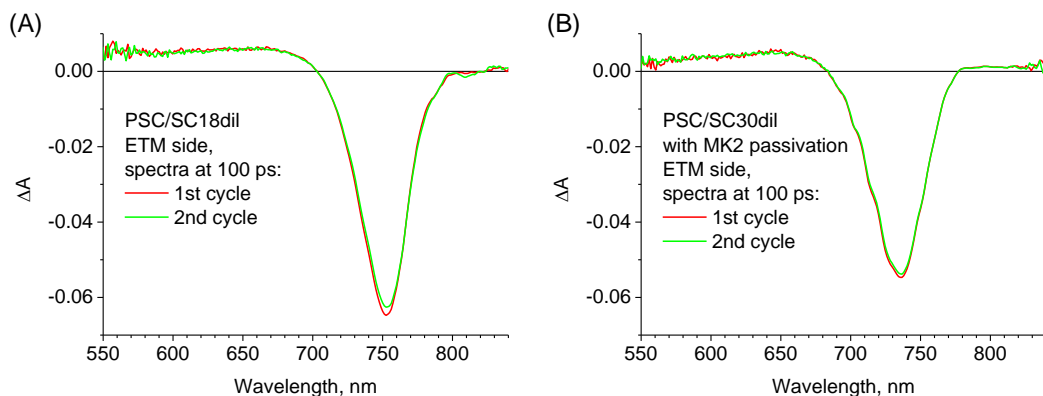


Figure S10. Transient absorption spectra for PSC with **SC18dil** layer (A) and with **SC30dil** layer passivated with MK2 dyes (B), both measured at 100 ps for different consecutive cycles at ETM side. The pump fluence was $30 \mu\text{J}/\text{cm}^2$.

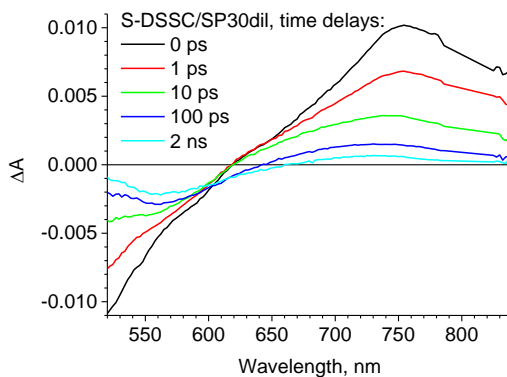


Figure S11. Transient absorption spectra at selected time delays between pump and probe pulses for S- DSSC cell with **SP30dil** layer pumped from HTM side. The excitation wavelength was 500 nm at $100 \mu\text{J}/\text{cm}^2$ fluence.

Table S1. Parameters of the different mesoporous titania layers:

Abbreviation	Deposition method	Particle size [nm]	Preparation	Resulted layer thickness [nm]
SC18dil	Spin-Coating	18	Dyename DN-GPS-18TS paste diluted 1:6 in ethanol	300-350
SC30dil	Spin-Coating	30	GreatCell Solar 30NR-D paste diluted 1:6 in ethanol	150-200
SP30	Screen-Printing	30	Dyename DN-GPS-30TS paste without any dilution	2500-3000
SP30dil	Screen-Printing	30	Dyename DN-GPS-30TS paste diluted 2:1 in (cellulose + ethanol + alpha-terpineol)	1300-1500

Table S2. Averaged photovoltaic parameters and their errors (standard deviation) of the different cells:

Sample	V_{oc} [V]	J_{sc} [mA/cm ²]	FF	PCE [%]
L-DSSC/Phen/SP30	0.85 ± 0.01	7.79 ± 0.25	0.66 ± 0.03	4.32 ± 0.02
L-DSSC/Phen/SP30dil	0.88 ± 0.01	7.43 ± 0.10	0.69 ± 0.01	4.43 ± 0.02
PSC/SC30dil	1.08 ± 0.01	22.5 ± 2.1	0.63 ± 0.04	15.2 ± 2.3
S-DSSC/SC30dil	0.72 ± 0.01	0.95 ± 0.04	0.57 ± 0.01	0.39 ± 0.02
S-DSSC/SP30dil	0.45 ± 0.13	3.52 ± 0.32	0.35 ± 0.07	0.57 ± 0.23
S-DSSC/SP30	0.44 ± 0.03	2.67 ± 0.88	0.35 ± 0.03	0.41 ± 0.12

Table S3. Effects of spattered gold thickness and smaller or bigger active surface on the photovoltaic parameters of the cells:

Sample	Thickness [nm]	Surface [cm ²]	V_{oc} [V]	J_{sc} [mA/cm ²]	FF	PCE [%]	$Total APCE$
PSC/SC30dil	50-100	0.05	1.09	24.5	0.64	17.1	1.17
PSC/SC30dil	25-50	0.05	1.07	24.4	0.68	17.8	1.17
PSC/SC30dil	50-100	0.125	0.98	15.5	0.56	8.5	0.74
PSC/SC30dil	25-50	0.125	1.02	16.8	0.66	11.3	0.81
S-DSSC/SP30dil	50-100	0.05	0.32	3.83	0.28	0.34	0.59
S-DSSC/SP30dil	25-50	0.05	0.58	3.20	0.42	0.79	0.49

Effect of gold sputtering method

As reported, sputtering method may introduce additional series resistance between spiro-OMeTAD and Au or cause partial damage to the organic HTM, which results in lowering FF and, for very high resistance, even the photocurrent. To confirm this possibility we prepared the test PSCs with gold electrodes of larger surface (resulting in the active surface increase from 0.05 cm² to 0.125 cm²) and also we checked the effect of thinner gold layer (25-50 nm instead of 50-100 nm). As can be seen in Table S2, indeed the larger active surface decreases FF , while the shorter deposition increases FF .

Table S4. Average decrease of the amplitude for consecutive scans during transient absorption measurements of S-DSSC:

Sample and excitation side	Difference in the amplitude
SC30dil HTM side	-1%
SP30dil ETM side	+1.5%
SP30dil HTM side	-5%
SP30 ETM side	-12.5%
SP30 HTM side	-2.5%

Paper VI

**Complexity of Electron Injection Dynamics and Light Soaking Effects
in Efficient Dyes for Modern DSSC**

Glinka, A.; Kubicki, J.; Ziólek, M.

Energies, 2021, 14, 407.

Article

Complexity of Electron Injection Dynamics and Light Soaking Effects in Efficient Dyes for Modern DSSC

Adam Glinka *, Jacek Kubicki  and Marcin Ziółek * 

Quantum Electronics Laboratory, Faculty of Physics, Adam Mickiewicz University in Poznań, Uniwersytetu Poznańskiego 2, 61-614 Poznań, Poland; jacek.kubicki@amu.edu.pl

* Correspondence: adam.glinka@amu.edu.pl (A.G.); marziol@amu.edu.pl (M.Z.)

Abstract: Electron transfer dynamics in dye sensitized solar cells (DSSCs) employing triphenylamine Y123 dye were investigated by means of femtosecond broadband transient absorption spectroscopy in the visible and mid-IR range of detection. The electron injection process to the titania conduction band was found to appear biphasically with the time constant of the first component within 350 fs and that of the second component between 80 and 95 ps. Subsequently, the effects of continuous irradiation on the ultrafast and fast electron transfer processes were studied in the systems comprising Y123 dye or carbazole MK2 dye in combination with cobalt- or copper-based redox mediators: [Co(bpy)₃](B(CN)₄)_{2/3} (bpy = 2,2'-bipyridine) or [Cu(tmby)₂](TFSI)_{1/2} (tmby = 4,4',6,6' tetramethyl-2,2'-bipyridine, TFSI = bis(trifluoromethane)sulfonamide). We have found that the steady-state illumination led to acceleration of the electron injection process due to the lowering of titania conduction band edge energy. Moreover, we have observed that the back electron transfer to the oxidized dye was suppressed. These changes in the initial (up to 3 ns) charge separation efficiency were directly correlated with the photocurrent enhancement.

Keywords: dye sensitized solar cell; electron injection; light soaking; triphenylamine dye; carbazole dye; cobalt complex; copper complex; ultrafast VIS spectroscopy; ultrafast mid-IR spectroscopy



Citation: Glinka, A.; Kubicki, J.; Ziółek, M. Complexity of Electron Injection Dynamics and Light Soaking Effects in Efficient Dyes for Modern DSSC. *Energies* **2021**, *14*, 407. <https://doi.org/10.3390/en14020407>

Received: 12 December 2020

Accepted: 11 January 2021

Published: 13 January 2021

Publisher's Note: MDPI stays neutral with regard to jurisdictional claims in published maps and institutional affiliations.



Copyright: © 2021 by the authors. Licensee MDPI, Basel, Switzerland. This article is an open access article distributed under the terms and conditions of the Creative Commons Attribution (CC BY) license (<https://creativecommons.org/licenses/by/4.0/>).

1. Introduction

Dye sensitized solar cells (DSSCs) have been much improved since the breakthrough achieved by O'Regan and Graetzel in 1991 [1]. Although DSSC have been recently outperformed by other emerging photovoltaic technologies (including perovskite [2], quantum dot solar cells [3], and organic photovoltaics [4]) in terms of power conversion efficiency (PCE) in full sunlight conditions, they are experiencing a renaissance and have attracted interest again, thanks to their superior performance in low ambient light conditions [5–7]. Thus, such cells enable powering of the novel class of electronic devices networked on the Internet of Things (IoT) [5]. In the pursuit of more efficient, stable, environmentally friendly, and cheap DSSC systems, a great deal of widely used materials and compounds have been replaced by novel counterparts, setting new standards. In particular, the introduction of fully organic D-π-A dyes [8–11] replacing ruthenium complexes [12] permitted bypassing a problem of low abundance and high price of this element as well as the issue of relatively low extinction coefficients of its coordination compounds. Another milestone achievement has been the replacement of iodide/triiodide (I⁻/I₃⁻) redox couple by new generation of coordination compounds of cobalt (Co³⁺/Co²⁺) [9] and more environmentally friendly copper (Cu²⁺/Cu⁺) [13–15], which allowed achieving over 1.1 V open circuit voltages (V_{OC}) in highly efficient DSSCs.

Thanks to the advances in new compounds and materials design, the highest achieved PCEs has been pushed up to ~14% [16,17] at full sunlight and 32–34% [5,18] in ambient light conditions. At the same time, the above-mentioned advances have raised fundamental questions on the operation of systems comprising the state-of-the-art cell components. Although

the number of studies focused on triphenylamine (TPA) dyes in combination with transition metals coordination compounds as redox mediators is relatively high [10,15,16,19], only a few authors have brought up a topic of ultrafast electron transfer dynamics of the benchmark TPA dye: 3-{6-[4-[bis(2',4'-dihexyloxybiphenyl-4-yl) amino-]phenyl]-4,4-dihexyl-cyclopenta-[2,1-b:3,4-b'] dithiophene-2-yl]-2-cyanoacrylic acid coded as Y123 (or its popular counterpart coded as LEG4) [20,21], Supplementary Scheme S1A. In particular, no detailed information has been published on the examination of the excited state dynamics of Y123 interacting with mesoporous titania in broad visible light spectrum. This issue should be examined, especially in light of recent advances on new, more complex and highly efficient TPA dyes [17,22–24]. It is especially important to establish whether the dynamics of electron injection in the fully operating solar cells occurs on the ultrafast time scale up to single ps (like for many organic dyes for DSSC), or extends into much longer time scales, e.g., for some ruthenium compounds [25,26]. According to our knowledge, so far there have been only two reports about the electron injection dynamics for Y123. In the first report the process occurring within about 2 ps was detected using femtosecond diffuse reflectance spectroscopy [21]. In the second one, the contribution of the electron injection time constant of 12 ps was reported in the inert electrolyte, using the picosecond time-resolved transient absorption (TA) spectroscopy [20]. Surprisingly, this time constant has been extended to 25 ps in the samples with a solid state Cu-based electrolyte [20]. It should be noted that in both the above-mentioned papers, the electron injection time constant determination has been based on the transient absorption kinetics at a single probe wavelength in the visible range. Moreover, in the context of suggestions reported on the possibility of direct interfacial electron transfer [27] between the LEG4 dye ground state and the conduction band of titania, based on the theoretical studies [28], a comprehensive experimental study was needed to verify if this process took place. If it does take place and is thoroughly characterized, it could help bypass the most significant potential loss in the state of the art DSSCs, which is caused by the electron injection process [7,23], so it should not be disregarded.

Thanks to the advances in new compounds and materials design, the highest achieved PCEs has been pushed up to ~14% [16,17] at full sunlight and 32–34% [5,18] in ambient light conditions. At the same time, the above-mentioned advances have raised fundamental questions on the operation of systems comprising the state-of-the-art cell components. Although the number of studies focused on triphenylamine (TPA) dyes in combination with transition metals coordination compounds as redox mediators is relatively high [10,15,16,19], only a few authors have brought up a topic of ultrafast electron transfer dynamics of the benchmark TPA dye: 3-{6-[4-[bis(2',4'-dihexyloxybiphenyl-4-yl) amino-]phenyl]-4,4-dihexyl-cyclopenta-[2,1-b:3,4-b'] dithiophene-2-yl]-2-cyanoacrylic acid coded as Y123 (or its popular counterpart coded as LEG4) [20,21], Supplementary Scheme S1A. In particular, no detailed information has been published on the examination of the excited state dynamics of Y123 interacting with mesoporous titania in broad visible light spectrum. This issue should be examined, especially in light of recent advances on new, more complex and highly efficient TPA dyes [17,22–24]. It is especially important to establish whether the dynamics of electron injection in the fully operating solar cells occurs on the ultrafast time scale up to single ps (like for many organic dyes for DSSC), or extends into much longer time scales, e.g., for some ruthenium compounds [25,26]. According to our knowledge, so far there have been only two reports about the electron injection dynamics for Y123. In the first report the process occurring within about 2 ps was detected using femtosecond diffuse reflectance spectroscopy [21]. In the second one, the contribution of the electron injection time constant of 12 ps was reported in the inert electrolyte, using the picosecond time-resolved transient absorption (TA) spectroscopy [20]. Surprisingly, this time constant has been extended to 25 ps in the samples with a solid state Cu-based electrolyte [20]. It should be noted that in both the above-mentioned papers, the electron injection time constant determination has been based on the transient absorption kinetics at a single probe wavelength in the visible range. Moreover, in the context of suggestions reported on

the possibility of direct interfacial electron transfer [27] between the LEG4 dye ground state and the conduction band of titania, based on the theoretical studies [28], a comprehensive experimental study was needed to verify if this process took place. If it does take place and is thoroughly characterized, it could help bypass the most significant potential loss in the state of the art DSSCs, which is caused by the electron injection process [7,23], so it should not be disregarded.

Thus, in this work, we focused on analysis of the excited state dynamics and charge transfer processes occurring in DSSC systems comprising Y123 dye. We aimed at answering the questions about possible modes and solving the controversies (vide infra) about the dynamics of electron injection. To do this, we used femtosecond transient absorption in the broad visible spectral range as well as femtosecond transient absorption in the mid-IR range. To achieve better understanding of the processes observed, the transient absorption kinetics at many wavelengths were analyzed simultaneously by means of the global fit. Transient absorption techniques in both visible and IR ranges were used to study the electron injection dynamics in DSSCs since the initial systems with ruthenium compounds had already been extensively studied [26,29–31]. These techniques have been frequently used for DSSC with ruthenium and other organic dyes, as reviewed, e.g., in [25,32–36]. Moreover, our study was conducted on full operational DSSC samples as well as half cells based on sapphire substrates (transparent in mid-IR), however preserving all the same conditions relevant for studied processes. The dye cells used in this study were also subjected to constant illumination to study the changes that occur in the systems within the first hour of operation. In this way we could not only evaluate the proposed charge transfer model, but also reveal some new insights into the way that charge transfer phenomena in DSSCs change, due to the so called light soaking effects. They are commonly observed in DSSC systems [37–40] and have been usually assigned to the shifts of the conduction band edge [37,38] which could be caused by light induced changes in equilibrium of positively charged ions (Li^+ , H^+) and Lewis base (predominantly *tert*-butylpyridine—TBP) on the semiconductor/electrolyte interface [40]. Although the light soaking effect for DSSCs is very important, its detailed impact on electron injection and recombination dynamics in the studied systems has not been reported so far.

Besides the Y123 based cells, we used well-described systems based on carbazole MK2 dye (Supplementary Scheme S1B), extensively studied by our group for the last few years [41–45]. Both dyes were studied in combination with $[\text{Co}(\text{bpy})_3](\text{B}(\text{CN})_4)_{2/3}$ ($\text{bpy} = 2,2'$ -bipyridine) [9] and $[\text{Cu}(\text{tmby})_2](\text{TFSI})_{1/2}$ ($\text{tmby} = 4,4',6,6'$ tetramethyl-2,2'-bipyridine, TFSI = bis(trifluoromethane)sulfonamide) [15], providing new insights into the dynamics of electron separation and recombination in Y123 and their impact on photocurrent generation.

2. Materials and Methods

2.1. Device Fabrication

Unless otherwise stated, all the chemicals were purchased from Sigma-Aldrich (Saint Louis, MO, USA) and used without additional purification. The FTO (fluorine doped tin oxide) coated glass sheet (Sigma-Aldrich, Saint Louis, MO, USA, 2.2 mm thick, $13 \Omega \text{ sq}^{-1}$) was cleaned, the mesoporous titania layers (including pre- and post- TiCl_4 treatment) were deposited and the DSSCs were fabricated according to the procedures described elsewhere [45]. A layer of mesoporous titania of 2–3 μm in thickness, without a scattering film, was prepared by screen-printing technique, to provide sufficient light transmission for optical absorption measurements. The screen-printable 28–31 nm titania nanoparticles containing paste (DN-GPS-30TS) were provided by Dyenamo, Sweden. The compositions of solutions for titania sensitization were as follows: for Y123 (Dyenamo, Stockholm, Sweden) sensitized solar cells: 0.1 mM dye solution with 0.2 mM addition of cheno-deoxycholic acid (CDCA) in acetonitrile (ACN) and *tert*-butanol (*tert*-BuOH) 1:1 mixture, while for MK2 sensitized cells a 0.2 mM dye solution in toluene (TOL) was used. To some of the MK2 cells, 0.1 mM of CDCA was added. The electrolyte solution compositions were as follows:

Co-based—0.25 M $[\text{Co}(\text{bpy})_3](\text{B}(\text{CN})_4)_2$, 0.035 M $[\text{Co}(\text{bpy})_3](\text{B}(\text{CN})_4)_3$, 0.1 M LiClO_4 and 0.5 M TBP in ACN; Cu-based—0.2 M $[\text{Cu}(\text{tmby})_2](\text{TFSI})$, 0.04 M $[\text{Cu}(\text{tmby})_2](\text{TFSI})_2$, 0.1 M LiTFSI , 0.6 M TBP in ACN. In some indicated control cells, the electrolytes without TBP were used. Platinized counter electrodes for Co-based and poly-3,4 ethylenedioxythiophene (PEDOT) coated ones for Cu-based electrolyte mediated solar cells were prepared according to methods specified elsewhere [46].

Titania substrates for half-cells for mid-IR optical measurements were prepared according to the same procedures as for full DSSCs, but on 3 mm thick sapphire windows (Thorlabs) to provide transparency for mid-IR light. Sensitized titania substrates were sandwiched with blank sapphire window, with a 5 μL drop of the electrolyte inside and tightened with a gasket cut from Parafilm[®] inside a 3D printed frame presented in Supplementary Figure S1A.

2.2. Device Characterization

Steady state absorption spectra of sensitized or bare photoanodes were measured using a JASCO (Tokio, Japan) V-770 UV-VIS-NIR spectrophotometer equipped with 150 mm integrating sphere (LN-925). Current-voltage and incident photon to current efficiency (IPCE) spectra measurements were performed on the system coupling an Metrohm Autolab (Utrecht, Netherlands) M101 potentiostat and a photoelectric spectrometer (Instytut Fotonowy, Kraków, Poland) comprising a 150 W Xe lamp with an AM 1.5 G spectral filter adjusted to 100 mW cm^{-2} using a calibration cell (ABET-Technologies, Milford, CT, USA, model 15151).

The transient absorption (TA) systems (UV-VIS Helios spectrometer, Ultrafast Systems, Sarasota, FL, USA), and mid-IR PhaseTech Spectroscopy, Inc., Madison, WI, USA), 2D Quick Transient spectrometer, coupled with Spectra-Physics (Santa Clara, CA, USA) laser system, have been described in detail formerly [41,47]. The instrument response function (IRF) width was 100–200 fs and 350 fs (FWHM) for VIS and mid-IR experiments, respectively. In broadband VIS experiment, the pump pulse energies were set to different values providing approximately constant signal response for different wavelengths (20 nJ, 70 nJ and 200 nJ translating to 10 $\mu\text{J cm}^{-2}$, 35 $\mu\text{J cm}^{-2}$, and 100 $\mu\text{J cm}^{-2}$, respectively). In the mid-IR experiment, the pump pulse energies were set to 50 nJ, 100 nJ, and 500 nJ, which equals 200 $\mu\text{J cm}^{-2}$, 400 $\mu\text{J cm}^{-2}$, and 2 mJ cm^{-2} energy density. Transient absorption data were analyzed using the Surface Explorer software (Ultrafast Systems, Sarasota, FL, USA).

3. Results and Discussion

3.1. Monitoring Electron Injection in the Cells with Y123

In order to develop the model of charge transfer dynamics in the systems containing Y123 dye sensitized titania nanoparticles, we performed transient absorption measurements for full operational solar cells with Co- and Cu-based electrolytes (see the next section for the photovoltaic parameters of the samples). The data collected in 3 ns time window and 530–850 nm spectral range were analyzed by means of the singular value decomposition using 3 kinetic vectors. Subsequently, to obtain time constants and their wavelength dependent amplitudes (also called the pre-exponential factor spectra), three-exponential global analysis, including the convolution with IRF, was performed. Additionally, the constant offset component was incorporated, to take the residual spectra into account.

To get insight into the dynamics of excited state of Y123, the TA measurements were performed using three different pump wavelengths in the range of the dye's operation spectra. This strategy was chosen taking into account the hypothesis that that different electron injection processes might occur in the system with different contributions, depending on the excitation wavelengths. The range of the dye's operation was determined on the basis of the IPCE spectra shown in Supplementary Figure S1B. The IPCE onset wavelength in Y123 sensitized solar cells is equal to 700 nm and in our semi-transparent electrodes, 10% of the IPCE maximum was already reached at 640 nm. Thus, we have chosen it for the longest pump wavelength. The long wavelength response can be enhanced by the incorporation

of a thicker titania layer supported by scattering nanoparticles coating. However, such a construction of the solar cell does not provide sufficient quality of transient absorption measurements in the transmission mode.

Positive transient absorption signals in the visible light spectral range may originate from photon absorption from the excited electronic state of the dye to higher excited states of dye or may be due to absorption of a new species (e.g., oxidized dye). On the other hand, the negative signals are connected mainly with the ground state depopulation (bleaching) or stimulated emission. The components of transient absorption containing contributions from the decay of S_1 excited state as well as building up the band assigned to the oxidized state (manifested as a negative amplitude of pre-exponential factor) may be assigned to electron injection to the titania conduction band [25,35]. At the same time, the components related to the Y123 ground state recovery and the oxidized state band decay, should be linked to the undesired charge recombination process [48,49]. However, spectral and temporal overlapping of the TA signals originating from different processes, often makes a direct assignment of the obtained components to particular electron transfer processes arduous or even impossible. That is why different experimental approaches are usually required for proper charge transfer model elucidation. Therefore, in this work apart from the ultrafast transient absorption spectroscopy in the visible range, the ultrafast transient absorption spectroscopy in the mid-IR range was applied, which permits direct probing of the population of free electrons in titania conduction band [35,41,47].

Examples of original transient absorption spectra in the visible range for DSSCs with Y123 dye are shown in Supplementary Figure S2, while Figure 1 presents the pre-exponential factor spectra of the components obtained in the global analysis for pump wavelength at 560 nm. ΔA stands for the difference between the absorbances with and without a pump pulse. The spectrum of the fastest (1–2 ps) component contains a negative amplitude (or indentation in the positive amplitude) in the range matching the fluorescence spectrum (see Supplementary Figure S3). That is why this feature may be interpreted as stimulated emission decay. Another important feature of the first component is the positive band with the maximum around 700 nm, which should be related to the transition between S_1 state and one of higher excited electronic states of the dye (see the results in solution in Supplementary Figure S4). Supplementary Figure S5 shows the pre-exponential factor spectra for different pump wavelengths (480 and 640 nm) at pump pulse energies tuned to have similar amplitude of TA signal. With increasing pump wavelength, the peak of the first component is shifted to the blue and approaches a central wavelength of the similar positive band present in the second (10–20 ps) component (Figure 2, the longer the pump wavelength, the smaller the difference between the band maxima of the first and second components). Supplementary Table S1 collects the time constants for all components at three excitation wavelengths.

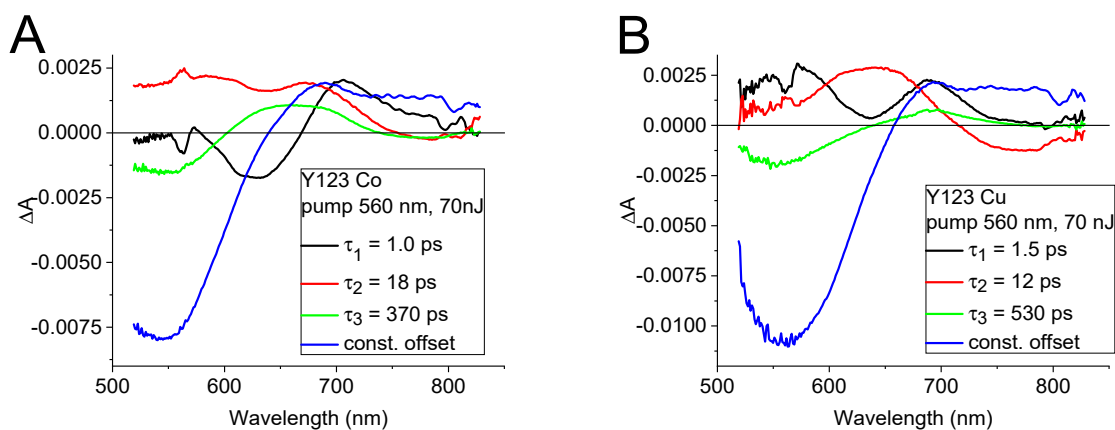


Figure 1. Pre-exponential factor spectra associated with the indicated time constants for a model with a three-exponential function with an offset for DSSC with Y123 dye and (A) cobalt- and (B) copper-based electrolyte for pump wavelength 560 nm.

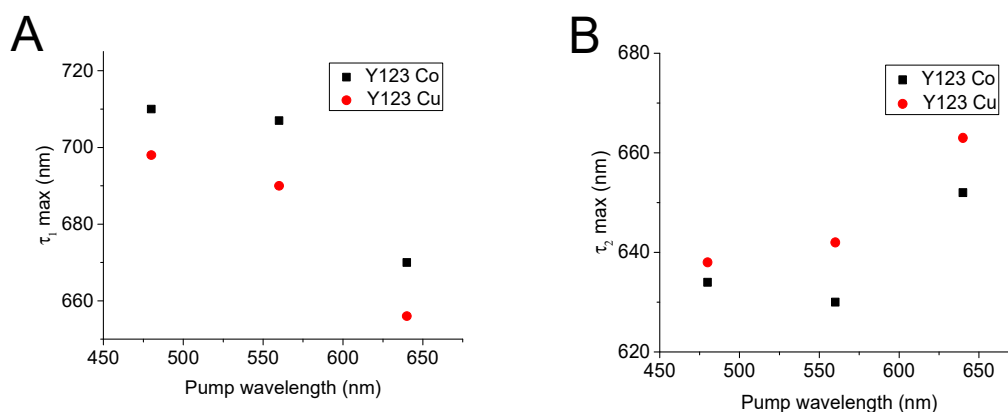


Figure 2. Maxima of the positive band in pre-exponential factor spectra of the (A) first and (B) second component of the global analysis for Y123 solar cells.

The wavelength-dependent amplitude of the second component contains also a negative signal or an indentation in the positive signal in the range between 700 nm and 850 nm, which can be assigned to the stimulated emission and/or to building up of the oxidized state population (the rise of its transient absorption can be visible as the second peak in the photoinduced absorption measurements [46]). For the samples containing a cobalt redox mediator, the positive band in the short wavelength part of the spectra, may be distorted by the residuum of the stimulated emission from hot (Franck–Condon) S_1 state of the dye. Small shifts (~ 10 nm) between the spectra recorded in Co and Cu based electrolytes, observed, e.g., in the positions of bleach bands in Figure 1, the positions of the absorption maxima in Figure 2, and IPCE spectra in Supplementary Figure S1B should be also noticed. These shifts probably originate from the slightly different solvation of the dye in the presence of the two electrolytes and can explain a small difference in the shape of the wavelength dependent spectra of the same transient absorption component for the two electrolytes (Figure 1 and Supplementary Figure S5).

The spectral evolution of the first two components observed with decreasing pump photon energy, indicates that τ_1 time constant can be associated with the hot S_1 state while τ_2 can be associated with a decay of the relaxed S_1 state. Similar behavior can be observed in the global analysis of transient absorption of Y123 in solution (Supplementary Figure S4), for which the second (~ 220 ps) component contains the bleach recovery and excited state decay, and the first (~ 2 ps) constituent exhibits Gaussian-like derivative shape, indicating a band shift typical of the excited state relaxation and solvation. In the presence of titania, both decays (of hot and relaxed S_1 state) must be affected by electron transfer to the semiconductor's conduction band, thus for DSSC samples we can assign the shortening of τ_1 and τ_2 to the process of carrier injection. Even though the TA measurements with detection in visible light were conducted using different pump wavelengths approaching the IPCE spectrum onset as close as possible maintaining reliable TA signal and reasonable pump pulse energy, we did not find any strong evidence for interfacial electron transfer occurring directly from the dye's ground state to the titania conduction band (CB).

The third (370–530 ps) component contains a negative band in the range of steady-state absorption of the dye, so we identify this decay as the dye ground state recovery connected with semiconductor-oxidized dye recombination. In the DSSCs systems studied using this method, the recombination component spectrum should match that of the constant offset (the decay with infinite time constant relative to a temporal range ~ 3 ns of our ultrafast spectrometers), which contains the ground state bleach and oxidized dye spectra [41]. In this case, the third component does not show positive amplitudes in the same range that we have previously assigned to building up of the oxidized dye band, caused by electron

injection (>700 nm). This fact suggests that the electrons may be injected in a time scale beyond the second component and thus may contribute to the third one too.

Therefore, we used time resolved infrared absorption spectroscopy, to directly observe the population of electrons injected to the titania conduction band. The measurements were performed on half-cells on the sapphire window (instead of FTO glass) and are described in the experimental section. The pump wavelength was set to 500 nm and the TA signal was monitored at the central wavelength equal to 4780 nm, away from the Y123 molecular vibrations. Thus, the recorded signal is exclusively proportional to the population of the electrons injected to the titania conduction band.

Figure 3 shows the kinetic traces measured at three different pump pulse energies, together with the fitted functions. Independently of the applied pump pulse energy, the population of electrons injected to the titania conduction band rises biphasically with the first rise in the instantaneous component (within IRF duration of 350 fs) and the second rise between 80 ps and 95 ps. For higher pump pulse energy, a higher value of the second time constant (Supplementary Table S2) is observed. However, the contribution of the second component drops relative to that of the first instantaneous component, with increasing pump pulse energy (Figure 3B). This observation could be explained assuming that higher density of charge injected in titania CB during the first instantaneous process, lifts up the quasi Fermi level, and reduces the driving force for electron transfer. Additionally, at high pump pulse energy, the slower injection is masked by more pronounced fast recombination to oxidized dye, which appears in the 500 nJ kinetics as the fast (<1 ps) decay. In general, the back electron transfer may also contribute to 100 nJ and 50 nJ kinetics, but to a much lower extent. We can also conclude, that in the operational conditions (low pump intensities) the slower component (~80 ps) brings the highest contribution.

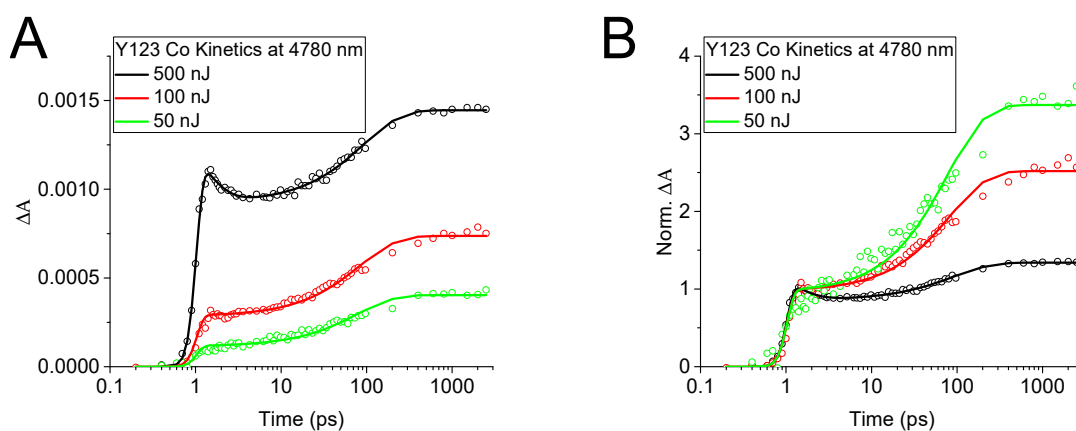


Figure 3. Kinetic traces at 4780 nm for Y123 samples cells with sapphire substrate at different pump intensity (points) with the fitted function (solid lines) (A) as measured and (B) normalized. The time zero was shifted to 1 ps in order to present the time axis in logarithmic scale. The parameters of the fits are given in Supplementary Table S2.

The initial signal magnitude dependence on the pump pulse energy is linear, thus, we can exclude any artifacts originating from two-photon absorption. To exclude other contributions, we performed experiment in the same conditions on the half-cell comprising bare titania without a dye (Supplementary Figure S7) and additionally in the area without titania, to exclude window's, solvent's and redox mediator's contributions. The second measurement did not reveal any signal higher than the noise level. However, the magnitude of the bare titania initial signal made nearly a half of the initial response of Y123 sensitized half-cell. No rise of the signal, but only a decay was revealed. It can be ascribed to the absorption of photons associated with transitions of electrons trapped within the mesoporous titania bandgap, but it must be noted that, in the presence of a dye characterized by a high extinction coefficient (the sensitized photoanode's absorbance was >1.5), competing in pump photons absorption, this contribution can be neglected.

The conclusion that can be drawn from the above experimental evidence is that electron injection into the solar cells sensitized with Y123 dye takes place on several time scales extending from sub-ps or single ps (from the dyes hot excited S_1 Frank–Condon (F-C) state) to about 80 ps (from the relaxed excited state). The contribution of the latter is dominant at low pump pulse energy, so also very likely in the operating 1 Sun conditions. The 80 ps component observed in mid-IR experiments corresponds partially to the second component (10–20 ps) and partially to the third component (370–530 ps) in VIS range. The latter contains also the contribution of electron recombination.

Supplementary Scheme S2 shows the proposed kinetic model of the electron injection taking place in the cells comprising Y123 dye. We believe that our results explain the previous discrepancies in the reported electron injection time constants for this dye: 2 ps in [21] and 12 ps or 25 ps in [20], which lie between the fastest and the slowest electron injection components revealed in this study. Most probably, the above time constants determined from transient absorption kinetics at a single wavelength (690 nm in [21] and 650 nm in two different environments in [20]) contained the specific partial contributions of the injection processes from the hot S_1 and relaxed S_1 states. As we have showed above, the contributions of the hot and relaxed states to the injection process are different at different probing wavelengths in the visible range. Moreover, for the Y123 dye the pre-exponential factor spectra were also slightly spectrally shifted depending on the used electrolyte (Co or Cu based). Therefore, depending on the environment and probing wavelength, the single kinetics can contain different contributions of the fast and slow electron injection components. On the contrary, the approach proposed by us (direct monitoring of electron population in the CB of titania by means of the ultrafast mid-IR spectroscopy accompanied with the broadband analysis in the visible range to assign the observed kinetics components to different states) permits revealing the global picture of the electron injection in the cells comprising Y123 and related dyes.

3.2. Photovoltaic Performance and Continuous Irradiation Effects

The photovoltaic parameters of our solar cell samples are given in Table 1. The performance of DSSCs prepared in this study departs from the highest reported for analogous systems in terms of the photocurrent density (J_{SC}) (7.0, 7.5 and 9.2 mA cm^{-2} vs. 14.6, 15.5 and 15.1 mA cm^{-2} for Y123 $\text{Co}^{3+/2+}(\text{bpy})_3$ [11], Y123 $\text{Cu}^{2+/+}(\text{tmby})_2$ [15] and MK2 $\text{Co}^{3+/2+}(\text{bpy})_3$ [50], respectively) and in terms of the fill factor (FF) (0.57, 0.6 and 0.65 vs. 0.64, 0.7 and 0.75, respectively).

Table 1. Photovoltaic parameters of the studied solar cells (before irradiation)¹.

Cell	PCE [%]	Voc [V]	FF	Jsc [mA cm^{-2}]	Total APCE
Y123 $\text{Co}^{3+/2+}(\text{bpy})_3$	3.8	0.96	0.57	7.03	0.69
error	0.2	0.01	0.02	0.15	0.02
Y123 $\text{Cu}^{2+/+}(\text{tmby})_2$	4.7	1.06	0.60	7.47	0.73
error	0.2	0.01	0.01	0.06	0.01
MK2 $\text{Co}^{3+/2+}(\text{bpy})_3$	5.1	0.85	0.65	9.22	0.71
error	0.2	0.01	0.02	0.11	0.01

¹ PCE, power conversion efficiency; V_{OC} , open circuit voltage; J_{SC} , short circuit photocurrent density; FF, fill factor. Parameters were averaged from at least three devices. Errors were calculated as the standard deviation of the mean value.

Lower J_{SC} values can be attributed to lower light harvesting efficiency. As indicated in the Materials and Methods section, we use a thin and optically transparent titania layer (of only 2–3 μm in thickness) without the scattering part to allow transient absorption measurements in the transmission mode. Lower FF values are probably due to the utilization of standard commercially available titania paste without further modification and optimization for specific dye-redox mediator system (e.g., tuning the porosity). However, decent V_{OC} values matching the best reported, indicate good quality of prepared samples. To compare samples of different light harvesting efficiency in terms of the photocurrent

generation efficiency, we calculated the total absorbed photon to current efficiency (Total APCE), the parameter which is a short circuit photocurrent density corrected for the number of absorbed photons [46]. It should be also noted that our Total APCE values are quite close to the best IPCE values reported for the optimized cells (~80%), which means that the conclusions regarding electron injection dynamics should also be valid for the best performing cells with the scattering layer. We also prepared and studied the cells with MK2 dyes and $\text{Cu}^{2+}/^+(\text{tmby})_2$ redox couple, but they suffered from significantly smaller photocurrents than those of our other cells, which is presented and discussed in SI.

In order to examine the effects occurring in the solar cells upon irradiation, all characterization measurements were performed before and after continuous 30 min long irradiation at full sunlight (AM 1.5 G conditions). In Table 2, the ratios of the photovoltaic parameters measured after and before continuous irradiation lasting 30 min are given. The ratios are the averages of the three series prepared on different days, and each of the series contained at least three cells of the same type.

Table 2. The ratios of photovoltaic parameters measured after and before 30 min continuous irradiation.

Cell	PCE Ratio	Voc Ratio	FF Ratio	Jsc Ratio
Y123 $\text{Co}^{3+}/^{2+}(\text{bpy})_3$	0.99	0.96	0.98	1.04
Y123 $\text{Cu}^{2+}/^+(\text{tmby})_2$	0.81	0.96	0.82	1.03
MK2 $\text{Co}^{3+}/^{2+}(\text{bpy})_3$	1.04	0.96	1.03	1.04

The cells were irradiated in short-circuit conditions, however comparable changes were observed in open circuit conditions during our preliminary studies. Prior to the first measurements the cells were stored in the dark. A common modification observed in all studied systems is the drop in V_{OC} and rise in J_{SC} , which is a frequently observed trade-off situation occurring when the potential of the conduction band edge is shifted towards more positive values [37,38]. The above phenomenon can be explained by intercalation of lithium cations and the protons [40] present due to inevitable content of trace amounts of water in the electrolyte and mesoporous photoanode. Intercalation of both cation types to titania may be intensified by the attraction of negative charge, injected to titania when the solar cell was under irradiation. The FF changes were incoherent but implied the PCE changes.

To get a deeper insight into the reasons for photovoltaic parameters change, and to reveal the irradiation effects on the charge transfer dynamics, we will compare below the results obtained in the global analysis of TA data from the measurements performed before and after irradiation. Exemplary results for Y123 and MK2 cells are shown in Figure 4 and Supplementary Figure S6. Similarly, as in Figure 1, these figures present the pre-exponential factor spectra (wavelength-dependent amplitudes) associated with the indicated time constants obtained in the global analysis. Negative amplitudes in pre-exponential factor spectra correspond to the rise of ΔA signal (e.g., due to the rise of transient absorption bands or the recovery of the ground state of the dye or the decay of population of the transient states which emit light (stimulated emission band)), while the positive amplitudes are related to the decay of ΔA (e.g., due to the decay of population of the transient states which absorb light in the spectral range of our interest). Figure 4A,B (Y123 cells pumped at 560 nm after irradiation) should be compared with Figure 1A,B (before irradiation), Supplementary Figure S6 (Y123 cells pumped at 480 and 640 nm after irradiation) with Supplementary Figure S5 (before irradiation), and Figure 4D (MK2 cells after irradiation) with Figure 4C (before irradiation). Table 3 collects the time constants of the components presented in Figures 1 and 4.

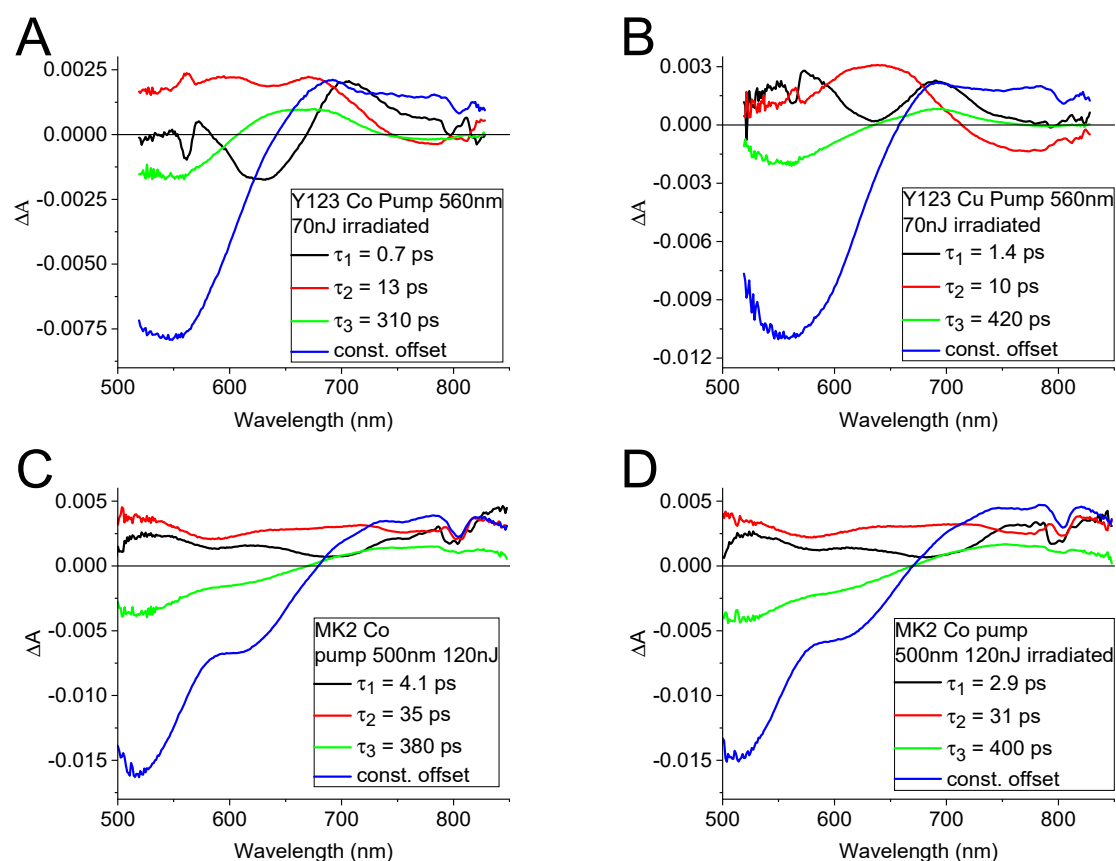


Figure 4. Results of the global analysis of transient absorption data using a three-exponential function with a constant offset for DSSC with Y123 dye and (A) cobalt- and (B) copper-based electrolyte after 30 min irradiation (compare with Figure 1) and DSSC with MK2 dye and cobalt-based electrolyte before (C) and after (D) irradiation.

Table 3. Comparison of time constants obtained in the global analysis of transient absorption measurements conducted before and after irradiation and shown in Figure 4, Supplementary Figures S5 and S6.

	Fresh			Irradiated		
	τ_1 [ps]	τ_2 [ps]	τ_3 [ps]	τ_1 [ps]	τ_2 [ps]	τ_3 [ps]
Y123 Co ^{3+/2+} (bpy) ₃ ^a	1.0	18	370	0.7	13	310
Y123 Cu ^{2+/+} (tmby) ₂ ^a	1.5	12	530	1.4	10	420
MK2 Co ^{3+/2+} (bpy) ₃ ^b	4.1	35	380	2.9	31	400

^a 560 nm excitation (480 nm and 640 nm given in Supplementary Table S1), ^b 500 nm excitation.

Our interpretation of the transient absorption measurements collected for Y123 sensitized solar cells is provided in the previous part of this paper. On the other hand, MK2 dye was extensively studied by our group and we based our interpretation on the previous reports [41–45]. Namely, we attributed the two faster (3–4 ps and 30–35 ps, black and red lines in Figure 4C,D) components to electron injection process. Similarly, as for Y123, the justification is that their pre-exponential factor spectra contain positive contributions from the decaying absorption from S₁ excited electronic state (to the higher excited electronic states of the dye) and they contain indentation originating from stimulated emission (with minima at about 700 nm for the faster component and redshifted to about 750 nm in the slower component, the latter due to thermalization of hot excited state). Slightly faster electron injection for MK2 dye relative to that for Y123 dye (the slowest component 30–35 ps for MK2 versus 80–95 ps for Y123) is probably due to the differences in the dyes structures and dye-titania electron coupling, as the difference between the dye LUMO and titania CB potentials is similar for both dyes (0.39 V for MK2 [51] and 0.44 V for Y123 [46]). The

pre-exponential factor spectra of the third component (green line in Figure 4C,D) match the spectra of constant offset constituent (blue line in Figure 4C,D, containing ground state depopulation recovery and the oxidized dye spectra decay) therefore, represent back electron transfer (recombination) from titania conduction band to the oxidized form of the MK2 dye.

The nature of the wavelength dependent pre-exponential factor spectra remains unchanged by irradiation (see Figures 1 and 4, the relative amplitudes of the pre-exponential factor spectra are similar before and after irradiation). However, clear changes in the associated time constants are observed (Figures 1 and 4, Table 3).

The fastest injection components (τ_1) recorded for the Y123 sensitized cells pumped at 560 nm are shortened: τ_1 from 1.0 ps to 0.7 ps and from 1.5 ps to 1.4 ps, while τ_2 from 18 ps to 13 ps and from 12 ps to 10 ps for cobalt- and copper-based electrolyte respectively. Therefore, the effect is more pronounced for the samples with $\text{Co}^{3+/2+}(\text{bpy})_3$. Similar acceleration of the injection process is observed for the MK2 sensitized cells (from 4.1 ps to 2.9 ps for τ_1 and from 35 ps to 31 ps for τ_2). The above effect should be attributed to the shift of the CB edge to more positive potentials, causing an increase in the driving force for electron injection. It is obviously connected with the photovoltage–photocurrent trade-off effect described earlier. It should be noted that the trends in the changes in the electron injection time constants (and also the recombination time constants discussed later) were confirmed for at least three different series of the same type of the cells prepared and measured on different days. However, the exact reductions of injection time constants were slightly different between the series.

Electron injection acceleration is unlikely to be the only cause of rise in the photocurrent density, because the quantum yield of this process should be already high enough as the internal conversion (which is the only process competing with the injection) occurs in solution on a time scale ~ 220 ps for Y123 (previous section) and ~ 500 ps for MK2) [43]. Therefore, for better understanding of the light soaking effects, the recombination processes should be considered too. For all MK2 cells, we observed slight but regular increase in the recombination time constant upon irradiation, while for Y123 cells no systematic changes in back electron transfer dynamics could be revealed (these results are consistent with the long-time scale recombination measured in inert cells and presented in Supplementary Figure S8). However, as we have shown before, the time constant of the recombination does not need to be related to the quantum yield of this unwanted process [43]. The kinetic traces at selected wavelength can better show the efficiency of electron recombination. Therefore, we took advantage of the TA kinetics at 700 nm, representing the decay of the dye's oxidized state and thereby, the CB-dye recombination for the cells comprising Y123 dye, and 750 nm for the DSSCs based on MK2 (Supplementary Figure S9). The ratio of the residual (at 3 ns time delay) and maximal signal values of the recombination kinetics (S_{RES} parameter), can be a good representation of the charge separation efficiency in a short time scale as we have shown in our previous studies of DSSCs exploiting organic sensitizers [41,43,44,46,52].

In Figure 5 we present correlations between the Total APCE (photocurrent corrected on the number of absorbed photons) and the S_{RES} parameter values. In general, we can conclude that the residual signal representing differences in charge separation efficiency is well correlated with the Total APCE. Therefore, an increase in the photocurrent upon irradiation can be directly related to the fast charge transfer dynamics that we observed in transient absorption experiment. This conclusion is coherent with our previous reports on organic sensitizers [41,43,44,46,52]. In order to get more information about the factors causing changes in the DSSCs operation upon continuous irradiation, we prepared several modified DSSCs systems based on MK2 dye (with no TBP in the electrolyte solution, with addition of co-adsorbate (CDCA) and with copper- instead of cobalt-based electrolyte).

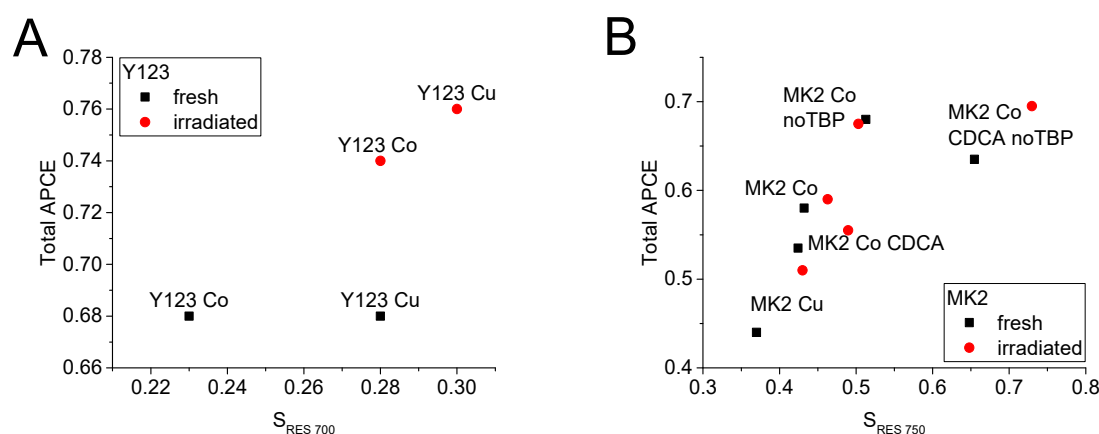


Figure 5. The correlations between Total APCE and recombinant kinetics residual signal at 700 nm for Y123 (A) and 750 nm for MK2 (B). The kinetics are given in Figure S8. Data points represent individual samples.

As mentioned before, we ascribed the effect of photocurrent enhancement to the cations of lithium and hydrogen intercalating into titania crystal lattice. Considering the shifts (correlated increase in Total APCE and S_{RES}) of the data points caused by irradiation shown in Figure 5B, we can conclude that the additives modifying the semiconductor/dye/electrolyte interface may retard the access of cations to the semiconductor's surface. Therefore, in the samples containing CDCA and/or TBP the irradiation accelerates the process of intercalation. On the other hand, it can be noticed that the sample without additives (MK2 Co noTBP) was not significantly affected by illumination. Furthermore, the Total APCE value was already relatively high, suggesting that the equilibrium was already achieved without hindrance by the additives. Another important observation is the high parallelism of the above-mentioned shifts, supporting a strong relationship between the short circuit photocurrent and the ultrafast charge separation efficiency.

4. Conclusions

In this study, we have proposed a model of charge transfer processes occurring on the dye/semiconductor interface, typical of DSSCs comprising Y123 dye and titania nanoparticle mesoporous layer. The electron injection was found to occur biphasically with the faster phase occurring within 350 fs (the resolution of mid-IR transient absorption setup) and the second one between 80 ps and 95 ps. According to the measurements performed in the visible range of detection at three different pump wavelengths, we ascribed the faster component to the injection of the electron from the hot S_1 (Frank-Condon) state and the slower constituent was assigned to the injection from the relaxed S_1 state. The contribution of the slower injection component was found to be more significant than that of the faster one, in the experiments using low pump pulse energy, and therefore it should be dominant in operational conditions.

Considering the fact that the Y123 (or its analogues) is one of the best performing sensitizers, its relatively slow electron injection should be accepted as fast enough in the absence of relevant competing deactivation processes occurring in the picosecond time scale. This should be important information for further tuning of relative excited state and CB edge energy levels, the driving force for electron injection. Despite the attempt to pump the dye in the transient absorption experiment as close as possible to the long wavelength edge of its operational spectrum, no evidence of interfacial electron transfer occurring directly from the Y123 dye's ground state to the titania conduction band was found.

In the second part of the study, we have examined the effects of illumination of the solar cells on the charge transfer rates in the Y123 sensitized solar cells and compared them with those for the systems comprising MK2 dye. The injection processes were found to be accelerated in the systems with both dyes, which was assigned to decreasing energy of the CB edge during illumination. On the other hand, the electron back transfer from

the semiconductor's conduction band to the oxidized dye was found to be slowed down in the MK2 based cells and unchanged in the systems comprising Y123. The lowering contribution of back electron transfer (estimated from the population of the oxidized dye at 3 ns) was directly correlated with the photocurrent increase upon illumination of the cells.

We believe that our efforts focused on the understanding of the electron transfer processes, occurring with involvement of Y123 dye which belongs to the most promising branch of sensitizers applied in cobalt- and copper-mediated DSSCs, will contribute to the further development of DSSC technology.

Supplementary Materials: The following are available online at <https://www.mdpi.com/1996-1073/14/2/407/s1>, Scheme S1: Molecular structures of the dyes, Scheme S2: Kinetic model for the electron injection from Y123 dye, Figure S1: Photo of the half-cell on sapphire substrate and IPCE and absorbance spectra, Figure S2: Pseudo-color 2D spectra of TA data for DSSC, Figure S3: Absorption and fluorescence spectra of the dyes solutions, Figure S4 TA data of Y123 solution, Table S1: Time constants obtained in the global analysis of TA, Figures S5 and S6: Pre-exponential factor spectra of DSSCs with Y123, Table S2: Time constants of fitted mid-IR TA kinetics, Figure S7: mid-IR control measurements, Figure S8: TA kinetics of non-irradiated/irradiated DSSCs with Y123 and MK2 and inert electrolyte, Figure S9: Kinetics of TA for Y123 and MK2 at 700 nm and 750 nm respectively Table S3: PV parameters of the cells with MK2 and Cu-based electrolyte, Figure S10: μ s-ms TA kinetics and electron lifetimes in DSSC with MK2 and Cu-based electrolyte.

Author Contributions: Conceptualization, A.G. and M.Z.; methodology, A.G. and M.Z.; validation, A.G. and M.Z.; formal analysis, A.G. and M.Z.; investigation, A.G., J.K., and M.Z.; resources, M.Z.; samples preparation, A.G.; writing—original draft preparation, A.G.; writing—review and editing, A.G., J.K., and M.Z.; visualization, A.G. and M.Z.; supervision, M.Z.; funding acquisition, M.Z. All authors have read and agreed to the published version of the manuscript.

Funding: This research was funded by NCN (National Science Centre, Poland), grant number 2015/18/E/ST4/00196.

Institutional Review Board Statement: Not applicable.

Informed Consent Statement: Not applicable.

Data Availability Statement: Not applicable.

Acknowledgments: We wish to thank Mateusz Gierszewski for kind assistance in samples preparation and Gotard Burdziński for help in nanosecond flash photolysis control measurements (Figures S8 and S10A). Our gratitude goes to Marina Freitag for the possibility of electron lifetime measurements (Figure S10B).

Conflicts of Interest: The authors declare no conflict of interest.

References

1. O'Regan, B.; Grätzel, M. A low-cost, high-efficiency solar-cell based on dye-sensitized colloidal TiO₂ films. *Nature* **1991**, *353*, 737–740. [[CrossRef](#)]
2. Kim, J.Y.; Lee, J.-W.; Jung, H.S.; Shin, H.; Park, N.-G. High-Efficiency perovskite solar cells. *Chem. Rev.* **2020**, *120*, 7867–7918. [[CrossRef](#)] [[PubMed](#)]
3. Chebrolov, V.T.; Kim, H.-J. Recent progress in quantum dot sensitized solar cells: An inclusive review of photoanode, sensitizer, electrolyte, and the counter electrode. *J. Mater. Chem.* **2019**, *7*, 4911–4933. [[CrossRef](#)]
4. Zhang, Z.; Yuan, J.; Wei, Q.; Zou, Y. Small-Molecule electron acceptors for efficient non-fullerene organic solar cells. *Front. Chem.* **2018**, *6*, 414. [[CrossRef](#)] [[PubMed](#)]
5. Michaels, H.; Rinderle, M.; Freitag, R.; Benesper, I.; Edvinsson, T.; Socher, R.; Gagliardi, A.; Freitag, M. Dye-Sensitized solar cells under ambient light powering machine learning: Towards autonomous smart sensors for the internet of things. *Chem. Sci.* **2020**, *11*, 2895–2906. [[CrossRef](#)]
6. Freitag, M.; Teuscher, J.; Saygili, Y.; Zhang, X.; Giordano, F.; Liska, P.; Hua, J.; Zakeeruddin, S.M.; Moser, J.-E.; Grätzel, M.; et al. Dye-Sensitized solar cells for efficient power generation under ambient lighting. *Nat. Photonics* **2017**, *11*, 372–378. [[CrossRef](#)]
7. Freitag, M.; Boschloo, G. The revival of dye-sensitized solar cells. *Curr. Opin. Electrochem.* **2017**, *2*, 111–119. [[CrossRef](#)]
8. Koumura, N.; Wang, Z.S.; Mori, S.; Miyashita, M.; Suzuki, E.; Hara, K. Alkyl-Functionalized organic dyes for efficient molecular photovoltaics. *J. Am. Chem. Soc.* **2006**, *128*, 14256–14257. [[CrossRef](#)]

9. Feldt, S.M.; Gibson, E.A.; Gabrielsson, E.; Sun, L.; Boschloo, G.; Hagfeldt, A. Design of organic dyes and cobalt polypyridine redox mediators for high-efficiency dye-sensitized solar cells. *J. Am. Chem. Soc.* **2010**, *132*, 16714–16724. [[CrossRef](#)]
10. Ellis, H.; Eriksson, S.K.; Feldt, S.M.; Gabrielsson, E.; Lohse, P.W.; Lindblad, R.; Sun, L.; Rensmo, H.; Boschloo, G.; Hagfeldt, A. Linker unit modification of triphenylamine-based organic dyes for efficient cobalt mediated dye-sensitized solar cells. *J. Phys. Chem.* **2013**, *117*, 21029–21036. [[CrossRef](#)]
11. Tsao, H.N.; Yi, C.; Moehl, T.; Yum, J.H.; Zakeeruddin, S.M.; Nazeeruddin, M.K.; Grätzel, M. Cyclopentadithiophene bridged donor-acceptor dyes achieve high power conversion efficiencies in dye-sensitized solar cells based on the tris-cobalt bipyridine redox couple. *ChemSusChem* **2011**, *4*, 591–594. [[CrossRef](#)] [[PubMed](#)]
12. Nazeeruddin, M.K.; Kay, A.; Rodicio, I.; Humphry-Baker, R.; Mueller, E.; Liska, P.; Vlachopoulos, N.; Graetzel, M. Conversion of light to electricity by cis-X2bis(2,2'-bipyridyl-4,4'-dicarboxylate)ruthenium(II) charge-transfer sensitizers (X = Cl-, Br-, I-, CN-, and SCN-) on nanocrystalline titanium dioxide electrodes. *J. Am. Chem. Soc.* **1993**, *115*, 6382–6390. [[CrossRef](#)]
13. Bai, Y.; Yu, Q.; Cai, N.; Wang, Y.; Zhang, M.; Wang, P. High-Efficiency organic dye-sensitized mesoscopic solar cells with a copper redox shuttle. *Chem. Commun.* **2011**, *47*, 4376–4378. [[CrossRef](#)] [[PubMed](#)]
14. Freitag, M.; Giordano, F.; Yang, W.; Pazoki, M.; Hao, Y.; Zietz, B.; Gra, M.; Hagfeldt, A.; Boschloo, G. Copper phenanthroline as a fast and high-performance redox mediator for dye-sensitized solar cells. *J. Phys. Chem.* **2016**, *120*, 9595–9603. [[CrossRef](#)]
15. Saygili, Y.; Söderberg, M.; Pellet, N.; Giordano, F.; Cao, Y.; Munoz-García, A.B.; Zakeeruddin, S.M.; Vlachopoulos, N.; Pavone, M.; Boschloo, G.; et al. Copper bipyridyl redox mediators for dye-sensitized solar cells with high photovoltage. *J. Am. Chem. Soc.* **2016**, *138*, 15087–15096. [[CrossRef](#)] [[PubMed](#)]
16. Kakiage, K.; Aoyama, Y.; Yano, T.; Oya, K.; Fujisawa, J.; Hanaya, M. Highly-Efficient dye-sensitized solar cells with collaborative sensitization by silyl-anchor and carboxy-anchor dyes. *Chem. Commun.* **2015**, *51*, 15894–15897. [[CrossRef](#)]
17. Ji, J.M.; Zhou, H.; Eom, Y.K.; Kim, C.H.; Kim, H.K. 14.2% efficiency dye-sensitized solar cells by co-sensitizing novel thieno[3,2-b]indole-based organic dyes with a promising porphyrin sensitizer. *Adv. Energy Mater.* **2020**, *10*, 1–12. [[CrossRef](#)]
18. Cao, Y.; Liu, Y.; Zakeeruddin, S.M.; Hagfeldt, A.; Grätzel, M. Direct contact of selective charge extraction layers enables high-efficiency molecular photovoltaics. *Joule* **2018**, *2*, 1108–1117. [[CrossRef](#)]
19. Michaels, H.; Benesperi, I.; Edvinsson, T.; Muñoz-García, A.B.; Pavone, M.; Boschloo, G.; Freitag, M. Copper complexes with tetradentate ligands for enhanced charge transport in dye-sensitized solar cells. *Inorganics* **2018**, *6*, 53. [[CrossRef](#)]
20. Cao, Y.; Saygili, Y.; Ummadisingu, A.; Teuscher, J.; Luo, J.; Pellet, N.; Giordano, F.; Zakeeruddin, S.M.; Moser, J.-E.; Freitag, M.; et al. 11% efficiency solid-state dye-sensitized solar cells with copper(II/I) hole transport materials. *Nat. Commun.* **2017**, *8*, 15390. [[CrossRef](#)]
21. Ghadiri, E.; Zakeeruddin, S.M.; Hagfeldt, A.; Gratzel, M.; Moser, J.E. Ultrafast charge separation dynamics in opaque, operational dye-sensitized solar cells revealed by femtosecond diffuse reflectance spectroscopy. *Sci. Rep.* **2016**, *6*, 24465. [[CrossRef](#)] [[PubMed](#)]
22. Yao, Z.; Guo, Y.; Wang, L.; Hao, Y.; Guo, Y.; Franchi, D.; Zhang, F.; Kloo, L.; Sun, L. Energy-Loss reduction as a strategy to improve the efficiency of dye-sensitized solar cells. *Sol. RRL* **2019**, *3*, 1900253. [[CrossRef](#)]
23. Zhang, W.; Wu, Y.; Bahng, H.W.; Cao, Y.; Yi, C.; Saygili, Y.; Luo, J.; Liu, Y.; Kavan, L.; Moser, J.E.; et al. Comprehensive control of voltage loss enables 11.7% efficient solid-state dye-sensitized solar cells. *Energy Environ. Sci.* **2018**, *11*, 1779–1787. [[CrossRef](#)]
24. Ren, Y.; Flores-Díaz, N.; Zhang, D.; Cao, Y.; Decoppet, J.D.; Fish, G.C.; Moser, J.E.; Zakeeruddin, S.M.; Wang, P.; Hagfeldt, A.; et al. Blue photosensitizer with copper(II/I) redox mediator for efficient and stable dye-sensitized solar cells. *Adv. Funct. Mater.* **2020**, *30*, 1–7. [[CrossRef](#)]
25. Martín, C.; Ziólek, M.; Douhal, A. Ultrafast and fast charge separation processes in real dye-sensitized solar cells. *J. Photochem. Photobiol. Photochem. Rev.* **2016**, *26*, 1–30. [[CrossRef](#)]
26. Gierszewski, M.; Grądzka, I.; Glinka, A.; Ziólek, M. Insights into the limitations of solar cells sensitized with ruthenium dyes revealed in time-resolved spectroscopy studies. *Phys. Chem. Chem. Phys.* **2017**, *19*, 20463–20473. [[CrossRef](#)] [[PubMed](#)]
27. Fujisawa, J.I. Interfacial charge-transfer transitions for direct charge-separation photovoltaics. *Energies* **2020**, *13*, 2521. [[CrossRef](#)]
28. Fujisawa, J.I.; Hanaya, M. Light harvesting and direct electron injection by interfacial charge-transfer transitions between TiO₂ and carboxy-anchor dye LEG4 in dye-sensitized solar cells. *J. Phys. Chem.* **2018**, *122*, 8–15. [[CrossRef](#)]
29. Lindström, H.; Södergren, S.; Solbrand, A.; Rensmo, H.; Hjelm, J.; Hagfeldt, A.; Lindquist, S.-E. Li⁺ ion insertion in TiO₂ (Anatase). 2. Voltammetry on nanoporous films. *J. Phys. Chem.* **1997**, *101*, 7717–7722. [[CrossRef](#)]
30. Ellingson, J.R.; Asbury, J.B.; Ferrere, S.; Ghosh, H.N.; Sprague, J.R.; Lian, T.; Nozik, A.J. Sub-Picosecond injection of electrons from excited {Ru(2,2'-bipy-4,4'-dicarboxy)₂(SCN)₂} into TiO₂ using transient mid-infrared spectroscopy. In Proceedings of the 12th International Conference on Photochemical Conversion and Storage of Solar Energy, Berlin, Germany, 9–14 August 1998.
31. Hilgendorff, M.; Sundström, V. Dynamics of electron injection and recombination of dye-sensitized TiO₂ particles. *J. Phys. Chem.* **1998**, *102*, 10505–10514. [[CrossRef](#)]
32. Durrant, J.R.; Haque, S.A.; Palomares, E. Towards optimisation of electron transfer processes in dye sensitised solar cells. *Coord. Chem. Rev.* **2004**, *248*, 1247–1257. [[CrossRef](#)]
33. Andersen, N.A.; Lian, T. Ultrafast electron transfer at the molecule-semiconductor nanoparticle interface. *Annu. Rev. Phys. Chem.* **2005**, *56*, 491–519. [[CrossRef](#)] [[PubMed](#)]
34. Ardo, S.; Meyer, G.J. Photodriven heterogeneous charge transfer with transition-metal compounds anchored to TiO₂ semiconductor surfaces. *Chem. Soc. Rev.* **2009**, *38*, 115–164. [[CrossRef](#)] [[PubMed](#)]

35. Katoh, R.; Furube, A. Electron injection efficiency in dye-sensitized solar cells. *J. Photochem. Photobiol. Photochem. Rev.* **2014**, *20*, 1–16. [[CrossRef](#)]
36. Ponseca, C.S.; Chábera, P.; Uhlig, J.; Persson, P.; Sundström, V. Ultrafast electron dynamics in solar energy conversion. *Chem. Rev.* **2017**, *117*, 10940–11024. [[CrossRef](#)]
37. Listorti, A.; Creager, C.; Sommeling, P.; Kroon, J.; Palomares, E.; Fornelli, A.; Breen, B.; Barnes, P.R.F.; Durrant, J.R.; Law, C.; et al. The mechanism behind the beneficial effect of light soaking on injection efficiency and photocurrent in dye sensitized solar cells. *Energy Environ. Sci.* **2011**, *4*, 3494–3501. [[CrossRef](#)]
38. Cabau, L.; Pellejà, L.; Clifford, J.N.; Kumar, C.V.; Palomares, E. Light soaking effects on charge recombination and device performance in dye sensitized solar cells based on indoline-cyclopentadithiophene chromophores. *J. Mater. Chem.* **2013**, *1*, 8994–9000. [[CrossRef](#)]
39. Gao, J.; El-zohry, A.M.; Trilaksana, H.; Gabrielsson, E.; Leandri, V.; Ellis, H.; Amario, L.D.; Safdari, M.; Gardner, J.M.; Andersson, G.; et al. Light-Induced interfacial dynamics dramatically improve the photocurrent in dye-sensitized solar cells: An electrolyte effect. *ACS Appl. Mater. Interfaces* **2018**, *10*, 26241–26247. [[CrossRef](#)]
40. Gao, J.; Yang, W.; El-Zohry, A.M.; Prajapati, G.K.; Fang, Y.; Dai, J.; Hao, Y.; Leandri, V.; Svensson, P.H.; Furó, I.; et al. Light-Induced electrolyte improvement in cobalt tris(bipyridine)-mediated dye-sensitized solar cells. *J. Mater. Chem.* **2019**, *7*, 19495–19505. [[CrossRef](#)]
41. Sobuś, J.; Kubicki, J.; Burdziński, G.; Ziótek, M. Carbazole dye-sensitized solar cells studied from femtoseconds to seconds—effect of additives in cobalt- and iodide-based electrolytes. *ChemSusChem* **2015**, *8*, 3118–3128. [[CrossRef](#)]
42. Sobuś, J.; Gierczyk, B.; Burdziński, G.; Jancelewicz, M.; Polanski, E.; Hagfeldt, A.; Ziótek, M. Factors affecting the performance of champion silyl-anchor carbazole dye revealed in the femtosecond to second studies of complete ADEKA-1 sensitized solar cells. *Chem. Eur. J.* **2016**, *22*, 15807–15818. [[CrossRef](#)] [[PubMed](#)]
43. Gierszewski, M.; Glinka, A.; Gradzka, I.; Jancelewicz, M.; Ziótek, M. Effects of post-assembly molecular and atomic passivation of sensitized titania surface: Dynamics of electron transfer measured from femtoseconds to seconds. *ACS Appl. Mater. Interfaces* **2017**, *9*, 17102–17114. [[CrossRef](#)] [[PubMed](#)]
44. Glinka, A.; Gierszewski, M.; Ziótek, M. Effects of aqueous electrolyte, active layer thickness and bias irradiation on charge transfer rates in solar cells sensitized with top efficient carbazole dyes. *J. Phys. Chem.* **2018**, *122*, 8147–8158. [[CrossRef](#)]
45. Pydzińska-Białek, K.; Glinka, A.; Drushliak, V.; Nowaczyk, G.; Florczak, P.; Ziótek, M. Impact of improvements in mesoporous titania layers on ultrafast electron transfer dynamics in perovskite and dye-sensitized solar cells. *Phys. Chem. Chem. Phys.* **2020**, *22*, 21947–21960. [[CrossRef](#)] [[PubMed](#)]
46. Glinka, A.; Gierszewski, M.; Gierczyk, B.; Burdziński, G.; Michaels, H.; Freitag, M.; Ziótek, M. Interface modification and exceptionally fast regeneration in copper mediated solar cells sensitized with indoline dyes. *J. Phys. Chem.* **2020**, *124*, 2895–2906. [[CrossRef](#)]
47. Idígoras, J.; Burdziński, G.; Karolczak, J.; Kubicki, J.; Oskam, G.; Anta, J.A.; Ziótek, M. The impact of the electrical nature of the metal oxide on the performance in dye-sensitized solar cells: New look at old paradigms. *J. Phys. Chem.* **2015**, *119*, 3931–3944. [[CrossRef](#)]
48. Haque, S.A.; Tachibana, Y.; Willis, R.L.; Moser, J.E.; Grätzel, M.; Klug, D.R.; Durrant, J.R. Parameters influencing charge recombination kinetics in dye-sensitized nanocrystalline titanium dioxide films. *J. Phys. Chem.* **2000**, *104*, 538–547. [[CrossRef](#)]
49. Nelson, J.; Haque, S.A.; Klug, D.R.; Durrant, J.R. Trap-Limited recombination in dye-sensitized nanocrystalline metal oxide electrodes. *Phys. Rev.* **2001**, *63*, 205321. [[CrossRef](#)]
50. Xiang, W.; Huang, W.; Bach, U.; Spiccia, L. Stable high efficiency dye-sensitized solar cells based on a cobalt polymer gel electrolyte. *Chem. Commun.* **2013**, *49*, 8997–8999. [[CrossRef](#)]
51. Wang, Z.S.; Koumura, N.; Cui, Y.; Takahashi, M.; Sekiguchi, H.; Mori, A.; Kubo, T.; Furube, A.; Hara, K. Hexylthiophene-Functionalized carbazole dyes for efficient molecular photovoltaics: Tuning of solar-cell performance by structural modification. *Chem. Mater.* **2008**, *20*, 3993–4003. [[CrossRef](#)]
52. Gierszewski, M.; Glinka, A.; Gradzka, I.; Gierczyk, B.; Ziótek, M. Testing new concepts in solar cells sensitized with indoline dyes—Alkoxysilyl anchoring group, molecular capping, and cobalt-based electrolyte. *J. Phys. Chem.* **2018**, *122*, 25764–25775. [[CrossRef](#)]

Supporting Information

for

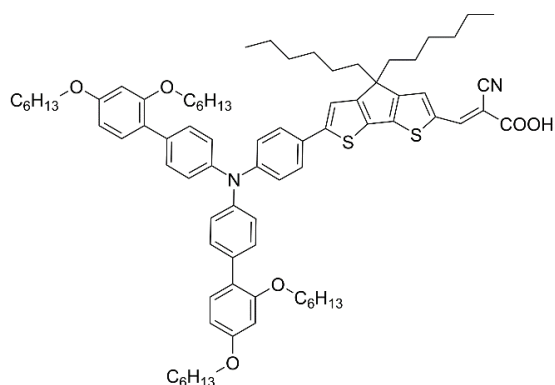
Complexity of Electron Injection Dynamics and Light Soaking Effects in Efficient Dyes for Modern DSSC

Adam Glinka^{1*}, Jacek Kubicki¹ and Marcin Ziólek^{1*}

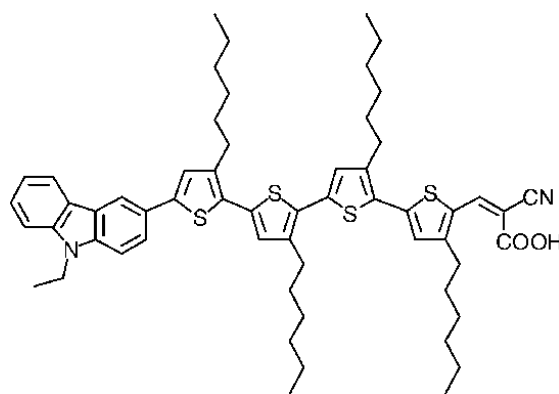
¹ *Quantum Electronics Laboratory, Faculty of Physics, Adam Mickiewicz University in Poznań, Uniwersytetu Poznańskiego 2, 61-614 Poznań, Poland.*

* corresponding authors, emails: adam.glinka@amu.edu.pl (AG) and marziol@amu.edu.pl (MZ)

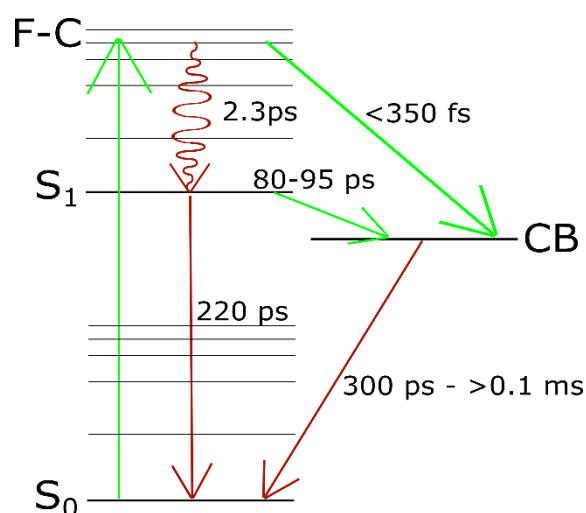
A



B



Scheme S1. Molecular structures of Y123 (A) and MK2 (B)



Scheme S2. Kinetic model of the electron injection from dye to the conduction band of titania in the cells comprising Y123 dye. Green and wine red arrows represent desired and undesired processes, respectively. The vibrational relaxation ($F-C \rightarrow$ relaxed S_1) and internal conversion ($S_1 \rightarrow S_0$) time constants are given based on our TA measurements of Y123 in solution. However, it should be noted that the internal conversion of Y123 attached to nanoparticles was reported to be equal to 750 ps while measured at mesoporous Al_2O_3 substrate [1]. Therefore, the quantum yield of electron injection from Y123 should be close to 100 % from both hot and relaxed excited state.

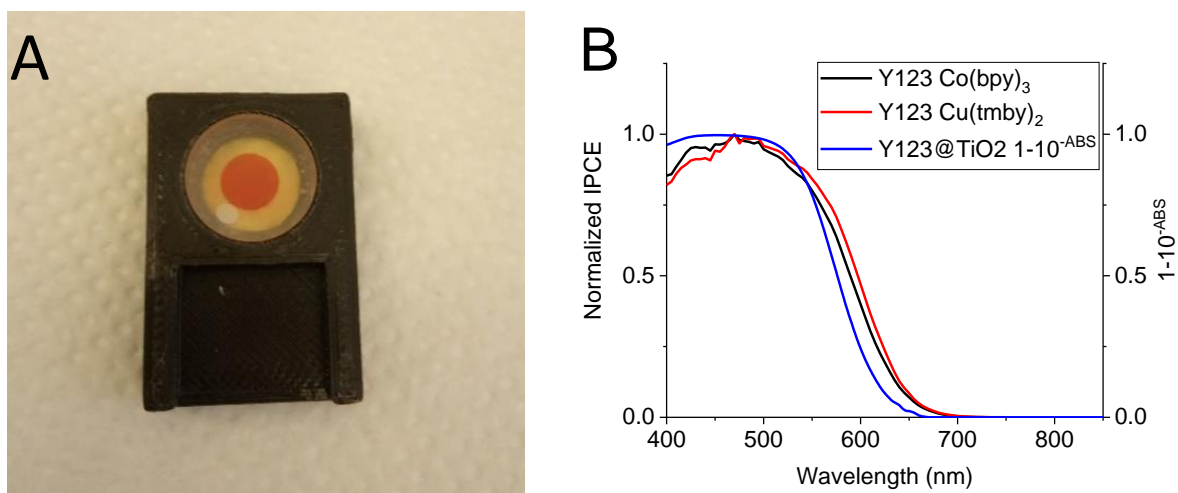


Figure S1. (A) Photo of the half-cell comprising titania sensitized with Y123 dye and cobalt-based electrolyte. The windows are 3mm thick sapphire plates provided by Thorlabs. (B) Normalized IPCE spectra of solar cells containing Y123 in combination with Co- and Cu-based electrolyte in comparison with the dye's absorbance spectra.

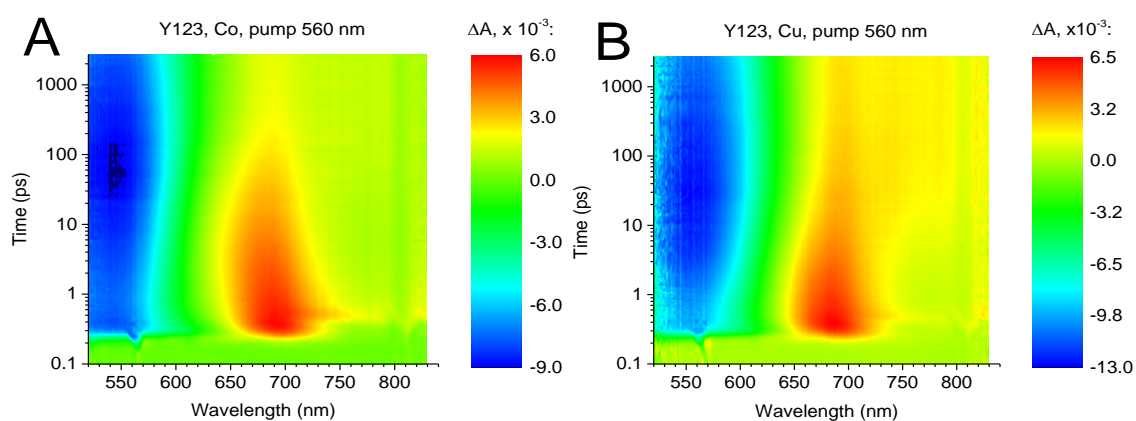


Figure S2. Pseudo-color 2D spectra of original transient absorption data for DSSCs with Y123 dye and (A) cobalt- and (B) copper- based electrolyte. The time zero was shifted to 0.3 ps in order to present the time axis in logarithmic scale.

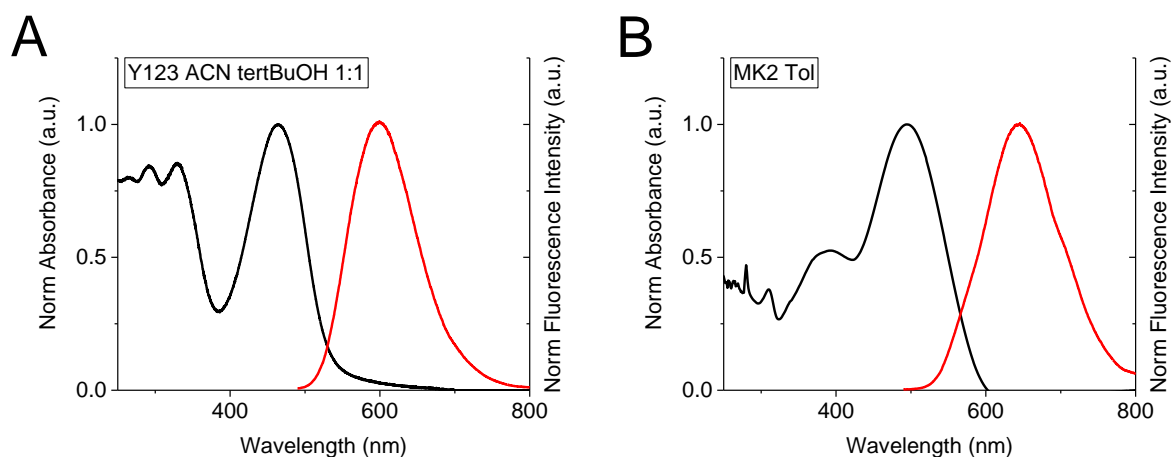


Figure S3. Normalized absorption and fluorescence spectra of the solutions used for sensitization by Y123 dye (A) and MK2 dye (B).

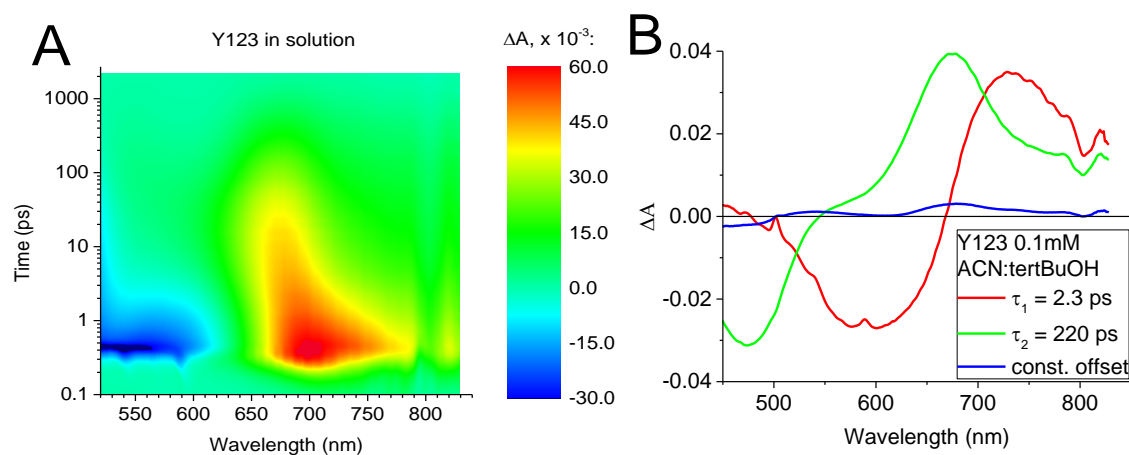


Figure S4. Pseudo-color 2D spectra of original data. The time zero was shifted to 0.3 ps in order to present the time axis in logarithmic scale (A), and global analysis of transient absorption spectra (B) of Y123 in ACN:tert-BuOH solution. The fastest component of about 2 ps should be assigned to the relaxation and solvation process in S_1 state. The shape of its amplitude spectra (negative values below 650 nm and positive above 650 nm) indicate the red shift of transient absorption spectra. The second component of 220 ps represents the decay of the relaxed S_1 state. The small residual component might be due to the triplet state populated with low quantum yield.

Table S1. Time constants obtained in the global analysis of the transient absorption of the solar cells sensitized with Y123 dye and collected for different pump wavelengths.

Co fresh				Cu fresh		
Wavelength [nm]	τ_1 [ps]	τ_2 [ps]	τ_3 [ps]	τ_1 [ps]	τ_2 [ps]	τ_3 [ps]
480	1.7	23	480	1	11	490
560	1	18	370	1.5	12	530
640	1.3	17	400	2	20	380

Co irradi				Cu irradi		
Wavelength [nm]	τ_1 [ps]	τ_2 [ps]	τ_3 [ps]	τ_1 [ps]	τ_2 [ps]	τ_3 [ps]
480	0.6	14	340	0.4	8.3	620
560	0.7	13	310	1.4	10	420
640	1.5	15	360	2.7	28	610

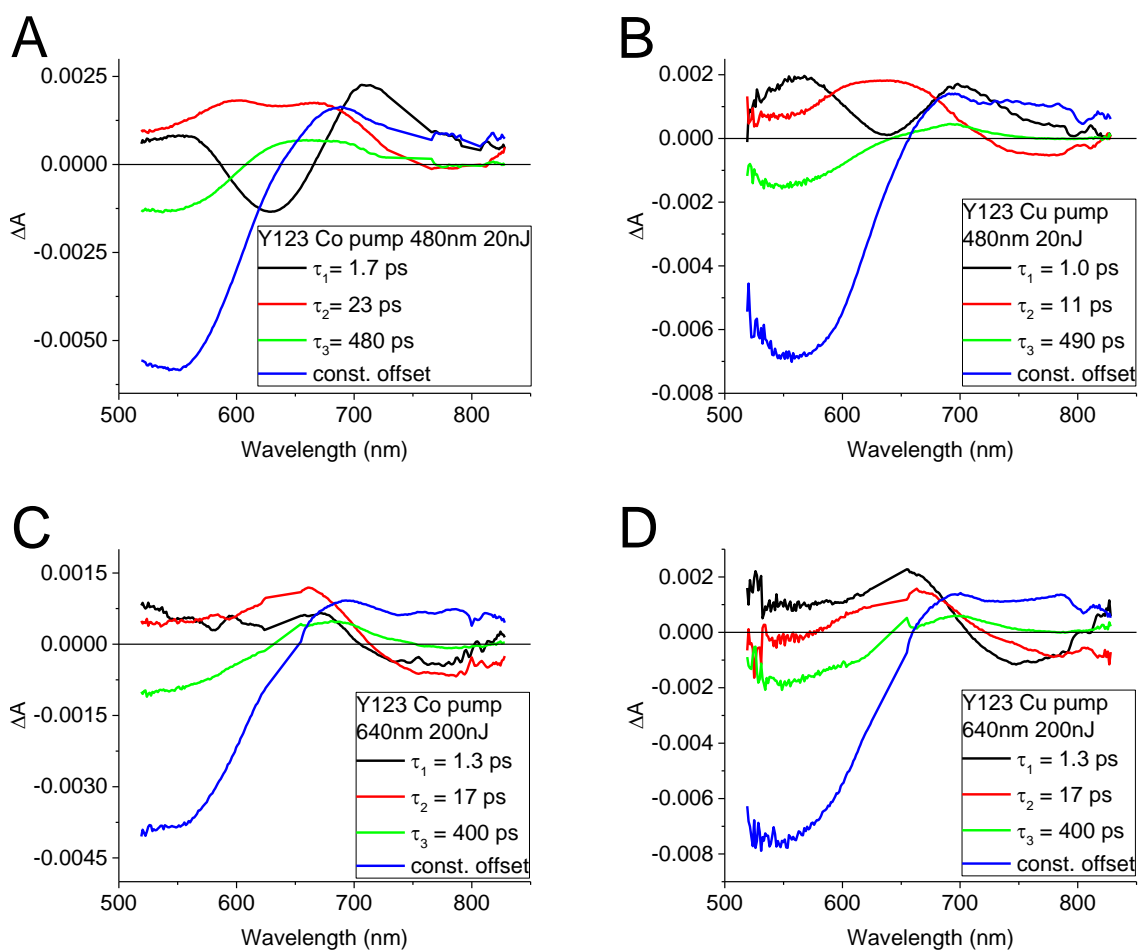


Figure S5. Pre-exponential factor spectra associated to the indicated time constants for a model with a three-exponential function with an offset for DSSC with Y123 dye and cobalt- (A,C) and copper- (B,D) based electrolyte, collected for 480 nm (A,B) and 640 nm (C,D). The fitted time constants for three pump wavelengths are compared in Table S1.

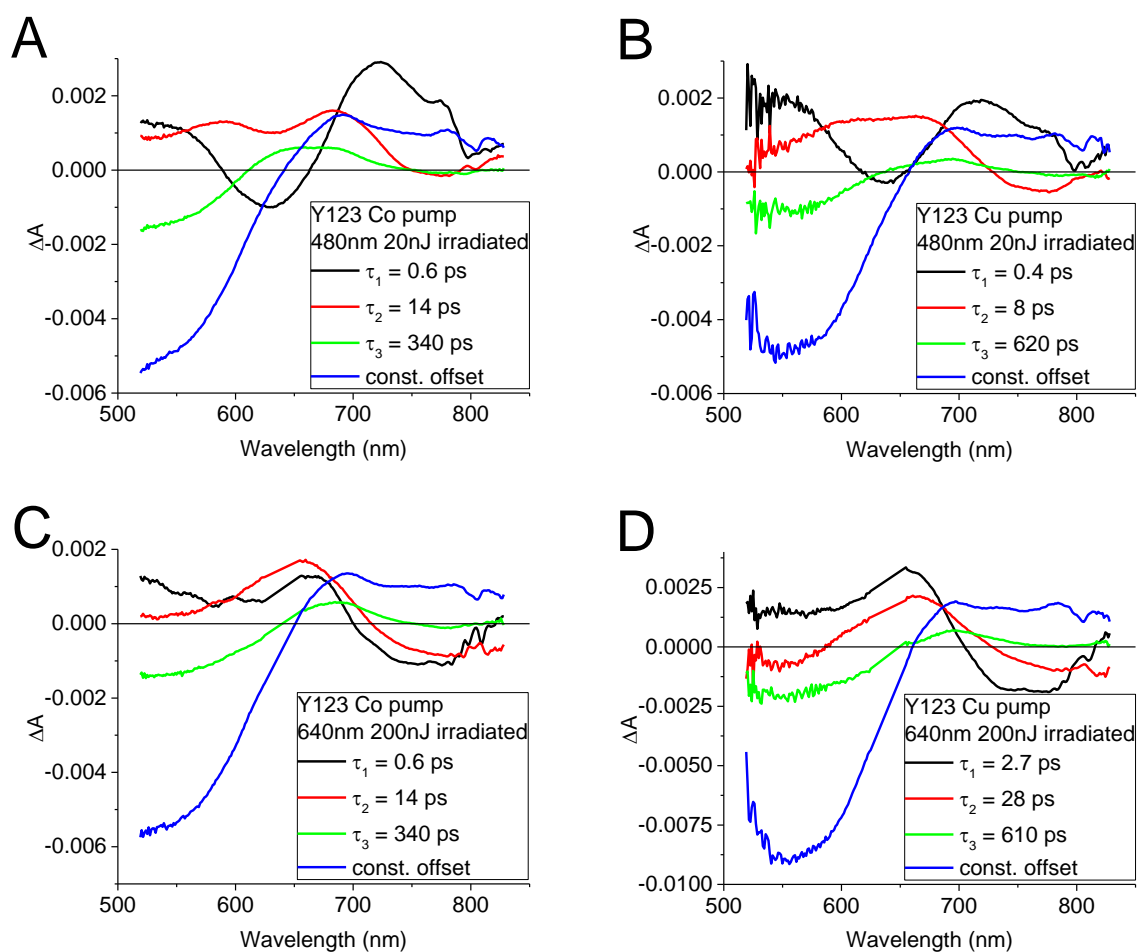


Figure S6. Pre-exponential factor spectra associated to the indicated time constants for a model with a three-exponential function with an offset for irradiated DSSC with Y123 dye and cobalt- (A,C) and copper- (B,D) based electrolyte, collected for 480 nm (A,B) and 640 nm (C,D).

Table S2. Time constants of the poly-exponential functions fitted to the transient absorption kinetics measured at 4780nm wavelength (Figure 3)

Pump pulse energy	Injection fast component	Injection slow component	Contribution of the slower component to the final signal	Recombination component
500 nJ	350 ± 10 fs	93 ± 1 ps	25%	820 ± 10 fs
100 nJ	350 ± 10 fs	85 ± 1 ps	60%	-
50 nJ	350 ± 10 fs	79 ± 1 ps	70%	-

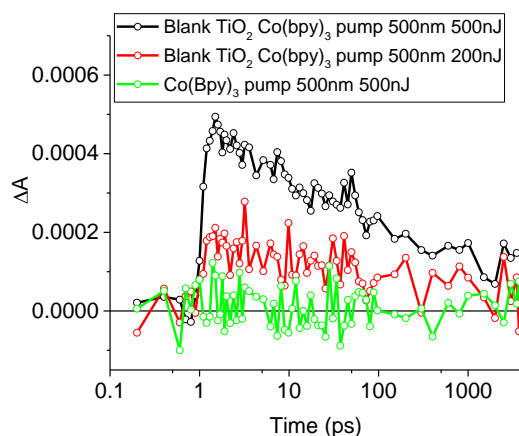


Figure S7. Kinetics of transient absorption at 4780nm collected to exclude the contribution of artifacts from pure TiO_2 and electrolyte to the injection kinetics. The time zero was shifted to 1 ps in order to present the time axis in logarithmic scale.

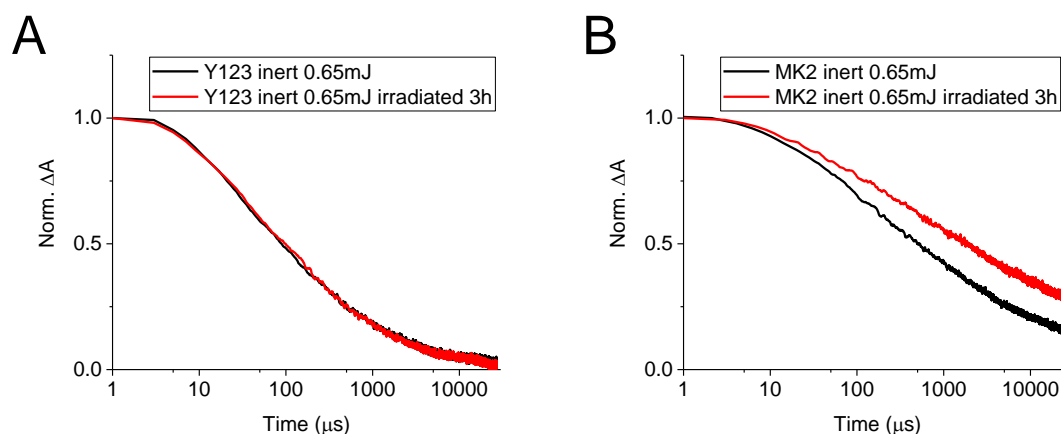


Figure S8. Transient absorption kinetics of the cells containing Y123 (A) and MK2 (B) dyes and inert electrolyte (solution without the addition of redox couple) measured at 700 nm. Transient absorption kinetics in ns-ms timescale were recorded on a nanosecond flash photolysis setup based on a Q-switched Nd:YAG laser as a pump and a 150 W Xe arc lamp as a probe. The pump pulses were set to 532 nm wavelength with 0.65 mJ energy. The probe spectrum was confined using a 10 nm at full width at half maximum (FWHM) band pass interference filter to limit the influence of high intensity probe light on the measured kinetics. The signal was detected by a photomultiplier (R928 Hamamatsu) coupled to a digital oscilloscope (Tektronix TDS 680 C).

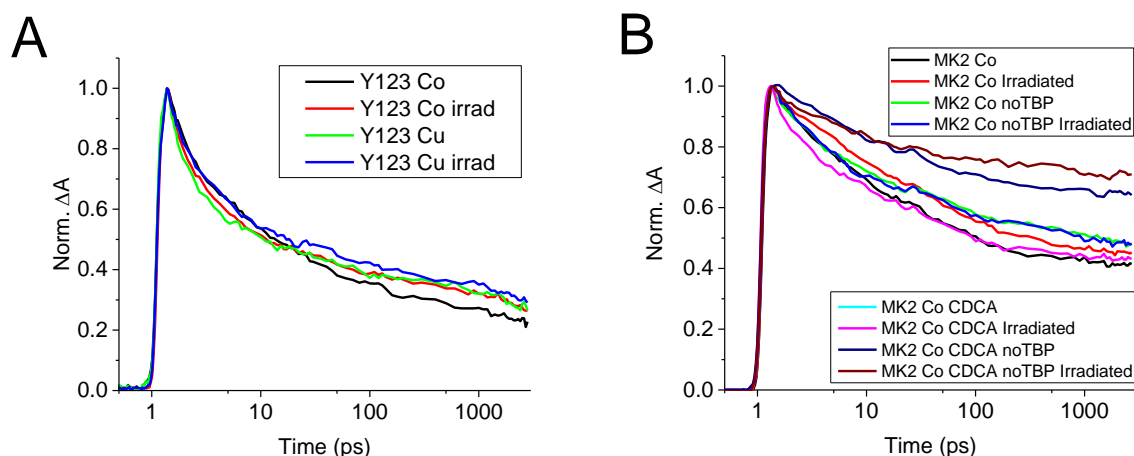


Figure S9. Kinetics of transient absorption of Y123 sensitized cells at 700 nm (A) and MK2 sensitized solar cells at 750nm (B). The time zero was shifted to 1 ps in order to present the time axis in logarithmic scale.

Solar cells with MK2 dye and copper-based electrolyte

Solar cells comprising MK2 dye and $\text{Cu}^{2+/+}(\text{tmby})_2$ exhibited relatively low PCE due to modest J_{SC} and V_{OC} (the latter quite low for copper-based electrolyte). One of the possible reasons for low J_{SC} could be insufficient driving force for dye regeneration. The redox potential of $\text{Cu}^{2+/+}(\text{tmby})_2$ redox couple is equal to -0.87 V vs SHE [2], what gives only 0.08 V over -0.95 V vs SHE for MK2 [3]. Therefore we measured the kinetics of the transient absorption at 700 nm representing the decay of oxidized dye caused by desired reduction reaction involving Cu^+ species (Figure S10A). The time constant of the decay was equal to 7.8 μs . This means that the regeneration process occurs approximately twice slower than 4 μs for MK2 with $\text{Co}^{3+/2+}(\text{bpy})_3$ measured in comparable experimental conditions [4]. However it should be still fast enough taking into account that the kinetics of the competing recombination process (black curve in Figure S10A) is orders of magnitude slower.

The difference in PCE should be rather attributed to low in comparison with Y123 electron lifetime (Figure S10B) explaining both low J_{SC} and V_{OC} values and indicating severe electron recombination from titania to the oxidized form of the redox mediator in the absence of bulky blocking dye moieties in MK2 dye [5].

Table S3. Photovoltaic parameters of the cells comprising MK2 and copper-based electrolyte ^a

	PCE [%]	Voc [V]	FF	Jsc [mA cm ⁻²]	Total APCE
MK2 Cu^{2+/+}(tmby)₂	2.2	0.82	0.76	3.50	0.37
error	0.1	0.01	0.01	0.17	0.02

^a PCE, power conversion efficiency; V_{OC}, open circuit voltage; J_{SC}, short circuit photocurrent density; FF, fill factor. Parameters were averaged from at least three devices. Errors were calculated as the standard deviation of the mean value.

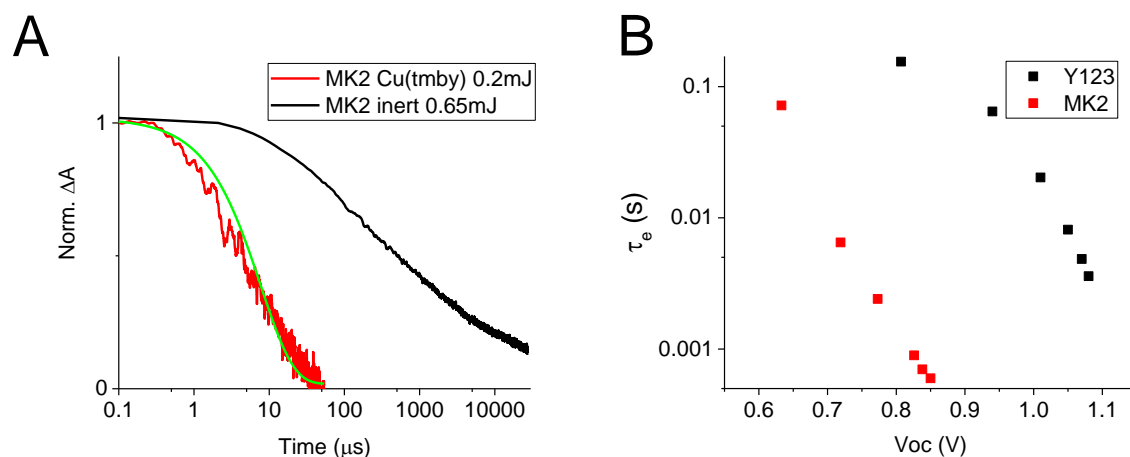


Figure S10. Transient absorption kinetics of the cells containing MK2 dye and copper-based and inert electrolyte (solution without the addition of redox couple) measured at 700 nm. Pump wavelength was set to 532 nm. Time constant of the fitted curve was equal to $7.8 \pm 0.1 \mu\text{s}$ (A), small light perturbation electron lifetime measurements of the cells comprising Y123 and MK2 dyes in combination with Cu^{2+/+}(tmby)₂ redox couple (B). Electron lifetimes were obtained using a Dyenamo Toolbox setup. Measurements were performed in open circuit conditions. A square wave modulated white light illumination was applied and the photovoltage response was acquired and analyzed by a dedicated software using the first order kinetics model.

The effect of light soaking is very pronounced and beneficial for cells comprising MK2 and Cu^{2+/+}(tmby)₂ (Table S4: 25% rise of photocurrent density, beneficial FF change and finally over 30% PCE enhancement).

Table S4. The ratios of photovoltaic parameters measured after and before 30 min continuous irradiation of the cells comprising MK2 and copper-based electrolyte

	PCE ratio	Voc ratio	FF ratio	Jsc ratio
MK2 Cu^{2+/+}(tmby)₂	1.31	1.00	1.06	1.25

Taking into account the magnitude of this light soaking effect and severe titania-electrolyte recombination as the bottleneck in hereby discussed system, it seems reasonable to

suspect that the boost of the photovoltaic performance could be attributed (except the factors discussed in the main part of this work) to the slowdown of the titania-electrolyte recombination dynamics. This could be related with the advantageous modifications in coordination spheres of the Cu²⁺ complexes with participation of the TBP [6–9] associated with the alterations in Li⁺ and H⁺ and the Lewis base equilibrium on the titania/dye/electrolyte interface mentioned in the main part of the work. However, despite being tempting, elucidation of this phenomena exceeds the scope of this work.

References

1. Cao, Y.; Saygili, Y.; Ummadisingu, A.; Teuscher, J.; Luo, J.; Pellet, N.; Giordano, F.; Zakeeruddin, S.M.; Moser, J.-E.; Freitag, M.; et al. 11% efficiency solid-state dye-sensitized solar cells with copper(II/I) hole transport materials. *Nat. Commun.* **2017**, *8*, 15390.
2. Saygili, Y.; Söderberg, M.; Pellet, N.; Giordano, F.; Cao, Y.; Munoz-García, A.B.; Zakeeruddin, S.M.; Vlachopoulos, N.; Pavone, M.; Boschloo, G.; et al. Copper Bipyridyl Redox Mediators for Dye-Sensitized Solar Cells with High Photovoltage. *J. Am. Chem. Soc.* **2016**, *138*, 15087–15096.
3. Kakiage, K.; Aoyama, Y.; Yano, T.; Otsuka, T.; Kyomen, T.; Unno, M.; Hanaya, M. An achievement of over 12 percent efficiency in an organic dye-sensitized solar cell. *Chem. Commun.* **2014**, *50*, 6379–6381.
4. Sobuś, J.; Gierczyk, B.; Burdziński, G.; Jancelewicz, M.; Polanski, E.; Hagfeldt, A.; Ziótek, M. Factors Affecting the Performance of Champion Silyl-Anchored Carbazole Dye Revealed in the Femtosecond to Second Studies of Complete ADEKA-1 Sensitized Solar Cells. *Chem. - A Eur. J.* **2016**, *22*, 15807–15818.
5. Glinka, A.; Gierszewski, M.; Gierczyk, B.; Burdziński, G.; Michaels, H.; Freitag, M.; Ziótek, M. Interface Modification and Exceptionally Fast Regeneration in Copper Mediated Solar Cells Sensitized with Indoline Dyes. *J. Phys. Chem. C* **2020**, *124*, 2895–2906.
6. Saygili, Y.; Stojanovic, M.; Michaels, H.; Tjepelt, J.; Teuscher, J.; Massaro, A.; Pavone, M.; Giordano, F.; Zakeeruddin, S.M.; Boschloo, G.; et al. Effect of Coordination Sphere Geometry of Copper Redox Mediators on Regeneration and Recombination Behavior in Dye-Sensitized Solar Cell Applications. *ACS Appl. Energy Mater* **2018**, *1*, 4950–4962.
7. Ho, W.L.; Katz, M.J.; Deria, P.; Ili, G.E.C.; Pellin, M.J.; Farha, O.K.; Hupp, J.T. One Electron Changes Everything. A Multispecies Copper Redox Shuttle for Dye-Sensitized Solar Cells. **2016**.
8. Wang, Y.; Hamann, T.W. Improved Performance Induced by in-situ Ligand Exchange Reactions of Copper Bipyridyl Redox Couples in Dye-Sensitized Solar Cells. **2018**, 1–14.
9. Furer, S.O.; Milhuisen, R.A.; Kashif, M.K.; Raga, S.R.; Acharya, S.S.; Forsyth, C.; Liu, M.; Frazer, L.; Duffy, N.W.; Ohlin, C.A.; et al. The Performance-Determining Role of Lewis Bases in Dye-Sensitized Solar Cells Employing Copper-Bisphenanthroline Redox Mediators. **2020**, *2002067*, 1–13.

Appendix

Appendix

Other published articles:

- 1 **Insights into the limitations of solar cells sensitized with ruthenium dyes revealed in time-resolved spectroscopy studies**

Gierszewski, M.; Grądzka, I.; **Glinka, A.**; Ziótek, M.

Phys. Chem. Chem. Phys. **2017**, *19*, 20463-20473

- 2 **Co-sensitization effects of indoline and carbazole dyes in solar cells and their neutral-anion equilibrium in solution**

Gierszewski, M.; **Glinka, A.**; Ziótek, M.

Under preparation.

List of conference contributions:

- 1 **International Conference on Hybrid and Organic Photovoltaics 2017**, 21-24.05 2017, Lausanne, Switzerland. Oral contribution entitled: **Effects of postassembly molecular and atomic passivation of sensitized titania surface on dynamics of electron transfer measured from femtoseconds to seconds**

- 2 **Polish Photoscience Seminar 2018**, 11-14.06.2018, Krutyń, Poland. Oral contribution entitled: **Factors affecting ultrafast electron transfer processes in solar cells sensitized with top efficient carbazole dyes**

- 3 **Polish Photoscience Seminar 2019**, 16-19.06.2019, Zagnańsk, Poland. Oral contribution entitled: **Effects of Interface Modifications on Charge Transfer and Separation in Copper Mediated Solar Cells Sensitized with Exceptionally Fast Regenerated Indoline Dyes**

- 4 **Dyename DSSC conference**, 14-15.10 2019 Uppsala, Sweden. Poster entitled: **Effects of Interface Modifications on Charge Transfer and**

Separation in Copper Mediated Solar Cells Sensitized with Exceptionally Fast Regenerated Indoline Dyes

5

International Conference on Hybrid and Organic Photovoltaics 2020, 26-29.05 2017, online conference. Poster entitled: Charge Transfer and Separation on Modified Interfaces of Copper Mediated Solar Cells Sensitized with Indoline and Triphenylamine Dyes

mgr inż. Adam Glinka

Zakład Elektroniki Kwantowej

Wydział Fizyki

Uniwersytet im. Adama Mickiewicza w Poznaniu

Oświadczenie

Oświadczam, że jako autor niniejszej rozprawy doktorskiej opartej o cykl opublikowanych artykułów naukowych, jestem współautorem wszystkich publikacji wchodzących w jej skład:

- 1 Effects of Post-Assembly Molecular and Atomic Passivation of Sensitized Titania Surface: Dynamics of Electron Transfer Measured from Femtoseconds to Seconds.**
Gierszewski, M.; **Glinka, A.**; Gradzka, I.; Jancelewicz, M.; Ziółek, M.
ACS Appl. Mater. Interfaces **2017**, *9*, 17102–17114.
- 2 Effects of Aqueous Electrolyte, Active Layer Thickness and Bias Irradiation on Charge Transfer Rates in Solar Cells Sensitized with Top Efficient Carbazole Dyes.**
Glinka, A.; Gierszewski, M.; Ziółek, M.
J. Phys. Chem. C **2018**, *122*, 8147–8158.
- 3 Testing New Concepts in Solar Cells Sensitized with Indoline Dyes—Alkoxysilyl Anchoring Group, Molecular Capping, and Cobalt-Based Electrolyte.**
Gierszewski, M.; **Glinka, A.**; Gradzka, I.; Gierczyk, B.; Ziółek, M.
J. Phys. Chem. C **2018**, *122*, 25764–25775.
- 4 Interface Modification and Exceptionally Fast Regeneration in Copper Mediated Solar Cells Sensitized with Indoline Dyes.**
Glinka, A.; Gierszewski, M.; Gierczyk, B.; Burdziński, G.; Michaels, H.; Freitag, M.; Ziółek, M.
J. Phys. Chem. C **2020**, *124*, 2895–2906.
- 5 Impact of Improvements in Mesoporous Titania Layers on Ultrafast Electron Transfer Dynamics in Perovskite and Dye-Sensitized Solar Cells.**
Pydzińska-Białek, K.*; **Glinka, A.***; Drushliak, V.; Nowaczyk, G.; Florczak, P.; Ziółek, M.
Phys. Chem. Chem. Phys. **2020**, *22*, 21947–21960.

* autorzy przyczynili się w równym stopniu

6 **Complexity of Electron Injection Dynamics and Light Soaking Effects in Efficient Dyes for Modern DSSC**

Glinka, A.; Kubicki, J.; Ziółek, M.

Energies, **2021**, 14, 407.

Poprzez moje uczestnictwo w pracach nad artykułem nr 5, rozumie się wkład w jej część dotyczącą ogniw DSSC.

W ramach prac eksperymentalnych związanych z przygotowaniem wszystkich artykułów z cyklu, byłem odpowiedzialny za przygotowanie ogniw DSSC zgodnie z procedurami opisanymi w rozprawie i artykułach, przy czym w pracach 1 i 3 dzieliłem te obowiązki z Dr inż. Iwoną Grądzką-Kurzaj.

Również w ramach udziału we wszystkich artykułach, wykonywałem samodzielnie bądź asystowałem w pomiarach charakterystyk prądowo-napięciowych, absorpcji stacjonarnej oraz absorpcji przejściowej w zakresie widzialnym i bliskiej podczerwieni z rozdzielczością femtosekundową.

Ponadto w związku z przygotowaniem artykułów nr 1-4 wykonywałem lub brałem udział w pomiarach widm IPCE oraz z wykorzystaniem spektroskopii impedancyjnej.

Dodatkowo, w artykule nr 4 wykonałem pomiary absorpcyjne w zakresie podczerwieni, pomiary czasów życia elektronów w paśmie przewodnictwa tlenku tytanu, pomiary foto-indukowanej absorpcji oraz pomiary elektrochemiczne. Brałem również udział w pomiarach absorpcji przejściowej z rozdzielczością nanosekundową.

Byłem również odpowiedzialny za wykonanie pomiarów absorpcji przejściowej w zakresie średniej podczerwieni z rozdzielczością femtosekundową w ramach prac związanych z artykułem nr 6.

Asystowałem również przy wykonaniu zdjęć z wykorzystaniem skaningowego mikroskopu elektronowego zamieszczonych w artykule nr 5.

We wszystkich artykułach cyklu brałem również udział w pracach na etapie obróbki i analizy danych pomiarowych oraz dyskusji wyników. W szczególności przeanalizowałem wyniki i

sformułowałem wnioski w artykułach nr 2,4 i 6. Ponadto w pracach nr 4-6 miałem szczególny wkład w tworzenie koncepcji badań oraz zaplanowanie wykonanych eksperymentów.

Brałem również udział w edycji lub pisaniu fragmentów wszystkich manuskryptów a teksty artykułów 2,4 i 6 napisałem w większości samodzielnie.

Adam Głuch

Poznań, dnia 12.04.2021

Prof. dr hab. Marcin Ziótek
Wydział Fizyki
Uniwersytet im. Adama Mickiewicza w Poznaniu
ul. Uniwersytetu Poznańskiego 2
61-614 Poznań
e-mail: marziol@amu.edu.pl

Oświadczenie o współautorstwie w publikacjach

W związku z rozprawą doktorską mgr. inż. Adama Glinki, którego jestem promotorem, oświadczam, że jestem współautorem następujących publikacji, które weszły w skład jego rozprawy doktorskiej:

1. M. Gierszewski, A. Glinka, I. Grądzka, M. Jancelewicz, M. Ziótek, *Effects of Post-Assembly Molecular and Atomic Passivation of Sensitized Titania Surface: Dynamics of Electron Transfer Measured from Femtoseconds to Seconds*, ACS Appl. Mater. Interfaces, **9** (2017) 17102-17114.
2. A. Glinka, M. Gierszewski, M. Ziótek, *Effects of Aqueous Electrolyte, Active Layer Thickness and Bias Irradiation on Charge Transfer Rates in Solar Cells Sensitized With Top Efficient Carbazole Dyes*, J. Phys. Chem. C, **122** (2018) 8147-8158.
3. M. Gierszewski, A. Glinka, I. Grądzka, B. Gierczyk, M. Ziótek, *Testing New Concepts in Solar Cells Sensitized with Indoline Dyes—Alkoxy-silyl Anchoring Group, Molecular Capping, and Cobalt-Based Electrolyte*, J. Phys. Chem. C, **122** (2018) 25764-25775.
4. A. Glinka, M. Gierszewski, B. Gierczyk, G. Burdzinski, H. Michaels, M. Freitag, M. Ziótek, *Interface Modification and Exceptionally Fast Regeneration in Copper Mediated Solar Cells Sensitized with Indoline Dyes*, J. Phys. Chem. C, **124** (2020) 2895-2906.
5. K. Pydzińska-Białek, A. Glinka, V. Drushliak, G. Nowaczyk, P. Florczak, M. Ziótek, *Impact of improvements in mesoporous titania layers on ultrafast electron transfer dynamics in perovskite and dye-sensitized solar cells*, Phys. Chem. Chem. Phys., **22** (2020) 21947-21960.
6. A. Glinka, J. Kubicki, M. Ziótek, *Complexity of Electron Injection Dynamics and Light Soaking Effects in Efficient Dyes for Modern DSSC*, Energies, **14** (2021) 407.

Mój udział w powyższych publikacjach polegał na sprawowaniu merytorycznej opieki nad pomiarami, dyskusji wyników, uczestniczeniu w pomiarach z użyciem femtosekundowej absorpcji przejściowej i analizie uzyskanych wyników, a także na pisaniu fragmentów manuskryptów i ich korekcie.

Z poważaniem,



Marcin Ziótek

Poznań, 12.04.2021

dr Mateusz Gierszewski
Zakład Elektroniki Kwantowej
Wydział Fizyki UAM
mgiersz@amu.edu.pl

Oświadczenie

Jako współautor publikacji włączonych do przygotowania rozprawy doktorskiej przez Pana mgr inż. Adama Glinkę, chciałbym określić swój udział w procesie przygotowania wymienionych niżej publikacji naukowych.

Wspólnym mianownikiem mojego udziału była odpowiedzialność za aspekty chemiczne pojawiające się w artykułach, w tym za przygotowanie roztworów stosowanych barwników oraz elektrolitów o odpowiednim składzie i stężeniu (w niektórych przypadkach stosując nowatorskie rozwiązania, które nie zostały dotychczas opisane w literaturze). Ponadto, brałem czynny udział w przygotowaniu artykułów, analizie i interpretacji uzyskanych rezultatów. Szczegółowe informacje o wykonanych zadaniach zostały zawarte przy każdym artykule.

- 1. M. Gierszewski, A. Glinka, I. Grądzka, M. Jancelewicz, M. Ziółek, *Effects of Post-Assembly Molecular and Atomic Passivation of Sensitized Titania Surface: Dynamics of Electron Transfer Measured from Femtoseconds to Seconds*, ACS Appl. Mater. Interfaces, 9 (2017) 17102-17114.**

Przeprowadzenie i interpretacja niektórych pomiarów fotowoltaicznych dla badanych fotoogniw sensybilizowanych barwnikami: MK-2 oraz ADEKA-1 w różnych konfiguracjach, dostosowanie i przeprowadzenie procedury „multi-capping” dla badanych fotoogniw, przeprowadzenie i interpretacja niektórych badań z zakresu elektrochemicznej spektroskopii impedancyjnej (między innymi analiza R_{CT} , C_{μ} , electron lifetime oraz charge collection efficiency), udział w interpretacji części rezultatów pomiarów femtosekundowej absorpcji przejściowej.

2. A. Glinka, M. Gierszewski, M. Ziótek, *Effects of Aqueous Electrolyte, Active Layer Thickness and Bias Irradiation on Charge Transfer Rates in Solar Cells Sensitized With Top Efficient Carbazole Dyes*, J. Phys. Chem. C, 122 (2018) 8147-8158.

Przygotowanie elektrolitów wodnych o określonych wartościach pH. Rejestracja i interpretacja niektórych wyników z zakresu elektrochemicznej spektroskopii impedancyjnej (analiza R_{CT} , C_{μ} , wyznaczenie parametrów „m” oraz „ α ” dla fotoogniw sensybilizowanych barwnikami ADEKA-1 oraz MK-2 wypełnionych elektrolitami na bazie acetonitrylu oraz wody (różne pH). Udział w pomiarach i interpretacji z zakresu femtosekundowej absorpcji przejściowej.

3. M. Gierszewski, A. Glinka, I. Grądzka, B. Gierczyk, M. Ziótek, *Testing New Concepts in Solar Cells Sensitized with Indoline Dyes—Alkoxyethyl Anchoring Group, Molecular Capping, and Cobalt-Based Electrolyte*, J. Phys. Chem. C, 122 (2018) 25764-25775.

Przygotowanie wstępu teoretycznego do artykułu. Interpretacja rezultatów pomiarów fotowoltaicznych dla ogniw sensybilizowanych barwnikami D149 oraz D149Si. Optymalizacja procedury „multi-capping” dla tych układów. Określenie stabilności skonstruowanych fotoogniw w czasie. Interpretacja niektórych rezultatów pomiarów EIS (analiza R_{CT} , C_{μ} , wyznaczenie parametrów „m” oraz „ α ”), udział w pomiarach i interpretacji rezultatów z zakresu femtosekundowej absorpcji przejściowej.

4. A. Glinka, M. Gierszewski, B. Gierczyk, G. Burdzinski, H. Michaels, M. Freitag, M. Ziótek, *Interface Modification and Exceptionally Fast Regeneration in Copper Mediated Solar Cells Sensitized with Indoline Dyes*, J. Phys. Chem. C, 124 (2020) 2895-2906.

Wykonanie obliczeń teoretycznych (DFT oraz TD-DFT) dla barwników D205 oraz D205Si stosowanych przy przygotowaniu badanych w artykule ogniw DSSC, interpretacja i opis uzyskanych rezultatów. Rejestracja widm fluorescencji barwników D205 oraz D205Si. Wyznaczenie wartości molowego współczynnika absorpcji dla D205Si w acetonitrylu.

M. Gierszewski

Wrocław, dnia 09.04.2021

Dr inż. Iwona Grądzka-Kurzaj
adres służbowy: XTPL S.A.,
Stabłowicka 147, 54-066 Wrocław
e-mail: iwona.gradzka-kurzaj@xtpl.com

Oświadczenie o współautorstwie w publikacji

Oświadczam, że jestem współautorem następującej publikacji, która weszła w skład rozprawy doktorskiej mgr. inż. Adama Glinki:

M. Gierszewski, A. Glinka, I. Grądzka, M. Jancelewicz, M. Ziółek, *Effects of Post-Assembly Molecular and Atomic Passivation of Sensitized Titania Surface: Dynamics of Electron Transfer Measured from Femtoseconds to Seconds*, ACS Appl. Mater. Interfaces, **9** (2017) 17102-17114.

Mój udział w powyższej publikacji polegał na przygotowaniu części fotoogniw barwnikowych, dyskusji wyników i korekcie manuskryptu.

podpis



Prof. UAM dr hab. Błażej Gierczyk
Uniwersytet im. Adama Mickiewicza w Poznaniu
Wydział Chemii
Uniwersytetu Poznańskiego 8
61-614 Poznań
e-mail: blazej.gierczyk@amu.edu.pl

Poznań, 10.04.2021

Oświadczenie o współautorstwie w publikacjach

Oświadczam, że jestem współautorem następujących publikacji, które weszły w skład rozprawy doktorskiej mgr. inż. Adama Glinki:

1. M. Gierszewski, A. Glinka, I. Grądzka, B. Gierczyk, M. Ziółek, *Testing New Concepts in Solar Cells Sensitized with Indoline Dyes—Alkoxyethyl Anchoring Group, Molecular Capping, and Cobalt-Based Electrolyte*, J. Phys. Chem. C, **122** (2018) 25764-25775.
2. A. Glinka, M. Gierszewski, B. Gierczyk, G. Burdzinski, H. Michaels, M. Freitag, M. Ziółek, *Interface Modification and Exceptionally Fast Regeneration in Copper Mediated Solar Cells Sensitized with Indoline Dyes*, J. Phys. Chem. C, **124** (2020) 2895-2906.

Mój udział w powyższych publikacjach polegał na syntezie oraz analizie przy pomocy spektroskopii NMR sililowych pochodnych barwników D149 i D205, które były wykorzystane do przygotowania fotoogniw.


Błażej Gierczyk

Poznań, dnia 19 kwietnia 2021 r

Dr Mariusz Jancelewicz
Centrum NanoBioMedyczne UAM
ul. Wszechnicy Piastowskiej 3
61-614 Poznań
e-mail: marjan7@amu.edu.pl

Oświadczenie o współautorstwie w publikacji

Oświadczam, że jestem współautorem następującej publikacji, która weszła w skład rozprawy doktorskiej mgr. inż. Adama Glinki:

M. Gierszewski, A. Glinka, I. Grądzka, M. Jancelewicz, M. Ziólek, *Effects of Post-Assembly Molecular and Atomic Passivation of Sensitized Titania Surface: Dynamics of Electron Transfer Measured from Femtoseconds to Seconds*, ACS Appl. Mater. Interfaces, **9** (2017) 17102-17114.

Mój udział w powyższej publikacji polegał na pokryciu elektrod warstwami Al_2O_3 metodą ALD (Atomic Layer Deposition).

M. Jancelewicz

Poznań, 8 kwietnia 2021

prof. dr hab. Gotard Burdziński
Zakład Elektroniki Kwantowej, Wydział Fizyki UAM
e-mail: gotardb@amu.edu.pl

Oświadczenie o udziale w manuskrypcie mgra Adama Glinki

Mój udział w manuskrypcie pracy

A. Glinka, M. Gierszewski, B. Gierczyk, G. Burdziński, H. Michaels, M. Freitag, M. Ziólek, Interface Modification and Exceptionally Fast Regeneration in Copper Mediated Solar Cells Sensitized with Indoline Dyes, J. Phys. Chem. C, 124 (2020) 2895-2906.

jest skromny i dotyczy (1) przygotowania spektrofotometru do nanosekundowej absorpcji przejściowej w zakresie UV-vis, (2) nadzorowaniu przebiegu eksperymentów na tej aparaturze, jak i (3) zaproponowania drobnych korekt do finalnej formy tekstu manuskryptu.

Gotard Burdziński



Newcastle, 16 March 2021

Hannes Michaels

Uppsala University

hannes.michaels@kemi.uu.se

Co-author statement

I declare that I am the co-author of the publication:

Interface Modification and Exceptionally Fast Regeneration in Copper Mediated Solar Cells Sensitized with Indoline Dyes, Adam Glinka, Mateusz Gierszewski, Błażej Gierczyk, Gotard Burdziński, Hannes Michaels, Marina Freitag, and Marcin Ziółek, *The Journal of Physical Chemistry C* **2020** *124* (5), 2895-2906, DOI: 10.1021/acs.jpcc.9b11778

My contribution consisted of assistance in the fabrication and characterization of D205/D205Si and Y123 dye-sensitized solar cells.

Hannes Michaels

A handwritten signature in black ink, appearing to read 'Hannes Michaels', with a long horizontal flourish extending to the right.

Newcastle, 16 March 2021

Marina Freitag

Newcastle University

marina.freitag@newcastle.ac.uk

Co-author statement

I declare that I am the co-author of the publication:

Interface Modification and Exceptionally Fast Regeneration in Copper Mediated Solar Cells Sensitized with Indoline Dyes, Adam Glinka, Mateusz Gierszewski, Błażej Gierczyk, Gotard Burdziński, Hannes Michaels, Marina Freitag, and Marcin Ziótek, *The Journal of Physical Chemistry C* **2020** 124 (5), 2895-2906, DOI: 10.1021/acs.jpcc.9b11778

My contribution consisted of assistance in the conceptualization and supervision of the project.

A handwritten signature in black ink, appearing to read 'M. Freitag', with a long horizontal flourish extending to the right.

Marina Freitag

Poznań, dnia 12.04.2021r.

Katarzyna Pydzińska-Białek
Wydział Fizyki UAM,
ul. Uniwersytetu Poznańskiego 2,
61-614 Poznań
e-mail:
katarzyna.pydzinska@amu.edu.pl

Oświadczenie o współautorstwie w publikacji

Oświadczam, że jestem współautorem następującej publikacji, która weszła w skład rozprawy doktorskiej mgr. inż. Adama Glinki:

K. Pydzińska-Białek, A. Glinka, V. Drushliak, G. Nowaczyk, P. Florczak, M. Ziółek, *Impact of improvements in mesoporous titania layers on ultrafast electron transfer dynamics in perovskite and dye-sensitized solar cells*, Phys. Chem. Chem. Phys., **22** (2020) 21947-21960.

Mój udział w powyższej publikacji związany był z częścią dotyczącą fotoogniw perowskitowych. Uczestniczyłam w ich przygotowaniu, pomiarach i analizie uzyskanych wyników, a także brałam udział w korekcie manuskryptu.

Katarzyna
Pydzińska-Białek

Poznań, dnia 08.04.2021

Mgr Viktoriia Drushliak
adres służbowy:
Zakład Fizyki Dielektryków p. 160
ul. Uniwersytetu Poznańskiego 2, 61-614 Poznań
e-mail: vikdru@amu.edu.pl

Oświadczenie o współautorstwie w publikacji

Oświadczam, że jestem współautorem następującej publikacji, która weszła w skład rozprawy doktorskiej mgr. inż. Adama Glinki:

K. Pydzińska-Białek, A. Glinka, V. Drushliak, G. Nowaczyk, P. Florczak, M. Ziólek, *Impact of improvements in mesoporous titania layers on ultrafast electron transfer dynamics in perovskite and dye-sensitized solar cells*, Phys. Chem. Chem. Phys., **22** (2020) 21947-21960.

Mój udział w powyższej publikacji związany był z częścią dotyczącą fotoogniw perowskitowych. Uczestniczyłam w ich przygotowaniu, pomiarach i analizie uzyskanych wyników, a także brałam udział w edycji manuskryptu.

podpis

Viktoriia Drushliak

Poznań, dnia 14 kwietnia 2021 r.

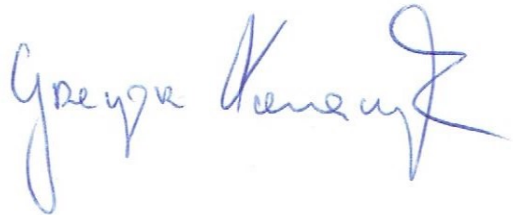
Dr Grzegorz Nowaczyk
Centrum NanoBioMedyczne UAM
ul. Wszechnicy Piastowskiej 3
61-614 Poznań
e-mail: nowag@amu.edu.pl

Oświadczenie o współautorstwie w publikacji

Oświadczam, że jestem współautorem następującej publikacji, która weszła w skład rozprawy doktorskiej mgr. inż. Adama Glinki:

K. Pydzińska-Białek, A. Glinka, V. Drushliak, G. Nowaczyk, P. Florczak, M. Ziólek, *Impact of improvements in mesoporous titania layers on ultrafast electron transfer dynamics in perovskite and dye-sensitized solar cells*, Phys. Chem. Chem. Phys., **22** (2020) 21947-21960.

Mój udział w powyższej publikacji polegał na wykonaniu zdjęć przekrojów poprzecznych elektrod do fotoogniw za pomocą techniki SEM (Scanning Electron Microscopy) oraz pomocy przy nakładaniu złotych elektrod na fotoogniwa.



Poznań, dnia 16.04.2021

Dr Patryk Florczak
Centrum NanoBioMedyczne UAM
ul. Wszechnicy Piastowskiej 3
61-614 Poznań
e-mail: patryk.florczak@amu.edu.pl

Oświadczenie o współautorstwie publikacji

Oświadczam, że jestem współautorem następującej publikacji, która weszła w skład rozprawy doktorskiej mgr. inż. Adama Glinki:

K. Pydzińska-Białek, A. Glinka, V. Drushliak, G. Nowaczyk, P. Florczak, M. Ziółek, *Impact of improvements in mesoporous titania layers on ultrafast electron transfer dynamics in perovskite and dye-sensitized solar cells*, Phys. Chem. Chem. Phys., **22** (2020) 21947-21960.

Mój udział w powyższej publikacji polegał na pomocy przy przygotowaniu fotoogniw perowskitowych w atmosferze beztlenowej w komorze rękawicowej.

podpis

Patryk Florczak

dr hab. Jacek Kubicki, profesor UAM
Wydział Fizyki
Uniwersytet im. Adama Mickiewicza w Poznaniu
ul. Uniwersytetu Poznańskiego 2
61-614 Poznań
e-mail: jacek.kubicki@amu.edu.pl

Poznań, dnia 08.04.2021

Oświadczenie o współautorstwie w publikacji

Oświadczam, że jestem współautorem następującej publikacji, która weszła w skład rozprawy doktorskiej mgr. inż. Adama Glinki:

A. Glinka, J. Kubicki, M. Ziółek, *Complexity of Electron Injection Dynamics and Light Soaking Effects in Efficient Dyes for Modern DSSC*, *Energies*, **14** (2021) 407.

Mój udział w powyższej publikacji polegał na nadzorowaniu pomiarów przy użyciu femtosekundowej absorpcji przejściowej w bliskiej podczerwieni (mid-IR), dyskusji wyników i korekcie manuskryptu.

Jacek Kubicki

Oświadczenie

Niniejszym oświadczam, że przedkładaną rozprawę doktorską pt.:

Wyznaczanie dynamiki i wydajności transferu ładunku w fotoogniwach sensybilizowanych barwnikami karbazolowymi, indolinowymi i trifenyloaminowymi

(ang. *Determination of charge transfer dynamics and efficiency in solar cells sensitized with carbazole indoline and triphenylamine dyes*),

napisałem samodzielnie. Oznacza to, że przy pisaniu pracy, poza niezbędnymi konsultacjami, nie korzystałem z pomocy innych osób, a w szczególności nie zlecałem opracowania rozprawy lub jej istotnych części innym osobom, ani nie odpisywałem tej rozprawy lub jej istotnych części od innych osób. Równocześnie oświadczam, że jestem świadomy, że w sytuacji, gdyby powyższe oświadczenie okazało się nieprawdziwe, decyzja o nadaniu mi stopnia naukowego doktora zostanie cofnięta.

mgr inż. Adam Glinka

